SCHOLARLY PUBLICATIONS

A CURRENT AWARENESS BULLETIN
OF RESEARCH OUTPUT

@DTU

(48th Edition)

DECEMBER 2016

BY: CENTRAL LIBRARY

DELHI TECHNOLOGICAL UNIVERSITY
(FORMERLY *DELHI COLLEGE OF ENGINEERING)*
GOVT. OF N.C.T. OF DELHI
SHAHBAD DAULATPUR, MAIN BAWANA ROAD
DELHI 110042

PREFACE

This is the **Forty eight** Issue of Current Awareness Bulletin started by Delhi Technological University, Central Library. The aim of the bulletin is to compile, preserve and disseminate information published by the faculty, students and alumni for mutual benefits. The bulletin also aims to propagate the intellectual contribution of Delhi Technological University (DTU) as a whole to the academia.

The bulletin contains information resources available in the internet in the form of articles, reports, presentations published in international journals, websites, etc. by the faculty and students of DTU. The publications of faculty and student which are not covered in this bulletin may be because of the reason that the full text either was not accessible or could not be searched by the search engine used by the library for this purpose.

The learned faculty and students are requested to provide their uncovered publications to the library either through email or in CD, etc to make the bulletin more comprehensive.

This issue contains the information published during **December 2016**. The arrangement of the contents is alphabetical. The full text of the article which is either subscribed by the university or available in the web is provided in this bulletin.

Central Library

CONTENTS

1. A Mean Point Based Convex Hull Computation Algorithm, 3.Digvijay Singh, Hemang Sarkar and ***3.L.N. Das***, Applied Mathematics, DTU

2. A Novel Approach for Text Extraction from Natural Scene Images, ***3.N. Jayanthi***, ***3.Abhilash Gaur*** and ***3.S. Indu***, ECE, DTU

3. A Novel red emitting Eu3+ doped Calcium Aluminozincate Phosphor for Applications in w-LEDs, ***6.Sumandeep Kaur, 3.M. Jayasimhadri*** and ***3.A.S.Rao***, Applied Physics, DTU

4. A Priority Based WSN Clustering of Multiple Sink (Scenario using Artificial Bee Colony Algorithm, ***3.Ravi Teja*** and ***3.Dr.S.Indu,*** ECE, DTU

5. A Review on Study on Effect of Various Admixtures on Geotechnical Properties of Expansive Soils, ***3.Raju Sarkar, 6.Ankur Mudgal, 6.Sandeep Bhaskar, 6.Varun Gupta*** and ***6.Ritesh Kurar***, Civil Engineering, DTU

6. A study of perceived quality of life of people in Gujarat, Rajesh Handa and ***3.Dr. G.C. Maheshwari***, Management, DTU

7. Analysis of Calorimetric Measurement Bismuth and Tin System, Kapil, C.K Behra and ***7.Ravinder Kumar***, DTU

8. Application of Fuzzy Logic and Fuzzy Systems in Machining: A Literature Review, ***6.S. Singhal***, ***3.Ranganth M.S***., ***6.R. Batra*** and ***6.S. Nanda***, Mechanical, Production & Industrial and Automobile Engineering, DTU

9. Autonomous payload drop system using mini Unmanned Aerial Vehicles, ***8.Rohan Pratap Singh*** and ***8.Akash Garg***, ECE, DTU

10. Building Concordant Ontologies for Drug Discovery, Hande Küçük-McGinty, ***3.Saurabh Mehta***, Yu Lin, Nooshin Nabizadeh, Vasileios Stathias, Dusica Vidovic, Amar Koleti, Christopher Mader, Jianbin Duan, Ubbo Visser and Stephan Schürer, Applied Chemistry, DTU

11. Cyclone Frame Prediction by Gaussian Mixture Modeling of the Three Penultimate Time-Lapse Frames, ***3.Seba Susan***, ***3.Achin Saxena***, ***3.Anuvart Budhwar***, ***3.Akshay Takhi*** and ***3.Abhishek Varshney***, CSE, DTU

12. Design and Analysis of DC-DC Boost Converter, ***3.JN Rai***, ***3.Nikhil Gupta*** and ***3.Prashant Bansal***, Electrical Engineering, DTU

13. Design of Single mode Bismuth oxide fiber for generation of Slow light, ***3.Utkarsh Nigam***, Than Singh Saini and ***3.Ajeet Kumar***, Applied Physics, DTU

14. DFAL Based Flexible Multi-Modulo Prescaler, ***3.Nitish***, ***3.Neeta Pandey***, Kirti Gupta and ***3.Manu Kumar Saini***, ECE, DTU

15. Dispersion Engineered Photonic Crystal Fiber Structure for Nonlinear Applications, ***6.AGN Chaitanya***, Than Singh Saini and ***3.Ajeet Kumar***, Applied Physics, DTU

16. Dynamic Analysis and Control of a Full Car Vehicle Model through Bondgraphs, ***6.Ashish Gupta*** and ***3.Vikas Rastogi***, Mechanical Engineering, DTU

17. Ever Increasing Cost of Knowledge: Challenges for Libraries for Electronic Resources A Case Study, Narender Kumar and ***4.1Dr. (Mrs.)Lalita***, DTU

18. Experimental and Theoretical Analysis of Connector Offset Optical Fiber Refractive Index Sensor, Vanita Bhardwaj, ***3.Kamal Kishor*** and Vinod Kumar Singh, Applied Physics, DTU

19. Failure analysis of a first stage IN738 gas turbine blade tip cracking in a thermal power plant, ***3.Sushila Rani***, ***3.Atul K. Agrawal*** and ***3.Vikas Rastogi***, Mechanical, Production, Industrial and Automobile Engineering, DTU

20. Forward scattering by the cylindrical dielectric nanoparticle, ***3.Reena***, ***3.Yogita Kalra*** and ***3.R.K. Sinha***, Applied Physics, DTU

21. Gate Drain Underlapped-PNIN-GAA-TFET for Comprehensively Upgraded Analog/RF Performance, ***3.Jaya Madan*** and ***3.Rishu Chaujar***, Engineering Physics, DTU

22. Green synthesis of multi metal- citrate complexes and their characterization, ***3.Usha Raju***, ***3.Sudhir G. Warkar*** and ***3.Anil Kumar***, Applied Chemistry, DTU

23. Intrinsic half metallicity in lithium terminated zigzag grapheme nanoribbons, ***3.Neha Tyagi***, Neeraj K. Jaiswal, Varun Sharma, Kamal K. Jha and Pankaj Srivastava, Applied Physics, DTU

24. Model of quality of life in Gujarat: A subjective approach, Rajesh Handa, ***3.Dr. G.C. Maheshwari***, Management, DTU

25. Modified Tang's Current Comparator and Its Application to Full Flash and Two-Step Flash Current Mode ADCs, Veepsa Bhatia and ***3.Neeta Pandey***, ECE, DTU

26. Molecular Chaperones and Ubiquitin Proteasome System in Tumor Biogenesis: An Overview, ***3.Saurabh Kumar Jha***, ***3.Niraj Kumar Jha***, ***3.Pravir Kumar*** and ***3.Rashmi K Ambasta***, Biotechnology, DTU

27. Molecular modeling and lead design of substituted zanamivir derivatives as potent anti-influenza drugs, ***3.Dhwani Dholakia***, Sukriti Goyal, Salma Jamal, Aditi Singh, ***3.Asmita Das*** and Abhinav Grover, Biotechnology, DTU

28. Novel Method for Ancient Indian Coins Classification, ***3.N. Jayanthi***, ***3.Prateek Tripathi***, ***3.Snigdhaa Hasija*** and ***3.S.Indu***, ECE, DTU

29. Analysis of Calorimetric Measurement Bismuth and Tin System, Kapil, C.K Behra and ***7.Ravinder Kumar***, Metallurgical Engineering, DTU

30. Optical logic operation using universal NOR gate***, 3.Preeti Rani***, ***3.Yogita Kalra*** and ***3.R. K. Sinha*** Applied Physics, DTU

31. Policy Issues On Cloud Computing In India- A Comparative Landscape, Dr. Rajat Agarwal, Vatsal Chanana and ***8.Rishabh Chanana***, DTU

32. Recommender system with grey wolf optimizer and FCM***, 3.Rahul Katarya*** and ***3.Om Prakash Verma***, CSE, DTU

33. Robust Pedestrian Tracking using improved Tracking-Learning-Detection algorithm, ***3.Ritika Verma*** and ***3.Indu Sreedevi,*** DTU

34. SBS based slow-light generation in rectangular lattice graded-index photonic crystal fiber: Design and analysis, ***3.Sandeep Yadav***, ***3.Ajeet Kumar***, Than Singh Saini and Ravindra Kumar Sinha, DTU

35. Search for Eco-friendly Alternatives Refrigerants in Vapor Compression Refrigeration Systems for Reducing Global Warming and Ozone Depletion, ***3.R. S. Mishra***, Mechanical Engineering, DTU

36. Security Framework for Portable NFC Mobile Based Health Record System, ***3.Divyashikha Sethia***, ***3.Daya Gupta*** and Huzur Saran, CSE, DTU

37. Slow-Light Generation Based on Stimulated Brillouin Scattering in Single-Mode Er-Doped Tellurite Photonic Crystal Fibers ***3.Shubham Sharma***, ***3.Varsha Jain***, ***3.Ajeet Kumar*** and Than Singh Saini, Applied Physics, DTU

38. Study of Natural Gas Engine using non-premixed combustion model, ***3.Raj Kumar Singh***, ***3.Aditya Kumar Singh*** and ***3.Aditya Anand***, Mechanical Engineering, DTU

39. Supercontinuum Generation in Ge11.5As24Se64.5 based Chalcogenide Few-Mode Fiber, ***3.Priti1, 3.Ajeet Kumar*** and Than Singh Saini, Applied Physics, DTU

40. The Smart Number Plate, ***8.Vanshaj Sikri***, ECE, DTU

41. Theoretical Modelling of Kelvin Helmholtz Instability Driven by an Ion Beam in a Negative Ion Plasma, ***3.Kavita Rani*** and Suresh C. Sharma, Applied Physics, DTU

42. A Study Of Sense Of Well-Being And Perceived Quality Of Life Of People In Central Gujarat, Rajesh Handa and ***3.Dr. G.C.Maheshwari***, Management, DTU

43. A STUDY OF SENSE OF WELL-BEING AND PERCEIVED QUALITY OF LIFE OF PEOPLE IN NORTH GUJARAT & CENTRAL GUJARAT, Rajesh Handa1, ***3.Dr. G.C.Maheshwari***, Management, DTU

44. Ultra broadband mid-IR supercontinuum generation in Ge11.5As24Se64.5 based chalcogenide graded-index photonic crystal fiber: design and analysis, ***3.A. G. N. Chaitanya, 3.Than Singh Saini, 3.Ajeet Kumar*** and Ravindra Kumar Sinha, Applied Physics, DTU

45. Understanding Various Technologies with Perspective of Energy and Environmental Audit: Review, ***6.Harwinder Singh, 6.Aftab Anjum, 6.Mohit Gupta, 6.Aadish Jain*** and ***6.Amrik Singh***, Mechanical Engineering, DTU

1. *Chancellor*

2. *Pro Vice Chancellor* ***2.1.*** *Ex Pro Vice Chancellor*

3. *Faculty* ***3.1.*** *Ex Faculty*

4. *Teaching-cum-Research Fellow* ***4.1.****Asst. Librarian*

5. *Alumni*

6. *Research Scholar* ***6.1.*** *Ex Research Scholar*

7. *PG Scholar* ***7.1.*** *Ex PG Scholar*

8. *Undergraduate Student* ***8.1.*** *Ex Undergraduate Student*

American Journal of Engineering Research (AJER) 2016
American Journal of Engineering Research (AJER)
e-ISSN: 2320-0847 p-ISSN : 2320-0936
Volume-5, Issue-11, pp-70-75
www.ajer.org
Research Paper Open Access

A Mean Point Based Convex Hull Computation Algorithm

Digvijay Singh[1], Hemang Sarkar[2], L N Das[3]
[1,2](Department of Applied Mathematics, Delhi Technological University, India)
[3](Associate Professor, Department of Applied Mathematics, Delhi Technological University, India)

ABSTRACT: *The optimal solution of a Linear Programming problem (LPP) is a basic feasible solution and all basic feasible solutions are extreme or boundary points of a convex region formed by the constraint functions of the LPP. In fact, the feasible solution space is not always a convex set so the verification of extreme points for optimality is quite difficult. In order to cover the non-convex feasible points within a convex set, a convex hull is imagined so that the extreme or boundary points may be checked for evaluation of the optimum solution in the decision-making process. In this article a computer assisted convex hull computation algorithm using the Mean Point and Python code verified results of the designed algorithm are discussed.*

Keywords: *Boundary points, Convex set, Convex hull, Extreme points, Mean Point, LPP*

I. INTRODUCTION

In Euclidean space, a convex set is the region such that, for every pair of points within the region, every point on the straight-line segment that joins the pair of points is also within the region. The convex hull or convex envelope of a set *X* of points in the Euclidean plane or Euclidean space is the smallest convex set that contains *X*. The domains and ranges of the functions for many linear programming problems' constraints are hyper-planes which are convex sets. The solution processes of optimization problems are computed by improving the finite set of feasible points by means of a suitable iterative algorithm. The set of feasible points in many situations are not defined in the convex set forms. Therefore, a minimum convex set containing the feasible solution set in the form of a convex hull is computed first to decide the possible convex polyhedron that contain the basic feasible solution (BFS) as its vertices.

In computational geometry, several algorithms are proposed for the computation of the convex hull of a finite set of points with various computational complexities. The convex hull computation is the framing of a convex shape that can represent the required convex feasible region for the constrained optimization problem. The time complexity of the corresponding algorithm is usually estimated in terms of n - the number of input points of the finite set and/or h - the number of points on the boundary of the convex-hull. If the time complexity depends on h, then the algorithm is output sensitive. There are several algorithms available in the convex- hull computation algorithm literature.

The notable algorithms are Gift wrapping planar algorithm of Jarvis [1], Graham Scan algorithm [2], Chan's algorithm [3], The ultimate planar convex hull algorithm of Kirkpatrick & Seidel [4] and Akl-Toussaint heuristic algorithm [5]. In section II, we present the pseudocode of the algorithm. Then in section III, we give a step by step description of the algorithm. Section IV presents the analysis of the computational complexity of the algorithm followed by section V where the outputs of the Python code for the algorithm are presented.

II. PSEUDOCODE OF THE PROPOSED ALGORITHM

```
check_counter_clockwise(prev, nxt, curr)
1-  value = (nxt.x - prev.x)*(curr.y - prev.y) - (nxt.y - prev.y)*(curr.x - prev.x)
2-  if value > 0:
```

```
3-      return False
4-  else:
5-      return True
```

convexhull(list A):

1- mean_x = mean x-coordinate in list A
2- mean_y = mean y-coordinate in list A
3- M = [mean_x, mean_y]
4- max_point = point in list A with maximum x coordinate (take the first instance in case of multiple instances)
5- min_point = point in list A with minimum x coordinate
6- Initialise empty lists Q_1 = [ ], Q_2 = [ ], Q_3 = [ ], Q_4 = [ ]
7- for i = 1 to n:
8- If i doesn't correspond to max_point or min_point:
9- d = distance between A[i] and M
10- a = positive angle in degrees that the line joining A[i] with M makes with the line joining M with max_point in the counterclockwise direction
11- Append [A[i].x, A[i].y, d, a] to Q_1, Q_2, Q_3 or Q_4 according to the quadrant of A[i] with respect to M
12- Sort Q_1, Q_2, Q_3 and Q_4 according to distance parameter stored at each index
13- q_1 = length(Q_1), q_2 = length(Q_2), q_3 = length(Q_3) and q_4 = length(Q_4)
14- Initialise circular linked as convex_hull and insert max_point and min_point in it
15- while max(q_1, q_2, q_3, q_4) > 0:
16- Take out the last element from each of Q_1, Q_2, Q_3 and Q_4 (if it exists) and insert it in sorted order with respect to angle parameter in convex_hull
17- prev = convex_hull.head, curr = prev.next, nxt = curr.next
18- while curr is not convex_hull.head:
19- if check_counter_clockwise(prev, nxt, curr) is false:
20- curr = nxt
21- nxt = nxt.next
22- prev.next = curr
23- else:
24- prev = prev.next
25- curr = curr.next
26- nxt = nxt.next
27- Print convex_hull to get the points on the boundary of the convex hull in counterclockwise direction

III. DESCRIPTION OF THE ALGORITHM

(1) The input is a list of n pairs $[x, y]$ which denotes the set of input points on the X-Y plane for which we have to find the convex hull.

(2) Find the mean x- coordinate and the mean y- coordinate. Label this point as M[mean_x, mean_y]. This is the mean point.

(3) Since the two points with the maximum x coordinate and the minimum x coordinate have to be a part of the convex hull, we find them both and store them in max_point and min_point respectively.

(4) Initialise four lists labeled as Q_1, Q_2, Q_3 and Q_4 which denote the four quadrants when we draw imaginary X-Y axes by setting the origin at the point M. The positive direction of this X axis is the extension of the line segment joining M to the point max_point.

(5) The points- max_point and min_point are not put in any of these lists. Put every other input point in exactly one of these four lists by comparing their x coordinates and y coordinates with that of point M.

(6) Each value in these four lists is of the form [x coordinate, y coordinate, distance, angle]. Here distance is

the distance of the point from M. The angle is found as the inverse tangent of the ratio of length of y component (of line joining point to the M) with the x component (of the same line joining point to M) in degrees, and the points are considered from all four quadrants Q_1, Q_2, Q_3 and Q_4. We then add 360º to the values that are negative in order to store all angles as positive values.

(7) Sort the values in the four lists individually according to the distance parameter.

(8) Initialize a circular linked list called convex_hull and insert in it the two points: max_point and min_point. The head of the linked list points to the node corresponding to max_point. The node for max_point points to the node containing min_point which, in turn points to the head. This linked list at the end of the algorithm will have all the vertices of the convex hull in anti-clockwise direction starting at max_point. The nodes in this linked list will also be of the form [x coordinate, y coordinate, distance, angle]. Suppose curr is a node then curr.next gives us the node that comes after curr in the linked list.

(9) Let q_1, q_2, q_3 and q_4 be the number of points in Q_1, Q_2, Q_3 and Q_4 respectively. Repeat the steps (10) to (12) while $max(q_1, q_2, q_3, q_4) > 0$.

(10) Remove the last element from each list (if it exists otherwise pass) and store it in a new list temp_list. The last element is the current element with the maximum distance from M in that list. Whenever we remove an element, we decrease the corresponding variable q_1, q_2, q_3 or q_4.

(11) The number of elements in temp_list will be at most 4. We now insert these points into convex_hull based upon the angle parameter. The convex_hull list must always be in sorted order with respect to angle of the nodes starting at the first node (max_point with angle 0°). We insert a node with angle B between nodes with angles A and C if A< B < C. Note that a node might have to be inserted after the last node and before the head node if its angle is greater than every value in the list.

(12) After the insertion of the new nodes, we test whether the points can be a part of the boundary of the convex hull or not. In convex_hull, we start from the head node (max_point) and take three consecutive nodes at a time. These three points are in the counterclockwise direction since we inserted them in sorted order. Let these points be $prev: (x_1, y_1)$, $curr: (x, y)$ and $nxt: (x_2, y_2)$ in this order. These may be a part of the convex hull if and only if

$$(1): (x_2 - x_1)(y - y_1) - (y_2 - y_1)(x - x_1) \geq 0$$

If this value comes out to be negative, we delete the node curr denoting the point (x, y) and set $prev = (x_1, y_1)$, $curr = (x_2, y_2)$ and $nxt = nxt.next$

Otherwise, $prev = (x_1, y_1)$, $curr = (x_2, y_2)$ and $nxt = nxt.next$

This step is terminated when we go around the list once and reach the head of convex_hull again.

(13) After the while loop in from steps (9) to (12) ends, print the values in convex_hull starting from the head to get the vertices of the convex hull boundary in counter clockwise direction. These points are on the boundary of the convex hull.

IV. DESCRIPTION OF COMPUTATIONAL COMPLEXITY OF ALGORITHM AND INFERENCE

If we consider basic mathematical operations to run in constant time, we can see that the execution time of steps (2) to (6) is $O(n)$. Using a sorting algorithm like the merge sort or the quick sort, step (7) runs in $O(nlogn)$ time. This is so because we can argue that on average, one quadrant as defined above will have $\lfloor \frac{n}{4} \rfloor$ number of points.

The while loop started in step (9) executes as long as $q_1 > 0$ or $q_2 > 0$ or $q_3 > 0$ or $q_4 > 0$. The average number of times the while loop will run is thus $\lfloor \frac{n}{4} \rfloor$.

In each iteration of the while loop, we extract at most one point from each of the four quadrants and insert these points at their appropriate positions into convex_hull. After this, we iterate over this circular linked list considering three consecutive points at a time. Assume that we are at the i^{th} iteration and let the length of the

circular linked list be $L(i)$.

(2): $L(1) = 2$

We insert 1, 2, 3 or 4 points into this linked list in sorted order. Let $a(i)$ be the number of points inserted into the linked list in the ith iteration.

We have to count the average (expected) number of comparisons that are done for each of these insertions. For the first insertion, the expected number of comparisons will be $\frac{L(i)+1}{2}$. For the second insertion, the expected number of comparisons will be $\frac{L(i)+2}{2}$. Similarly, we can find the expected number of comparisons for the other two points. Hence the average number of comparisons will be:

(3): $$\frac{(L(i)+1)+f(a(i),2)(L(i)+2)+f(a(i),3)(L(i)+3)+f(a(i),4)(L(i)+4)}{2}$$

where the function $f(x,y)$is defined as:

(4): $f(x,y) = 1\ if x \geq y$ otherwise $f(x,y) = 0$

Since we are looking for an upper-bound to the number of comparisons, we assume that we make all four insertions in each case. The length of the list now is $(L(i) + 4)$ and we also see that the number of comparisons on average is $(2L(i) + 5)$ from (3).

After the insertions are done, we go around the list once and delete some point(s) based on the inequality (1). This adds to $(L(i) - 1)$ more operations. The number of the operations in the while loop started in step (9) of the algorithm is:

(5): $$2L(1) + 2L(2) + \ldots + 2L\left(\left\lfloor\frac{n}{4}\right\rfloor\right) + 5\left\lfloor\frac{n}{4}\right\rfloor + L(1) + L(2) + \ldots + L\left(\left\lfloor\frac{n}{4}\right\rfloor\right) - \left(\left\lfloor\frac{n}{4}\right\rfloor\right)$$

Whenever we have u points, in the worst case we can delete $(u - 3)$ of them when we iterate around the list taking three consecutive points at a time. The minimum number of points deleted here can be 0. The expected number of deletions will be thus $\frac{(u-3)}{2}$. We also defined h - as the number of points which form the boundary of the convex hull. Assuming uniform distribution, we can claim that after i iterations, we will have $\left\lfloor\frac{4hi}{n}\right\rfloor$ number of points in our convex_hull which are a part of the boundary. These can't be deleted when we make a transition from the iteration $i$to the iteration $(i + 1)$of the while loop.

The expected length of the list after the deletion will be

(6): $$L(i+1) = (L(i) + 4) - \left(\frac{L(i)+4-\left\lfloor\frac{4hi}{n}\right\rfloor-3}{2}\right)$$

(7): $$2L(i+1) = L(i) + 7 + \left\lfloor\frac{4hi}{n}\right\rfloor$$

Putting values of i from 1 to$\left\lfloor\frac{n}{4}\right\rfloor$ in (7) and adding the equations vertically, we get:

(8): $L(1) + L(2) + \ldots + L\left(\left\lfloor\frac{n}{4}\right\rfloor\right) = O(nh)$

Using (8) with (5), we can see that the average runtime of the algorithm will be $O(n\log n) + O(n) + O(nh) = O(nh)$. This algorithm is thus output sensitive. In cases where $h < \log(n)$, the runtime will be $O(n\log n)$.

The worst case occurs when all of the input points lie on the boundary of the convex hull, because then no point is deleted as we go from the i^{th} iteration to the $(i+1)^{th}$ iteration as discussed above and then we can show that the runtime is achieved by setting $n = h$ to get $O(n^2)$.

V. VERIFICATION OF CONVEX HULL COMPUTATIONAL ALGORITHM IN PYTHON CODE

We have encoded the above described algorithm in Python version 3.4 and used "matplotlib" to plot the geometric shape of the computed circular linked list of the points that forms the boundary shape of the convex hull. The set of input points were generated by pseudo random number generator function in the random module of Python. Instance outputs for the algorithm at $n = 10,100$ and 1000 are shown in Fig.1, Fig.2 and Fig.3 respectively. The point shown in red colour is the Mean Point for the input set. The dashed vertical and horizontal lines drawn through this point denote the imaginary X and Y axes required to separate the input set into Q_1, Q_2, Q_3 and Q_4. The points on the boundary of the convex hull region (both vertices and non-vertices) are shown in green colour and the interior points are shown in blue colour.

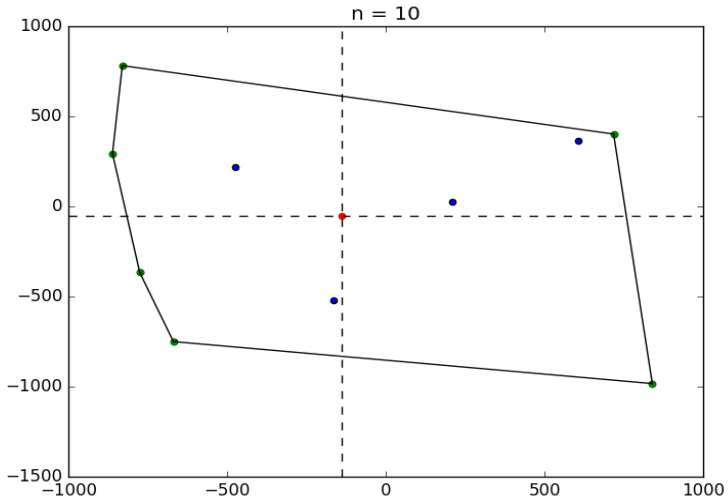


Fig. 1

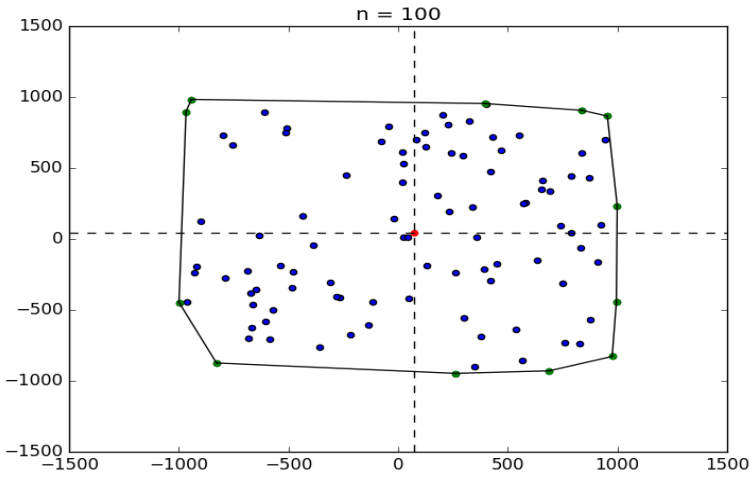


Fig. 2

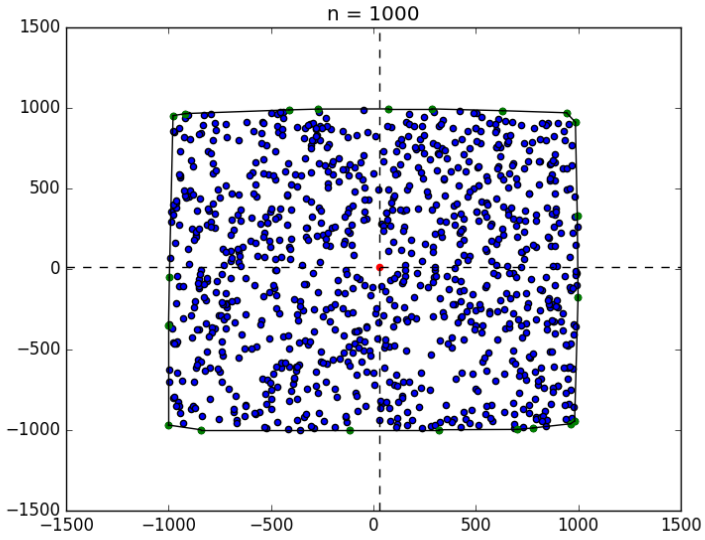


Fig. 3

VI. CONCLUSION

The discussed convex hull computation algorithm uses the mean point to find the polar angles and distances of all the input points and then with the help of a circular linked list implementation keeps track of all the points on the boundary of the convex hull. The average case time complexity of the algorithm is $O(nh)$. Thus, the runtime of the algorithm is the same as that of Jarvis [1].

REFERENCES

[1]. R. A. Jarvis. On the identification of the convex hull of a finite set of points in the plane. *Inform. Process. Lett., 2:18–21, 1973.*

[2]. Graham, R. L.: An efficient algorithm for determining the convex hull of a finite planar set. *Information processing letters1, 132-133 (1972)*

[3]. Chan, T.M. *Discrete Comput Geom (1996)16: 361. doi:10.1007/BF02712873*

[4]. Kirkpatrick, D. G., Seidel, R. (1986) The ultimate planar convex hull algorithm, *SIAM journal on Computing 15 (1), 287-299, doi:10.1137/0215021*

[5]. Selim G. Akl, & G. T, Toussaint, (1978) A fast convex hull algorithm, *Information Processing Letters, vol 7, pp 219-222.*

Accepted Manuscript



A novel red emitting Eu^{3+} doped calcium aluminozincate phosphor for applications in w-LEDs

Sumandeep Kaur, M. Jayasimhadri, A.S. Rao

PII: S0925-8388(16)34068-3

DOI: 10.1016/j.jallcom.2016.12.150

Reference: JALCOM 40072

To appear in: *Journal of Alloys and Compounds*

Received Date: 9 August 2016

Revised Date: 28 October 2016

Accepted Date: 12 December 2016

Please cite this article as: S. Kaur, M. Jayasimhadri, A.S. Rao, A novel red emitting Eu^{3+} doped calcium aluminozincate phosphor for applications in w-LEDs, *Journal of Alloys and Compounds* (2017), doi: 10.1016/j.jallcom.2016.12.150.

This is a PDF file of an unedited manuscript that has been accepted for publication. As a service to our customers we are providing this early version of the manuscript. The manuscript will undergo copyediting, typesetting, and review of the resulting proof before it is published in its final form. Please note that during the production process errors may be discovered which could affect the content, and all legal disclaimers that apply to the journal pertain.

ACCEPTED MANUSCRIPT

A novel red emitting Eu^{3+} doped Calcium Aluminozincate Phosphor for Applications in w-LEDs

Sumandeep Kaur, M. Jayasimhadri * and A.S.Rao*

Department of Applied Physics, Delhi Technological University, Bawana Road, New Delhi-110 042, India.

Abstract

A novel calcium aluminozincate phosphor doped with Eu^{3+} ions has been synthesized by conventional solid state reaction method and characterized by using X-ray diffraction (XRD), Scanning Electron Microscope (SEM), Diffuse Reflectance Absorbance (DRA) and Spectrofluorophotometer to study the structural, morphological and photoluminescence (PL) properties. All the XRD peaks are matching well with the standard ICDD card confirm that the prepared phosphors consist of single phase orthorhombic structure ($Ca_3Al_4ZnO_{10}$) having Pbc2 space group. The PL spectra recorded under near-UV/blue excitations demonstrates a very distinct and intense red emission from all the phosphors. In the present investigation, we found that 2 mol% of Eu^{3+} ions concentration is optimum in this host to give intense red emission. This result is also in consistent with the CIE chromaticity coordinates measured from the PL spectra of the samples under investigation. The results obtained for the optimized phosphor in the present investigation such as PL and CIE coordinates (x= 0.629 and y= 0.370) are close to the commercial red phosphor Y_2O_2S: Eu^{3+} (x= 0.622 and y= 0.351) and also very near to the coordinates specified by National Television Standard Committee (NTSC).

Corresponding authors:* ***E-mail:* drsrallam@gmail.com, Tel: +91-85860 39007
jayaphysics@yahoo.com, Tel: +91-9013553360

ACCEPTED MANUSCRIPT

1. Introduction

Energy became an essential commodity in our lives and the demand for energy in various sectors of the present society is increasing day by day. Lighting plays a vital role in our lives as well as in commerce and industry worldwide as it consumes large amount of the total energy produced. Energy efficiency is one of the most effective and challenging means to meet the ever growing demand of energy worldwide. Realizing the need of high efficiency lighting devices, various scientists across the world are working to meet this challenge. The rapid scientific quest for achieving the energy efficient light sources, white light emitting diodes (w-LEDs) open up opportunities in the general lighting market. Lighting applications using LEDs, organic LEDs, or light emitting polymers are commonly refers to Solid State Lighting (SSL). Now a days, SSL technology is emerging as a promising one to replace the conventional lighting sources such as incandescent bulbs, fluorescent lamps and high intensity discharge lamps due to their unique features such as high efficiency, compact and rigid structure, longer lifetime and their efficiency in power saving [1-2]. SSL technology also contributes immensely to the reduction of greenhouse gases and thereby helps in protecting the environment [3-4]. The history of solid state lighting dates back to 1907 when H.J. Round discovered a green glow in the silicon carbide diode junction [5]. However this major invention remained unnoticed for a longer period. A significant development in this direction took place when Shuji Nakamura fabricated double-hetrostructured InGaN/GAN blue LED chips in 1993 [6]. The first white light emitting diode was brought in to the commercial market by Nichia Corporation in 1996 [7]. From that time onwards, the search for the most efficient w-LEDs became a thrust area and the scientists are striving hard to bring out financially viable and environmental friendly w-LEDs needed for lighting industries.

There are various approaches to get efficient solid state sources for white light generation [8, 9]. However two different prominent methods are employed most commonly. The first one is using phosphor free RGB-LEDs. In this method light from three monochromatic LED sources, red, green and blue (RGB) are mixed directly so as to produce a white light. Second one is phosphor based, i.e., phosphor-converted white LEDs (pc-white LEDs) method. Nowaday pc-white LEDs approach has been paid much attention when compared with phosphor free RGB-LED approach for preparing w-LEDs. The main disadvantage of the RGB-LED approach is that, it requires different driving currents for individual LED to tune it for white light generation. In the pc-w-LEDs approach, phosphors are coated on NUV/blue LEDs in which part of NUV/blue light is converted into white light either by a combination of blue LED and yellow phosphor or UV LED coupled with mixture of RGB phosphors. The commercially available blue-emitting LED (InGaN) with the combination of yellow phosphor (YAG: Ce^{3+}) gives white light having fast luminescence decay time. Despite the various advantages, its luminescence suffers some limitations such as poor color rendering index (CRI) , high correlated colour temperature (CCT), low chromatic stability due to lack of red component which restricts its application in SSL devices [2, 10-13]. Moreover, tricolor phosphors based w-LEDs consist of NUV chip coated with appropriate mixture of RGB (red, green, and blue) phosphors. However, the disadvantage of using tricolour phosphors is the inconsistency in decay process of different components which leads to change in colour with time. Also the commercial sulfide red phosphor Y_2O_2S: Eu^{3+} is chemically unstable and less efficient as compared to the green (ZnS: Cu^{+}, Al^{3+}) and blue phosphors ($BaMgAl_{10}O_{17}$: Eu^{2+}) [14-16]. So it is essential to develop the most promising and efficient red phosphor needed from the perspective of chemical stability and high luminescent efficiency for the preparation of w-LEDs. All the aforementioned issues prompted us to take up an investigation on a new phosphor suitable for bright red light with high CRI and brightness [17]. It is well known that

rare earth's (RE) are excellent activator ions in a host matrix and found numerous applications in optical materials. Though the host matrix has negligible influence on the luminescence of RE ions, their energy levels are greatly affected by the crystal field symmetry of the host lattice. Due to a large number of absorption and emission bands arising from various transition levels, rare earth ions activated phosphors found applications in display devices. Among all the RE ions, europium serves as one of the most important candidate for tremendous application in luminescence, density optical storage and biomedical applications due to its energy level structure and high luminescence efficiency [18, 19].

In recent times, various inorganic oxide host materials such as binary and ternary compounds of phosphates, silicates, molybdates, tungstate, aluminates, tantalates, etc., have been rigorously studied for their electric, optical, magnetic, photocatalytic, cohesive, chromic, and multiferroic behaviour [20-29]. Nowadays, ternary oxide phosphors are gaining much attraction for their application in luminescence. Ternary compounds based on CaO-Al_2O_3-MO (M = Mg, Co, Zn) have not been explored much for its application in luminescence [15, 30, 31]. Pondering on all the aforementioned scientific applications of LED phosphors and considering the scientific patronages offered by the ternary oxide phosphors, we prepared a germane phosphor system namely calcium aluminozincate $Ca_3Al_4ZnO_{10}$ (CAZ) doped with Eu^{3+} ions at different concentrations using solid state reaction method and studied its structural, morphological, PL studies in order to explore the possibility of using these new phosphors for future photonic devices in general and w-LEDs in particular.

2. Experimental

Calcium Aluminozincate [$Ca_{3-x}Al_4ZnO_{10}$: xEu^{3+} (x = 0.0, 1.0, 2.0, 3.0, and 4.0 mol%) (CAZ: Eu)] Phosphors were synthesized taking analytical grade CaO, Al_2O_3, ZnO and Eu_2O_3 as chemical precursors using the conventional solid state reaction method. The appropriate

amounts of the aforementioned chemicals were collected in an agate mortar and grinded for an hour by adding acetone for uniform mixing of the constituent chemicals. The grinded samples were collected in an alumina crucible and placed inside a programmable muffle furnace at 700 ˚C for two hours and then sintered at different temperature ranging from 1100 to 1300 ˚C for five hours to obtain a pure phase. The sintered samples were naturally cooled down to the room temperature and again grinded for various characterizations.

X-Ray diffraction pattern measurements were performed on a high-resolution X-ray Bruker D8 Advance Diffractometer having nickel filtered Cu-Kα radiation (λ=1.54Å) operating at 40 kV and 40 mA in the 2θ angle range 20° to 70°. The morphology of the as prepared phosphor was studied by using scanning electron microscope (Hitachi S3700N) and the diffuse reflection spectra of powder samples were recorded with Pelkin-Elmer Lambda 35 UV/Vis/NIR Spectrometer in the UV-Visible range. The PL excitation and emission spectra were measured using Shimadzu RF-5301 PC-Spectrofluorophotometer equipped with a Xenon arc lamp as the source of excitation. All the characterizations were performed at room temperature.

3. **Results and Discussion.**

3.1. Phase Identification:

Fig. 1 represents the X-ray diffraction patterns of CAZ powder phosphor sintered at the different temperatures in the process of obtaining pure phase. From Fig.1 it is observed that the intensities of the impurity peaks are decreasing gradually with increasing the sintering temperature of the sample and exhibiting pure phase for the as prepared phosphor sintered at 1300 ^{o}C. All the diffraction peaks of the CAZ phosphor sintered at 1300 ^{o}C matches well with the standard PDF4 + International Crystallographic Diffraction Database (ICDD) card no. 04-009-7304 and confirms the single phase formation of an orthorhombic structure with a

space group Pbc2 for CAZ. The characteristic structural units for CAZ are five-membered tetrahedral rings with Ca^{2+} ion inside them. The oxygen atom forms deformed octahedral in the form of antiprisms. The aluminium and zinc form three-membered tetrahedral rings parallel to yx-plane which is connected with the similar rings along x-axis on their common vertex and with other two rings connected by double helical axis forming continuous layers. These layers are interconnected by metaaluminate chains of Al tetrahedral forming a continuous 3D structure [32]. Fig. 2 represents the X-Ray diffraction patterns for CAZ: xEu (x = 0.0, 1.0, 2.0 and 3.0 mol%). No impurity peak was observed in diffraction patterns confirms the successful doping of Eu^{3+} ions in the host lattice. The absence of any second phase implies that the Eu^{3+} ions are not influencing the crystal structure of the host lattice due to similar ionic radii of six coordinated Ca^{2+} = 1.0 Å; Eu^{3+} = 0.947 Å. The lattice parameters were found to be *a = 5.142 Å, b = 16.751 Å, c = 10.721 Å*, with cell volume *V = 923.438 Å*^{3} having number of atoms per unit cell, *N = 4*. The Williamson-Hall method is used to calculate the crystallite size and strain [33]. The Williamson- Hall equation is given by:

$$\beta cos\theta = \left(\frac{k\lambda}{D}\right) + 4\varepsilon sin\theta \qquad (1)$$

Where, k is shape factor, λ is the wavelength of X-rays used, *D* is the average crystallite size, β is full width at half maximum (FWHM) of the observed diffraction peak, θ is the diffraction angle in radian, and ε is strain. The obtained crystallite size is 52.0, 69.5, 74.2, and 92.7 nm and strain is 0.00029, 0.00092, 0.00382, and 0.0094 for CAZ: xEu (x = 0.0, 1.0, 2.0 and 3.0 mol%). The crystallite size is also estimated by using Debye-Scherrer equation $D = k\lambda/\beta cos\theta$.. The average crystallite sizes were found to be 51.6, 63.3, 70.5, and 84.3 nm for CAZ: xEu (x = 0.0, 1.0, 2.0 and 3.0 mol%) phosphor, respectively which is in good agreement with that calculated from W-H method. The increase in crystallite size with

concentration of Eu^{3+} ion accredited to the increase in strain introduced due to the replacement of Ca^{2+} ions by Eu^{3+} ions of smaller radii [34].

3.2. Morphology:

Figs. 3a and 3b represent the surface morphology of undoped and 2.0 mol% Eu^{3+} doped CAZ phosphor sample sintered at 1300 ^{o}C. The observed SEM images exhibit inhomogeneous and uneven particles with an average size falling in the range between 2-10 μm. The observed micron size of particles is very much suitable to be use as potential luminescent material [35].

3.3. Diffuse Reflectance Spectra:

Fig.4 shows the diffuse reflectance absorbance spectra of CAZ: xEu (x = 0.0 and 2.0 mol%). Generally, the optical properties changes when impurity ions are doped in the host matrix [36]. CAZ phosphor doped with 2.0 mol% Eu^{3+} ions shows the absorption band in the range 390-525 nm due to the presence of Eu^{3+} ions, which were found to be consistent with those observed in excitation spectra. In the process of finding the optical band gap of the prepared samples, we have converted the diffuse reflectance spectra into Kulbeka-Munk function as follows:

$$F(R) = (1 - R)^2/2R \quad (2)$$

where, $F(R) = K/S$ is the Kulbelka –Munk function or absolute reflectance of the host lattice, K is the molar absorption coefficient, S is the scattering coefficient [18]. The relation between absorption coefficient (α) and energy band gap (E_g) is given by Tauc equation:

$$\alpha h\nu = C(h\nu - E_g)^n \quad (3)$$

Where, $h\nu$ is the photon energy, C is energy independent constant, and n is a constant related to the transition (n = 1/2, 2, 1/3, 3 for direct allowed, indirect allowed, direct forbidden, and

indirect forbidden transitions, respectively). Since α is proportional to F(R), the above equation can be rewritten as:

$$F(R)h\nu = C(h\nu - E_g)^n \quad (4)$$

The band gap for pure CAZ and 2.0 mol% Eu^{3+} doped CAZ samples were measured by calculating *F(R)* and plotting a graph between $(F(R)h\nu)^2$ and $h\nu$ (Tauc plot), for direct allowed transition as show in the inset of Fig. 4. The intercept of the tangent to the X-axis gives a good approximation of the band gap energy. The calculated band gap for CAZ: xEu^{3+} (x = 0.0, and 2.0 mol% of Eu^{3+} ions) was observed to be approximately 3.34 and 3.36 eV respectively, by extrapolating the Kulbelka-Munk absorption coefficient related spectrum. The calculated values of band gap represent insignificant change with the doping of activator ions [19]. With the addition of dopant into the host lattice, a slight expansion in the unit cell tends to narrower the conduction and valence band which cause the broadening in the band gap. [37]

3.4. Luminescent Properties:

The PL excitation and PL emission spectra of CAZ: xEu (x = 1.0, 2.0, 3.0, and 4.0 mol%) are represented in Fig. 5 and 6, respectively. Fig.5 shows the excitation spectra of CAZ: xEu (x = 1.0, 2.0, 3.0, and 4.0 mol%) phosphor in the wavelength range 225-550 nm by monitoring emission wavelength at 615 nm. Two broad excitation bands were observed in the range 250-300 nm and 320-360 nm, indicates the presence of charge transfer band (CTB) and host band respectively in the host matrix. The CTB corresponds to the electronic transition from the 2p orbital of O^{2-} to the 4f orbital of Eu^{3+}, and it is related to the covalency between O^{2-} and Eu^{3+} and coordination environment of Eu^{3+} [38]. The narrow excitation peaks at a wavelength of 360, 379, 391, 412, 462, and 529 nm were observed as associated with intra-4f transitions of Eu^{3+} ions designated to $^7F_0 \rightarrow {}^5D_4$, $^7F_0 \rightarrow {}^5L_7$, $^7F_0 \rightarrow {}^5L_6$, $^7F_0 \rightarrow {}^5D_3$, $^7F_0 \rightarrow {}^5D_2$, and

$^7F_0 \rightarrow {}^5D_1$ transitions, respectively [38-40]. Among all the peaks, the one at a 462 nm wavelength has the highest intensity and the peak at 391 nm has the intensity closer to the intensity observed at 462 nm. These two intense peaks observed at 462 and 391 nm conspicuously speak that the phosphor under investigation can be excited by n-UV and Blue LED chips. Fig. 6(a) represents the PL emission spectra of CAZ phosphor doped with 2.0 mol % Eu^{3+} ions under different excitation wavelengths. From Fig. 6(a), it can be seen that, the phosphor under investigation gives maximum emission intensity under 462 nm excitation. The emission intensity observed under 391 nm excitation wavelength is also very closer to that observed at 462 nm excitation. Fig. 6(b) and Fig. 6(c) represent the emission spectra of CAZ: xEu (x = 1.0, 2.0, 3.0, and 4.0 mol%) recorded by exciting the samples at 462 nm and 391 nm wavelengths respectively, which are similar from the perspective of peak position and intensity. Sharp emission peaks observed at 553, 578, 588, 615, 653 and 701 nm and in both the emission spectra were assigned to $^5D_1 \rightarrow {}^7F_2$, $^5D_0 \rightarrow {}^7F_0$, $^5D_0 \rightarrow {}^7F_1$, $^5D_0 \rightarrow {}^7F_2$, $^5D_0 \rightarrow {}^7F_3$, and $^5D_0 \rightarrow {}^7F_4$ transitions, respectively [41, 42]. Splitting of $^5D_0 \rightarrow {}^7F_1$, and $^5D_0 \rightarrow {}^7F_2$ levels into two peaks because of stark effect indicates the presence of Eu^{3+} ions at two or more site symmetries in the phosphor under investigation [43]. It is well known that because of stark effect, the emission transitions can split into a maximum of the *2J+1* stark level, where *J* is the total angular momentum [44]. The emission transitions $^5D_0 \rightarrow {}^7F_1$ and $^5D_0 \rightarrow {}^7F_2$ observed in the emission spectra are attributed to the magnetic dipole (MD) and forced electric dipole (ED) transitions, respectively. The hypersensitive forced ED transition is more intense than allowed MD transition indicating Eu^{3+} ions are located at the sites with no inversion symmetry [42, 45]. The intensity ratio of $^5D_0 \rightarrow {}^7F_2$ to $^5D_0 \rightarrow {}^7F_1$ transition gives the asymmetric ratio, which tells us the degree of distortion on the inversion symmetry of Eu^{3+} ions in the lattice. Such ratio was found to be in the range from 1.4 to 1.6 for different concentration of Eu^{3+} ions in the phosphor under investigation indicates that the Eu^{3+} ions are

present at a high symmetry site. The slight variation observed in asymmetric ratio indicates consistency in symmetry of Eu^{3+} ions with varying concentration [46, 47].

From the emission spectra, it is observed that emission intensity initially increases up to 2.0 mol% of Eu^{3+} ions, and then gradually decreases with further increase in Eu^{3+} ion concentration. As the concentration of Eu^{3+} ion increases, the distance between the Eu^{3+} ions becomes smaller which favours the non-radiative pathway by energy transfer among Eu^{3+} ions which leads to luminescence quenching. In general there are three mechanisms responsible for non-radiative energy transfer including exchange interaction, radiation re-absorption and electric multipolar interaction among activator ions [48]. The energy transfer between Eu^{3+} ions depends on the shortest average distance (critical distance R_c) between Eu^{3+} - Eu^{3+} ions at a critical concentration (mol %) X_c of Eu^{3+} ions. The critical distance R_c [34, 49] can be determined from the equation given by:

$$R_c \approx 2\left[\frac{3V}{4\pi X_c N}\right]^{\frac{1}{3}} \quad (5)$$

where, V is the volume of the unit cell, N is the number of cations per unit cell. For CAZ system V = 923.438 $Å^3$, N = 4, X_c = 0.02 (2.0 mol%). By using the above experimental data, the critical distance was estimated to be 29.16 Å. This is far larger than the critical distance needed (5 Å) for exchange interaction to takes place. The huge difference in critical distance conspicuously speaks that the exchange interaction is not responsible for energy transfer, and multipolar interaction may be the most appropriate mechanism in the present case [50]. According to Dexter Theory, if the energy transfer occur by electric multipolar interaction, the probability of energy transfer between the activator ions is inversely proportional to the Q^{th} power of R (Q = 6, 8, and 10 corresponding to electric dipole-dipole, dipole-quadrupole, and quadrupole-quadrupole interactions, respectively), where R is the distance between activator ions.

The emission intensities and the corresponding doping concentration of activator ions are related as [37, 51]

$$\frac{I}{x} = K\{1 + \beta(x)^{\frac{Q}{3}}\}^{-1} \quad (6)$$

where *I* is the luminous intensity, *x* is the mole concentration of activator ions, *Q* represents the interaction type, *K* and β are constants for the same excitation condition in a given host. From the Huang's description for luminous intensity and mole fraction [52], the luminous intensity and the mole fraction of activator ions can be reduced to:

$$log\frac{I}{x} = A - \frac{Qlog(x)}{3} \quad (7)$$

where, A is independent of doping concentration. To estimate the value of Q, the graph between *log(I/x)* versus *log(x)* is plotted as shown in Fig. 7. The calculated value of Q is 5.94, which is in proximity to 6 implying energy transfer mechanism occurs due to electric dipole-dipole interaction [53].

On the basis of the observed photoluminescence spectrum of as-prepared Eu^{3+} doped CAZ powder, schematic energy transfer mechanism is represented in Fig. 8 where the Eu^{3+} ions excited to higher energy levels and then returns to the lower energy levels either by the radiative or non-radiative transitions. The upward and downward arrows indicate the excitation and radiative emission respectively which are shown by solid lines and non-radiative emission transitions are shown by dotted lines. The possible non-radiative transition channels might be either due to Resonant Energy Transfer (RET) or cross-relaxation (CR). The possible cross-relaxation channels for depopulating $^5D_1$, $^5D_2$ and $^5D_3$ higher levels are $^5D_1 + {}^7F_0 \rightarrow {}^5D_0 + {}^7F_3$ (CRC1), $^5D_2 + {}^7F_0 \rightarrow {}^5D_0 + {}^7F_5$ (CRC2), $^5D_2 + {}^7F_0 \rightarrow {}^5D_1 + {}^7F_4$ (CRC3), $^5D_3 + {}^7F_0 \rightarrow {}^5D_1 + {}^7F_6$ (CRC4) and $^5D_3 + {}^7F_0 \rightarrow {}^5D_2 + {}^7F_4$ (CRC5), respectively as shown in Fig. 8 [54].

3.5. Colorimetric Studies:

To evaluate the colorimetric performance of the CAZ: xEu phosphors (x = 1.0, 2.0, 3.0 and 4.0 mol%), the Commission Internationale de I'Eclairage (CIE) chromaticity coordinates were calculated using emission spectrum (λ_{ex} = 391 and 462 nm). The chromaticity coordinates (x,y) for the prepared samples were estimated as (0.627, 0.372), (0.629, 0.370), (0.626, 0.374) and (0.627, 0.372) (λ_{ex} = 391 nm) and (0.614, 0.384), (0.614, 0.385), (0.615, 0.384), and (0.615, 0.383) (λ_{ex} = 462 nm) for 1.0, 2.0, 3.0 and 4.0 mol% of Eu^{3+} ions, respectively. The calculated CIE chromaticity coordinates for CAZ: xEu (x = 1.0, 2.0, 3.0 and 4.0 mol%) are closer to the commercial red phosphor of Y_2O_2S: Eu^{3+} (x = 0.622, y = 0.351) and also close to the National Television Standard Committee (NTSC) standard value of red phosphor (x = 0.670, y = 0.330) [48]. The CIE chromaticity coordinates for the optimized concentration of Eu^{3+} ions for λ_{ex} = 391 nm and 462 nm are shown in Fig. 9. The Correlated Colour Temperature (CCT) has been estimated using McCamy's polynomial formula [55]:

$$CCT = -449n^3 + 3525n^2 - 6823.3n + 5520.33 \quad (8)$$

Where $n = (x-x_e)/(y-y_e)$ represent the inverse slope line and x_e = 0.3320, y_e = 0.1860, are the coordinates for epicenter. The calculated CCT were found to be 1951, 1994, 1930, 1954 K for the spectra recorded at λ_{ex} = 391 nm and 1792, 1788, 1798 and 1801 K for spectra recorded at λ_{ex} = 462 nm for 1.0, 2.0, 3.0 and 4.0 mol % of Eu^{3+} ions, respectively. The above results suggest that the as prepared CAZ: xEu phosphor can be used as potential red phosphor in white LEDs.

4. Conclusions.

Monophase calcium aluminozincate phosphor doped with different molar concentrations of Eu^{3+} ions (0.0, 1.0, 2.0, 3.0 and 4.0 mol %) have been synthesized by conventional solid state reaction technique at 1300 ^oC. It's structural, morphological, and optical properties have been studied using XRD, SEM, DRA and PL spectral studies. The particle size has been found to

be in the micron range having inhomogeneous structure. The band gap has been found to be 3.34 and 3.36 eV for pure and optimized samples respectively. The photoluminescence study shows that the prepared sample exhibits two strong emission bands at 588 and 615 nm corresponding to $^5D_0 \rightarrow {}^7F_1$, and $^5D_0 \rightarrow {}^7F_2$ transitions respectively, of which, the band at 615 nm is more intense under n-UV and blue excitations than the other one. The optimal doping concentration of Eu^{3+} ions is 2.0 mol%, beyond which the luminescence concentration quenching is obtained. The CIE chromaticity coordinates for all the samples are found to lie in red region. The CIE chromaticity coordinates for the optimized concentration i.e., 2.0 mol% of Eu^{3+} are (x= 0.629 and y= 0.370) and (x= 0.614 and y= 0.385) at λ_{ex} = 391 nm and 462 nm respectively, which is close to the commercial red phosphor Y_2O_2S: Eu^{3+} (x= 0.622 and y= 0.351) and also to the standard chromaticity of x=0.67 and y=0.33 for the NTSC system. From the PL studies and calculated CIE chromaticity coordinates, it is concluded that the calcium aluminozincate phosphor is a potential candidate for red emission and is useful for the development of w-LEDs.

Acknowledgements:

One of the authors, Ms. Sumandeep Kaur is very much thankful to Council of Scientific & Industrial Research (CSIR)-University Grants Commission (UGC), Govt. of India, New Delhi for awarding her with Junior Research Fellowship (JRF) (Roll No.513 560) to carry out the present research work.

ACCEPTED MANUSCRIPT

References

[1] H. Hagemann, H. Bill, J. M. Rey, F. Kubel, L. Calame, D. Lovy, J. Phys. Chem. C. 119 (2015) 141-147.

[2] X. Li, J. D. Budai, F. Liu, J. Y. Howe, J. Zhang, X-J Wang, Z. Gu, C, Sun, R. S. Meltzer, Z. Pan, Light Sci Appl. 2 (2013) 1-8.

[3] S. Mishra, G. Swati, B. Rajesh, K. Tyagi, B. Gahtori, B. Sivaiah, N. Vijayan, M. K. Dalai, A. Dhar, S. Auluck, M. Jayasimhadri, D. Haranath, Luminescence DOI 10.1002/bio.2966.

[4] J. Geng, C. Yu, H. Wu, B. Wu, L. Tian, J. Lumin. 140 (2013) 71-73.

[5] H.J. Round, The Electrical World 49 (1907) 309-310

[6] G.Fasol, S.Nakamura, The Blue Laser Diode:GaN based blue light emitters and lasers, Springer, Berlin (1997)

[7] R. Mirhosseini, M.F. Schubert, S. Chhajed, J. Cho, J.K. Kim, E.F. Schubert, Opt. Express. 17 (2009) 10806–10813.

[8] J. McKittrick, L.E.Shea-Rohwer, J.Am.Ceram.Soc. 97 (2014) 1327-1352.

[9] C.C.Lin, Liu, J.Phys.Chem.Lett. 2 (2011) 1268-1277

[10] Y. Li, Y. Shi, and Y. Wang, ECS J. Solid State Sci. Light Technol. 2 (2013) R208-R213.

[11] X. Yang, J. Liu, H. Yang, X. Yu, Y. Guo, Y. Zhou, J. Liu, J. Mater. Chem. 19 (2009) 3771-3774.

[12] A. J. Fernández-Carrión, M. Ocaña, J. García-Sevillano, E. Cantelar, A. I. Becerro. J. Phys. Chem. C. 118 (2014) 18035-18043.

[13] W. B. Im, N. N. Fellows, S. P. DenBaars, R. Seshadri, Y-Il Kim, Chem. Mater. 21 (2009) 2957-2966.

[14] S. Som, P. Mitra, V. Kumar, V. Kumar, J.J. Terblans, H.C. Swart, S.K. Sharma, Dalton Trans. 43 (2014) 9860-9871.

[15] B. Hallstedt, J. Am. Ceram. Soc. 78 [1] (1995) 193-198.

[16] S. Neeraj, N. Kijima, A.K. Cheetham, Chem. Phys. Lett. 387 (2004) 2–6.

[17] M. Marius, E. J. Popovici, L Barbu-Tudoran, E. Indrea, A. Mesaros, Ceram. Int. 40 (2014) 6233-6239.

[18] Y.C. Wu, D.Y. Wang, T.M. Chen, C.S. Lee, K.J. Chen, and H.C. Kuo, ACS Appl. Mater. Inter. 3 (2011) 3195-3199.

[19] R. Koferstein, L. Jager, and S. G. Ebbinghaus, Solid State Ionics. 249-250 (2013) 1-5.

[20] K. Zaghib, A. Mauger, J. B. Goodenough, F. Gendron, C. M. Julien, Chem. Mater. 19 (2007) 3740-3747.

[21] X. Pardal, F. Brunet, T. Charpentier, I. Pochard, A. Nonat, Inorg. Chem. 51 (2012) 1827-1836.

[22] T. Endo, Y. Doi, M. Wakeshima, Y. Hinatsu, Inorg. Chem. 49 (2010) 10809-10814.

[23] L. Mohapatra, K. Parida, M. Satpathy, J. Phys. Chem. C. 116 (2012) 13063-13070.

[24] P. Patureau, M. Josse, R. Dessapt, J-Y. Mevellec, F. Porcher, M. Maglione, P. Deniard, C. Payen, Inorg. Chem. 54 (2015) 10623-10631.

[25] K. Fukuda, K. Akatsuka, Y. Ebina, M. Osada, W. Sugimoto, M. Kimura, T. Sasaki, Inorg. Chem. 51 (2012) 1540-1543.

[26] S. R. Jansen, H. T. Hintzen, R. Metselaar, J. Phys. Chem. B. 102 (1998) 5969-5976.

[27] M-R. Li, P. W. Stephens, M. Retuerto, T. Sarkar, C. P. Grams, J. Hemberger, M. C. Croft, D. Walker, M. Greenblatt, J. Am. Chem. Soc. 136 (2014) 8508-8511.

[28] J. Praveen Kumar, G.K. Prasad, J.A. Allen, P.V.R.K. Ramacharyulu, K. Kadirvelu, B. Singh, J. Alloy. Compd. 662 (2016) 44-53.

[29] Z. Fu, P. Liu, J. Ma, B. Guo, X. Chen, H. Zhang, Mater. Res. Bull. 77 (2016) 78-83.

[30] B. Vazquez, L. M. Torres-Martinez, N. Alvarez, J. F. Vente, P. Quintana, J. Solid State Chem. 166 (2002) 191-196.

[31] R.S. Bhavsar, R.B. Kharat, Mater. Chem. Phys. 80 (2003) 143-149.

[32] V. D. Barbanyagre, T. I. Timoshenko, A, M. Ilyinets, and V. M. Shamshurov, Powder Diffr. 12 (1997) 22-26.

[33] A.K. Vishwakarma, K. Jha, M. Jayasimhadri, B. Sivaiah, B. Gahtori, and D. Haranath, Dalton Trans. 44 (2015) 17166-17174.

[34] Maheshwary, B.P. Singh, J. Singh, R.A. Singh, RSC Adv. 4 (2014) 32605–32621.

[35] A.K. Vishwakarma, K. Jha, M. Jayasimhadri, A. S. Rao, K. Jang, B. Sivaiah, and D. Haranath, J. Alloys Compd. 622 (2015) 97-101.

[36] Y. Li, Z. Zhao, Z. Song, R. Wan, J. Qiu, Z. Yang, Z. Yin, X. Liu, Q. Liu, and Y. Zhou, J. Am. Ceram. Soc. 98 (2015) 2170-2176.

[37] B. Y. Huang, B. L. Feng, L. Luo, C. L. Han, Y. T. He, Z. R. Qiu, Mater. Sci.Eng., B, 212 (2016) 71-77.

[38] Y. Tian, X. Qi, X. Wu, R. Hua, and B. Chen, J. Phys. Chem. C. 113 (2009) 10767-10772.

[39] Y. Wu, Z. Sun, K. Ruan, Y. Xu, H. Zhang, J. Lumin. 155 (2014) 269-274.

[40] Q. Xiao, Y. Liu, L. Liu, R. Li, W. Luo, and X. Chen, J. Phys. Chem. C. 114 (2010) 114, 9314-9321.

[41] Q. Ju, Y. Liu, R. Li, L. Liu, W. Luo, and X. Chen, J. Phys. Chem. C. 113 (2009) 2309-2315.

[42] Marcos V. dos S, Rezende, C. William A. Paschoal, Opt. Mater. 46 (2015) 530-535.

[43] V.R.L. Constantino, M.A. Bizeto, H.F. Brito, J. Alloy Compd. 278 (1998) 142-148.

[44] H. Steinkemper, S. Fischer, M. Hermle, J. C. Goldschmidt, New J. Phys. 15 (2013) 53033-53048.

[45] T. C. Ozawa, K. Fukuda, K. Akatsuka, Y. Ebina, T. Sasaki, Chem. Mater. 19 (2007) 6575-6580.

[46] J. Hou, P. Chen, G. Zhang, Y. Fang, W. Jiang, F. Huang, Z. Mad, J. Lumin. 146 (2014) 97-101.

[47] Z.W. Zhang, L.J. Wang, L. Han, F. Han, X.X. Ma, X.Q. Li, D.-J. Wang, Mater. Lett. 160 (2015) 302-304.

[48] Q. Xu, J. Sun, D. Cui, Q. Di, and J. Zeng, J. Lumin. 158 (2015) 301-305.

[49] Z. Ci, Q. Sun, S. Qin, M. Sun, X. Jiang, X. Zhang, and Y. Wang, Phys. Chem. Chem. Phys. 2014, 16, 11597-11602.

[50] J. Zhong, W. Zhuang, X. Xing, R. Liu, Y. Li, Y. Liu, and Y. Hu, J. Phys. Chem. C. 119 (2015) 5562-5569.

[51] Y. Tian, B. Chen, R. Hua, N. Yu, B. Liu, J. Sun, L. Cheng, H. Zhong, X. Li, J. Zhang, B. Tian and H. Zhong, CrystEngComm, 14 (2014) 1760-1769.

[52] Y. Tian, B. Chen, B. Tian, R. Hua, J. Sun, L. Cheng, H. Zhong, X. Li, J. Zhang, Y. Zheng, T. Yu, L. Huang, Q. Meng, J. Alloys Compd., 509 (2011) 6096-6101.

[53] G.P. Darshan, H.B. Premkumar, H. Nagabhushana, S.C. Sharma, S.C. Prashanth, B. D. Prasad, J. Colloid Interface Sci. 464 (2016) 206-218.

[54] B. Tian, B. Chen, Y. Tian, X. Li, J. Zhang, J. Sun, H. Zhong, L. Cheng, S. Fu, H. Zhong, Y. Wang, X. Zhang, H. Xiac, and R. Hua, J. Mater. Chem. C. 1 (2013) 2338-2344.

[55] A. K. Vishwakarma, M. Jayasimhadri, J. Lumin. 176 (2016) 112-117.

ACCEPTED MANUSCRIPT

Figure Captions:

Fig. 1: XRD pattern of $Ca_3Al_4ZnO_{10}$ at different temperatures along with standard diffraction pattern of $Ca_3Al_4ZnO_{10}$.

Fig. 2: XRD pattern of $Ca_{3-x}Al_4ZnO_{10}$: xEu^{3+} (x = 0.0, 1.0, 2.0 and 3.0 mol%) along with standard diffraction pattern of $Ca_3Al_4ZnO_{10}$.

Fig. 3(a): SEM image of $Ca_3Al_4ZnO_{10}$.

Fig. 3(b): SEM image of $Ca_{3-x}Al_4ZnO_{10}$; xEu^{3+} (x = 2.0 mol%).

Fig. 4: The Diffuse Reflectance Absorbance of $Ca_{3-x}Al_4ZnO_{10}$; xEu^{3+} (x = 0.0 and 2.0 mol%). (Inset: Tauc plot for band gap measurements).

Fig. 5: The excitation spectra of $Ca_{3-x}Al_4ZnO_{10}$: xEu^{3+} (x = 1.0, 2.0, 3.0 and 4.0 mol%) at 615 nm emission wavelength.

Fig. 6(a): The emission spectra for $Ca_{3-x}Al_4ZnO_{10}$: xEu^{3+} (x = 2.0 mol%) monitored at different excitation wavelengths.

Fig. 6(b): The emission spectra of $Ca_{3-x}Al_4ZnO_{10}$: xEu^{3+} (x = 1.0, 2.0, 3.0 and 4.0 mol%) under 462 nm excitation wavelength.

Fig. 6(c): The emission spectra of $Ca_{3-x}Al_4ZnO_{10}$: xEu^{3+} (x = 1.0, 2.0, 3.0 and 4.0 mol%) under 391 nm excitation wavelength.

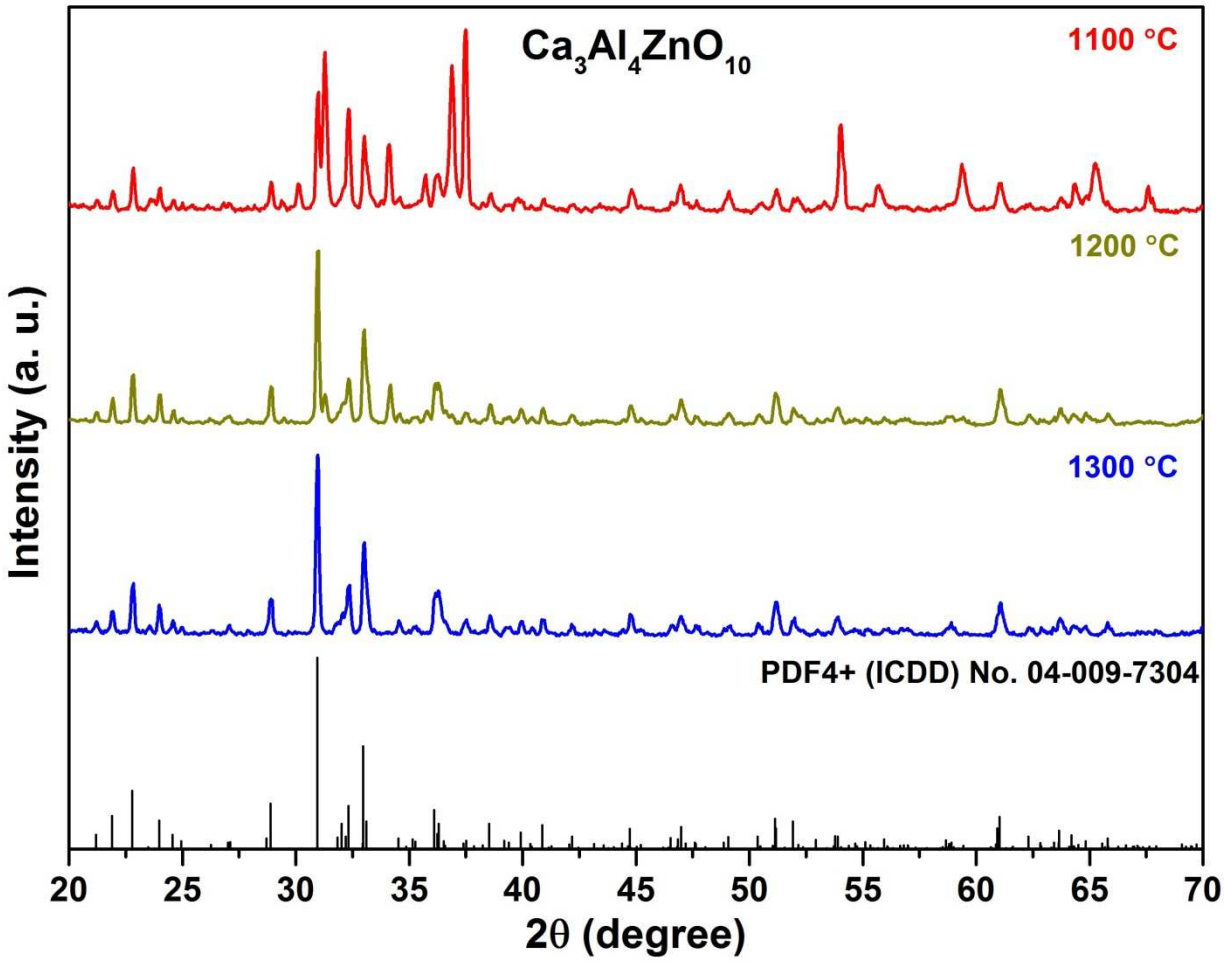
Fig. 7: Plot of log(I/x) vs log(x).

Fig. 8: Partial Energy level diagram and possible cross-relaxation channels of Eu^{3+} ion doped CAZ phosphor.

Fig. 9: CIE Chromaticity Diagram of CAZ phosphor doped with 2.0 mol% of Eu^{3+} ions at 391 and 462 nm excitation wavelengths.

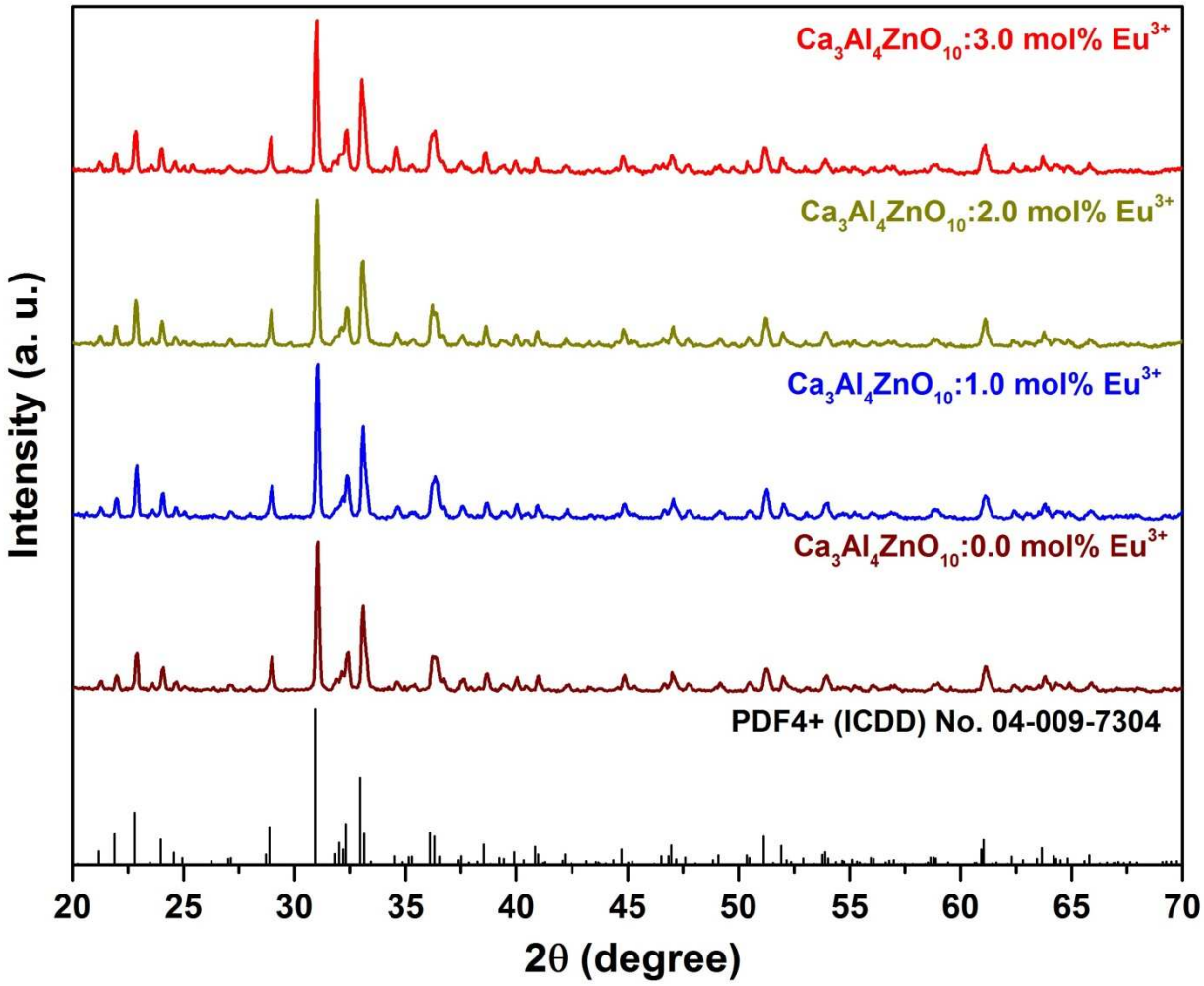
ACCEPTED MANUSCRIPT

Fig. 1:



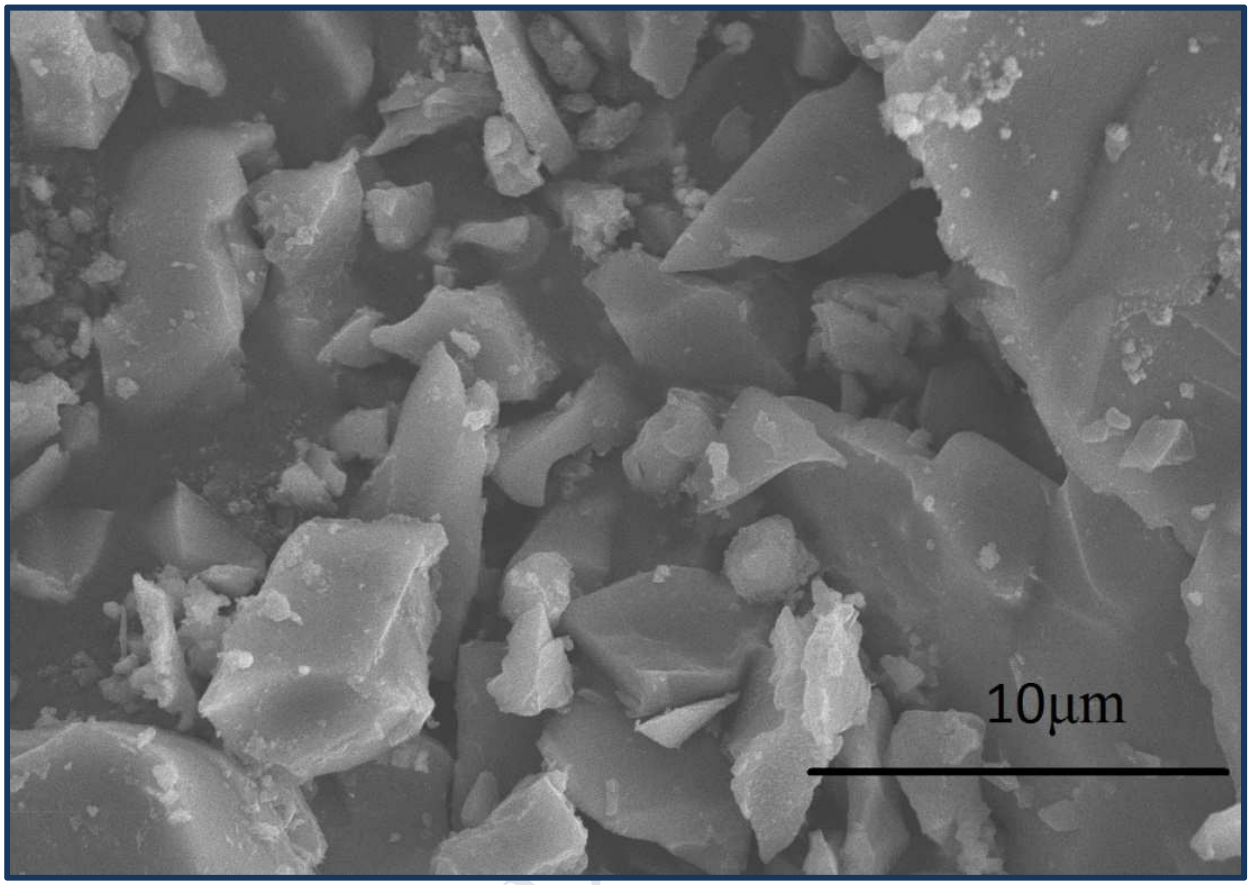
ACCEPTED

Fig. 2:


Ca3Al4ZnO10:3.0 mol% Eu3+
Ca3Al4ZnO10:2.0 mol% Eu3+
Ca3Al4ZnO10:1.0 mol% Eu3+
Ca3Al4ZnO10:0.0 mol% Eu3+
PDF4+ (ICDD) No. 04-009-7304
Intensity (a. u.)
20
25
30
35
40
45
50
55
60
65
70
2θ (degree)

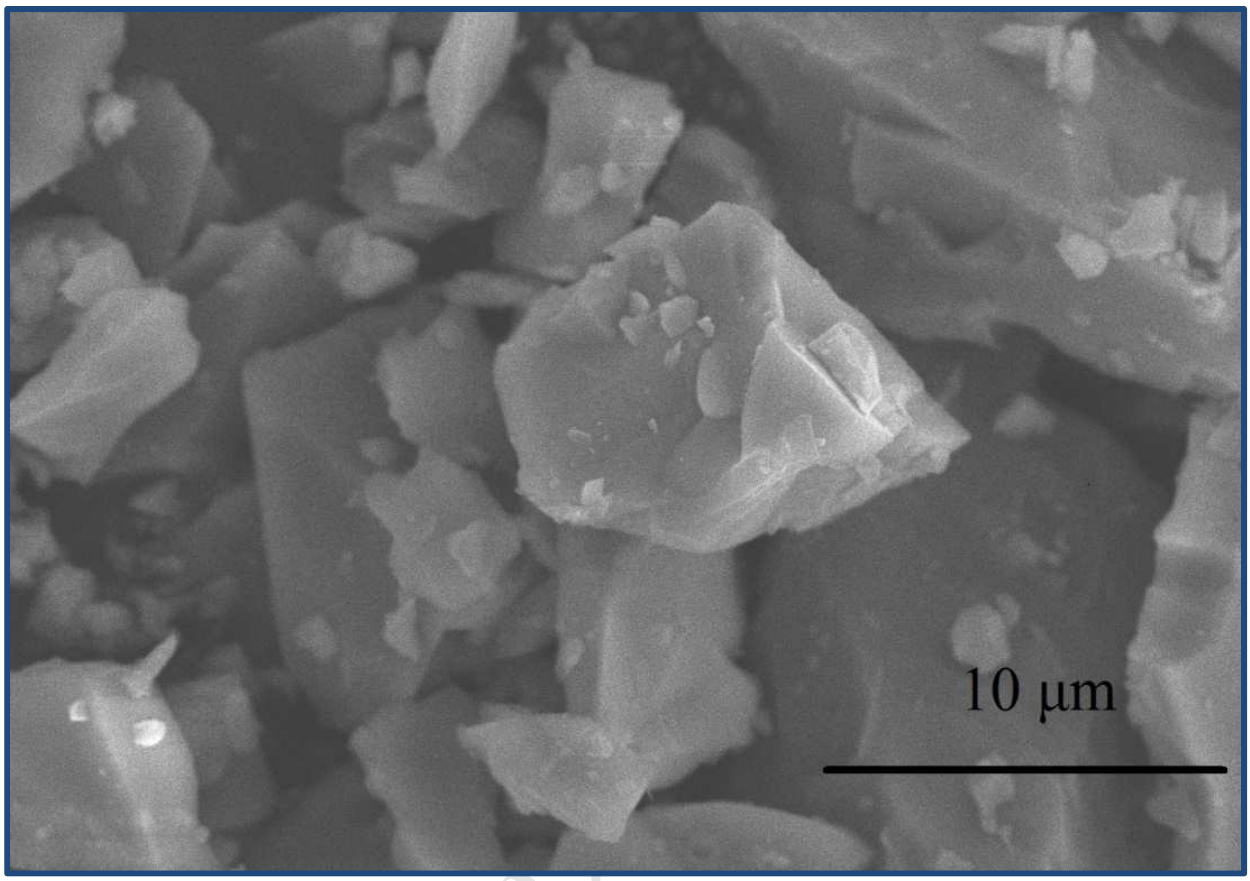
ACCEP

Fig. 3(a):



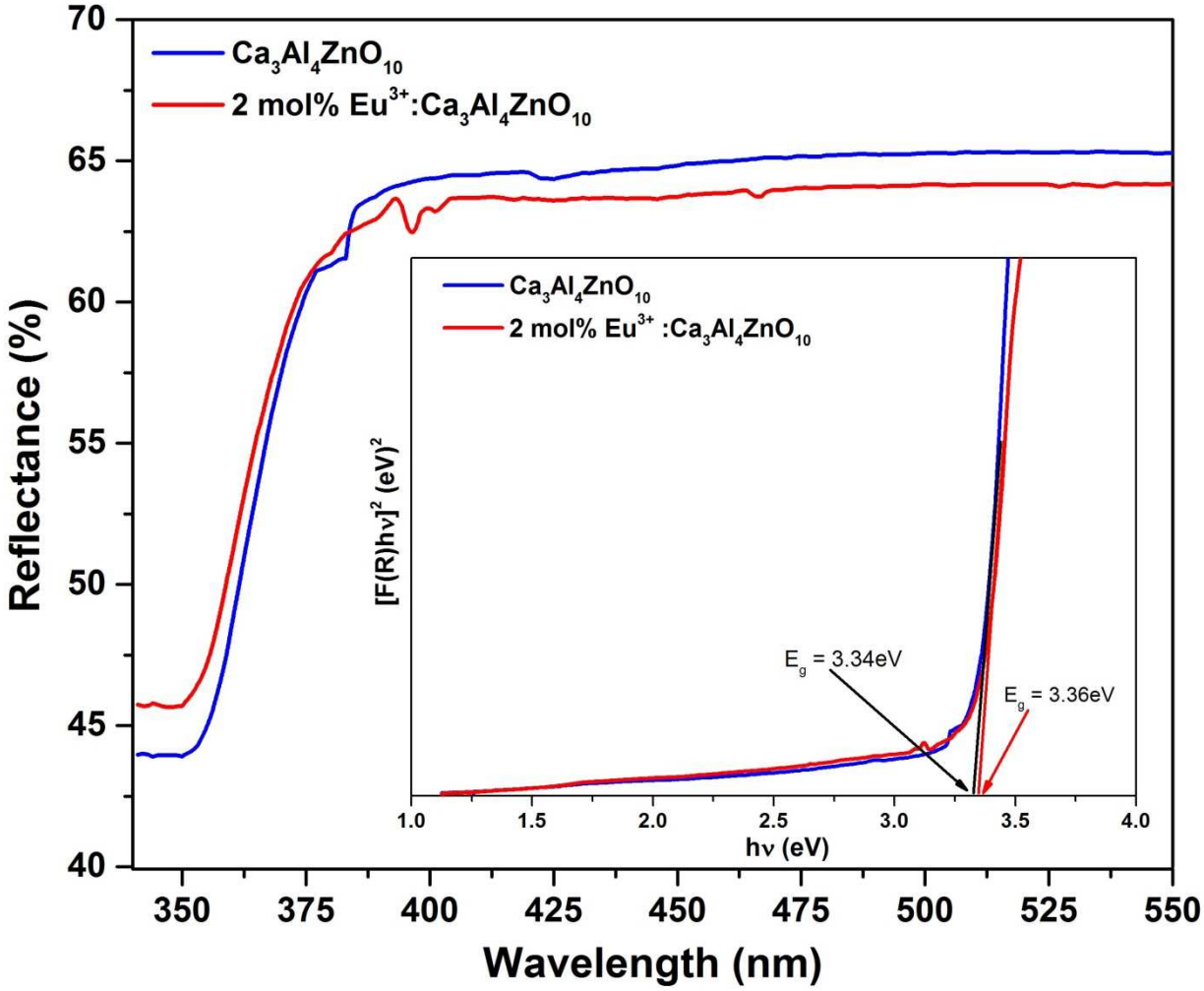
ACCEPTED

Fig. 3(b):



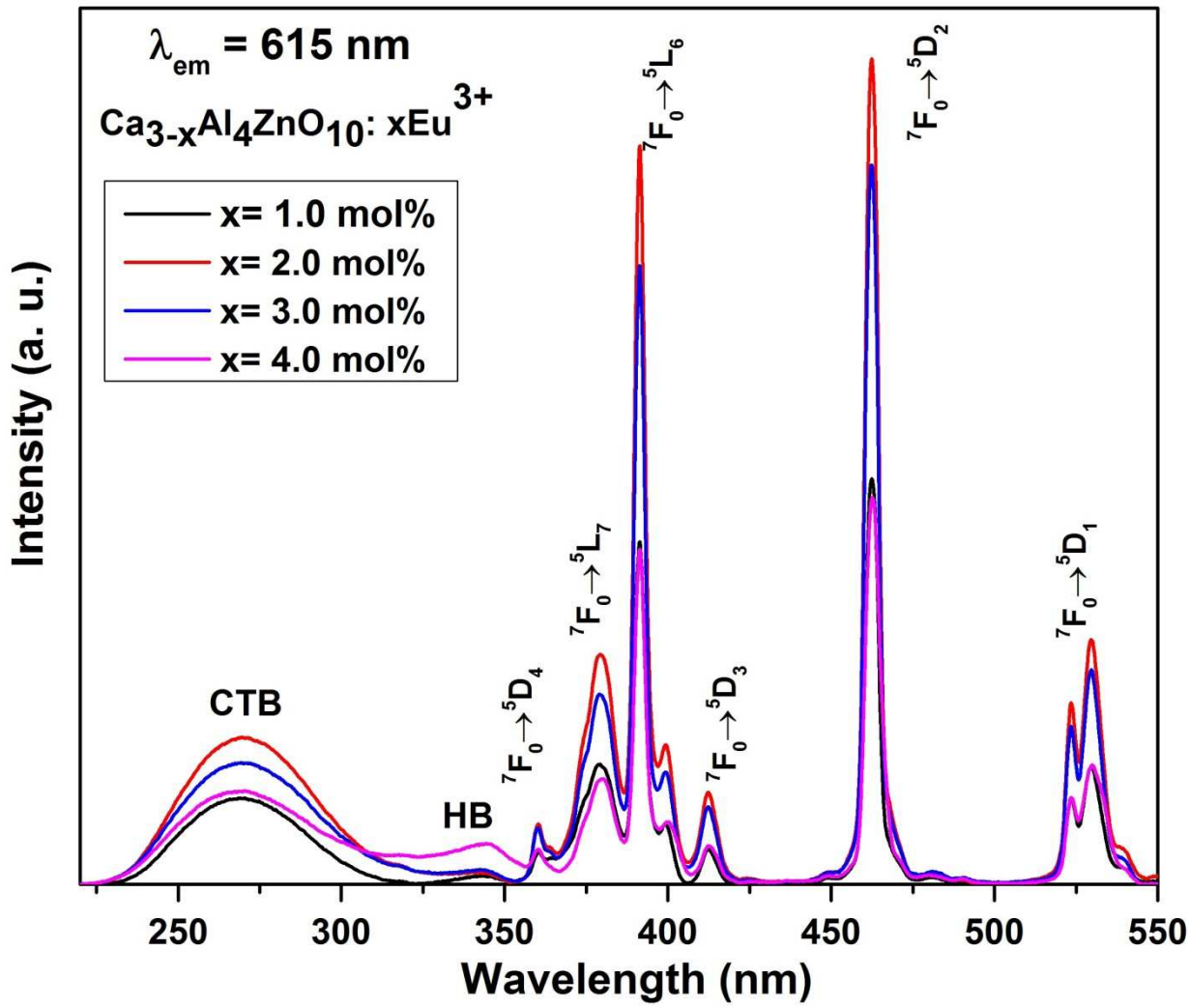
ACCEPTED

Fig. 4:



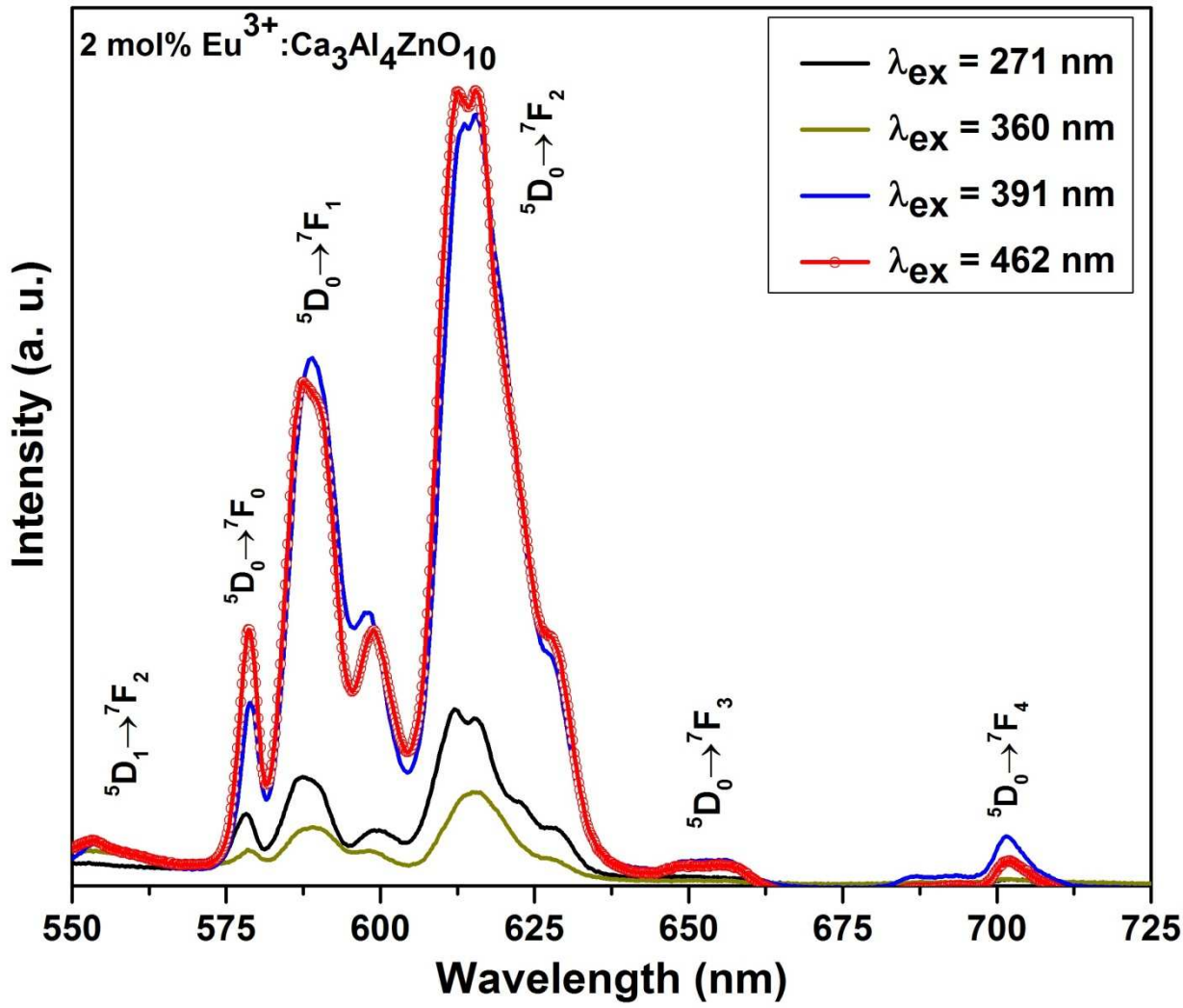
ACCEPTED

Fig. 5:



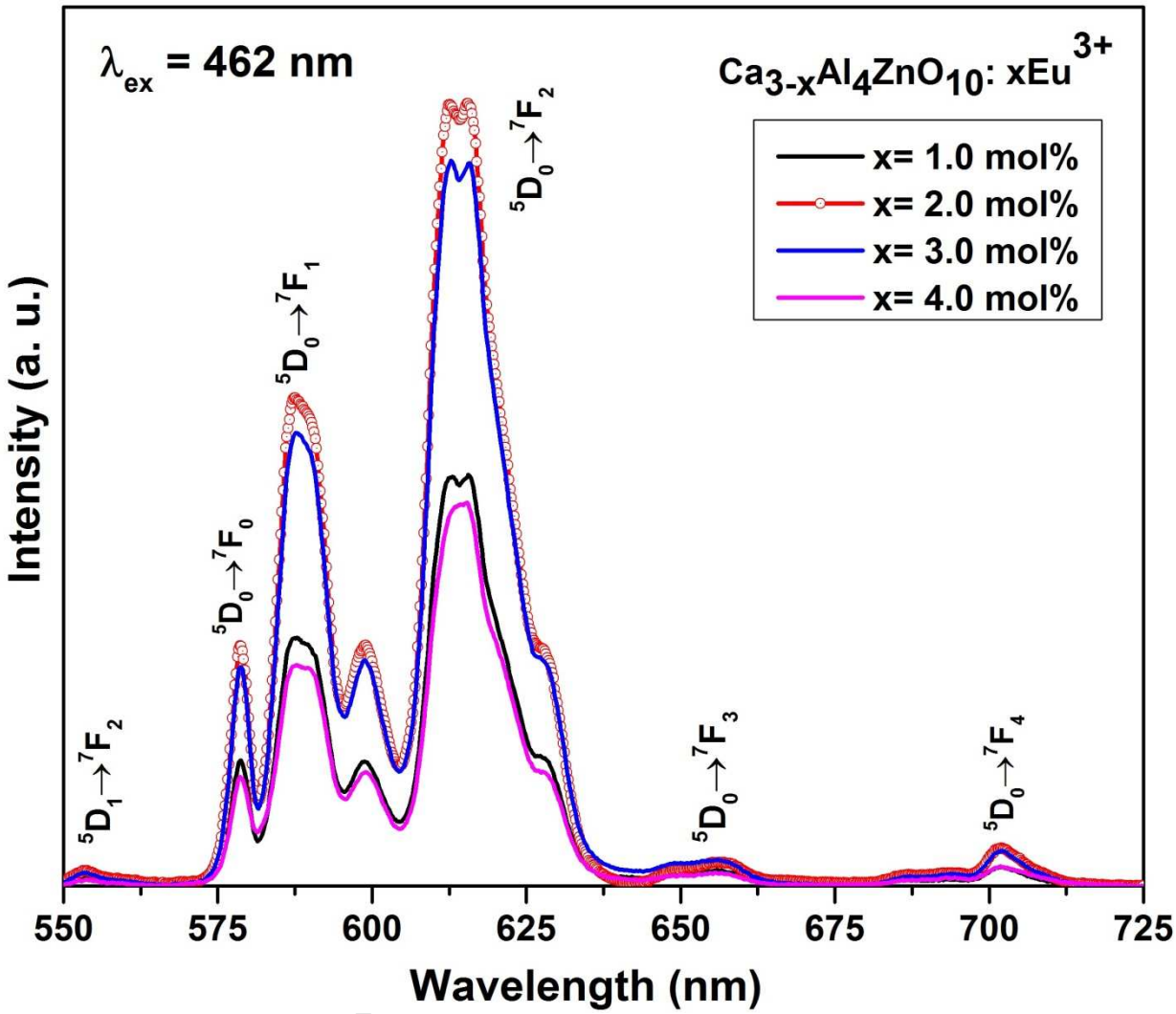
ACCEPTED MANUSCRIPT

Fig. 6(a):


2 mol% Eu3+:Ca3Al4ZnO10
λex = 271 nm
λex = 360 nm
λex = 391 nm
λex = 462 nm
5D1→7F2
5D0→7F0
5D0→7F1
5D0→7F2
5D0→7F3
5D0→7F4
Intensity (a. u.)
Wavelength (nm)
550
575
600
625
650
675
700
725

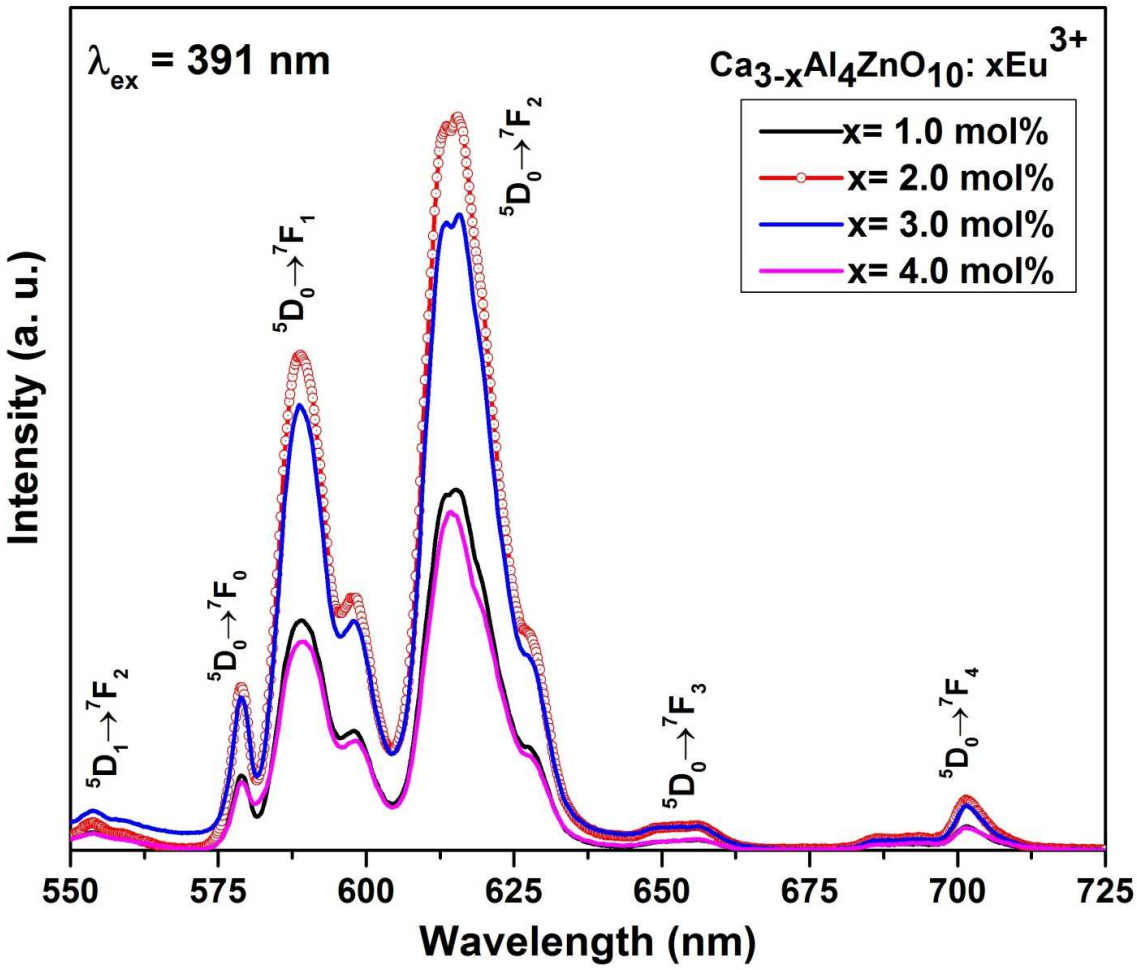
ACCEP

Fig. 6(b):



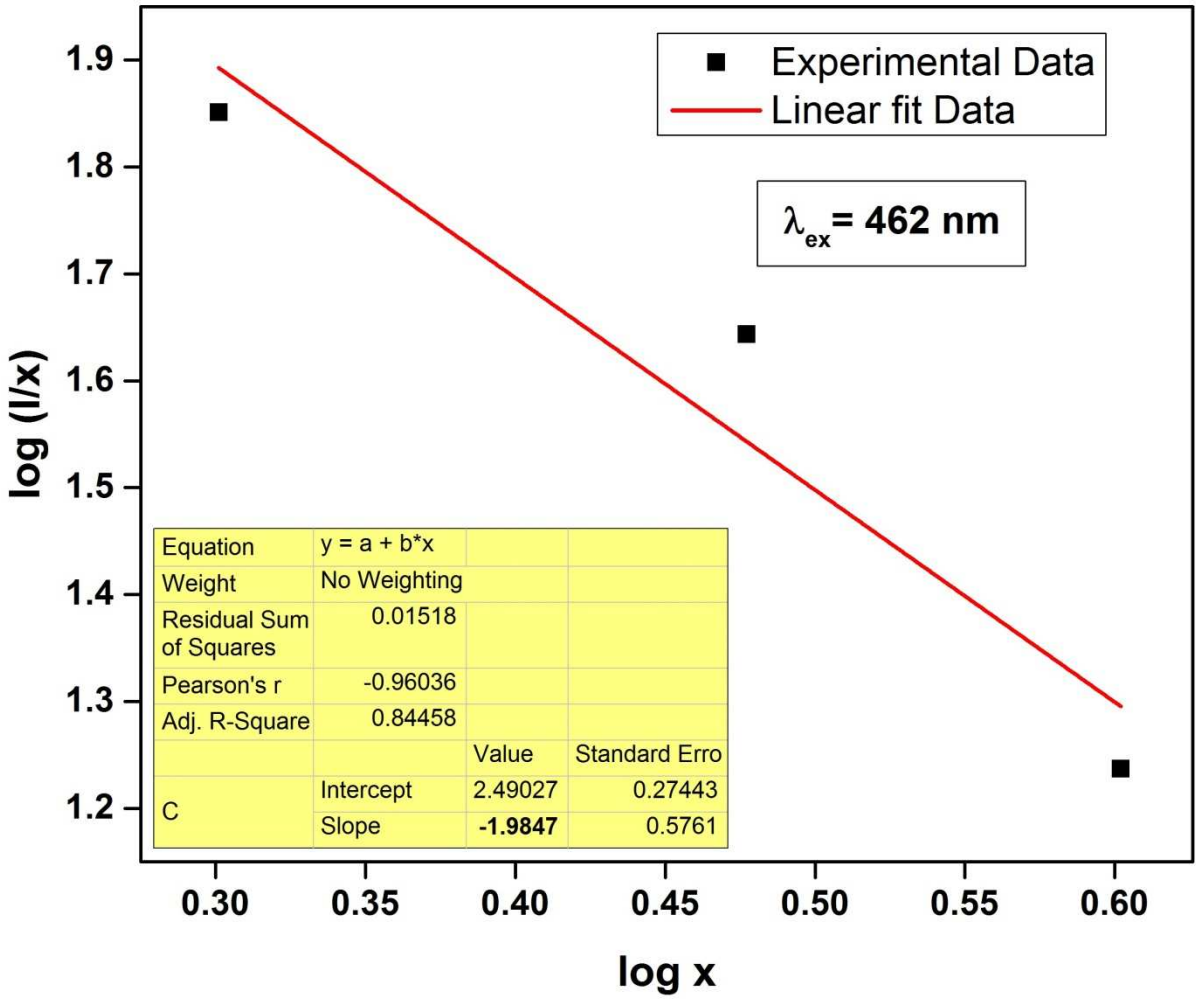
ACCEPTED MANUSCRIPT

Fig. 6(c):



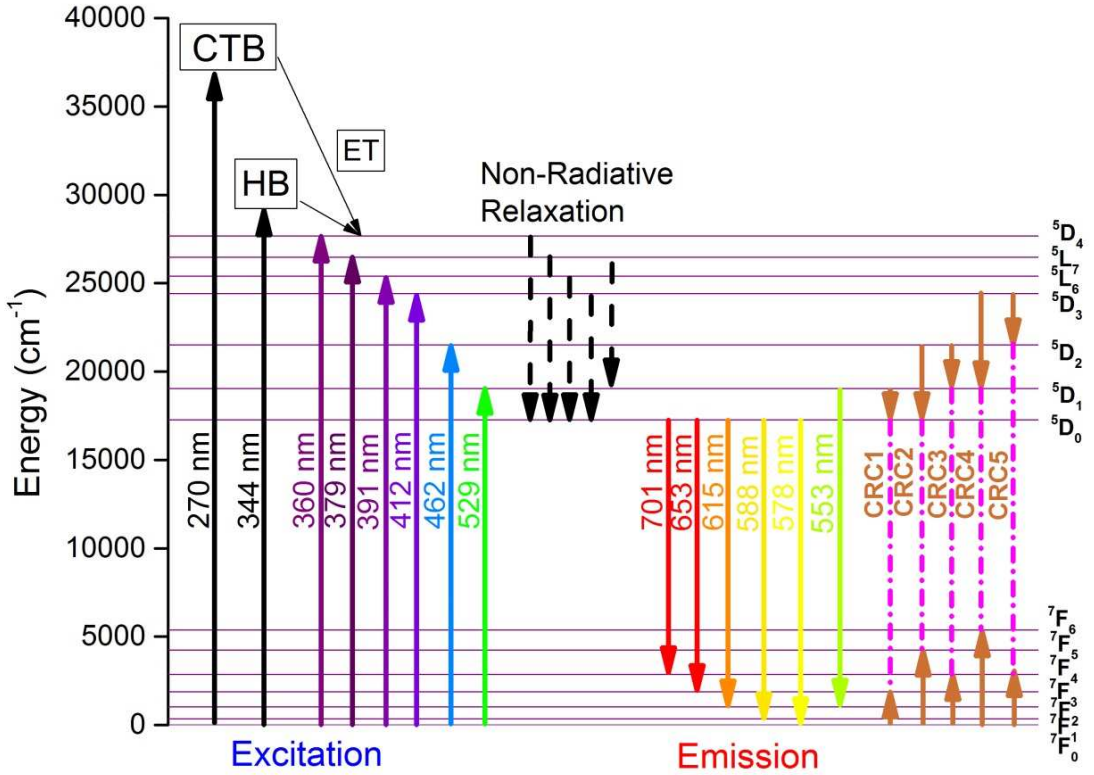
ACCEPTED

Fig. 7:



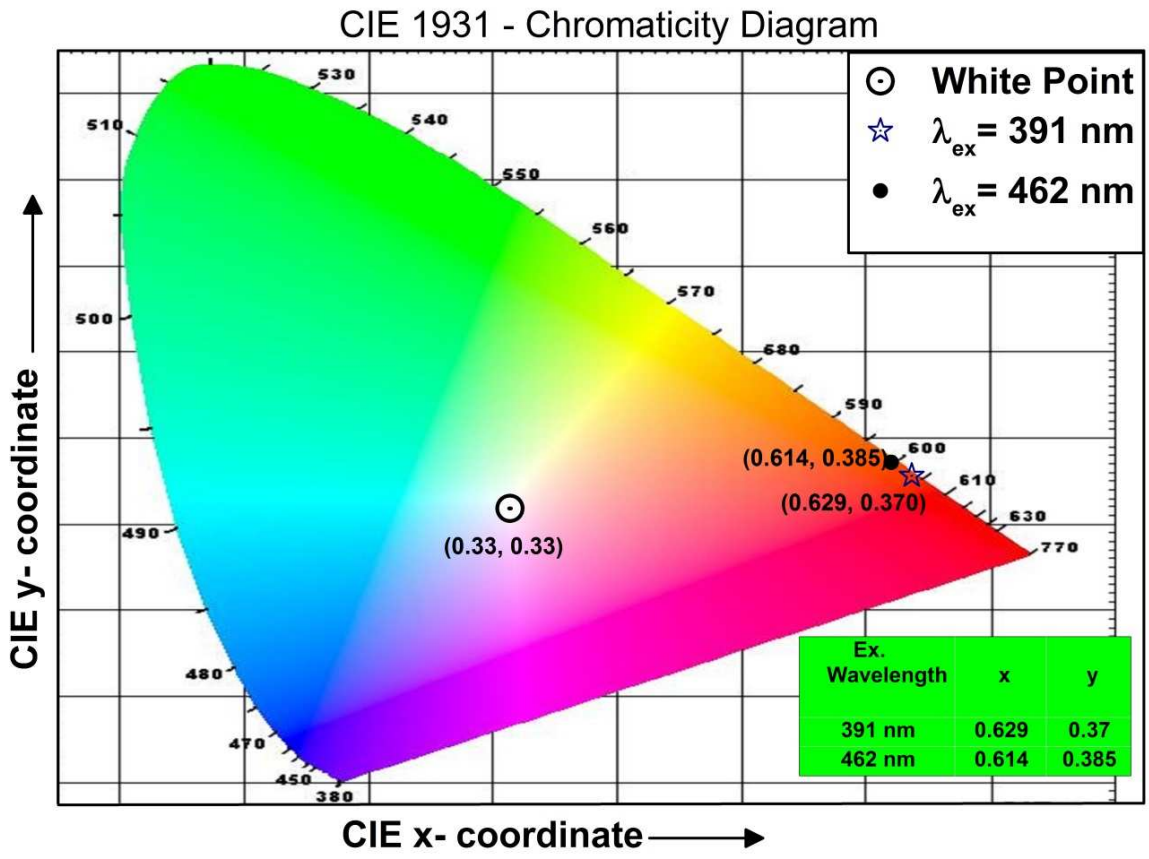
ACCEPTED

Fig. 8:



ACCEPTED MANUSCRIPT

Fig. 9:



ACCEPTED

ACCEPTED MANUSCRIPT

Highlights

- Novel $Ca_{3-x}Al_4ZnO_{10}$: xEu^{3+} phosphor prepared by using solid state reaction method.
- XRD studies confirm single phase orthorhombic structure with Pbc2 space group.
- Under n-UV/blue excitation the phosphors are showing bright visible red emission.
- Calculated CIE coordinates are close to the commercial red phosphor (Y_2O_2S: Eu^{3+}).
- Results suggest that this phosphor can be used as red component for RGB w-LEDs

ACCEPTED MANUSCRIPT

A Priority Based WSN Clustering of Multiple Sink Scenario using Artificial Bee Colony Algorithm

Ravi Teja
Department of Electronics and Communication Engineering
Delhi Technological University
New Delhi, India

Dr. S. Indu
Department of Electronics and Communication Engineering
Delhi Technological University
New Delhi, India

***Abstract*—Wireless Sensor Networks are limited by the battery lifetime of the sensor nodes as well as gateways and should be able to send useful packets to the Sink. Therefore, energy efficiency and data packets are the primary parameters which have to be considered while designing clustering and routing algorithms for WSN. This paper presents an energy efficient as well as a priority based wireless sensor network clustering and routing algorithm for a multiple sink scenario using Artificial Bee Colony Optimization with a multi objective fitness function which takes into account the priority of each sink, energy of gateway, sensor and distance of sensor node to the gateway which reduces the energy consumption of the network and ensures the sinks with more priority receive more packets. The proposed algorithm has been extensively tested in MATLAB and the results are shown in terms of data packets sent to each sink, the total energy of gateways, the total energy of sensors, dead nodes in each round and the lifetime of the network.**

Keywords—Wireless Sensor Network, Artificial Bee Colony Optimization, Multiple Sink, Clustering, Priority, Routing.

I. INTRODUCTION

Wireless Sensor Networks consists of sensors, gateways (cluster head) and sinks which communicate with each other in order to extract some useful information with minimal power dissipation and maximum coverage of the scenario. These networks are used in a wide range of applications ranging from space science to disaster management. But they are limited by the battery lifetime of the sensor nodes as well as that of gateways. Therefore, the main constraint in deploying the Wireless Sensor Network is the design of the algorithms that try to minimize the energy dissipation of nodes in each round without any significant loss and delay of information.

Clustering and routing algorithms have been applied to wireless sensor networks for the gateway assignment, for determining the optimal path to communicate the information to the sink, in order to increase energy efficiency and for maximum coverage of the scenario. Clustering algorithms divide the whole scenario into smaller bunches of regions based on certain factors which may include energy of node, energy of gateway, transmission range and priority while routing algorithms are used to assign the optimal path for every sensor node to send its data to sink via gateways or other sensor nodes which depends on the application.

The rest of the paper is organized as follows. Section II presents the related work, where some of the existing literature is highlighted; Section III presents the problem statement where some of the limitations of existing algorithm are shown and presents the advantages of the proposed algorithm. Section IV presents a brief summary of the proposed work and Section V shows the Simulation results. Finally, Section VI shows the Conclusion.

II. RELATED WORK

Many clustering algorithms have been proposed for Wireless Sensor Network whose main focus is on energy efficiency, deployment of sensor nodes and coverage of the scenario. Leach Algorithm [1] was one of the earliest proposed algorithms for WSN clustering for energy efficiency, cluster head is elected in each round in a cluster based on certain probability which forwards the data packet of each sensor in that cluster to sink and cluster head changes in each round. A priority based clustering for WSN was proposed in [2], sensor node with heavier traffic was given more priority than others and analysis was performed using Imbedded Markov Scheme. Gravity algorithm was implemented in WSN clustering in [3] for multiple sink scenario and the simulation results showed that power consumption was lower in scenario in comparison to the single sink scenario. A multiple sink approach in which Integer Linear Programming (ILP) was used to find the optimal location of sink for energy efficiency was proposed in [4]. Particle Swarm Optimization was used to reduce the hop distance between the sink and sensor node in [5] for multiple sink deployment in which the whole scenario was divided into multiple clusters with each cluster containing one sink for reducing the energy consumption of sensor nodes and Particle Swarm Optimization was applied for optimal deployment of multiple sink in [6] which was used for energy efficiency and lifetime balancing. A priority based clustering to reduce traffic for controlling network overload was implemented using congestion aware routing in [7] and ECPSOA was used for routing recovery protocol in WSN with multiple sinks in [8].

Artificial Bee Colony Optimization [9] is an evolutionary algorithm with a very fast convergence rate based on nonlinear programming techniques and is a new swarm the intelligence algorithm inspired by intelligent foraging of honey bees during their search for food. The algorithm is used to find a globally optimal solution for a given problem, especially when the solution space is very large. It improves the available solutions

978-1-5090-1022-6/16/$31.00 ©2016 IEEE

using the existing solution and a randomly chosen candidate solution.

III. Problem Statement

Existing algorithms don't take into account the priority assigned to each sink for clustering and routing. There are many applications, especially in defense applications where some of the base stations have more priority to receive information in comparison to others and simultaneously we have to ensure that, WSN networks are limited by energy of gateways as well as the sensor nodes. So there is a need for designing an algorithm which takes into account both the energy consumption of network, energy of sensor nodes and gateways as well as prioritization of base stations. Therefore, in order to address these issues we have designed a clustering algorithm for gateway assignment as well as a sink assignment to each sensor node based on artificial bee colony optimization with a multi objective fitness function which is used in clustering as well as routing for a WSN scenario which takes into account the energy of the sensors, energy of the gateways, distance of gateway to sensor node and priority assigned to each sink. The advantage of our algorithm is that it increases the energy efficiency of the network and simultaneously ensures the integrity of data so that only the sinks with more priority receive maximum packets.

IV. Proposed Algorithm

A Two-dimensional rectangular space is created with predefined maximum and minimum values of the x and y coordinates. A Fixed number of Sensors and gateways are deployed in the scenario with random locations and a total of 5 sinks are deployed in the area with fixed locations. Energy of sensor nodes are initialized, gateways are given extra energy due to their more energy consumption while sinks have unlimited energy. Clustering is performed using Artificial Bee Colony Optimization. An initial population of bees is created with each bee representing a two dimensional array; each element of array will contain cluster head (gateway) assigned to that particular sensor node element as well as the sink assigned to the sensor which is same as the sink assigned to the gateway of that sensor. The fitness value of each bee is calculated using a multi-objective fitness using Eq. 1 which has to be maximized that takes into account the following parameters:-

i) Distance between the sensor node and the cluster head (gateway)
ii) Energy of the Sensor Node
iii) Energy of the Gateway
iv) Priority of Sink assigned to that Node

$$Fitness = k1*E_S + k2*(1/Dist(node, gateway)) + k3*E_G + k4*Priority_S \quad (1)$$

Fitness=Fitness value of each bee
E_S=Energy of sensor
E_G=Energy of Gateway
Priority_S=Priority of Sink assigned to that sensor
k1, k2, k3, k4=Constants.
Subsequent better population is created using Eq. 2.

$$Gw(i) = Gw(i) + r*(Gw(i) - Gw(j)) \quad (2)$$

$Gw(i)$ = Existing Bee

$Gw(j)$ =Randomly Chosen Bee

r =Random Number Between -1 and 1

Ceil function is used if the gateway or sink number is a fraction; if the gateway or sink value exceeds maximum value, then it is assigned random gateway or sink and vice-versa. Sensor Network with the best fitness value is chosen as the final network for simulation. For each sensor, the routing path or the data packet will be first transmitted from the sensor to gateway, gateway aggregates all the data packets received by it from all the sensors which are assigned to it and the data is directly forwarded by the gateway to the assigned sink. The energy consumption of nodes and gateways is based on the energy model in [10]. Simulation results are also shown in terms of total packets received by each sink, round at which first sensor node dies and lifetime of sensor network which is equal to round at which first gateway dies.

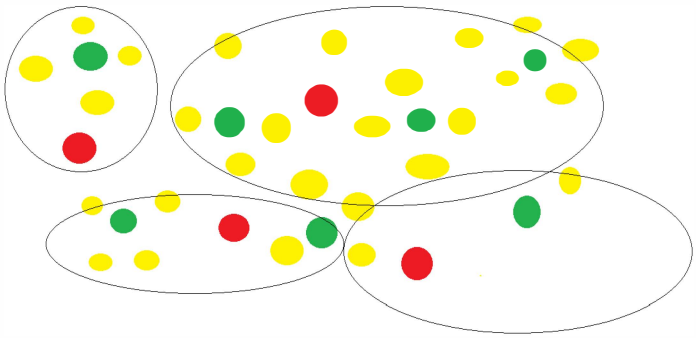


Fig.1. Clustering of Scenario- Sensors marked with Yellow color, Gateways with Green and Sinks with Red.

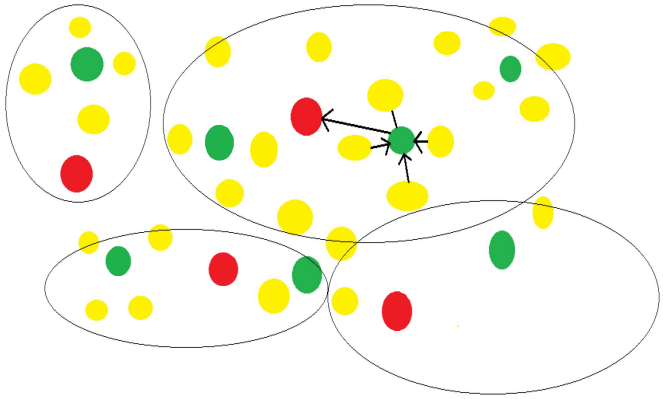


Fig.2. Routing of data packets of Sensor via assigned Gateway to assigned Sink

V. Simulation Results

The proposed algorithm was implemented in MATLAB IDE. A rectangular scenario of 100x100 m was created which can be varied depending on the application. Total number of sensors was set to 150, gateways to 20, there were 5 sinks in the scenario and Priority of Sink at (25, 25) is least (5^{th}), Priority of Sink at (75, 25) is (4^{th}), Priority of Sink at (25, 75)

is 3rd, Priority of Sink at (75, 75) is 2nd and Priority of Sink at (50, 50) is highest. The energy of the sensors was initialized to 0.1J, gateways to 0.5J. The number of bees was set to 50; iterations for further improvement using ABC were set to 10 while the number of rounds of communication of sensor nodes to sink of WSN was set to 8000. Fig.3 shows the WSN scenario after optimization using Artificial Bee Colony Algorithm. Fig.4 and Fig.5 shows the number of dead nodes, the number of dead gateways with rounds, the number of dead nodes and gateways increases with time and the rate at which the gateways and sensors die also increases with time. Fig.6 shows the total packets sent in each round, the rate of packets sent decreases with time and suddenly the value is very less in higher rounds because of high death rate of sensors. Fig.7 and Fig.8 shows the total energy of nodes and gateways with rounds. Fig 9-13 shows the packets received by each sink in each round; sinks with the more priority received maximum packets. Fig.14 shows the number of sensors assigned to each gateway and Fig.15 shows the numbers of sensors assigned to each sink, sinks with more priority are assigned more sensors. Table-1 shows the lifetime of WSN which is equal to the round at which the first gateway is dead and packets received by each sink. Sinks with more priority (1st and 2nd) receive maximum packets. Sink with most priority received less information than Sink with 2nd because the energy and distance were also considered during the assignment of gateways and sink.

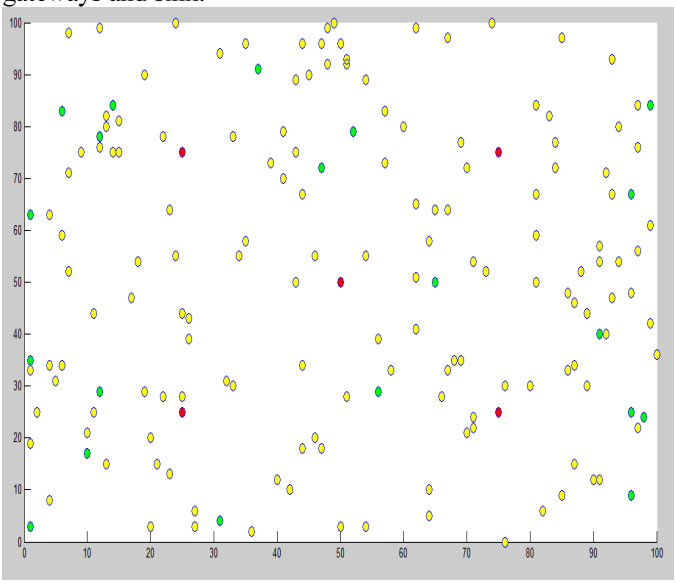


Fig.3. WSN Scenario using the Proposed Algorithm

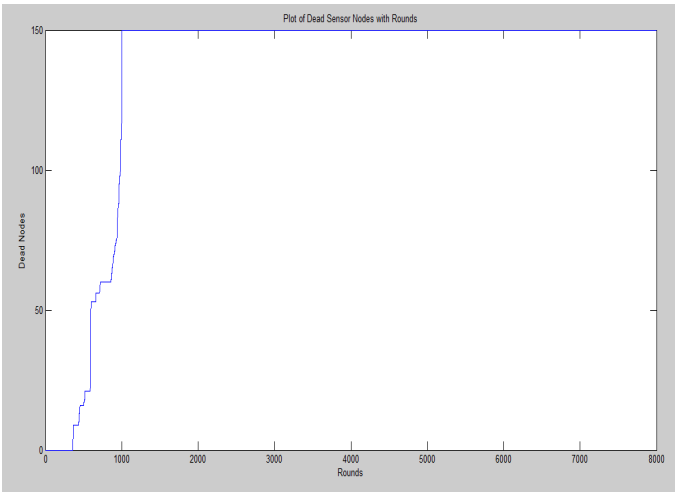


Fig.4. Number of Dead Sensor Nodes with Rounds

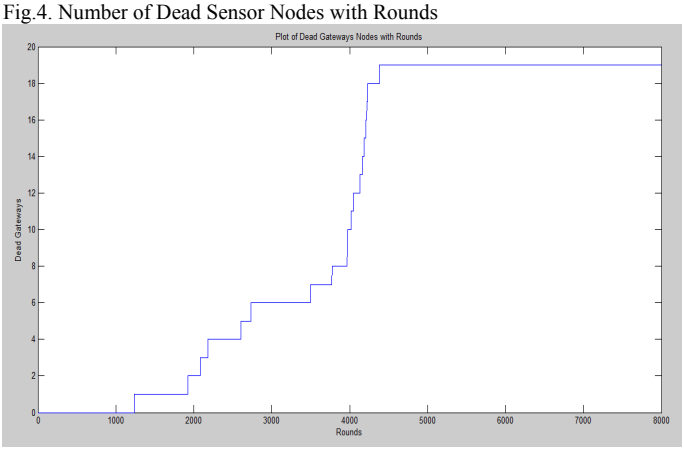


Fig.5. Number of Dead Gateways with Rounds

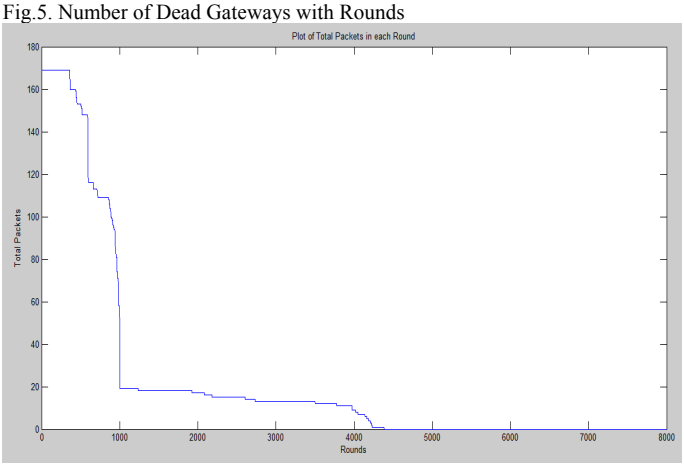


Fig.6. Total Packets Sent in each Round with Time

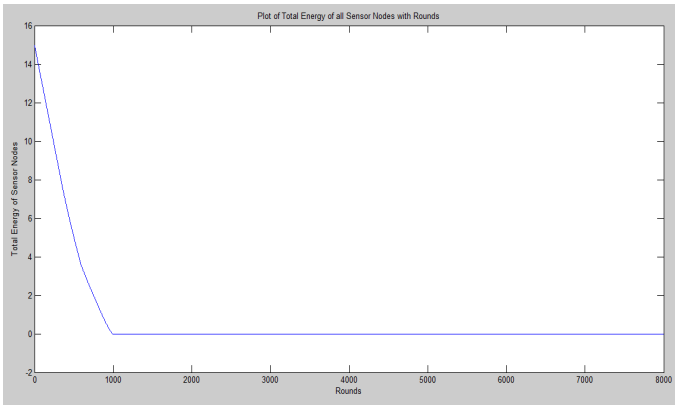


Fig.7. Total Energy of Sensor Nodes with Rounds

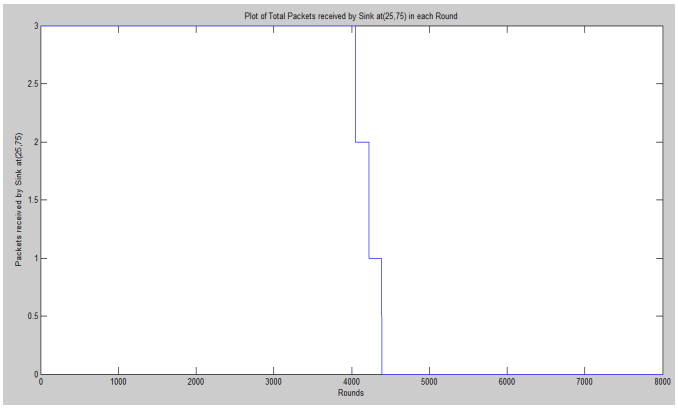


Fig.11. Total Packets Received by Sink at (25,75) in each round

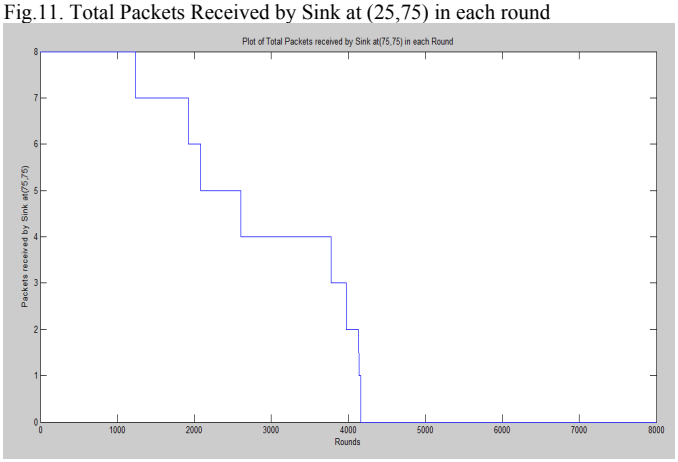


Fig.8. Total Energy of Gateways with Rounds

Fig.12. Total Packets Received by Sink at (75,75) in each round

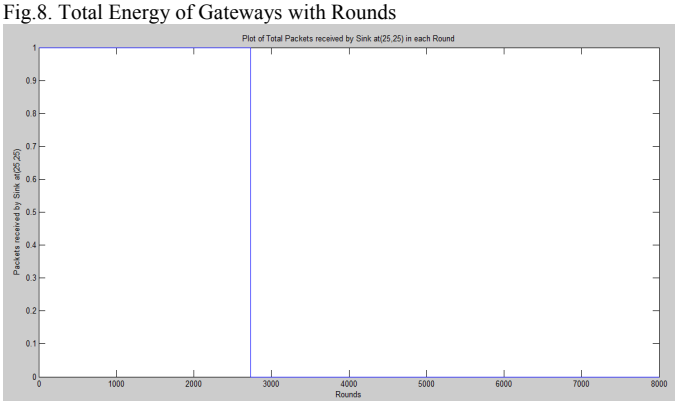


Fig.9. Total Packets Received by Sink at (25,25) in each round

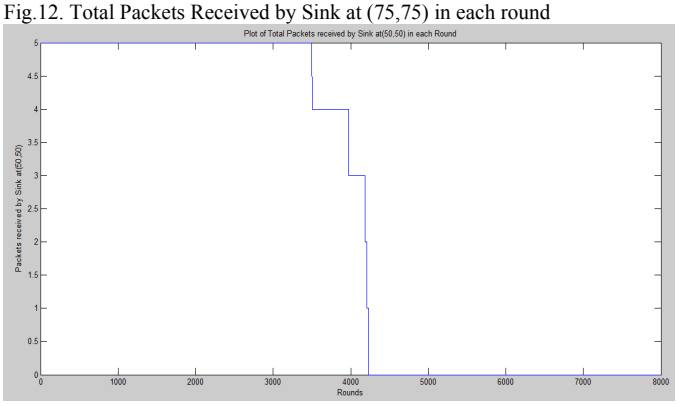


Fig.13. Total Packets Received by Sink at (50,50) in each round

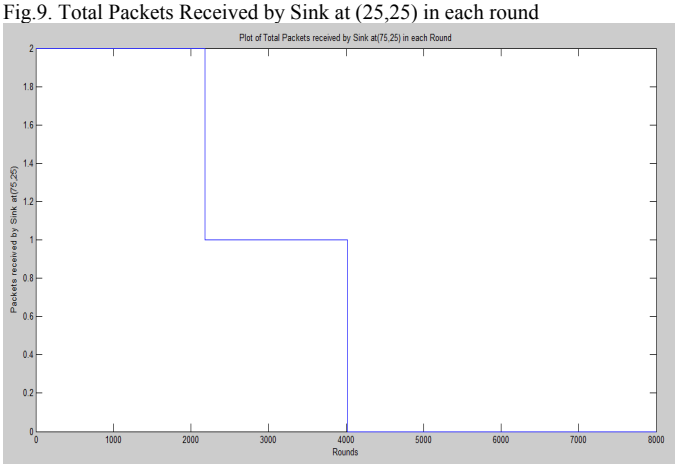


Fig.10. Total Packets Received by Sink at (75,25) in each round

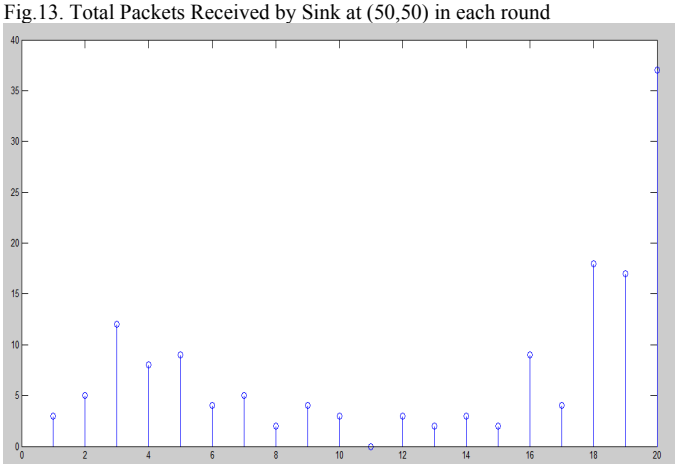


Fig.14. Total Sensor Nodes assigned to each Gateway

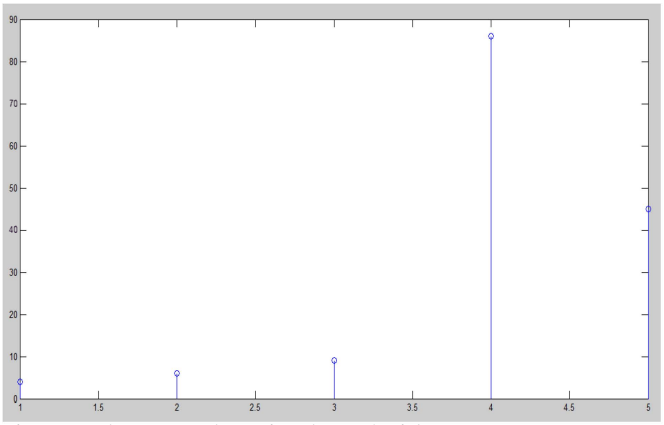


Fig.15. Total Sensor Nodes assigned to each Sink

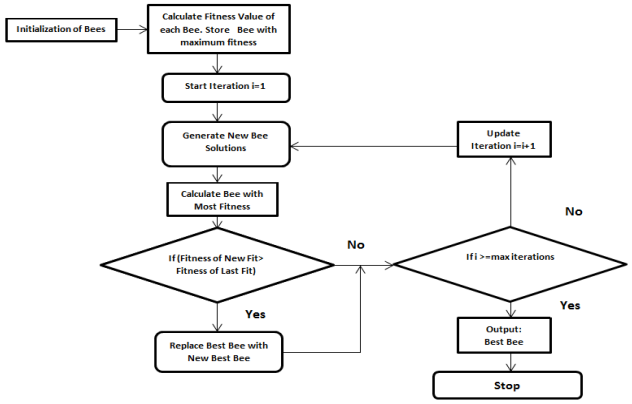


Fig 16 Flowchart of Proposed Algorithm

Total Packets Received By Sink at (25,25)	2733
Total Packets Received By Sink at (75,25)	6197
Total Packets Received By Sink at (25,75)	12652
Total Packets Received By Sink at (75,75)	23891
Total Packets Received By Sink at (50,50)	20088
Lifetime of Network (Round at which first gateway is dead)	1234
Round at which first sensor is dead	361

Table.1. Simulation Results

Number of Sensor Nodes	150
Number of Gateway	20
Number of Sinks	5
Energy of Sensor	0.1 J
Energy of Gateway	0.5 J
k1	0.01
k2	0.01
k3	1
k4	0.0004
Number of Bees	50
Number of Iterations	10
Maximum Rounds	8000

Table.2 Parameters used in the Scenario

VI. Conclusion

This paper presents a novel Priority based clustering and routing algorithm for Wireless Sensor Network of a Multiple Sink Scenario based on Artificial Bee Colony Optimization. A multi-objective fitness function was used to find optimal clustering using energy of node, energy of gateway, priority of sink assigned to the sensor node and distance of gateway to node. The simulation results were shown in terms of number of packets received by each sink, total energy of sensor nodes, total energy of gateways, dead nodes, dead gateways with rounds, the total sensors assigned to each gateway, the total gateways assigned to each sink and the lifetime of the sensor network. Sink with more priority received more packets in comparison to others, also sink with less priority, but which has gateway at less distance from sensor nodes also receives more packets in comparison to more prior sinks which shows the effectiveness of the proposed algorithm.

References

[1] Wendi Rabiner Heinzelman, Anantha Chandrakasan, and Hari Balakrishnan, "Energy Efficient Communication Protocol for Wireless Sensor Networks", 33rd Hawai International Conference on System Science, IEEE, 2000, pp. 4-7.

[2] Zhuguan Liang and Dongfeng Zhao, "A Priority-based polling scheme for Clustering Wireless Sensor Network MAC Protocols," The 1st International Conference on Information Science and Engineering ICISE, 2009 , pp. 2488-2491.

[3] M. Gracio A.R and Ihan Martoyo, "Gravity Algorithm for Wireless Sensor Networks with Multiple Sinks", 17th Asia-Pacific Conference on Communications (APCC), 2011, pp. 121-126.

[4] Leila Ben Saad and Bernard Tourancheau, "Multiple Mobile Sinks Positioning in Wireless Sensor Networks for Buildings", Third International Conference on Sensor Technologies and Applications, 2009, pp. 264-270.

[5] Deepak R Dandekar and P R Deshmukh, "Energy Balancing Multiple Sink Optimal Deployment in Multi-hop Wireless Sensor", 3rd IEEE International Advance Computing Conference (IACC), 2013, pp. 402-412.

[6] Mohan Kadasali ,Geetha N B and Mohamed Rafi, " An Energy Efficient Data Collection Scheme for Multiple Sink in Wireless Sensor Network", International Journal of Innovative Research in Computer and Communication Engineering, Vol.3, Issue.4, April 2015, pp. 2780-2784.

[7] Swimpy Pahuja and Ram Kumar Ankit Verma Sandeep Negi and Himanshu Arora, " Priority Based Approach against Congestion in Sensor Network", 2011 Annual IEEE India Conference, pp. 1-4.

[8] YiFan Hu , XiaoMing Wu, FuQiang Wang, Xiangzhi Liu, Hua Han,"A Novel Routing Recovery Strategy Based on Particle Swarm Optimization for Wireless Sensor Networks with Multiple Mobile Sink", 13th International Conference on Control, Automation, Robotics & Vision, 10-12th December 2014 (ICARCV 2014), pp. 681-686

[9] D. Karaboga, "AN IDEA BASED ON HONEY BEE SWARM FOR NUMERICAL OPTIMIZATION", TECHNICAL REPORT-TR06, Erciyes University, Engineering Faculty, Computer Engineering Department 2005, pp. 1-10.

[10] Heinzelman, W.B., et al., 2002, "Application specific protocol architecture for wireless microsensor networks", IEEE Transactions on Wireless Communication, pp. 660–670.

3rd International Conference on Recent Innovations in Science, Technology, Management and Environment
Indian Federation of United Nations Associations, New Delhi, India (ICRISTME-16)
18th December 2016 , www.conferenceworld.in ISBN: 978-93-86171-13-9

A STUDY OF PERCEIVED QUALITY OF LIFE OF PEOPLE IN GUJARAT

Rajesh Handa[1], Dr. G.C.Maheshwari[2].

[1]*Rajesh Handa, Management, Manish Institute of Management, Gujarat, (India)*
[2]*Dr. G.C.Maheshwari, Management, Delhi Technological University, Delhi, (India)*

ABSTRACT

This paper examined the perceived quality of life (well-being) of people of Gujarat state, with a 410 adult sample. It investigated first Overall life satisfaction with the help of "satisfaction with life scale" (standardized scale by Dinner). Second, the relation between demographic characteristics like gender, age, education, marital status, income and locality with perceived quality of life. Employing descriptive approaches through a modified questionnaire (Life-domain satisfaction scale). Parametric tests used like One-sample t-test, Independent sample t-test, One Way Annona for hypothesis testing.

Keywords: Well-being, Perceived Quality of Life, Overall Life-satisfaction, Satisfaction with life scale, Life domain satisfaction scale.

I INTRODUCTION

"Quality of life and its assessment is a challengeable task; still to improve it is a primary goal of any government & Individuals too. By many years we are measuring quality of life in terms of HDI (Human development Index) and accordingly ranking of the nations takes place which shows their well-being and quality of life in the country. HDI is an objective approach to access quality of life. But the second approach to measure Quality of life is subjective approach which we called perceived quality of life or happiness. Many researches has contributed their work in measuring PQOL or happiness of the nations and now a days World happiness Index is one of popular approach to measure the quality of life. As we noticed countries like Bhutan had focused on GNP (Gross national happiness) instead of GDP." This study is also an approach towards measuring PQOL of individuals in Gujarat.

II OBJECTIVES

I. To access global life satisfation of the inhabitants of Gujarat.
II. To examine whether perceived quality of life varies with sex, age, marital status, education status, income level and locality.

ISBN: 978-93-86171-13-9

III RESEARCH METHODOLOGY

- Research type: Quantitative Research.
- Descriptive Research.
- Population: Gujarat.
- Data used: Primary.
- Data Collection Tool: Structured Questionnaire
- Data Collection method: Survey (personal interaction).
- Survey method: Convenience Sampling (Non-Probability).
- Sample unit: People (ordinary resident).
- Sample Size: 410 respondents.

IV LIMITATIONS OF THE STUDY

i. Under certain time limit 425 samples has collected, out of which 410 sample became part of this study.
ii. Sampling frame was not present. Non-random, Convenience sampling method has used.
iii. Respondent has limited to working class people with certain age limit (25-55), education (S.S.C. Pass and above.) and income levels (1.20 lakh to 10 lakhs).

V RESEARCH TOOLS USED

1. Global life satisfaction scale.
2. Life domain satisfaction scale.

5.1 Reliability Check

1. Global life satisfaction scale.

Reliability Statistics

Cronbach's Alpha	N of Items
.700	5

Table: 1

***Interpretation*:** Cronbachs Alpha value **0.700 = 0.7**. This is a good sign of reliability.

2. Life domain satisfaction scale.

Reliability Statistics

Cronbach's Alpha	N of Items
.933	38

Table: 2

***Interpretation*:** Cronbach's Alpha value **0.933 > 0.7**. This is a good sign of reliability.

VI RESEARCH HYPOTHESIS

Hypothesis 1: People are not neutral towards their perceived QOL.

Hypothesis 2: Males and females vary significantly in their perceived QOL.

Hypothesis 3: Individuals belonging to different age groups vary significantly in their perceived QOL.

Hypothesis 4: Individuals belonging to different education status vary significantly in their perceived QOL.

Hypothesis 5: Individuals belonging to different marital status vary significantly in their perceived QOL.

Hypothesis 6: Individuals belonging to different income groups vary significantly in their perceived QOL.

Hypothesis 7: Perceived QOL vary with individuals belonging to Central Gujarat, South Gujarat, Saurastra and North-Gujarat.

Hypothesis 8: Perceived QOL vary with individuals belonging to rural and urban Gujarat.

VII HYPOTHESIS TESTING

1. H_O: Peoples are neutral about their perceived quality of life.

   H_1: People are not neutral about their perceived quality of life

One-Sample Test

	Test Value = 4					
	t	df	Sig. (2-tailed)	Mean Difference	95% Confidence Interval of the Difference	
					Lower	Upper
sw	23.680	409	**.000**	1.05756	.9698	1.1454

Table: 3

Interpretation: Here, p-value **0.000 < 0.05**, so we reject null hypothesis. Alternate hypothesis is accepted. People are not neutral about their perceived quality of life. Peoples are somewhat satisfied toward their perceived quality of life.

2. H_O: There is no significant difference between Males and females in their PQOL.

   H_1: There is significant difference between Males and females in their PQOL.

Independent Samples Test

		Levene's Test for Equality of Variances		t-test for Equality of Means						
		F	Sig.	t	df	Sig. (2-tailed)	Mean Difference	Std. Error Difference	95% Confidence Interval of the Difference	
									Lower	Upper
sw	Equal variances assumed	12.595	**.000**	-.531	408	.596	-.05245	.09873	-.24654	.14164
	Equal variances not assumed			-.481	178.588	**.631**	-.05245	.10909	-.41072	.16283

Table: 4

Interpretation: Here, p-value **0.631 > 0.05**, so we fail to reject null hypothesis. Null hypothesis is accepted. There is no significant difference between males and females in their perceived QOL.

3. H_0: There is no significant difference Individuals belonging to different age groups in their perceived QOL.
H_1: There is significant difference between individuals belonging to different age groups in their perceived QOL.

Levene's Test of Equality of Error Variances[a]

Dependent Variable: sw

F	df1	df2	Sig.
.119	2	407	**.888**

Tests the null hypothesis that the error variance of the dependent variable is equal across groups.

a. Design: Intercept + Age

Table: 5

Tests of Between-Subjects Effects

Dependent Variable: sw

Source	Type III Sum of Squares	df	Mean Square	F	Sig.
Corrected Model	4.434[a]	2	2.217	2.734	**.066**
Intercept	7141.012	1	7141.012	8805.969	.000
Age	4.434	2	2.217	2.734	**.066**
Error	330.048	407	.811		
Total	10821.840	410			
Corrected Total	334.482	409			

a. R Squared = .013 (Adjusted R Squared = .008)

Table: 6

sw

Tukey HSD[a,b,c]

Age	N	Subset
		1
26-35	264	**4.9947**
36-45	92	**5.0935**
46-55	54	**5.3037**
Sig.		.056

Means for groups in homogeneous subsets are displayed.

Based on observed means.

The error term is Mean Square (Error) = .811.

a. Uses Harmonic Mean Sample Size = 90.427.

b. The group sizes are unequal. The harmonic mean of the group sizes is used. Type I error levels are not guaranteed.

c. Alpha = .05.

Table: 7

Findings: Levene's test = 0.888, it shows homoscedascity. Basic condition of constant error variance has sustained. Model is insignificant (0.066 > 0.05). Adjusted R square is 8%.

Interpretation: Here, p-value **0.066 > 0.05**, so we fail to reject null hypothesis. Null hypothesis accepted.There is no significant difference between individuals belonging to different age groups varies significantly in their perceived QOL**.**

4. H_0: There is no significant difference between Individuals belonging to different education status in their perceived QOL.

H_1: There is significant difference between Individuals belonging to different education status vary significantly in their perceived QOL.

Levene's Test of Equality of Error Variances[a]

Dependent Variable: sw

F	df1	df2	Sig.
.690	2	407	**.502**

Tests the null hypothesis that the error variance of the dependent variable is equal across groups.

a. Design: Intercept + Education.

Table: 7

Tests of Between-Subjects Effects

Dependent Variable: sw

Source	Type III Sum of Squares	df	Mean Square	F	Sig.
Corrected Model	.452[a]	2	.226	.275	**.759**
Intercept	8145.840	1	8145.840	9925.336	.000
Education	.452	2	.226	.275	**.759**
Error	334.030	407	.821		
Total	10821.840	410			
Corrected Total	334.482	409			

a. R Squared = .001 (Adjusted R Squared = -.004)

sw

Tukey HSD[a,b,c]

Education	N	Subset 1
Below graduate	65	4.9877
Graduate	122	5.0508
Post graduate or above.	223	5.0816
Sig.		.729

Means for groups in homogeneous subsets are displayed.

Based on observed means.

The error term is Mean Square (Error) = .821.

a. Uses Harmonic Mean Sample Size = 106.892.

b. The group sizes are unequal. The harmonic mean of the group sizes is used. Type I error levels are not guaranteed.

c. Alpha = .05.

Findings: Levene's test = 0.502, it shows homoscedascity. Basic condition of constant error variance has sustained. Model is insignificant (0.759 > 0.05). Adjusted R square is 0%.

Interpretation: Here, p-value **0.0759 > 0.05**, so we fail to reject null hypothesis. Null hypothesis accepted. There is no significant difference between Individuals belonging to different education status in their perceived QOL.

5. H_0: There is no significant difference between Individuals belonging to different marital status in their perceived QOL.

H_1: There is significant difference between Individuals belonging to different marital status vary significantly in their perceived QOL.

Independent Samples Test

		Levene's Test for Equality of Variances		t-test for Equality of Means						
		F	Sig.	t	df	Sig. (2-tailed)	Mean Difference	Std. Error Difference	95% Confidence Interval of the Difference	
									Lower	Upper
sw	Equal variances assumed	.537	**.464**	-3.641	408	**.000**	-.36829	.10114	-.56711	-.16947
	Equal variances not assumed			-3.603	174.765	.000	-.36829	.10221	-.57001	-.16657

Table: 9

Interpretation: Here, p-value **0.000 < 0.05**. So we reject our null hypothesis. Alternate hypothesis accepted .There is significant difference between Individuals belonging to different marital status in their perceived QOL.

6. H_0: There is no significant difference between Individuals belonging to different income groups in their perceived QOL.

H_1: There is significant difference between Individuals belonging to different income groups vary significantly in their perceived QOL.

Levene's Test of Equality of Error Variances[a]

Dependent Variable: sw

F	df1	df2	Sig.
.313	2	407	**.732**

Tests the null hypothesis that the error variance of the dependent variable is equal across groups.

a. Design: Intercept + Income

Table: 11

Tests of Between-Subjects Effects

Dependent Variable: sw

Source	Type III Sum of Squares	df	Mean Square	F	Sig.
Corrected Model	13.047[a]	2	6.524	8.260	**.000**
Intercept	7774.319	1	7774.319	9843.832	.000
Income	13.047	2	6.524	8.260	**.000**
Error	321.435	407	.790		
Total	10821.840	410			
Corrected Total	334.482	409			

a. R Squared = .039 (Adjusted R Squared = .034)

sw

Tukey HSD[a,b,c]

Income	N	Subset	
		1	2
Lower income group	186	4.8688	
Middle income group	172		**5.1791**
Higher income group	52		**5.3308**
Sig.		1.000	.455

Means for groups in homogeneous subsets are displayed.
Based on observed means.
The error term is Mean Square (Error) = .790.
a. Uses Harmonic Mean Sample Size = 98.616.
b. The group sizes are unequal. The harmonic mean of the group sizes is used. Type I error levels are not guaranteed.
c. Alpha = .05.

Findings: Levene's test = 0.732, it shows homoscedascity. Basic condition of constant error variance has sustained. Model is significant (0.000< 0.05). Adjusted R square is 3%.

Interpretation: Here, p-value **0.000 < 0.05.** So we reject null hypothesis. Alternate hypothesis accepted. There is significant difference between Individuals belonging to different income groups vary significantly in their perceived QOL. PQOL of middle income group and higher income group are significantly higher than lower income group.

7. H_0: There no significant difference in PQOL of Individuals belonging to Central Gujarat, South Gujarat, Saurastra and North-Gujarat.

H_1: There significant difference in PQOL of Individuals belonging to Central Gujarat, South Gujarat, Saurastra and North-Gujarat.

Levene's Test of Equality of Error Variances[a]

Dependent Variable: sw

F	df1	df2	Sig.
1.565	3	406	**.197**

Tests the null hypothesis that the error variance of the dependent variable is equal across groups.

a. Design: Intercept + Res3

Table: 13

Tests of Between-Subjects Effects

Dependent Variable: sw

Source	Type III Sum of Squares	df	Mean Square	F	Sig.
Corrected Model	1.852[a]	3	.617	.754	**.521**
Intercept	10271.484	1	10271.484	12537.152	.000
Res3	1.852	3	.617	.754	**.521**
Error	332.629	406	.819		
Total	10821.840	410			
Corrected Total	334.482	409			

a. R Squared = .006 (Adjusted R Squared = -.002)

Table: 14

sw

Tukey HSD[a,b,c]

Residence3	N	Subset 1
Central-Gujarat	97	4.9567
South-Gujarat	87	5.0345
Saurastra	100	5.0760
North-Gujarat	126	5.1365
Sig.		.494

Means for groups in homogeneous subsets are displayed.
Based on observed means.
The error term is Mean Square (Error) = .819.
a. Uses Harmonic Mean Sample Size = 100.654.
b. The group sizes are unequal. The harmonic mean of the group sizes is used. Type I error levels are not guaranteed.
c. Alpha = .05.

Findings: Levene's test = 0.197, it shows homoscedascity. Basic condition of constant error variance has sustained. Model is insignificant (0.521 > 0.05). Adjusted R square is 0%.

Interpretation: Here, p-value **0.197 > 0.05.** So we fail to reject null hypothesis. Null hypothesis accepted. There no significant difference in PQOL of Individuals belonging to Central Gujarat, South Gujarat, Saurastra and North-Gujarat.

8. H_0: There is no significant difference between Individuals belonging to Rural Gujarat and Urban Gujarat in their perceived QOL.

H_1: There is no significant difference between Individuals belonging to Rural Gujarat and urban Gujarat in their perceived QOL.

Group Statistics

	Residence2	N	Mean	Std. Deviation	Std. Error Mean
sw	Rural	122	5.0213	.90465	.08190
	Urban	288	5.0729	.90532	.05335

Table: 15

Independent Samples Test

		Levene's Test for Equality of Variances		t-test for Equality of Means						
		F	Sig.	t	df	Sig. (2-tailed)	Mean Difference	Std. Error Difference	95% Confidence Interval of the Difference	
									Lower	Upper
sw	Equal variances assumed	.004	**.952**	-.528	408	.598	-.05161	.09777	-.24381	.14060
	Equal variances not assumed			-.528	228.134	.598	-.05161	.09774	-.24420	.14099

Table: 16

Interpretation: Here, p-value **0.952 > 0.05.** So we fail to reject null hypothesis. Null hypothesis accepted. There no significant difference between in PQOL of Individuals belonging to Rural Gujarat and Urban Gujarat.

VIII CONCLUSION

People of Gujarat are somewhat satisfied towards overall life satisfaction. Perceived Quality of life does not associated with gender difference. Perceived Quality of life does not associated with different age groups. Perceived Quality of life does not associated with education status of individuals. Perceived Quality of life is associated with marital status Marrieds are more satisfied than unmarried. Perceived Quality of life is associated with income levels of individuals. Higher income group and middle income group are found more satisfied than lower income group in PQOL. Perceived Quality of life does not associated with different geographical areas of Gujarat like Central Gujarat, South Gujarat, Saurastra and North Gujarat. Perceived Quality of life does not associate with different areas of Gujarat based on urban and rural.

REFERENCES

1. R. Handa & G.C. Maheshwari (2016). A study of sense of well-being and perceived quality of life of people in Central Gujarat, International Journal of Science Technology and Management, Vol. No.5, Issue No. 11, pp 198-207.
2. W. Asyraf, & B. Afthanorhan (2013), A comparison of partial least square structural equation modeling (PLS-SEM) and covariance based structural equation modeling (CB-SEM) for confirmatory factor analysis, International journal of engineering science and innovative technology (IJESIT), Vol.2, Issue 5, pp 198-205.
3. P. Conceicao & R. Bandura (2008), Measuring Subjective Well-being: A Summary Review of the Literature United Nations Development Programme, USA.
4. S. Dasgupta & S. Majumdar (2000), Sense of well-being and perceived quality of life in Culcutta, In Advance in quality of life theory and research, Kluwer Academic publishers, Netherlands, Pp 65-79.
5. E. Diener, R. Emmons, R, Larsen & S. Griffen (1985), The Satisfaction with Life. Scale, Journal of Personality Assessment, 49, 1.
6. N. Gjoksi (2010), National approaches to measure wealth and well-being in the context of sustainable development. ESDN Case Study No.4.
7. I. Gough (2003), Human Well-being: Bridging Objective and Subjective Approaches. ESPANET Conference, 13-15 November, 2003, Copenhagen.
8. R, Haq (2009). Measuring Human Wellbeing in Pakistan: Objective versus Subjective Indicators, European Journal of Social Science, Volume 9, 3.
9. S, Hicks, J, Newton, J, Haynes & J. Evans (2011), Measuring Children's and Young People's Well-being, Office for National Statistic and BRASS, Cardiff University.

10. D. Kahneman (2006), Developments in the Measurement of Subjective Wellbeing, Journal of Economic Perspective, Volume 20, Number 1, Pages 3-24.
11. D. Kahneman, E. Diener & N. Schwarz (1999). Well-being: The Foundations of Hedonic Psychology, Russell SAGE Foundation, New York.
12. T. Kashdan (2002), The Assessment of Subjective Wellbeing (Issues Raised By the Oxford Happiness Questionnaire). Personality and Individual Difference, 36, 1225-1232.
13. M. Rapley (2003), Quality of Life Research, SAGE Publications, New Delhi.
14. C. Smith, & P. M. Clay (2010), Measuring Subjective and Objective Well-being: Analysis from Five Marine Commercial Fisheries. Human Organization, Volume 69, No.2.

International Journal of Research in Engineering and Innovation (IJREI)

Home page http:// www.ijrei.com

Analysis of Calorimetric Measurement Bismuth and Tin System

Kapil [1], C.K Behra[2], Ravinder Kumar[3]

[1]M.Tech Student, Department of Metallurgical Engineering, IIT, BHU Varanasi, India
[2] Department of Metallurgical Engineering, IIT, BHU Varanasi, India
[3]M.Tech Student, Delhi Technological University, New Delhi, India

Keywords

Drop Calorimeter
Calisto Software
Sapphire,
Enthalpy

Abstract

Lead-free soldering alloys with low melting point suitable for use in soldering joints are very essential. Use of lead as a solder is considered dangerous for the environment due to the huge number of printed circuit board and electronic devices, pipe joints etc. needed to be recycled from dumps.

In this work the metallic samples were prepared from Bi in the mass range from 0.75gm. Samples of Sn were dropped into the bath of Bi by using an automatic dropping device System required 40min time interval after every sample of dropped. Calorimetric measurements was done at temperature 830K. The Integral and partial enthalpy of mixing was calculated at this temperatures. The Integral enthalpy of mixing in Bi- Sn system at 830K is endothermic in nature throughout the composition and its maximum value at X_{sn} = 0.6, is 1005.9061 respectively. © 2016, ijrei.com. All rights reserved

1. Introduction

Development of new lead-free solder requires a database. The database will help us to avoid complicated and time consuming experiments. Information on thermodynamic properties such as mixing enthalpies is indispensable for the accurate thermodynamic optimization of phase diagrams, for the development of a lead-free solder database, and for the prediction of physical and chemical properties, such as surface tension and viscosity.

It is not possible so far to substitute lead by any single metal in the conventional lead-tin solder. So the attempt has been made to substitute lead by more than one metal. These systems are called multicomponent metallic solution. Like In- Sn- Bi, In-Sn-Zn, and In-Sn-Bi-Zn

Higher temperatures dramatically reduce the firmness of the solder joint during thermal cycling, due to greater plastic deformation of the solder and recrystallization and grain growth inside the solder. At such high temperatures, the mechanical properties of the conventional alloys Sn62/Pb36/Ag2 (melting point 179°C) and Sn63/Pb37 (melting point 183°C) deteriorate. In the manufacturing environment, the only risk is caused by breathing in floating, dried powder particles, or through the occurrence of gross mistakes in safety measures. A greater danger lies in the contamination of groundwater and soil by electronics scrap (disposal of electronic circuit and solder dross). Several proposals have been made to ban the use of lead in electronics.

2. Experimental Setup & Procedure

- All experimental measurements were performed by using the calorimetric drop method. Calorimetric measurements were carried out by using the MHTC96 high temperature drop calorimeter from Setaram, France.
- It is a calorimeter with a thermopile of 20 thermocouples and a graphite tube resistance furnace operating up to 1723K. Control and data evaluation were performed using the software provided by the manufacture. To prevent oxidation of the samples all measurements were taken in a atmosphere of flowing argon.
- All measurements were carried out in an alumina crucible.

Corresponding author: Kapil
Email address: kapil.tyagipr@gmail.com
Copyright©ijrei.com

- A motorized dropping device is placed on the top of the calorimeter. 23 samples can be installed at a time into it. It also consists of a vacuum pump.
- An alumina tube connects the furnace to the dropping device. Sample is dropped from dropping device to the alumina crucible (placed in the furnace) by this tube.
- Control and data evaluation were performed using the software provided by the manufacturer

The starting materials are the metals reagent grade as powder. In (purity > 99.9%; 1µm<Ø<2µm), Bi (purity > 99.95%; Ø< 25µm) and Sn (purity > 99.9985%, Ø<20µm). The Stoichiometric mixtures, in the appropriate molar ratio were carefully homogenized inside a glove box under purified argon gas in an agate mortar and compacted into 6mm diameter pellets. The pellets were cut into pieces and transferred from the glove box to the calorimeter using a special Ar-tight container in order to prevent any oxidation with air atmosphere. The Ar gas pressure and time in Analysis chamber is 1.5 bar & 15 min. while for furnace it is 1.5 bar & 2 min 30 sec. The starting samples were placed alternatively in the container with reference •-alumina used for calibration. The enthalpy variations of •-alumina between room and experimental temperatures are well established by Sabbah et al. [1]

Figure 1: Drop Calorimeter Device

Governing Equation

Heat capacity

If there is not a transition or reaction occurring within the sample on the temperature range, the following heat relation is obtained

, " , =

It is needed to repeat sample drops at different temperatures in order to determine the variation of heat versus sample temperature. From the derivation of this curve according to temperature the variation of the sample heat capacity is obtained on the measured temperature range.

Determination of enthalpy of transition

For the temperature range under investigation, the sample can undergo a structure change (melting, crystallization, phase transition ,). The measured heat will contain the heat capacity contribution before and after the transformation and the corresponding heat of transition

, " , = "+ + "+ "+ + " + "+

To obtain the heat of transition, the Cp variation has to be calculated before and transition. The difference between the two curves provides the heat value.

Where

- T_D = Dropping (Room) Temperature
- T_{Tr} = Transformation Temperature
- " = Enthalpy change during transformation
- Tm = Melting Point
- $\int H_{Tf}$ = Enthalpy change during melting
- T_C = Temperature of the Calorimeter at which experiment is carried out.

*Transformation phase may or may not be present in the system. C_p was calculated using the following relation taken from the Metallurgical Thermochemistry book [27].

Cp = a+bT

Where a and b are the constants and T is temperature in Kelvin. Values of a and b are taken from the book. All the experiments was carried out at a calorimeter temperature of 830 K and drop temperature was 293K.

, " , = = . D

Alpha alumina (•-Al2O3) was used for the calibration of the calorimeter for each experiment. Alpha alumina does not react with the molten alloy of Bi-Sn due to its high melting point. Molecular weight of the •-Al2O3 = 101.9613. $\int H$ Reaction for •-Al2O3 is zero. The molar enthalpy difference for •-Al2O3 Standard Reference Material 720 was taken from Standard Reference Material 720 Synthetic Sapphire certificate issued by National Bureau of Standards Certificate, Washington.

, " , = D

4.1.3 Enthalpy calculation:

The measured enthalpy (integrated heat flow at constant pressure) is given by

$$" = , " , + "$$

Where the number of moles of the added sample is $H_{sample, Tc}$ enotes molar enthalpies at calorimetric temperature and $H_{sample, TD}$ denotes molar enthalpies at drop (room) temperature. $\Delta H_{reaction}$ is the enthalpy of reaction due to addition of i. number of moles.

Because of the relatively small mass added the Partial enthalpy can be directly calculated as

$$" = \frac{"}{\quad}$$

The integral enthalpy of mixing was calculated by summarizing the respective reaction enthalpies and division by the total molar amount of substance.

$$" = \frac{S"}{(+ S)}$$

Calibration constant (K) calculation:

Calibration constant was calculated using area under the peak of dropped α-Al_2O_3 samples

$$" = , " ,$$

$$= \frac{}{"}$$

Where n_i is the number of moles of dropped α-Al_2O_3 samples. A is area under the peak in micro-volt second (m-s). " is the heat absorbed in joule by n_i number of moles of α-Al_2O_3.

Results & Discussion

Molten Bi Held at temperature 38 K according to pre-set time range in program and Sn dropped in the crucible at a regular interval of 40 mins with the help of motorizing dropping device.

Graph-1: Peak areas with enthalpy values

Table1 Molar mixing Enthalpies with composition

Xsn	ΔH_{MIX} (Joule/mole)
0.1	40.27759
0.2	151.754
0.3	292.1128
0.4	469.3475
0.5	570.039
0.6	605.922
0.7389	569.9107
0.8093	450.1246
0.832	392.1039
0.8498	339.8457
0.8642	286.1929
0.8861	229.9907
0.8946	165.0691
0.9019	85.15358

Calibration constant was calculated using area under the peak of dropped α-Al_2O_3 samples

Table2: Partially Enthalpies with730 Kcomposition[5]

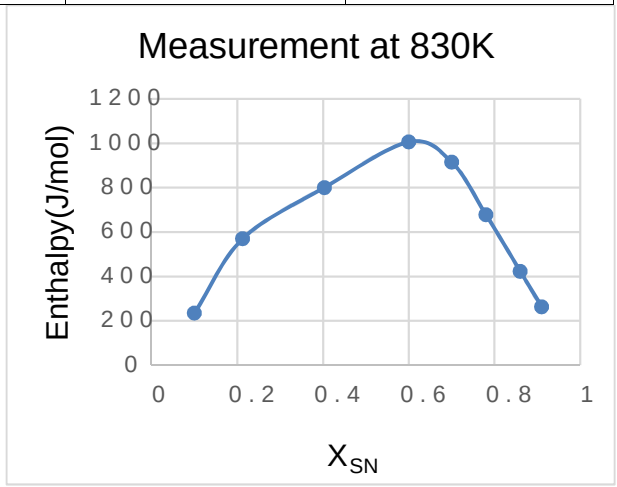
Xsn	Partial Enthalpy (J/mole)
0.1	1352.665878
0.2	606.035198
0.3	515.5397029
0.4	945.0941891
0.5	883.0229295
0.6	667.9512507
0.7389	535.4989169
0.7796	106.1237565
0.832	-3.890277147
0.8642	-30.5927125
0.8946	-104.2914341
0.9019	-370.2476901

Table- 3: Integral Enthalpies of mixing at 830K

X_{sn}	€• MIX (J/mol)
	Experimental valuesat 830K
0.1	234.92128
0.2126	570
0.40295	745
0.6	1005.9061
0.7	915.2765
0.78	678.7265
0.86	423.5942
0.91	263.36614

Comparison of Model values [3] to experimental values

	€• MIX (J/Mole)	
	Experimental values at 730K	Theoretical Values at 608K
0.1	135.2776	20.91
0.2	221.754	62.73
0.3	292.1128	83.64
0.4	469.3475	104.55
0.5	589.039	154.55
0.6	612.922	346.37
0.7	570.678	104.55
0.8	400.126	62.64
0.9	165.1536	2091



Partial Enthalpy values at 830K

X_{sn}	€• partial (J/mol)
	Experimental values at 830K
0.1	2364.1027
0.2126	2058.12752
0.40295	1158.32547
0.6	628.76927
0.7	137.91588
0.78	-89.168
0.86	-122.07893
0.91	-98.79091

Variation of Mixing Enthalpies with X_{sn} [5]

comparison data analysis between Literature data & our experimental data

we find that first the value of Enthalpy is increasing with composition of Sn and at X_{SN} = 0.59, the value of Enthalpy is Maximum for all the temperatures. This is an agreement with the literature. That means at this point reaction is more Endothermic in nature and after this composition Enthalpy goes on decreasing as shown in Fig. R. Hultgrenet[3] have got the maximum value of enthalpy at X_{sn} = 0.6 is „† $_{mix}$ = 146.37 J/mol at 608K1. we have obtained the maximum values of enthalpy at X_{sn} = 0.6 is † $_{mix}$=1005.9061 J/mol at 830K, and is „† $_{mix}$ = 612.33 J/mol at 730 K [5]. It has been observed that enthalpy of mixing in the system Bi- Sn is more endothermic in nature with the temperature.

It is observed that partial enthalpy of mixing decreases temperature. The experimental values show some scatter from the literature [3,4]. The reason for the scatter may be due to different techniques used for the experimental measurement in the Bi-Sn system. The second reason may be the experiments are carried out at different temperatures. For example the Partial enthalpies values obtained from the literature are calculated values from EMF measurement but our values are obtained directly from the enthalpy measurement by calorimeter at 730K and 830 K.

Conclusion

The Enthalpy change of Bi- Sn system is measured at temperature 608K & 830K by Drop calorimetric technique and following conclusions are made. The Integral enthalpy of mixing in Bi- Sn system at 608K and 830K is endothermic in nature throughout the composition and its maximum value at X_{sn} = 0.6, is 346.37 J/mol and 1005.9061 respectively

The partial molar enthalpy of Sn is endothermic in nature and decreases with the composition of tin for most of the composition except Sn rich composition.

The experimental values are compared with the literature and found some scatter due to difference in experimental constraints.

References

[1] R. Sabbah, Xu-Wu An, J.S. Chickos, M.L. Planas Leitão, M.V. Roux, Thermochim.Acta 331 (1999) 93–204.

[2] O.Kubaschewski, E.LL. Evans, C.B. Alcock, "Metallurgical Thermochem" V4 (1967) [28]

[3] R. Hultgren, Raymond L.Orr, Philip D. Anderson. Selected values of Thermodynamic properties of metals and alloys V2(1963), pp 549-554

[4] Hing-feng Yanga, Feng-ling Chena, Wojciech Gierlotkaa Hsiehc, Li-ling Huanga Materials Chemistry and Physics 112 (2008) pp. 94–103.

[5] Kapil, Sunil kumar, Avnish kumar, calorimetric measurement on Bi-Sn system IJRMET VOL5 spl nov2014

Proceedings of the 2016 International Conference on Industrial Engineering and Operations Management
Kuala Lumpur, Malaysia, March 8-10, 2016

Application of Fuzzy Logic and Fuzzy Systems in Machining: A Literature Review

S. Singhal*, Ranganth M.S., R. Batra, S. Nanda
Department of Mechanical, Production & Industrial and Automobile Engineering
Delhi Technological University
New Delhi, India
shubhamsinghal_dtu@yahoo.co.in

Abstract— Fuzzy Logic has found popularity in the academic community and widespread use in the industry due to ever increasing complexities in systems, at the core of which lies vagueness, uncertainty and imprecision in information. The proposition of fuzzy set theory, specifically Fuzzy Inference Systems (FIS) led to an explosion of its application in diverse fields including manufacturing especially machining owing to their ability to handle numeric and linguistic information in the same framework. This literature review focuses on the use of FIS in various aspects of machining including process selection, parametric optimization, decision making, etc. The emphasis is first laid down on a review of various fuzzy tools and their evolution & application in past two decades. It is then shifted to area specific applications of FIS and its combination with neural networks. This review provides an effective insight into the world of intelligent and intuitive systems developed to mimic the human minds' capabilities in an efficient manner. It concludes with the fact that more emphasis can be laid on the use of fuzzy based systems in certain aspects of machining whereas application specific adaption of the concepts seem less popular.

Keywords— fuzzy logic; fuzzy inference system; machining; set membership; ANN; Taguchi method

I. INTRODUCTION

The history and foundations of Artificial Intelligence can be traced back to a conference in 1956 held in Dartmouth College where the term was originally coined. Since then it has emerged from being a mere theory to a concept with rampant application in intelligent computing systems nowadays. Zadeh's article on proving convexity of disjoint fuzzy sets in 1965 paved the way for their popularity and acceptability in the academia but still found very limited use in the industry. Fuzzy systems are applied to artificial intelligence for representing the knowledge of experts or acquired through learning process. Additionally, fuzzy systems provide a rich and robust method of building systems that include multiple conflicting, cooperating, and collaborating knowledge. It is a method specifically developed to incorporate uncertainty by processing information termed as grey (white for perfect information and black for complete absence of information) into a decision making model.

Essentially, fuzzy logic allows for considering reasoning that is approximate rather than precise by use of linguistic variables as both inputs and responses. Fuzzy based inference systems or FIS provide a much simplified platform where the development and analysis of models require reduced development time than other approaches. This has resulted in its widespread within the industry as well for a wide variety of applications. It considers variables to be included in a set based on their degrees of membership, rather than absolute membership. Instead of precision and accuracy, fuzzy logic carries along a level of tolerance for imprecision. Fuzzy logic attempts to mimic the human mind to effectively employ modes of reasoning that are approximate rather than exact. By allowing for the inclusion of imprecision in memberships, fuzzy logic allows for the detection of imprecise dependencies among concepts [1]. The approach differs from the use of crisp sets in which an element is either a member of the set or not. Fuzzy sets, on the other hand, allow elements to be partially in a set. Each element is given a degree of membership in a set. This membership value can range from 0 (not an element of the set) to 1 (a member of the set). It is clear that if one only allows the extreme membership values of 0 and 1, then this would actually be equivalent to crisp sets. A membership function is the relationship between the values of an element and its degree of membership in a set [2].

A fuzzy inference system (FIS) is a system that uses fuzzy set theory to map inputs to outputs (or responses). The most popular and widely used FIS are Mamdani and Sugeno types. They comprise of a fuzzification interface, a rule database, a decision making unit and defuzzification interface as shown in Fig. 1. The first two parts of the fuzzy inference process, fuzzifying the inputs and applying the fuzzy operator, are the same in both the types. The main difference lies in the fact that output membership functions in Sugeno type are either linear or constant. Although the Mamdani type system has gained widespread acceptance owing to it being intuitive and well suited to human input, Sugeno type systems are still considered a notch higher due to computational efficiency, suitability to mathematical analysis and guaranteed continuity of output surfaces [3].

© IEOM Society International

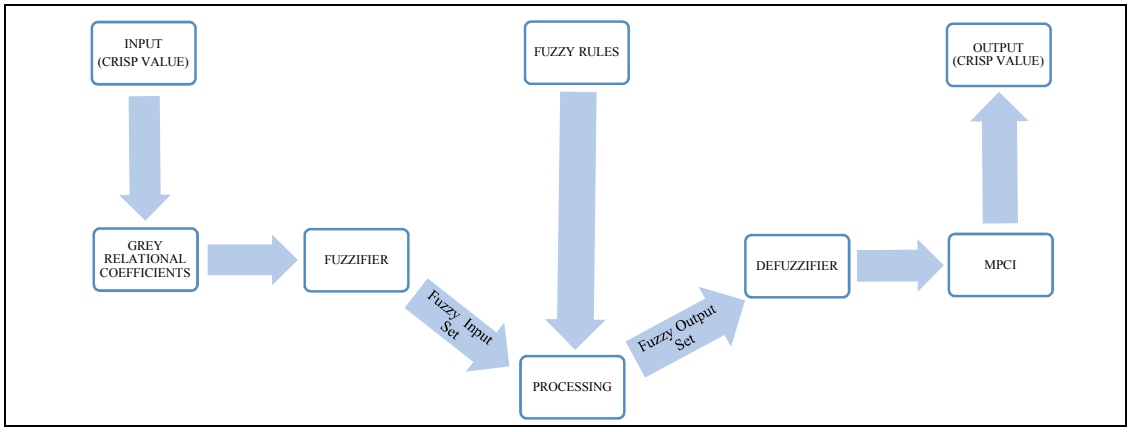


Fig. 1. Flow chart representing Fuzzy Inference System

This research focuses on application of these intelligent systems to machining and attempts to find the reason behind its widespread acceptance beginning with small history of evolution of artificial intelligence and fuzzy logic. It then gives a clear picture regarding the background of the techniques prominently used and fuzzy logic as a whole. The study then clearly demarcates the application of FIS and fuzzy techniques in a variety of industries and research purposes.

II. LITERATURE REVIEW

A. History

Long before the methodology of fuzzy logic had emerged, ancient Greek philosophy conceived the traditional notions of set membership and logic. The efforts of Aristotle and the philosophers who preceded him were largely responsible for the success of mathematics. The postulation of the so-called "Laws of Thought" was the result of their efforts to develop a concise theory of logic, and later mathematics [4]. One of these laws is the "Law of the Excluded Middle" which states that every proposition must either be true or false. But when the first interpretation of this law was proposed by Parminedes (around 400 B.C.), strong objections emerged; one of these was a proposal by Heraclitus that things can be simultaneously True and not True. It was Plato who laid the foundation for what has become fuzzy logic, indicating that there could be a third region (beyond True and False) where these opposites "toppled about". Hegel, Marx, and Engels were among the modern philosophers of those times who echoed thoughts of Plato. The first attempts for formulation of a multi-valued logic were made around the end of the nineteenth century. But it was Pole Jan Lukasiewicz who first introduced a well-known system of multi-valued logic of Aristotle in the 1920s. In his system of logic, Lukasiewicz defined a third truth value other than true and false [5]. But in 1930s, some renowned mathematicians such as Brouwer, and von Neumann proposed the possibility of an infinite number of truth values.

B. Background

Lotfi A. Zadeh, a professor for computer science at the University of California in Berkeley, pioneered Fuzzy Logic in 1965 [6, 7, 8] to address the issues of application complexities arising due to nonlinearities, poorly defined dynamics, absence of a priori information, imprecision, uncertainties and vague description of the system [9]. He laid the foundation of fuzzy sets which he defined as 'a class of objects with a continuum of grades of membership' [6]. He made the use of some of the notions of set membership such as union, intersection, complement, relation, etc. in the same sense as they are used in set membership. At that time, his concept had to face a lot of criticisms, some of which were from his colleagues. A few mathematicians thought that the notions of fuzzy would encourage some sort of imprecise thinking while others believed 'fuzzification' is a kind of scientific permissiveness. Due to the aforementioned reasons, fuzzy logic developed slowly and its applications came into light after a long time. First industrial applications of fuzzy logic were observed in Europe in 1970s. Later, it became popular because of ease of application in decision making and data analysis.

Decision making problems involves many ambiguous and vague objectives and constraints. Therefore, a robust performance evaluation method is a requisite process. In real world problems, these evaluation techniques can handle cases of subjectivity, fuzziness and imprecise information and the implementation of fuzzy sets theory can provide a more precise and optimized value in evaluation systems [10]. Several researchers have emulated the above approach through analytical hierarchy process (AHP), for example in personnel selection [11, 12] and shipping performance evaluation [13], where all the fuzzy sets were aggregated for evaluation.

© IEOM Society International

TABLE I. SELECTED LITERATURE REVIEW OF FUZZY LOGIC'S APPLICATION IN MACHINING PROCESSES

Topic	Author(s)/Year	Description
Optimization of Machining Processes	Fang and Jawahir (1994)	Proposes integrated fuzzy-sets models to assess total machining performance in finish turning
	Tarng, Tseng and Chung (1997)	Develops fuzzy pulse discriminator to organize various discharge pulses in EDM process for optimizing machining productivity
	Kuo and Cohen (1998)	Applies integrated approach of artificial neural networks (ANNs) and fuzzy logic for manufacturing process control
	Lin, Wang, Yang and Tarng (2000)	An establishment of a multi-response performance index using Taguchi fuzzy-based approach to improve EDM process
	Lin, Chung and Huang (2001)	Fabricates multi-variables fuzzy logic controller aiming to improve machining accuracy at corner parts for wire-EDM
	Lin, Lin and Ko (2002)	Compares optimization results of grey relation analysis and fuzzy-based Taguchi method
	Lo (2003)	Predicts workpiece surface roughness in end milling using adaptive network based fuzzy inference system (ANFIS) model
	Lin and Lin (2005)	Multi-objective optimization of EDM process using grey-fuzzy logic
	Tzeng and Chen (2007)	An application of fuzzy logic along with Taguchi methods to study the correlation between machining accuracy and precision
	Hsu and Shu (2008)	Predicts manufacturing process capability based on Taguchi index using two fuzzy inference criteria
	Çaydaş, Hasçalık and Ekici (2009)	Predicts wire-EDM process parameters using adaptive network based fuzzy inference system (ANFIS) model
	Ramanujan et al. (2014)	Employs fuzzy based Principal component function to optimize multi-response during dry turning operation
Selection of Performance Parameters	Balazinski, Bellerose and Czogala (1994)	Use of compositional rule of inference (CRI) to generate fuzzy decision support system (FDSS)
	Baradie (1997)	Computerizes Machining Data Handbook to facilitate machining data selection based on fuzzy logic
	Hashmi, Baradie and Ryan (1998)	Selection of cutting conditions in machining operations based on fuzzy control techniques
	Yilmaz, Eyercioglu and Gindy (2006)	Intelligent selection of EDM process parameters by means of user-friendly fuzzy-expert system

C. Application: Optimization of Machining Processes

Researchers have attempted to apply methodology of fuzzy systems in a wide domain. One of these is the optimization of machining with the application of fuzzy system. The implementation of fuzzy system proved to be highly helpful in case of very complex or highly nonlinear processes, in the absence of any simple mathematical model or the need of processing of expert knowledge. Tarng, Tseng and Chung (1997) used fuzzy set theory to develop a new pulse discriminator in electric discharge machining (EDM) process. In EDM process, cutting performance indexes such as material removal rate (MRR) and surface roughness have strong relationship with the EDM discharge pulses. Hence it is very important to develop a pulse discriminator in order to classify various discharge pulses in EDM for optimization of machining productivity. The fuzzy pulse discriminator (FPD) consisted of a fuzzifier, a knowledge base and an inference engine. In FPD, the EDM discharge pulses were classified based on the linguistic rules attained from the knowledge of experts and expressed mathematically through the fuzzy sets theory. Since the membership functions of FPD have a great influence on its classification performance, the relevant membership functions have been synthesized automatically with the application of a machine learning method. This method was based on a simulated annealing algorithm which is a heuristic search technique. This approach can classify EDM discharge pulses correctly and instantly under varying cutting conditions [14]. The aim of the work done by Tzeng and Chen (2007) was to develop a robust, versatile and high speed EDM technique. This was achieved by optimizing the machining precision and accuracy with the application fuzzy logic analysis incorporation with the Taguchi dynamic method. They employed a fuzzy logic system to study the association of machining precision with machining accuracy. The fuzzy system is composed of a fuzzifier, an inference system, a data base, a rule base and defuzzifier, and further used ANOVA to determine the process parameters that significantly affect the multiple performance characteristics (MPCs) and a confirmatory test of the calculated optimal process showed that targeted MPCs have improved [15]. Lin, Wang, Yang and Tarng applied the Taguchi

method with fuzzy logic to improve the electrical discharge machining (EDM) process with multiple performance characteristics (MPCs) by transforming the optimization of these complicated MPCs into the optimization of a single multiple response performance index (MRPI). The Taguchi method can optimize performance characteristics by adjusting the process parameters and increase the insensitivity of the performance of the system to sources of variation. As a result, the Taguchi method has become a powerful tool in the design of experiment (DOE) methods. It uses a special orthogonal array design to study the entire parameter space preventing the conduction of a large number of experiments. Considering the MPCs (electrode wear ratio (EWR) and material removal rate (MRR)), the machining parameters such as the workpiece polarity, pulse-on time, duty factor, open discharge voltage, discharge current and dielectric fluid are optimized. A fuzzy reasoning of the MPCs has been carried out by the fuzzy logic unit. The fuzzy logic unit comprises a fuzzifer, membership functions, a fuzzy rule base, an inference engine, and a defuzzifer [16].

Ramanujan, Venkatesan, Saxena, Pandey, Harsha et al. attempted to combine the multi-responses of the dry turning operation into a single multiple performance index using principal component function based on fuzzy system as well as design of experiment based on Taguchi method. The aim of their work was to optimize the machining parameters during dry turning operation of Inconel 625 to minimize surface roughness and power consumption and maximize material removal rate. The entire machining parameter space is investigated using L9 orthogonal array. The fuzzy reasoning grades are evaluated and are optimized using the Taguchi method. A hybrid principal component analysis based on fuzzy system was employed because it takes into account all the principal components to obtain the multiple performance index which leads to the reduction in errors [17]. Hsu and Shu developed a realistic approach to work on imprecise output data observed during the measurements of the products quality. They introduced a general method which combines the vector of fuzzy numbers to produce the membership function of fuzzy eliminator of the Taguchi index for further process capability testing. The Taguchi index, also called the loss-based process capability index C_{pm}, was proposed by Hsiang and Taguchi (1985) to measure process capability, wherein the output process data is precise. Process capability index provides statistical measures to check whether a process binds to the specified manufacturing capability prerequisite. In this approach, Hsu and Shu proposed two fuzzy inference criteria, the critical value and the fuzzy P-value, to assess the manufacturing process capability based on C_{pm}. They applied the proposed methodology to the luminous intensity of LED sources data to check for its applicability [18].

Lin, Chung and Huang (2001) tried to improve the wire-EDM machining accuracy at corner parts without compromising with its cutting feed rate. They presented a new control strategy based on fuzzy logic to improve the cutting precision. With the application of fuzzy logic control, software implementation and incorporation of expert knowledge without any need for an explicit mathematical model can be done easily. The fuzzy rules are developed based on the physical characteristics and experimental data of the wire-EDM process and on the past experience of the operator. Using this approach, machining errors of corner parts are found to be reduced to less than 50% of those in normal machining, while the machining process time is increased not more than 10% of the normal value [19]. In finish turning operation, the interrelated machining parameters are present which make it is difficult to evaluate the total machining performance (TMP) including surface finish, tool wear rate, dimensional accuracy, cutting power and chip breakability. Fang and Jawahir provided a new technique to evaluate each facet of the TMP in finish turning of steels. They established a machining reference database providing a fundamental and quantitative standard and a knowledge pool giving all the major factors influencing the TMP. The effects of these factors have been quantified with the application of fuzzy-set method. They proposed a series of fuzzy-set models to evaluate quantitative values of the TMP for any specific input conditions, encompassing work material properties, tool geometries, chipbreaker types and cutting conditions [20].

Fuzzy logic coupled with artificial neural networks (ANN) has been utilized in a wide range of domains. Çaydaş, Hasçalık and Ekici (2009) adopted an adaptive neuro-fuzzy inference system (ANFIS) model for predicting the average surface roughness and white layer thickness (WLT) in the wire-EDM process. ANFIS model is made by the fusion of fuzzy inference system (FIS) and artificial neural network (ANN) approaches as it uses the FIS modeling function and the ANN learning ability. A hybrid learning algorithm, which merges the gradient method with the least squares method to optimize the process parameters, forms the basis of this model. The machining parameters which were input to the model are pulse duration, open circuit voltage, dielectric flushing pressure and wire feed rate. Fuzzy if-then rules of Sugeno type make the rule base of ANFIS. To predict the desired performance parameters, the authors performed normalization of measured performance parameters using standard min-max normalization methodology, feature reduction using principal component analysis (PCA) and ANFIS tests using computer simulation. It was concluded that the proposed approach can be of great use for optimization of surface roughness and WLT in the wire-EDM process [21]. Kuo and Cohen (1998) proposed a self-organizing and self-adjusting fuzzy model (SOSAFM) which was based on the integration of fuzzy logic and ANN. They presented an online estimation system which can be applied in the manufacturing control area. In this approach, Kohonen's feature mapping is employed to divide the inputs and outputs to the system and error back propagation (EBP)-type learning algorithm is used to improve training parameters of ANNs. Evaluation of the proposed methods was done by conducting some physical experiments for manufacturing process control. SOSAFM is found to be better than the multiple regression and artificial neural network both with respect to speed and accuracy for the purpose of multi-sensor integration [22]. For predicting the surface roughness of the workpiece after the completion of end milling process, Lo (2003) employed an adaptive-network based fuzzy

© IEOM Society International

inference system (ANFIS). Considering that spindle speed, feed rate and depth of cut are the three parameters of milling process that have a major influence on the surface roughness, these performance parameters were analyzed. A comparison between the triangular and trapezoidal membership functions was made during the training process of ANFIS to examine the accuracy in predicting the surface roughness by these two membership functions. Results showed very satisfactory predicting accuracy when either of the membership functions is used while the prediction accuracy of ANFIS has reached as high as 96% when a triangular membership function is employed [23].

Many researchers adopted grey relational analysis based on the grey system theory to solve the complicated interrelationships among the multiple responses. In their paper, Lin and Lin also attempted the application of grey-fuzzy logic based on orthogonal array for the optimization of electrical discharge machining (EDM) process with MPCs. The effects of machining parameters (pulse on time, duty factor and discharge current) to the MPCs (EWR, MRR and surface roughness) were studied and analyzed. The experimental plan was designed based on L9 orthogonal array. Grey relational coefficient (GRC) for each process response is calculated to analyze the degree of relation of the multiple responses. Fuzzy reasoning of the MPCs is done using fuzzy logic and the experimental data was analyzed using the technique of analysis of variance (ANOVA). It was concluded that these approaches could greatly improve the process responses such in the EDM process [24]. Lin, Lin and Ko (2002) applied the grey relational analysis based on an orthogonal array and fuzzy-based Taguchi method for improving MPCs in the electrical discharge machining (EDM) process. The influence of the machining parameters (pulse on time, duty factor, and discharge current) on the MPCs (electrode wear ratio, material removal rate, and surface roughness) is investigated. The entire machining parameter space is investigated using L9 orthogonal array. The grey relational analysis method comprises of grey relational generation, calculation of grey relational coefficient and computation of grey relational grade to convert the optimization of complicated MPCs into optimization of a single grey relational grade. In fuzzy-based Taguchi method, S/N ratio corresponding to each MPC is evaluated and fuzzified and fuzzy reasoning grade is obtained by using the max–min fuzzy inference and centroid defuzzification methods to convert the optimization of complicated MPCs into optimization of a single fuzzy reasoning grade. Both approaches can produce very similar experimental results but the calculation using the grey relational analysis is much simpler than that the fuzzy logic analysis [25].

D. Application: Selection of Performance Parameters

Machining data play a vital role in the efficient utilization of machine tools and thus significantly influences the overall manufacturing costs. Machining Data Handbook [26], published by Metcut Research Associates, is a vast information source that compiles machining data for different combinations of tool-work. Baradie (1997) suggested the need and importance of computerization of the Machining data Handbook which would provide an easy access to an immense collection of machining data and lead to the integrated automation of the manufacturing process. He demonstrated the implementation of a fuzzy logic model for metal cutting operation to develop a computerized machining database system that could be a great aid to the process planner for establishment of the strategy for selecting machining data for a specific machining process [27]. In Machinability data hand book [26], one may find different tool materials possible for each work material and hardness. So it proves to be an ample way for selecting cutting parameters in machining processes. But in some cases, uncertainty may occur if more than one choice is applicable for a particular cutting condition. To overcome this problem, Hashmi, Baradie and Ryan (1998) applied fuzzy logic principles for selection process. The material hardness and the cutting speed are considered the fuzzy input and output variables respectively. The fuzzy if-else rules are synthesized based on the information extracted from the used machine tool. The triangular shaped membership functions are employed for both input and output. He compared the cutting speed values predicted using the fuzzy logic model with the speed values recommended by the Machinability Data Handbook and the results showed a good correlation between two speed values [28].

Balazinski, Bellerose and Czogala (1994) developed a fuzzy decision support system (FDSS) based on the compositional rule of inference (CRI). CRI preserves a maximum amount of information contained in the rules and the observations. It is based on the inference method of approximate reasoning applied for handling imprecise information. They attempted the application of FDSS to the choice and modification of cutting parameters considering metal cutting processes to be stochastic, nonlinear and ill-defined. The reasonable results showed that the proposed method would be appropriate for such kinds of decision problems [29]. The parameter selection of the EDM is an obscure problem which is difficult to model as it depends on heuristics and is based on experts' experiences. Fuzzy set theory can play a major role in such problems and fuzzy logic can be employed to emulate the performance of the expert and provide decision making abilities in the presence of certain degree of vagueness. Following this approach, Yilmaz, Eyercioglu and Gindy (2006) developed a user-friendly intelligent system based on fuzzy logic to make the selection of EDM parameters easy and accurate. A compact selection method is used based on expert rules which are evaluated by the fuzzy set theory. A fuzzy model has been developed which uses fuzzy expert rules, triangular membership functions for fuzzification and centroid area method for defuzzification processes. A system has been implemented based on the proposed model which helps an unskilled user to select important parameters according to the specific operation [30].

© IEOM Society International

III. CONCLUSION

This study is based on a state-of-the-art literature review of the application of fuzzy logic and fuzzy systems in various sectors of manufacturing, specifically machining processes. Firstly, a brief definition of fuzzy logic and fuzzy inference system is provided. It is followed by a brief description of origin of the notion of fuzzy logic and stating the reasons responsible for the success & wide acceptability of fuzzy logic as a concept efficiently mimicking the human mind. The research includes the work done in the field of manufacturing based on fuzzy system. From the literature available, it was concluded that fuzzy logic has a wide area of application where imprecise and vague information is available but leaves a room for a more specialized application and adaptation for the industry. Fuzzy Inference Systems (FIS) have been found to be the most commonly applied fuzzy tool for processing information and data incorporating uncertainty. The concepts have gained wide popularity within the academic community as a research subject for machining applications like EDM, turning, milling etc. and other manufacturing processes like injection molding. It was observed that the fuzzy based concepts have been complementing other intelligent systems like Artificial Neural Networks (ANN) and widely contributing to the field of machine learning. Fuzzy logic has also found use in selection of performance parameters in conjugation with preexisting handbooks. This calls for a more adaptive approach to this largely academic concept which gives due emphasis to taking fuzzy concepts out of research laboratories to factories.

REFERENCES

[1] A. Azadegan, L. Porobic, S. Ghazinoory, P. Samouei and A.S. Kheirkhah, "Fuzzy logic in manufacturing: a review of literature and a specialized application", International Journal of Production Economics, vol. 132, issue 2, pp. 258-270, 2011.

[2] http://www.cs.princeton.edu/courses/archive/fall07/cos436/HIDDEN/Knapp/fuzzy002.htm.

[3] http://in.mathworks.com/help/fuzzy/comparison-of-sugeno-and-mamdani-systems.html.

[4] S. Korner, "Laws of thought," Encyclopedia of Philosophy, Vol. 4, MacMillan, NY: 1967, pp. 414-417.

[5] C. Lejewski, "Jan Lukasiewicz," Encyclopedia of Philosophy, Vol. 5, MacMillan, NY: 1967, pp. 104-107.

[6] L.A. Zadeh, "Fuzzy Sets," Information and Control, 1965.

[7] L.A. Zadeh, "Outline of A New Approach to the Analysis of Complex Systems and Decision Processes", 1973.

[8] L.A. Zadeh, "Fuzzy algorithms," Info. & Ctl., Vol. 12, pp. 94-102, 1968.

[9] M. F. Azeem, "Fuzzy inference system– theory and applications", InTech, Croatia, April, 2012, ISBN 978-953-51-0525-1.

[10] D. Zhou, J. Ma, E. Turban, N. Bolloju, "A fuzzy set approach to the evaluation of journal grades", Fuzzy Sets and Systems, Volume 131, Issue 1, Pages 63-74, 1 October 2002.

[11] Saaty, T. (1995). The Analytic Hierarchy Process: RWS publications Pittsburgh, PA.

[12] F.A. Taylor III, A.F. Ketcham, D. Hoffman, "Personnel evaluation with AHP", Management Decision, Vol. 36 Iss: 10, pp.679 – 685, 1998.

[13] T. Chou, & G. Liang, "Application of a fuzzy multi-criteria decision-making model for shipping company performance evaluation", Maritime Policy & Management, 28(4), pp. 375-392, 2001.

[14] Y. S. Tarng, C. M. Tseng and L. K. Chung, "A Fuzzy Pulse Discriminating System For Electrical Discharge Machining", International Journal of Machine Tools and Manufacture, Vol. 37, No. 4, pp. 511-522, 1997.

[15] Y. F. Tzeng and F. C. Chen, "Multi-objective optimization of high speed electrical discharge machining process using a Taguchi fuzzy-based approach", Materials and Design, Vol. 28, pp. 1159 – 1168, 2007.

[16] J. L. Lin, K. S.Wang, B. H. Yan, and Y. S. Tarng, ''Optimization of the electrical discharge machining process based on the Taguchi method with fuzzy logics'' Journal of Materials Processing Technology,Vol.102, pp.48-55, 2000.

[17] R. Ramanujam, K. Venkatesan, Vimal Saxena, Rachit Pandey, T. Harsha, Gurusharan Kumar, "Optimization of Machining Parameters Using Fuzzy Based Principal Component Analysis during dry turning operation of Inconel 625 – A hybrid approach", Procedia Engineering, Volume 97, pp. 668-676, 2014.

[18] Bi-Min Hsu, Ming-Hung Shu, "Fuzzy inference to assess manufacturing process capability with imprecise data", European Journal of Operational Research, Volume 186, Issue 2, pp. 652-670, 16 April 2008.

[19] C. T. Lin, I. F. Chung, and S. Y. Huang, "Improvement of machining accuracy by fuzzy logic at corner parts for wire-EDM", Fuzzy Sets and Systems, Vol. 122, pp. 499 – 511, 2001.

[20] X. D. Fang and I. S. Jawahir, "Predicting total machining performance in finish turning using integrated fuzzy-set models of the machinability parameters", International Journal of Production Research, Vol. 32, Issue 4, pp. 833 – 849, 1994.

[21] U. Çaydaş, A. Hasçalık, S. Ekici, "An adaptive neuro-fuzzy inference system (ANFIS) model for wire-EDM", Expert Systems with Applications, Volume 36, Issue 3, Part 2, pp. 6135-6139, April 2009.

[22] R.J. Kuo, P.H. Cohen, "Manufacturing process control through integration of neural networks and fuzzy model", Fuzzy Sets and Systems, Volume 98, Issue 1, pp. 15-31, 16 August 1998.

[23] Ship-Peng Lo, "An adaptive-network based fuzzy inference system for prediction of workpiece surface roughness in end milling", Journal of Materials Processing Technology, Volume 142, Issue 3, pp. 665-675, 10 December 2003.

[24] J. L. Lin and C.L. Lin, "The use of grey-fuzzy logic for the optimization of the manufacturing process", Journal of Materials Processing Technology, pp. 9 – 14, November 2005.

© IEOM Society International

[25] C. L. Lin, J. L. Lin, and T. C. Ko, "Optimisation of the EDM Process Based on the Orthogonal Array with Fuzzy Logic and Grey Relational Analysis Method", The International Journal of Advanced Manufacturing Technology, Volume 19, Issue 4, pp. 271 - 277, February 2002.

[26] Metcut Research Associates Inc., Machining Data Handbook, 3rd edn, Vols I and 2. Cincinnati, 1980.

[27] M. A. El-Baradie, "A fuzzy logic model for machining data selection", International Journal of Machine Tools and Manufacture, Vol. 37, No. 9, pp. 1353 – 1372, 1997.

[28] K. Hashmi, M.A El-Baradie, and M. Ryan, "Fuzzy-logic based intelligent selection of machining parameters", Journal of Materials Processing Technology, Vol. 94, Issues 2–3, pp 94–111, September 1999.

[29] M. Balazinski, M. Bellerose, E. Czogala, "Application of fuzzy logic techniques to the selection of cutting parameters in machining processes", Fuzzy Sets and Systems, Volume 63, Issue 3, pp. 307-317, 10 May 1994.

[30] O. Yilmaz, O. Eyercioglu , and N. N. Z. Gindy, "A user-friendly fuzzy-based system for the selection of electro discharge machining process parameters", Journal of Materials Processing Technology, Vol. 173, No. 3, pp. 363 - 371, March 2006.

BIOGRAPHY

Shubham Singhal is a student of Mechanical Engineering at Delhi Technological University, New Delhi, India. He has been involved in several research projects with Centre for Advanced Studies and Research in Automobile Engineering (CASRAE), DTU and many governmental organizations. His research interests inlcude manufacturing, machining, mechatronics and robotics, six sigma, IC engines and parametric optimization. He wishes to pursue his research in Robotics specializing in Humanoid robots after graduation. He is a member of ASME, IET, IEEE, SAE and IMechE.

Dr. Ranganath M. Singari is currently the Associate Professor, Department of Production & Industrial Engineering, Delhi Technological University. He is a Post Graduate and Doctorate from University of Delhi. He has made contribution in the areas of Production Engineering, Metal Cutting and Automation. He is a Life member of Indian Society of Technical Education, Computer Society of India and Indian Society of Mechanical Engineering. He has published more than 50 research papers in the area of Productio Engineering.

Rushil Batra is a student of Mechanical Engineering at Delhi Technological University, New Delhi, India. He has led the braking system and manufacturing departments in SAE BAJA team of the university. He has done research projects with automobile manufacturers and governmental organizations. His research interests include manufacturing, process engineering, non-conventional machining, lean management, operations management and ergonomics. He wishes to pursue his research in Production & Industrial Engineering after graduation. He is an active member of SAE, SME and IMechE.

Sahil Nanda is a student of Mechanical Engineering at Delhi Technological University, New Delhi, India. He has done research projects with Indian Railways and many governmental organizations. His research interests inlcude manufacturing, machining, lean transformation, six sigma, SCM and automotive systems. He wishes to do a job specializing in Manufacturing or Automotive Engineering after graduation. He is a member of IEEE, IET, SAE and IMechE.

© IEOM Society International

Autonomous payload drop system using mini Unmanned Aerial Vehicles

Rohan Pratap Singh
Department of Electrical and Electronics Engineering
Delhi Technological University, Delhi, India

Akash Garg
Department of Electronics and Communication Engineering
Delhi Technological University, Delhi, India

Abstract- This paper describes a novel mechanism for the airdrop of a small payload from a mini - Unmanned Aerial Vehicle (UAV). The primary objectives were to drop a payload from the UAV in such a way that it falls within the threshold radius around the target location. The payload drop triggered is executed after taking into account various factors including the speed, altitude and heading of the UAV, the wind speed, drag force experienced by the payload, and the target coordinates. The firmware of the open source autopilot, Pixhawk, was modified as per the requirements. An accuracy of around 70% was achieved when threshold radius was kept at 7 meters around the target location and the payload was dropped from altitudes ranging from 100 – 200m.
Keywords – Payload drop algorithm, projectile from UAV, autopilot firmware.

I. INTRODUCTION

UAV, an acronym for Unmanned Aerial Vehicle, is in essence an aircraft with no human pilot on board. The primary function of an Unmanned Aerial Vehicle is ISTAR which stands for information, surveillance, target acquisition and reconnaissance. In recent years, the application base of UAVs has expanded exponentially. They are being utilized in various sectors including military, defense and border patrolling, journalism, scientific researches, disaster relief, agriculture and many more [1].

A new era has begun with the attempts to employ UAVs in tasks other than just surveillance like payload delivery at specified coordinates. The object to be dropped can range from medicines, food for disaster relief programs to potential weapons, bombs in a war etc., thus leading to optimal utilization of UAVs in every sector [1-3]. This paper is thus intended to provide a working mechanism of airdrop along with flight test results.

The rest of the paper is organized as follows: Algorithm for conducting the payload drop is described in section II. Flight test results are shown in section III and finally, conclusion and references in IV and V respectively.

II. PROPOSED ALGORITHM

Calculation of payload Release Point –

The trajectory of the payload will be that of a projectile once released from the aircraft.

To evaluate the GPS coordinates of the Release Point, range of the projectile is needed to be calculated first.
Let us assume that the instant of calculating the range of the projectile,
Aircraft velocity (relative to the ground) = u,
Aircraft altitude (above ground level) = H,
and Wind speed (relative to the ground) = w

The autopilot firmware employs the inbuilt barometer for estimating the altitude, the external air speed measurement sensor for estimating wind speed, and the inbuilt IMU for estimating the aircraft velocity.

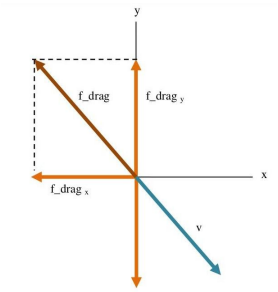


Figure 1: A projectile in flight with velocity v and grad

The drag force due to wind is taken to be proportional to the square of the velocity with respect to the payload [4-5].

The program to calculate the range of the projectile is written in C++ and is based upon the following algorithm:

Step 1: Record the following parameters at the given instant from the corresponding sensors:
Aircraft altitude (above ground level),
Aircraft velocity relative to the ground,
Wind speed relative to the aircraft,

The mass of the payload, its surface area, drag coefficient and air density are constant parameters stored in the FCS before-hand.

Step 2: Calculate the constant q in terms of the above parameters. 'q' is given by,

$$q = \tfrac{1}{2}(PCA)$$

where, P = density of air
C = drag coefficient
A = surface area of the payload

Step 3: Choose time interval $\Delta t = 0.02$sec. Set maximum number of iterations (N) = 3000.

Step 4: Iterate steps 4a through 4e while number of iterations < N.

Step 4a: Calculate the new components of acceleration in the horizontal and vertical directions,

$$acc_x = -(q/m)v_x^2 \; ; \qquad acc_y = g - (q/m)v_y^2 \; ;$$

Step 4b: Calculate the new components of velocity in the horizontal and vertical directions,

$$v_x` = v_x + acc_x \, \Delta t \; ; \qquad v_y` = v_y + acc_y \, \Delta t \; ;$$

Step 4c: Calculate horizontal and vertical distance of projectile from the aircraft at the end of interval,

$$x` = x + v_x \Delta t + \tfrac{1}{2}(acc_x)(\Delta t)^2 \; ; \qquad y` = y + v_y \Delta t + \tfrac{1}{2}(acc_y)(\Delta t)^2 \; ;$$

Step 4d: Update the value of range, altitude and total time

$$x = x` \; ; \quad y = y` \; ;$$
$$t = t + \Delta t$$

Step 4e: Check if y == H, then range = x. Exit from the loop. Else continue.

Step 10: End

The above algorithm calculates the range R of the projectile if the payload is released at that particular instant.

After estimating the value of range R, we need to calculate the GPS coordinates of the release point (RP_{lat} , RP_{lon}). It is calculated as follows:

$\tan \theta$ = (target long – current long)/(target lat – target long)

RP_{lat} = target lat – R * sin θ
RP_{long} = target long – R * cos θ

Therefore, the predicted release point is (RP_{lat} , RP_{lon}).

We now proceed to explain the entire payload release algorithm

Payload release algorithm –

An algorithm was developed for calculating the release coordinates before executing the payload drop. The algorithm was programmed into the Flight Control System (FCS) onboard the UAV. The payload can be released by triggering a servo connected to an auxilliary PWM channel of the onboard FCS. The developed algorithm accounts for following factors in order to execute an accurate drop: aircraft velocity, aircraft altitude, wind velocity, aircraft current location coordinates, and target coordinates. Weight of the payload and its approximate drag coefficients have been hard coded into the software.

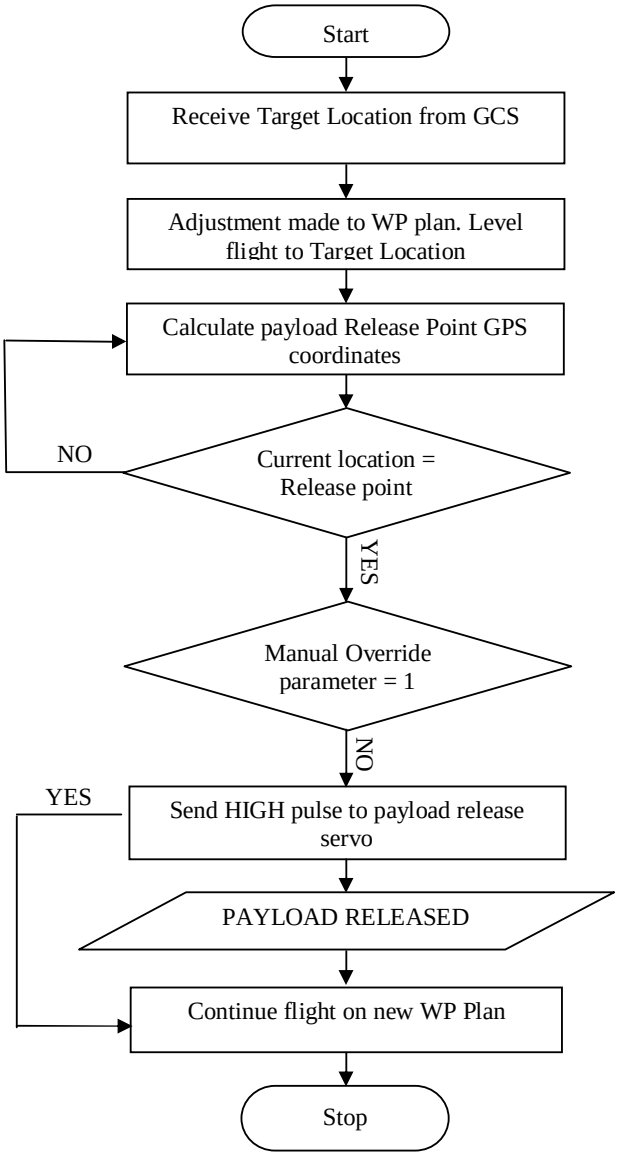


Figure 2: Flowchart for payload drop algorithm

The proposed algorithm waits for the Ground control station to communicate the target location coordinates to the on board FCS via the telemetry link. Upon receiving the target location, the FCS makes minor modification to the aircraft's trajectory by adjusting the way-points such that the trajectory is now in a straight line passing over the target location. The FCS then evaluates the release point by assuming constant wind velocity and aircraft's altitude and velocity from the current point to the estimated release point. This evaluation is done in a loop until the release point is reached and the drop mechanism is triggered.

As a safety procedure, the FCS checks for an override parameter before finally triggering the payload release. The override parameter can be set or reset manually from the Ground control station.

The above algorithm may fail if the calculated range of the projectile is greater than the distance between the aircraft current location and the target location. This can happen if the aircraft velocity is too high.

III. Experiment and Result

A. Hardware Description –

AIRFRAME

The entire testing was carried out on a foam based COTS airframe. It is high winged airframe with a wingspan of 2.5m and the tail configured to an H. The electric propulsion motor is installed in a pusher configuration. Air titan is an EPO foam built frame which makes it light weight as well as strong. Also, EPO foam can be easily repaired. The wings of the frame come pre strengthened with carbon fiber spars embedded near the leading edge. The frame demonstrates rolling takeoff and landing. After thoroughly examining the space inside the fuselage at the C.G. of the frame, the unavailability of space for installing the payload system was felt and hence the entire payload drop system was accommodated outside the fuselage under the belly. However to achieve this the ground clearance of the frame was increased using the modified nose gear.

The payload drop system consists of two wooden cuffs with 2 degree of motions along with a thick iron strip. The payload to be dropped (here bottle) is fitted inside the space provided by wooden cuffs and the cuffs are closed or opened depending on the position of the iron strip. A high torque metal gear servo motor was required which could easily control the lock positioning. It was found that HiTec HS-645MG servo motor provided the much required torque and hence the lock system could be controlled with ease

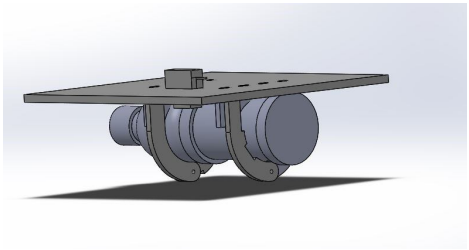


Figure 3: CAD model of payload drop mechanism

AVIONICS

The avionics used in the system can be classified into following sub-sections

1. Propulsion
2. Payload
3. Communication
4. Autopilot and other flight control systems

The paper will introduce each avionics sub-section with a detailed description.

Propulsion: A brushless Electric out-runner motor of 500 kV with 1.5 kW power rating is used as the propulsion system of the frame. Lithium-polymer batteries were used to power both avionics and propulsion system since the energy density of these batteries is greater than lithium-ion batteries.

Payload: Payload could be defined as the extra material apart from propulsion motor, batteries and avionics peripherals which could be carried by the unmanned Aerial Vehicle. In this case the payload is the water bottles of weight 250g which will be dropped during the flight of the vehicle.

Autopilot: A number of autopilots were considered. Since it was required to modify the firmware of the autopilot according to the requirements, Pixhawk, which is an open source autopilot was chosen. Moreover it also provided the liberty to form new parameters e.g. the bull's eye or the target GPS coordinates, the threshold radius etc. the values of which could be provided by the user at real time during the execution of the airdrop.

Telemetry: A pair of 3DR telemetry radio with 433 MHz diploe antenna was used to obtain the telemetry data of the UAV like altitude, distance to home, pitch, roll, yaw etc. One of the telemetry unit was mounted on the UAV and connected to the Pixhawk, was paired to the one present at the ground control station, connected to Mission Planner and thus setting up the telemetry connection.

GPS: GPS module connected to Pixhawk provided the GPS location of the UAV. A module with very small error and negligible Electromagnetic Interference from the surrounding was chosen since the GPS location of the release of the Payload was required to be as accurate as possible.

Airspeed Sensor: A digital differential airspeed sensor was used to measure the air pressure during the flight of the UAV. Air pressure was required so as to estimate the force of drag acting on the object dropped and thus influencing the release coordinates of the bottle.

B. Flight test results –

The system was first tested using Software-in –the-loop (SITL) simulation. After the execution of safe flights along with appreciable results on SITL it was decided to test the system manually on-field. A series of manual flights were conducted to validate the algorithm proposed in the paper. The Airdrop task was attempted during various different wind conditions, however the accuracy obtained was approximately close even in variant conditions, thus generalizing the algorithm.

Table 1: Tabular representation of flight test results

S.NO	Altitude(m)	Wind Speed (m/s)	Aircraft velocity (m/s)	Distance from target(m)
1	101	3.3	12	5
2	103	3.5	14	3
3	107	3.1	11	8
4	102	3.9	13	4
5	104	4.1	11	5
6	112	3.5	15	7
7	116	3.7	15	9
8	118	4.2	13	8
9	111	4.3	14	4
10	116	3.8	14	8
11	122	3.9	12	9
12	126	4.2	11	11
13	124	4.3	15	10
14	120	4.1	13	9
15	123	4.4	14	13
16	155	3.8	14	15
17	159	4.4	15	14
18	152	4.1	15	16
19	155	3.9	11	17
20	161	4.5	14	16

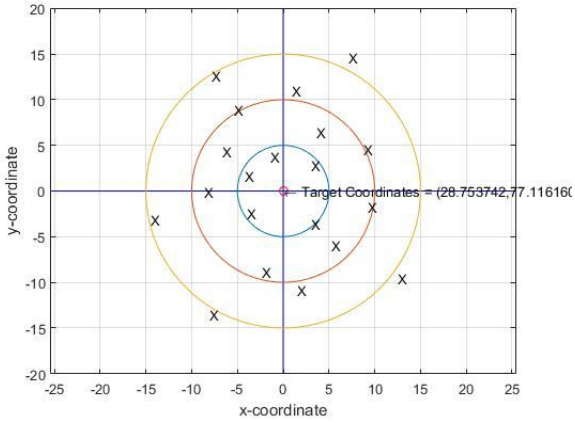
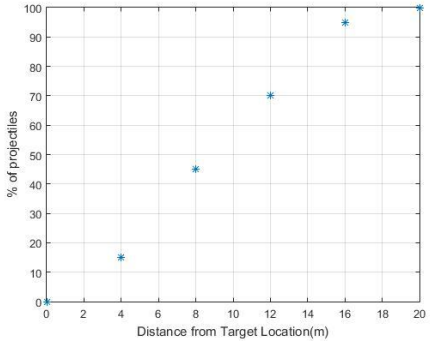


Figure 4: Payload landing points with respect to Target Location

The flight test data was analyzed to find the ratio of projectiles within a threshold radius from the target location. Percentage of projectiles falling within the threshold radius was plotted. Threshold radii considered: 4m, 8m, 12m, 16m and 20m from the target location. The plot is shown in figure 5.



X-axis: Threshold radius from the target
Y-axis: Percentage of projectiles

Figure 5: Percent of projectiles landing within threshold radius

IV.CONCLUSION

In this paper, we present a novel system for the airdrop of a small payload from a UAV. The algorithm was successfully flight tested in over 20 flights. The results depicted an accuracy of over 70 percent when the threshold distance is about 12 meters from the target location, and over 95 percent for a threshold distance of 16 meters. The results prove that the proposed method is a viable solution for autonomously dropping payload in a specified region. Hence, this method can be successfully implemented on a mini UAV for dropping up to 250g of payload with satisfactory accuracy. The accuracy of the method can certainly be improved by taking into account the direction of wind. The number of iterations can be increased and time interval can be decreased for range calculations. Thus, UAVs can be successfully used for implementing payload drop[6]. The above research proves that there is ample ground for future research in this field.

REFERENCE

[1] Sonia Waharte and Niki Trigoni, "Supporting Search and Rescue Operations with UAVs ", International Conference on Emerging Security Technologies, 2010

[2] Yogianandh Naidoo, Riaan Stopforth, and Glen Bright, "Development of an UAV for Search & Rescue Applications", IEEE Africon 2011 - The Falls Resort and Conference Centre, Livingstone, Zambia, 13 - 15 September 2011

[3] Charles W. Hewgley and Oleg A. Yakimenko,"Precision Guided Airdrop for Vertical Replenishment of Naval Vessels", 20th AIAA Aerodynamic Decelerator Systems Technology Conference and Seminar, 4 - 7 May 2009, Seattle, Washington

[4] G. W. Parker, "Projectile motion with air resistance quadratic in the speed", *American Journal of Physics*, vol. 45, *No. 7, July 1977*.

[5] Michael A. B. Deakin and G. J. Troup, “Approximate trajectories for projectile motion with air resistance”, American Association of Physics Teachers, Vol. 66, No. 1, January 1998

[6] Siri Holthe Mathisen, “High Precision Deployment of Wireless Sensors from Unmanned Aerial Vehicles”, Master of Science in Cybernetics and Robotics, May 2014.

Building Concordant Ontologies for Drug Discovery

Hande Küçük-McGinty[1], Saurabh Mehta[2,3], Yu Lin[2], Nooshin Nabizadeh[2], Vasileios Stathias[2], Dusica Vidovic[2], Amar Koleti[2], Christopher Mader[2], Jianbin Duan[1,2], Ubbo Visser[1], Stephan Schürer[,2,5]*

1 Department of Computer Science, University of Miami, Coral Gables, FL
2 Center for Computational Science, University of Miami, Coral Gables, FL
3 Department of Applied Chemistry, Delhi Technological University, Delhi, India
5 Department of Molecular and Cellular Pharmacology, Miller School of Medicine, University of Miami, FL

***Abstract*— In this study we demonstrate how we interconnect three different ontologies, the BioAssay Ontology (BAO), LINCS Information FramEwork ontology (LIFEo), and the Drug Target Ontology (DTO). The three ontologies are built and maintained for three different projects: BAO for the BioAssay Ontology Project, LIFEo for the Library of Integrated Network-Based Cellular Signatures (LINCS) project, and DTO for the Illuminating the Druggable Genome (IDG) project. DTO is a new ontology that aims to formally describe drug target knowledge relevant to drug discovery. LIFEo is an application ontology to describe information in the LIFE software system. BAO is a highly accessed NCBO ontology; it has been extended formally to describe several LINCS assays. The three ontologies use the same principle architecture that allows for re-use and easy integration of ontology modules and instance data. Using the formal definitions in DTO, LIFEo, and BAO and data from various resources one can quickly identify disease-relevant and tissue-specific genes, proteins, and prospective small molecules. We show a simple use case example demonstrating knowledge-based linking of life science data with the potential to empower drug discovery.**

Keywords— drug discovery; bioinformatics; cheminformatics

I. INTRODUCTION

Big data are ubiquitous in business, technology and science. Life science research data are no exception. However, the nature of research data, in particular in the life sciences brings additional challenges due to broad diversity of data types and formats, the quick evolution of knowledge and advancements in technologies to generate data. Despite large investments in information systems in the pharmaceutical industry and non-profit research organizations, the difficult problem of describing, organizing, integrating, analyzing diverse, fast evolving and large scale data in the context of biological knowledge remains a critical and not fully solved challenge.

In this study we demonstrate in a simple case study how to represent and organize such data better by using Semantic Web technologies. Although this approach is not novel, we contribute by leveraging three ontologies developed in our group and that are largely aimed at addressing different aspects of drug discovery data.

The BioAssay Ontology (BAO) [3] has been developed to formally describe knowledge of chemical biology assays and screening results using Description Logic (DL) [14] and OWL (OWL2.0) [17]. The first version of BAO [9] focused on High Throughput Screening (HTS) assays and contained descriptions of many assays from PubChem. BAO since evolved to better integrate with other ontologies and better align with established upper level models and improve usability. BAO was also extended to support profiling assays such as those in LINCS [21]. The systems biology nature of LINCS data required a formal model to describe the relations of cells, disease, tissues and relevant bio-molecules, such as proteins, transcribed genes, used in different roles the various assays. The LINCS Information FramEwork (LIFE) [20] was developed to process, integrate, query, and explore this data. The LIFE application ontology (LIFEo) was developed as a knowledge model to capture the relevant relationships to facilitate this functionality. The Drug Target Ontology (DTO) is being developed as a reference framework to formalize knowledge about drug targets in the context of simple assays and more complex model systems; it is developed as part of the Illuminating the Druggable Genome (IDG) project [22]. For example DTO can readily be used in BAO or in LINCS to describe protein targets in an assay or known targets of small molecule drugs.

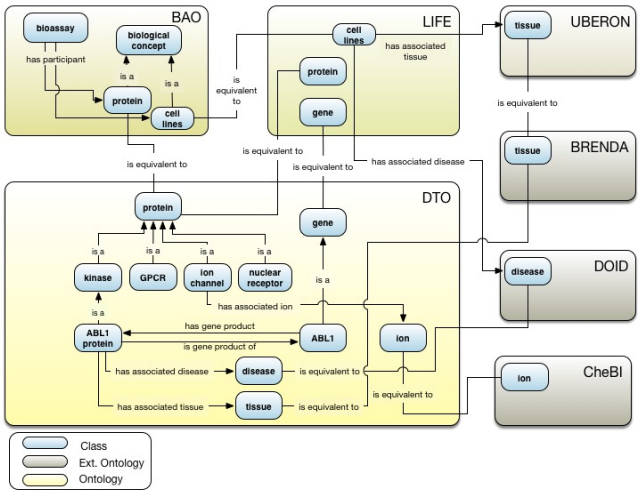


Figure 1 BAO, LIFEo, and DTO with select external ontologies

II. METHODS

All three ontologies (BAO, LIFEo, and DTO) are built using the OWL language. They all use the same approach of modular architectures to facilitate maintenance and re-use [1]. For the construction of DTO we developed tools (using Java and the OWL API) to semi-automate the ontology building process; modularization in DTO further separates algorithm-generated components from expert-generated ones.

Modeling of the data requires a complex and sequential approach. BAO contains formal definitions of assay-related concepts, LIFEo contains axioms for various bio-molecules and their relationships to the assays, cells, tissues, etc, while DTO contains axioms to formalize drug target knowledge. The ontologies have been designed to complement each other and to be compatible. All ontologies make extensive use of external ontologies.

The concepts for BAO ontology are either created by our group, or extracted from external ontologies and used with their own URIs. LIFEo formally describes data generated in the LINCS project's Data and Signature Generating Centers (DSGCs). Finally, for DTO we formally describe drug target data that are the focus of the IDG Project. We further use public databases, such as UniProt [27], in an effort to cross reference and map terms.

We used Protégé [29] to add the manual axioms, Fact ++ [12] reasoner to reason the query view that we created and used Virtuoso [37] as our triple store.

III. RESULTS

A. BioAssay Ontology (BAO)

BAO [3] was designed and implemented to axiomize knowledge about bioassays. As the content expanded with the addition of LINCS assays, an architectural change was implemented to the ontology so that it can maintain its core while importing external ontologies for existing information. Current version of BAO has >3300 classes, >420,000 axioms and 165 object properties.

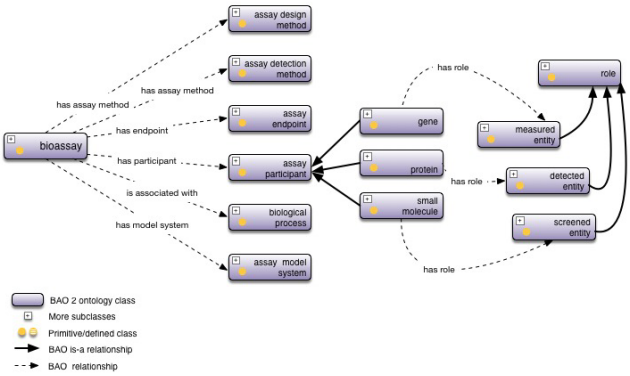


Figure 2 Concepts for Modeling of Bioassays in BAO.

Briefly, the implemented modular architecture divides the ontology into layers, starting with the vocabularies, followed by modules with BAO-native axioms, and finally, different views of the ontology can be created by combinations of modules that can contain the native as well as the external axioms. An important feature of this modularization is that it allows to create a BFO-founded version for ontology authoring and integration with other resources, but also a BAO-native version for users; since most users are not familiar with BFO terms. In addition to the ontology architecture of BAO, we aimed to standardize the assay descriptions by creating metadata and design patterns for the formal definitions. LINCS assays were axiomized in BAO using the model previously described [38] and shown in Figure 2.

B. LINCS Information FramEwork Ontology (LIFEo)

The Library of Integrated Network-Based Cellular Signatures (LINCS) project aims to create a network-based understanding of biology by cataloging changes in gene expression and other cellular processes that occur when cells are exposed to a variety of perturbing agents. LINCS aims to use computational tools to integrate this diverse information into a comprehensive view of normal and disease states that can be applied for the development of new biomarkers and therapeutics [21]. The diverse datasets of LINCS are generated via various assays; in each assay biological molecules occur in different *roles*; formalizing this information facilitates the integration of this data and allows asking potentially novel complex queries.

To accomplish this, we have formalized LINCS assays in BAO. The systems biology nature of LINCS data required a new model we called the LIFE ontology. LIFEo is an application ontology designed to handle the different biological molecules and model systems (in particular cell lines and cells), their relationships to other concepts, such as disease and tissue and assays and their roles. LIFEo contains >49000 classes, >132,000 axioms and 62 object properties (including direct and indirect imports from BAO, DTO and other, external ontologies). By using a modular approach, LIFEo is aiming to create a useful model of how the different metadata components in LINCS align across the entire project.

The first version of LIFEo supported eight assays, namely: KINOMEscan, KiNativ, Cue Signal Response, P100, 2-Color-Apoptosis, 3-Color-Apoptosis, Cell Cycle State, and Cell Growth Assays [21].

Although LINCS assays are diverse with respect to assay technology, the detection method, model systems, and metadata entities, the main point of LIFEo is to provide an integrative model that facilitates context-specific analysis by formalizing the most important relationships.

In addition to the gene and protein modules of the LIFE ontology, we have a module for cells that are used as model systems in the various assays. They are grouped into four main categories: stem cells, primary cells, differentiated cells, and cell lines. Cell lines then are grouped by using the organs from which they were derived using UBERON.

C. Drug Target Ontology (DTO)

DTO is being created as part of the IDG project. An important goal of the IDG project is to catalyze the development of chemical probes and drug development entry points for understudied, yet relevant protein targets in the four most

commonly targeted protein families (G-protein coupled receptors (GPCR), nuclear receptors, ion channels, and kinases) by integrating all available information and making it available as actionable knowledge. The current version of DTO consists of asserted class hierarchies of the ~1800 protein targets, > 13,000 classes and > 214,000 axioms.

DTO is designed to work with other ontologies, such as BAO and thus can be used to describe proteins in LINCS assays.

DTO content is being curated from various sources and the details of the development of DTO will be described elsewhere. DTO content is further annotated and linked by various ontologies. To facilitate the construction of DTO, we wrote various scripts using Java to retrieve information from databases and ontologies. These databases include UniProt and NCBI databases for ENTREZ IDs for the genes, and ChEBI [33] for ions and other small molecules. Further information from the DISEASES and TISSUES databases are incorporated [36].

We retrieved the proteins, with their tissue and disease relationships with the confidence scores that are given to the relationships. We put this data into our database and use this information while creating the ontology's axioms that refer to the probabilistic values of the relationships.

a) Knowledge Modeling of the Drug Target Ontology:

Drug Target Ontology (DTO) uses various external databases and ontologies to retrieve information. The information is retrieved via web-based applications and in-house-built scripts. The data that is used to build DTO is then housed in an internal database. To facilitate ontology development and maintenance, such as frequent updates and synchronization to other data sources, we use Java, OWL API and Jena to build modules of the ontology in a semi-automated. The details of the specific modularization architecture are shown in Figure 3.

b) Improved Modular Architecture for the Drug Target Ontology:

In contrast to BAO, which is primarily constructed manually by experts formalizing axioms, DTO integrates lots of information from different resources. We therefore separated a further module category built using only automated scripts. These are imported into modules that incorporate expert-built axioms. This way, updates from the database will not overwrite expert-modeled content.

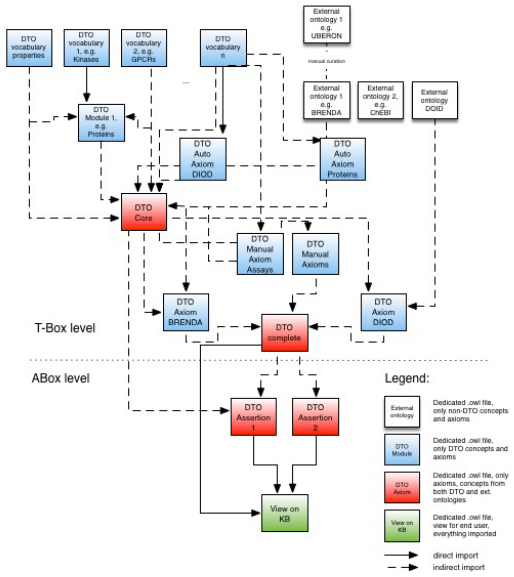


Figure 3 Modular Architecture of DTO

First, we determine the abstract horizon between TBox and ABox. Tbox contains modules, which define the conceptualization without dependencies. These modules are self-contained and well-defined with respect to the domain and they contain concepts, relations, and individuals. We can have *n* of these modules.

Second, once the *n* modules are defined, the modules with axioms that can be generated automatically are created. Those modules have interdependent axioms. At this level one could create any number of gluing modules, which import other modules without dependencies or with dependencies. It also is self-contained. This means that there is no outside term or relationship in the files.

Third, this level contains axioms created manually; however the axioms generated are independent and self-contained. The manual modules are an optional level and they inherit the axioms created automatically. A good example of axioms that may be seen in this level are axioms for protein modifications and mutations, which have been challenging modeling questions. At this level, the self-contained DTO_core is also generated with the existing modules.

Fourth, at this level we can design modules that import modules from our domain of discourse, and also from third party ontologies. Third party ontologies could be large, therefore a suitable module extraction method (e.g. Java programs using OWL API and Jena) can be used to extract only part of those ontologies (*vide supra*). We would model this in the DTO_complete level. We can have one DTO_complete file or multiple files, each may be modeled for a different purpose, e.g., tailored for various research groups. Once these ontologies are imported, the alignment takes place. The alignments are defined for concepts and relations using equivalence or subsumption DL constructs. The alignment depends on the domain experts and/or cross-references made in the ontologies. For DTO, the most significant alignment made

is between UBERON [23] and BRENDA [24] ontologies for the tissue information.

Fifth, release the TBox based on the modules created from the third phase. Depending on the end-users, the modules are combined without loss of generality. With this methodology we make sure that we only send out physical files that contain our (and the absolute necessary) knowledge.

Sixth, at this level, the necessary modules ABoxes are created. ABoxes can be loaded to a triple store or to a distributed file system in a way that one could achieve pseudo-parallel reasoning.

Seventh, at this level we define *views on the knowledge base*. These are files that contain imports (both direct and indirect) from various TBoxes and ABoxes modules for the end-user. It can be seen as a *view*, using database terminology.

D. Use Case Example Query

Since BAO, LIFEo, and DTO have been constructed using a modular approach, we are able to create different *views* that would help to integrate and query relevant data, for example in the drug-discovery domain. We extracted the LINCS assays from BAO by using Jena [6], and OWL API, used the cell line module from LIFEo, and the targets from Drug Target Ontology (DTO) in order to query the following use case.

1) Query

What are the kinases used in the LINCS assays that measure protein binding and have strong evidence for being associated with cancer? Further, what are the relevant compounds targeting these kinases and are therefore relevant for the disease? What other data support the compound-disease association? The generic example cancer, is meant only for illustrative purposes.

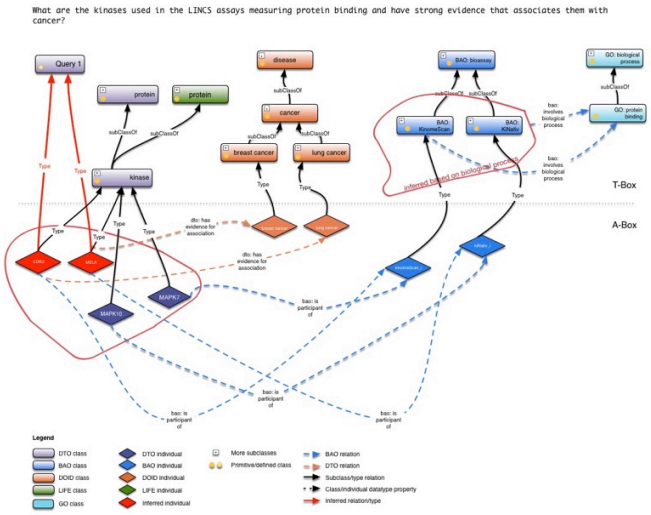


Figure 4 Illustration of the example query using the three ontologies

2) Results

This query aims to retrieve assay specific proteins based on the assays of interest. It works in two parts. In the first part we used the molecular function that is measured (i.e. protein binding) to infer the bioassays of interest. This information is formally described in BAO. We then identified the kinases used in these assays using the LINCS data axioms related with kinases in LIFEo. Finally by using DTO, we get the intersection of this subset of kinases with the kinases that have strong evidence for associations with cancer. The disease and tissue information related with different genes and proteins is formalized in DTO as described above. We further analyzed the results by using the compound data in the LIFEo. We queried the compounds used both in KINOMEscan (KS) and KiNativ (KN) assays.

Table 1 Results for the Query

Assays	**Results for Kinases**		
	Protein Name	***Gene***	***Disease***
KS& KN	cyclin-dependent kinase 2	CDK2	cancer
KS& KN	cyclin-dependent kinase 16	CDK16	cancer
KS	death-associated protein kinase 3	DAPK3	cancer
KS& KN	insulin-like growth factor 1 receptor	IGF1R	cancer
KS& KN	interleukin-1 receptor-associated kinase 1	IRAK1	cancer
KS	maternal embryonic leucine zipper kinase	MELK	cancer

Table 2 Small Molecules and Proteins that are used in KS and KN Assays

Small Molecule Name	Small Molecule LINCS ID	Proteins
OTSSP167	LSM-6340	CDK2, DAPK3, IGF1R, IRAK1, MELK
5z-7-oxozeaenol	LSM-43344	CDK2, CDK16, IRAK1,MELK
XMD16-144	LSM-43287	CDK2, IRAK1
Sorafenib	LSM-1008	CDK2, IRAK1,CDK16
GW-5074	LSM-1029	CDK2, IRAK1
SB590885	LSM-1046	CDK2, IRAK1
PLX-4720	LSM-1049	CDK2, IRAK1
AZ-628	LSM-1050	CDK2, IRAK1
PLX4032	LSM-1068	CDK2, IRAK1
NPK76-II-72-1	LSM-1070	CDK2, IRAK1
Torin1	LSM-1079	CDK2, IRAK1
Torin2	LSM-1080	CDK2, IRAK1
XMD11-50	LSM-1086	CDK2, IRAK1
JWE-035	LSM-1092	CDK2, IRAK1
XMD8-85	LSM-1093	CDK2, IRAK1
XMD8-92	LSM-1094	CDK2, IRAK1
XMD-12	LSM-1106	CDK2, IRAK1
Ibrutinib	LSM-1129	CDK2
XMD11-85h	LSM-5577	CDK2, IRAK1
QL-X-138	LSM-5803	CDK2, IRAK1
WZ3105	LSM-5970	CDK2, CDK16, IRAK1
HG-6-64-01	LSM-43248	CDK2, IRAK1

We combined the resulting kinases of Query1 with the 22 compounds. Table 2 shows the specific kinases that were targets of the same assays as the 22 compounds used both in KINOMEscan and KiNativ assays.

In summary, assays with their molecular functions of interest are axiomized in BAO. Kinases have assay related axioms in LIFEo, which we retrieve as the second step in the query. We then explore more about the proteins by using the axioms related with their associated disease information from DOID [8] encoded in the DTO. As cell lines are linked to diseases, compounds can further be identified based on the growth inhibition assays.

Our results showed us that with the three ontologies, BAO, LIFEo, and DTO, we were able to connect different data types and content related to drug-discovery data. The uniform architecture along with the complex and sequential modeling templates we use for the diverse types of data, allows us to combine different modules and create different views in order to reach the components of interest faster.

IV. Discussion

Here we presented three ontologies built for three related, yet different projects, and how they can work together in queries crossing several concepts important for drug discovery. This is facilitated by the similar modular architectures of the ontologies, which enable their integration of diverse information into a triple store.

BAO has been developed to formalize complex chemical biology assays, such as HTS assays, which are one of the primary methods to identify novel entry points for drug discovery projects. BAO facilitates re-use of this data. LIFEo provide a simple model to address the systems biology aspects, specifically relations of disease model systems, tissues, protein targets, small molecules and assays. DTO describes drug targets formally and integrates information from many sources. All ontologies utilize external ontologies, which serve as an integration point, such as disease and tissue.

BAO was used in the BioAssay Research Database (BARD) software system [19] and it is used in several projects and organizations [36] after we had initially demonstrated its use in the semantic software application BAOSearch (http://baosearch.ccs.miami.edu/). We have also used BAO to describe omics profiling assays in the LINCS program via the LINCS Information Framework (LIFE) (http://life.ccs.miami.edu/).

DTO provides a formal classification of four protein families based on function and phylogenetic and describes their clinical classifications and relations to diseases and tissue expression. DTO is already used in the IDG main Portal Pharos (https://pharos.nih.gov/) and the TinX software application (http://newdrugtargets.org/) to prioritize drugs by novelty and importance. DTO is publicly available at http://drugtargetontology.org/, where it can be visualized and searched.

We have illustrated how DTO, LIFEo, and BAO and included external ontologies are used to describe, integrate, and query drug discovery related data. We are also in the process of integrating these knowledge models with the recently released LINCS Data Portal (http://lincsportal.ccs.miami.edu/). For the purpose of this paper, we have integrated only a part of the available LINCS data in a local triple store to demonstrate the basic concept of our approach of integration. Much more work is required to fully integrate and model all LINCS data. As we expand the LINCS and DTO knowledge models, we can construct more complex queries. A particular goal is to enable the context-sensitive integration and querying of data. We will also integrate further ontologies for example the Cell Line Ontology (CLO) to formalize LINCS cell lines.

We continue to develop BAO and DTO to maximize their utility for the research community. We are constructing a more advanced LINCS MetaData Ontology towards the goal of a comprehensive systems-based model of LINCS signature and drug discovery data.

Acknowledgment

This work was supported by grants U54CA189205 (Illuminating the Druggable Genome Knowledge Management Center, IDG-KMC) and U54HL127624 (BD2K LINCS Data Coordination and Integration Center, DCIC). The IDG-KMC is a component of the Illuminating the

Druggable Genome (IDG) project (https://commonfund.nih.gov/idg) awarded by the NCI. The BD2K LINC DCIC is awarded by the National Heart, Lung, and Blood Institute through funds provided by the trans-NIH Library of Integrated Network-based Cellular Signatures (LINCS) Program (http://www.lincsproject.org/) and the trans-NIH Big Data to Knowledge (BD2K) initiative (http://www.bd2k.nih.gov). Both IDG and LINCS are NIH Common Fund projects.

REFERENCES

[1] Abeyruwan, Saminda, et al. "Evolving BioAssay Ontology (BAO): modularization, integration and applications." *Journal of biomedical semantics* 5.1 (2014): 1.

[2] Oprea, Tudor I., et al. "Systems chemical biology." *Nature chemical biology*3.8 (2007): 447-450.

[3] Visser Ubbo; Abeyruwan Saminda; Vempati Uma; Smith Robin P; Lemmon Vance; Schurer Stephan C., "BioAssay. Ontology, a semantic description of bioassays and high-throughput screening results " *BMC bioinformatics* 12 (2011): 257.

[4] Harmar, Anthony J., et al. "IUPHAR-DB: the IUPHAR database of G protein-coupled receptors and ion channels." *Nucleic acids research* 37.suppl 1 (2009): D680-D685.

[5] Stevens, Robert, Carole A. Goble, and Sean Bechhofer. "Ontology-based knowledge representation for bioinformatics." *Briefings in bioinformatics* 1.4 (2000): 398-414.

[6] Carroll, Jeremy J., et al. "Jena: implementing the semantic web recommendations." *Proceedings of the 13th international World Wide Web conference on Alternate track papers & posters*. ACM, 2004.

[7] Hille, Bertil. *Ion channels of excitable membranes*. Vol. 507. Sunderland, MA: Sinauer, 2001.

[8] Kibbe, Warren A., et al. "Disease Ontology 2015 update: an expanded and updated database of human diseases for linking biomedical knowledge through disease data." *Nucleic acids research* 43.D1 (2015): D1071-D1078.

[9] Schürer, Stephan C., et al. "BioAssay ontology annotations facilitate cross-analysis of diverse high-throughput screening data sets." *Journal of biomolecular screening* 16.4 (2011): 415-426.

[10] Gene Ontology Consortium. "Gene ontology consortium: going forward."*Nucleic acids research* 43.D1 (2015): D1049-D1056.

[11] Brinkman, Ryan R., et al. "Modeling biomedical experimental processes with OBI." *Journal of biomedical semantics* 1.1 (2010): 1.

[12] Tsarkov, Dmitry, and Ian Horrocks. "FaCT++ description logic reasoner: System description." *Automated reasoning*. Springer Berlin Heidelberg, 2006. 292-297.

[13] Dumontier, Michel, and Melanie Courtot. "Proceedings of the 8th International Workshop on OWL: Experiences and Directions." (2011).

[14] Baader, Franz. *The description logic handbook: Theory, implementation and applications*. Cambridge university press, 2003.

[15] Hitzler, Pascal, Markus Krotzsch, and Sebastian Rudolph. *Foundations of semantic web technologies*. CRC Press, 2009.

[16] Gruber, Thomas R., Nicola Guarino, and Roberto Poli. "Formal ontology in conceptual analysis and knowledge representation." *Chapter" Towards principles for the design of ontologies used for knowledge sharing" in Conceptual Analysis and Knowledge Representation* (1993).

[17] W3C Owl Working Group. "{OWL} 2 Web Ontology Language Document Overview." (2009).

[18] Xiang, Zuoshuang, et al. "OntoFox: web-based support for ontology reuse."*BMC research notes* 3.1 (2010): 175.

[19] Howe, E. A., et al. "BioAssay Research Database (BARD): chemical biology and probe-development enabled by structured metadata and result types."*Nucleic acids research* (2014): gku1244.

[20] Library of Integrated Network-based Cellular Signatures (LINCS) Information FramEwork, http://life.ccs.miami.edu/life/, Last visited on 05/05/2016

[21] Library of Integrated Network-Based Cellular Signatures (NIH LINCS) program, http://www.lincsproject.org/, Last visited on 05/05/2016

[22] Illuminating the Druggable Genome | NIH Common Fund, https://commonfund.nih.gov/idg/index, Last visited on 05/05/2016

[23] Mungall, Christopher J., et al. "Uberon, an integrative multi-species anatomy ontology." *Genome Biol* 13.1 (2012): R5.

[24] Maglott, Donna, et al. "Entrez Gene: gene-centered information at NCBI."*Nucleic acids research* 33.suppl 1 (2005): D54-D58.

[25] Gremse, Marion, et al. "The BRENDA Tissue Ontology (BTO): the first all-integrating ontology of all organisms for enzyme sources." *Nucleic acids research* 39.suppl 1 (2011): D507-D513.

[26] Gaulton, Anna, et al. "ChEMBL: a large-scale bioactivity database for drug discovery." *Nucleic acids research* 40.D1 (2012): D1100-D1107.

[27] UniProt Consortium. "UniProt: a hub for protein information." *Nucleic acids research* (2014): gku989.

[28] Callahan, Alison, et al. "RegenBase: a knowledge base of spinal cord injury biology for translational research." *Database* 2016 (2016): baw040.

[29] Protégé, http://protege.stanford.edu/, Last visited on 06/10/2015

[30] Smith, Barry, Anand Kumar, and Thomas Bittner. "Basic formal ontology for bioinformatics." *Journal of Information Systems* (2005): 1-16.

[31] Dumontier, Michel, and Robert Hoehndorf. "Realism for scientific ontologies."*FOIS*. 2010.

[32] Gaulton, Anna, et al. "ChEMBL: a large-scale bioactivity database for drug discovery." *Nucleic acids research* 40.D1 (2012): D1100-D1107.

[33] Degtyarenko, Kirill, et al. "ChEBI: a database and ontology for chemical entities of biological interest." *Nucleic acids research* 36.suppl 1 (2008): D344-D350.

[34] Wache, Holger, et al. "Ontology-based integration of information-a survey of existing approaches." *IJCAI-01 workshop: ontologies and information sharing*. Vol. 2001. 2001.

[35] Clark AM, Bunin BA, Litterman NK, Schürer SC, Visser U. (2014) Fast and accurate semantic annotation of bioassays exploiting a hybrid of machine learning and user confirmation. *PeerJ.*,**14**(2), e524.

[36] Pletscher-Frankild, Sune, et al. "DISEASES: Text mining and data integration of disease–gene associations." *Methods* 74 (2015): 83-89.

[37] Erling, Orri, and Ivan Mikhailov. "RDF Support in the Virtuoso DBMS."*Networked Knowledge-Networked Media*. Springer Berlin Heidelberg, 2009. 7-24.

[38] Vempati, Uma D., et al. "Formalization, annotation and analysis of diverse drug and probe screening assay datasets using the BioAssay Ontology (BAO)." *PloS one* 7.11 (2012): e49198.

Based on all the reviewers' request, we added pages with larger figures.
We couldn't see a way to add supplementary materials.

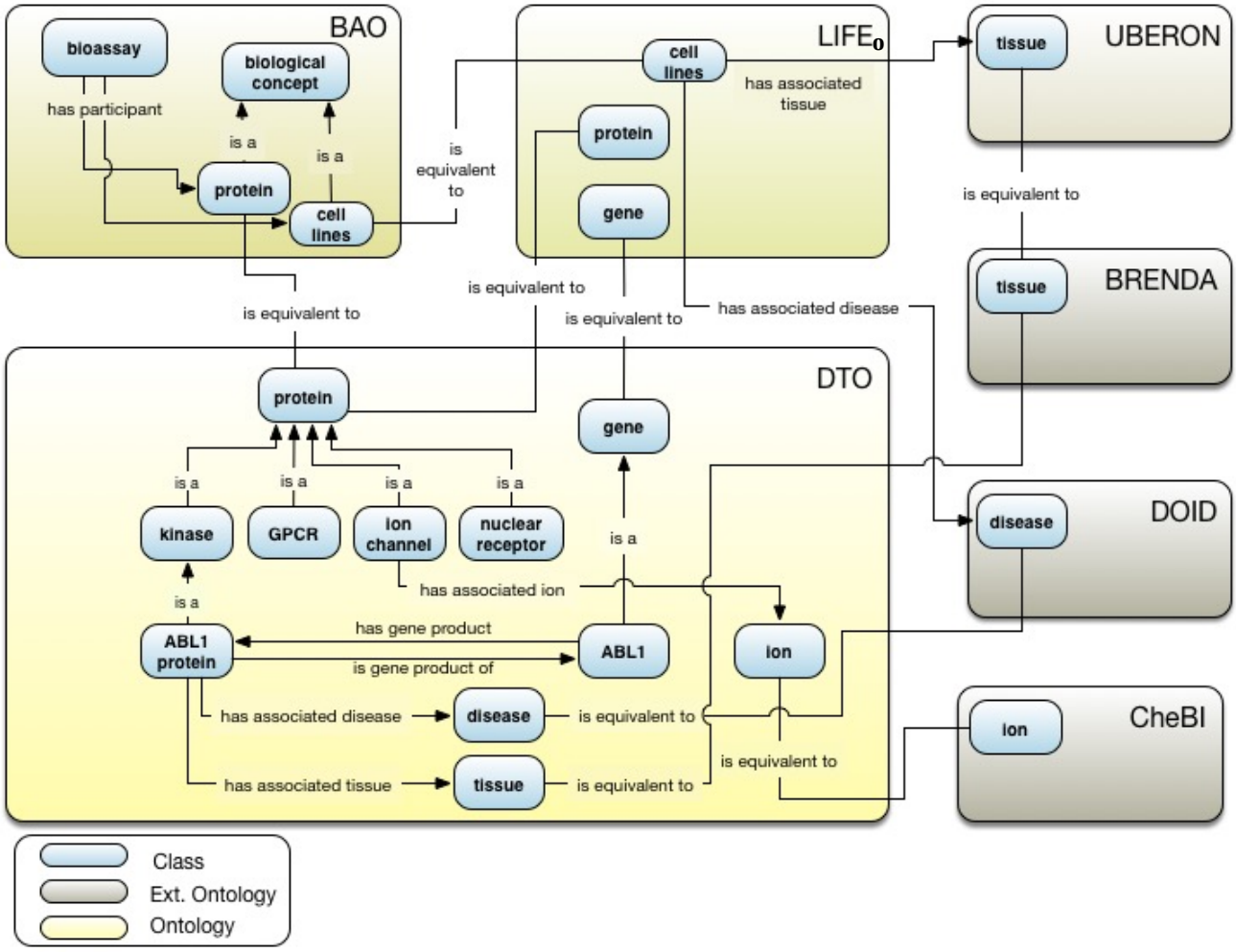


Figure 1

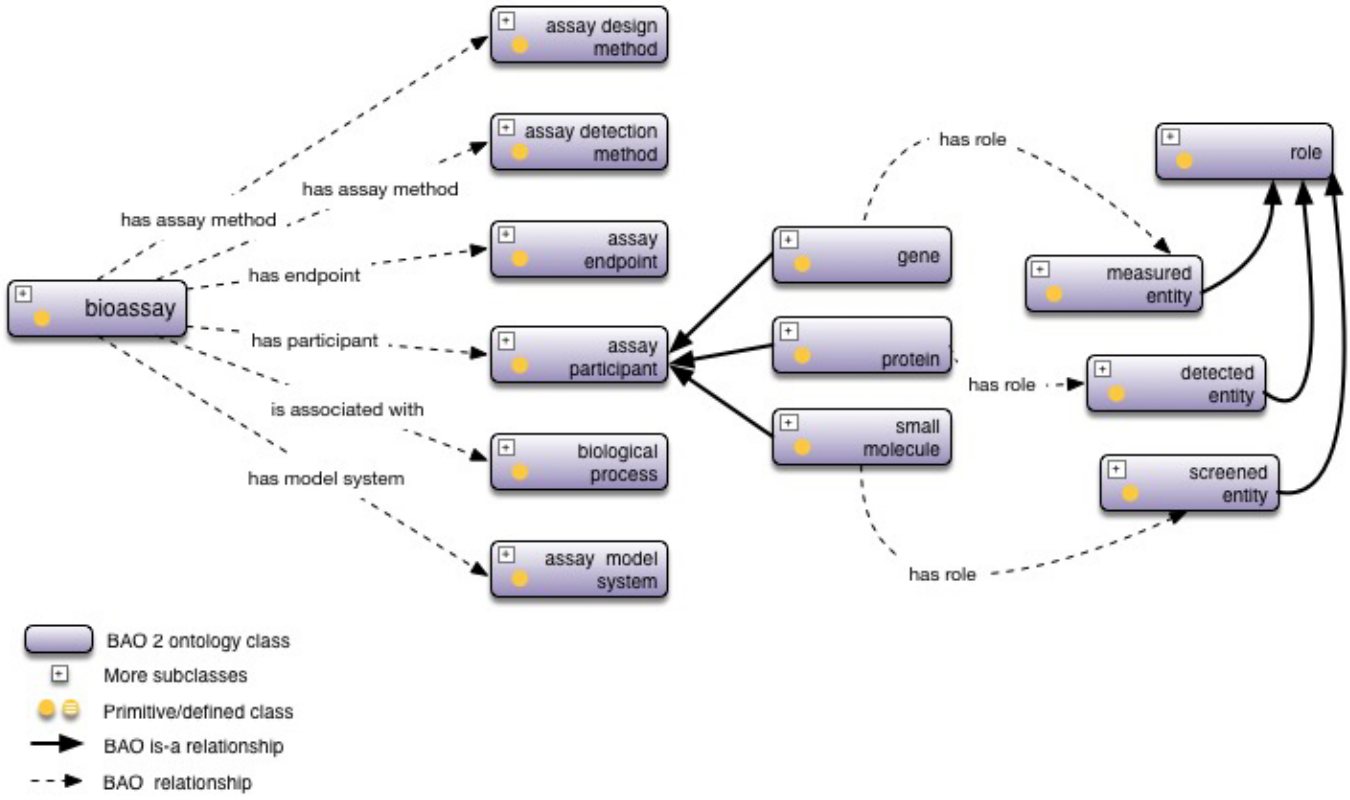

assay design method
assay detection method
assay endpoint
assay participant
biological process
assay model system
bioassay
has assay method
has assay method
has endpoint
has participant
is associated with
has model system
has role
role
gene
protein
small molecule
measured entity
detected entity
screened entity
has role
has role
BAO 2 ontology class
More subclasses
Primitive/defined class
BAO is-a relationship
BAO relationship

Figure 2

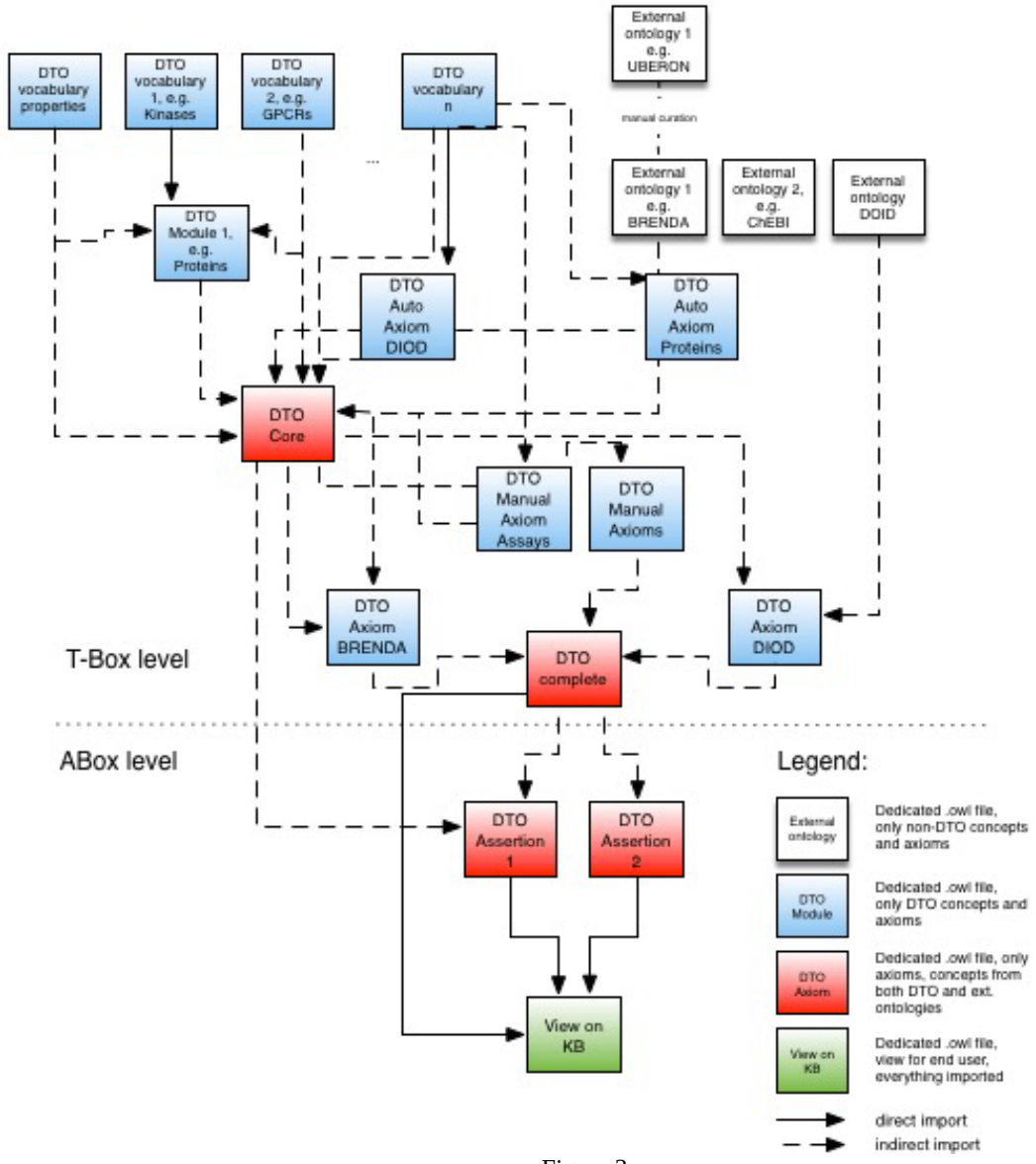

DTO vocabulary properties
DTO vocabulary 1, e.g. Kinases
DTO vocabulary 2, e.g. GPCRs
DTO vocabulary n
External ontology 1 e.g. UBERON
manual curation
External ontology 1 e.g. BRENDA
External ontology 2, e.g. ChEBI
External ontology DOID
DTO Module 1, e.g. Proteins
DTO Auto Axiom DIOD
DTO Auto Axiom Proteins
DTO Core
DTO Manual Axiom Assays
DTO Manual Axioms
DTO Axiom BRENDA
DTO Axiom DIOD
DTO complete
T-Box level
ABox level
DTO Assertion 1
DTO Assertion 2
View on KB
Legend:
External ontology
Dedicated .owl file, only non-DTO concepts and axioms
DTO Module
Dedicated .owl file, only DTO concepts and axioms
DTO Axiom
Dedicated .owl file, only axioms, concepts from both DTO and ext. ontologies
View on KB
Dedicated .owl file, view for end user, everything imported
direct import
indirect import

Figure 3

What are the kinases used in the LINCS assays measuring protein binding and have strong evidence that associates them with cancer?

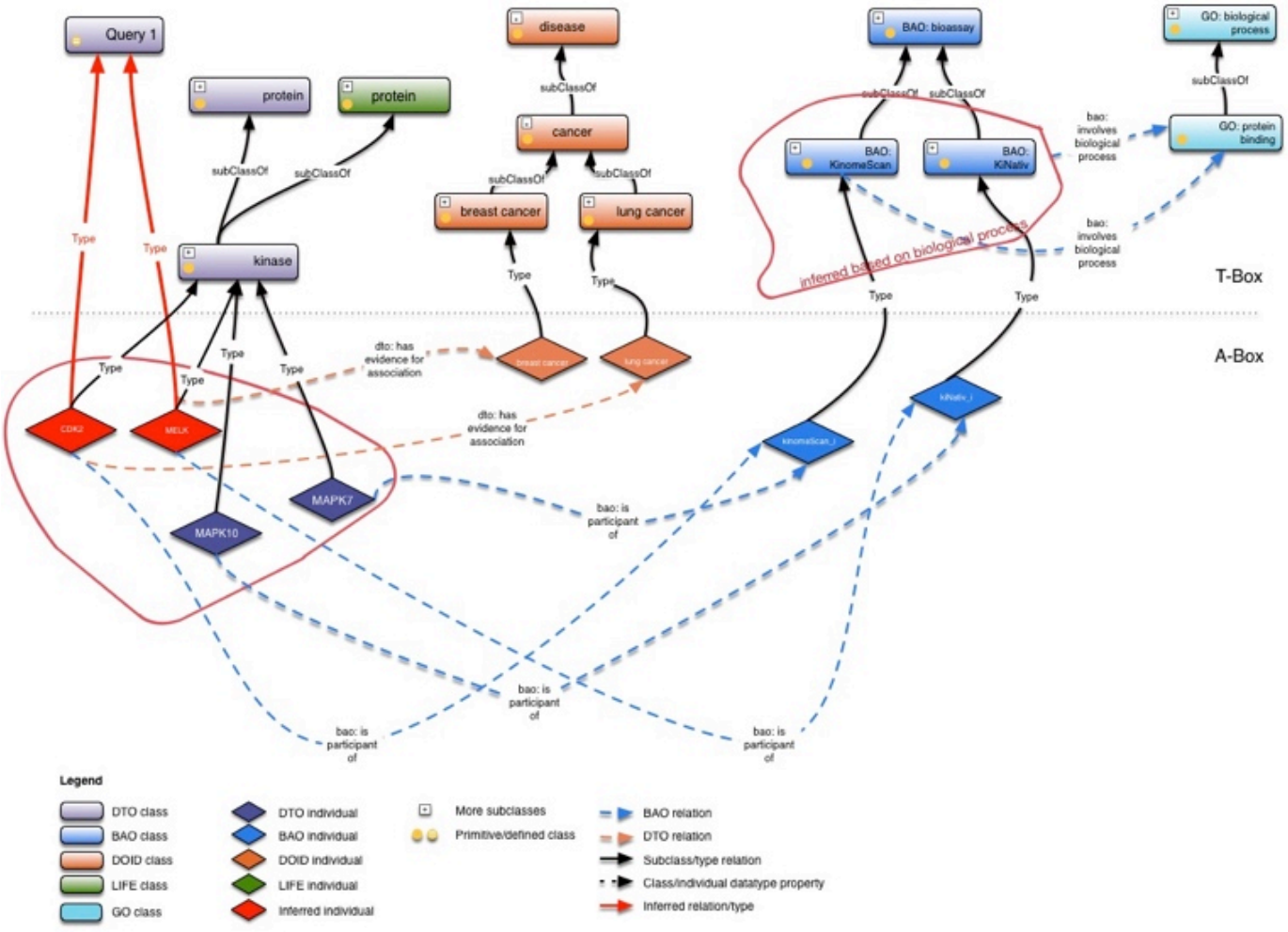


Figure 5

J Indian Soc Remote Sens
DOI 10.1007/s12524-016-0644-8

SHORT NOTE

Cyclone Frame Prediction by Gaussian Mixture Modeling of the Three Penultimate Time-Lapse Frames

Seba Susan[1] · Achin Saxena[1] · Anuvart Budhwar[1] · Akshay Takhi[1] · Abhishek Varshney[1]

Received: 3 November 2015 / Accepted: 23 November 2016
© Indian Society of Remote Sensing 2016

Abstract A fast cyclone frame prediction is proposed in this paper that fits a Gaussian Mixture model on the spatio-temporal data extracted from the three penultimate time-lapse frames, prior to fuzzy regression. Unlike the previous work in Verma and Pal (In: Applied Imagery Pattern Recognition Workshop (AIPR), pp. 1–8, 2010) that models the entire history on a per pixel basis, a single Gaussian mixture is used for fitting the spatio-temporal data within the time-span of the last three frames, making the process faster and more accurate. The increase in accuracy is attributed to the fact that cyclones evolve over time and thus the recent frames give a more meaningful insight into the predictions for the next frame. The number of components in the Gaussian mixture is determined from the occurrence of equally likely modes that correspond to high entropy peaks. Our results on satellite videos of recent cyclones that hit the Indian seas show a high accuracy of frame prediction.

Keywords Fuzzy Gaussian regression · Cyclone frame prediction · Image prediction · Non-extensive entropy with Gaussian gain · Gaussian mixture model

Introduction

The prediction of future frames of a cyclone video is crucial to timely intervention on the part of the authorities for preventive measures and relief operations. Since the frames of the video captured by the satellite are about 30 min apart, future frame prediction when done with accuracy provides sufficient time for guiding rescue operations. Several cyclone frame prediction schemes can be found in literature. Verma and Pal (2010) proposed Gaussian mixture modeling of the entire history of each pixel for each of the color R, G, B channels followed by fuzzy regression. An improvisation using artificial neural networks and dimensionality reduction was proposed by Verma (2012) and that using PNN (Huang et al. 2016). The Adaptive Network based Fuzzy Inference System (ANFIS) together with dimensionality reduction was used for predicting future cyclone frames based on the spatio-temporal and color information of each pixel (Verma 2012). Spatio-temporal regression that incorporates clustering was used to predict satellite frames in Shukla et al. (2014). The study of extreme storms in Economou et al. (2014) indicates that the severe cyclone behaviour deepens explosively with no warning whatsoever, and so we devise a technique in this paper that models the spatio-temporal information in the last three frames only, prior to fuzzy regression for predicting satellite frames.

Proposed Cyclone Frame Prediction by Gaussian Mixture Modeling of the Three Penultimate Frames and Fuzzy Regression

In our method, for each of the R, G, B color planes, we fit a M-component Gaussian Mixture Model (GMM) to the 11-dimensional feature vector emanating from every pixel position compiled from the three penultimate frames t, t−1, t−2. The 11-dimensional feature vector **v** defined at pixel position (x, y) comprises of the intensities at locations: (x, y, t), (x, y, t−1), (x, y−1, t−1), (x−1, y, t−1), (x, y+1,

✉ Seba Susan
seba_406@yahoo.in

[1] Department of Computer Science and Engineering, Delhi Technological University, New Delhi 110042, India

Published online: 03 December 2016

t−1), (x+1, y, t−1), (x, y, t−2), (x, y−1, t−2), (x−1, y, t−2), (x, y+1, t−2), (x+1, y, t−2). The model parameters are then used in the fuzzy rule base regression (Verma and Pal 2010) for the future frame prediction at the location (x, y, t+1) based on the 10-dimensional input **u** of (x, y, t), (x, y−1, t), (x−1, y, t), (x, y+1, t), (x+1, y, t), (x, y, t−1), (x, y−1, t−1), (x−1, y, t−1), (x, y+1, t−1), (x+1, y, t−1) obtained from the frames t and t−1. The advantage of our method is the saving in computational overhead due to the consideration of the three penultimate frames for modeling the data instead of modeling the entire history at each pixel position as in Verma and Pal (2010). The methodology is explained below in more detail.

- For predicting the (t+1)th frame from the tth, (t−1)th and (t−2)th frames, do:
  - For each R, G, B, channel do:
    1. Compile the 11-dimensional feature vector **v** at each pixel position from the frames t, t−1, t−2.
    2. Model **v** using a Gaussian Mixture Model $\{\{\mu_m, \sum_m\}, \alpha_m\}$, $m = 1, 2,\ldots, M$ with the number of components M varying from 2 to 20. The model parameters $\{\mu_m, \sum_m\}$ are determined by Expectation–Maximization. As per Susan and Kumar (2016), select the optimal number of Gaussian mixture components as the one for which the mixture probabilities $\{\alpha_m\}$ contribute maximum entropy i.e. $M_{opt} = \arg\max_{\forall M=2,3,..20} \sum_{m=1}^{M} \alpha_m e^{-\alpha_m^2}$, with the entropy function $\sum_{m=1}^{M} \alpha_m e^{-\alpha_m^2}$ being the non-extensive entropy with Gaussian gain (Susan and Hanmandlu 2013) that is non-additive and interprets events from entropy peaks.
    3. For the GMM with M_{opt} components, estimate the model parameters and use these for predicting the frame t+1 by fuzzy regression given the 10-dimensional input **u**, using the conditional expectation formulae in Verma and Pal (2010).

Experimental Results and Discussions

The satellite videos of *Nargis* (https://www.youtube.com/watch?v=i9O4elfEneQ&app=desktop) the severe cyclone that hit the shores of Myanmar in 2008 and *Hudhud* (https://www.youtube.com/watch?v=TaSCW0r4pHs) that hit the eastern shores of India in 2014, are used for the experimentation. The satellite videos comprise of the time-lapse frames (half-hourly) that are colorized using the infra-red imagery in meteorological satellites. The high-resolution images of dimensions in the order of 600 × 700 are resized to 108 × 192 for ease of computations. Our coding was done in MATLAB 7.10 on a 2.6 GHz PC and require only a few minutes for execution. The proposed algorithm successfully predicted the last video frame as shown in Fig. 1 more accurately as compared to the original fuzzy rule based Gaussian regression (Verma and Pal 2010) which is also corroborated from Table 1 that evaluates the predicted result based on the CIM, PSNR, SSIM and NQM metrics. For the results of Verma and Pal (2010) we set the number of components to four [as per the case example given in Verma and Pal (2010)] per mixture per pixel to save computations and time. Figure 2 shows the recursive frame prediction results for both methods in which each frame predicted serves as the input for predicting the next frame. The last frame in the recursive process is predicted one and a half hours in advance. Though a decline in accuracy is generally observed over time, the decline is slight for our method and the values are overall high. Our work on image prediction could be similarly extended to the prediction of thunderstorms,

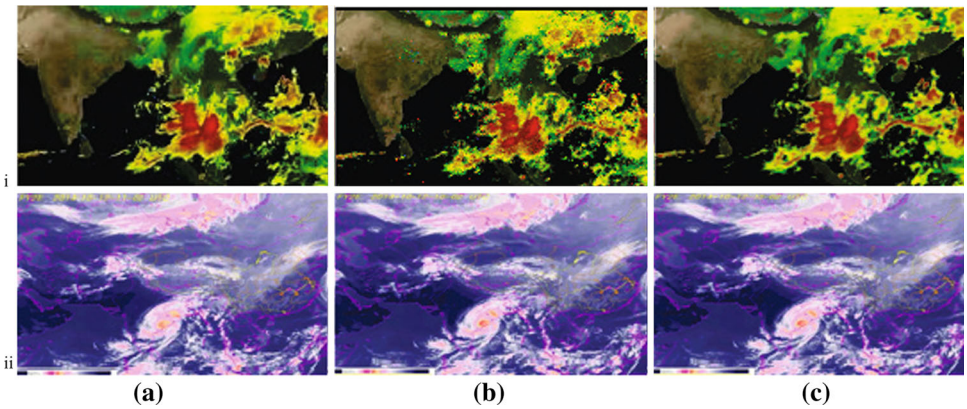


Fig. 1 Frame prediction results for the (i) *Nargis* and (ii) *Hudhud* cyclones, **a** Original frames, **b** predicted frames by fuzzy regression (Verma and Pal 2010), **c** predicted frames by the proposed method

Table 1 Accuracy of the last frame prediction for the cyclone videos (using different metrics)

Cyclone (frame predicted)	Method	Number of training frames required	CIM-Red	CIM-Green	CIM-Blue	CIM (mean)	PSNR	MSSIM	NQM
Nargis (193rd)	Fuzzy Gaussian regression (Verma and Pal 2010)	192	0.9908	0.9918	0.9463	0.9763	21.06	0.8043	12.52
	Proposed method	3	0.9916	0.9752	0.9834	0.9834	22.69	0.8435	12.59
Hudhud (171st)	Fuzzy Gaussian regression (Verma and Pal 2010)	170	0.9749	0.9481	0.9247	0.9492	19.82	0.6960	9.48
	Proposed method	3	0.9641	0.9549	0.9855	0.9682	24.38	0.8440	11.28

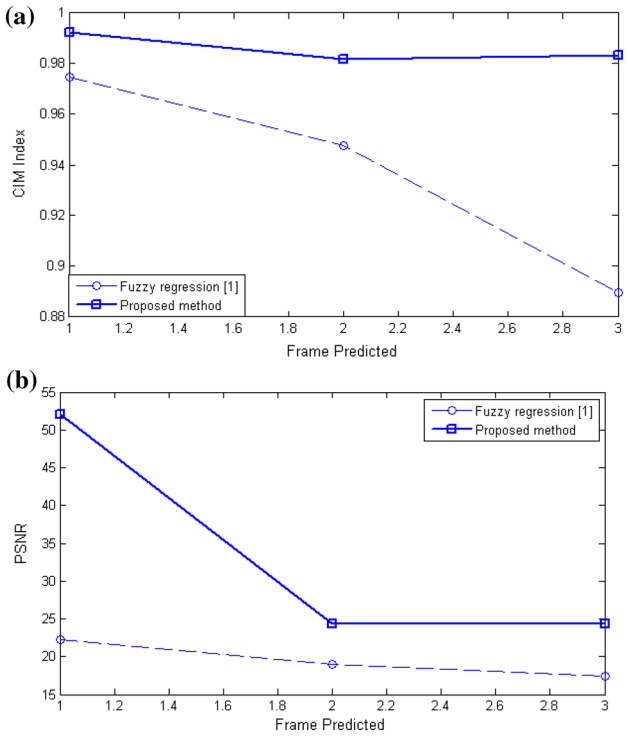


Fig. 2 Frame prediction accuracy in terms of the **a** (mean) CIM, **b** PSNR metrics for three consecutive frames computed recursively, for cyclone *Hudhud* (Frames predicted recursively in the order: 168,169,170 given frames 1–167)

cloudbursts and other temporally evolving forces in nature, and this forms the future scope of our work.

Conclusion

A fast and accurate cyclone frame prediction is proposed in this paper that uses Gaussian mixture modeling with fuzzy rule based regression on the spatio-temporal data contained in the three penultimate time-lapse frames of the cyclone video. The optimal number of components of the mixture is determined from the maximum entropy of mode probabilities. Comparison of our frame prediction results with the fuzzy regression technique, on videos of some recent Indian cyclone affirms the efficiency of our approach.

References

Economou, T., Stephenson, D. B., & Ferro, C. A. T. (2014). Spatio-temporal modelling of extreme storms. *The Annals of Applied Statistics, 8*(4), 2223–2246.

Huang, X., Guan, Z., He, L., Huang, Y., & Zhao, H. (2016). A PNN prediction scheme for local tropical cyclone intensity over the South China Sea. *Natural Hazards, 81*(2), 1249–1267.

Shukla, B. P., Kishtawal, C. M., & Pal, P. K. (2014). Prediction of satellite image sequence for weather nowcasting using cluster-based spatiotemporal regression. *IEEE Transactions on Geoscience and Remote Sensing, 52*(7), 4155–4160.

Susan, S., & Hanmandlu, M. (2013). A non-extensive entropy feature and its application to texture classification. *Neurocomputing, 120*, 214–225.

Susan, S., & Kumar, A. (2016). Auto-segmentation using mean-shift and entropy analysis. In *2016 3rd International Conference on Computing for Sustainable Global Development (INDIACom)* (pp. 292–296). IEEE.

Verma, N. K. (2012). Future image frame generation using artificial neural network with selected features. In *2012 IEEE Applied Imagery Pattern Recognition Workshop (AIPR)* (pp. 1–8).

Verma, N. K. (2012). Generation of future image frames using adaptive network based fuzzy inference system on spatiotemporal framework. In *2012 IEEE Applied Imagery Pattern Recognition Workshop (AIPR)* (pp. 1–8).

Verma, N. K., & Pal, N. R. (2010). Prediction of satellite images using fuzzy rule based Gaussian regression. In *2010 IEEE 39th Applied Imagery Pattern Recognition Workshop (AIPR)* (pp. 1–8).

Volume 4, Issue 3 (2016) 499-502 ISSN 2347 - 3258
International Journal of Advance Research and Innovation

Design and Analysis of DC-DC Boost Converter

JN Rai, Nikhil Gupta, Prashant Bansal
Department of Electrical Engineering, Delhi Technological University, India

Article Info

Article history:
Received 20 January 2016
Received in revised form
10 June 2016
Accepted 28 September 2016
Available online September 2016

Keywords
Converter, Power MOSFET, MATLAB, Inductor Design

Abstract

This paper demonstrates the design of a working prototype of 5-12V DC-DC Boost Converter. The boost converter circuit is designed using MOSFET, Resistor, Capacitor, Inductor and Diode. The key principle that drives the boost converter is the tendency of an inductor to resist changes in current. Inductor is designed using ferrite pot core and windings. This paper briefly reviews the technology used in switched mode power supplies for DC to DC conversion for transferring energy from input to output. Simulation studies are performed using MATLAB tool to validate the proposed scheme as well as hardware practical results.

1. Introduction

The widespread use of battery operated portable devices such as cell phones and laptops has created the need for DC to DC conversion power supplies such as switched mode power supplies. The prominence of distributed energy sources such as solar photovoltaic systems, which produce DC power has created a demand for DC to DC converters. DC converters are widely used for traction motor control in electric automobiles, trolley cars, marine hoists, forklifts trucks, and mine haulers. They provide high efficiency, good acceleration control and fast dynamic response. They can be used in regenerative braking of DC motors to return energy back into the supply. This attribute results in energy savings for transportation systems with frequent steps. DC converters are used in DC voltage regulators; and also are used, with an inductor in conjunction, to generate a DC current source, specifically for the current source inverter.[1] In this paper, some mathematical derivations are given first, and second, simulated and experimental results are provided to verify the effectiveness of the proposed voltage-boosting converter topology.

2. Mathematical Model

The mathematical model for boost converter performance formulae described by as follows:

Calculation

Basic formula

$$(V_o)/V_i = 1/(1-D) \quad (1)$$

Where V_o = Output voltage

V_i = Input voltage

D = Duty cycle

Solving for V_o = 12V and V_i=5 V

We get D=59 %

Also the Ripple Current comes to be:

$$\text{Ripple Current} = V_i(V_o-V_i)/fLV_o \quad (2)$$

And the Ripple Voltage is:

$$\text{Ripple Voltage} = (I_o*D)/ F_c \quad (3)$$

3. Test Setup

The boost converter was built on a standard breadboard. The 5V DC input voltage was supplied by a DC source. All DC measurements were taken using multimeter and all waveforms were obtained via an oscilloscope. To build this boost converter that meets the team specifications the team needs the power stage that will provide the 12V output from a 5 V input. To set the desired frequency for this converter we need to design a pulse width modulation (PWM) circuit up to 20 kHz to drive the boost converter. For PWM circuit we used a Power MOSFET.[5]

3.1 Theoretical values

To obtain the necessary boosting action, the 100 uH inductor was increased to a 122 uH. In order to eliminate noise at the output, all wire lengths were shortened. To eliminate noise from the ground plane, 47 uF capacitors were added to the input and the output of the circuit. The 1.68 uF capacitor was increased to 47uF, in order to decrease the output ripple.

4. Simulation Result

Simulation of Boost Converter in MATLAB, Simulation with 5V dc battery, duty cycle 50 and frequency 20 KHz

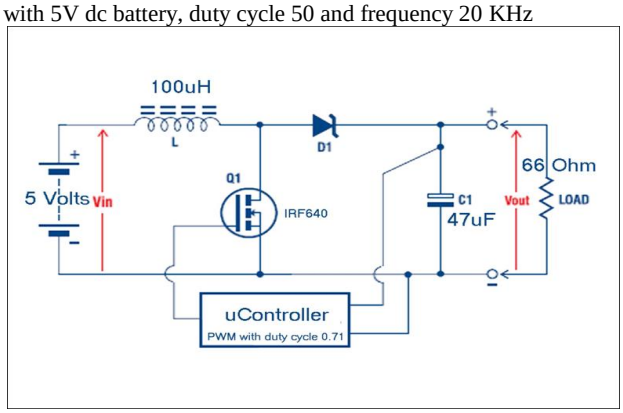


Fig.1: Boost Converter Design Circuit

Corresponding Author,
E-mail address: nikhigupta240@gmail.com
All rights reserved: http://www.ijari.org

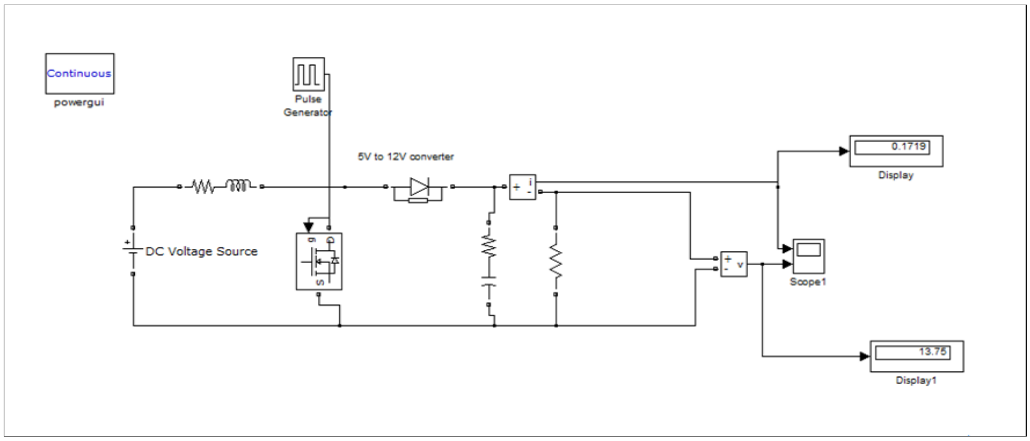


Fig.2: Simulink model of boost converter

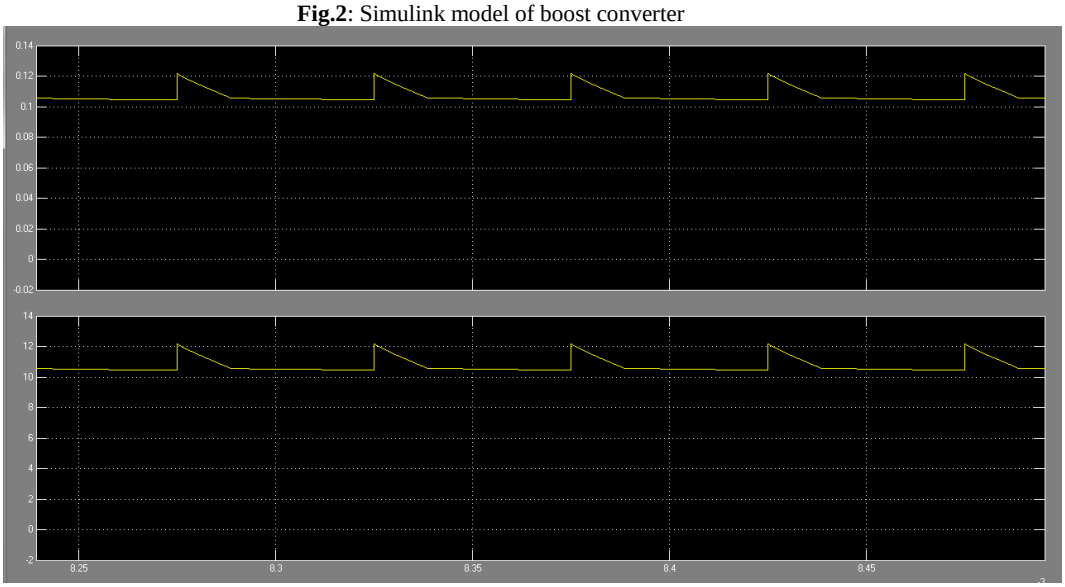


Fig. 3: Zoomed Output and Plots of Output Voltage and Current Waveform



Fig.4 Experimental Output and Plots of Output Voltage

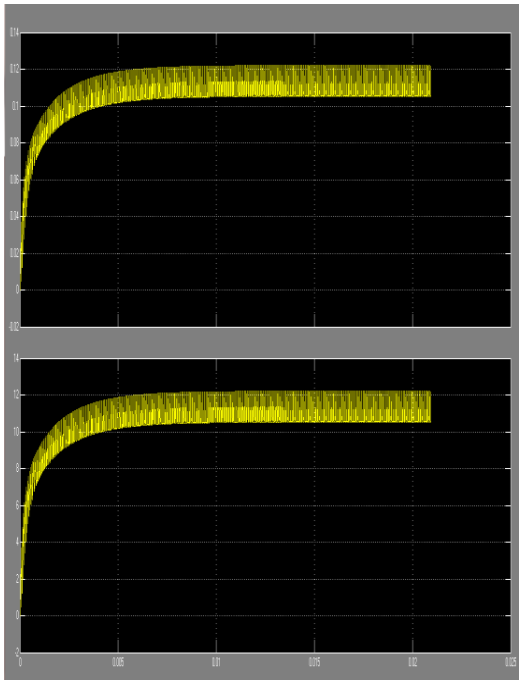


Fig.5: Output and Plots of Output Voltage and Current Waveform

4.1 Variation in Output current and voltage with the Duty cycle, Inductance and Capacitance.

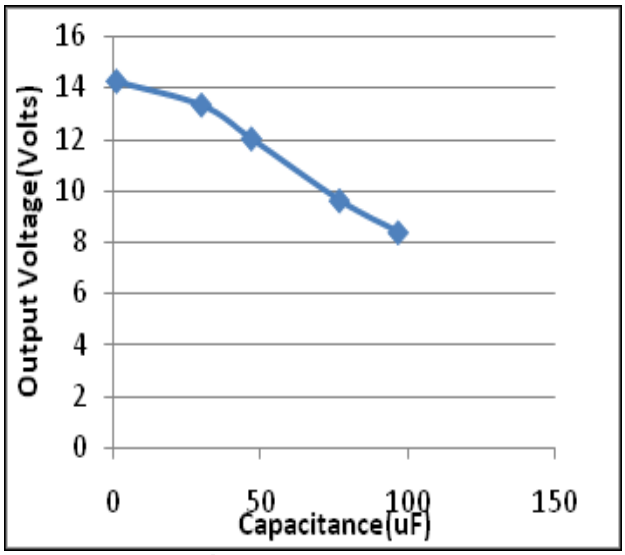


Fig.6 Output voltage versus capacitance

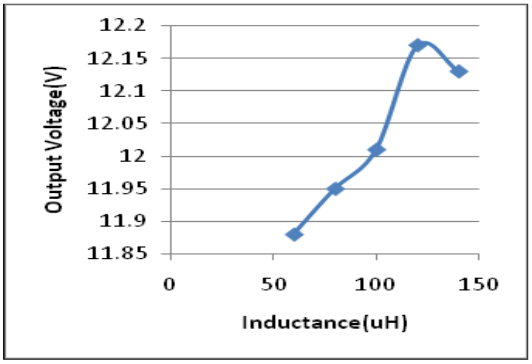


Fig.8 Output voltage versus inductance

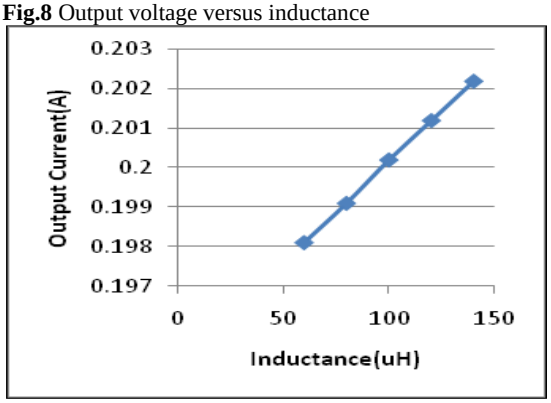


Fig.7 Output current versus capacitance

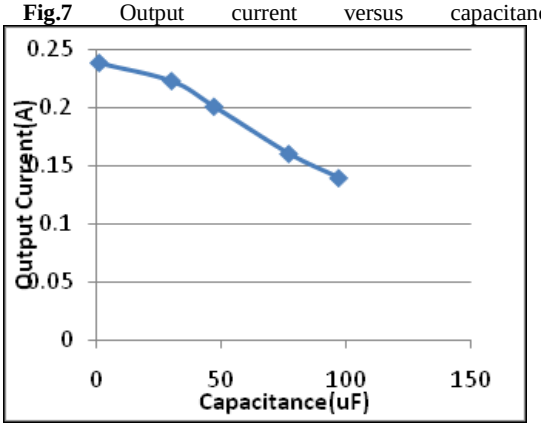


Fig.9 Output current versus inductance

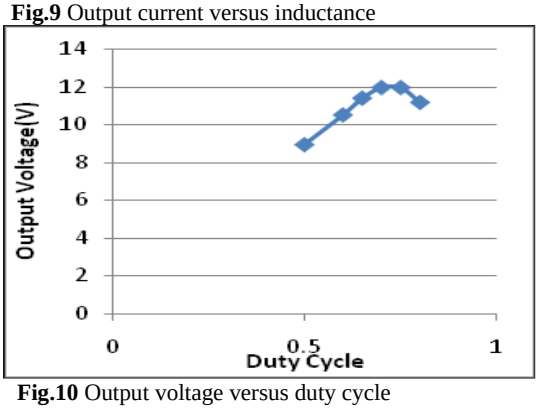


Fig.10 Output voltage versus duty cycle

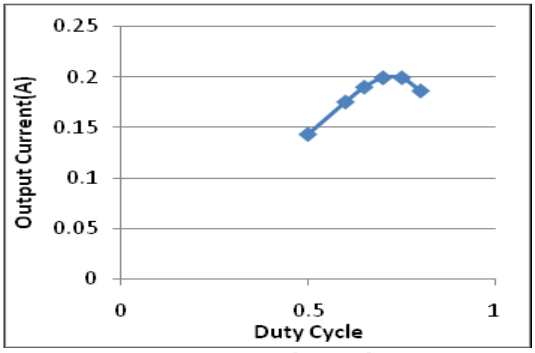


Fig.11: Output current versus duty cycle

5. Result and Discussion

All of the specifications stated previously have been met by this boost converter design. The output voltage across the output capacitor is 12V with a maximum output ripple of 1.6%.The power efficiency of the circuit exceeds 80 % for the load range of 4-5W. However an additional constraint needs to be put on the load. The load must not exceed 5 W.

Addition of Heat Sink was very important role as on Physical touch heat sink also gets hot. So it can damage the MOSFET without heat sink or a smaller heat sink. Use of electronic inductor is avoided due to low current carrying capacity. Value of the inductor should be 1.2 to 2.5 times more than the calculated value. Inductor core should be strictly locked so that there is no air gap.

As duty cycle increases output voltage and current increases to certain extent and then decreases as losses increase beyond that value duty cycle. With the increase in inductance the output voltage also increases to certain extent and then it decreases as losses increase beyond that value of inductance. For maximum efficiency voltage boosting should be 2 to 3.

6. Conclusions

The average output voltage of the converter practically comes to be 11.2V as compared to the 13.75V form the Simulink. The efficiency of the converter comes out to be 80%. Practically there is a dip in output voltage waveform as compared to the Simulink output voltage waveform.

References

[1] K. I. Hwu, C. F. Chuang, and W. C. Tu, "High Voltage-Boosting Converters Based on Bootstrap Capacitors and Boost Inductors" IEEE Trans. On Industrial Elec., Vol., 60 No 6, June 2013.

[2] D. Nicolae, C. Richards, and J. van Rensburg. Boost converter with improved transfer ratio, in Proc. IEEE IPEC, 2010, pp. 76–81.

[3] Ned Mohan et.al. Power electronics. John Wiley and Sons, 1989.

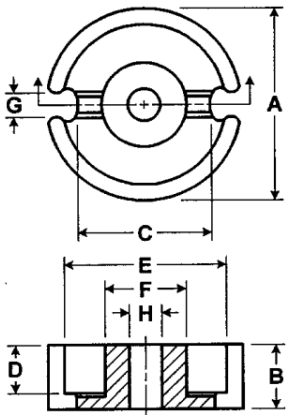
[4] Dr. P.S. Bhimra. Power Electronics. Khanna publishers. New Delhi, India

[5] Ramshaw, R.S. Power electronics, Thyrsitor controlled power for electric Motors' London: chapman & Hall ltd., 1982.

[6] Fairchild Semiconductor Reference Data Sheet: IRF840B.

[7] Muhammad H.Rashid 'Power Electronics Circuits, Devices and Application' third edition, Pearson Education, Inc.2004.

Appendix



DIMENSIONS

	inches	mm		inches	mm
A	.709 ± .015	18 ± .381	2D	.284 min.	7.2 min.
B	.210 + .000 - .005	5.33 + .000 - .127	E	.590 min.	14.98 min.
2B	.420 + .000 - .010	10.67+ .000 - .254	F	.299 max.	7.59 max.
C	.515 nom.	13.08 nom.	G	.162 min.	4.1 min.
D	.142 min.	3.6 min.	H	.122 ± .003	3.10 ± .076

MAGNETIC DATA

MAGNETIC PATH LENGTH (cm)	2.59	CORE WEIGHT (grams per set)	7.3
EFFECTIVE AREA (cm^2)	.429	Wa Ac ‡ (cm4)	.073
VOLUME (cm^3)	1.11	‡ Product of window area & core area, 1 sec. standard bobbin.	

NOTE: Minimum core area .360 cm^2

Design of Single mode Bismuth oxide fiber for generation of Slow light

Utkarsh Nigam[1], Than Singh Saini[2], Ajeet Kumar[1]*

[1]Advanced Photonics Simulation Research Lab., Department of Applied Physics, Delhi Technological University, Delhi-110042, India
[2]CSIR-Central Scientific Instruments Organization, Sector-30, Chandigarh-160 030, India
**ajeetdph@gmail.com*

Abstract: A theoretical design is proposed for single mode bismuth oxide fiber for slow light generation at 1550nm. A time delay of 104.45ns is obtained for maximum allowed pump power of976mW.

OCIS CODES: (060.4370) Nonlinear optics, fibers; (060.2430) Fibers, single-mode;(190.5890) Scattering, stimulated;(290.5900) Scattering, stimulated Brillouin.

Introduction:

Slow light means to limit the velocity of light by reducing group velocity. Nowadays, many applications of slow light are being researched upon in an attempt to produce better optical based communication systems. Some applications of slow light are optical buffering, data synchronization, optical memories, optical signal processing, microwave photonics and precise interferometric instruments [1-5].

Slow light can be generated using scattering effects of non-linear optics. In scattering effects, energy gets transferred from one light wave to another wave at a longer wavelength or lower energy. The lost energy is absorbed by the molecular vibrations, or phonons, in the medium. The most important types of nonlinear scattering within optical fibers are stimulated Brillouin scattering (SBS) and stimulated Raman scattering (SRS).SBS is a resonant nonlinear optical interaction with the material that results in transmitted light being scattered back towards the input [6-9].

In this paper, we have designed and analyzed a single mode bismuth oxide fiber based on SBS. We have calculated the maximum allowable pump power in order to avoid distortion of optical pulse and the corresponding time delay obtained. The variation of time delay with pump power and fiber length has been simulated numerically.The simulated results indicate that the time delay in proposed fiber can be tuned with the pump power and thereby tunable slow light features can be obtained from proposed fiber structure.

Design of fiber:

Figure 1(a). shows the transverse cross-sectional view of the proposed fiber structure. For core we have used bismuth oxide with diameter of 1.32 µm (d_1) and refractive index of 2.22(n_1) with tellurite used as cladding material with a diameter of 13 µm (d_2) and refractive index of 2.03 (n_2).The PML layer is of 1µm (x) thickness. Figure 1(b) shows the electric field distribution of the fundamental mode at 1.55µm.This core radius is chosen using the single mode operation condition, V< 2.4048.

$$\mathrm{V} = \frac{2\pi \times a \times ({n_1}^2 - {n_2}^2)^{1/2}}{\lambda}$$

where V is normalized frequency parameter, a is core radius, n_1 is core refractive index, n_2 is cladding refractive index and λ is wavelength.

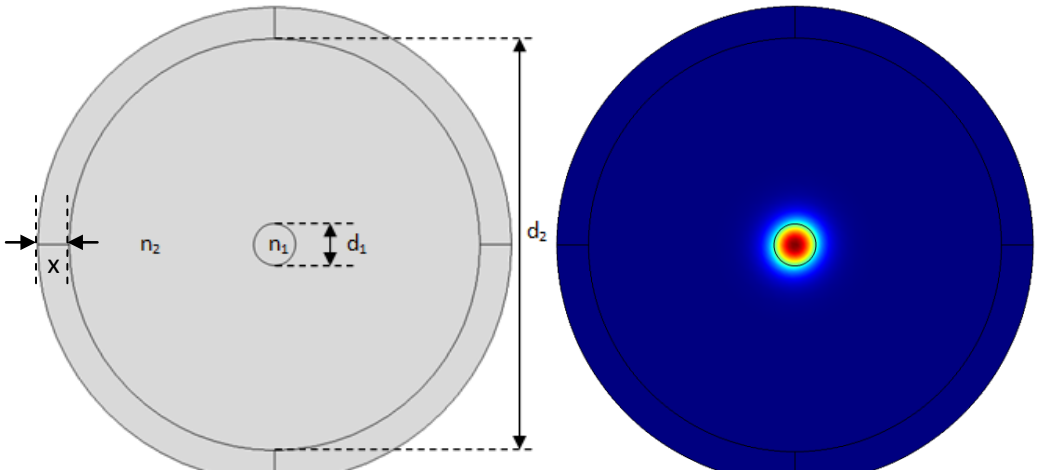


Figure 1 (a) Transverse cross-sectional view of fiber; **(b)** Electric field distribution at 1.55 µm

Simulated results:

In this paper, we have simulated results over a 1m long Bismuth oxide fiber, the intrinsic properties of the material have been taken from the Refs. [10,11]. Specifically, refractive index of material of the core is 2.22 at 1550nm, the Brillouin gain coefficient, $g_B = 6.43 \times 10^{-11}$ m/W, Brillouin gain bandwidth, $\Delta\nu_B$= 32MHz, fiber loss = 0.8 dB/m (i.e. α = 0.1842/m), and the polarization factor, K = 0.667. Using above-mentioned parameters and the mode effective area, $A_{eff} = 1.82\ \mu m^2$ for our design, we have calculated maximum allowable pump power as 976.3mW and a corresponding time delay of 104.45ns. Beyond this pump power distortion of the optical wave will occur. Pump power is the most important parameter in deciding the feasibility of a design. In this paper, we have investigated the variation of time delay with pump power as illustrated in Fig. 2(a).The time delay increases with increase in pump power applied on the fiber. The influence of fiber length on time delay per unit power (ps/mW) is illustrated in Fig. 2(b). The time delay per unit pump power increases with increase in real fiber length. The maximum time delay per unit power is obtained as 382.76 ns for a length of 5 m.

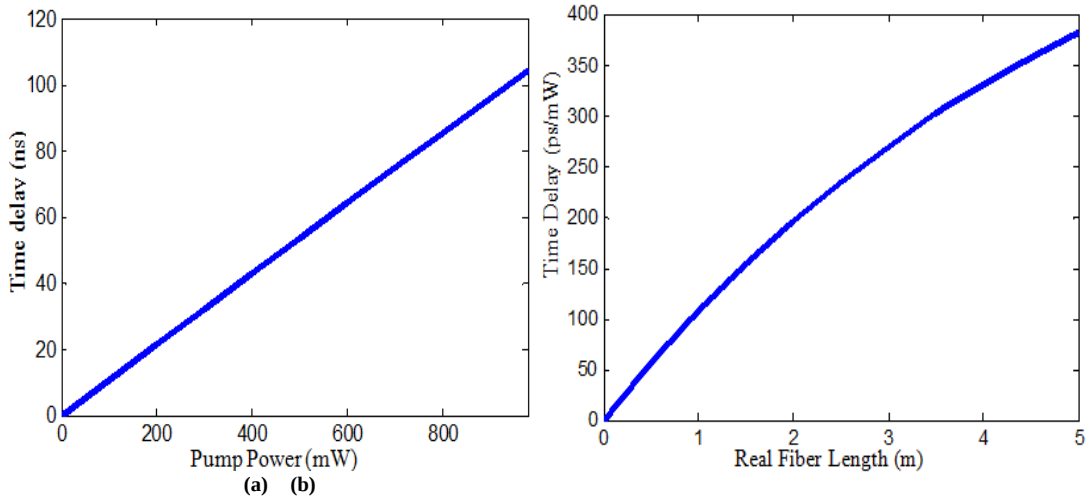


Figure 2 (a): Time delay as a function of Pump power; **(b)** Time delay as a function of Real fiber length.

Conclusion

In conclusion, we have designed and numerically analyzed a highly nonlinear single mode step index bismuth oxide fiber for slow light generation based on stimulated Brillouin scattering. The fiber characteristics for slow light such as maximum allowable pump power and time delay experienced by the pulse for proposed fiber has been calculated. The time delay of 104.45 ns is achieved for 1m long single mode bismuth oxide fiber for the pump power of 976.3mW. The simulated results indicate that the time delay in this fiber can be easily tuned with pump power, which means generation of tunable slow light. These Bismuth oxide fibers are expected to have potential applications in realization of compact slow light devices.

References:

[1] T. S. Saini, A. Kumar, R. K. Sinha, "Slow light generation in single-mode tellurite fibers," Journal of Modern Optics, **62** (7), 508–513 (2015).

[2] R. K. Sinha,A. Kumar and T. S. Saini, "Analysis and Design of Single-Mode As_2Se_3-Chalcogenide Photonic Crystal Fiber for Generation of Slow Light With Tunable Features," IEEE J.Sel.Top. Quant.Electron.**22**(2), 4900706(2016).

[3] T. S. Saini, A. Kumar, R. K. Sinha," Stimulated Brillouin Scattering Based Tunable Slow Light in Tellurite Photonic Crystal Fiber," Proc. of Photonics 2014: 12th International Conference on Fiber Optics and Photonics, OSA 2014, December 13-16, 2014,IIT Kharagpur, WB, India, T3A.28; DOI: 10.1364/PHOTONICS.2014.T3A.28

[4] J. T. Mok and B. J. Eggleton, "Expect more delays," Nature, **433**,811–812 (2005).

[5] M. Santagiustina et al., "Slow light devices and their applications tomicrowaves and photonics," IEEE Photon. Soc. Newslett., **26** (1),5–12(2012).

[6] G. P. Agrawal, *Nonlinear Fiber Optics*. New York: Academic, 1995,pp. 370–385.

[7] E. P. Ippen and R. H. Stolen, "Stimulated Brillouin scattering in optical fibers," Appl. Phys. Lett., **21**, 539–540 (1972).

[8] A. Kobyakov, M. Sauer, and D. Chowdhury, "Stimulated Brillouin scattering in optical fibers," Adv. Opt. Photon., **2**, 1–59 (2010).

[9] F. H. Tithi,M. S. Islam, Md. T. A. Tanna, "Overview of Stimulated Brillouin Scattering Effect and Various Types of Method to Eliminate this Effect," International J. Computer Applications, **92**(7)(2014).

[10] Qin, G.; Sotobayashi, H.; Tsuchiya, M.; Mori, A.; Suzuki, T.; Ohishi, Y. J., " Stimulated Brillouin Scattering in a Single-Mode Tellurite fiber for Amplification, Lasing, and Slow Light Generation,"Lightwave Technology,**26**, 492–498 (2008).

[11] J. H. Lee, T. Tanemura, K. Kikuchi, T. Nagashima, T. Hasegawa, S.Ohara, and N. Sugimoto, "Experimental comparison of a Kerr nonlinearity figure of merit including the stimulated Brillouin scattering threshold for state-of-art nonlinear optical fibers," *Opt. Lett.*, vol. 30, 2005, pp. 1698–1700.

14.139.251.107 {ts '2016-12-26 04:28:31'}

ISSN: 2395-1680 (ONLINE)
DOI: 10.21917/ijme.2016.0047

DFAL BASED FLEXIBLE MULTI-MODULO PRESCALER

Nitish[1], Neeta Pandey[2], Kirti Gupta[3] and Manu Kumar Saini[4]
[1,2,4]*Department of Electronics and Communication Engineering, Delhi Technological University, India*
E-mail: [1]nitish.nitish7593@gmail.com, [2]n66pandey@rediffmail.com, [4]manuksaini@gmail.com
[3]*Department of Electronics and Communication Engineering, Bharati Vidyapeeth's College of Engineering, India*
E-mail: [3]kirtigupta22@gmail.com

Abstract

The quest to have longer battery life and reduced packaging cost has been motivating factor behind developing low power circuits for different applications. Research in adiabatic logic has recently gained momentum and diode free adiabatic logic (DFAL) is one among promising variant. This paper presents a diode free adiabatic logic (DFAL) based flexible multi-modulo prescaler. It provides frequency division of 32, 33, 47, 48, 64, 65, 79 and 80 based upon the value of control signals. The functionality and performance of the proposed prescaler is investigated through TSPICE simulations by using 0.18 micron TSMC technology parameters. The performance parameters average power dissipation, time delay and PDP of the DFAL based circuit are compared with its static CMOS counterpart and a maximum power saving of 84.6% is achieved.

Keywords:

CMOS, DFAL, Dual-Modulo Prescaler, Multi-Modulo Prescaler

1. INTRODUCTION

There is immense increase in the number of components that are placed on same piece of silicon which may be attributed to aggressive and continual feature size reduction. Coupled with this is proliferation in the demand of portable consumer products and high-end circuits which culminates into shorter battery life in case the former one and requirement of cooling packages in the later. Thus the focus on low power consumption which was earlier limited to a class of integrated circuits has become part of almost every design. The research efforts have been made at various levels of VLSI design abstractions and methodologies have been worked upon. At circuit level, adiabatic logic has emerged as promising low power technique and is based on energy recycling [1-5]. Many variants of adiabatic logic namely: Two-Phase Adiabatic Static CMOS logic (2PASCL) [6], Clocked Cascadable Adiabatic Logic (CCAL) [7], Glitch Free Cascadable Adiabatic Logic (GFCAL) [8], Quasi-Static Energy Recovery logic (QSERL) [10], Positive feedback adiabatic logic (PFAL) [10], Efficient Charge Recovery Logic (ECRL) [11] and Diode Free Adiabatic Logic (DFAL) [12] are available in open literature. These styles differ in terms of the type of power supply used and path between power supply and output node.

Most of these families suffer from limitations such as large time delay, output degradation and leakage of current etc. As DFAL [12] has low power dissipation and lower PDP with respect to static CMOS and other existing adiabatic logic families, therefore it is chosen for further exploration. Different applications such as basic logic gates, full-adder, positive and negative edge triggered D-flip flop; multiplier and prescalers are developed in recent past [12-15]. A prescaler is used to divide input frequency to a lower frequency based on the division ratio (N). A flexible multi-modulo prescaler is a block which gives multiple division of frequency by making use of dual modulo prescaler. It is a constituent block of frequency synthesizers [16] and is generally employed in mobile TV, data bus synchronizer, co-prime division pre-scaler and parallel path frequency divider circuit etc. [17]. Since prescaler is a circuit which operates at higher frequency, hence power dissipation in the circuitry is very high. In this paper, DFAL based multi-modulo prescaler is proposed and its performance is examined.

In section 2, a brief description of DFAL is given. Section 3 begins with proposed DFAL-based flexible multi-modulo prescaler architecture, followed by operation of the circuit in various frequency divisions such as divide by 32, 33, 47, 48, 64, 65, 79 and 80. The proposed circuit is verified in section 4 using TSPICE simulations and performance analysis for power dissipation, time delay and power delay product has been done for each of the frequency divisions. The results of the DFAL based circuit at each frequency division are compared with the corresponding CMOS counterpart, at a frequency range of 5-100MHz. Finally, the conclusion is stated from the analysis of the results in section 5.

2. DIODE FREE ADIABATIC LOGIC (DFAL) FAMILY

The generalized block diagram of DFAL family [15] is shown in the Fig.1.

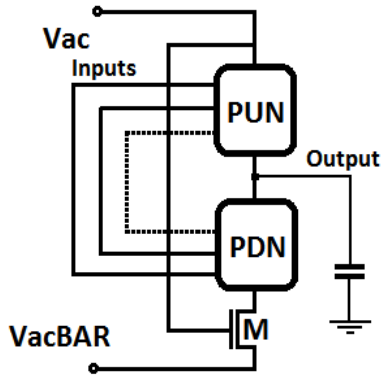


Fig.1. Generalized block diagram of DFAL family [13]

The structure is similar to CMOS logic but differ by adding an additional NMOS transistor 'M' and using split level sinusoidal power supply (V_{ac} and V_{acBAR}). It comprises of a pull-up network (PUN) and a pull-down network (PDN) for complementary operation. Transistor '*M*', driven by V_{ac}, is responsible for discharging of output and show significant power reduction by offering much smaller resistance than other adiabatic logic families to discharge the output node [7].

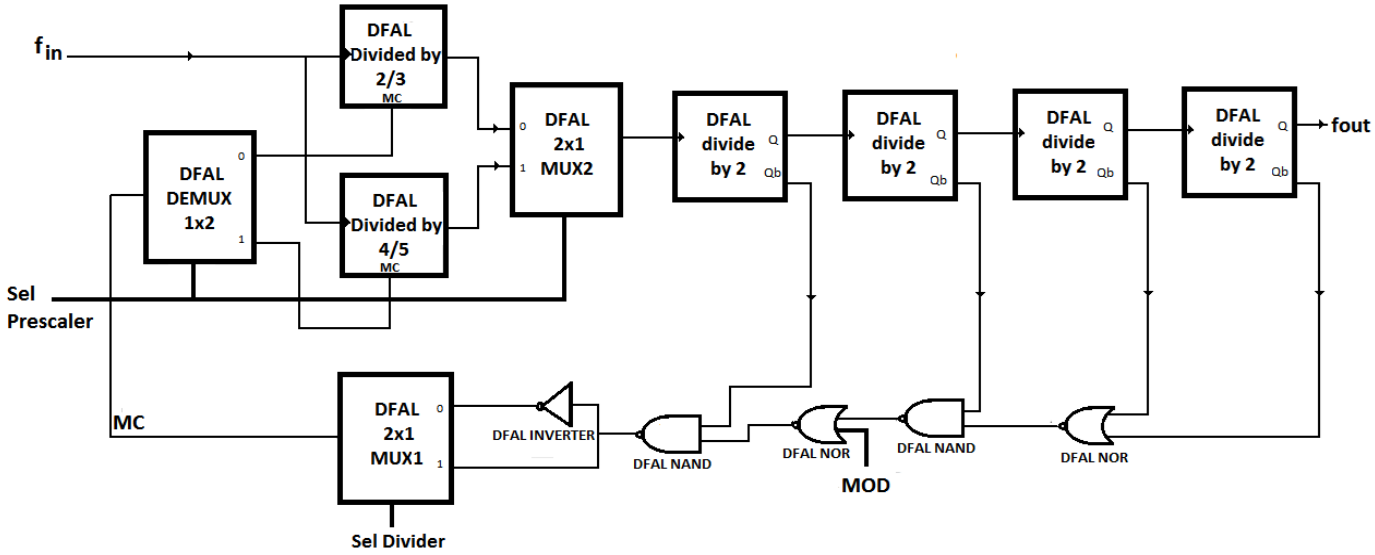


Fig.2. Proposed architecture for the flexible DFAL based multi-modulo prescaler

A DFAL gate operates in two phases namely, hold phase and the evaluation phase depending on the power supply value. In the hold phase, V_{ac} ramps down and V_{acBAR} ramps up the gate is in hold phase and no switching activity takes place, irrespective of the output voltage and inputs. Alternatively, when V_{ac} ramps up and V_{acBAR} ramps down the circuits enters evaluation phase. Depending upon the inputs the output follows the power supply signal. That is, if inputs are such that the PUN is active then the output node follows the V_{ac} signal (ramps up) otherwise for activated PDN, the output node follows the V_{acBAR} (ramps down) signal.

3. PROPOSED MULTI-MODULO PRESCALER

A prescaler is a constituent block of any communication systems. It is a circuit block used for lowering the frequency of signal (f_{in}) by factor (X). Some of the existing prescaler in DFAL family include Frequency divide-by-2, frequency divider-by-3, prescaler by 3 with 50% duty cycle and prescaler by 5 with 50% duty cycle. In this paper, a flexible multi-modulo prescaler, a major block in multi-band flexible divider in a frequency synthesizer is worked upon. The proposed architecture and the operation of the flexible multi-modulo prescaler are presented.

3.1 ARCHITECTURE

The proposed architecture for a DFAL based flexible multi-modulo prescaler circuit as shown in Fig.2. It consists of two dual-modulo prescalers i.e. 2/3 and 4/5, an asynchronous divide by 16 circuit, two multiplexers (MUX1 and MUX2), a demultiplexer (DEMUX) and few combinational gates for intermediate signal generations. There are three control signals modulo control (MOD) signal, Sel Prescaler, Sel Divider used for the selection of the divide by factor. The input signal with frequency (f_{in}) is fed to the dual-modulo prescaler block then depending upon the value of Sel prescaler and an intermediate MC control signal either 2/3 or 4/5 gets selected. The signal passes further through the asynchronous divide by 16 circuits. The intermediate signals of the divide-by-2 circuits in connection with the control signal modulo control MOD are used to generate appropriate inputs to the Sel Divider multiplexer. The output of the multiplexer then forms the MC signal used for prescalers selection. The DFAL based block diagram of the individual constituents such as dual modulo 2/3 prescaler dual modulo 4/5 prescaler and 1×2 DEMUX and 2×1 MUX are shown in Fig.3 for complete reference.

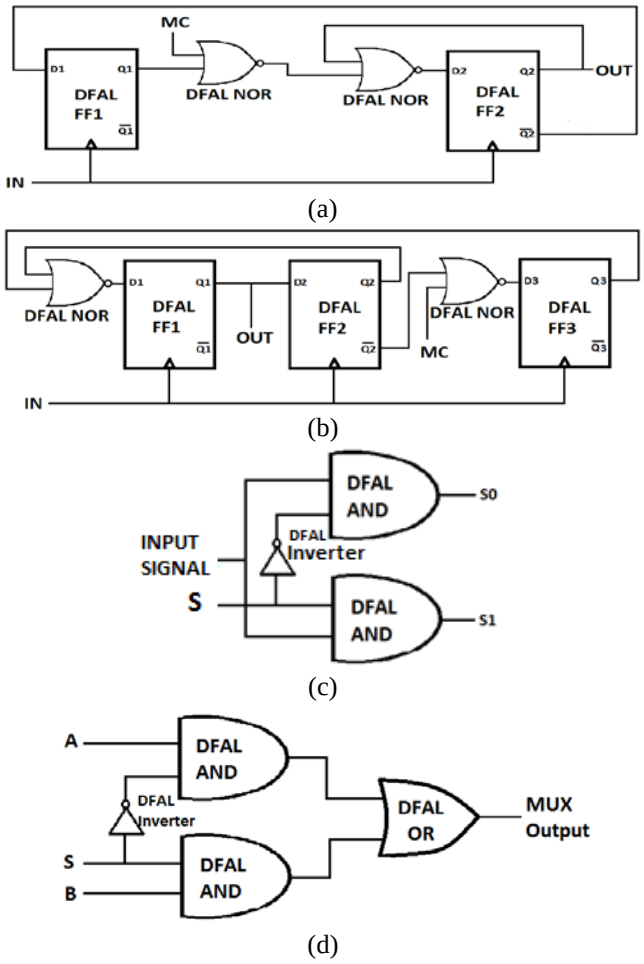


Fig.3. Block diagram of a) dual modulo 2/3 Prescaler b) dual modulo 4/5 Prescaler c) 1×2 DEMUX d) 2×1 MUX

3.2 OPERATION OF THE CIRCUIT

The proposed architecture provides frequency division factor N depending upon Sel Prescaler, Sel Divider and MOD control signals. The frequency division factor N for various combinations of control signals are enlisted in Table.1. Based on the proposed architecture, it is clear that the selection of dual modulo prescalers (2/3 and 4/5) is decided by "Sel Prescaler" and mode control (MC) signals. For Sel Prescaler = 0, the MC signal is sent to 2/3 modulo prescaler through DEMUX and the output of the 2/3 modulo prescaler is selected using MUX2 with further connects to divide by 16 block and gives frequency division at $f_{out.}$ Similarly, for Sel Prescaler = 1, the 4/5 modulo prescaler path is enabled i.e. the MC signal is given to 4/5 prescaler using DEMUX and the output of the 4/5 prescaler connects to the divide by 16 block. It is evident now that the generation of the appropriate MC signal is thus essential. The Sel Divider and MOD control signals along with the combinational gates generates the MC signal. An in-depth discussion on its generation for all the combination of the control signals is presented further.

Table.1. Frequency division in accordance to Selection Control signal for proposed circuit

SEL Prescaler	SEL Divider	MOD	Frequency division factor N
0	1	1	32
0	1	0	33
0	0	0	47
0	0	1	48
1	1	1	64
1	1	0	65
1	0	0	79
1	0	1	80

3.2.1 Case 1: Select Prescaler = 0, SEL Divider = 1, MOD = 1

When MOD is at logic 1, the NOR gate gives logic 0 irrespective of its second input. This logic 0 signal when passed to NAND gate gives logic 1 always and the MUX1 gets two signals either logic 1 or 0 at its input. Now if "SEL Divider" signal = 1, then the MUX1 will select logic 1 and set MC = 1. Now this MC control signal will enable divide by 2 out of 2/3. After the selection of divide by 2 modulo in the asynchronous block of divide by 16, it will give a resultant frequency division of 32 at the f_{out}. A pictorial representation of the selection is shown in Fig.4 where continuous line signifies that the block is in use while the dotted line denotes non usage.

3.2.2 Case 2: Select Prescaler = 0, SEL Divider = 1, MOD = 0

If MOD is logic 0 then the combinational part of the proposed circuit is enabled. Now "Sel Divider" = 1 enables the input of the MUX1 coming out from the NAND gate. This give rise to frequency division of 33 though the dual modulo 2/3 prescaler.

3.2.3 Case 3: Select Prescaler = 0, SEL Divider = 0, MOD = 1

When MOD is logic 1 the NOR gate gives logic 0 irrespective of its second input. This logic 0 signal when passed to NAND gate gives logic 1 always and the MUX1 gets two signals either logic 1 or 0 at its input. Now if "Sel Divider" signal=0, then the MUX1 will select logic 0 and set MC = 0. Now this MC control signal will enable divide by 3 out of 2/3. After the selection of divide by 3, modulus the asynchronous block of divide by 16 will give a resultant frequency division of 48 at the f_{out}.

3.2.4 Case 4: Select Prescaler = 0, SEL Divider = 0, MOD = 0

If MOD is logic 0 then the combinational part of the proposed circuit is enabled. Now "Sel Divider" = 1 enables the input of the MUX1 coming out from the NAND gate. This will give rise to frequency division of 47 though the dual modulo 2/3 prescaler.

3.2.5 Case 5: Select Prescaler = 1, SEL Divider = 1, MOD = 1

When MOD is logic 1 the NOR gate gives logic 0 irrespective of its second input. This logic 0 signal when passed to NAND gate gives logic 1 always and the MUX1 gets two signals either logic 1 or 0 at its input. Now if "Sel Divider" signal=1, then the MUX1 will select logic 1 and set MC=1. Now this MC control signal will enable divide by 4 out of 4/5. After the selection of divide by 4, modulus the asynchronous block of divide by 16 will give a resultant frequency division of 64 at the f_{out}.

3.2.6 Case 6: Select Prescaler = 1, SEL Divider = 1, MOD = 0

If MOD is logic 0 then the combinational part of the proposed circuit is enabled. Now "Sel Divider" = 1 enables the input of the MUX1 coming out from the NAND gate. This will give rise to frequency division of 65 though the dual modulo 2/3 prescaler.

3.2.7 Case 7: Select Prescaler = 1, SEL Divider = 0, MOD = 1

When MOD is logic 1 the NOR gate gives logic 0 irrespective of its second input. This logic 0 signal when passed to NAND gate gives logic 1 always and the MUX1 gets two signals either logic 1 or 0 at its input. Now if "Sel Divider" signal=0, then the MUX1 will select logic 0 and set MC=0. Now this MC control signal will enable divide by 5 out of 4/5. After the selection of divide by 5, modulus the asynchronous block of divide by 16 will give a resultant frequency division of 80 at the f_{out}.

3.2.8 Case 8: Select Prescaler = 1, SEL Divider = 0, MOD = 0

If MOD is logic 0 then the combinational part of the proposed circuit is enabled. Now "Sel Divider" = 1 enables the input of the MUX1 coming out from the NAND gate. This will give rise to frequency division of 79.

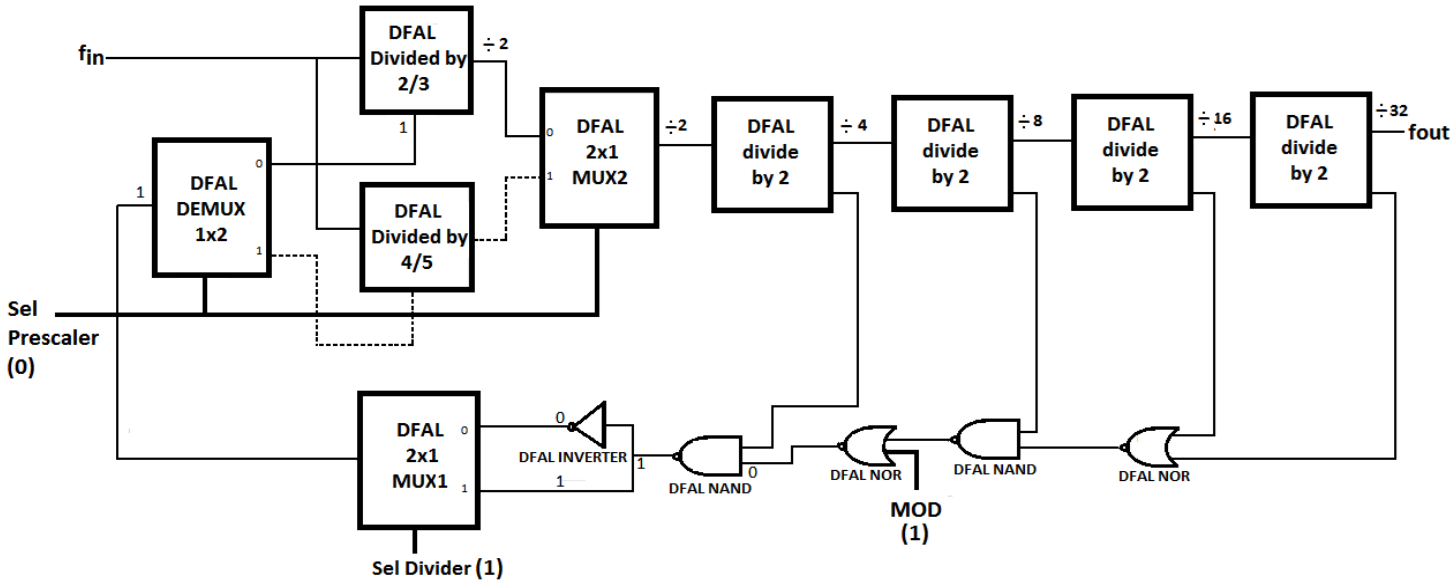


Fig.4. Proposed architecture operating as Divide by 32 prescaler under case 1

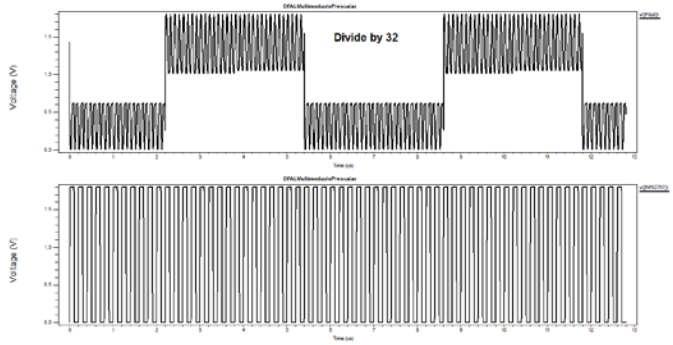
4. SIMULATION RESULTS

The functionality of the proposed flexible multi-modulo prescaler is verified for all division factors through TSPICE simulations using 180 nm CMOS technology parameters. The performance of the proposed DFAL prescalers is compared with its CMOS counterpart in terms of power dissipation, time delay and power delay product (PDP) for varying input frequency ranging from 5MHz to 80MHz. For DFAL circuits, the input frequency is kept half of supply clock frequency. Load capacitance and transistor aspect ratio of 100 fF and 540 nm/180 nm respectively are taken in simulations for both the styles. The section first functionally verifies the feasibility of the proposed flexible multi-modulo prescaler and then presents the simulation results for the performance evaluation.

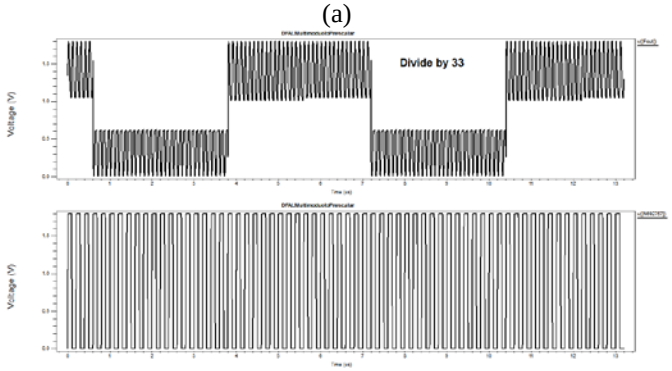
The results for proposed circuits are compared with the results of its CMOS counterpart in the subsections below for all the different frequency divisions i.e. 32, 33, 47, 48, 64, 65, 79 and 80.

4.1 FUNCTIONAL VERIFICATION OF THE PROPOSED ARCHITECTURE

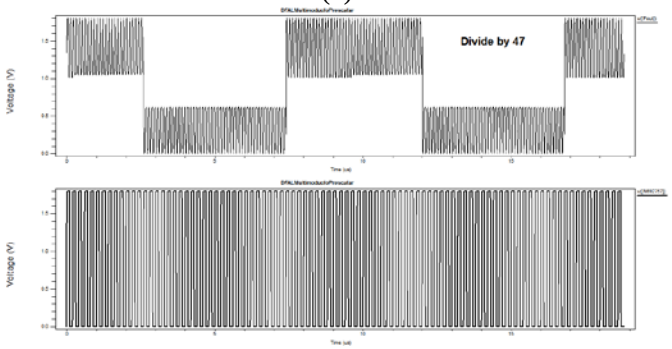
The proposed DFAL based flexible multi-modulo prescaler is configured for different frequency division factor i.e. 32, 33, 47, 48, 64, 65, 79 and 80 according to Table.1. For operation as divide by 32 prescaler (case 1), the control signals Sel Prescaler, Sel Divider and MOD logic levels are set to low, high and high respectively. The output waveform for the first two divide by 32 cycles of the proposed divide by 32 prescaler is shown in Fig.5(a). The waveforms corresponding to the different cases II-case VIII are shown in Fig.5(b)-Fig.5(h). It can be observed that the proposed DFAL based flexible multi-modulo prescaler is able to conform to the required functionality. Similar waveforms were obtained from the CMOS based prescalers and are omitted.



(a)



(b)



(c)

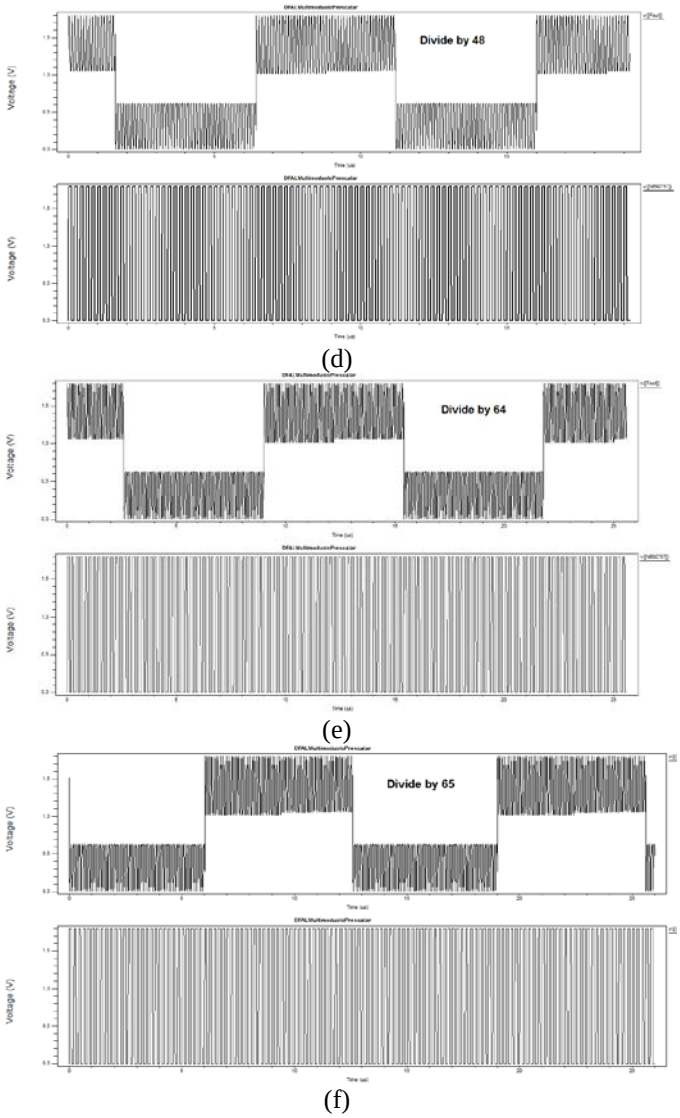


Fig.5. Simulation waveforms of Prescalers a) case 1: Divide by 32 b) case 2: Divide by 33 c) case 3: Divide by 47 d) case 4: Divide by 48 e) case 5: Divide by 64 f) case 6: Divide by 65 g) case 7: Divide by 79 h) case 8: Divide by 80

4.2 PERFORMANCE EVALUATION

The performance of the proposed DFAL based flexible multi-modulo prescaler is evaluated in terms of power, delay and PDP. A complete listing of the values of these parameters for all the cases of DFAL and CMOS based prescalers are summarized in Table.2.

Table.2. Summary of Simulation Results

Frequency / Style	5 MHz	10 MHz	16 MHz	25 MHz	50 MHz	62.5 MHz	100 MHz	Max % improvement w.r.t. CMOS
Divide-by-32								
Power Dissipation (uW)								
Static CMOS	8.66	10.84	13.48	17.48	28.27	34.83	40.71	80.48%
DFAL	1.69	3.26	5.26	8.32	18.66	24.75	33.39	
Time Delay (ns)								
Static CMOS	1.00	1.25	1.37	1.37	1.36	1.36	1.37	
DFAL	2.98	2.60	2.36	2.13	1.81	1.75	1.70	
PDP (fJ)								
Static CMOS	8.66	13.55	18.46	23.94	38.44	47.36	55.77	41.92%
DFAL	5.03	8.47	12.41	17.72	33.77	43.31	56.76	
Divide-by-33								
Power Dissipation (uW)								
Static CMOS	8.74	10.89	13.51	17.53	28.33	34.88	40.84	80.89%
DFAL	1.67	3.23	5.22	8.26	18.55	24.62	33.22	

Time Delay (ns)								
Static CMOS	1.03	1.26	1.32	1.37	1.37	1.37	1.36	
DFAL	2.97	2.62	2.37	2.12	1.82	1.74	1.70	
PDP (fJ)								
Static CMOS	9.00	13.72	17.83	24.01	38.81	47.78	55.54	45%
DFAL	4.95	8.46	12.37	17.51	33.76	42.83	56.47	
Divide-by-48								
Power Dissipation (uW)								
Static CMOS	8.32	10.14	12.42	15.73	24.54	30.01	35.70	82.81%
DFAL	1.43	2.72	4.38	6.89	16.08	21.30	28.70	
Time Delay (ns)								
Static CMOS	1.00	1.21	1.32	1.37	1.37	1.36	1.36	
DFAL	2.95	2.64	2.38	2.15	1.81	1.74	1.70	
PDP (fJ)								
Static CMOS	8.32	12.26	16.39	21.55	33.61	40.81	48.55	49.40%
DFAL	4.21	7.18	10.42	14.81	29.10	27.06	48.79	
Divide-by-47								
Power Dissipation (uW)								
Static CMOS	8.30	9.88	12.34	15.67	24.66	30.19	35.96	82.41%
DFAL	1.46	2.77	4.46	7.03	16.39	21.71	29.31	
Time Delay (ns)								
Static CMOS	1.00	1.30	1.33	1.36	1.37	1.36	1.37	
DFAL	3.00	2.67	2.37	2.13	1.81	1.74	1.72	
PDP (fJ)								
Static CMOS	8.30	12.84	16.41	21.31	33.78	41.05	49.26	47.29%
DFAL	4.38	7.39	10.57	14.97	29.66	37.77	50.41	
Divide-by-64								
Power Dissipation (uW)								
Static CMOS	8.54	9.67	11.61	14.64	22.60	27.74	32.92	84.31%
DFAL	1.34	2.47	3.96	6.29	14.88	19.72	26.57	
Time Delay (ns)								
Static CMOS	0.86	1.25	1.32	1.36	1.36	1.36	1.36	
DFAL	2.94	2.63	2.35	2.13	1.81	1.74	1.69	
PDP (fJ)								
Static CMOS	7.34	12.08	15.32	19.91	30.73	37.72	44.77	46.46%
DFAL	3.93	6.49	9.30	13.39	26.93	34.31	44.90	
Divide-by-65								
Power Dissipation (uW)								
Static CMOS	8.60	9.67	11.69	14.75	22.75	28.09	33.20	84.19%
DFAL	1.36	2.50	4.00	6.34	15.01	19.89	26.81	
Time Delay (ns)								
Static CMOS	0.93	1.25	1.32	1.37	1.37	1.36	1.36	
DFAL	2.97	2.63	2.36	2.13	1.82	1.73	1.69	
PDP (fJ)								
Static CMOS	7.99	12.08	15.43	20.20	31.16	38.20	45.15	49.56%
DFAL	4.03	6.57	9.44	13.50	27.31	34.40	45.30	

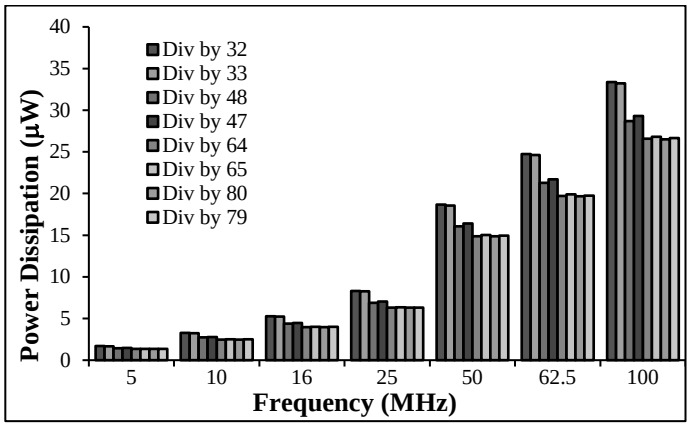
Divide-by-80								
Power Dissipation (uW)								
Static CMOS	8.44	9.67	11.52	14.51	22.43	27.55	32.62	84.12%
DFAL	1.34	2.48	3.98	6.29	14.86	19.66	26.49	
Time Delay (ns)								
Static CMOS	0.83	1.23	1.33	1.36	1.37	1.36	1.36	
DFAL	2.94	2.61	2.36	2.16	1.82	1.74	1.68	
PDP (fJ)								
Static CMOS	7.00	11.89	15.32	19.73	30.72	37.46	44.36	43.86%
DFAL	3.93	6.47	9.39	13.58	27.04	34.20	44.50	
Divide-by-79								
Power Dissipation (uW)								
Static CMOS	8.70	9.88	11.88	15.03	22.83	28.47	33.64	84.60%
DFAL	1.34	2.49	4.00	6.31	14.93	19.75	26.64	
Time Delay (ns)								
Static CMOS	0.94	1.25	1.32	1.36	1.37	1.36	1.36	
DFAL	2.95	2.60	2.35	2.10	1.81	1.75	1.73	
PDP (fJ)								
Static CMOS	8.17	12.35	15.68	20.44	31.27	38.71	45.75	51.65%
DFAL	3.95	6.47	9.40	13.25	27.02	34.56	46.08	

The simulated results can be analyzed as,

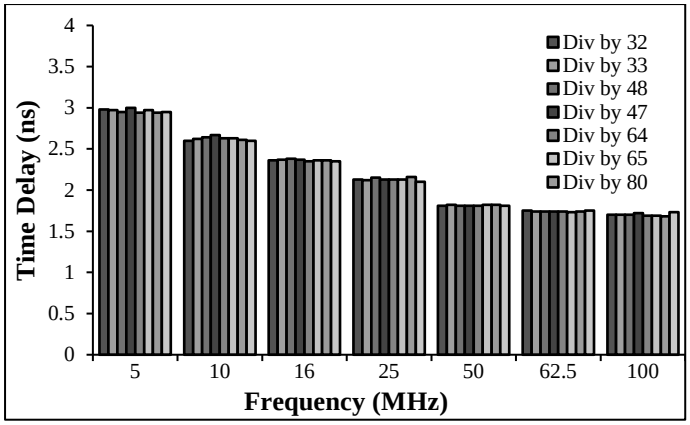
1. The DFAL based flexible multi-modulo prescaler show lower power values in comparison to CMOS based. A maximum power saving of 84.6 % w.r.t CMOS based prescaler is achieved with DFAL based prescaler.
2. An increased in the delay values of the proposed DFAL prescaler is achieved w.r.t CMOS based prescaler. This behavior matches to the basic nature of adiabatic circuits of achieving low power operation by having large delay values.
3. The DFAL based prescaler outperforms in terms of PDP values for all the measured frequencies. This indicates that the power saving is more than speed degradation.

To study the behavior of the proposed DFAL based prescaler at different frequencies a bar graph representation is plotted in Fig.6. The analysis can be summarized as:

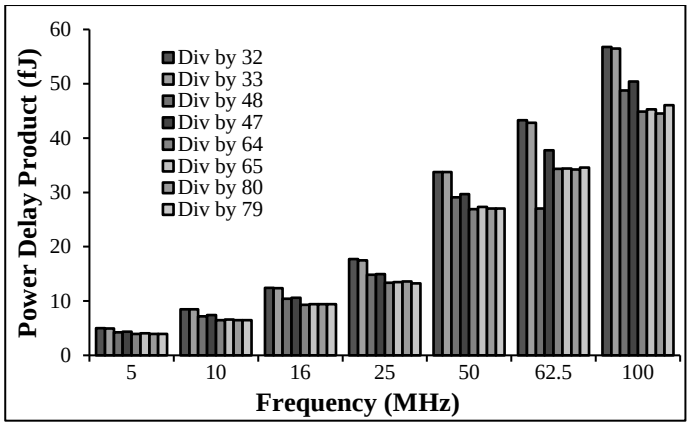
1. There is a rising trend in the power consumption of the prescalers w. r. t. increasing input frequency whereas a falling trend is observed for the delay values.
2. The PDP curve show an increasing trend w. r. t. input frequency as the increase in power is much more pronounce than the reduction in the delay values.
3. The delay values of the prescaler configured for all the cases show almost same delay values at a particular input frequency.



(a)



(b)



(c)

Fig.6. Performance evaluation of the DFAL multi-modulo prescaler configured for all at different frequency

5. CONCLUSION

A new DFAL based architecture for flexible multi-modulo prescaler has been presented in this paper which is a constituent block of frequency synthesizer. The proposed architecture shows better performance for various frequency divisions i.e. 32, 33, 47, 48, 64, 65, 79 and 80 with respect to static CMOS in terms of PDP and power dissipation under varying clock frequency. From the analysis of power dissipation results, DFAL based flexible multi–modulo prescaler shows average maximum power dissipation reduction of 84.6% among various frequency divisions.

The detailed study of the proposed circuit shows that the DFAL based circuit surpasses the CMOS based industry standard in terms of lower power dissipation. Since there is a significant reduction in power, the proposed circuit can be used in many applications of frequency synthesizers such as mobile phones, GPS systems walkie-talkies, satellite receivers with a much better performance and higher efficiency. Also, since the proposed architecture can provide multiple frequency synthesis, it may be useful in different scenarios for different applications which require a specific frequency synthesis. Hence DFAL can be a suitable alternative of conventional CMOS for low power in many existing and future applications.

REFERENCES

[1] Philip Teichmann, "*Adiabatic Logic in Future Trend and System Level Perspective*", 1st Edition, Springer Series in Advance Microelectronics, 2012.

[2] W.C. Athas, L.J. Svensson, J.G. Koller, N. Tzartzanis and E. Ying-Chin Chou, "Low-Power Digital Systems based on Adiabatic Switching Principles", *IEEE Transactions on Very Large Scale Integration Systems*, Vol. 2, No. 4, pp. 398-407, 1994.

[3] G. Dickinson and J.S. Denker, "Adiabatic Dynamic Logic", *IEEE Journal of Solid-State Circuits*, Vol. 30, No. 3, pp. 311-315,1995.

[4] D. Maksimovic, V.G. Oklobdzija, B. Nikolic and K.W. Current, "Clocked CMOS Adiabatic Logic with Integrated Single-Phase Power Clock Supply", *IEEE Transactions on Very Large Scale Integration Systems*, Vol. 8, No. 4, pp. 460-463, 2000.

[5] W.C. Athas, L.J. Svensson, J.G. Koller, N. Tzartzanis and E. Ying-Chin Chou, "Low-Power Digital Systems based on Adiabatic-Switching Principles", *IEEE Transactions on Very Large Scale Integration Systems*, Vol. 2, No. 4, pp. 398-407, 1994.

[6] Nazrul Anuar, Yasuhiro Takahashi and Toshikazu Sekine, "Two Phase Clocked Adiabatic Static CMOS Logic and its Logic Family", *Journal of Semiconductor Technology and Science*, Vol. 10, No. 1, pp. 1-10, 2010

[7] He Li, Yimeng Zhang and Tsutomu Yoshihara, "Clocked CMOS Adiabatic Logic with Low-Power Dissipation", *Proceedings of International Conference in SoC Design Conference*, pp. 64-67, 2013.

[8] N.S.S. Reddy, M. Satyam, K.L. Kishore, "Cascadable Adiabatic Logic Circuits for Low-Power Applications", *IET Circuits Devices and Systems*, Vol. 2, No. 6, pp. 518-526, 2008.

[9] Yibin Ye and K. Roy, "QSERL: Quasi-Static Energy Recovery Logic", *IEEE Journal of Solid-State Circuits*, Vol. 36, No. 2, pp. 239-248, 2001.

[10] A. Blotti and R. Saletti, "Ultra Low-Power Adiabatic Circuit Semi-Custom Design", *IEEE Transactions on Very Large Scale Integration Systems*, Vol. 12, No. 11, pp. 1248-1253, 2004.

[11] Yong Moon and Deog Kyoon Jeong, "An Efficient Charge Recovery Logic Circuit", *IEEE Journal of Solid-State Circuits*, Vol. 31, No. 4, pp. 514-522, 1996.

[12] Shipra Upadhyay, R.A. Mishra, R.K. Nagaria and S.P. Singh, "DFAL: Diode-Free Adiabatic Logic Circuits", *ISRN Electronics*, Vol. 2013, No. 673601, pp. 1-12, 2013.

[13] Himanshu Puri, Kshitij Ghai, Kirti Gupta and Neeta Pandey, "A Novel DFAL based Frequency Divider", *Proceedings of International Conference on Signal Processing and Integrated Networks*, pp. 526-530, 2014.

[14] Nitish, Neeta Pandey, Rajeshwari Pandey and Kirti Gupta, "DFAL based Implementation of Frequency Divider-By-3", *Proceedings of Annual India Conference*, pp. 1-6, 2015.

[15] Neeta Pandey, Nitish, Kirti Gupta and Twinkle Kuhar, "Prescaler for Diode Free Adiabatic Logic family", *Proceedings of International Conference on Computational Techniques in Information and Communication Technologies*, pp. 481-485, 2016.

[16] Hongyu Wang, Paul Brennan and Dai Jiang, "A Generic Multi-Modulus Divider Architecture for Fractional-N Frequency Synthesisers", *Proceedings of IEEE International Frequency Control Symposium Joint with the 21st European Frequency and Time Forum*, pp. 261-265, 2007.

[17] B.M. Miller, "Multi-Modulus Prescaler with Synchronous Output", Available at: http://www.google.co.in/patents/US6614870.

Dispersion Engineered Photonic Crystal FiberStructure for Nonlinear Applications

AGN Chaitanya[1], Than Singh Saini[2], Ajeet Kumar[1]*

[1]Advanced Photonics Simulation Research Lab., Department of Applied Physics,Delhi Technological University, Delhi-110042, India
[2]CSIR-Central Scientific Instruments Organization, Sector-30, Chandigarh-160 030, India
**ajeetdph@gmail.com*

Abstract. We report a promising design of As_2Se_3 Chalcogenide based graded index photonic crystal fiber dispersion engineered at 3.1 μm wavelength and has potential application in field of nonlinear optics like supercontinuum generation.

OCIS codes: (320.6629**)** Supercontinuum generation; (260.2030) Dispersion; (190.4390) Nonlinear optics.

1.**Introduction**

The supercontinuum generation and slow-light generation are very important nonlinear phenomena in the field of nonlinear optics [1]. Supercontinuum generation has found applications in the field of frequency metrology, optical coherence tomography, molecular spectroscopy, biomedical imaging, gas sensing, food quality control and early cancer detection[2-6]. Slow-light generation has found application in the field of optical buffering, optical switching, microwave photonics [7-11]. With improvement in purification and fabrication techniques and also with invention of new fabrication methods more complex and better design in wide variety of optically transparent materials is being introduced in the field of optics. Supercontinuum generation is due to the interplay of linear effect of dispersion and nonlinear effects such as self phase modulation, cross phase modulation, stimulated Raman scattering, four wave mixing etc [3]. For any nonlinear application the two important pre-requisites are zero dispersion at pump wavelength and least effective mode area [1]. These two conditions ensure a high nonlinear coefficient γ resulting in optimised output either a very broad spectrum in case of supercontinuum generation or increased time delay in case of slow-light generation.

In this paper, we have designed an As_2Se_3 chalcogenide based graded index photonic crystal fiber, dispersion engineered to have zero dispersion at 3.1 μm. The effect of variation of position and radius of air hole of inner ring on dispersion has been discussed. The variation of effective area and nonlinear coefficient with respect to wavelength has been demonstrated. The nonlinear refractive index of the material is calculated using Kraimer-Kronig transformation equation at 3.1 μm.

2**. Design of proposed photonic crystal fiber**

The transverse cross sectional view of the proposed PCF structure is illustrated in Fig.1 (*a*). To achieve high nonlinear coefficient and zero dispersion at pump wavelength As_2Se_3 based chalcogenide graded index PCF is designed. As shown in Fig.1 (*a*) the design consists of three layers of air holes. Pitch or position of air hole of each layer is different and can be independently varied. Λ_1, Λ_2, Λ_3 are the distances between the center of the PCF to the center of the air hole of inner, intermediate/middle and outer ring respectively.r_1, r_2, andr_3 are the radius of the air holes of inner, intermediate and outer ring respectively. The shape of the core is hexagonal. The inner ring consists of six air holes, intermediate ring consists of eight air holes and outer ring consists of twelve air holes. Fig. 1(*b*) represents the electric field pattern of the fundamental mode at 3.1 μm.The value of r_n/Λ_nincreases gradually with the order of ring. In other words the effective refractive index of the cladding monotonically decreases, as we move outwards from the axis of the PCF and hence the structure is named as 'graded-index'.The proposed design has a strong control over dispersion profile and zero dispersion wavelength (ZDWL). The normalized electric field pattern of the propagating mode is shown in Figure 1(b).

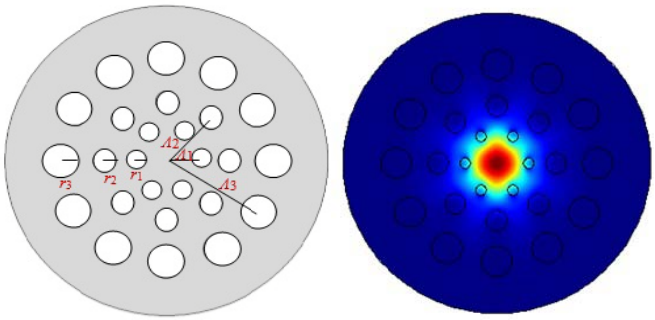


Fig 1: (a) Geometrical view of the proposed graded index PCF (b) Electric field pattern of the propagating mode at 3.1 µm.

3.**Dispersion Characteristics**

The effective refractive index (n_{eff}) is obtained by finite element based full-vectorial method using the COMSOL Multiphysics software. The dispersion D is calculated using [12]

$$D(\lambda) = -\frac{\lambda}{c}\frac{d^2 n_{eff}}{d\lambda^2}\ ps/nm.km \quad (1)$$

The dispersion obtained using Eq. (1) comprises of both material and waveguide dispersion since Thomson Sellmeier's equation is considered while calculating n_{eff} of fundamental mode [13].

$$n(\lambda) = \sqrt{[1+\lambda^2[A_0^2/(\lambda^2 - A_1^2) + A_2^2/(\lambda^2 - 1 9^2) + A_3^2/(\lambda^2 - 4\times A_1^2)]} \quad (2)$$

where, A_0 = 2.234921, A_1= 0.24164, A_2= 0.347441 and A_3= 1.308575.

The variation in radius has significant influence on dispersion characteristics. As the radius of the air hole is increased the ZDWL shifts towards shorter wavelength as shown in Fig 2(a). The effective mode area also decreases with increase in radius of the air hole. The variation in dispersion characteristics due to variation in Λ_1 has been displayed in Fig 2(b). If Λ_1 is increased the effective mode area increases without any significant change in effective refractive index and hence ZDWL shifts towards shorter wavelength. The dispersion at 3.1 µm was -0.7 ps/nm.km

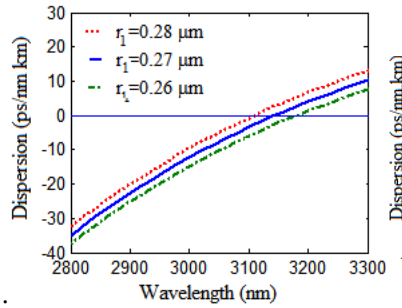


Fig 2(a). Effect of variation of radius on dispersion

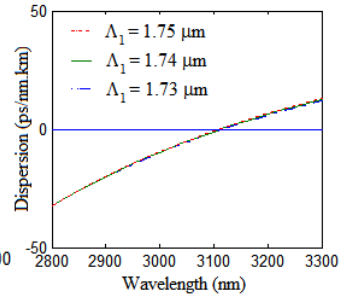


Fig 2(b) Effect of variation of position on dispersion

4.**Nonlinear Characteristics**.

The nonlinear refractive index n_2 is obtained using Kraimer's-Kronig transformation equation given by [14, 15]

$$n_2(\nu) = 1.7\times10^{-18}(n^2+2)^3(n^2-1)\left(\frac{\sigma}{n\times E_s}\right)^2 F\left(\frac{h\nu}{E_g}\right) \quad (3)$$

For As_2Se_3 at 3.1 µm, n= 2.789 obtained from Eqn(2), σ=0.283 nm, E_s = 4.1 eV, E_g= 1.7 eV and F(hν/E_g) is about 1.3. The n_2 obtained from the above Eqn (3) at 3.1 µm is 6.31x10^{-18} m^2W^{-1}. The nonlinear coefficient γ is obtained using [1]

$$\gamma = \frac{2\pi n_2}{\lambda A_{eff}(\lambda)} m^{-1}W^{-1} \qquad (4)$$

The nonlinear coefficient can be optimised by reducing effective mode area and chosing a material with high nonlinear coefficient. The variation of nonlinear coefficient and effective area against wavelength is shown in Fig 3 (a). As the wavelength increases the effective area increases and hence the nonlinear coefficient decreases. The increase in effective area is due to lower confinement of the fundamental mode by the photonic crystal fiber. Figure 3(b) shows the dispersion characteristics of the photonic crystal fiber at optimised parameter. The nonlinear coefficient at 3.1 μm is 2.29 $m^{-1}W^{-1}$.

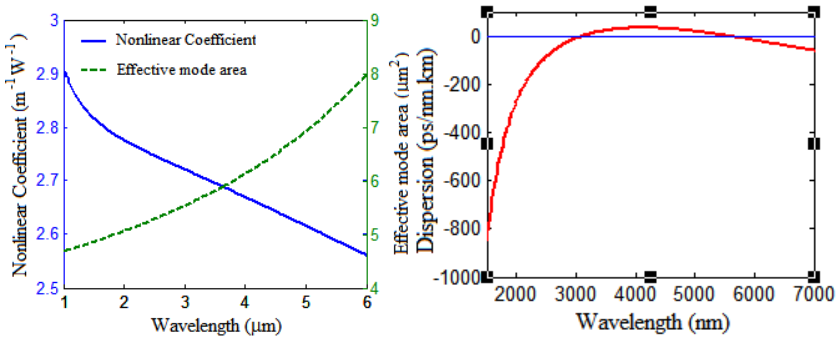


Fig 3(a)Variation of effective area and nonlinear coefficient 3(b) Dispersion at optimised parameter

5. Conclusion

A low dispersion of -0.7 ps/nm.km has been obtained at Λ_1 = 1.75 μm, Λ_2 =2.50 μm, Λ_3 =3.90 μm and the radius of air holes r_1= 0.28 μm r_2= 0.40 μm and r_3= 0.60 μm. A high nonlinear coefficient of 2.29 $m^{-1}W^{-1}$ has been achieved with the above mentioned parameters.The dispersion at lower wavelength is high, but has flat response at mid-IR region. This design can be used for supercontinuum generation in mid-IR region since the dispersion has minimum variation in this region. The proposed PCF can be used for broadband supercontinuum generation which has potential application in the field of medicine, biomedical imaging, security etc. The proposed design can also be used for slow light generation which has potential application in field of optical communication.

References:

[1]G.P. Agrawal, *Nonlinear Fiber Optics 5th ed.*
[2]K.M. Hillgsoe, T.V. Andersen, H.W. Paulsen, C.K. Widsen, K. Molmer, S Kading, R. Krishansen, K.P. Hansen and J.J. Larsen " Supercontinuum generation in photonic crystal fiber with two zero dispersion wavelength", Opt. Exp, (2004), 18299-308.
[3]J. Hu, C.R. Menyuk, L.B. Shaw, J.S. Sanghera and I.D. Aggarwal "Maximising bandwidth of supercontinuum generation in As_2Se_3 chalcogenide fibers" Opt. Exp. 18(3), (2010), 6722-6739.
[4] T. S. Saini, A. Kumar, R. K. Sinha, "Broadband mid-infrared supercontinuum spectra spanning 2 – 15 μm using As_2Se_3 chalcogenide glass triangular-core graded-index photonic crystal fiber," *IEEE/OSA J. Lightwave Technol.*33(18), (2015) 3914 – 3920.
[5] T. S. Saini, A. Kumar, R. K. Sinha, "Broadband mid-IR supercontinuum generation in As_2Se_3 based chalcogenide photonic crystal fiber: A new design and analysis," *Opt. Commun*. 347, (2015),13 – 19.
[6] I.D. Aggarwal and J.S. Sanghera, "Development and application of chalcogenide glass optic fiber at NRL", J.Opt. electron Adv Matter, (2002). 665-678.
[7]T. Baba "Slow light in photonic crystals" Nat Photonics, 2, (2008), 465-473.
[8]T. S. Saini, A. Kumar, R. K. Sinha, "Stimulated Brillouin scattering based tunable slow light in tellurite photonic crystal fiber," *Proc*. Photonics 2014: 12th International Conference on Fiber Optics and Photonics @ OSA 2014, IIT Kharagpur, WB, India, December 13-16, 2014, T3A.28
[9]C. Florea,M. Bashkansky, J. Sanghera, I. Aggarwal, Z. Dutton "Slow-light generation through Brillouin scattering in As_2S_3 fibers 32(2),, (2009), 358-361,
[10]R. K. Sinha, A. Kumar, T. S. Saini, "Analysis and Design of Single-Mode As_2Se_3-Chalcogenide Photonic Crystal Fiber for Generation of Slow Light with Tunable Features," *IEEE J. Sel. Topics Quant. Electron.* 22(2), (2016), 4900706.
[11] T. S. Saini, A. Kumar, R. K. Sinha, "Slow light generation in single-mode tellurite fibers," *J. Modern Optics* 62(7), (2015),508 – 513.
[12]John M. Senior "Optical Fiber Communication, Principles and Practice", 3rd Ed 2013.
[13] W. Yuan "2-10 μm Mid-infrared Supercontinuum Generation in As2Se3 Photonic Crystal Fiber" Laser physics Lett. 10(9), (2013), 095107
[14] M. Sheik-Bahae, D. C. Hutchings, D. J. Hagan, and E. W. Van Stryland, ''Dispersion of bound electron nonlinear refraction in solids,'' IEEE J. Quantum Electron. 27, (1991),1296–1309.
[15] G. Lenz, J. Zimmermann, T. Katsufuji, M. E. Lines, H. Y. Hwang, S. Spalter, R. E. Slusher, S.-W. Cheong, J. S. Sanghera, I. D. Aggrawal, ''Large Kerr effect in bulk Se based chalcogenide glasses,'' Opt. Lett.25, (2000), 254–256.

DESIDOC Journal of Library & Information Technology, Vol. 36, No. 6, November 2016, pp. 437-442 DOI: 10.14429/djlit.36.6.10380
© 2016, DESIDOC

Ever Increasing Cost of Knowledge: Challenges for Libraries for Electronic Resources A Case Study

Narender Kumar* and Lalita**

**University of Delhi, Delhi - 110 007*
E-mail: narenderkumar59@yahoo.com
***Delhi Technological University, Delhi 110 042*
E-mail: lalitakumar69@gmail.com

ABSTRACT

The article highlights the total expenditure on various databases in general and subject-wise by University of Delhi and discusses an annual average increase in foreign databases and impact of exchange rates on expenditure. It highlights the cumulative annual growth rate in general and subject-wise also. The various reasons presented by the publishers for increase in subscription are also discussed. The paper also presents solutions to meet the challenge of ever increasing cost of databases.

Keywords: Electronic databases, cost of knowledge, database subscription

1. INTRODUCTION

Libraries are spending bulk of its financial allocations to have access to the information needed by its users. Academic librarians in the last year about the allocation of their collections budgets, most mention that 70 % to 90 % is devoted to electronic resources with the remainder to print materials[1]. However, the question remains that whether the libraries will be able to sustain the subscription of various databases being subscribed by keeping in view the price cap and the impact of currency exchange rates. A case study of university of delhi has taken to discuss the impact of price cap along with exchange rates on sustainability of e-resources. Based on the empirical data a projection is made for the next ten years regarding expected growth in the prices of e-resources and need of the financial allocations for retaining the subscription of databases.

The University of Delhi with modest beginning with just three colleges, two faculties (Arts and Science) and about 750 students has now become one of the India's largest institutions of higher learning, and among the largest in the world. Presently the university has 85 constituent and affiliated colleges, 16 faculties, 82 departments and 14 centres. The total number of students enrolled in the university during the academic year 2014-15 was 6,28,443. Of these 2,03,460 students were enrolled in the colleges, 17,098 in the university departments, 3,91,344 in the school of open learning and 16,541 in the Non-collegiate women's education board2.

2. METHODOLOGY

Subscription costs of all the databases being subscribed by university of delhi in original cost were collected. The original cost, in case of foreign databases, converted into at exchange rates of reserve bank of India as on 1st January of the concerned year. Since bulk of the budget of electronic databases is being spent on foreign databases the cost only of foreign database has been analysed on the basis of various indicators like average increase, cumulative average increase, subject wise expenditure and growth in subscription rates, tables and graphs are prepared. On the basis of analysis, a projected growth for next 10 years has been made references are given as per IEEE.

3. EXPENDITURE ON E-RESOURCES

Being ranked number one among the universities it has been spending substantial amount on electronic resources since 2006 besides getting access through INFLIBNET. In fact University of Delhi is the highest subscriber of databases among the universities in India. It has access to science direct, sage online, wiley online, lexis-nexis, scopus, springer online, scifinder, IEL onlinemention few. University of delhi has also been ranked one for usage of INFLIBNET databases. University of Delhi also purchased number of archives, e.g., Science Direct, Sage Online, Emerald Management Extra, etc., in the year 2010.

Table 1 provides a glimpse of spending on e-resources and number of electronic databases being subscribed by university of delhi since 2006. Table 1 and Fig. 1 reveal that the university has started subscription of electronic databases for it users in 2006 with 14 foreign databases spending approx 1.23 crore which has enhanced to 4.02 crore in the current year i.e., 2016 Delhi University renewed the subscription of 47 databases (39 foreign and 8 Indian) and adding two new foreign database.

Received 18 September 2016, revised 9 October 2016, online published 30 November 2016

Table 1. Expenditure on electronic resources

Year	Foreign databases		Indian databases		Total	
	No.	Expenditure in	No.	Expenditure in	No.	Expenditure in
2006	14	12270120	0	0	14	12270120
2007	17	17415888	0	0	17	17415888
2008	24	18854626	0	0	24	19017548
2009	27	34788511	3	213340	30	35001851
2010	47	63300121	9	1073610	56	64373731
2011	45	25695354	8	1045233	53	26740587
2012	44	30266700	8	1574181	52	31840881
2013	44	33308376	8	1686332	52	34994708
2014	44	38526137	8	1707832	52	40233969
2015	41	33901499	8	1764553	49	35666052
2016	39	37070090	8	1717001	47	38787091

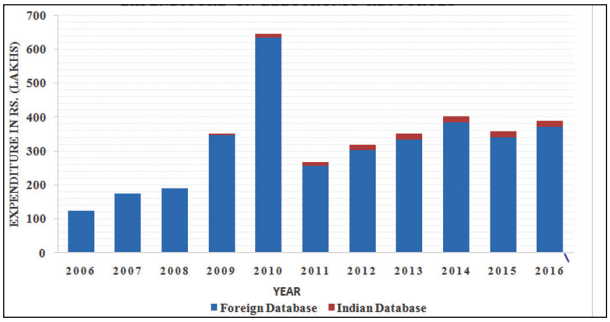


Figure 1. Expenditure on electronic resources.

The CAGR of expenditure incurred on the subscription of e-resources has been 9.60 since 2006.

4. SUBJECT-WISE EXPENDITURE ON E-RESOURCES

The expenditure on various subjects incurred on subscription of e-resources has also been analysed on the basis of their broad subjects and is presented (in %) as Table 2 and Fig. 2. Regarding expenditure on difference subjects an analysis reveals that database belonging to science subjects consume most of the financial allocation which vary from 57.91 % to 80.34 % of total expenditure on e-resources before INFLIBNET started giving access to important databases in 2010. In the current year, the library spent approx 40 % on sciences, 26 % on social sciences, and 1.55 % on arts or humanities databases.

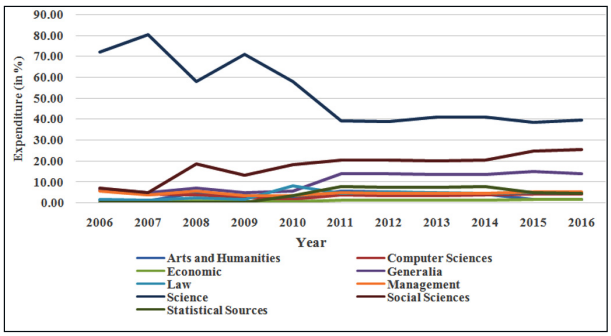


Figure 2. Subject-wise expenditure (per cent).

5. ANNUAL AVERAGE INCREASE IN FOREIGN DATABASES AND IMPACT OF EXCHANGE RATES

Fig. 3. shows the impact of exchange rates on subscription of electronic databases a study of fluctuation in exchange rates is also done in which reveals that exchange rates do impact the expenditure on electronic

Table 2. Subject-wise expenditure on e-resources (per cent)

Subject	2006	2007	2008	2009	2010	2011	2012	2013	2014	2015	2016
Arts and humanities	1.31	0.88	4.60	3.21	2.19	5.48	5.27	4.56	4.06	1.55	1.55
Computer sciences	5.86	4.13	3.77	2.40	1.48	3.60	3.48	3.37	3.61	4.04	4.07
Economics	0.00	0.00	0.60	0.42	0.31	1.11	1.19	1.19	1.19	1.44	1.43
Generalia	6.73	4.85	6.91	4.94	5.56	13.97	13.71	13.48	13.30	14.90	13.90
Law	1.76	1.33	2.21	1.62	7.95	4.30	5.02	4.74	4.32	4.93	4.39
Management	5.54	3.82	5.46	3.47	3.39	4.68	4.55	4.49	4.32	5.34	5.25
Sciences	71.88	80.34	57.91	71.05	57.98	38.99	38.87	40.90	40.99	38.35	39.44
Social sciences	6.92	4.65	18.53	12.89	17.94	20.09	20.40	19.96	20.40	24.53	25.35
Statistical sources	0.00	0.00	0.00	0.00	3.20	7.78	7.50	7.30	7.83	4.92	4.62

resources in Fig. 3. The exchange rates of $ have increased by 49.92 % followed by € 41.82 % and £ 16.74 % since 2006. Regarding comparative CAGR of three currencies, the $ has been increasing @ 3.99 %, € by 3.56 % and £ by 1.56 % per annum. Due to the fluctuation in exchange rates an overall increase in the last ten year subscription of foreign database has been 45.01 % in terms of original currency which rose to 112.6 % when into. The decreasing trends is emerging from the Table for the last three years as the average increase was 2.84 %, 3.22 and -0.5 for 2014, 2015 and 2016, respectively. This trends matches with the EBSCO projections for the same period.[3,4,5] Another reason for decreasing trends during the last three years could be intensive negotiation by the university of delhi.

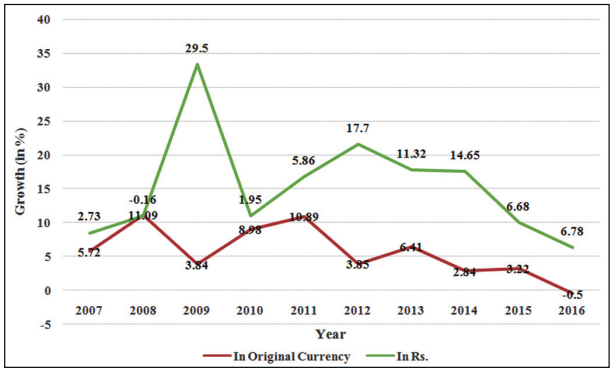


Figure 3. Annual average growth of foreign database.

6. SUBJECT-WISE INCREASE IN FOREIGN DATABASES AND IMPACT OF EXCHANGE RATES

Table 3 provides an analysis of percentage of budget for e-resources is being spend on various subjects. Further analysis of subscription prices of foreign databases (in their original currency) by subjects reveals that there has always been positive increase every year in case of databases belonging to science, management, and social science whereas in other subjects there has been a negative growth also in some years. Databases belong to sciences have shown highest increase (83.75 %) in subscription prices followed by economics (67.22 %), management (47.09 %), computer science (43.27 %), generalia (36.84 %), social sciences (29.41 %), law (23 %) and arts and humanities (8.84 %). Subscription prices of statistical sources have shown negative trends as their prices are reduced by 1.05 %.

On analysis of the impact of exchange rates, it is revealed that despite the negative growth (-1.05 %) in statistical databases in their original currency there has been a positive growth (25.26 %) when converted the into original currency. Subscription prices of science databases have enhanced by 179.54 % though the growth in original currency was 83.75 % and in arts and humanities prices have gone up by 64.83 % in although increase in original currency was only 8.84 %.

7. CUMULATIVE ANNUAL GROWTH RATE (CAGR)

The cumulative annual growth rate (CAGR) in various subjects and overall of the entire databases since 2006 being subscribed by University of Delhi is shown in Table 4. and Fig. 4. These show the CAGR of various databases according to their subjects. Table 4 reveals that in totality the CAGR is 9.60 % per annum.

The CAGR in case of databases originated from other countries is 3.80 % before currency impact. However,

Table 4. Cumulative annual growth rates (subject-wise)

Subject	Cumulative annual growth rate (□)
Arts and humanities	7.10
Computer sciences	7.63
Economics	10.28
Generalia	8.43
Law	7.59
Management	7.89
Sciences	12.64
Social sciences	9.37
Statistical sources	4.57
Indian databases	11.51
Total	9.60

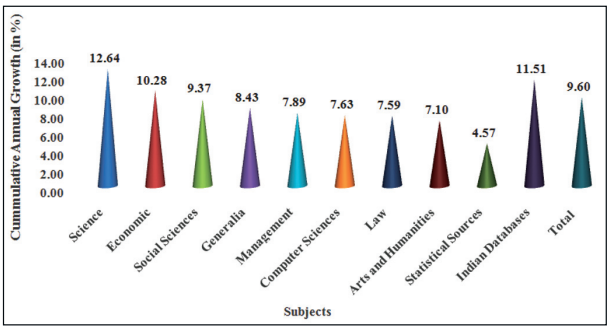


Figure 4. Cummulative annual growth rate (CAGR).

when the original currency is converted into Indian currency the CAGR climbs to 9.25 % per annum for foreign databases. The databases originated from India are also in fact having higher CAGR i.e., 11.51 % compared to foreign databases (9.25 %) in terms of as regards to the CAGR, in relation to various subjects (foreign databases only) it has been revealed that the subscription rate of science databases has the highest CAGR account for 12.64 % followed by economics (10.28 %), social sciences (9.37 %), generalia (8.43 %), management (7.89 %), computer science (7.63 %), law (7.59 %), and lowest is arts and humanities which is 7.10 %.

Table 3. Subject-wise increase in foreign databases

Subjects	2007		2008		2009		2010		2011		2012		2013		2014		2015		2016		Over All	
	OC	Rs.	OC	Rs.	OC	Rs.	OC	Rs.	OC	Rs.	OC	Rs.	OC	Rs.	OC	Rs.	OC	Rs.	OC	Rs.	OC	Rs.
Arts and Humanities	0.00	-4.68	0.00	-10.66	-6.01	30.65	4.02	-4.98	4.32	0.40	0.00	15.15	4.36	10.17	0.13	8.86	1.52	3.79	0.00	8.83	8.84	64.83
Computer Sciences	4.58	0.00	2.00	2.78	-5.19	13.81	22.33	15.11	2.02	-1.89	3.19	14.86	4.76	10.15	1.82	19.01	5.62	1.59	4.89	10.44	43.27	110.29
Economics					4.99	28.38	6.01	5.46	38.61	30.82	10.10	23.24	4.97	10.95	2.95	9.20	3.48	15.59	-16.75	-11.99	67.72	175.65
Generalia	12.77	10.22	4.17	-5.33	3.75	23.04	7.94	3.52	23.81	12.24	1.47	15.55	3.66	9.85	1.61	12.08	3.41	7.83	-4.18	2.39	36.84	92.35
Law	2.50	7.29	34.15	10.87	5.00	38.04	4.76	-7.35	15.67	12.22	0.19	20.28	3.74	5.36	-8.93	3.60	-0.93	1.10	-8.40	0.20	23.00	82.83
Management	1.08	-2.34	22.33	13.05	0.55	15.54	8.34	1.34	3.18	0.22	2.68	16.06	4.84	10.95	1.51	9.76	2.33	11.16	1.00	6.64	47.09	109.61
Sciences	9.30	6.38	16.41	4.53	9.74	39.58	10.15	2.63	8.01	5.49	6.77	20.62	10.56	16.00	3.39	16.80	4.45	8.71	4.82	13.04	83.75	179.54
Social Sciences	0.10	-4.68	0.00	15.02	5.33	35.75	4.66	-3.60	4.26	2.45	6.65	21.15	3.52	9.58	2.58	13.44	3.19	5.50	1.99	11.00	29.41	86.05
Statistical Sources										-16.86	0.00	8.66	13.90	9.59	19.28	37.61	1.25	-7.36	0.00	5.88	-1.05	25.26

8. REASONS FOR CHANGE IN PRICES IN DATABASES

Offer Price: Publishers/aggregators/vendors of electronic databases offer heavy discounted subscription prices of their databases in the beginning to promote their product(s) and enhance the price after getting popularity.

Change in Tier: In some cases if the usage go up and cross the certain level they increase the price and place the institution on a higher tier, hence, require to pay more to access the database.

Acquisition and Mergers of Publisher: Whenever there is change in the ownership of publishing house the pricing of e-databases get changed.

9. FUTURE PROJECTION BASED ON CAGR

Table 5. and Fig. 5 show EBSCO's projecting prices of the serials for many years[3-5]. They projected 6-8 % for 2014, 5-7 % for 2015 and 4-6 % for 2016 before currency impact. From the projections it has been notice that every year expected increase is dropping by one percent. On the basis of present study attempt has been made to project the increase for retaining the subscription of existing databases for the next ten years. The projection has been made on the basis of 2016 as base year.

Figure 5. Future projection on the basis of CAGR.

As per CAGR in various subjects and in totality the multidisciplinary academic institutions libraries have to double its financial allocation in next 8 years to retain the subscription of the existing databases. Future is tenser for the libraries, like, CSIR, IITs, NIITs, Indian Institute of Science, etc., extensively subscribing science databases as they have to double their existing finance in the next six years. Doubling period of existing finance is 10 years for subjects, like, arts and humanities, computer science, law. In case of economics and social sciences the existing finance has to be doubled within 7 years.Management libraries should convert it financial allocations for retaining existing management databases within the period of 9 years.

Table 5. Future projection on the basis of CAGR

Subject	CAGR	2017	2018	2019	2020	2021	2022	2023	2024	2025	2026
Arts and humanities	7.10	107.10	114.70	122.85	131.57	140.91	150.92	161.63	173.11	185.40	198.56
Computer sciences	7.63	107.63	115.84	124.68	134.19	144.43	155.45	167.31	180.08	193.82	208.61
Economics	10.28	110.28	121.62	134.12	147.91	163.11	179.88	198.37	218.76	241.25	266.05
Generalia	8.43	108.43	117.57	127.48	138.23	149.88	162.52	176.22	191.07	207.18	224.64
Law	7.59	107.59	115.76	124.54	133.99	144.16	155.11	166.88	179.55	193.17	207.84
Management	7.89	107.89	116.40	125.59	135.50	146.19	157.72	170.16	183.59	198.08	213.70
Sciences	12.64	112.64	126.88	142.92	160.98	181.33	204.25	230.06	259.14	291.90	328.80
Social sciences	9.37	109.37	119.62	130.83	143.08	156.49	171.15	187.19	204.73	223.92	244.90
Statistical sources	4.57	104.57	109.35	114.35	119.57	125.04	130.75	136.73	142.97	149.51	156.34
Indian databases	11.51	111.51	124.34	138.66	154.62	172.41	192.26	214.39	239.06	266.58	297.26
Total	9.60	109.60	120.12	131.65	144.29	158.14	173.33	189.97	208.20	228.19	250.10

10. SOLUTIONS OF PROBLEMS

Librarians are walking on the double-side edge weapon. One side they have to find the solution for rising cost of e-databases, especially, foreign databases and on other side ever increasing exchange rates. They have to strike a right balance between ever increasing information needs of the users and availability of resources in the library to satisfy those information needs.

Fortunately, the developments in information technology create new opportunities for librarians. The following are some suggestive solutions to meet these challenges.

10.1 National Consortia

Since information should be considered as national resource, there is an urgent need to set up a national consortium by the Government of India who would be responsible to provide any information/documents needed by any person/institution/libraries, etc., in India. National library consortia will have an advantage to have expert's knowledge not only for selecting the resources but also to negotiate the prices of e-resources.

10.2 Library Cooperation

During the print era, the libraries used to subscribe only core titles of periodicals which were useful to meet the objective of the institution. For auxiliary titles they used to depend on the other libraries. They received documents not available in their collection on ILL.

Instead of subscribing bundle collection and try to be self-sufficient, the libraries should scribe only core titles and for auxiliary titles they should get cooperation from other libraries.

10.3 Access Versus Ownership

Introduction of new pricing models by publishers such as licensing (rather than subscription) and access fees for e-information sources and relatively favourable offers for consortia agreements has made the economics of cooperation more visible.

10.4 Pay Per View Transactions

Users tend to download a single article number of times without realising the cost of download. Sometime they download articles after seeing the catchy titles of the articles though not related to their area of study. The libraries don't keep the record who is downloading what, why', and how many times and even for whom (for himself or for someone else). Even usages of many e-resources that are fully subscribed indicate low. Moreover, experts are raising questions on the usage statistics provided by the publishers. To tackle this problem the libraries may adopt the policy to pay for per view transaction. This will help libraries not only to lower the cost but also to maintain the records regarding who is using what and why.

10.5 Multiyear Price Cap Agreement

Another solution to the problem is to enter with publishers/aggregators/vendors multi-year agreements in which price cap is fixed if the library agrees to renew the subscription of the database for years. They agreed to keep the capped pricing as low as 3-5 % for libraries who agree to purchase the database for multiple years.

10.6 Return on Investment Study

It is a high time for libraries in India to do research on return on investment (ROI) which would help in identifying the impact of the usage of electronic journals on the activity of publishing articles by university-affiliated researchers. In particular, it analyses the impact of the usage of e-journals on the scientific production (publications, citations) by domain and type of institution. It develops indicators of causal relationships between usage, publications and citations, and analyses the evolution of the phenomena of causality in time[6].

10.7 Discontinuation of Print Journal

In India, some of the libraries are still maintaining the print run despite the availability of the same title in e-format. The libraries need to reformulate this policy

and discontinue the print run of the journal hence, save the expenditure of the library.

10.8 Just in Time Access

Libraries have been subscribing number of databases in anticipation of demand, i.e., 'Just-in-Case' users need any article the library doesn't to contact the publisher. In this, there are chances that there may not be enough demand for the database justifying its subscription. In 'Just in Time', the libraries acquire the document after receiving the demand from the user. 'Just in time' access satisfies information needs of scholars and keeps cost down as compared to 'Just-in-case'

10.9 Open Access Resources

Libraries must be upto date with the ever evolving information landscape and always on the hunt for reduced costs for accessing scholarly quality information. So far these free resources have been used to supplement and add value to the library's collection. The evaluation of the free internet resources that have been 'added' to the library's collection is ongoing, hopefully to allow for the cancellation of equivalent for-fee resources.

11. CONCLUSIONS

Expenditure on subscription of e-resources has been increasing at the rate of 9.60 % per annum since 2006. The University of Delhi spends most on science databases (58-80 %) and least on arts and humanities. Overall increase in the last 10 year subscription of foreign databases has been 45.01 % in terms of original currency which rises to 112.6 % in terms of the $ (increasing @ 3.99 %), € by 3.56 % and £ by 1.56 % per annum since 2006. Therefore libraries should add an additional 5-7 % to the estimated price increases while preparing a budget. Databases belong to sciences have shown highest increase (83.75 %) in subscription prices followed by economics (67.22 %), management (47.09 %), computer science (43.27 %), generalia (36.84 %), social sciences (29.41 %), law (23 %) and arts and humanities (8.84 %). Subscription prices of statistical sources have shown negative trends as their prices are reduced by 1.05 %.

The CAGR for databases originated from other countries is 3.80 % before currency impact but rose to 9.25 % per annum after converting. Regarding various subjects (foreign databases only), science databases have the highest CAGR (12.64 %) followed by economics (10.28 %), social sciences (9.37 %), generalia (8.43), management (7.89 %), computer science (7.63 %), law (7.59 %), and lowest is arts and humanities (7.10 %). Therefore, it is suggested that the libraries should add an additional 5-7 % to the estimated price increases while preparing a budget.

Information should be considered as national resource there is an urgent need to set up a national consortium. Instead of subscribing bundle collection and try to be self-sufficient the libraries should subscribe only core titles and for auxiliary titles, they should get cooperation from other libraries. The libraries may adopt the policy to pay-for-per view transaction to reduce the expenditure. Another solution to the problem is to enter with publishers/ aggregators/vendors multi-year agreements in which price cap is fixed if the library agreed to renew the subscription of the database for years. The libraries need to discontinue the print run of the journals whose e-access is available. Use 'Just'-in-time' policy instead of 'Just-in-Case' to arrest the increasing trend of expenditure on electronic resources. Libraries must keep up to date with the ever evolving information landscape always on the hunt for reduced costs for accessing scholarly quality information. So far these free resources have been used to supplement and add value to the library's collection.

REFERENCES

1. Breeding, Marshal. Balancing the management of electronic and print resources. *Computers in Libraries,* 2014, **34** (5).
2. University of Delhi. 92nd Annual Report: 2014-2015. S.l.: University of Delhi, 2016. p. 15.
3. EBSCO. EBSCO releases 2014 serials price projection report. PR web: Online visibility from vocus. 26 September 2013. http://www.prweb.com/releases/2014serials/priceprojections/prweb11164612.htm. (accessed on 18 July 2016.)
4. Ebsco serials price projections for 2015. Ebscohost. (Online) 25 September 2014. https://www.ebscohost.com/promomaterials/serials_price_projections_for_2015.pdf (accessed on 18 July 2016).
5. EBSCO serials price projections for 2016. Ebscohost. (Online) 29 September 2015. https://www.ebscohost.com/promomaterials/EBSCOSerialspriceprojectionreport2016.pdf. (accessed on 18 July 2016).
6. Schopfel, Joachim. Electronic resources in academic context: Return on investment. *Technische Universitat Dortmund*. (Online) 24 January 2014. https://www.ub.uni-dortmund.de/listen/inetbib/msg52312.html. (accessed on 8 August 2016).

Contributor

Dr Narender Kumar is working as Deputy Librarian, Central Library, University of Delhi. A doctorate from University of Delhi. He began his career from British Council Division Library, Delhi and further moved to College of Business Studies, University of Delhi as Librarian. During his service, he has participated as resource person at several workshops and seminars related to his profession.

Plasmonics
DOI 10.1007/s11468-016-0473-1

Experimental and Theoretical Analysis of Connector Offset Optical Fiber Refractive Index Sensor

Vanita Bhardwaj[1] · **Kamal Kishor**[2] · **Vinod Kumar Singh**[1]

Received: 20 September 2016 / Accepted: 25 November 2016
© Springer Science+Business Media New York 2016

Abstract In this paper, a high sensitive connector offset optical fiber sensor is employed to detect the refractive index of liquid. The configuration chosen for this experiment is formed by lateral core offset fusion splicing of no-core fiber (NCF) between the single mode fibers (SMF) and cladding modes are excited by misalignment. The sensing principle for refractive index detection is based on Mach-Zehnder Interferometer (MZI) principle and the experiment is carried out by immersion of device in NaCl solutions of different refractive indices. Such refractive index sensor exhibits high sensitivity 197.33 nm/RIU for the surrounding refractive index variation from 1.333 to 1.380, and the result shows the excellent agreement with theoretical analysis. Compared to other sensors, the proposed device has the potential to provide high sensitivity, ease of fabrication, low cost, compact size, and linear response. Thus, it can be used in many applications such as bio-sensors, chemical sensor, temperature sensor, and pressure sensor.

✉ Vanita Bhardwaj
vanitabhardwaj@ap.ism.ac.in

Kamal Kishor
kishorkamal1@rediffmail.com

Vinod Kumar Singh
singh.vk.ap@ismdhanbad.ac.in

[1] Department of Applied Physics, Indian Institute of Technology (Indian School of Mines), Dhanbad 826004, India

[2] TIFAC-Centre of Relevance & Excellence in Fiber Optics & Optical Communications, Applied Physics Department, Delhi Technological University (Formerly Delhi College of Engineering), Bawana Road, Delhi 110042, India

Keywords No core fiber · Core-offset · Mach-Zehnder interferometer · Refractive index

Introduction

Various biological, chemical and physical parameters require refractive index detection. Thus, for refractive index measurement, fiber optic refractive index sensors, like interferometeric sensors [1–6] and sensors based on long-period gratings [7], tilted fiber Bragg gratings [8], tapered fiber [9], Surface plasmon resonance [10] and photonic crystal fiber [11, 12], have been of great interest due to various desirable advantages. Optical fiber-based refractive index possesses many advantages of small size, easy fabrication, high sensitivity and light weight. The measurement of refractive index sensing is very much important in the variety of applications including the inspection of solute concentration and quality control in the monitoring of food engineering processes. The measurements of refractive index of liquids imply its applications in optical, physical, chemical and biological fields. Numerous structures have been proposed for refractive index sensing using various configurations such as double cladding [13], core offset splice [14, 15], concatenating tapers [16] and peanut-shaped structures [17]. The in-line MZIs are fabricated by a splitter, combiner to observe the coupling and recouping of core-cladding modes. These kinds of sensors have been widely used to investigate the temperature [18, 19], strain [20], refractive index [21–23], and liquid level [24]. Compared to other sensors, the sensor based on the core offset structure is more economic owing to low cost and its ease of fabrication.

In this letter, we present a highly sensitive connector lateral core offset optical fiber refractive index sensor based on MZI. The sensing result depends on the

Published online: 06 December 2016

interference between the core mode and cladding modes in the sensing length, in which the cladding modes get excited because of the mismatch-core splicing interface and the surrounding medium. Thus, the transmission shifts with variation of surrounding medium, which makes it possible to detect the refractive index of unknown solutions. The reason why we employ such structure is that SMF-NCF can easily excite the higher order cladding modes and core offset helps to excite the lower-order cladding modes. The order of cladding modes can be easily monitored by changing the length of NCF. The refractive index sensitivities in some investigations are positive [25–27] where as in some other investigations are negative [28, 29]. Here, the negative and positive sensitivity are due to the different cladding mode excitements, and these cladding modes have different response to the surrounding environmental refrac tive index. Therefore, in our present work, we will focus on the investigation of refractive index.

Sensor Fabrication

The sensing device, as shown in Fig. 1, is a composition of SMF_1-NCF-SMF_2 spliced with lateral core offset fusion splicing with SMF_3. The device is fabricated by using short section of a NCF (diameter 96 μm) spliced between two single mode fibers with core/cladding diameter of 8.5 μm/125 μm. Then, the free end of SMF_2 is fusion spliced to another lead out SMF_3 together with laterally core offset of 15 μm. The whole fabrication process involves only splicing and using inexpensive fibers, making it low cost. Moreover, the 10 mm length of NCF is enough to expand the mode field efficiency.

Experimental Setup and Principle

The experimental set up for investigating sensing properties is shown in Fig. 2. Light from broadband source was coupled into the sensing device. The output transmission spectrum was recorded and analyzed by optical spectrum analyzer (OSA). During sensing experiment, the environmental temperature was kept at 25 °C. The first taper SMF_1-NCF due to core diameter difference, couples a part of light from the core mode into the cladding modes. Then, the part of light in cladding modes coupled back into the core at the lead out SMF_2 fiber. The core offset SMF_3 was used to receive and transmits the generated interference pattern of different order cladding modes.

The sensing structure was placed in NaCl and water solutions. When light from broad band source guided into lead SMF_1 further passes through the NCF, the fundamental modes will spread out widely and different order cladding modes get excited causes interference which was then coupled back into the core of SMF_2. No overlapping between core mode fields and cladding mode fields was seen as the lateral core offset was larger than the core diameter of SMF. Due to phase difference of core and cladding modes, a MZI is realized. If only two modes are considered, then the interference pattern of sensing structure can be expressed as

$$I = I_1 + I_2 + 2\sqrt{I_1 I_2}\cos(\Phi_m) \tag{1}$$

where I_1 and I_2 are the propagating lights travelling through the core and cladding of fiber, respectively. Here, core offset was introduced to increase extinction ratio. The extinction ratio for the interferometer is small without introducing an offset. Thus, to obtain high interference depth, we introduce offset with SMF_3. The extinction ratio (ER) of interferometer can be expressed as

$$\mathrm{ER} = 10\log\left[\left(1+\sqrt{I_1 I_2}\right)/\left(1-\sqrt{I_1 I_2}\right)\right]^2, \tag{2}$$

where I_1 and I_2 are distributed power in the lower and higher order modes, respectively. The ER decreases with decrement of power.

From Eq. (1), the intensity of the interference signal reaches its minimum value when Φ_m becomes an odd times number of π. Considering Eq. (1) that the interference signal

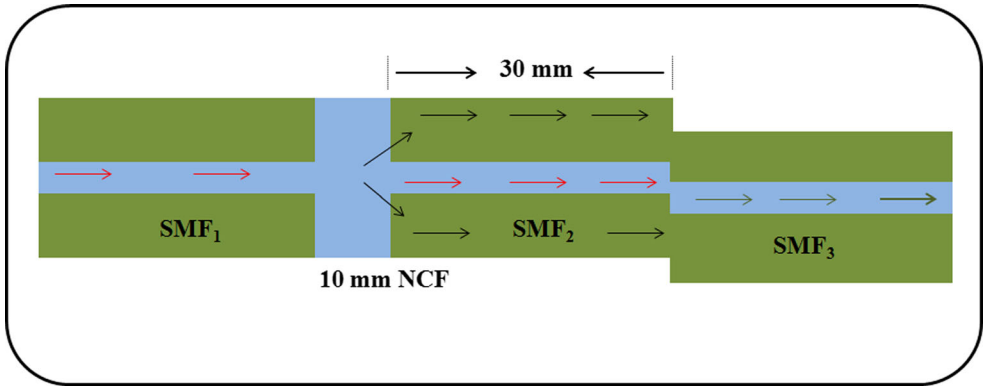


Fig. 1 Schematic of the proposed sensing structure

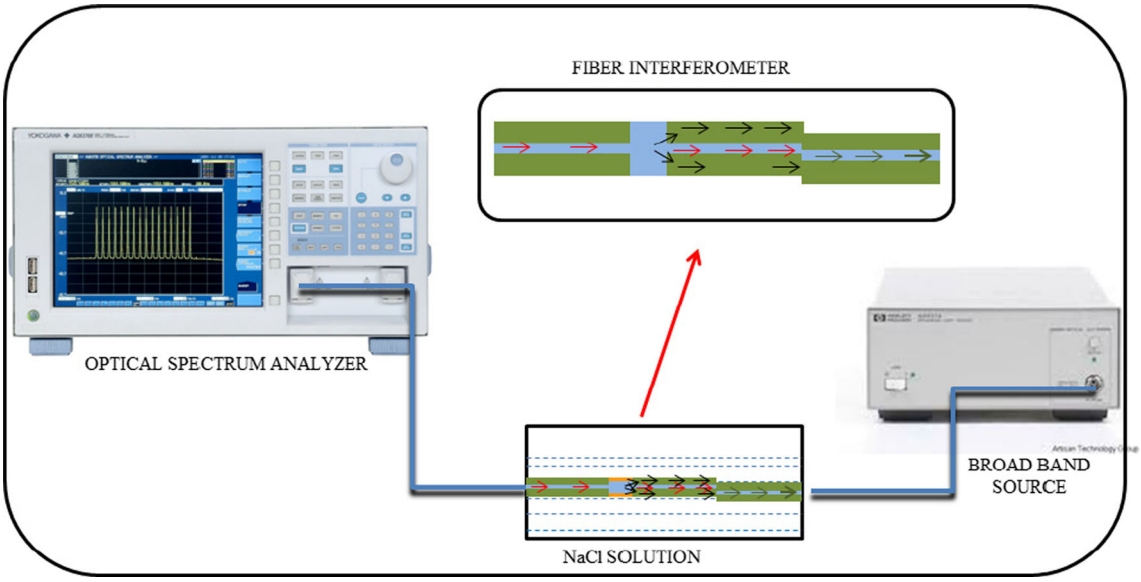


Fig. 2 Experimental set for investigating refractive index sensing properties

reaches its minimum value when $\Delta\Phi = (2m + 1)\pi$. Thus, the dip wavelength of the spectrum can be expressed as

$$\lambda = \frac{2\Delta n_{\text{eff}} L}{2n + 1} \tag{3}$$

where λ is the wavelength of the transmission dip and n is the integer. When the ellipsoidal structure is dipped in different RI liquids, the effective RIs of cladding modes get influenced but the core mode is unaffected. So the effective refractive index between the core and cladding mode $\Delta n_{\text{eff}} = \left(n_{\text{eff}}^{\text{core}} - n_{\text{eff}}^{\text{clad}}\right)$ decreased by $\delta n_{\text{eff}}^{m}$. Thus, when the Δn_{eff} decreased by $\delta n_{\text{eff}}^{m}$, the wavelength shifts towards the shorter wavelength by,

$$\delta\lambda_n \approx \frac{2\delta n_{\text{eff}}^{m} L}{2n + 1} \tag{4}$$

Thus, the interferometer can be used to monitor the surrounding RI. It is clear from Eq. (4) that the sensitivity of the interferometer depends on length L but for compact sensor, L should not be too long.

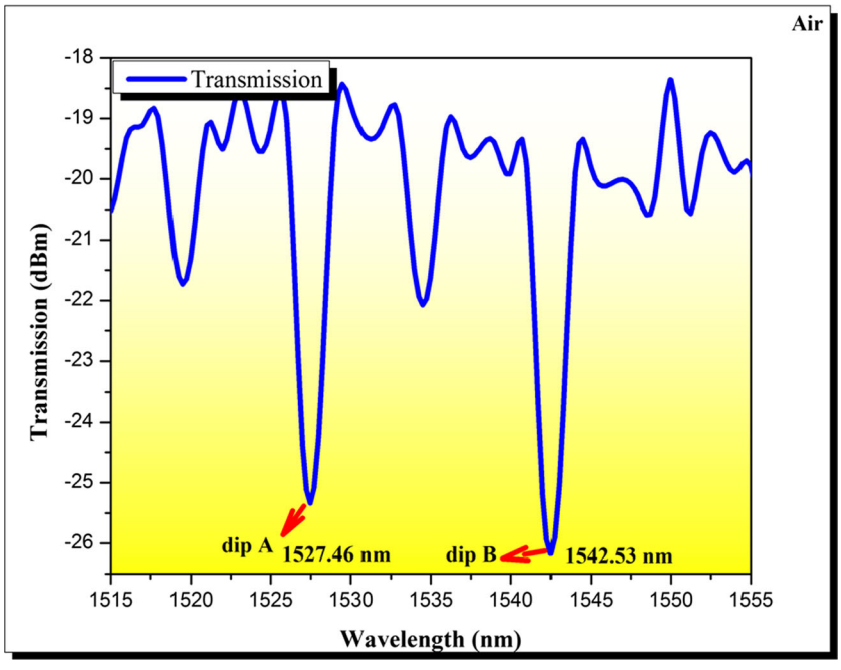


Fig. 3 Transmission spectra of the interferometer in air

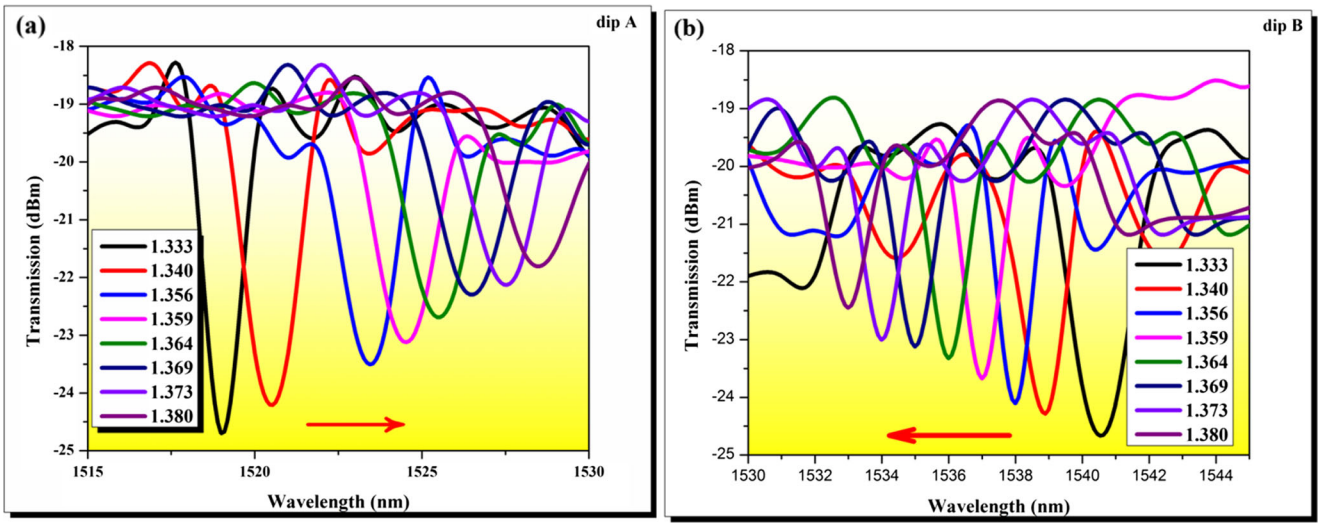


Fig. 4 Transmission spectra of the proposed interferometer at different refractive index of a NaCl solution **a** dip A and **b** dip B

Result and Discussion

The interferometer was immersed in liquid solutions for refractive index testing. NaCl and water solutions with different concentrations were used for refractive index testing. Since the bending, twisting or rotation of fiber will lead to variation in interference spectrum, some part of power in the dominant interference modes coupled into the weak modes. In order to avoid bending, the sensor was kept straight during the measurements. The light source was used to inject a light into the interferometer and the transmission spectrum was recorded by OSA. The light intensity from broadband source is mainly distributed in the core and strong cladding mode. The interference pattern is generated by the interference of the core modes with dominant cladding modes. Figure 3 shows the interference pattern in air.

The transmission spectra for interferometer with different refractive index are shown in Fig. 4.

The experimental result shows that dip A shows red shift whereas dip B shows blue shift with variation of refractive index. The sensitivity obtained for dip A and dip B are 197.33 and −153.91 nm/RIU, respectively (shown in Fig. 5). Here, we obtained positive sensitivity for dip A and negative sensitivity for dip B. The negative sensitivity of dip B is due to the excitement of the core mode and lower order cladding modes whereas the positive sensitivity is due to the participations of the core modes with higher order cladding modes. Such positive and negative sensitivity with changed dip indicates that the interference between cladding modes participates in the modulation of the sensitivity. The overall response of the spectrum is due to the combined effect of the core modes with lower and higher order cladding modes.

However, sensitivity of device can be further enhanced by using metal coating on sensing region of fiber probe to make it surface plasmon resonance-based sensor [30].

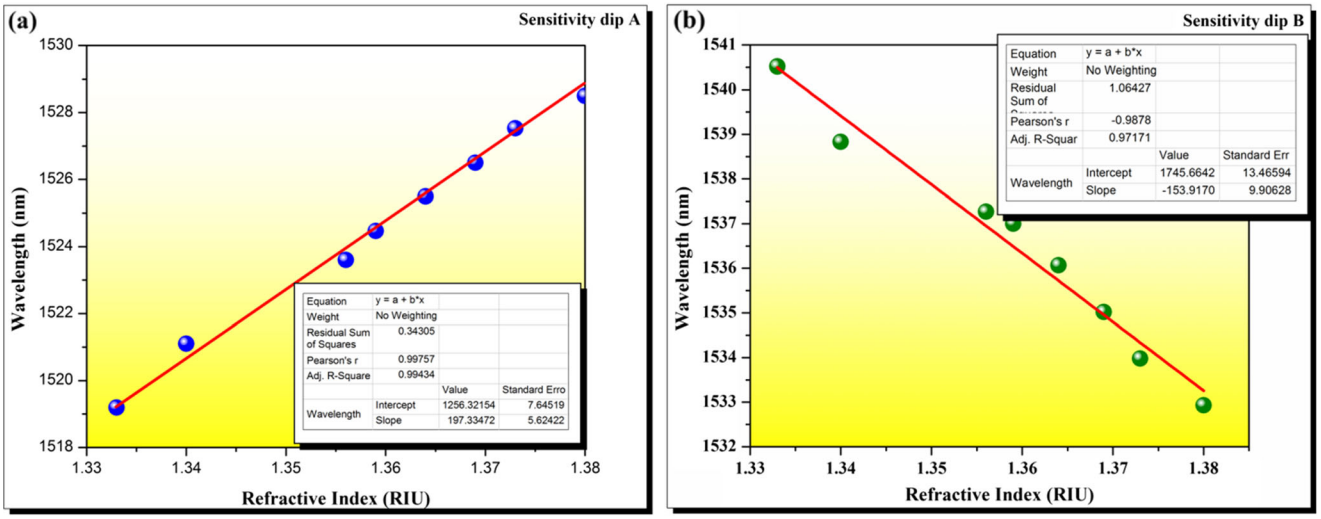


Fig. 5 Recorded wavelength as a refractive index function of NaCl solution for **a** dip A and **b** dip B

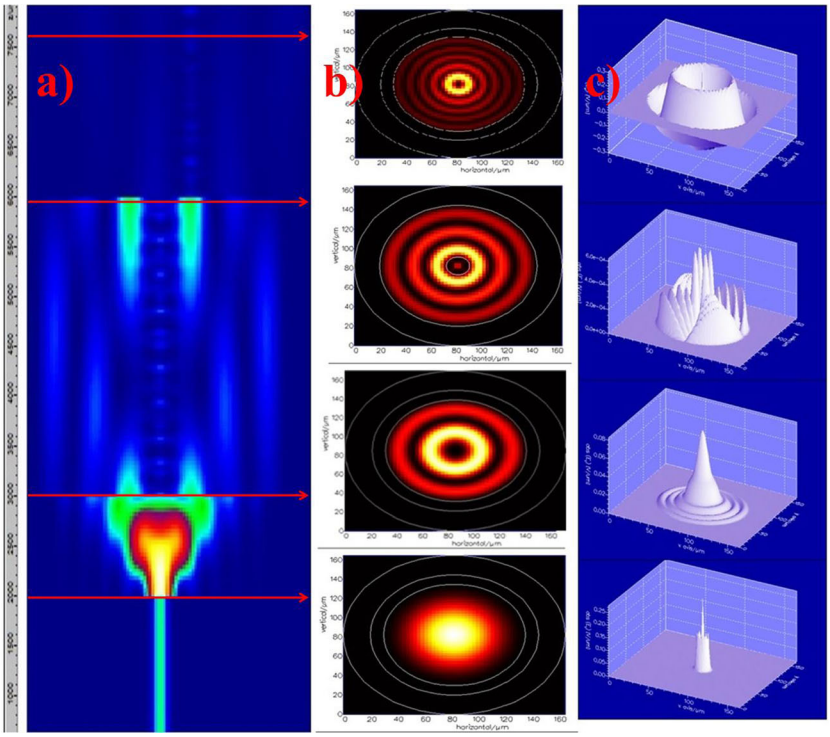


Fig. 6 Simulation of the optical field profile calculating with Eigen mode expansion method

Simulations

Modelling and simulation for reported sensor are performed using FIMWAVE simulation package of Photon Design, UK to verify the experimental results. The input field is given to the sensing structure. A light beam from the lead in fiber spreads out into the NCF. The field pattern shows that because of multimode interference, the core modes from lead in SMF almost vanish. Then, the light from NCF is injected into the SMF_2. Eigen mode expansion method is used to study the light propagation in reported sensor.

Figure 6 shows the field propagations and cross-sectional views of the field pattern and the transmission spectrum obtained from simulated results. For modelling the effect of refractive index, the refractive index of solution found to increase from 1.333 to 1.380. The result obtained by simulation is shown in Fig. 7. It is observed that central wavelength shifts towards shorter wavelength. Sensitivity has been calculated with the linear fitting of curve, obtained from refractive index as a function of wavelength. However, it is difficult to predict a quantitative description to the refractive index response of each cladding modes because it is difficult to calculate the

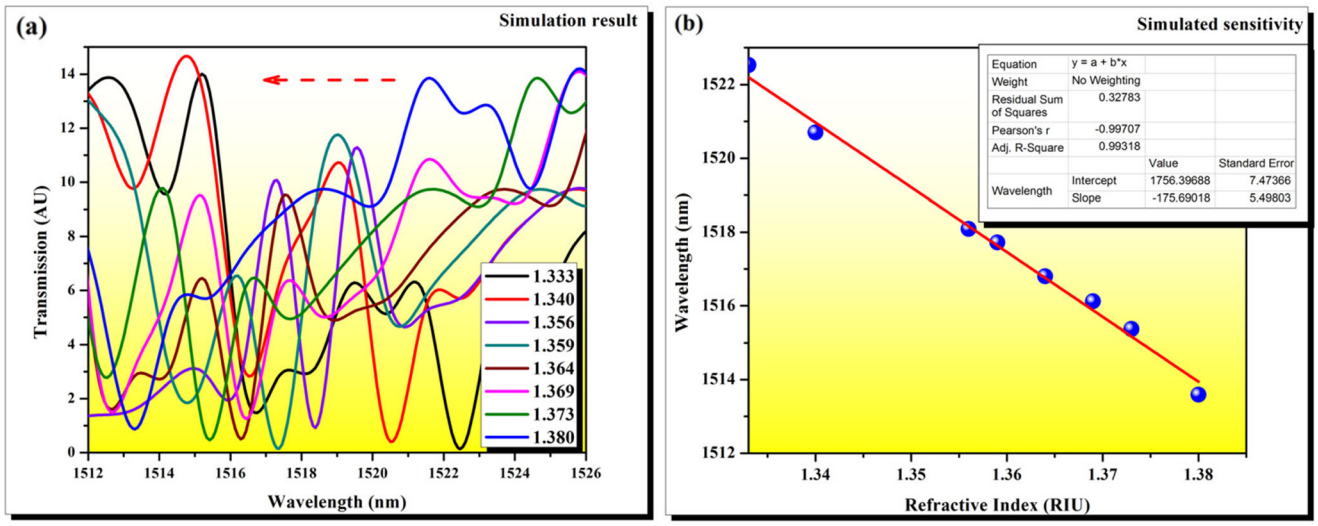


Fig. 7 **a** Simulated transmission spectra of the proposed interferometer. **b** Simulated sensitivity at different refractive index of a NaCl solution

exact order and energy of each cladding modes due to the some unknown exact parameters of fibers and fiber structure.

From the spectrum, we can see that, with the increment of refractive index, the transmission dip shifts towards shorter wavelength. It means that the refractive index sensitivity coefficient is positive. The sensitivity obtained from theoretical simulation is 175.69 nm/RIU which closer to sensitivity obtained for dip B (197.33 nm/RIU) from experimental analysis.

Conclusion

In conclusion, investigation of liquid refractive index using connector offset optical fiber sensor based on MZI realized by using NCF and connector offset SMF have been fabricated and demonstrated. The transmission spectrum was obtained by participation of core mode and strong cladding modes. Therefore, the refractive index variation was detected by shifts in wavelength. The experimental result shows that device has a linear refractive index sensitivity of 197.33 nm/RIU (R^2 = 0.994) and −153.91 nm/RIU (R^2 = 0.971) and this experimental result is also verified by theoretical result with sensitivity 175.69 nm/RIU in the RI 1.333 to 1.380. The calculated results may be considered as an important step towards sensing applications in the field of other sensing parameters such as chemical, pressure, and biological sensor.

Acknowledgements This work is supported by the Indian Institute of Technology (Indian School of Mines), Dhanbad, India for providing financial support, Electrical Engineering Department and Physics Department of IIT MADRAS for providing the experimental research facilities to carry out this research work.

References

1. Wang Q, Wei W, Guo M, Zhao Y (2016) Optimization of cascaded fiber tapered Mach-Zehnder interferometer and refractive index sensing technology. Sens. and Actuator B: Chem. 222:159–165
2. Pang F, Liu H, Guo H et al (2011) In fiber Mach-Zehnder interferometer based double cladding fibers for refractive index sensor. IEEE Sensors J 11(10):2395–2400
3. Bhardwaj V, Singh VK (2016) Fabrication and characterization of cascaded tapered Mach-Zehnder interferometer for refractive index sensing. Sens and Actuator A: Phy 244:30–40
4. Wang Y, Shen C, Lou W, Shentu F (2016) Polarization-dependent humidity sensor based on an in-fiber Mach-Zehnder interferometer coated with grapheme oxide. Sens and Actuator B: Chem 234:503–509
5. Gutierrez J et al (2016) Switchable and multi-wavelength linear fiber laser based on Fabry-Perot and Mach-Zehnder interferometer. Opt Commun 374:39–44
6. Raji Y, Lin H, Ibrahim S, Mokhtar M, Yusoff Z (2016) Intensity-modulated abrupt tapered fiber Mach-Zehnder interferometer for the simultaneous sensing of temperature and curvature. Opt. & Laser Techn. 86:8–13
7. Chong JH, Shum P, Haryono H et al (2004) Measurements of refractive index sensitivity using long-period grating refractometer. Opt Commun 229:65–69
8. Liang W, Huang Y, Xu Y et al (2005) Highly sensitive fiber Bragg grating refractive index sensor. Appl Phys Lett 86:151122
9. Qiu H, Xu S, Jiang S et al (2015) A novel graphene based tapered optical fiber sensor for glucose detection. Appl Surf Sci 329:390–395
10. Bevenot X, Trouillet A (2002) Surface plasmon resonance hydrogen sensor using an optical fibre. Meas Sci Technol 13(1):118–124
11. Gangwar R, Bhardwaj V, Singh VK (2016) Magnetic field sensor based on selectively liquid fluid infiltrated dual core photonic crystal fiber. Opt Eng 55:026111–026115
12. Gangwar R, Singh VK (2015) Refractive index sensor based on selectively liquid fluid infiltrated dual core photonic crystal fiber. Photon Nano Str 15:46–52
13. Lvanov O, Chertoriyskiy (2015) Fiber-optic bend sensor based on double cladding fiber. J Sens. 726793–6
14. Tian Z, Yam S, Loock H (2008) Single-mode fiber refractive index sensor based on core-offset attenuators. IEEE Photon Technol Lett 20:1387
15. Zhao Y, Li XG, Cai L (2015) High sensitive Mach-Zehnder interferometric refractive index sensor based on core-offset single mode fiber. Sens Actuators A: Phy 223:119–124
16. Zhang AP, Shao LY, Ding JF, He S (2005) Sandwiched long-period gratings for simultaneous measurement of refractive index and temperature. IEEE Photon Technol Lett 17(11):2397–2399
17. Huang R, Ni K, Ma Q, Wu X (2016) Refractormeter based on a tapered Mach–Zehnder interferometer with peanut-shape structure. Opt & Laser in Eng 83:80–82
18. Singh A, Enles D, Sharma A, Singh M (2014) Temperature sensitivity of long period fiber grating in SMF-28 fiber. Optik 125:457–460
19. Wang P et al (2013) Fiber tip high temperature sensor based on multimode interference. Opt Lett 38:4617–4620
20. Frazao O, Santos JL (2004) Simultaneous measurement of strain and temperature using a Bragg grating structure written in germanosilicate fibres. J. Opt. A, pure Appl Opt 6(6):553–556
21. Sai V, Kundub T, Mukherji S (2009) Novel U-bent fiber optic probe for localized surface plasmon resonance based biosensor. Biosens Bioelectron 24:2804–2809
22. Kulchin YN, Vitrik OB, Dyshlyuk AV, Zhou Z (2013) Conditions for surface plasmon resonance excitation by whispering gallery modes in a bent single mode optical fiber for the development of novel refractometric sensors. Laser Phys 23(8):085105
23. Kishor K, Baitha MN, Sinha RK, Lahiri B (2014) Tunable negative refractive index metamaterial from V-shaped SRR structure: fabrication and characterization. J Opt society of America 31(7):1410–1414
24. Dhara P, Singh VK (2015) Effect of MMF stub on the sensitivity of a photonic crystal fiber at 1550 nm. Opt Fiber Techn 21:154–159
25. Domingues M et al (2006) Cost effective refractive index sensor based on optical fiber micro cavities produced by the catastrophic fuse effect. Measurement 77:265–268
26. Wang Z, Tan Z et al (2016) Liquid level sensor based on fiber ring laser with single-mode-offset coreless-single-mode fiber structure. Opt Laser Technol 84:59–63
27. Wang JN, Tang JL (2012) Photonic crystal fiber Mach-Zehnder interferometer for refractive index sensing. Sensors 12(3):2983–2995
28. Zhang S, Zhang W, Geng P, Geo S (2013) Fiber Mach-Zehnder interferometer based on concatenated down- and up-tapers for refractive index sensing applications. Opt Commun 288:47–51
29. Yin G, Lou S, Zou H (2013) Refractive index sensor with asymmetrical fiber Mach–Zehnder interferometer based on concatenating single-mode abrupt taper and core-offset section. Opt & Laser Techn 45:294–300
30. Bhatia P, Gupta BD (2011) Surface plasmon resonance based fiber optic refractive index sensor: sensitivity enhancement. Appl Opt 50(14):141473

Case Studies in Engineering Failure Analysis 8 (2017) 1–10

Contents lists available at ScienceDirect

Case Studies in Engineering Failure Analysis

journal homepage: www.elsevier.com/locate/csefa

Failure analysis of a first stage IN738 gas turbine blade tip cracking in a thermal power plant

Sushila Rani*, Atul K. Agrawal, Vikas Rastogi

Department of Mechanical, Production, Industrial and Automobile Engineering, Delhi Technological University, Delhi 110042, India

ARTICLE INFO

Article history:
Received 22 August 2016
Received in revised form 8 November 2016
Accepted 21 November 2016
Available online 5 December 2016

Keywords:
First stage gas turbine blade
IN738LC nickel alloy
SEM
Corrosion pits
Coating degradation
TCP

ABSTRACT

This research paper deals with the investigation of causes of failure of the first stage gas turbine blade of 30 MW gas turbine having tip cracks at the trailing as well as leading edge. This blade is made of nickel based super alloy IN738LC, having directional solidified grain structure and contains aluminide coating ($Pt–Al_2$) by diffusion process. The main focus of the paper is evaluation of tip crack at the trailing edge and further degradation of blade coating. The investigations included the visual observations, material composition analysis, scanning electron microscopy (SEM) and energy dispersive spectroscopy (EDS). During examination of the failed blade, it is found that the blade surface is completely degraded due to overheating. Corrosion pits are formed on the blade surface, these pits act as a notch to produce stress concentrations and cracks is initiated due to fatigue which further propagate due to hot corrosion. It is also reported that the Al-Pt coating is completely degraded, heavily oxidized. From these investigations, it is concluded that the failure of gas turbine blade takes place due to the combined effect of surface degradation caused by overheating, oxidation, hot corrosion and degradation of coating heavily oxidized.

© 2016 The Author(s). Published by Elsevier Ltd. This is an open access article under the CC BY-NC-ND license (http://creativecommons.org/licenses/by-nc-nd/4.0/).

1. Introduction

Turbine blade failure occurs time to time in power plants. To increase the reliability and efficiency of turbine, it is necessary to perform detailed investigations of the failed turbine blade. The most common failure mechanisms exist in turbine blade includes fatigue [1,12], creep [2,4,10], oxidation [2,3], degradation of coating of turbine blade [2,5,10,11], corrosion [4,5,7,10], erosion [4] and surface degradation due to overheating [9]. However, the degree of deterioration of individual blade differs due to operating temperature, rotational speed, mode of operations, total service time and manufacturing differences [2]. The failure of gas turbine blade is due to the combination of aforesaid failure mechanisms.

This paper presents failure analysis of a first stage gas turbine blade of 30 MW gas turbine. The investigations includes the visual observations, material composition analysis, scanning electron microscopy (SEM) and energy dispersive spectroscopy (EDS).

* Corresponding author.
E-mail addresses: sranidtu@gmail.com (S. Rani), akadce@gmail.com (A.K. Agrawal), rastogivikas@yahoo.com (V. Rastogi).

http://dx.doi.org/10.1016/j.csefa.2016.11.002
2213-2902/© 2016 The Author(s). Published by Elsevier Ltd. This is an open access article under the CC BY-NC-ND license (http://creativecommons.org/licenses/by-nc-nd/4.0/).

2. Background

The first stage gas turbine blade of 30 MW gas turbine made of nickel based super alloy Inconel 738LC, having operating temperature 1104 °C, pressure 10 kgf/cm^2 and rotates at 5135 rpm was investigated. The analyzed blade is physically damaged after rendering useful life of 72,000 h and having cracks at the tip of trailing and leading edge (Fig. 1). This blade is made by investment casting process, having directional solidified grain structure and contains aluminide coating (Pt–Al2) by diffusion process [2,3] (Fig. 2). The gas turbine operates on compressed natural gas at Indraprastha Gas Power Plant, located in India.

3. Experimental details

A failed first stage gas turbine blade was collected from power plant. The blade has tip cracks on both leading edge and trailing edge [4]. In order to identify the root causes of blade failure, three specimens about 1 cm^2 were cut over the trailing edge by wire cutting process. Next, these specimens are polished using standard metallographic techniques and etched with acetone [5]. Hitachi S-3700N scanning electronic microscope (SEM) equipped with an X-ray energy dispersive spectrometer (EDS) was used to observe fracture surface morphology, microstructure and chemical compositions at different regions over the trailing edge of turbine blade [4].

4. Results and discussions

4.1. Visual examination

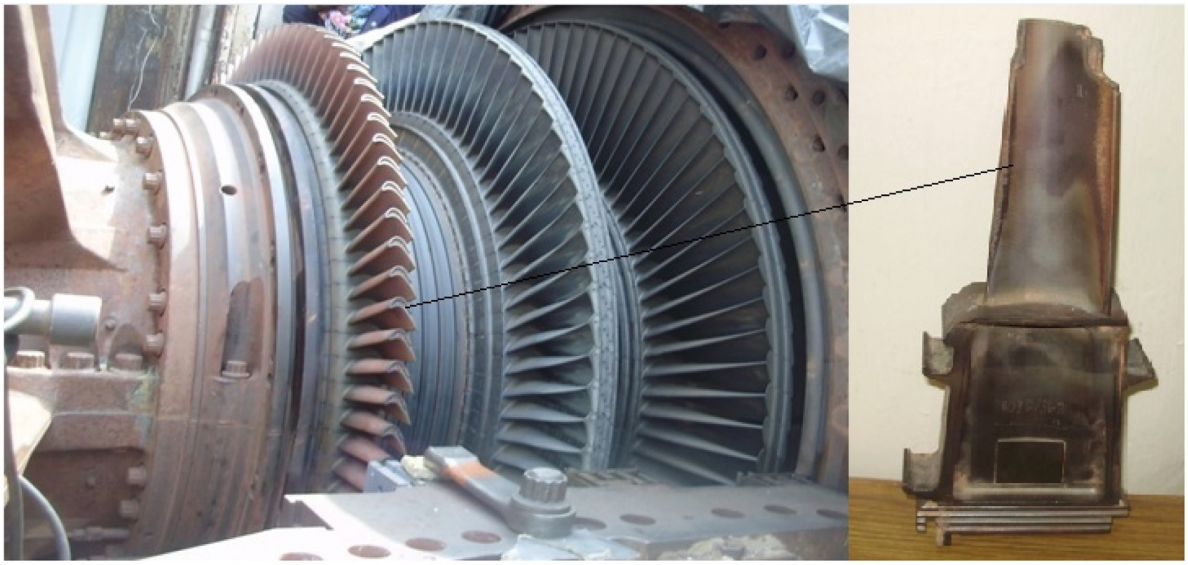
The failed blade is shown in Fig. 3. The blade was cracked at the tip of leading edge and at the tip of trailing edge. It is evident from the figure that surface of turbine blade become dark and erosion also found on both sides of the leading and the trailing edge.

4.2. Chemical Analysis

Optical Emission Analyzer spectrometer model- 49 DV4 is used to determine chemical composition of blade material. The alloy composition (%wt) of failed turbine blade and IN738LC alloy is given in Table 1.The result shows that the blade material is in accordance with nickel based super alloy Inconel 738.

4.3. Microstructure Evaluation

The microstructure investigation of the crack at the tip of trailing edge was carried out. Further, samples were prepared to investigate degradation of turbine blade surface and the blade coating. For evaluating microstructure, a reference sample i.e. specimen 3 was cut and prepared from the root of blade as shown in Fig. 4. The microstructure of the root sample is shown in



Figs. 1–2. (1) Internal view of 30 MW Gas Turbine. (2) First stage Gas Turbine Blade.

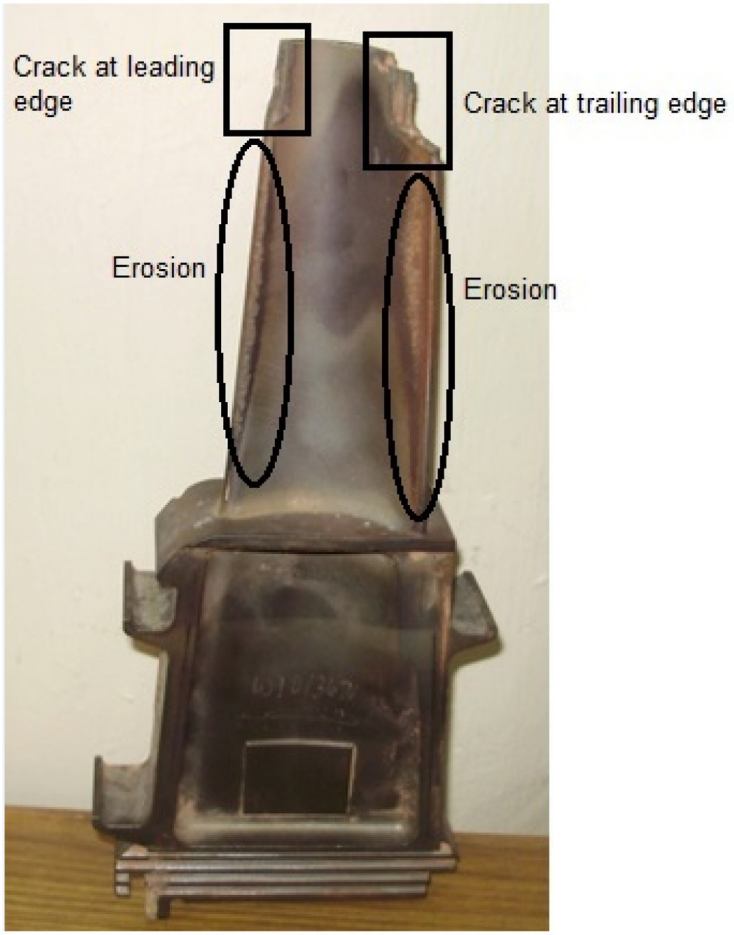


Fig. 3. Crack and Erosion on the leading and trailing edge.

Table 1
The Chemical composition of Inconel 738LC superalloy (wt%).

Alloy	Cr	Co	Al	W	Ti	Ta	Ni
IN738LC	16	8.3	3.4	2.6	3.4	1.75	Remaining
Failed Blade at surface	14.22	8.92	2.07	2.51	5.16	6.33	58.80
Failed blade at a depth of 4 mm from surface	15.03	7.9	3.1	2.4	2.9	1.60	Remaining

Fig. 5 consists of carbides of MC precipitated on grain boundaries and grain interior and matrix [8]. An EDS spectrum of specimen 3 is shown in Fig. 6.

Fig. 7 shows surface degradation by the formation of needle separation topologically closed packed phase (TCP), which occur due to overheating. This structure instability of the alloy results decrease in strength and ductility of alloy [9].

4.4. Crack evaluation

The crack initiation and propagation in the gas turbine blade are due to the combinations of thermal stress and environment. The surface metal of the turbine blade degraded due to presence of TCP phases and results in pit formation as shown in Fig. 8. An EDS spectrum of these pits confirmed the presence of corrosion products, sulphur and oxygen as shown in Fig. 9. The crack initiates readily because of these corrosion pits as they act as a notch to produce stress concentrations [4]. The corrosion products penetrate deeply into metal through these initiated cracks (Fig. 10) and results in crack propagation (Fig. 11). During crack propagation, hot corrosion [5–7,10] occurs and causes enlargement of crack area. (Fig. 12) shows rapid oxidation at high temperature in the presence of sodium sulfate which combine with chromium to form a mixture of salts and sulphur. This released sulphur penetrates inward and react with chromium to form chromium sulfide in the substrate. Further, sulfides are converted to complex unstable metal oxides as corrosion proceeds. It is evaluated that the crack initiation is due to fatigue and its propagation results in hot corrosion and oxidation.

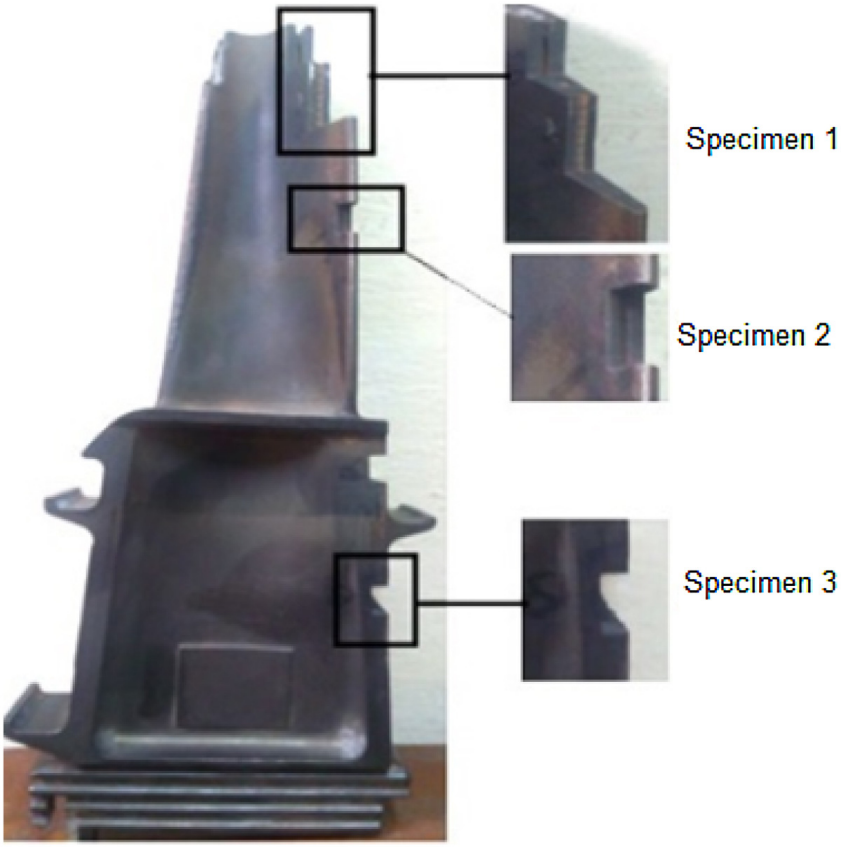


Fig. 4. Locations of specimens cut over trailing edge.

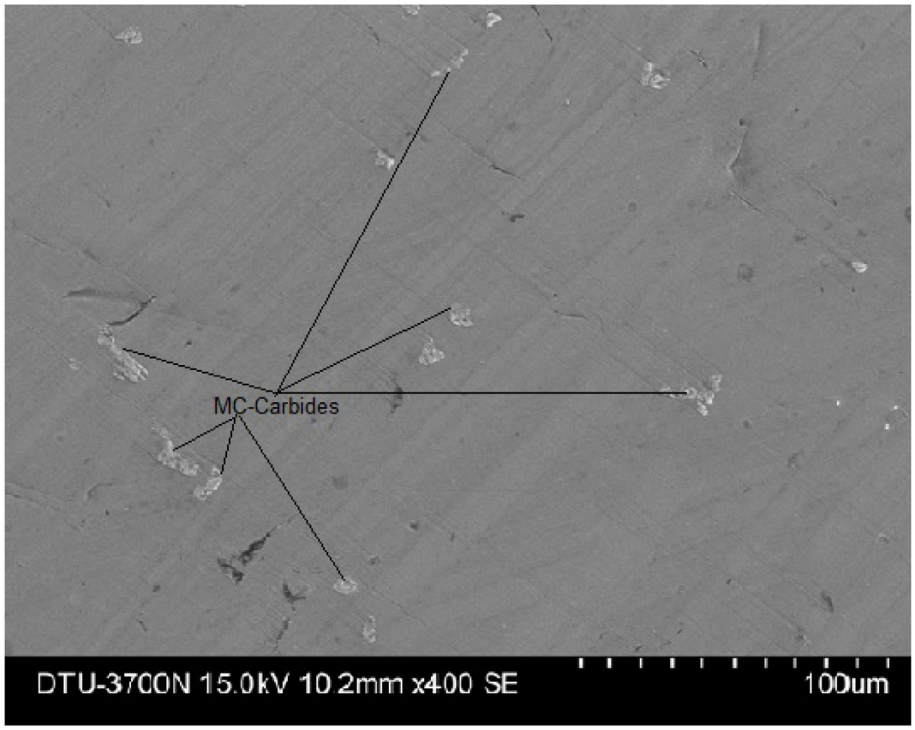


Fig. 5. MC-Carbides in the matrix and grain boundaries.

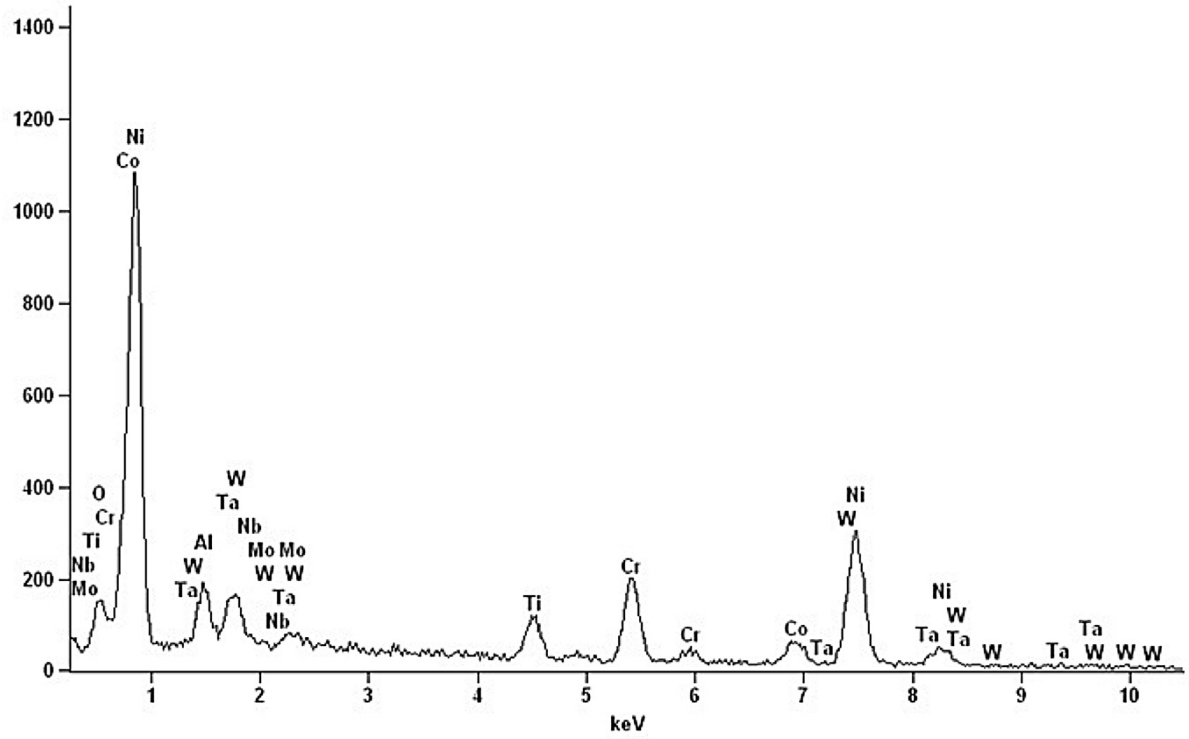


Fig. 6. An EDS Spectrum of specimen 3 of turbine blade material.

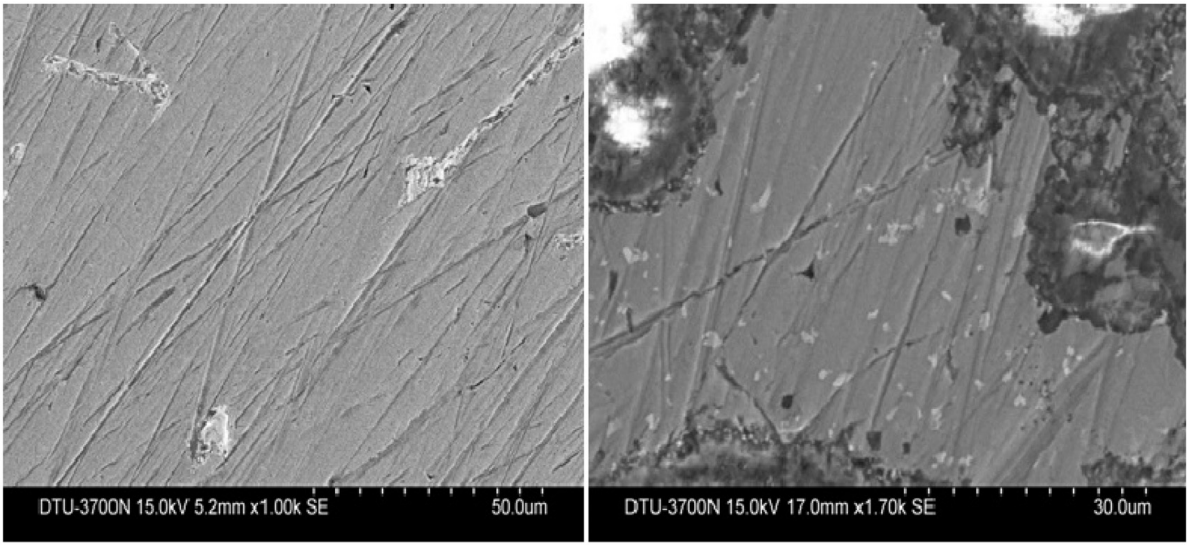


Fig. 7. Topologically closed packed (TCP) phases occur due to overheating, surface degradation.

4.5. Degradation of Blade coating

The deterioration of turbine blade coating is shown in Fig. 13. This coating consists of four zones. The external surface layer has $PtAl_2$ particles and form external zone. These $PtAl_2$ particles dissolve to NiAl which is finely dispersed in the base metal matrix to form single phase platinum rich Beta Nickel-Aluminium [(Ni, Pt) Al or (β)] and form intermediate zone. The internal zone is refractory (Cr, W, and Mo) rich inter diffusion zone. The fourth zone consists of nickel based super alloy IN738 base metal [2,10,11].

In this case, the degradation of coating occurs due to oxidation of Al-Pt coating. The aluminium diffuses to form protective Al_2O_3 on the blade surface. The reddish color of blade surface occurs due to this oxidation. This oxide is removed due to erosion. In turn, the coating provides additional aluminium to form new aluminium oxide. The chemistry of coating by

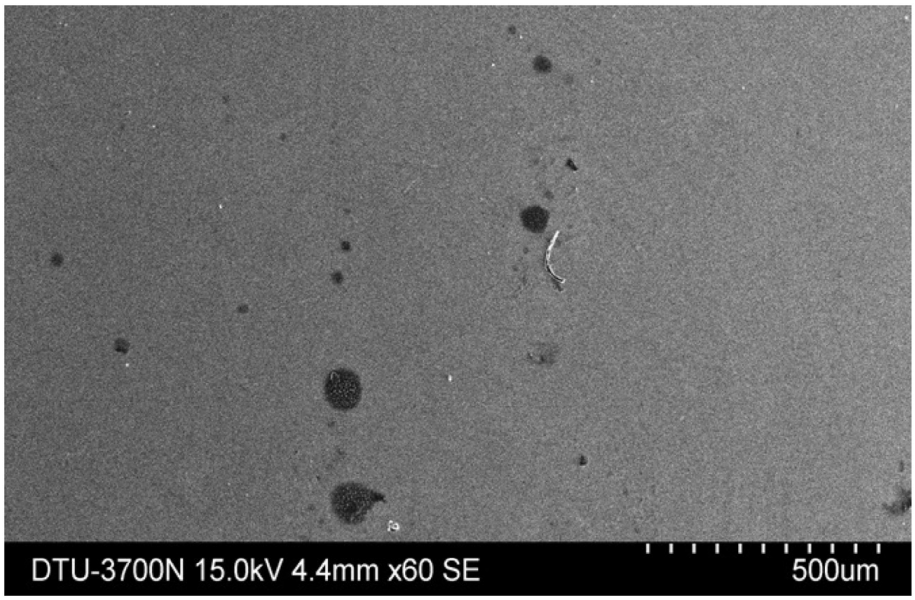


Fig. 8. Corrosion pits act as a notch to produce stress concentration.

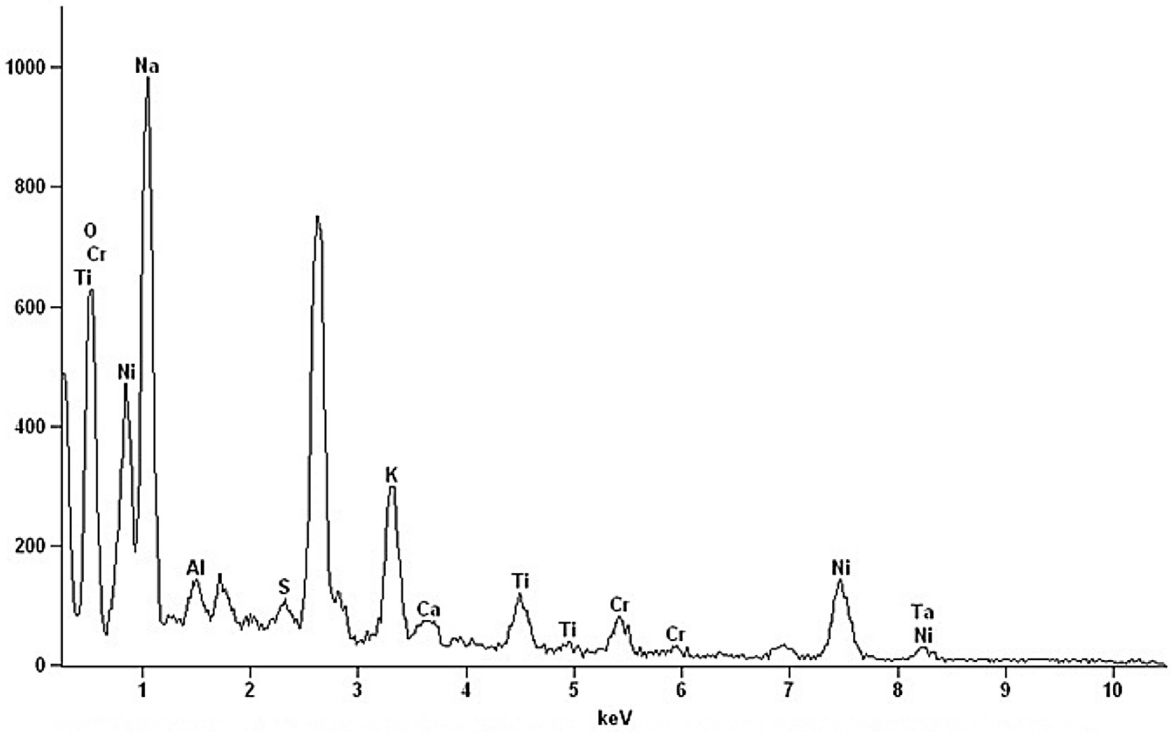


Fig. 9. An EDS Spectrum of corrosion pit identifies the presence of corrosion products, sulphur & Oxygen.

weight percent shows that the oxygen concentration increased as high as 26.64% and aluminium is reduced by 10%. This reduction in aluminium content proves that coating is consumed offer no protection to base metal.

The single phase platinum rich Beta Nickel-Aluminium [Ni Al (β)] discompose to bi phase γ' [$(Ni, Pt)_3$ Al +β]. The aluminium is consumed, the β phase cannot survive and hence only γ' exists. Since Ni and other element go into solid solution, this discomposes to γ and γ' (Fig. 14). Finally coating is consumed completely and only γ exists [2,10].

5. Discussions

The material composition of blade material on the surface of blade and at a depth of 4 mm from surface has been determined using Optical Emission Analyzer spectrometer. By comparing material composition of blade at a depth of 4 mm from surface with IN738 alloy, it is concluded that the blade does not failed due to material defects [12].

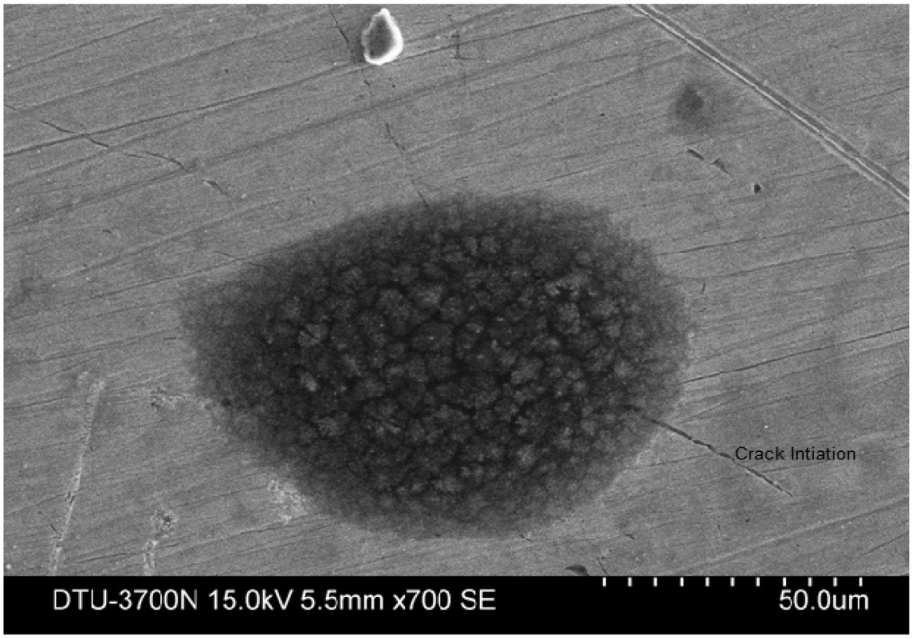


Fig. 10. Crack initiation due to Fatigue.

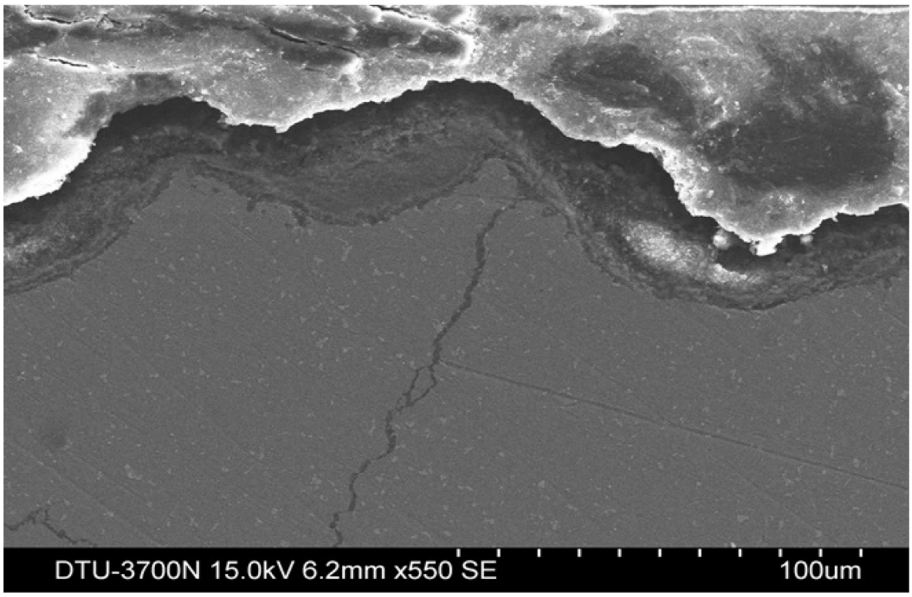


Fig. 11. Crack propagation due to penetration of sulphur and oxygen into substrate.

From microstructure and EDS spectrum obtained using Hitachi S-3700N scanning electronic microscope (SEM) equipped with an X-ray energy dispersive spectrometer (EDS), it is evaluated that the turbine blade is failed due to presence of topologically closed packed phase (TCP) on blade surface which results in the formation of corrosion pits. The corrosion products penetrate deeply into metal through these initiated cracks and results in crack propagation, hot corrosion occurs. At high temperature, sodium sulfate which combine with chromium to form a mixture of salts and sulphur which penetrates inward and react with chromium to form chromium sulfide in the substrate. Further, sulfides are converted to complex unstable metal oxides. It is concluded that blade is failed due to hot corrosion and oxidation.

In service, at high temperature MC-carbides transforms to $M_{23}C_6$–carbides.

The degradation of coating occurs due to oxidation of Al-Pt coating. The oxygen concentration increased as high as 26.64% and aluminium is reduced by 10% as shown in Fig. 9. The coating is heavily oxidized and offers no protection to the base metal.

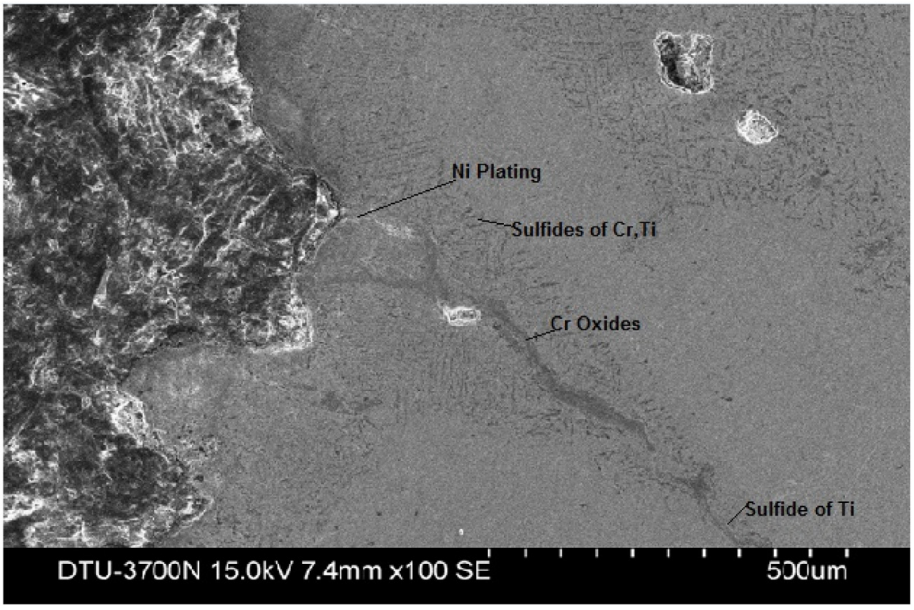


Fig. 12. Hot Corrosion: Subscales of sulfides and oxides.

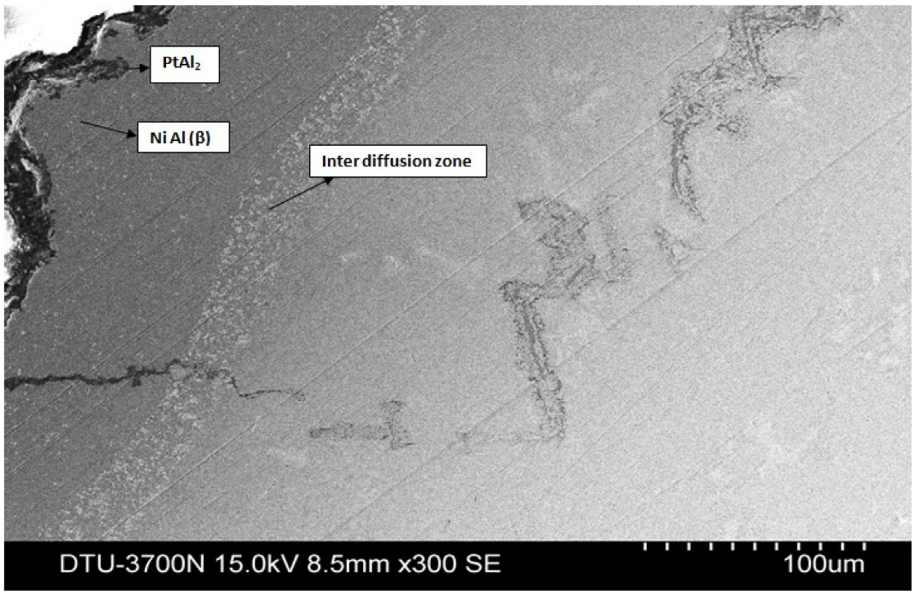


Fig. 13. Microstructure of Platinum-Aluminide Coating.

The dark color of blade surface is due to formation of oxides. These oxides are removed due to erosion, which is caused by the catalyst particles that flow in the hot gas stream. These catalysts also adhere and deposit in the path of channels and results in high heat buildup. This will lead to radial blade tip cracking.

6. Prevention approaches against future failures

Generally, the life of turbine first stage gas turbine blade is approximately 72,000 h. During this life span it should be undergoing into a repair session after rendering useful life of 24,000 h. In this repair session blade undergoing routine maintenance that includes proper cleaning of cooling holes, recoating of turbine blade with thermal barrier coating (TBC) and area rebuilt at non pressure sides has been included. TBC consists of two coats namely 'bond coat' and 'top coat'. 'Bond coat' is an oxidation and corrosion resistant inner layer and 'top coat' is an insulating ceramic outer layer [13,14].

Secondly, proper selection of alloy element for manufacturing of turbine blades is major concern. During overheating the surface of the blade is degraded due to the formation of TCP, which is further responsible for the formation of corrosion pits that leads to hot corrosion and oxidation. The material used for manufacturing of gas turbine blade must be corrosion

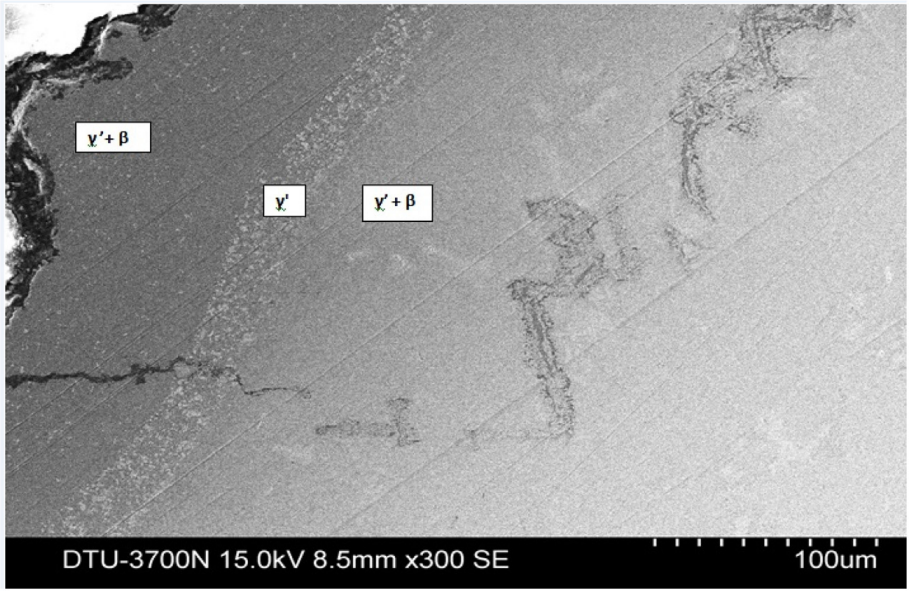


Fig. 14. Phase changes during consumption of coating.

resistant. The most effective hot corrosion resistance alloy element is chromium. The chromium combines with oxygen to form Cr_2O_3, which prevents dissolution of protective oxide scale. In order to obtain good hot corrosion resistance, a minimum of 16 wt% Cr is needed in Ni based super alloy IN738LC. At high temperature, the high percentage of chromium form topologically closed packed phase (TCP), which may decrease the strength of alloying long term [15,16,17].

The turbine blades in service are mostly failed due to presence of high amplitude resonant stresses [18]. In order to reduce resonance amplitudes, friction dampers are used between bladed disks. This is metallic piece which is placed between adjacent blades. By placing damper the structure become stiffer and hence reduces amplitude of resonance stresses [19,20].

7. Conclusions

1 Based upon the chemical composition determined using Optical Emission Analyzer spectrometer, it is concluded that the blade does not failed due to material defects.
2 From microstructure and EDX spectrum obtained using Hitachi S-3700N scanning electronic microscope (SEM) equipped with an X-ray energy dispersive spectrometer (EDS), it is evaluated that the turbine blade is failed due to surface degradation caused by overheating, hot corrosion and oxidation.
3 In this case, the degradation of coating occurs due to oxidation of Al-Pt coating. The coating is heavily oxidized and offers no protection to base metal. The dark color of the blade surface is due to the presence of oxides.
4 It is found that the blade has been failed due to combined effect of surface degradation caused by overheating, oxidation, hot corrosion and degradation of coating, heavily oxidized.
5 To prevent future failures of first stage IN738LC gas turbine blade, repair session after rendering useful life of 24,000 h, selection of proper corrosion resistant alloy and placing of friction dampers between bladed disks has been discussed.

Acknowledgements

The first stage failed gas turbine blade is provided by Indraprastha Gas Power Plant, Delhi. The authors would be thankful to Physics Department of Delhi Technological University for help in conducting experiments in Nanotechnology laboratory.

References

[1] Kim H. Crack evaluation of the fourth stage blade in a low -pressure steam turbine. Eng Fail Anal 2011;18:907–13.
[2] Mazur Z, Ramirez A, Amezcua CA. Failure analysis of a gas turbine blade made of Inconel 738LC alloy. Eng Fail Anal 2005;12:474–86.
[3] Varda N, Ekerim NA. Failure analysis of gas turbine blade in a thermal power plant. Eng Fail Anal 2007;14:743–9.
[4] Xie Y, Wang M, Zhang G. Analysis of super alloy turbine blade tip cracking during service. Eng Fail Anal 2006;13:1429–36.
[5] Khajavi MR, Shariat MH. Failure of first stage turbine blades. Eng Fail Anal 2004;11:589–97.
[6] Technical Data -NiPERA, IN_738Alloy_PreliminaryData_497_.pdf.
[7] Eliaz N, Shemesh G, Latanision RM. Hot corrosion in gas turbine component. Eng Fail Anal 2002;9:31–43.
[8] Tawancy HM, Hadhrami LM. Degradation of turbine blades and vanes by overheating in a power plant. Eng Fail Anal 2009;16:273–80.
[9] Rybhinov AI, Gestov LB, Mozhaiskaya NV. Operation experience with cast rotor blades made of Russian alloys in stationary gas turbines. Therm Eng 2012;59(3)242–9 © Pleiades Publishing, Inc..

[10] M.T. Naeem, S.A. Jazayeri, N. Rezamahdi. Failure analysis of gas turbine blades Proceedings of the 2008 IAJC-IJME International Conference 120 ENG 108.
[11] Dowson P, Dowson D. Selection of material and material related processes for FCC power recovery turbines. Thirty eight turbo machinery symposium. . p. 187–212.
[12] Bhagi L, Rastogi V, Gupta P. Fractographic investigations of the failure of L-1 low pressure steam turbine Naeem blade. Case Stud Eng Fail Anal 2013;1:72–8.
[13] Nicholls JR. Smart overlay coating: concepts and practice. J Surf Coat Technol 2002;149:236–44.
[14] Strawbridge A, Evans HE, Ponton CB. Spallation of oxide scales from NiCrAlY Overlay coatings. Mater Sci Forum 1997;251–254:365–72.
[15] Goebel JA, Pettit FS, Goward GW. Mechanisms for the hot corrosion of nickel-base alloys. Metall Trans 1973;4:261–78.
[16] Otsuka N, Rapp RA. Hot corrosion of preoxidized Ni by a thin fused Na_2SO_4 film at 900 °C. J Electrochem Soc 1990;137(1):46–52.
[17] Eliaz N, Shemesh G. Hot corrosion in gas turbine components. Eng Fail Anal 2002;9:31–43.
[18] Griffin JH. Friction damping of resonant stresses in gas turbine engine airfoils. J Eng Power ASME 1980;102:329–33.
[19] Petrov EP. Explicit finite element models of friction dampers in forced response analysis of bladed disks. J Eng Gas Turbines Power 2008130: 022502-1-11.
[20] Griffin JH. An integrated approach for friction damper design. J Vib Acoust 1990;112:175–82.

Forward scattering by the cylindrical dielectric nanoparticle

Reena,[1] Yogita Kalra,[1] and R.K. Sinha*[1,2]

[1]*TIFAC-center of Relevance and Excellence in Fiber Optics and Optical Communication, Department of Applied Physics, Delhi Technological University (Formerly Delhi College of Engineering, University of Delhi), Bawana Road, Delhi-110042, India*

[2] *CSIR-Central Scientific Instruments Organisation, Sector 30 C, Chandigarh-160 030, India*

**Email: dr_rk_sinha@yahoo.com*

Abstract: Forward scattering by the cylindrical dielectric nanoparticle in the near infrared region has been reported. Entire light scatter is scatttered in the forward direction at the interference of the electric and magnetic dipoles.

OCIS codes: (040.6040) Silicon; (260.5740) Resonance; (290.0290) Scattering

1. Introduction

Scattering of the light has been studied for many years due its application in the field of nanoantennas, photovoltaics and also in biomedicine [1-3]. Metallic split ring resonators have been used for many years to create artificial magnetism [4]. But there was an issue of heating losses in the metals. To avoid these types of losses, dielectric nanoparticles have been chosen now to produce artificial magnetism. Optically induced magnetic dipole can be formed in the dielectric nanoparticles at the particular frequency which is impossible in naturally occurring materials [5, 6]. Electric dipole is also formed in these nanoparticles at slightly higher frequency to that of magnetic dipole. This can be well explained by the Mie resonance in dielectric spherical and cylindrical nanoparticles [7].

In this paper, dielectric cylindrical nanoparticle has been considered. Electric and magnetic dipoles have been induced in the particle at the wavelength of resonance. Further, at the wavelength at which the electric and magnetic dipoles interfere, far field has been calculated using the finite element method. Using far field pattern, it has been analyzed that whole of the light has been scattered in the forward direction. This unidirectional scattering can be used for the design of optical nanoantennas.

2. Design

A Silicon (Si) nano-cylinder of radius ‘r = 80 nm’ and height ‘h = 200 nm’ has been considered. A plane wave propagating in the z direction, along the height of the nano-cylinder is made incident on it. Electric field ‘E’ and magnetic field ‘H’ are along y axis and x axis, respectively. Parameters of the nanoparticle are chosen such that electric and magnetic dipoles are created in the optical region.

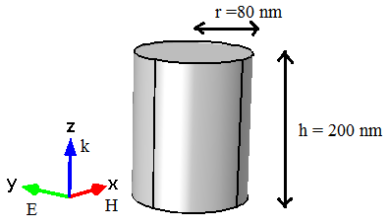


Figure 1. Schematic diagram of the cylindrical nanoparticle

3. Results and discussion

When light of a particular wavelength falls on the dielectric nano-cylinder, it creates magnetic dipole. To find this particular wavelength, scattering cross section has been calculated using the formula [5]

$$\sigma_{sca}^{p} = \frac{\langle P_{sca,ED} \rangle}{I_0} \tag{1a}$$

$$\sigma_{sca}^{m} = \frac{\left\langle P_{sca,MD} \right\rangle}{I_0} \tag{1b}$$

where, $\left\langle P_{sca,ED} \right\rangle$ and $\left\langle P_{sca,MD} \right\rangle$ are the power scattered by electric dipole and magnetic dipole and I_0 is the incident power density. These powers scattered by the electric and magnetic dipoles can be expressed as

$$\left\langle P_{sca,ED} \right\rangle = \frac{c^2 k_0^4 z_0}{12\pi} |\, p \,|^2 \tag{2a}$$

$$\left\langle P_{sca,MD} \right\rangle = \frac{c^2 k_0^4 z_0}{12\pi} |\, m \,|^2 \tag{3a}$$

where, c, k_0 and z_0 are the speed of light in vacuum, free space wavenumber and impedance, respectively. Electric dipole p and magnetic dipole m can be calculated as

$$p = \varepsilon_0 (1 - \varepsilon_r) \oint_V E(r') dV' \tag{4a}$$

$$m = \frac{i\omega(1-\varepsilon_r)}{2c} \oint_V [r \times E(r')] dV' \tag{4b}$$

where, ε_0 is the vacuum permittivity, r and r' are the observation point and source point, respectively, c is the speed of light in vacuum and ε_r is the relative permittivity of the nanoparticle.

Scattering cross section of the cylindrical nanoparticle has been shown in the figure 2(a). Here, peak of the electric dipole has been shown by the blue curve and peak of the magnetic dipole has been shown by the green curve. Modes of electric dipole and magnetic dipole have been shown in the figures 2(b) and 2(c) respectively.

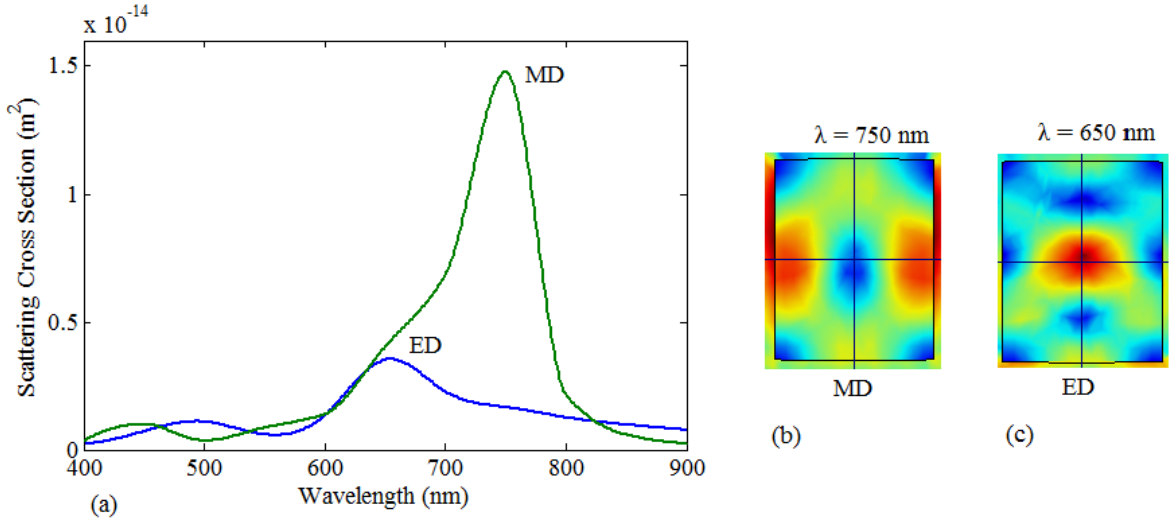


Figure 2 (a) Scattering spectra of the cylindrical nanoantenna with blue curve peak showing position of electric dipole and green curve peak denotes magnetic dipole position (b) Mode of magnetic dipole at wavelength λ = 750 nm (c) Mode of electric dipole at wavelength λ = 650 nm

Figure 2(a) shows that the electric dipole and magnetic dipole interfere at the wavelength of 820 nm. Further, far field has been calculated at λ = 820 nm as shown in the figure 3. Figure 3 shows that there is a complete scattering

of light in the forward direction without side lobes or back lobes. Thus, the entire light is scattered in the forward direction because electric and magnetic dipoles are in phase at this wavelength.

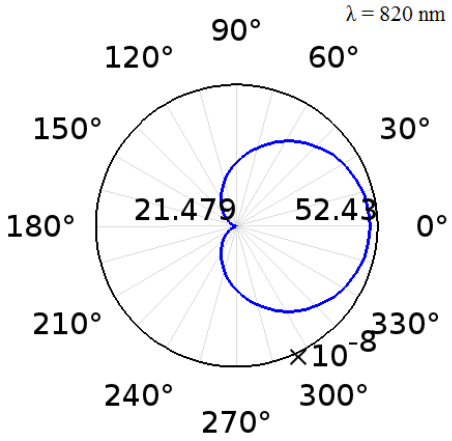


Figure 3. Far field of the nano-cylinder at the wavelength λ = 820 nm.

4. Conclusion

In this paper, electric and magnetic dipoles have been induced in the cylindrical Si nanoparticle using the plane wave propagating in the longitudinal direction of the cylinder. Scattering spectra has been calculated to find the position of the electric and magnetic dipoles. Further, far field pattern has been calculated at the wavelength of interference of electric and magnetic dipoles. It has been shown that the complete forward scattering takes place at λ = 820 nm. Thus, cylindrical dielectric nanoparticles can be used in the design and development of optical nanoantennas.

5. Acknowledgments

Authors gratefully (i) acknowledge the initiatives and support from TIFAC-Center of Relevance and Excellence in Fiber Optics and Optical Communication at Delhi College of Engineering, now DTU, and Delhi under Mission REACH Program of Technology vision-2020, Government of India and Support through (ii) DST-RMES (Indo-Russian) joint research project on "All Dielectric, Plasmonic and Hybrid Photonic Nanostructures" and (iii) DST-RFBR (Indo-Russian) joint research project on "From Plasmonics to Dielectric and Hybrid nanoantennas: Novel approaches to control electromagnetic waves and light."

6. References

[1] L. Novotony and N. Van Hulst, "Antennas for light," Nat. Photonics **5**, 83-90 (2011)

[2] H. A. Atwater and A. Polman, "Plasmonics for improved photovoltaic devices,"Nat. Mater.**9**, 205–213 (2010).

[3] D. Sikdar, I. D. Rukhlenko, W. Cheng and M. Premaratne, "Optimized gold nanoshell ensembles for biomedical applications,"Nanoscale Res. Lett. **8**, 142-146 (2013).

[4] R. Marqués, J. Martel, F. Mesa and F. Medina, "Left-handed-media simulation and transmission of EM waves in subwavelength split ring resonator loaded metallic waveguides," Physical Review Letters, **89**(18), 183901 (2002).

[5] D. Sikdar, W. Cheng and M. Premaratne, "Optically resonant magneto-electric cubic nanoantennas for ultra-directional light scattering" Journal of Applied Physics **117**, 083101 (2015).

[6] R. Gomez-Medina, B. Garcia-Camara, I. Suarez-Lacalle, F. Gonzalez, F. Moreno, M. Nieto-Vesperinas, andJ. J. Saenz, "Electric and magnetic dipolar response of germanium nanospheres: Interference effects, scattering anisotropy, and optical forces," J. Nanophotonics 5, 053512 (2011).

[7] Zhao Q., Zhou J., Zhang F. and Lippens D., "Mie resonance-based dielectric metamaterials," Mater. Today12, 60-69 (2009).

Superlattices and Microstructures 102 (2017) 17–26

Contents lists available at ScienceDirect

Superlattices and Microstructures

journal homepage: www.elsevier.com/locate/superlattices

Gate Drain Underlapped-PNIN-GAA-TFET for Comprehensively Upgraded Analog/RF Performance

Jaya Madan, Rishu Chaujar*

Microelectronics Research Lab, Department of Engineering Physics, Delhi Technological University, Bawana Road, Delhi, 110042, India

ARTICLE INFO

Article history:
Received 15 November 2016
Accepted 16 December 2016
Available online 18 December 2016

Keywords:
Band to band tunneling (BTBT)
Source pocket
Gate-drain underlapping (GDU)
Parasitic capacitance
Tunneling FET (TFET)

ABSTRACT

This work integrates the merits of gate-drain underlapping (GDU) and N+ source pocket on cylindrical gate all around tunnel FET (GAA-TFET) to form GDU-PNIN-GAA-TFET. It is analysed that the source pocket located at the source-channel junction narrows the tunneling barrier width at the tunneling junction and thereby enhances the ON-state current of GAA-TFET. Further, it is obtained that the GDU resists the extension of carrier density (built-up under the gated region) towards the drain side (under the underlapped length), thereby suppressing the ambipolar current and reducing the parasitic capacitances of GAA-TFET. Consequently, the amalgamated merits of both engineering schemes are obtained in GDU-PNIN-GAA-TFET that thus conquers the greatest challenges faced by TFET. Thus, GDU-PNIN-GAA-TFET results in an up-gradation in the overall performance of GAA-TFET. Moreover, it is realised that the RF figure of merits FOMs such as cut-off frequency (f_T) and maximum oscillation frequency (f_{MAX}) are also considerably improved with integration of source pocket on GAA-TFET. Thus, the improved analog and RF performance of GDU-PNIN-GAA-TFET makes it ideal for low power and high-speed applications.

© 2016 Published by Elsevier Ltd.

1. Introduction

From the last few decades, CMOS technology is efficiently meeting the growing demand for various viable integrated circuits ICs by providing the low power consumption required for low power battery operated portable devices such as wireless devices, laptops, mobile phones, etc. [1]. However, relentless downscaling of MOSFET (metal oxide semiconductor field effect transistors) to below sub-22 nm technology node has stemmed into serious short channel effects (SCEs) [2]. These SCEs or the non-ideal effects, impede the MOSFET performance and thereby enforces a call for the novel devices that utilizes new device physics other than the thermionic emission of the carrier (as driven by MOSFET). In this regard, tunneling field effect transistor (TFET) that uses the band to band tunneling (BTBT) principle is reported as an energy efficient electronic device for acquiring sub- 60mV/decade subthreshold swing (SS) [3,4]. Along with steep SS, TFET offers lower I_{OFF} (of the order of 10^{-17}–10^{-18} A) owing to the large tunneling barrier width at the source-channel (or the tunneling junction) for lower gate bias, which reduces the tunneling probability of carrier from the valence band of the source to the conduction band of the channel at low gate bias [5,6]. Thus, the lower I_{OFF} and steeper SS offered by TFET provides lower leakage current and lower static power dissipations. Hence, TFET becomes an attractive device for ultra low power applications. However, the exponential dependence of BTBT on the lateral electric field, which is lower in conventional TFET leads to low efficiency of BTBT,

* Corresponding author.
E-mail addresses: jayamadan.2012@gmail.com (J. Madan), rishu.phy@dce.edu (R. Chaujar).

http://dx.doi.org/10.1016/j.spmi.2016.12.034
0749-6036/© 2016 Published by Elsevier Ltd.

even at high gate bias. This, lesser BTBT rate of carriers leads to low I_{ON} of TFET; and limits the TFET for high-speed analog applications [7]. To enhance the ON-state current in TFETs many device and material engineering schemes have been reported such as multi-gate architecture TFET (double gate, gate all around architectures) [8], dual material gate [9], heterogate dielectric [10], source N^+ pocket [11,12], narrow band gap materials [13] etc.

In this work, a N^+ source pocket is implanted at the source-channel junction. This N^+ source pocket modulates the energy band profile at the tunneling junction and thereby enhances the lateral electric field [11]. The enhanced lateral electric field reduces the tunneling barrier width at the source-channel junction and thereby increases the tunneling probability of electrons and thus, the I_{ON} of TFET. Moreover, an improved reliability of PNIN-TFET is reported in Ref. [14], in comparison with conventional PIN-TFET. Furthermore, the fabrication process of PNIN architecture is also reported in Ref. [12], in which after defining the gate metal the tilt angled implant is used to form the source N+ pocket.

Another major impedes suffered by TFET is ambipolar conduction i.e. the conduction in both positive and negative gate bias regions [15,16]. The main reason of ambipolar conduction in TFET is tunneling at the drain-channel junction for negative gate bias, caused by the lowering of barrier width at the drain-channel junction at negative gate bias. The ambipolar conduction in TFETs hampers TFET applicability for digital applications. Many device engineering schemes have been reported for lowering the ambipolar current such as gate-drain underlapping (GDU) or shortened metal gate [17], asymmetric source-drain doping [6], hetero gate dielectric [18], heterojunction TFET [19], etc.

In GDU scheme, the underlapped metal gate near drain side resists the extension of carrier density that is built-up under the gated region towards the drain side or beneath the underlapped region. Thus, the underlapped gate metal reduces the ambipolar conduction [20]. In addition to the reduction in ambipolar conduction, the underlapped metal engineering scheme also reduces the gate to drain parasitic capacitance (C_{gd}), which is a major obstacle of TFET for circuit designing. However, the hetero gate dielectric engineering scheme also reduces the ambipolar current, but it has implications on enhanced parasitic capacitance due to the presence of high-k dielectric near source-channel junction [21]. Therefore, in this work, the short metal gate or the GDU engineering scheme is considered for reducing the ambipolar current in TFET. In addition to GDU, asymmetric source-drain doping has also been incorporated to support the reduced ambipolar conduction further. Moreover, a cylindrical GAA architecture is considered to enhance the electrostatic control of gate over the channel region.

This work is organized as follows; Section 2 describes the device structures that are under considerations and their parameters used in the simulations. In Section 3, the simulation models are explained, and the calibration of simulation work with experimental data is also shown that ensures the feasibility of models used in TCAD simulations. Section 4 firstly refers the optimization of GDU engineering scheme in terms of gate-drain underlap length and then it describes the comparative analysis of GAA-TFET, GDU-GAA-TFET, PNIN-GAA-TFET and GDU-PNIN-GAA-TFET in terms of various analog and RF figure of merits. Finally, section 5 concludes the entire work.

2. Device architecture and parameters

ATLAS device simulator has been used to simulate GAA-TFET with GDU and N^+ source pocket. Fig. 1(a) shows the schematic structure of GDU-PNIN-GAA-TFET used for simulation. Moreover, for better understanding, the 2D schematic cross-

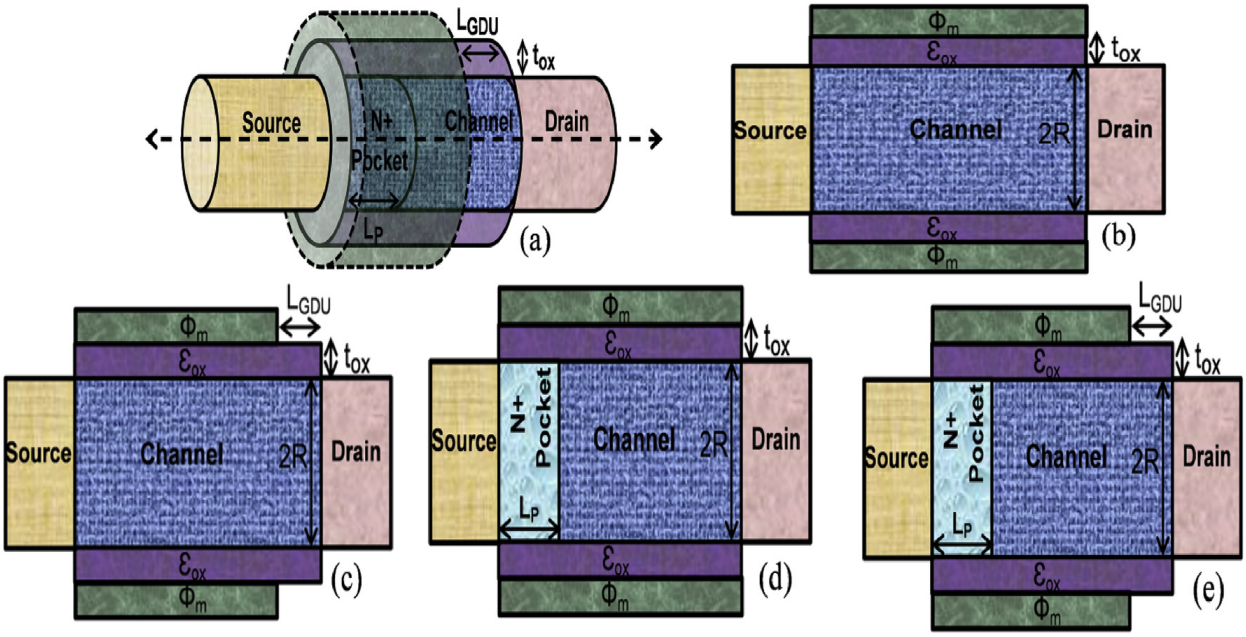


Fig. 1. (a) Simulation structure of GDU-PNIN-GAA-TFET. Schematic 2-D cross-sectional view of (b) GAA-TFET, (c) GDU-GAA-TFET, (c) PNIN-GAA-TFET, and (d) GDU-PNIN-GAA-TFET.

sectional view of GAA-TFET, GDU-GAA-TFET, PNIN-GAA-TFET and GDU-PNIN-GAA-TFET has also been shown in Fig. 1(b–d). The design variables for acquiring an optimized GDU-PNIN-GAA-TFET are gate-drain underlapping length (L_{GDU}), source pocket doping (N_P) and source pocket width (L_P). For PNIN-GAA-TFET, source pocket is optimized for better I_{ON}/I_{OFF} ratio, V_{th}, and SS by tuning L_p and N_p. It is obtained that at $L_p = 4$ nm and $N_p = 4 \times 10^{19}$ cm^{-3} respectively, the PNIN engineering scheme is optimized in terms of high I_{ON}/I_{OFF} ratio, low-V_{th} and low SS. The GDU engineering scheme is also optimized by altering the L_{GDU} for acquiring an optimum analog performance and parasitic capacitances.

The minimum parasitic capacitances and high I_{ON}/I_{OFF} ratio are obtained at $L_{GDU} = 15$ nm. Therefore, for GDU engineering scheme, L_{GDU} is optimized at 15 nm. Typical default device design parameters used in simulations are listed in Table 1. Silicon is used as source, drain and channel material. To constrain the ambipolarity effect, i.e. tunneling at drain-channel junction source is heavily doped in comparison with drain. The optimum value of gate metal work function of 4.3eV has been chosen for better OFF-state characteristics for all the device architectures under consideration i.e. GAA-TFET, GDU-GAA-TFET, PNIN-GAA-TFET, and GDU-PNIN-GAA-TFET.

3. Model validation

3.1. Simulation methodology

All simulations have been performed using the ATLAS device simulator [22]. To account the spatial variation dependence of electric field on energy bands, the nonlocal BTBT model is considered, rather the local models that make a triangular approximation and thereby assumes a constant electric field throughout the tunneling barrier regime. Thus, the nonlocal BTBT model takes into account the electrons energy for evaluating electric field at the individual mesh points in the simulated device structure, rather assuming a constant electric field as in local BTBT models such as Kane model [23]. Thus, more realistic results have been obtained by incorporating the nonlocal BTBT model. As tunneling current have strong band gap dependent and the band gap of semiconductor reduces for heavily doped semiconductors thus, the band gap narrowing model is also employed to consider the effects of degenerately doped source/drain. In addition, for accounting the carrier distribution, the Fermi-Dirac statistics is invoked. To describe the carrier's recombination Shockley Read Hall (SRH) recombination model is activated. Along with this, concentration and field dependent mobility model is also employed. The numerical methods used to mathematically solve the carrier transport equation are: Gummel (decoupled) and Newton's (Fully coupled). In this work the parasitic capacitances are extracted through small signal AC analysis (after solving the constant DC bias). The parasitic capacitances between each electrodes are evaluated at constant frequency i.e. 1 MHz.

3.2. Calibration with experimental data

To validate the simulation setup, the simulation models have been calibrated with the experimental results. In this respect, the GAA TFET is designed with the same structural device parameters as in Ref. [24]. To calibrate the Non-local BTBT model, the tunneling masses were adjusted from their default values to make it best fit with the experimental data. The adjusted value of me.tunnel $= 0.22 m_o$ and mh.tunnel $= 0.52\ m_o$. Where; m_o is the rest mass of electron. Fig. 2(a) shows the transfer characteristics of the data obtained by simulation results along with the extracted data from the reference [24]. A close match achieved between the TCAD simulation results, and the experimental characteristics validate the models parameters used in the simulation.

4. Results analysis

4.1. Impact of Gate-Drain Underlapping length: An optimization study

This subsection presents a comparative analysis of transfer characteristics and parasitic capacitances with the aim of attaining an optimized gate metal underlapping length (L_{GDU}) for GDU-GAA-TFET. To investigate an optimized L_{GDU} for the

Table 1
Device default design parameters used in simulations.

Parameters	Value
Drain (N^+) doping N_d	5×10^{18} cm^{-3}
Source (P^+) doping N_s	1×10^{20} cm^{-3}
Channel radius R	10 nm
Source Pocket (N^+) doping N_p	4×10^{19} cm^{-3}
Source Pocket Width L_p	4 nm
Channel Length L_g	50 nm
Gate oxide thickness t_{ox}	2 nm
Gate metal workfunction Φ_M	4.3 eV
Gate dielectric ε_{ox}	3.9 SiO_2
Gate drain underlapping length L_{GDU}	15 nm

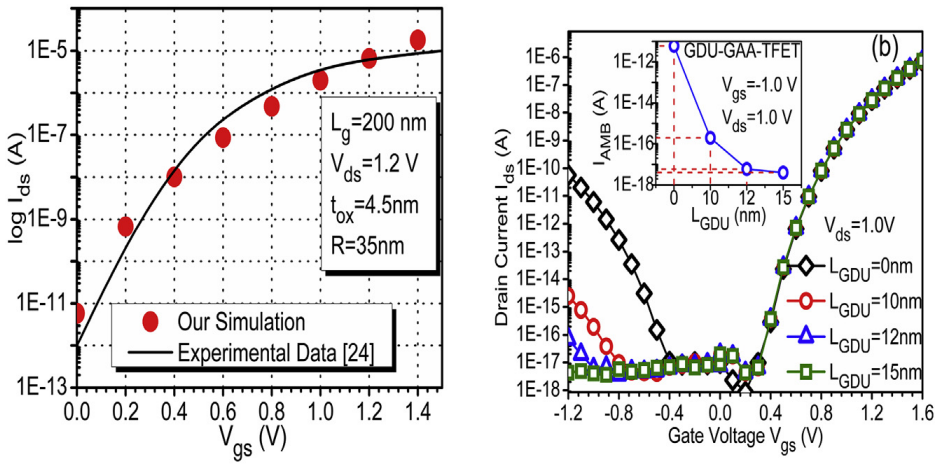


Fig. 2. (a) Calibration with the experimental data, transfer characteristics of the SiNW-TFET with 200-nm gate length at V_{ds} = 1.2 V, t_{ox} = 4.5 nm, and Radius = 35 nm. (b) Transfer characteristics of GDU-GAA-TFET at various L_{GDU}. Inset: I_{AMB} of GDU-GAA-TFET at various L_{GDU}.

GDU-GAA-TFET, the influence of L_{GDU} is studied on the transfer characteristics of GDU-GAA-TFET. From Fig. 2(b), it can be observed that underlapping the gate metal near drain side, affects the device characteristics only for negative gate bias (or the ambipolar current). Considerable suppression in ambipolarity is obtained with a shortened gate metal length. It is obtained that the ambipolar current (I_{AMB}) is reduced from an order of 10^{-12} A (for GAA-TFET) to 10^{-18} A (for GDU-GAA-TFET at L_{GDU} = 15 nm). However, as the tunneling junction is unaffected by the shortened gate metal (being at the drain-channel junction), the tunneling rate of electrons at source-channel junction remains immune against variations in L_{GDU} which is evident from the unaltered transfer characteristics for positive V_{gs} as shown in Fig. 2(b). Moreover, it is clearly evident that at L_{GDU} = 15 nm, I_{AMB} is significantly reduced, to an order of 10^{-18} A, that adequately overcome the challenges faced by TFET for digital applications. Thus, L_{GDU} = 15 nm is optimum from the perspective of I_{AMB} at the default design parameters mentioned in Table 1 for GDU-GAA-TFET.

Furthermore, it is requisite to study the intrinsic parasitic capacitances due to the fact that the important device design parameters such as the response time and the active power dissipation rely on these parasitic capacitances. Three main parasitic capacitances affect the device performance i.e. total gate capacitance (C_{gg}), gate to source capacitance (C_{gs}) and gate to drain capacitance (C_{gd}). The C_{gs} and C_{gg} of GDU-GAA-TFET at various L_{GDU} are examined as a function of both V_{gs} (at constant V_{ds} = 1.0 V) and V_{ds} (at constant V_{gs} = 1.2 V) and are shown in Fig. 3(a–b). It should be noted that L_{GDU} = 0 nm is the case of GAA-TFET. In Fig. 3(a) the solid fill notations used for C_{gg}, specifies a significant reduced in C_{gg} for GDU-GAA-TFET in comparison to GAA-TFET. The C_{gg} reduces by 38% for an increase in L_{GDU} from 0 nm (GAA-TFET) to 15 nm (GDU-GAA-TFET). However, the tunneling junction is immune to the underlapped length (being at the drain-channel junction), thereby the C_{gs} is almost unaltered for any variations in L_{GDU}. Also, the variations of these intrinsic capacitances are also analyzed as a function of V_{ds} at a constant V_{gs} as shown in Fig. 3(b). The C_{gg} of GDU-GAA-TFET at various L_{GDU} indicates a significant reduction in C_{gg} for shortened gate metal lengths, in comparison to GAA-TFET. Moreover, as the transfer characteristics for positive gate bias is immune towards variations in L_{GDU}, the V_{th}, SS, I_{ON}, I_{ON}/I_{OFF} ratio, g_m and other analog and electrical

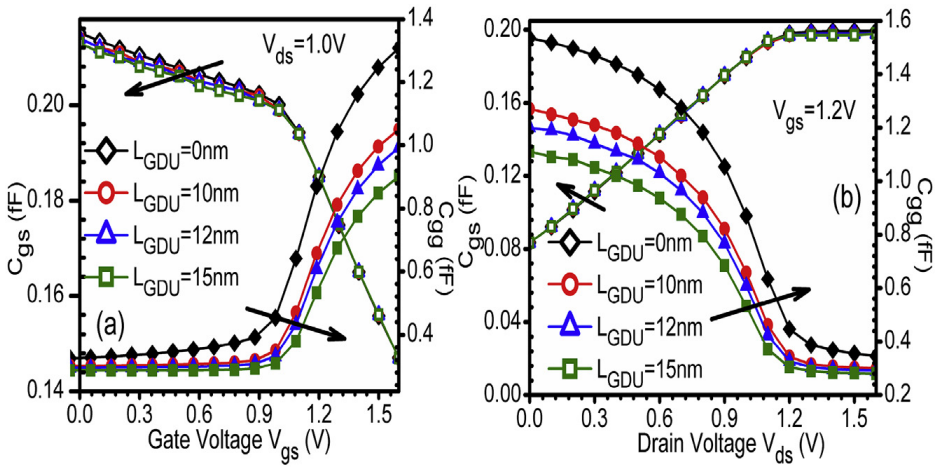


Fig. 3. C_{gs} and C_{gg} of GDU-GAA-TFET as a function of (a) V_{gs} at V_{ds} = 1.0 V (b) V_{ds} at V_{gs} = 1.2 V at various L_{GDU}. L_{GDU} = 0 nm signifies GAA-TFET.

parameters will also remain inviolate for variations in L_{GDU}. Thus, it is assessed that for $L_{GDU} = 15$ nm, GDU-GAA-TFET shows an optimum device performance in terms of I_{AMB} and parasitic capacitances.

4.2. Impact of Gate-Drain Underlapping and source pocket

This subsection presents the comparative analysis of GAA-TFET, GDU-GAA-TFET, PNIN-GAA-TFET, and GDU-PNIN-GAA-TFET, in terms of various analog and RF figure of merits such as: energy band diagrams (in ON-state and ambipolar-state), nonlocal BTBT rate of electrons, electric field, transfer characteristics, switching ratio, threshold voltage, subthreshold swing, parasitic capacitances, cutoff frequency (f_T) and maximum oscillations frequency (f_{MAX}). The default parameters for GDU architecture is $L_{GDU} = 15$ nm and for PNIN architecture is $N_p = 4 \times 10^{19}\text{cm}^{-3}$, $L_p = 4$ nm.

For analyzing the tunneling phenomenon, the energy band profiles of GAA-TFET, GDU-GAA-TFET, PNIN-GAA-TFET and GDU-PNIN-GAA-TFET in the ON-state ($V_{gs} = 1.2$ V and $V_{ds} = 1.0$ V) as well as for the ambipolar-state ($V_{gs} = -1.0$ V and $V_{ds} = 1.0$ V) are studied as shown in Fig. 4(a–b). It is clearly evident from Fig. 4(a) that the electron energy band profile is almost same for the GAA-TFET and GDU-GAA-TFET owing to the fact that GDU plays role for the negative gate bias to control the ambipolar current. However, the integration of source pocket at the tunneling junction or, for PNIN-GAA-TFET and GDU-PNIN-GAA-TFET, the bands at the tunneling junction bends steeply. This steeper band bending is due to the presence of N^+ source pocket, that lowers the barrier width and thereby enhances the probability of tunneling of electrons from valence band of source to conduction band of channel.

The energy band profile of all the aforementioned devices analyzed at the ambipolar state, is shown in Fig. 4(b). The broadened tunneling width at the drain-channel junction due to the underlapped metal gate that resists the tunneling of electrons at the drain-channel junction. This lowered tunneling due to the GDU thereby reduces the I_{AMB}, and makes the TFET eligible for digital switching applications.

Fig. 5 shows the comparison of the nonlocal-BTBT (N-BTBT) rate of electrons and electric field at the tunneling junction for different GAA-TFET configurations. In conventional GAA-TFET and GDU-GAA-TFET, the broader tunneling width contributes to the tremendously lower nonlocal BTBT rate of electrons. However, the steeper band bending attained by the N^+ source pocket considerably reduces the barrier width at the source-channel junction and thus enhances the N-BTBT rate of electrons as clearly shown in Fig. 5. The consequence of steeper band bending (obtained via N+ source pocket) is increased electric field for PNIN-GAA-TFET and GDU-PNIN-GAA-TFET. Quantitatively, the electric field is increased by 2.2 times with the application of N+ source pocket onto GAA-TFET.

The transfer characteristics of all the devices i.e. GAA-TFET, GDU-GAA-TFET, PNIN-GAA-TFET, and GDU-PNIN-GAA-TFET are shown in Fig. 6(a). It is evident that GAA-TFET suffers from lower I_{ON} and higher I_{AMB}. With the integration of GDU architecture on GAA-TFET, a significant reduction in I_{AMB} (from an order of 10^{-18}A to 10^{-12} A) is obtained. This decrease in I_{AMB} is due to the underlapping of gate metal near the drain-channel junction that resists the extension of carrier density towards the drain side and thus, repels the lowering of barrier width at the drain-channel junction (for negative V_{gs}) and thereby reduces the I_{AMB}. This reduced I_{AMB} thus overcomes the major challenges faced by TFET and makes it suitable for digital applications.

Furthermore, the amalgamation of N^+ pocket at the tunneling junction, enhances band bending at the source-channel junction [see Fig. 4(a)]. This steeper band bending thus increases the tunneling rate of electrons. Which thereby conquers the obstacle of lower I_{ON} of TFET, and hence I_{ON} increases from an order of 10^{-8} A (for GAA-TFET) to 10^{-4} A (for PNIN-GAA-TFET). Consequently, the integration of both the scheme i.e. GDU-PNIN-GAA-TFET improves both the hitches (i.e. lower I_{ON} and higher I_{AMB}) by enhancing the I_{ON} and reducing the I_{AMB} as evident by Fig. 6(a). The threshold voltage (V_{th}) and subthreshold swing (SS) of all the device architectures under considerations are shown in Fig. 6(b). The larger band bending at the

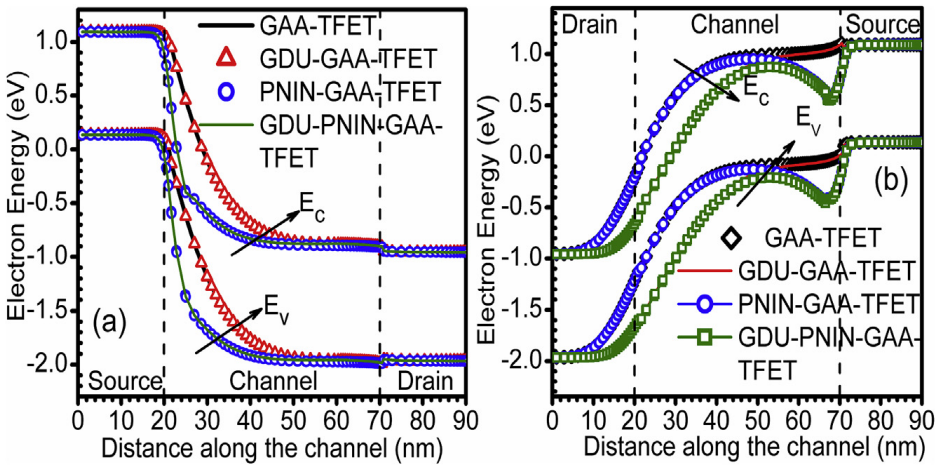


Fig. 4. Energy band diagram of GAA-TFET, GDU-GAA-TFET, PNIN-GAA-TFET and GDU-PNIN-GAA-TFET (a) in ON-state at $V_{gs} = 1.2$ V and $V_{ds} = 1.0$ V (b) in ambipolar state at $V_{gs} = -1.0$ V and $V_{ds} = 1.0$ V as a function of channel length. For GDU architecture $L_{GDU} = 15$ nm.

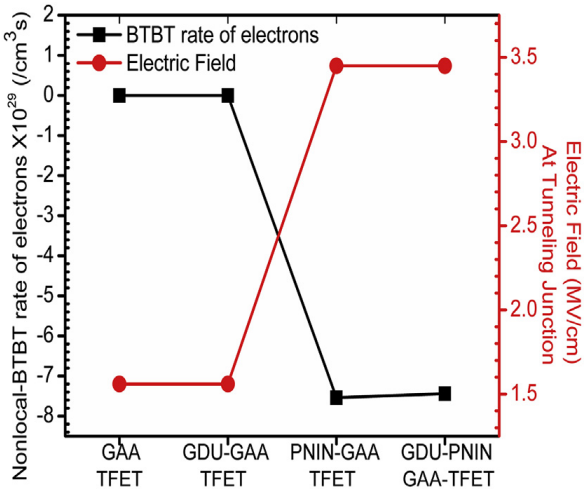
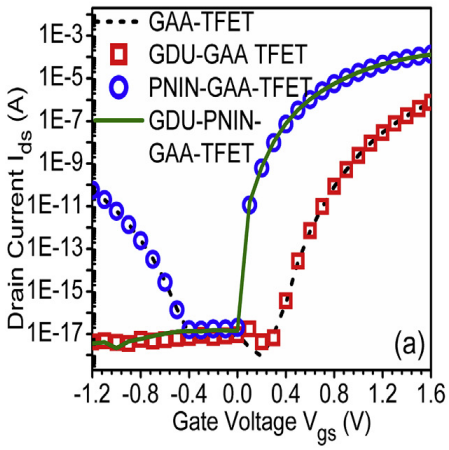


Fig. 5. Nonlocal BTBT rate and electric field at the tunneling junction of GAA-TFET, GDU-GAA-TFET, PNIN-GAA-TFET and GDU-PNIN-GAA-TFET at V_{gs} = 1.2 V and V_{ds} = 1.0 V.



Device architecture	SS (mV/decade)	V_{th} (@I_{ds}= 10^{-7}A) (V)
GAA-TFET	52.22	1.32
GDU-GAA-TFET	53.37	1.32
PNIN-GAA-TFET	17.41	0.41
GDU-PNIN-GAA-TFET	16.59	0.40

(b)

Fig. 6. (a) Transfer characteristics, (b) threshold voltage (V_{th}) and subthreshold swing (SS) of GAA-TFET, GDU-GAA-TFET, PNIN-GAA-TFET and GDU-PNIN-GAA-TFET at V_{ds} = 1.0 V.

tunneling junction for the PNIN-GAA-TFET switches ON TFET at the lower V_{gs}. Thus, there is a considerable reduction in the V_{th} for PNIN-GAA-TFET and GDU-PNIN-GAA-TFET in comparison with its conventional counterparts. Further, the integration of N^+ pocket in GAA-TFET enhances the I_{ON} without any degradation in the I_{OFF}, thereby reduces the SS of GAA-TFET by 3.14 times for PNIN-GAA-TFET.

The ambipolar current of TFETs is a major hindrance in the device designing for low power analog and digital applications. In this work, I_{AMB} is defined as the drain current at $V_{gs} = -1.0$ V and V_{ds} = 1.0 V and are plotted for all the aforementioned device architectures in Fig. 7(a). It is clearly evident from 8(a) that the GDU architecture suppresses the ambipolar current significantly. This suppressed I_{AMB} is attributed to the fact of reduced accumulations of electrons under the underlapped region. This reduction in accumulation in electrons broadens the barrier width between the channel and drain region and thereby reduces the tunneling probability of electrons at the drain-channel junction. Thus, the reduction in tunneling of electrons suppresses the I_{AMB}, from 10^{-12} A (for GAA-TFET and PNIN-GAA-TFET) to 10^{-18}A (for GDU-GAA-TFET and GDU-PNIN-GAA-TFET) as shown in Fig. 7(a). The switching (I_{ON}/I_{OFF}) ratio is an important parameter for digital circuit designing. In this work the I_{ON} and I_{OFF} are defined as the I_{ds} at V_{gs} = 1.2 V and 0 V respectively, at constant V_{ds} = 1.0 V. The presence of N^+ pocket enhances I_{ON} of the TFET significantly (without any degradation in the I_{OFF}) [see Fig. 6(a)], thus results in a considerable enhancement in the switching ratio of PNIN-GAA-TFET and GDU-PNIN-GAA-TFET to an order of 10^{12}. The enhanced I_{ON}/I_{OFF} ratio acquired by the source pocket at the tunneling junction thereby makes source pocket-PIN-GAA-TFET, a potential candidate for high switching speed applications.

Desiging the FETs for analog applications the crucial design parameters are the device efficiency (or the transconductance generation factor) and the output resistance (or the drain resistance). The device efficiency is evaluated as the ratio of transconductance to drive current i.e. g_m/I_{ds} at a constant drain voltage. g_m/I_{ds} is a measure of available gain per unit power dissipation. Further, a higher value of device efficiency is desirable for better analag performance. Fig. 8(a) shows the

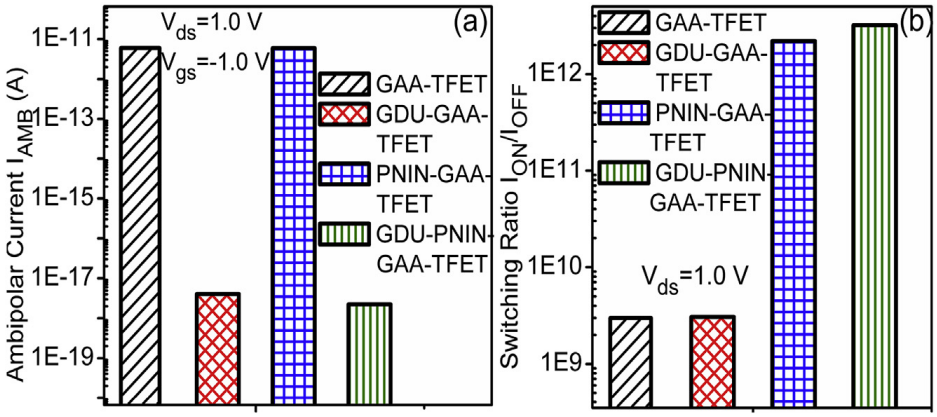


Fig. 7. (a) Ambipolar current (I_{AMB}) at $V_{gs} = -1.0$ V and $V_{ds} = 1.0$ V, (b) Switching ratio (I_{ON}/I_{OFF}) at $V_{ds} = 1.0$ V of GAA-TFET, GDU-GAA-TFET, PNIN-GAA-TFET and GDU-PNIN-GAA-TFET.

improved device efficiency of PNIN-GAA-TFET and GDU-PNIN-GAA-TFET in comparsion with GAA-TFET and GDU-GAA-TFET. This improvement is attributed to the presence of N^+ source pocket in PNIN architecture that enhances the tunneling rate and thus increases the drain current and the transconductance significantly. The enhanced device efficiency acquired for the PNIN-GAA-TFET and GDU-PNIN-GAA-TFET, reveals that the incorporation of N^+ source pocket enhances the amplification delivered by the device. Fig. 8(b) illustrates the output resistance (R_{out}) of all the devices under consideration. It is clearly evident that the R_{out} of PNIN-GAA-TFET and GDU-PNIN-GAA-TFET are appreciably improved in comparsion with GAA-TFET and GDU-GAA-TFET. This improvement in R_{out} for PNIN-GAA-TFET and GDU-PNIN-GAA-TFET is due to the enhanced drain current that increases the output conductance. Thereby the consequence of inverse relation of output conductance and R_{out} reduces the R_{out} from an order of $10^8\Omega$ (for GAA-TFET and GDU-GAA-TFET) to $10^5\Omega$ (for PNIN-GAA-TFET and GDU-PNIN-GDU-GAA-TFET). This improved device efficiency and R_{out} makes GDU-PNIN-GAA-TFET suitable for low power analog applications.

Merely increasing the I_{ON}, reducing the V_{th} and lowered SS does not sufficiently result in a superior TFET based circuit performance. However, the power dissipations and the propagation delay are the key performance metrics for designing digital circuits. The prime important device parameters that affects these performance metrics are the intrinsic parasitic capacitances. Thus, it is necessary to analyze the impact of integration of the aforementioned device engineering schemes on the bias dependence inherent parasitic capacitances. As reported in Refs. [25,26] that for TFET the inversion charge distribution and thus the partition of C_{gg} is entirely different from that of MOSFET. This results in unequal contribution of C_{gs} and C_{gd} to C_{gg}, in contrary to MOSFET in which $C_{gg}/2 \sim C_{gd} \sim C_{gs}$. For TFETs, the source-channel junction being reverse biased, effectively decouples the channel charge from the source. However, the degenerated (N^+) drain floods the channel region with electrons. Therefore, the channel charge is majorly coupled with the drain, and thus C_{gd} represents a major fraction of C_{gg}.

Fig. 9(a–d) shows the C_{gs} and C_{gg} as a function of V_{gs} and V_{ds}. Fig. 9(a–b) clearly illustrates that C_{gs} is lesser than C_{gg}, attributed to the larger C_{gd}. Fig. 9(a) shows that C_{gs} is immune to the integration of GDU engineering scheme because the metal is underlapped near the drain side. Moreover, it is analyzed that for shorter metal gate, the parasitic C_{gg} is considerably reduced, due to the reduction in C_{gd} for underlapped metal gate. Thus, C_{gg} is appreciably reduced for GDU-GAA-TFET and GDU-PNIN-GAA-TFET, in comparison with GAA-TFET. Quantitatively, C_{gg} is reduced by 29% with the integration of GDU engineering scheme onto GAA-TFET as shown in Fig. 9(b). In addition to this, at lower gate bias, the inversion layer is first formed near the drain side, and then with an increase in gate bias, the inversion layer extends towards the source side. Thus, C_{gg} increases with an increase in gate bias. Fig. 9(c–d) shows C_{gs} and C_{gg} for all the device design architectures as a function of V_{ds} at a constant V_{gs}. At $V_{gs} = 1.2$ V (TFET is in ON-state), an increase in V_{ds} pinches the inversion layer at the source side (in contrast to MOSFET, where pinch off occurs near drain side). Thereby, C_{gg} decreases with an increase in V_{ds}. Consistent with the above explanations for shortened metal gate, the C_{gs} remains unaltered with the incorporation of GDU architectures. However, the reduction in C_{gd} with GDU engineering scheme results into lowering of C_{gg} for GDU-GAA-TFET and PNIN-GDU-GAA-TFET in comparison with GAA-TFET and PNIN-GAA-TFET. Thus, as lower parasitic capacitances are needed for higher switching speed and lower static power dissipation, GDU-PNIN-GAA-TFET may act as a superior candidate to meet these requirements.

An important RF figure of merit for a tunnel FET is the unity current gain or the intrinsic f_T. It is defined as the frequency at which the short circuit current gain falls to 0 dB. Mathematically, the intrinsic f_T is defined as

$$f_T = \frac{g_m}{2\pi\left(C_{gs} + C_{gd}\right)} \tag{1}$$

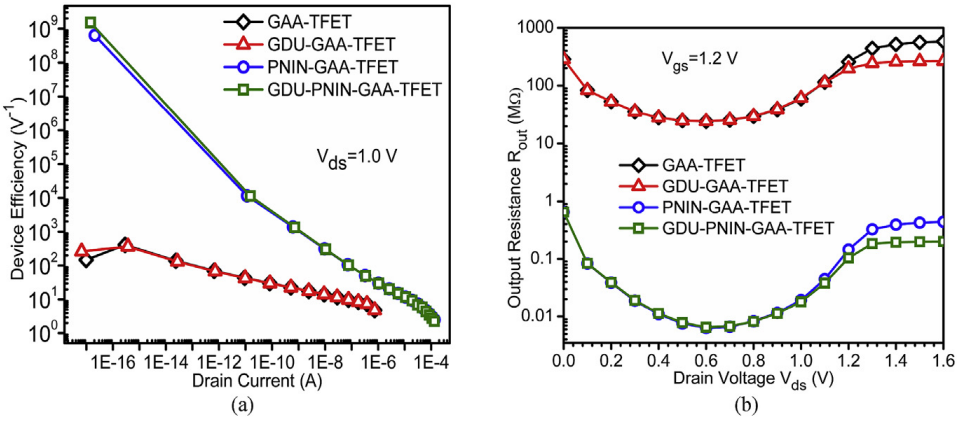


Fig. 8. (a) Device efficiency at V_{ds} = 1.0 V, (b) Output resistance (R_{out}) at V_{gs} = 1.2 V of GAA-TFET, GDU-GAA-TFET, PNIN-GAA-TFET and GDU-PNIN-GAA-TFET.

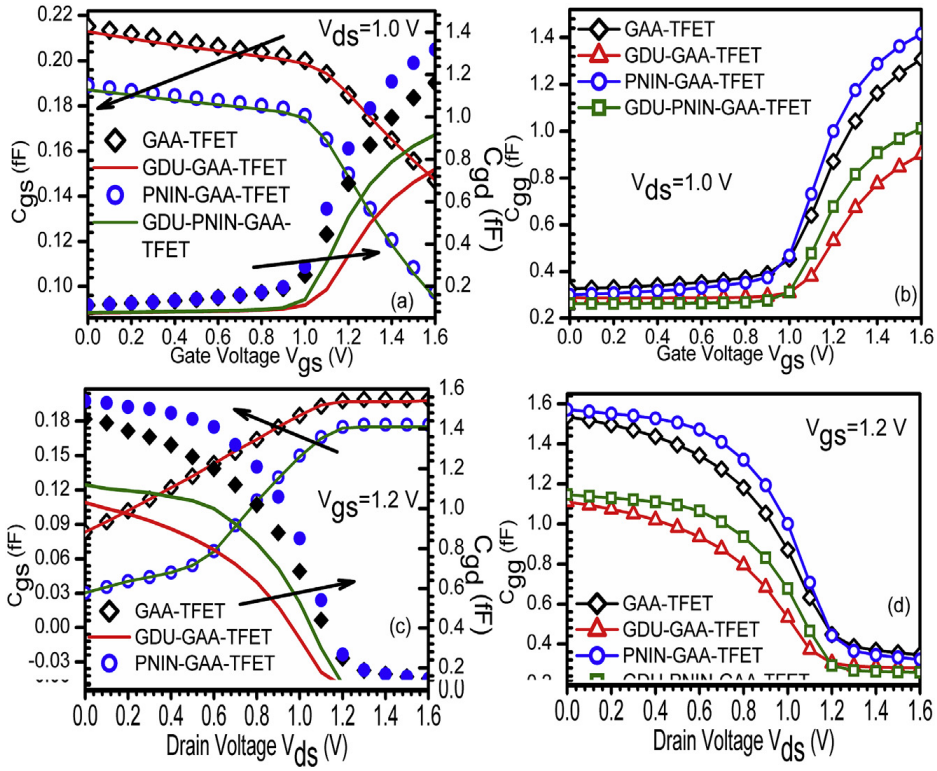


Fig. 9. (a) C_{gs} w.r.t. V_{gs} at V_{ds} = 1.0 V (b) C_{gg} w.r.t. V_{gs} at V_{ds} = 1.0 V (c) C_{gs} w.r.t. V_{ds} at V_{gs} = 1.2 V (d) C_{gg} w.r.t. V_{ds} at V_{gs} = 1.2 V of GAA-TFET, GDU-GAA-TFET, PNIN-GAA-TFET and GDU-PNIN-GAA-TFET.

Where g_m is the transconductance, C_{gs} and C_{gd} are gate to source and gate to drain intrinsic parasitic capacitances. The vital RF parameters needed for designing analog/RF electronic circuits are shown in Fig. 10(a–b). The variations of f_T as a function of gate bias for all the device designs under considerations are shown in Fig. 10(a). Result shows that as the V_{gs} increases, f_T of all the devices increases until it attains a peak value. The increase in f_T with V_{gs} is attributed to the narrower tunneling barrier width that increases the rate of carrier injection at the tunneling junction and thus, increases the drain current and the transconductance (first order derivative of drain current). f_T being directly proportional to the g_m, increases with V_{gs}, before attaining a peak value. It is observed that the enhanced drain current with source pocket incorporation enhances the transconductance and thereby enhances f_T (being directly proportional to g_m) for PNIN-GAA-TFET and GDU-PNIN-GAA-TFET in comparison with GAA-TFET and GDU-GAA-TFET. f_T is enhanced from an order of 10^8 Hz–10^{10} Hz with the integration of N^+ source pocket. The f_T and f_{MAX} of all the devices are also shown in Fig. 10(b). The frequencies at which the short circuit current gain and unilateral power gain drops to 0 dB are defined as the f_T and the f_{MAX} respectively. The f_T and f_{MAX} are tremendously enhanced for the cases of PNIN-GAA-TFET and GDU-PNIN-GAA-TFET in comparison with GAA-TFET and GDU-GAA-TFET, owing to the enhanced drain current and transconductance that enhance the current gain and the unilateral power gain and therefore results into a larger f_T and f_{MAX} as illustrated in Fig. 10(b). Thus, results indicate that with the integration of N^+

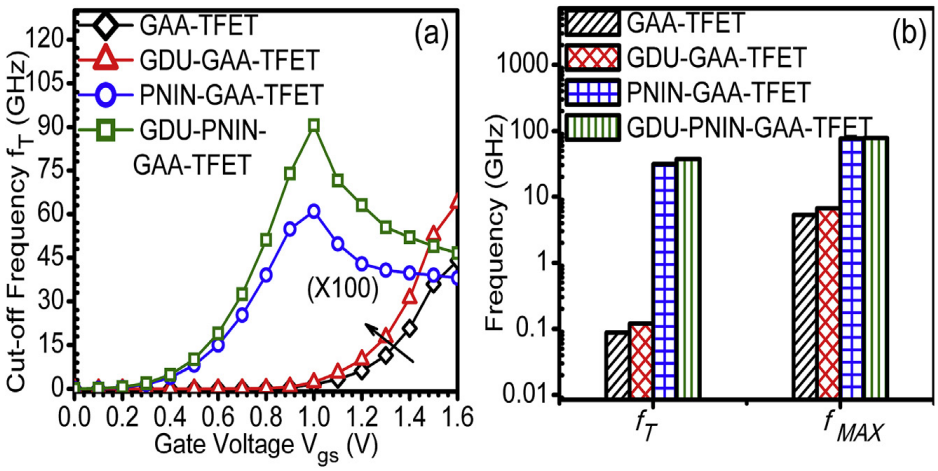


Fig. 10. (a) f_T as a function of gate bias, at constant $V_{ds} = 1.0$ V (b) f_T and f_{MAX} at $V_{gs} = 1.2$ V and $V_{ds} = 1.0$ V of GAA-TFET, GDU-GAA-TFET, PNIN-GAA-TFET and GDU-PNIN-GAA-TFET.

source pocket engineering, analog as well as the high-frequency performance of TFET are improved appreciably, making it a superior candidate for high switching speed electronics application.

5. Conclusion

In this work, gate drain underlapped N^+ source pocket gate all around tunnel FET (GDU-PNIN-GAA-TFET) is realized. In GDU-PNIN-GAA-TFET, the source pocket pedals the source-channel junction and thereby improves the ON-state characteristics of TFET along with a reduced threshold voltage; however, the GDU governs the drain-channel junction and thus controls the ambipolar conduction of the device. Results show a tremendously improved ON-state characteristics i.e. the I_{ON} to an order of 10^{-4} A together with suppressed ambipolar current to 10^{-18}A with the amalgamation of source pocket and GDU engineering schemes respectively onto GAA-TFET. Hence, the challenges faced by TFET that restricts it for the practical applications have been overcome. Further, the reduction in parasitic capacitances offered by GDU and enhanced transconductance acquired by N^+ pocket leads to a superior RF performance. The detailed insight demonstration in terms of analog/RF performance for GDU-PNIN-GAA-TFET may be beneficial for analog/RF circuit designers and it may also serves as a superior candidate for high speed and low power applications.

Acknowledgment

Authors would like to thank to Microelectronics Research Lab, Department of Engineering Physics Delhi Technological University to carry out this work. One of the authors (Jaya Madan) would like to thank University Grants Commission, Govt. of India, for providing the necessary financial assistance during the course of this research work.

References

[1] A.M. Ionescu, H. Riel, Tunnel field-effect transistors as energy-efficient electronic switches, Nature 479 (2011) 329–337.
[2] W.Y. Choi, B.-G. Park, J.D. Lee, T.-J.K. Liu, Tunneling field-effect transistors (TFETs) with subthreshold swing (SS) less than 60 mV/dec, IEEE Electron Device Lett. 28 (2007) 743–745.
[3] Y. Khatami, K. Banerjee, Steep subthreshold slope n-and p-type tunnel-FET devices for low-power and energy-efficient digital circuits, IEEE Trans. Electron Devices 56 (2009) 2752–2761.
[4] J. Madan, R. Chaujar, Interfacial charge analysis of heterogeneous gate dielectric-gate all around-tunnel FET for improved device reliability, IEEE Trans. Device Mater. Reliab. 16 (2016) 227–234.
[5] K. Boucart, A.M. Ionescu, Length scaling of the double gate tunnel FET with a high-k gate dielectric, Solid-State Electron. 51 (2007) 1500–1507.
[6] K. Boucart, A.M. Ionescu, Double-gate Tunnel FET with High-gate Dielectric, 2007.
[7] A. Villalon, G. Le Carval, S. Martinie, C. Le Royer, M.-A. Jaud, S. Cristoloveanu, Further insights in TFET operation, IEEE Trans. Electron Devices 61 (2014) 2893–2898.
[8] R. Gandhi, Z. Chen, N. Singh, K. Banerjee, S. Lee, CMOS-compatible vertical-silicon-nanowire gate-all-around p-type tunneling FETs with-mV/decade subthreshold swing, IEEE Electron Device Lett. 32 (2011) 1504–1506.
[9] J. Madan, R. Gupta, R. Chaujar, Mathematical modeling insight of hetero gate dielectric-dual material gate-GAA-tunnel FET for VLSI/analog applications, Microsyst. Technol. (2016) 1–8.
[10] W.Y. Choi, W. Lee, Hetero-gate-dielectric tunneling field-effect transistors, IEEE Trans. electron devices 57 (2010) 2317–2319.
[11] R. Jhaveri, V. Nagavarapu, J.C. Woo, Effect of pocket doping and annealing schemes on the source-pocket tunnel field-effect transistor, IEEE Trans. Electron Devices 58 (2011) 80–86.
[12] V. Nagavarapu, R. Jhaveri, J.C. Woo, The tunnel source (PNPN) n-MOSFET: a novel high performance transistor, IEEE Trans. Electron Devices 55 (2008) 1013–1019.
[13] E.-H. Toh, G.H. Wang, L. Chan, G. Samudra, Y.-C. Yeo, Device physics and guiding principles for the design of double-gate tunneling field effect transistor with silicon-germanium source heterojunction, Appl. Phys. Lett. 91 (2007) 243505.

[14] W. Cao, C. Yao, G. Jiao, D. Huang, H. Yu, M.-F. Li, Improvement in reliability of tunneling field-effect transistor with pnin structure, IEEE Trans. Electron Devices 58 (2011) 2122–2126.
[15] P.-F. Wang, K. Hilsenbeck, T. Nirschl, M. Oswald, C. Stepper, M. Weis, et al., Complementary tunneling transistor for low power application, Solid-State Electron. 48 (2004) 2281–2286.
[16] J. Madan, R. Chaujar, Gate drain-overlapped-asymmetric gate dielectric-GAA-TFET: a solution for suppressed ambipolarity and enhanced ON state behavior, Appl. Phys. A 122 (2016) 973.
[17] A.S. Verhulst, W.G. Vandenberghe, K. Maex, G. Groeseneken, Tunnel field-effect transistor without gate-drain overlap, Appl. Phys. Lett. 91 (2007) 053102.
[18] J. Madan, R. Gupta, R. Chaujar, Analytical drain current formulation for gate dielectric engineered dual material gate-gate all around-tunneling field effect transistor, Jpn. J. Appl. Phys. 54 (2015) 094202.
[19] U.E. Avci, I.A. Young, Heterojunction TFET scaling and resonant-TFET for steep subthreshold slope at sub-9nm gate-length, in: 2013 IEEE International Electron Devices Meeting, 2013, pp. 4.3. 1-4.3. 4.
[20] X. Wang, Y. Xiong, M. Tang, L. Peng, Y. Xiao, X. Xu, et al., A Si tunnel field-effect transistor model with a high switching current ratio and steep sub-threshold swing, Semicond. Sci. Technol. 29 (2014) 095016.
[21] I.M. Kang, J.-S. Jang, W.Y. Choi, Radio frequency performance of hetero-gate-dielectric tunneling field-effect transistors, Jpn. J. Appl. Phys. 50 (2011) 124301.
[22] I. Silvaco, ATLAS User's Manual, vol. 5, 2011. Santa Clara, CA, Ver.
[23] A. Biswas, S.S. Dan, C. Le Royer, W. Grabinski, A.M. Ionescu, TCAD simulation of SOI TFETs and calibration of non-local band-to-band tunneling model, Microelectron. Eng. 98 (2012) 334–337.
[24] Z. Chen, H. Yu, N. Singh, N. Shen, R. Sayanthan, G. Lo, et al., Demonstration of tunneling FETs based on highly scalable vertical silicon nanowires, IEEE Electron Device Lett. 30 (2009) 754–756.
[25] E. Gnani, E. Baravelli, A. Gnudi, S. Reggiani, G. Baccarani, Capacitance estimation for InAs Tunnel FETs by means of full-quantum k· p simulation, Solid-State Electron. 108 (2015) 104–109.
[26] S. Mookerjea, R. Krishnan, S. Datta, V. Narayanan, On enhanced Miller capacitance effect in interband tunnel transistors, IEEE Electron Device Lett. 30 (2009) 1102–1104.

Journal of Molecular Structure 1133 (2017) 90–94

Contents lists available at ScienceDirect

Journal of Molecular Structure

journal homepage: http://www.elsevier.com/locate/molstruc

Green synthesis of multi metal- citrate complexes and their characterization

Usha Raju, Sudhir G. Warkar, Anil Kumar*

Department of Applied Chemistry, Delhi Technological University, Bawana Road, Delhi, 110042, India

ARTICLE INFO

Article history:
Received 18 April 2016
Received in revised form
8 November 2016
Accepted 28 November 2016
Available online 29 November 2016

Keywords:
Citric acid
Multi metal-citrate complex
Hydrothermal synthesis
Fourier Transform Infrared Spectroscopy
Thermogravimetric analysis
Powder X-ray Diffraction

ABSTRACT

Four new multi metal-citrate complexes have been synthesized through green synthetic pathways. Their synthesis by hydrothermal route in the present research is decorated with features such as, a simple one pot synthesis, cost effectiveness, easy to scale up for commercial production, efficient synthesis conditions like mild temperature and shorter duration which further rules out the possibility of forming byproducts which may cause damage to the environment and being environmental benign as it eliminates the use and recovery of harmful organic solvents such as *N*, *N*- dimethyl formamide and *N*, *N*- diethyl formamide, used by the researchers in the past during the synthesis of similar metal- organic framework complexes. All four complexes are well defined crystalline materials with polynuclear multi metal-citrate framework having cubic crystal structure as indicated by their Powder X-ray Diffraction patterns. These complexes have been characterized by Fourier Transform Infrared Spectroscopy, Scanning Electron Microscopy, Energy Dispersive X-ray Spectroscopy, Thermogravimetric analysis and Powder XRD techniques.

© 2016 Elsevier B.V. All rights reserved.

1. Introduction

Over the past several years, a large community of researchers has focused its attention on the synthesis of metal- organic frameworks due to their wide range of applications namely catalysis [1,2], biological imaging [3], luminescence [4], magnetism [5], gas adsorption [6,7] and gas separation [8,9] etc. Extensive efforts have been made in the past to develop strategies for the synthesis of metal- organic frameworks with larger surface area for efficient uptake and storage of hydrogen-a future generation fuel. Metal-organic frameworks constitute a class of inorganic- organic hybrid materials which can store hydrogen at molecular level. These are highly porous crystalline materials consisting of metal ions or their clusters coordinated to organic linkers. When solvent guest molecules occupying their pores are removed during thermal evacuation or solvent exchange, a well defined porous structure of these complexes can be achieved without destabilizing the framework. Gases like hydrogen and carbon dioxide can be adsorbed in their pores by the process of physisorption. Moreover their highly crystalline and porous nature, tailored structures, ultra high surface area, tunable pore size and facile synthesis, makes metal- organic frameworks the most suitable materials for the uptake and storage of gases like hydrogen and methane [10]. These complexes have an added advantage as they can be synthesized by simple solvothermal or hydrothermal techniques. Metal- organic frameworks of transition metal ions with a variety of organic linkers have extensively been synthesized by solvothermal method using organic solvents mostly DMF (*N*, *N*- dimethylformamide) and DEF (*N*, *N*- diethylformamide). First water soluble iron-citrate complex was synthesized by Salifoglou [11]. Hydrothermal synthesis of metal- organic frameworks has been carried out by various scientists in the past [12–17]. Recently $Co_3(BTC)_2 \cdot 12H_2O$ (BTC = 1, 3, 5-benzene tricarboxylic acid) having micro porous channels has been synthesized hydrothermally which involves hydrogen bonding of the coordinated water molecules [18]. Metal- organic frameworks with diverse structures from different inorganic secondary building blocks can even be prepared using the same basic units just by adjusting the amount of water in the reaction mixture as reported by Kim [19]. Merrifield solid-phase peptide synthesis was used to synthesize multi metal- organic complexes bearing three to six

Abbreviations: MOF, Metal-organic framework; DMF, *N*, *N*- dimethyl formamide; DEF, *N*, *N*- diethyl formamide; PXRD, Powder X-ray Diffraction; FTIR, Fourier Transform Infrared Spectroscopy; TGA, Thermogravimetric analysis; EDX, Energy-dispersive X-ray spectroscopy; SEM, Scanning electron microscopy; FWHM, full width half maximum.

* Corresponding author.
E-mail address: anil_kumar@dce.ac.in (A. Kumar).

http://dx.doi.org/10.1016/j.molstruc.2016.11.084
0022-2860/© 2016 Elsevier B.V. All rights reserved.

metal atoms in a pre determined sequence [20]. To synthesize multiple metal atom molecules containing more than one type of metal is "*notoriously tough*". Such complexes may be used in highly selective catalytic reactions or "*cascading reactions*" [21,22]. Wang and co-workers have synthesized microcrystalline metal- organic framework-74 with 2, 4, 6, 8 and 10 divalent metal atoms [23]. Recently, Li and co-workers have claimed that mixed metal- MOFs show superior catalytic performance and have great potential in heterogeneous catalysis [24].

The present research aims to explore the complexation of metal ions or their clusters with citric acid linker through green synthetic pathways to form multi metal-citrate complexes which are expected to have larger surface area and efficient uptake and storage of hydrogen due to unique coordination properties of different metal ions. Out of several complexing agents, citric acid appears to be the most attractive option because of being a naturally occurring complexing agent and its environment friendly nature. An excellent chelating agent, citric acid can easily co-ordinate with different metals to form a variety of one, two and three dimensional complexes under mild conditions. Citric acid can form bidentate, tridentate, binuclear or polynuclear complexes with transition metals, alkali metals and actinides.

2. Experimental

2.1. Materials and physical measurements

All the chemicals used were commercially available analytical grade and used as obtained without further purification. Reactions were carried out in the air. Water used as a solvent was double distilled water with specific conductivity of 0.055 μS/cm. Powder X-ray diffraction (PXRD) patterns were recorded with a Bruker D8 ADVANCE X-ray powder diffractometer operated at 40 kV and 40 mA with monochromated CuKα radiation (λ = 1.5406 Å). Fourier transform infrared (FTIR) spectra were obtained in the wavenumber range of 4000–400 cm^{-1} by using a Nicolet 380 FTIR spectrometer with the KBr pellet technique. Scanning electron microscopy (SEM), to observe the microscopic morphology of the crystals and energy-dispersive X-ray spectroscopy to identify the relative elemental composition was carried out with a HITACHI S-3700N electron microscope with a "built-in" Energy Dispersive X-Ray Analyzer (EDX). Thermogravimetric analyses (TGA) were carried out on Mettler Toledo using software STAR^e SW 9.20.

2.2. Synthesis of multi metal-citrate complexes

Multi metal citrate complex **1** was synthesized by stirring the solution of $NiSO_4 \cdot 6H_2O$ and $ZnSO_4 \cdot 7H_2O$ (10 mmol each) with 20 mmol of citric acid monohydrate in 20 mL of double distilled water. The reaction mixture was initially heated and temperature of reaction vessel was kept between 30 and 40 °C for 1 h and stirring continued for 4 h. The pH of the reaction mixture was between 3 and 4. Upon cooling bluish green needle shaped crystalline product was obtained in 54% yield after 48 h. Complex **2** was synthesized according to above mentioned procedure by the complexation of citric acid monohydrate with $CuSO_4 \cdot 5H_2O$ and $FeSO_4 \cdot 7H_2O$ in a molar ratio of 2:1:1 using 20 mL of double distilled water as a solvent. Upon cooling yellowish green cubical crystals were obtained in 52% yield. In the synthesis of complex **3**, complexation of citric acid monohydrate was carried out with $CuSO_4 \cdot 5H_2O$, $FeSO_4 \cdot 7H_2O$ and $NiSO_4 \cdot 6H_2O$ taken in a molar ratio of 2:1:1:1 and dark green cubical crystals were obtained in 62% yield. The complex **4** was also synthesized by the same procedure, taking 10 mmol each of $CuSO_4 \cdot 5H_2O$, $FeSO_4 \cdot 7H_2O$, $NiSO_4 \cdot 6H_2O$, $ZnSO_4 \cdot 7H_2O$ and 20 mmol of citric acid monohydrate dissolved in 20 mL of double distilled water and dark green crystals of the complex **4** were separated out in 59% yield. The complexes **1**, **2**, **3** and **4** were washed with ice cold distilled water and dried in air. All four complexes have been characterized by Fourier Transform Infrared Spectroscopy, Scanning Electron Microscopy, Energy Dispersive Spectroscopy, Thermogravimetric analysis and Powder X-ray Diffraction techniques. The crystal structure of these complexes could not be established by single crystal X-ray diffraction, probably due to overlapping of reflections caused by their large unit cells [25].

3. Results and discussion

The FTIR spectroscopy of the multi metal-citrate metal organic frameworks in KBr indicates the presence of vibrationally active carboxylate group (Fig. 1). Both anti-symmetric and symmetric stretching vibrations of the carboxylate groups present in the co-ordinated citrate ligand are revealed by the FTIR spectrum of the complexes. Strong absorption bands between 1630-1600 cm^{-1} are assigned to anti-symmetric, while between 1450 and 1400 cm^{-1} are due to symmetric stretching vibrations of the carboxylate groups of citrate ligand. Due to acidic medium the intensities of these bands decrease [26]. The difference between the anti-symmetric and symmetric stretching vibrations in complex **1** and **2** being greater than 200 cm^{-1} indicates that the carboxylate groups of citrate ligand in these complexes are coordinated to metal ions in a mono dentate fashion [27], while a separation of 180–200 cm^{-1} in complex **3** and **4** refers to bidentate bridging bonding, the most preferred co-ordination of the carboxylate groups of citrate ligand in these complexes [28,29]. A peak at 1724.2 cm^{-1} and 1726.7 cm^{-1} in complex **1** and **2** respectively, suggests that a fraction of the hydrogen atoms of carboxylate group of citric acid remain bound while others are replaced by metal atoms forming multi-metal citrate complexes [30]. The absence of the characteristic valence vibrational band of the carboxyl group of citric acid between 1750 and 1720 cm^{-1} reflects the presence of complete deprotonated form of the citric acid in complexes **3** and **4** [31]. In addition the strong –OH stretching band in the range 3200–2500 cm^{-1} and in-plane and out-of-plane O-H bending bands of carboxylic acids at 1430 cm^{-1} and 930 cm^{-1} are absent in multi metal-citrate complexes [32]. Thus the hydroxyl group of citrate ligand is coordinated as shown by Hedwig and co-workers

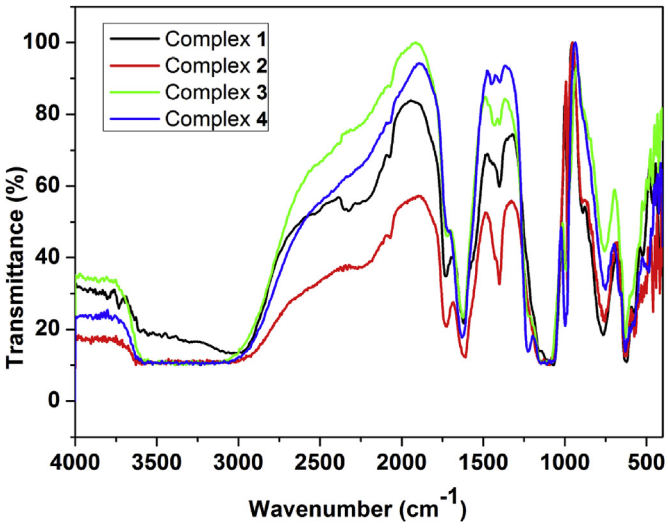


Fig. 1. IR spectrum of complexes **1**–**4** recorded in KBr.

through potentiometric and spectroscopic study for the synthesis of Ni(II) complex with citric acid in aqueous solution in the pH range of 3–6 [33]. The characteristic vibrational bands of alcoholic hydroxyl group of citric acid at 3450, 1290, 1265, 1165, 1125, 1060, 925, 890 and 820 cm^{-1} disappear in the FTIR spectrum of the prepared complexes [31]. A broad peak between 3700 and 3200 cm^{-1} in all the complexes is assigned to hydrogen bonding by hydroxyl group of coordinated water, lying between the tetrahedral and octahedral sheets in the complexes [32]. A layered structure similar to the one assigned to metal carboxylates by the researchers in the past is thus proposed for the hydrothermally synthesized multi metal-citrate complexes in the present research [34]. Two vibrational bands at around 760 cm^{-1} and 630 cm^{-1} confirm the presence of coordinated water molecules in the complexes [35]. The sharp peaks in Powder X-Ray diffraction pattern of the synthesized complexes reflect their highly crystalline nature of single phase (see Supporting information). $Sin^2\theta$ values of the diffraction lines give a set of integers and satisfy the equation given below obtained by combining Bragg's Law with the plane spacing equation for the cubic system, which confirms cubic lattice for the crystals [36].

$$\sin^2\theta \Big/ \left(h^2 + k^2 + l^2\right) = \sin^2\theta/s = \lambda^2 \Big/ 4a^2$$

(θ = Bragg's diffraction angle in radian, h k l = Miller indices, $s = h^2 + k^2 + l^2$ = an integer λ = wave length of the CuKα radiation (0.154056 nm), a = lattice constant).

The lattice parameters of these complexes were calculated by using the formula $a = d\,(h^2 + k^2 + l^2)^{1/2}$ where, a = lattice constant, d = inter planar distance and (h k l) are the Miller indices. The unit cell length of the cubic structure assigned to these complexes has been found to be 6 Å for complexes **1** and **2** and 7 Å for complexes **3** and **4**. The variation in lattice constants can be explained on the basis of difference in ionic radii of different metal ions [37]. The average crystallite size of the complexes was calculated using Scherrer formula: $\tau = K\lambda/\beta \cdot \cos\theta$ [38,39] where λ is the wave length of the CuKα radiation (0.154056 nm), K is shape factor a constant (0.94), β (FWHM) is the broadening of the diffraction line measured in radian at half of its maximum intensity, θ is Bragg's diffraction angle in radian. Table 1 depicts the crystallite size of the complexes in nanometers (D and λ have the same units of measurement).

The crystalline nature of these complexes is further supported by their SEM images and shown in Fig. 2. Energy-dispersive X-ray spectroscopy (EDX) was performed for the elemental analysis of the synthesized complexes, which confirms the presence of metals namely Ni, Zn, Fe, and Cu as targeted (see Supporting information). However, no chemical formula could be assigned to the complexes because electron dispersive spectroscopy was not able to detect carbon, as analysis of lighter elements such as Be, B, C, N, O and F is difficult with standard EDX technique [40].

3.1. Thermogravimetric analysis

The thermal behaviour of multi metal-citrate complexes was studied with their thermogravimetric analysis carried out in air as well as in an inert atmosphere of nitrogen by heating the samples

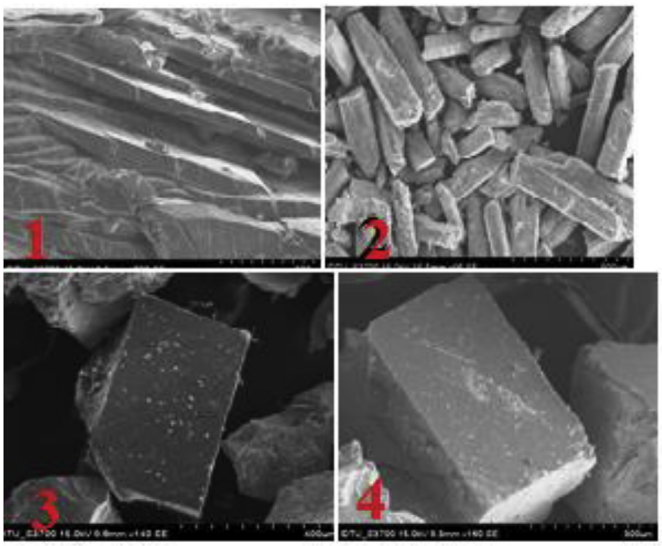


Fig. 2. SEM images of complexes **1**–**4**.

from ambient temperature to 1500 °C with a controlled heating rate of 10 °C/min and shown in Fig. 3 and Fig. 4. The thermogravimetric curve of complexes **1**, **3** and **4** shows four stage decomposition pattern, while the thermal decomposition of complex **2** occurs in three stages. The major weight loss in the temperature range 120 °C–150 °C in the first stage can be attributed to vaporization of lattice water in all the complexes [41]. The second stage reveals a small weight loss corresponding to coordinated water in all the complexes, followed by gradual weight loss in the temperature range 300 °C–700 °C. A large weight loss in third stage may

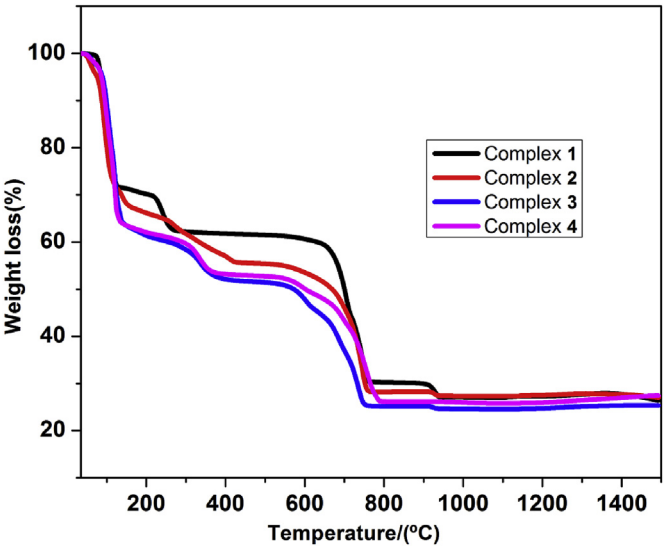


Fig. 3. Thermogravimetric curves of complexes **1**–**4** in air.

Table 1
Crystallite size of complexes **1**–**4** calculated using Scherrer formula.

Complex	2 Theta (degrees)	FWHM of 100% peak (degrees)	Crystallite size/(nm)	Lattice strain
1	48.00	0.232	39.16	0.0023
2	15.20	0.124	67.54	0.0041
3	31.96	0.206	41.92	0.0031
4	18.44	0.214	39.31	0.0058

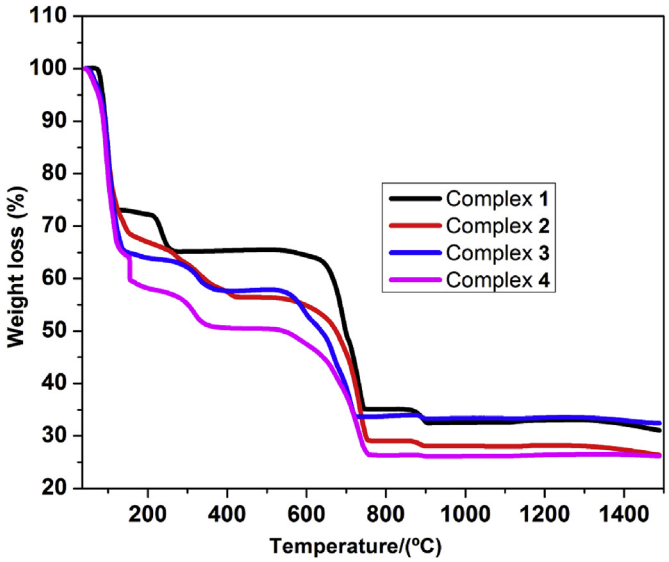


Fig. 4. Thermogravimetric curves of complexes **1**–**4** in nitrogen atmosphere.

be attributed to the decarboxylation of carboxylic acid groups of citrate moiety. The dehydration takes place at relatively higher temperatures during thermal analysis of the multi metal-citrate complexes due to an extensive array of hydrogen bonds in these complexes and probably due to "*resistance of crystal lattice*" to the water escaping as described by Rogan and Poleti [42]. The hydrogen bonding occurs between lattice water and coordinated water molecules and between coordinated water molecules and carboxyl oxygen atoms of citrate moiety to form a rigid three dimensional supramolecular structure with great stability [43]. Moreover decarboxylation of citrate ligand occurs at higher temperature as the thermal stability of citrate ligand increases on complexation with metal ions [44]. The residue contains mixed metal oxides as a result of decomposition of complexes in air. Pyrolysis of these complexes in an atmosphere of nitrogen leaves more residue as compared to their thermal decomposition in air due to carbon black formed from pyrolysis of citrate moiety.

4. Conclusion

Multi metal-citrate complexes prepared by the green synthetic pathways in the present research are polynuclear complexes with cubic geometry. The method has the merits of being a simple one pot synthesis, environmental benign. The established protocol eliminates the use and recovery of potentially harmful organic solvents such as DMF and DEF, cost effectiveness, efficient synthesis conditions like mild temperature and shorter duration which further rules out the possibility of forming byproducts which may cause damage to the environment. These complexes are expected to have better hydrogen adsorption and storage properties due to vacant coordination sites associated with a combination of different metal ions in the crystal structure upon removal of guest solvent molecules. Due to bidentate bridging mode of coordination of carboxylate groups of citrate moiety in complexes **3** and **4** with metal ions in contrast to complexes **1** and **2** (which show mono-dentate coordination of carboxylate groups with metal ions) may prove to be versatile materials for hydrogen storage. Also, these complexes can show reversible adsorption and desorption of gases through two or more cycles and may have the potential as mobile carriers of hydrogen, a future generation fuel to prevent further degradation of the environment.

Acknowledgements

Authors thank to DTU, Delhi, India for providing infrastructural facilities.

Appendix A. Supplementary data

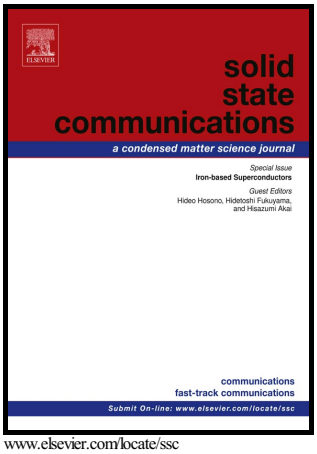
Supplementary data related to this article can be found at http://dx.doi.org/10.1016/j.molstruc.2016.11.084.

References

[1] T. Sawano, Z. Lin, D. Boures, B. An, C. Wang, W. Lin, Metal-organic frameworks stabilize mono(phosphine)- metal complexes for broad-scope catalytic reactions, J. Am. Chem. Soc. 138 (2016) 9783–9786.
[2] A. Henschel, K. Gedrich, R. Kraehnert, S. Kaskel, Catalytic properties of MIL-101, Chem. Commun. (2008) 4192–4194.
[3] D. Liu, K. Lu, C. Poon, W. Lin, Metal-organic frameworks as sensory materials and imaging agents, Inorg. Chem. 53 (2014) 1916–1924.
[4] L. Zhang, Z. Kang, X. Xin, D. Sun, Metal-organic frameworks based luminescent materials for nitroaromatics sensing, Cryst. Eng. Comm. 18 (2016) 193–206.
[5] M. Kurmoo, Magnetic metal-organic frameworks, Chem. Soc. Rev. 38 (2009) 1353–1379.
[6] R.Q. Zhong, R.Q. Zou, M. Du, T. Yamada, G. Maruta, S. Takeda, J. Li, Q. Xu, Metal-organic frameworks of manganese(ii) 4,4′- biphenyldicarboxylates: crystal structures, hydrogen adsorption, and magnetism properties, Cryst. Eng. Comm. 12 (2010) 677–681.
[7] B. Panella, M. Hirscher, Hydrogen physisorption in metal-organic porous crystals, Adv. Mater. 17 (2005) 538–541.
[8] R. Zou, A.I. Abdel-Fattah, H. Xu, Y. Zhao, D.D. Hickmott, Storage and separation applications of nanoporous metal-organic frameworks, Cryst. Eng. Comm. 12 (2010) 1337–1353.
[9] D. Britt, D. Tranchemontagne, O.M. Yaghi, Metal-organic frameworks with high capacity and selectivity for harmful gases, Proc. Natl. Acad. Sci. U. S. A. 105 (2008) 11623–11627.
[10] S. Kaskel, Porous metal-organic frameworks, p.1190-1249, in: Handbook of Porous Solids, Wiley Online Library, 2002.
[11] M. Matzapetakis, C.P. Raptopoulou, A. Tsohos, V. Papaefthymiou, N. Moon, A. Salifoglou, Synthesis, spectroscopic and structural characterization of the first mononuclear, water soluble iron- citrate complex, $(NH_4)_5Fe(-C_6H_4O_7)_2\cdot 2H_2O$, J. Am. Chem. Soc. 120 (1998) 13266–13267.
[12] O.M. Yaghi, H. Li, Hydrothermal synthesis of a metal- organic framework containing large rectangular channels, J. Am. Chem. Soc. 117 (1995) 10401–10402.
[13] C. Gabriel, C.P. Raptopoulou, A. Terzis, V. Tangoulis, C. Mateescu, A. Salifoglou, pH -specific synthesis and spectroscopic, structural, and magnetic studies of a chromium(III)- citrate species. Aqueous solution speciation of the binary chromium (III)- citrate System, Inorg. Chem. 46 (2007) 2998–3009.
[14] Y. Qi, F. Luo, Y. Che, J. Zheng, Hydrothermal synthesis of metal- organic frameworks based on aromatic polycarboxylate and flexible bis(imidazole) ligands, Cryst. Growth Des. 8 (2008) 606–611.
[15] E.Y. Choi, K. Park, C.M. Yang, H. Kim, J.H. Son, S.W. Lee, Y.H. Lee, D. Min, Y.U. Kwon, Benzene- templated hydrothermal synthesis of metal- organic frameworks with selective sorption properties, Chem. Eur. J. 10 (2004) 5535–5540.
[16] J.Y. Lu, M.A. Lawandy, J. Li, T. Yuen, C.L. Lin, A new type of two-dimensional metal coordination systems: Hydrothermal synthesis and properties of the first oxalate- bpy mixed- ligand framework [M (ox)(bpy)] (M = Fe(II), Co(II), Ni(II), Zn(II); ox = $C_2O_4^{2-}$; bpy = 4,4′-bipyridine), Inorg. Chem. 38 (1999) 2695–2704.
[17] D. Saha, T. Maity, S. Koner, Alkaline earth metal-based metal- organic framework: hydrothermal synthesis, X- ray structure and heterogeneously catalyzed Claisen- Schmidt reaction, Dalton Trans. 43 (2014) 13006–13017.
[18] J.L. Crane, K.E. Anderson, S.G. Conway, Hydrothermal synthesis and characterization of a metal- organic framework by thermogravimetric analysis, powder X- ray diffraction, and Infrared spectroscopy: an integrative inorganic chemistry experiment, J. Chem. Educ. 92 (2015) 373–377.
[19] J. Kim, Nanotechnology (IEEE- NANO), 10th IEEE Conference, 17–20 Aug. 2010, Seoul, 180-184.
[20] P. Vairaprakash, H. Ueki, K. Tashiro, O.M. Yaghi, Synthesis of metal- organic complex arrays, J. Am. Chem. Soc. 133 (2011) 759–761.
[21] News of the Week, Chemical & Engineering News, USA vol. 89 (2011), p. 8.
[22] K. Sajna, A.M. Fracaroli, O.M. Yaghi, K. Tashiro, Modular synthesis of metal-organic complex arrays containing precisely designed metal sequences, Inorg. Chem. 54 (2015) 1197–1199.
[23] L.J. Wang, H. Deng, H. Furukawa, F. Gandara, K.E. Cordova, D. Peri, O.M. Yaghi, Synthesis and characterization of metal- organic framework- 74 containing 2, 4, 6, 8, and 10 different metals, Inorg. Chem. 53 (2014) 5881–5883.
[24] (a) D. Sun, F. Sun, X. Deng, Z. Li, Mixed- metal strategy on metal- organic frameworks (MOFs) for functionalities expansion: Co substitution induces aerobic oxidation of cyclohexene over inactive Ni- MOF- 74, Inorg. Chem. 54

(2015) 8639–8643;
(b) U. Raju, A. Kumar, Storage of hydrogen: a future generation fuel, by Metal Organic Frameworks, Der Chem. Sin. 6 (2015) 25–29.
[25] M. Suga, S. Asahina, Y. Sakuda, H. Kazumori, H. Nishiyama, T. Nokuo, V. Alfredsson, T. Kjellman, S.M. Stevens, H.S. Cho, M. Cho, L. Han, S. Che, M.W. Anderson, F. Schuth, H. Deng, O.M. Yaghi, Z. Liu, H.Y. Jeong, A. Stein, K. Sakamoto, R. Ryoo, O. Terasaki, Recent progress in scanning electron microscopy for the characterization of fine structural details of nano materials, Prog. Solid State Chem. 42 (2014) 1–21.
[26] J. Lewis, R.G. Wilkins (Eds.), Modern Coordination Chemistry, Interscience Publishers, New York (, 1960.
[27] G.B. Deacon, R.J. Phillips, Relationships between the carbon- oxygen stretching frequencies of carboxylato complexes and the type of carboxylate coordination, Coord. Chem. Rev. 33 (1980) 227–250.
[28] K. Nakamoto, Infrared and Raman Spectra of Inorganic and Coordination Compounds, Wiley, New York (, 1978.
[29] Z. Nickolov, G. Georgiev, D. Stoilova, I. Ivanov, Raman and IR study of cobalt acetate dihydrate, J. Mol. Struct. 354 (1995) 119–125.
[30] R.C. Mehrotra, R. Bohra, Metal Carboxylates, Academic Press, New York, 1983.
[31] S.M. Tsimbler, L.L. Shevchenko, V.V. Grigoreva, The IR absorption spectra of the tartrate and citrate complexes of nickel, cobalt, and iron, J. Appl. Spectrosc. 11 (1969) 1096–1101.
[32] B. Stuart, Infrared Spectroscopy, Fundamentals and Applications, Wiley Online Library, 2004.
[33] G.R. Hedwig, J.R. Liddle, R.D. Reeves, Complex formation of nickel (II) ions with citric acid in aqueous solution: a potentiometric and spectroscopic study, Aust. J. Chem. 33 (1980) 1685–1693.
[34] O. M. Yaghi, Patent Number: 5648508, (1997).
[35] K. Nakamoto, Infrared and Raman Spectra of Inorganic and Co-ordination Compounds, fourth ed., John Wiley and Sons, 1986.
[36] R.D. Shannon, C.T. Prewitt, Revised values of effective ionic radii, Acta Cryst. 26 (1970) 1046–1048.
[37] B.D. Cullity, Elements of X-ray Diffraction, second ed., Addison Wesley, Publishing Company, USA, 1978.
[38] B.D. Cullity, S.R. Stock, Elements of X-Ray Diffraction, third ed., Prentice Hall, New York, 2001.
[39] A.L. Patterson, The Scherrer formula for X-Ray particle size determination, Phys. Rev. 56 (1939) 978–982.
[40] F.C. Miguens, M.L. de Oliveira, R.V. Marins, L.D. de Lacerda, A new protocol to detect light elements in estuarine sediments by X-ray microanalysis (SEM/EDS), J. Electron Microsc. 59 (2010) 437–446.
[41] C. Duval, Inorganic Thermogravimetric Analysis, Elsevier, Amsterdam, 1953.
[42] J. Rogan, D. Poleti, Thermal behaviour of mixed ligand Co(II), Ni(II) and Cu(II) complexes containing terephthalate ligands, Thermochim. Acta 413 (2004) 227–234.
[43] G.R. Desiraju, The supramolecular concept as a bridge between organic, inorganic and organometallic crystal chemistry, J. Mol. Struct. 374 (1996) 191–198.
[44] B. Mathew, S. Jacob, Thermogravimetric studies of the metal complexes of polystyrene-supported ethanolamine, Polym. Degrad. Stab. 54 (1996) 107–111.

Author's Accepted Manuscript



www.elsevier.com/locate/ssc

Intrinsic half metallicity in lithium terminated zigzag graphene nanoribbons

Neha Tyagi, Neeraj K. Jaiswal, Varun Sharma, Kamal K. Jha, Pankaj Srivastava

PII: S0038-1098(16)30329-5
DOI: http://dx.doi.org/10.1016/j.ssc.2016.11.022
Reference: SSC13087

To appear in: *Solid State Communications*

Received date: 31 March 2016
Revised date: 27 September 2016
Accepted date: 25 November 2016

Cite this article as: Neha Tyagi, Neeraj K. Jaiswal, Varun Sharma, Kamal K. Jha and Pankaj Srivastava, Intrinsic half metallicity in lithium terminated zigzag graphene nanoribbons, *Solid State Communications* http://dx.doi.org/10.1016/j.ssc.2016.11.022

This is a PDF file of an unedited manuscript that has been accepted fo publication. As a service to our customers we are providing this early version o the manuscript. The manuscript will undergo copyediting, typesetting, an review of the resulting galley proof before it is published in its final citable form Please note that during the production process errors may be discovered whic could affect the content, and all legal disclaimers that apply to the journal pertain

ACCEPTED MANUSCRIPT

Intrinsic half metallicity in lithium terminated zigzag graphene nanoribbons

Neha Tyagi[1*], Neeraj K. Jaiswal[2], Varun Sharma[3], Kamal K. Jha[4], Pankaj Srivastava[3]

[1]Department of Applied Physics, Delhi Technological University, Delhi-110042, India
[2]Discipline of Physics, Indian Institute of Information Technology, Design & Manufacturing, Jabalpur, Dumna Airport Road, Jabalpur-482005, India
[3]Nanomaterials Research Group, ABV-Indian Institute of Information Technology & Management, Gwalior-474015, India
[4]Indian Institute of Information Technology, Vadodara-382028, India
[*]Corresponding author: nehatyagi@dtu.ac.in

Accepted manuscript

Abstract

Half-metallic materials are the prime requisite for future spintronic devices. In present work, the possibility of half-metallic characteristic has been investigated in Li terminated zigzag graphene nanoribbons (ZGNR) using density functional theory. Two different configurations: (i) both edges Li termination (Li-both edges) and (ii) one edge Li termination (Li-one edge), have been examined in the present study. The calculated binding energy (ranging from -3.19 eV to -4.96 eV) confirms that both the considered configurations are energetically viable to obtain. All the considered structures settled in antiferromagnetic ground state which is more stable than that of spin compensated state. Further, it is revealed that upto 100% spin polarization can be achieved (without application of any external electric field) in ZGNR with Li-one edge. Moreover, the observed half-metallicity is found to be independent of the ribbon width and therefore pledges for applications in novel spin filtering devices.

Keywords

A. Graphene nanoribbon; A. lithium; D. binding energy; D. half-metal; D. spintronic

ACCEPTED MANUSCRIPT

1. Introduction

The search of novel materials for improved generation of future electronic devices is an area of active research. Nano-materials like graphene, a perfect 2-D sheet of carbon atoms [1-2], exhibit great potential for beyond Si electronic devices [3-6]. Moreover, future devices are supposed to be faster, smaller as well as eco-friendly in nature [7-9]. To meet these requirements, low power consumption is one of the important criteria that decide the adaptability of any device. Progressing in this direction, researchers are also investigating the new class of devices known as spintronic devices [10-12]. The spintronic devices will be governed by the electron spin rather than its charge as in conventional electronic devices. The prime requirement of these proposed spintronic devices are the materials that can differentiate the spin up electrons with those of spin down. Such materials, formally known as the half-metals, are rare to be found. However, researchers have shown that zigzag graphene nanoribbons (ZGNR) exhibit half-metallic properties in the presence of external electric field [13]. In other studies, it is revealed that the spin filtering properties (half metallicity) can be induced in ZGNR via doping of selective impurities at predefined sites [14-16]. Despite of these efforts, still the obtained spin polarization is not very promising. Although few reports are available to claim up to 100% spin polarization in GNR but it requires controlling the doping sites with atomic precision [16-19]. To obtain such structures, first we need to create a vacancy in the GNR network and then fill these vacant sites with guest atoms which make it difficult to experimentally realize these half-metallic GNR. Previous findings revealed that edge termination of GNR by metal atoms is energetically more favourable than the substitutional doping of the ribbons with same metal [18]. In the present work, we have investigated the possibility of half-metallicity in Li-terminated ZGNR and found promising results. The selection of Li is based on the fact that it can replace terminating H atoms at the edges of ZGNR due to its higher position (than that of H) in electro-potential series. Further, the edge termination is comparatively easier to control than that of substitutional doping by metal atoms. This indicates towards the practical viability of the proposed configurations to realize half-metallicity in GNR.

Accepted manuscript

ACCEPTED MANUSCRIPT

2. Computational Details

The proposed structures of Li-terminated ZGNR have been investigated using density functional theory (DFT) based first-principle calculations [20, 21]. The considered geometries have been modelled by using supercell approach. Owing to the quasi 1-D geometry of ribbons, the periodicity of the structures was maintained along *Z*-axis whereas the remaining two directions were kept confined. The k-point sampling of 1×1×50 points in Monkhorst Pack scheme [22] along with cut off energy of 70 Rydberg was used for the geometry optimization. Further, a vacuum region of 10 Å was also introduced in the supercell along *X* and *Y* directions to prevent interactions of structures with their replica. In order to account the exchange and correlation energy, we used generalised gradient approximation (GGA) with Perdew-Burke-Ernzerhof (PBE) parameterization [23]. For all the present calculations, double zeta plus polarized basis set was employed. The optimization was done self-consistently and cycle of optimization was continued taking the maximum force component of 0.04 eV/Å as the optimization criteria. Once, geometry has been optimized, the band structures and density of states (DOS) were computed with higher number of k-points. Moreover, to take width effects in to account, we considered ZGNR having widths from N_z = 4 to N_z=8. The nanoribbons width was defined equal to number of C-C pairs across the width. Present investigated structures are (i) both edges Li termination (Li-both edges) and (ii) one edge Li termination (Li-one edge). The width convention along with the schematics of considered structures is depicted in Fig. 1. For the calculation of transport properties, we used optimized geometries in two-probe configuration. The central channel region in two-probe geometry, between left and right electrodes, is seamlessly coupled with semi-infinite electrodes to avoid interface scattering at both the ends. The transport calculations were performed using the same parameters and models as explained in ref. [24].

Accepted manuscript

3. Results and Discussion

In the present study, structural and spintronic properties of ZGNR interacting with Li atoms as terminating elements, have been investigated. It is noticed that after optimization, ribbons adhere to their perfectly planar structure for Li-both edges as well as for Li-one edge. The terminating Li atoms form stable chemical bonds with the edge C atoms. The optimized Li-C bond length was found to be 1.97 Å which is consistent with the previous theoretical predictions [25]. It is revealed that Li-terminated ZGNR exhibit magnetic ground state. All

ACCEPTED MANUSCRIPT

the considered structures favour antiferromagnetic (AFM) coupling between edges which is about ~115-120 meV more stable than that of nonmagnetic (NM) state in Li-both edges. For Li-one edge this difference ranges ~83-98 meV. Similar AFM coupling has been noticed previously for pristine ZGNR [26]. The observed magnetic coupling is greater than that of the pristine ribbons [Table 1]. In order to examine the origin of observed magnetic ground state, we analysed spin compensated DOS for Li-both edges and Li-one edge ribbons as shown in Fig. 2(a) and 2(b) respectively. As the findings are similar, to be concise, the DOS have been depicted only for N_z =4. In both the cases, a sharp peak is noticed at the Fermi level which indicates that observed magnetic ground state arises due to magnetic stabilization. Moreover, the characteristic 1-D behaviour is also evident from the DOS profiles [shown by arrows in Fig. 2]. The observed magnetic stabilization ($E_{AFM} - E_{NM}$) of Li terminated ZGNR is presented in Table (1). Owing to this magnetic stabilization, splitting of electronic states takes place near the Fermi level which in turn gives rise to AFM ground state. The similar magnetic stabilization was previously observed for pristine ZGNR due to availability of sharp edge states at the Fermi level [26].

After determining most stable ground state, we next compared the structural stability of ribbons on the basis of binding energy (BE) calculations. The analysis of BE indicates that Li-one edge is energetically more favourable than Li-both edges [Table (1)]. The similar findings were obtained for ZGNR interaction with transition metals [24]. It is also noticed that widths do not play a significant role for structural stabilities of the configurations. This is due to the fact that chemical bonding between terminating Li and edge C atom is mediated via charge transfer at local level. For Li-both edges, 0.01e charge transfer takes place between Li and the nearest C atom. On the other hand, for Li-one edge, the edge C atom (bonded with Li) receives 0.023e charge from Li at one edge and donates 0.08e to the terminating H atom at opposite edge. Owing to this unequal charge transfer at opposite edges, the degeneracy of edge states is no more preserved in Li-one edge ZGNR as highlighted by the circle [Fig. 3(b)]. However, the equal charge transfer at opposite edges preserves the electronic states degeneracy in both edges Li terminated ZGNR as shown in Fig. 3(a) for representative width N_z =4. Further, each terminating Li atom contributes an additional electronic band near the Fermi level. For Li-both edges two such bands are observed whereas for Li-one edge only one additional band appears across the Fermi level as highlighted by arrows [Fig. 3(a)-(b)].

Accepted manuscript

ACCEPTED MANUSCRIPT

To investigate the spin dependent electronic properties of ribbon, we calculated spin polarized band structures and corresponding DOS. For Li-both edges, we observed that band structures exhibit degenerate energy states [Fig. 4 (a)-(c)]. Further, a number of conducting channels are noticed across the Fermi level which indicates their metallic behavior irrespective of ribbon width. The corresponding DOS and partial DOS (PDOS) have been presented in Fig. 5 for N_z =4. As expected from the preserved spin degeneracy of the energy states in band structures of Li-both edges, we observed equal and symmetric DOS for spin up and spin down electrons. Further, availability of DOS across the Fermi level further confirms its metallic character. Thus, for both edges Li-terminated structures, both types of spin play equal role towards the current conduction.

On the other hand, the spin polarized band structures of Li-one edge [depicted in Fig. 6 (a)-(c)], revealed broken degeneracy between opposite spin electrons. It is observed that Li-one edge turns the ribbon half-metallic (i.e. metallic for spin up electrons whereas semiconducting for spin down electrons). The broken degeneracy of electronic states is due to asymmetry of ribbons and hence, unequal charge transfer taking place at opposite edges. The Li terminating edge receives charge from terminating (Li) atom whereas opposite edge donates charge to the terminating H. Thus, an electrostatic potential difference is developed between opposite edges of ribbon. The π orbital of edge C atoms shift under the influence of this potential [27] which pushes the spin up and spin down electronic states in opposite directions and ultimately results into half-metallic character. Similar effect was also used to induce half metallicity in ZGNR by Wu et al. [28]. However, they could make half-metallic ZGNR only for wider ribbons having width N_Z >16. On contrary, the half metallicity proposed in the present work persists for widths as narrow as N_z =4. The considered ribbons (N_z = 4, 6, 8) are found to be metallic (semiconducting) for spin up (spin down) electrons. However, it is observed that for narrow ribbons, the highest valence band (HVB) for spin down electrons lie in the vicinity of Fermi level compared to that of wider ribbons. This is due to the fact that edges of ZGNR are under the influence of two competing effects (i) AFM coupling between opposite edges and (ii) the developed potential difference (arises due to charge donated at one edge and received at opposite edge). For narrow ribbons the AFM coupling is prevailing whereas for wider ribbons the developed potential difference becomes more effective. Therefore, HVB for spin down electron is shifted downward upto a greater extent in wider ZGNR. Further, the spin induced band gap (E_{sg}) is indirect in nature for all the widths and corresponding magnitude is presented in Table (1).

Accepted manuscript

ACCEPTED MANUSCRIPT

In order to understand the origin and behaviour of observed half metallicity in one-edge Li-terminated ribbons, the DOS and PDOS have also been analysed as depicted in Fig. 7. For Li-one edge structures, the DOS exhibits finite availability (absence) of states at the Fermi level for spin up (spin down) electrons. Since the findings are not affected by the ribbon width, to be concise, here we have shown DOS and PDOS plots only for $N_z = 4$. The half metallic gap of ~0.72 eV across the Fermi level for spin down states corresponds to observed electronic band structure [Fig. 6(a)]. Further, it can be noticed that electronic states are asymmetric for opposite spins which is due to broken spin degeneracy of the electronic states. Analysis of PDOS reveals that highest valence band peak for spin down states is mainly due to edge C atoms [Fig. 7(b)]. On the other hand, conduction band peaks are collective contribution of p-orbital of C and the terminating Li. Since this configuration is metallic for one type of spin and semiconducting for opposite spin, the structure acts as half-metal and is ideal for novel spin filtering devices. Here, 100% spin polarization is observed which indicates great potential of these structures for spintronic devices. Further, termination is comparatively easier to control as compared to selective doping (with foreign atoms), making it more simple and viable way to achieve high spin polarization. Another advantage of the present finding is that no external electric field is required to observe half metallic character in contrast to that of pristine ZGNR [13].

To demonstrate the spin filtering capability of Li-one edge ribbons, we have also calculated current-voltage (*I-V*) characteristics using two-probe models as adopted in previously [29]. The obtained *I-V* behavior has been plotted in Fig. 8 (for N_z =4). As expected, with increasing the applied bias voltage, current starts to increase for spin up electrons which is in consistent with its metallic behaviour of spin up electrons. On the other hand, current remains negligible for spin down electrons until the applied bias exceeds spin induced band gap as shown by red dashed lines in Fig. 8. Since the spin dependent band gap (~0.72 eV) is sufficiently larger than that of room temperature excitation energy (~0.025 eV), it is evident that Li-one edge ZGNR can act as a perfect spin filter. Such a spin filtering capability in the absence of any external electric field is of great importance for designing future memories and spin filtering devices.

For a further understanding of the observed *I-V* characteristics, we computed the transmission spectra (TS) for Li-one edge (N_z =4) for different bias voltages as depicted in Fig. 9. The perusal of TS indicates that for spin down states, value of transmission coefficient is zero in the vicinity of Fermi level which is in consistent with the observed semiconducting behavior

Accepted manuscript

ACCEPTED MANUSCRIPT

for spin down electrons. The current conduction is taking place only via spin up electrons. Therefore, TS further verifies the spin filtering capability of Li-one edge ZGNR as predicted by corresponding band structures and DOS investigations.

4. Conclusions

We have systematically examined the stability aspects of Li-terminated ZGNR and revealed their potential applications in spintronic devices. It is noticed that both the structures under investigation are energetically stable and exhibit AFM ground state. Li-one edge structures are found to be more stable than that of Li-both edges. Further, Li-one edge ZGNR is metallic (semiconducting) for spin up (spin down) electrons and therefore exhibit perfect half-metallic character which is not affected by their widths. The observed half metallicity is further supported by *I-V* characteristics and corresponding TS calculations. The importance of present work lies in the fact that observed half-metallicity persists without application of any electric field which makes present configurations preferable for spin filtering applications.

Acknowledgements

Authors are thankful to ABV- Indian Institute of Information Technology & Management, Gwalior for utilizing its computational facilities.

Accepted manuscript

References

[1] K.S. Novoselov, A.K. Geim, S.V. Morozov, D. Jiang, Y. Zhang, S.V. Dubonos, I.V. Grigorieva, A.A. Firsov, Electric field effect in atomically thin carbon films, Science 306 (2004) 666-69.

[2] A.K. Geim, K.S. Novoselov, The rise of graphene, Nat. Mater. 6 (2007) 183-91.

[3] B. Standley, W. Bao, H. Zhang, J. Bruck, C.N. Lau, M. Bockrath, Graphene-based atomic-scale switches, Nano Lett. 8 (2008) 3345-49.

[4] A.H.C. Neto, F. Guinea, N.M.R. Peres, K.S. Novoselov, A.K. Geim, The electronic properties of graphene, Rev. Mod. Phys. 81 (2009) 109-162.

[5] D.A. Abanin, L.S. Levitov, Quantized transport in graphene p-n junctions in magnetic field, Science 317 (2007) 641-43.

[6] Y. Zhang, Y.-W. Tan, H.L. Stormer, P. Kim, Experimental observation of the quantum Hall effect and Berry's phase in graphene, Nature 438 (2005) 201-04.

ACCEPTED MANUSCRIPT

[7] X. Liang, S. Wi, Transport characteristics of multichannel transistors made from densely aligned sub-10 nm half-pitch graphene nanoribbons, ACS Nano 6 (2012) 9700-10.

[8] F. Schedin, A.K. Geim, S.V. Morozov, E.W. Hill, P. Blake, M.I. Katsnelson, K.S. Novoselov, Detection of individual gas molecule adsorbed on graphene, Nat. Mater. 6 (2007) 652-55.

[9] X. Liang, Z. Fu, S.Y. Chou, Graphene transistor fabricated via transfer-printing in device active-areas on large wafer, Nano Lett. 7 (2007) 3840-44.

[10] W. Han, R.K. Kawakami, M. Gmitra, J. Fabian, Graphene spintronics, Nat. Nanotech. 9 (2014) 794-807.

[11] R. Farghadan, A. Saffarzadeh, Generation of fully spin-polarized currents in three-terminal graphene-based transistors, RSC Adv. 5 (2015) 87411-15.

[12] X.Q. Deng, Z.H. Zhang, G.P. Tang, Z.Q. Fan, C.H. Yang, Spin filter effects in zigzag-edge graphene nanoribbons with symmetric and asymmetric edge hydrogenations, Carbon 66 (2014) 646–653.

[13] Y.W. Son, M. L. Cohen, S. G. Louie, Half-metallic graphene nanoribbons, Nature 444 (2006) 347-49.

[14] J. Kang, F. Wu, J. Li, Doping induced spin filtering effect in zigzag graphene nanoribbons with asymmetric edge hydrogenation, Appl. Phys. Lett. 98 (2011) 083109-1-083109-3.

[15] S.L. Yan, M. Q. Long, X. J. Zhang, H. Xu, The effects of spin-filter and negative differential resistance on Fe-substituted zigzag graphene nanoribbons, Phys. Lett. A 378 (2014) 960-65.

[16] F. Zou, L. Zhu, K. Yao, Perfect spin filtering effect and negative differential behaviour in phosphorus-doped zigzag graphene nanoribbons, Sci. Rep. 5 (2015) 15966-1-15966-10.

[17] G.A. Nemnes, S. Antohe, Spin filtering in graphene nanoribbons with Mn-doped boron nitride inclusions, Mater. Sci. Eng., B 178 (2013) 1347-51.

[18] N.K. Jaiswal, P. Srivastava, Tailoring the electronic structure of zigzag graphene nanoribbons via Cu impurities, J. Comput. Theor. Nanosci. 10 (2013) 1441-45.

[19] B. Mandal, S. Sarkar, A. Pramanik, P. Sarkar, Doped defective graphene nanoribbons: a new class of materials with novel spin filtering properties, RSC Adv. 4 (2014) 49946-52.

Accepted manuscript

ACCEPTED MANUSCRIPT

[20] M. Brandbyge, J. L. Mozos, P. Ordejon, J. Taylor, K. Stokbro, Density-functional method for nonequilibrium electron transport, Phys. Rev. B 65 (2002) 165401-1-165401-17.

[21] www.quantumwise.com.

[22] H.J. Monkhorst and J. D. Pack. Special points for Brillouin-zone integrations. Phys. Rev. B, 13 (1976) 5188-92.

[23] J.P. Perdew, K. Burke, M. Ernzerhof, Generalized gradient approximation made simple, Phys. Rev. Lett. 77 (1996) 3865-1-3865-4.

[24] N.K. Jaiswal, P. Srivastava, Enhanced metallicity and spin polarization in zigzag graphene nanoribbons with Fe impurities, Physica E 54 (2013) 103-08.

[25] C. Uthaisar, D.J. Hicks, V. Barone, Li adsorption on edge-oxidized graphene nanoribbons predicted by DFT calculations, Surf. Sci. 619 (2014) 105-113.

[26] L. Pisani, J.A. Chan, B. Montanari, N.M. Harrison, Electronic structure and magnetic properties of graphitic ribbons, Phys. Rev. B 75 (2007) 064418-1-064418-9.

[27] Er-jun Kan, Z. Li, J. Yang, J. G. Hou, Half-metallicity in edge modified zigzag graphene nanoribbons, J. Am. Chem. Soc. 130 (2008) 4224-25.

[28] M. Wu, X. Wu, Y. Gao, X.C. Zeng, Materials design of half-metallic graphene and graphene nanoribbons, Appl. Phys. Lett. 94 (2009) 223111-1-223111-3.

[29] P. Srivastava , N.K. Jaiswal, G. Tripathi, Chloring sensing properties of zigzag boron nitride nanoribbons. Solid State Commun. 185 (2014) 41-46.

Accepted manuscript

ACCEPTED MANUSCRIPT

Figures

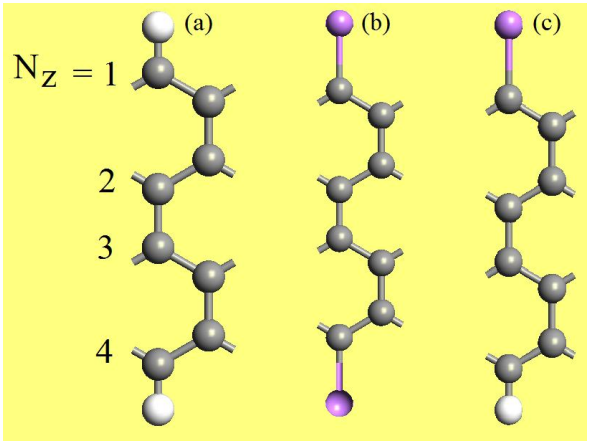


Fig.1 : The convention of defining the width of ZGNR and the considered structures of (a) Pristine (b) Both edges Li terminated ZGNR (c) One edge Li terminated ZGNR. The grey, white and purple spheres represent C, H and Li atoms respectively.

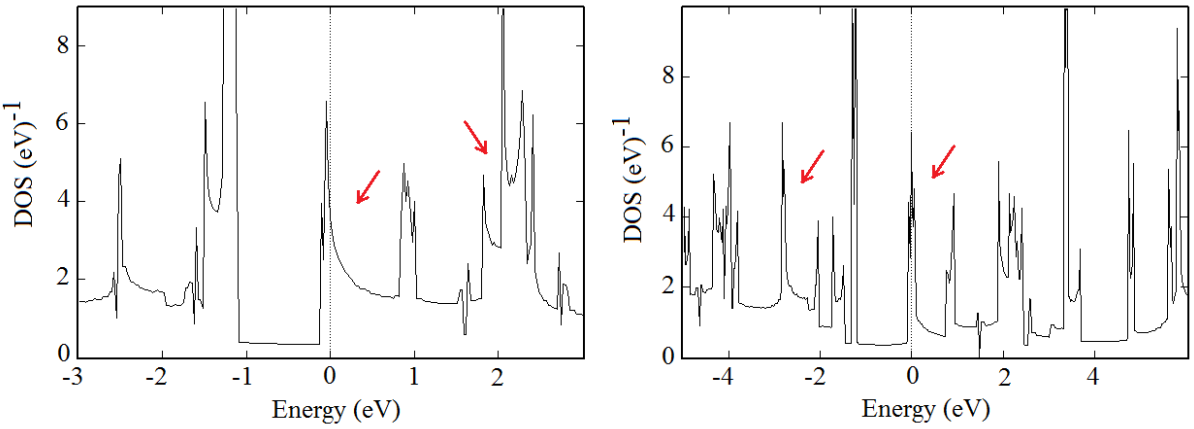


Fig. 2: Spin compensated density of states (DOS) profiles for (a) Both edges Li terminated ZGNR and (b) One edge Li terminated ZGNR. The dotted line at 0 eV represents the Fermi level.

ACCEPTED MANUSCRIPT

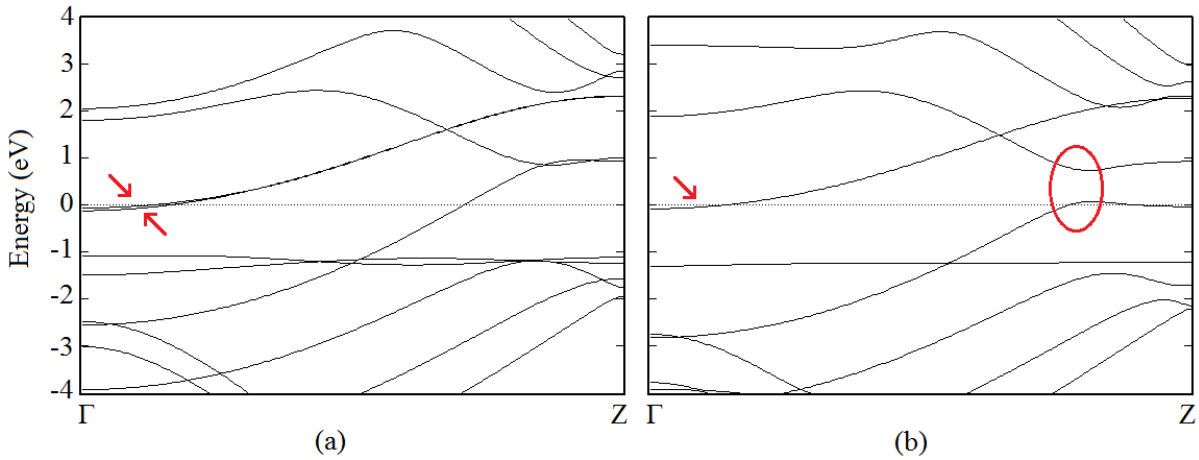


Fig. 3: The spin compensated band structures (N_z =4) for (a) Both edges Li terminated ZGNR and (b) One edge Li terminated ZGNR configurations. The dotted line at 0 eV represents the Fermi level.

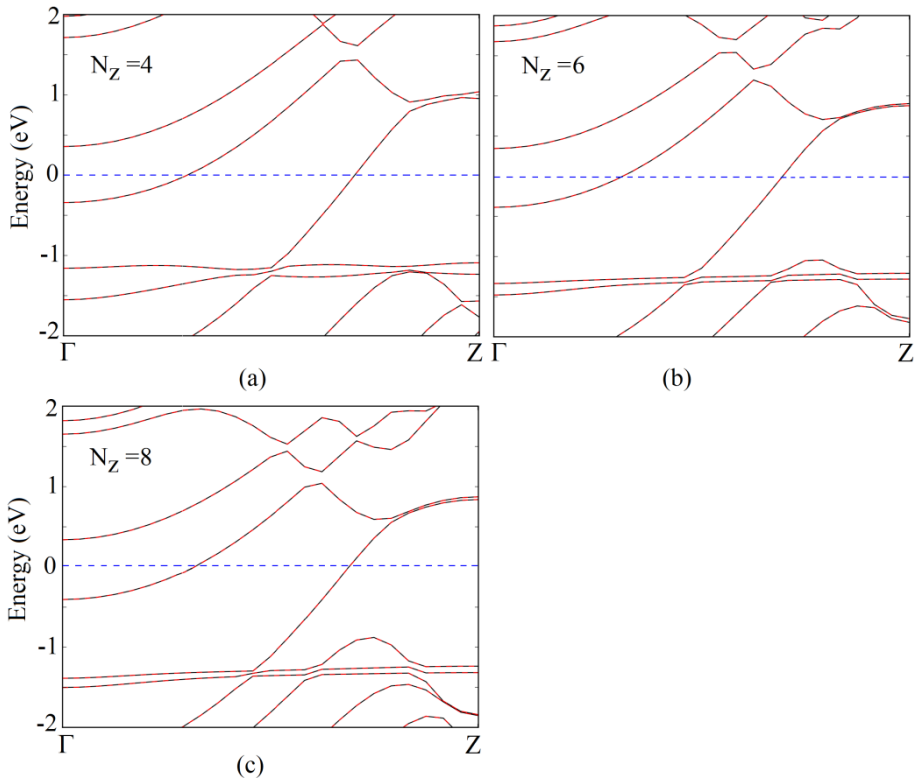


Fig. 4: The spin polarized band structures of both edges Li terminated ZGNR for (a) N_z = 4 (b) N_z = 6 and (c) N_z = 8. The dashed line at 0 eV represents the Fermi level.

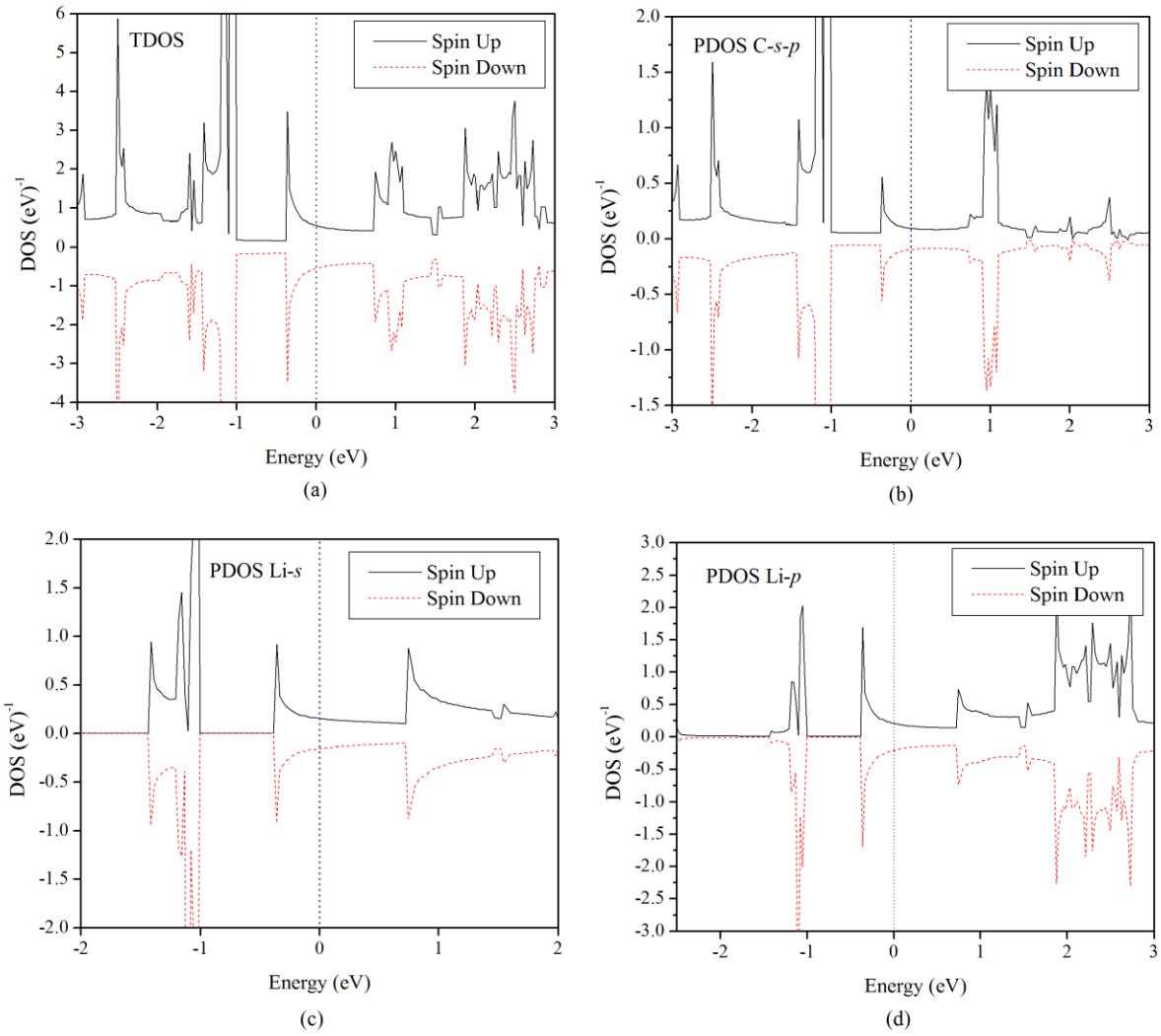


Fig. 5: The spin polarized DOS (N_z =4) for both edges Li terminated ZGNR (a) Total DOS (TDOS) and the partial DOS (PDOS) for (b) s and p orbital of edge C atoms (c) s orbital of Li (d) p orbital of Li. The vertical dashed line at 0 eV represents the Fermi level.

ACCEPTED MANUSCRIPT

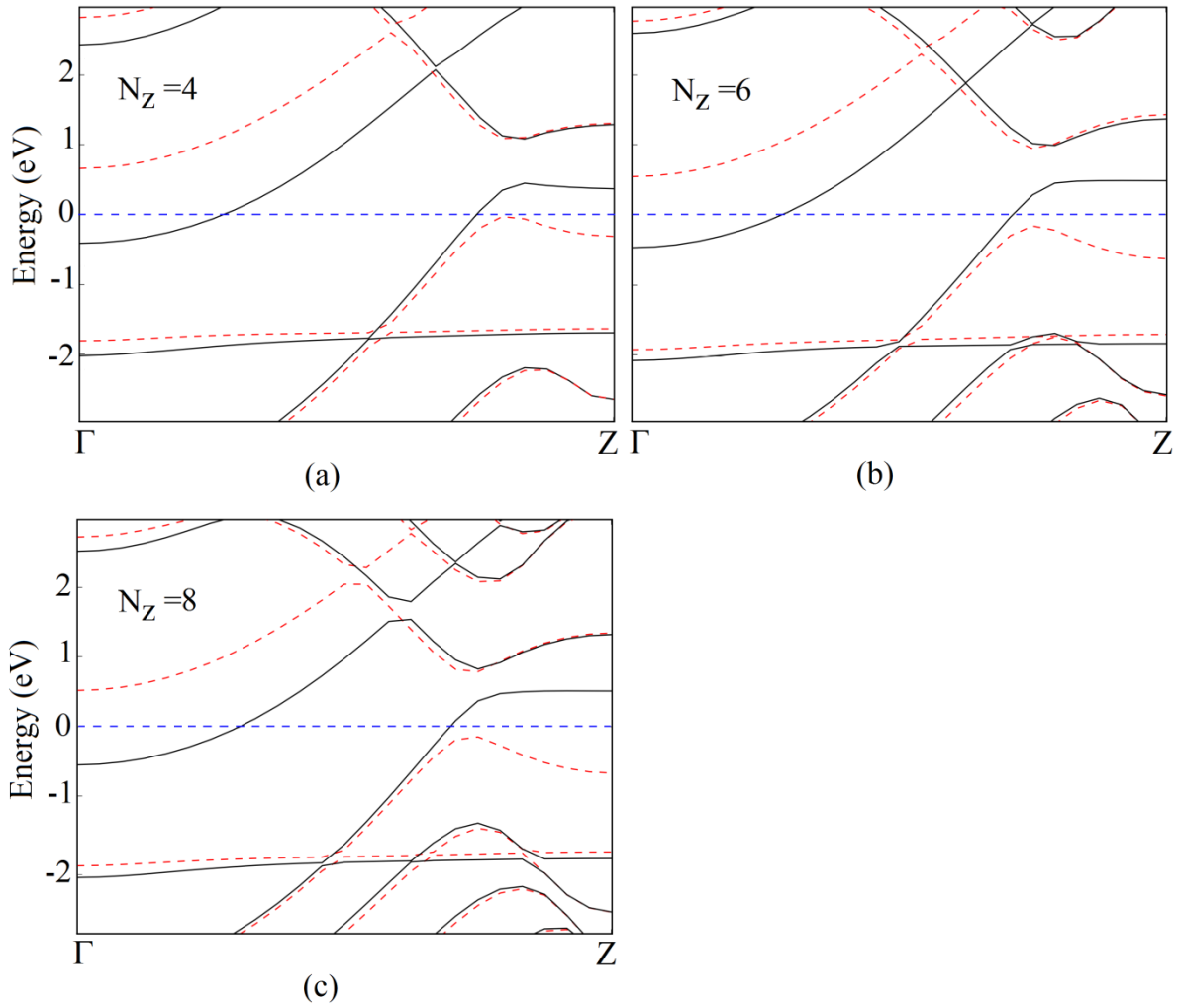


Fig. 6: The spin polarized band structures of one edge Li terminated ZGNR for (a) N_z = 4 (b) N_z = 6 and (c) N_z = 8. Solid (black) and dashed (red) lines represent the electronic states for spin up and spin down electrons respectively. The metallic behavior for spin up and semiconducting for the spin down electrons is evident for all considered nanoribbons width i.e. N_z = 4-8. The dashed line at 0 eV represents the Fermi level.

Accepted

ACCEPTED MANUSCRIPT

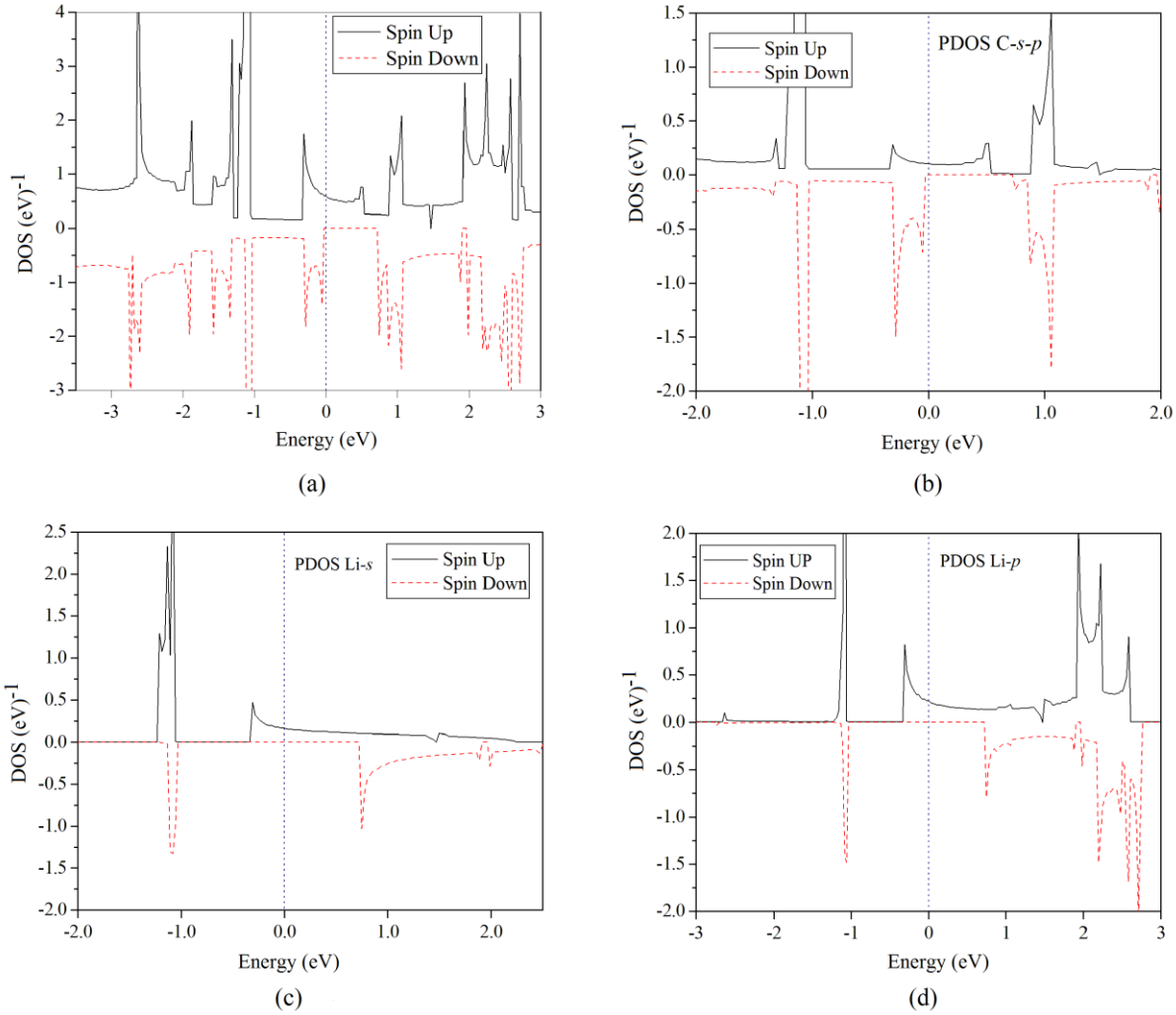


Fig. 7: The spin polarized DOS (N_z =4) for one edge Li terminated ZGNR (a) TDOS and the PDOS for (b) s and p orbital of edge C atoms (c) s orbital of Li (d) p orbital of Li. The vertical dashed line at 0 eV represents the Fermi level.

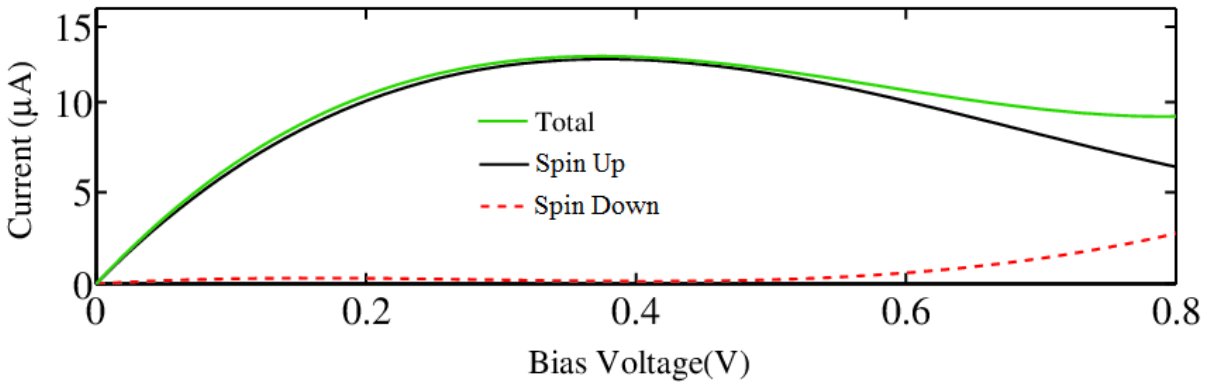


Fig.8: The calculated I-V characteristic of half-metallic ZGNR (N_z =4).

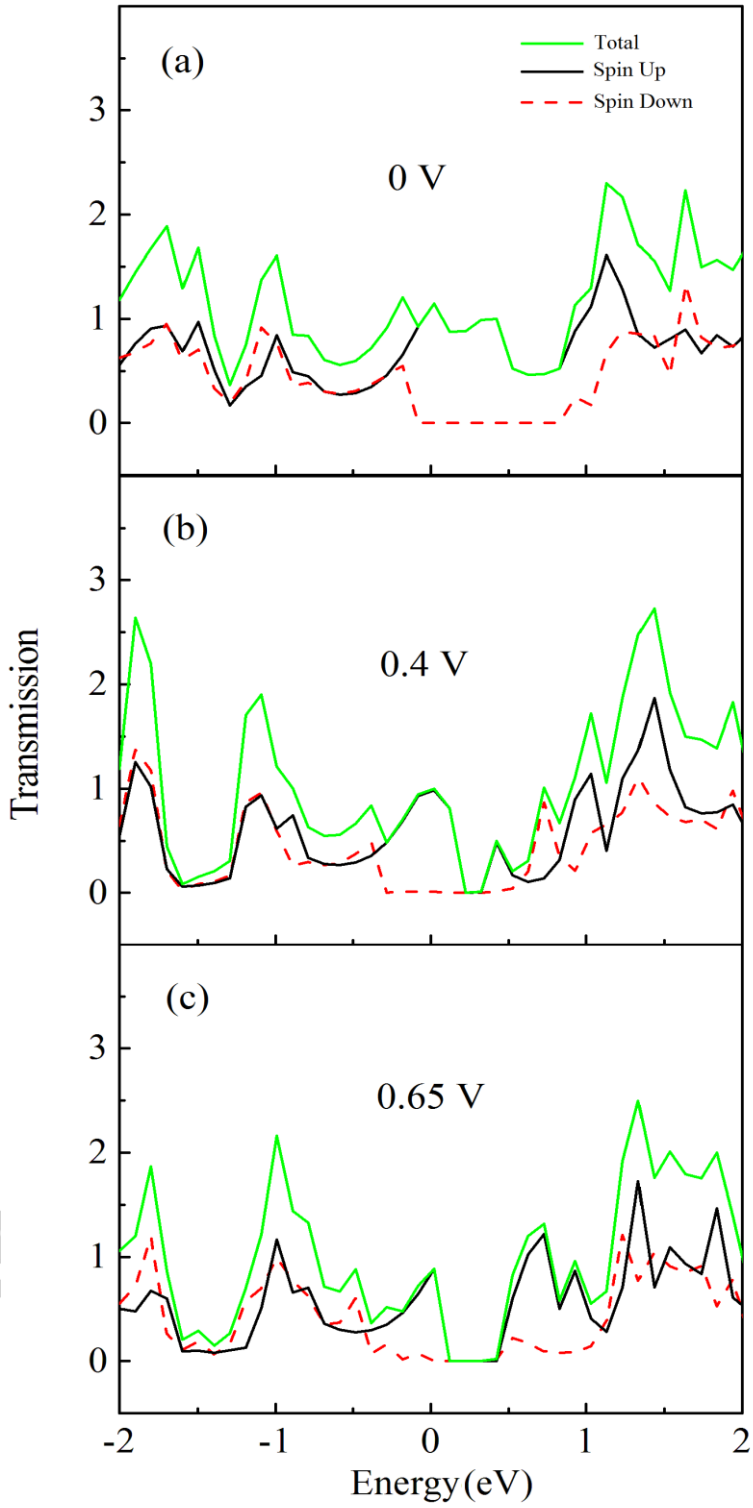


Fig. 9: The transmission spectra of half-metallic ZGNR (N_z =4) for the bias voltages as mentioned therein.

ACCEPTED MANUSCRIPT

Tables

Table 1: The calculated binding energy (BE), magnetic stabilization (E_{AFM} - E_{NM}), spin induced energy band gap (E_{sg}) as a function of ribbon widths.

Width (N_z)	Configuration	BE (eV)	E_{AFM} - E_{NM} (meV)	E_{sg} (eV)
4	Pristine	-6.58	60.5	0.64
	Li-both edges	-3.19	115.2	0
	Li-one edge	-4.93	83.6	0.72
6	Pristine	-6.59	70.1	0.57
	Li-both edges	-3.22	118.2	0
	Li-one edge	-4.94	95.2	0.68
8	Pristine	-6.59	70.2	0.51
	Li-both edges	-3.23	120.1	0
	Li-one edge	-4.96	98.7	0.65

Accepted manuscript

3rd International Conference on Recent Innovations in Science, Technology, Management and Environment
Indian Federation of United Nations Associations, New Delhi, India (ICRISTME-16)
18th December 2016 , www.conferenceworld.in ISBN: 978-93-86171-13-9

MODEL OF QUALITY OF LIFE IN GUJARAT: A SUBJECTIVE APPROACH

Rajesh Handa[1], Dr. G.C.Maheshwari[2]

[1]*Rajesh Handa, Management, Manish Institute of Management, Gujarat, (India)*
[2]*Dr. G.C.Maheshwari, Management, Delhi Technological University, Delhi, (India)*

ABSTRACT

This paper examined the perceived quality of life (Well- being) of people in Gujarat state, with a 410 adult sample. It investigated first exploring underlying constructs (factors) of defining quality of life. Employing descriptive approaches through a modified questionnaire (Life domain satisfaction scale). The survey instrument measures the residents' life satisfaction in many Life domains: Government satisfaction, Material possession satisfaction, Spirituality satisfaction, Physical health satisfaction, Environmental quality satisfaction, career satisfaction and Infrastructure satisfaction. EFA, Multiple Regression analysis, CB-SEM techniques used to predict perceived life-satisfaction and validate the model of Perceived Quality of Life.

Keywords: Well-being, Perceived Quality of Life, Life-satisfaction, Government satisfaction, Spirituality satisfaction.

I INTRODUCTION

"Quality of life and its assessment is a challengeable task; still to improve it is a primary goal of any government & Individuals too. By many years we are measuring quality of life in terms of HDI (Human development Index) and accordingly ranking of the nations takes place which shows their well-being and quality of life in the country. HDI is an objective approach to access quality of life. But the second approach to measure Quality of life is subjective approach which we called perceived quality of life or happiness. Many researches has contributed their work in measuring PQOL or happiness of the nations and now a days World happiness Index is one of popular approach to measure the quality of life. As we noticed countries like Bhutan had focused on GNP (Gross national happiness) instead of GDP." This study is also an approach towards measuring PQOL of Gujarat".

II OBJECTIVES

i. To explore different factors (domains of life satisfaction).
ii. To assess different domains of life satisfaction thus affects the overall life satisfaction of Individuals.

ISBN: 978-93-86171-13-9

III RESEARCH METHODOLOGY

- Research type: Quantitative Research.
- Descriptive Research.
- Population: Gujarat.
- Data used: Primary.
- Data Collection Tool: Structured Questionnaire
- Data Collection method: Survey (personal interaction).
- Survey method: Convenience Sampling (Non-Probability).
- Sample unit: People (ordinary resident).
- Sample Size: 410 respondents.

IV LIMITATIONS OF THE STUDY

i. Under certain time limit 300 samples has collected, out of which 410 sample became part of this study.
ii. Sampling frame was not present. Non-random, Convenience sampling method has used.
iii. Respondent has limited to working class people with certain age, education and income limitation.

V RESEARCH TOOLS USED

1. Global life satisfaction scale.
2. Life domain satisfaction scale.

5.1 Reliability Check

1. Global life satisfaction scale.

Reliability Statistics

Cronbach's Alpha	N of Items
.700	5

Table: 1

***Interpretation*:** Cronbachs Alpha value **0.700 = 0.7**. This is a good sign of reliability.

2. Life domain satisfaction scale.

Reliability Statistics

Cronbach's Alpha	N of Items
.933	38

Table: 2

***Interpretation*:** Cronbach's Alpha value **0.933 > 0.7**. This is a good sign of reliability.

VI RESEARCH HYPOTHESIS

Hypothesis 1: Sense of well-being is influenced by different domains of life. To determine which of these domains of life are related to global satisfaction or PQOL?

VII HYPOTHESIS TESTING

1. H_o: There is no significant relationship between overall life satisfaction and different domains of life.
   H_1: There is significant relationship between overall life satisfaction and different domains of life.

Exploratory Factor Analysis used for exploring underlying construct:

KMO and Bartlett's Test

Kaiser-Meyer-Olkin Measure of Sampling Adequacy.		**.886**
Bartlett's Test of Sphericity	Approx. Chi-Square	9321.048
	df	666
	Sig.	**.000**

Table: 3

∴KMO value ≅ **0.886** which is near to 0.9 consider as an excellent condition for factor analysis.

∴ Bartlett's Test of Sphericity Sig. 000 which shows it is not an identity matrix.

Total Variance Explained

Component	Initial Eigenvalues			Extraction Sums of Squared Loadings			Rotation Sums of Squared Loadings		
	Total	% of Variance	Cumulative %	Total	% of Variance	Cumulative %	Total	% of Variance	Cumulative %
1	11.186	30.232	30.232	11.186	30.232	30.232	4.494	12.146	12.146
2	3.355	9.069	39.301	3.355	9.069	39.301	3.538	9.561	21.707
3	2.422	6.546	45.846	2.422	6.546	45.846	3.112	8.410	30.117
4	2.113	5.710	51.557	2.113	5.710	51.557	2.866	7.747	37.864
5	1.742	4.708	56.264	1.742	4.708	56.264	2.856	7.718	45.582
6	1.605	4.338	60.602	1.605	4.338	60.602	2.744	7.416	52.999
7	1.405	3.797	64.399	1.405	3.797	64.399	2.680	7.244	60.243
8	1.042	2.817	67.216	1.042	2.817	67.216	2.580	6.973	**67.216**

ISBN: 978-93-86171-13-9

9	.970	2.622	69.838						
10	.862	2.330	72.168						
11	.835	2.256	74.424						
12	.779	2.105	76.529						
13	.748	2.021	78.550						
14	.650	1.756	80.307						
15	.606	1.637	81.943						
16	.551	1.490	83.433						
17	.507	1.369	84.802						
18	.484	1.308	86.110						
19	.464	1.254	87.364						
20	.425	1.149	88.513						
21	.406	1.098	89.611						
22	.376	1.017	90.629						
23	.349	.944	91.573						
24	.341	.921	92.494						
25	.317	.857	93.351						
26	.302	.817	94.168						
27	.271	.734	94.901						
28	.269	.726	95.628						
29	.250	.676	96.304						
30	.232	.628	96.932						
31	.213	.576	97.509						
32	.201	.542	98.051						
33	.191	.515	98.566						
34	.159	.430	98.995						
35	.141	.382	99.377						
36	.130	.352	99.729						
37	.100	.271	100.000						

REGRESSION ANALYSIS

Model Summary[b]

Model	R	R Square	Adjusted R Square	Std. Error of the Estimate	Durbin-Watson
1	.614[a]	.377	**.367**	.71889	**1.963**

a. Predictors: (Constant), Government satisfaction, Career satisfaction, Material Possession satisfaction, Spirituality satisfaction, Infrastructure satisfaction, Environmental satisfaction, Physical health satisfaction.

b. Dependent Variable: sw.

Table: 5

Interpretation: The Adjusted R square value tells us that our model accounts for 37% of variance which indicate it is a respective model as per social science research.

ANOVA[a]

Model		Sum of Squares	df	Mean Square	F	Sig.
1	Regression	125.659	7	17.951	34.736	**.000[b]**
	Residual	207.237	401	.517		
	Total	332.896	408			

a. Dependent Variable: sw

b. Predictors: (Constant), Government satisfaction, Career satisfaction, Material Possession satisfaction, Spirituality satisfaction, Infrastructure satisfaction, Environmental satisfaction, Physical health satisfaction.

Table: 6

Interpretation: sig.0.000 < .05 the model is significant. Null hypothesis rejected, alternate hypothesis accepted. There is significant relationship between overall life satisfaction and different domains of life.

Coefficients[a]

Model		Unstandardized Coefficients		Standardized Coefficients	t	Sig.	Collinearity Statistics	
		B	Std. Error	Beta			Tolerance	VIF
1	(Constant)	5.063	.036		142.418	.000		
	Government satisfaction	.122	.036	.135	3.431	.001	1.000	1.000
	Career satisfaction	**.246**	.036	.272	6.911	.000	1.000	1.000
	Material Possession satisfaction	**.370**	.036	.410	10.394	.000	1.000	1.000
	Spirituality satisfaction	.189	.036	.209	5.304	.000	1.000	1.000
	Infrastructure satisfaction	.097	.036	.108	2.729	.007	1.000	1.000
	Environmental satisfaction	.086	.036	.095	2.419	.016	1.000	1.000
	Physical health satisfaction	**.209**	.036	.232	5.886	.000	1.000	1.000

a. Dependent Variable: sw

Table: 7

Interpretation: All predictors variable's p <.05. T values of all predictor variables are high. So, all predictors variable are significant.

∴Multicollinearity check: No tolerance value less than 0.2 and no VIF value greater than 5 found. There is no sign of presence of multicollinearity.

Assumptions Check:

1. Mean of residuals is zero: satisfied.
2. Residuals are normally distributed: satisfied.
3. Error (Residual) variances are constant (Homoscedascity): satisfied.
4. There is no Multicollinearity: satisfied.
5. There is no auto co-relation (∴Durbin Watson value 1.963 ≅ 2.00 and this is cross-sectional data): satisfied.

VIIII VALIDITY ANALYSIS: PATH DIAGRAM

Covariance Based Structural Equation Modeling (CB-SEM).

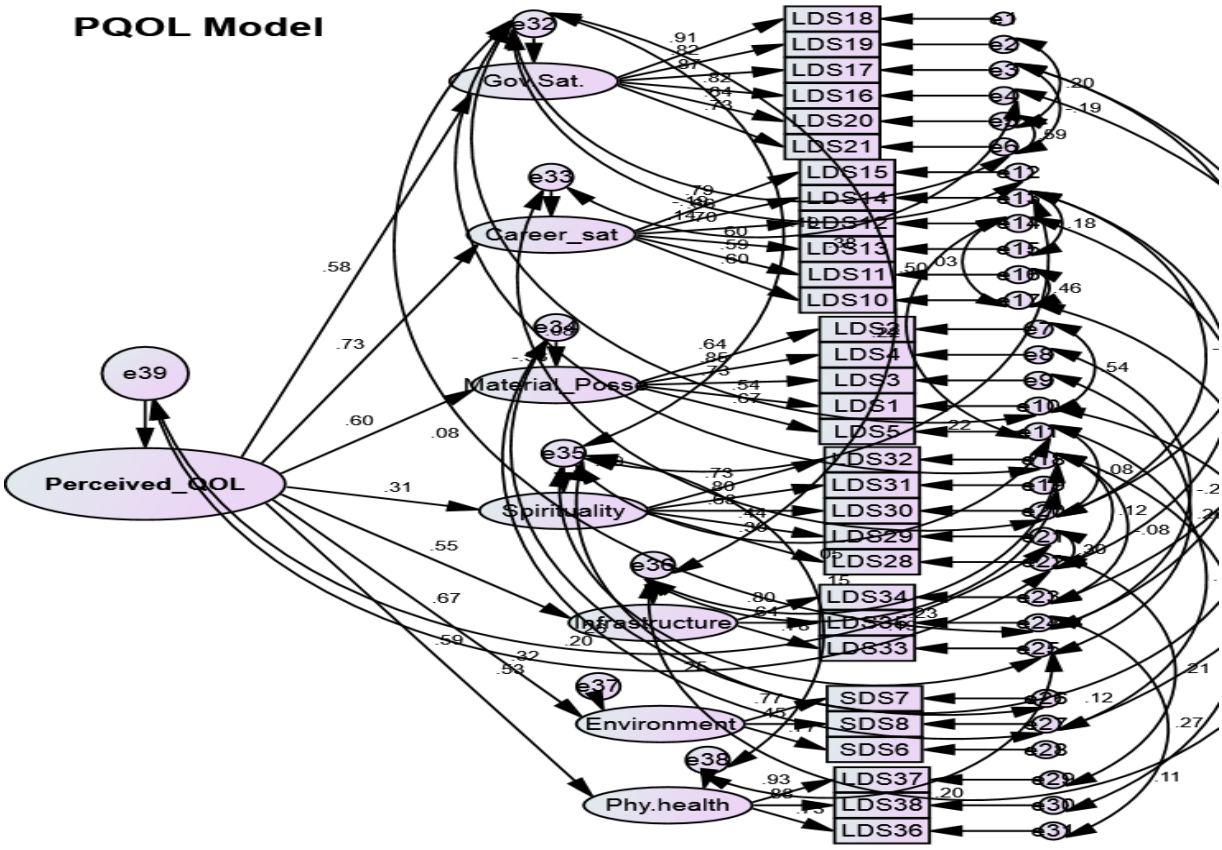


Fig: 1

MODEL FIT SUMMARY:

	Index	Level of acceptance	Observed value	Literature	Comments
Absolute fit	Chi-square	P > 0.05	0.051	Wheaton et. Al. (1997)	**Accepted**
	RMSEA	RMSEA < 0.08	0.033	Browne and Cudeck (1993)	**Accepted**
	GFI	GFI > 0.90	0.923	Joreskog and Sorbom (1984)	**Accepted**
Incremental fit	AGFI	AGFI > 0.90	0.900	Tanaka and Huba (1985)	**Accepted**
	CFI	CFI > 0.90	0.974	Bentler (1990)	**Accepted**
	TLI	TLI > 0.90	0.969	Bentler and Bonett (1980)	**Accepted**
	NFI	NFI > 0.90	0.921	Bollen (1989)	**Accepted**
Parsimonious fit	Chisq/df	Chisq/df < 5.0	1.441	Marsh and Hocevar (1985)	**Accepted**

Table: 8

IX CONCLUSION

Perceived quality of life is associated with different domains of life.The study found that all seven domains of life: Government satisfaction, Career satisfaction, Material possession satisfaction, Spirituality satisfaction, infrastructure satisfaction, Environmental quality satisfaction and Physical health satisfaction are significant in model. Domains like Material possession satisfaction, career satisfaction and physical health satisfaction shows high weightage in the PQOL model.

REFERENCES

1. R. Handa & G.C. Maheshwari (2016). A study of sense of well-being and perceived quality of life of people in Central Gujarat, *International Journal of Science Technology and Management, Vol. No.5, Issue No. 11, pp 198-207.*
2. W. Asyraf, & B. Afthanorhan (2013), A comparison of partial least square structural equation modeling (PLS-SEM) and covariance based structural equation modeling (CB-SEM) for confirmatory factor analysis, *International journal of engineering science and innovative technology (IJESIT), Vol.2, Issue 5, pp 198-205.*
3. P. Conceicao & R. Bandura (2008), Measuring Subjective Well-being: A Summary Review of the Literature United Nations Development Programme, USA.
4. S. Dasgupta & S. Majumdar (2000), Sense of well-being and perceived quality of life in Culcutta, *In Advance in quality of life theory and research, Kluwer Academic publishers, Netherlands, Pp 65-79.*
5. E. Diener, R. Emmons, R, Larsen & S. Griffen (1985), The Satisfaction with Life. Scale, *Journal of Personality Assessment, 49, 1.*
6. N. Gjoksi (2010), National approaches to measure wealth and well-being in the context of sustainable development. *ESDN Case Study No.4.*
7. I. Gough (2003), Human Well-being: Bridging Objective and Subjective Approaches. ESPANET Conference, 13-15 November, 2003, Copenhagen.
8. R, Haq (2009). Measuring Human Wellbeing in Pakistan: Objective versus Subjective Indicators, *European Journal of Social Science, Volume 9, 3.*
9. S, Hicks, J, Newton, J, Haynes & J. Evans (2011), Measuring Children's and Young People's Well-being, Office for National Statistic and BRASS, Cardiff University.
10. D. Kahneman (2006), Developments in the Measurement of Subjective Wellbeing, *Journal of Economic Perspective, Volume 20, Number 1, Pages 3-24.*
11. D. Kahneman, E. Diener & N. Schwarz (1999). Well-being: The Foundations of Hedonic Psychology, Russell SAGE Foundation, New York.
12. T. Kashdan (2002), The Assessment of Subjective Wellbeing (Issues Raised By the Oxford Happiness Questionnaire). Personality and Individual Difference, 36, 1225-1232.
13. M. Rapley (2003), Quality of Life Research, SAGE Publications, New Delhi.

To,

The Editor,

Journal of Electrical and Computer Engineering.

Dear Sir,

This is to hereby convey that for our research paper titled “Modified Tang’s Current Comparator and Its Application to Full Flash and Two-Step Flash Current Mode ADCs”, neither me nor my co-authors have any conflict of interest with anyone and that this is our original piece of work that has not been published elsewhere.

Thanks & Regards,

Veepsa Bhatia

Corresponding Author

Modified Tang's Current Comparator and Its Application to Full Flash and Two-Step Flash Current Mode ADCs

*Veepsa Bhatia, **Neeta Pandey

* Dept of ECE, Indira Gandhi Delhi Technical University for Women, Delhi, India, veepsa@gmail.com

** Dept of ECE, Delhi Technological University, Delhi, India, neetapandey06@gmail.com

Abstract- In this paper, a modification to an existing current comparator proposed by Tang has been presented. The circuit introduces a Flipped Voltage Follower (FVF) which replaces the source follower input stage of the existing current comparator of Tang. This modification culminates into higher speed especially at lower currents and lower power dissipation. The application of the proposed current comparator has also been put forth by implementing a 3-bit current mode (CM) ADC and a two-step 3-bit CM ADC. The theoretical propositions are verified through spice simulation using 0.18μm TSMC CMOS technology at a power supply of 1.8V. Propagation delay, power dissipation and power delay product (PDP) have been calculated for the proposed current comparator and process parameter variation has been studied. For both the implementations of ADCs, performance parameters namely DNL, INL, missing codes, monotonicity, offset and gain errors have been evaluated.

Keywords- Current Comparator, source follower, FVF, Process corners, Current mode Flash ADC, Two-step Flash ADC, DNL, INL.

1. Introduction

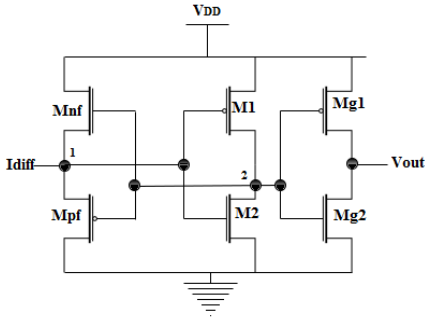
Current comparator circuit finds application in a wide variety of applications like nonlinear current mode signal processing and analog to digital converters (ADCs). Besides, low level, high speed current detection is also required in different light and radiation sensing applications, or controllability and reconfigurability issues in E-beam testing of integrated circuits. Further, subthreshold CMOS current mode computation architectures also require efficient detection of low current levels. Another lucrative option is requirement of current detection in IDDQ VLSI testing approaches [1]-[7]. Hence, a considerable amount of effort has been expended by the circuit designers and researchers into the area of design of efficient current comparators.

The basic functionality of a current comparator is to determine which of the two currents (I_{in} or I_{ref}) is greater and to present that decision as one of two voltage levels, established by the output's (V_{out}) limiting values. The output value is typically interpreted as logic '1' and '0' for further processing [8]. One of the two currents is generally a constant current called the reference current (I_{ref}) against which the input current is compared (I_{in}). This is shown by the following relation:

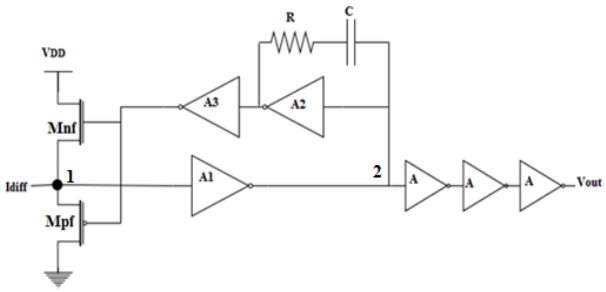
$$V_{out}(t) = \begin{cases} 1, I_{in}(t) > I_{ref}(t) \\ 0, I_{in}(t) < I_{ref}(t) \end{cases} \quad (1)$$

Numerous structures for current comparators have been put forth in the literature, of which the one proposed by Traff [9] (Fig. 1(a)) can be considered a pioneering structure which adheres to all the characteristics desirable of a current comparator viz. low input impedance, low power dissipation and moderate speed of operation.

It comprise of a source-follower input stage and a CMOS inverter. CMOS inverter provides positive feedback which helps achieve sufficient gain for amplifying small voltage variations at the input stage. This structure however, suffers from a problem of a deadband region wherein the input voltage to the inverter does not slew from rail to rail, making neither of the transistors in the source follower stage totally shutoff leading to non-zero DC power dissipation. To overcome this problem, a variety of modifications to the structure of Traff [9] have been presented in [10]-[17]. Of these, the one proposed Tang [15] is the most significant one in terms of giving the fastest response at low input currents and resolution. Tang [15] modifies the gain stage of Traff [9] by adding two more inverters (A2) and (A3) its feedback path apart from already existing inverter (A1) and source follower input stage Mnf and Mpf. A2 and A3 together act as a non-inverting amplifier, in order improve speed for low input currents. Circuit is depicted in Fig. 1(b).



(a)



(b)

Fig. 1 (a) Traff's [9] current comparator (b) Tang's [15] current comparator

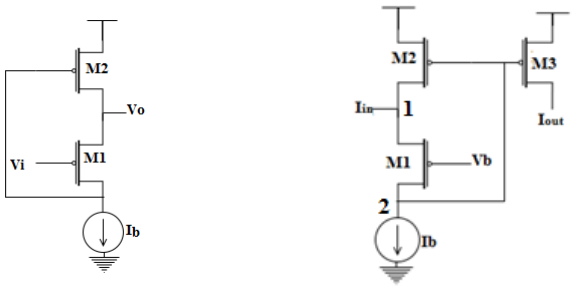
For a low input current, a small voltage change appears at the input node and node 1. However, amplification by A2 and A3 leads to significant change in the voltage at node 2, thus turning on input transistor Mnf or Mpf and activating the feedback loop. Hence the response time is considerably shortened.

In this paper, a modification to the circuit proposed by Tang [15] has been put forth. The input stage source follower has been replaced with a Flipped Voltage Follower Cell [FVF]. The authors have put forth a similar modification to Traff [9] in [18] and have obtained improved speed and power dissipation over the former. The similar approach has been adopted herein to modify Tang's [15] to develop a new current comparator structure. The proposed current comparator so developed has further been used to implement a 3-bit Full Flash and a Two-step CM Flash ADC.

2. The FVF Cell

The concept of FVF was put forth in [19]. The FVF, shown in Fig. 2 (a) is essentially a voltage follower with shunt feedback. It is low-power, low-voltage circuit having low impedance compared to basic source follower and current/voltage biasing. It employs two transistors M1 and M2. The shunt feedback ensures that transistor M2 remains always in on state independent of the power supply is given to the circuit. Further, due to current biasing the current through transistor M1 is held constant and it also remain on [19]-[20]. Thus change in output current does not affect the input current and V_{SG1} (which is a function of input current) remains almost constant across M1. This results in almost unity voltage gain or in other words output voltage follows input voltage. Further, since FVF can operate on very low supply voltage, thus it is a suitable structure of choice for design of low power current comparator design.

The FVF can also be used as a current sensing cell, shown in Fig. 2 (b). Its operation can be explained as follows- When an input current is applied at node 1 with all transistors properly biased to work in the saturation region, then due to the shunt feedback provided by transistor M2, the impedance at the input node becomes very low and, so the amount of current flowing into this node does not modify the value of the voltage developed at this node. Thus, the input node is capable of sourcing large current variations at the input and the FVF then translates them into compressed voltage variations at output node 2.



(a) (b)

Fig. 2 (a) An FVF cell (b) FVF Current Sensor [19]

3. Proposed Current Comparator

As mentioned before, the Tang's [15] circuit is a high speed circuit capable of giving good response at lower currents. However, it cannot be considered a complete current comparator as it does not calculate the difference between the two currents (input and reference) but takes a pre-calculated current difference (I_{diff}) at its input. Hence, the performance parameters as quantified by Tang [15] are somewhat deficient and are set to alter when a current differencing unit is appended on the input side. Thus, in this paper a modification of Tang [15] has been put forth. This structure introduces two-fold modification to Tang [15] by introducing the current differencing unit at the input side and the input source follower stage has been replaced with the FVF source follower stage to benefit from its advantages discussed in the previous section. Similar modification to Traff's [9] circuit has been proposed by the authors in [20]. Figure 3 shows the circuit diagram of the implementation.

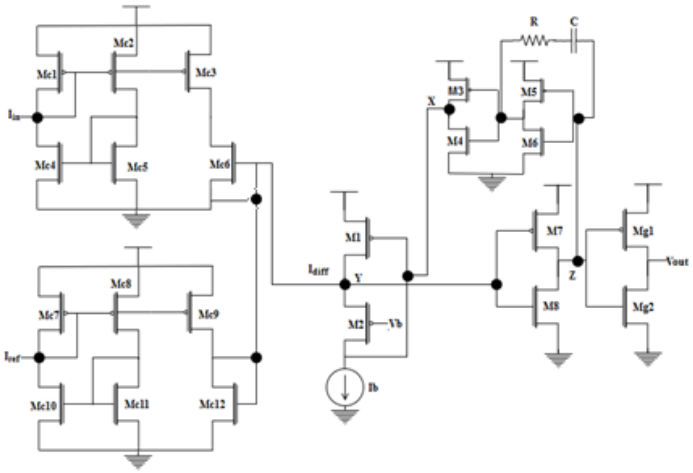


Fig. 3 Proposed Current Comparator

This implementation is a complete current comparator with the current differencing stage (Mc1-Mc12), gain stage (M1-M8) and the output stage (Mg1-Mg2). The current differencing

unit accepts two current I_{in} and I_{ref} and outputs current I_{diff}. The gain stage is a modification of the gain stage of Tang [15] wherein transistors (Mpf-Mnf) that form a source follower have been replaced by an FVF based source follower. The FVF source follower comprises of transistors M1 and M2 and biasing current source (I_b) which keeps M2 on and a biasing voltage source (V_b).

This is followed by a CMOS inverter (Mpf-Mnf) connected to the FVF current sensor in the feedback loop with two passive elements, a resistor R and a capacitor C placed in series in this feedback loop. These together form the gain stage of the proposed current comparator. Finally, the output stage is formed by a CMOS inverter Mg1-Mg2 that is connected to provide rail to rail swing at the output.

When I_{in} and I_{ref} are applied to the current differencing unit, it generates a current difference I_{diff}. This current applied to node Y of the gain stage is translated into corresponding voltage variations at the node Z. When I_{diff} is negative, the voltage developed at node Y is small which leads to a high voltage at node Z due to the inverting action of the CMOS inverter M7-M8. Consequently, the output of the output stage, Mg1-Mg2, goes low and hence the overall output of the current comparator from the output stage, with rail-to-rail swing, is a low.

When a low I_{diff} is applied, it introduces a slowly rising voltage at the node Y. This causes the output of the inverter M7-M8 to change slowly in response. Simultaneously, the current applied to node Y is translated into corresponding voltage variations at the node 'X'. These small voltage variations at 'X' are amplified by non inverting amplifier formed by M3-M4 and M5-M6, causing a change in the voltage at node Z which further activates the feedback loop, leading to faster switching. These inverters in the feedback path also serve to stabilize the voltage fluctuations at the output node V_{out}.

3.1 Simulation Results of the proposed current comparator

The theoretical proposition is verified through SPICE simulations using 0.18 μm TSMC CMOS technology parameters and a supply voltage of 1.8 V. An I_{in} of 3 μA with I_{ref} of 1 μA to obtain I_{diff} equal to 2μA is used for all simulations. The functionality of current comparator is shown in Fig. 4 along with that of Tang [15] under similar simulation conditions. The output voltage swing of 1.8V is obtained with a propagation delay of 2.1ns.

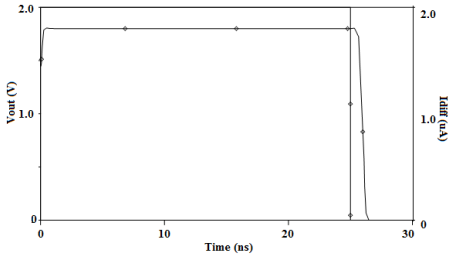
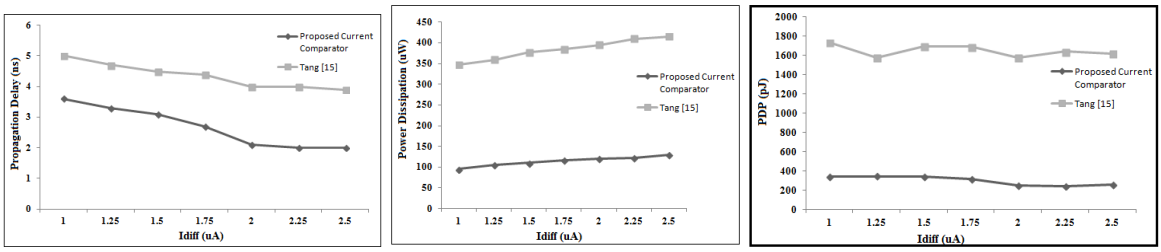


Fig. 4 Output for proposed comparator for Input current difference of 2μA.

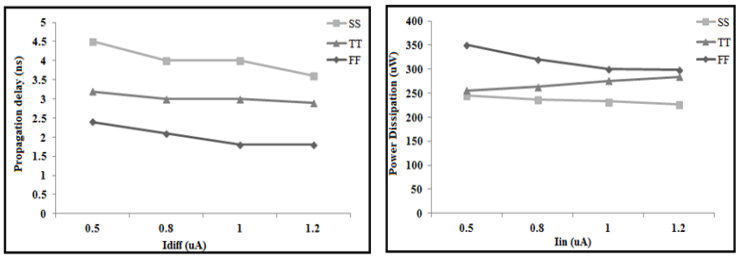


(a) (b) (c)

Fig. 5 Variation of (a) Delay (b) Power dissipation and (c) Power Delay Product versus Current Difference

The variation of performance parameters namely delay, power dissipation and power delay product (PDP) with input current difference have been evaluated and depicted via plots below. Figure 6 depicts various plots for performance parameters versus input current difference, specifically variation of input current difference with respect to delay in Fig. 5 (a), power dissipation in Fig. 5(b) and power delay product (PDP) in Fig. 5(c). It is observed that the propagation delay reduces with increasing current difference due to faster charging/discharging of the node capacitance while the power dissipation increases with current. PDP follows a reducing pattern with increasing current. As can be clearly observed, the proposed comparator outperforms Tang's [15] current comparator by being faster and power efficient thus offering a better PDP than the later.

Process corner analysis was also carried out on the proposed comparator to study its behavior under extreme cases of process mismatch between PMOS and NMOS during manufacturing. The impact of parameter variations on the performance of the proposed comparator at different design corners is also studied and the corresponding results for delay and power dissipation are depicted in Fig. 6(a) and (b) respectively. In this analysis, three corners exist, namely typical, fast and slow. Slow and Fast corners exhibit carrier mobilities that are higher and lower than normal respectively. Specifically, the corner FS represents fast NMOS and slow PMOS.



(a) (b)

Fig. 6 Effect of process corner variation on (a) delay (b) power dissipation

For the proposed current comparator, it is observed that the propagation delay is lower at the process corner FF while the power dissipation is higher than at process corner TT. Similarly, for process corner SS, a higher propagation delay is observed while the power dissipation is lower than at process corner TT.

4. Current Mode Flash ADC

As an application of the proposed comparator, a 3-bit current mode (CM) flash ADC is implemented, as represented in Fig. 7, wherein I_{in} and I_{refi} (i = 1, …, 7) represent input current and the reference currents of the ith comparator.

The value of the I_{refi} is determined by the input current range and the number of bits (n) in ADC output.

$$I_{refi} = \frac{Input\ current\ range}{2^{n}-1} \quad (2)$$

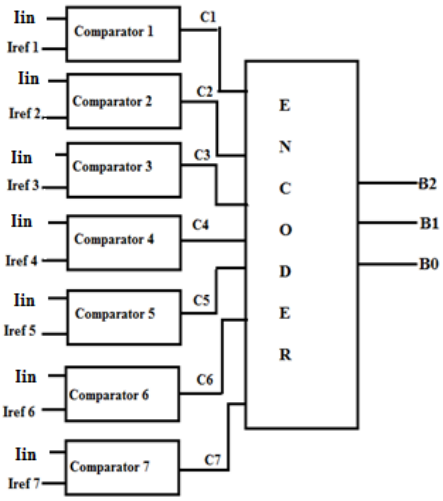


Fig. 7 A 3-bit CM Flash ADC

The number of current comparators to be employed for 3-bit conversion is given by 2^3-1=7. These current comparators receive progressively increasing reference currents (I_{refi}) as per Eqn. (2), the input current (I_{in}) is mirrored to all the current comparators. Each comparator

compares I_{in} to its respective reference current I_{refi}. Hence all comparators perform the comparison in a single step in parallel, so this structure is also called a parallel ADC or a single step ADC. The output of the comparators represents a thermometer code which is then converted into the corresponding binary code by a 7X3 encoder block. The comparator outputs are C7 (MSB), C6 to C2 and C1 (LSB). The encoder outputs are B2 (MSB), B1 and B0 (LSB), respectively.

A 7X3 CMOS encoder, shown in Fig. 8, has been designed for thermometer to binary conversion which remains the same for all these CM Flash ADCs..

The relation between comparator and encoder output is given by:

$$B_0 = C_1 \oplus C_2 \oplus C_3 \oplus C_4 \oplus C_5 \oplus C_6 \oplus C_7 \tag{3}$$

$$B_1 = \overline{C_4} C_2 + C_4 C_6 \tag{4}$$

$$B_2 = C_4 \tag{5}$$

where $\overline{C_4}$ represents the complement of C_4. The CMOS encoder circuit implemented is as shown in Fig. 8.

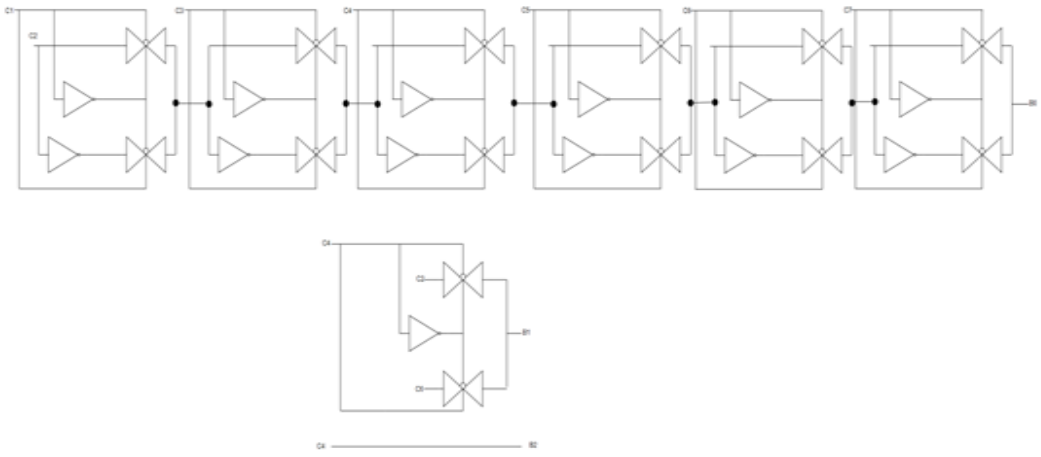


Fig. 8 7X3 CMOS Encoder

4.1 Simulation Results of the CM Flash ADC

The functionality of the CM Flash ADC has been demonstrated by simulations on PSPICE. The ADC response is shown in Fig. 9 for ramp input, to evaluate the performance of the comparator in ADC application.

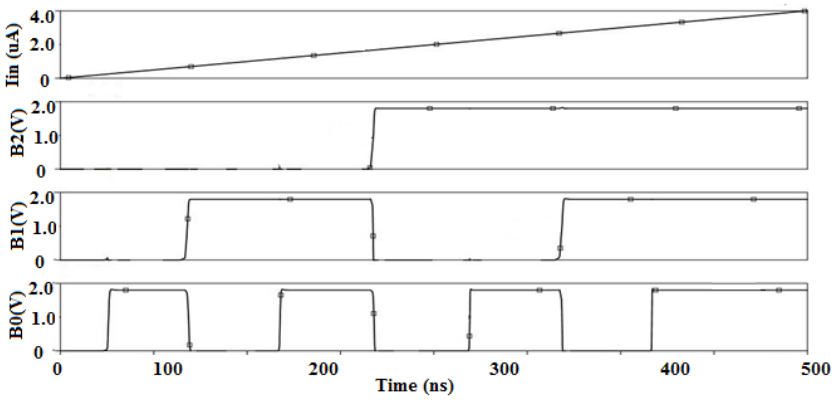
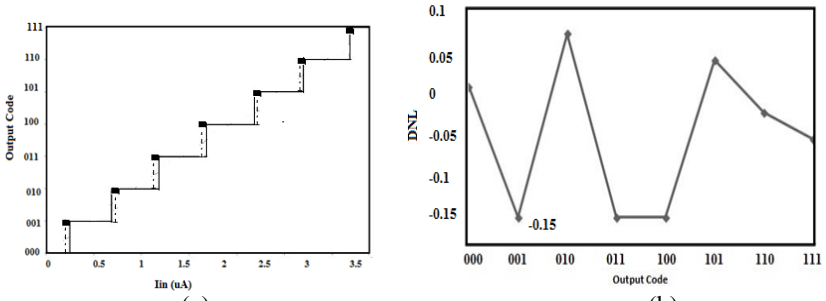


Fig. 9 CM Flash ADC-III output for ramp input

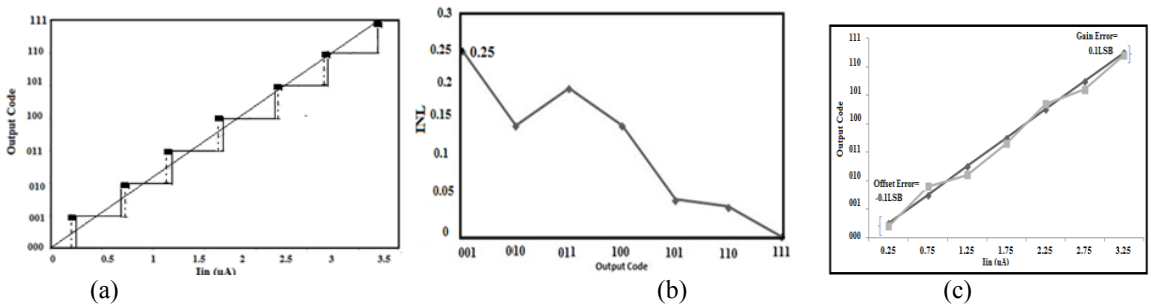
The ADC transfer characteristics are shown in Fig. 10(a) plotted alongside the characteristics of an ideal ADC. The Differential Non-Linearity (DNL) is computed to be -0.15 LSB and is plotted as in Fig. 10(b). It is clear that CM Flash ADC I does not suffer from any missing codes and gives a monotonic response



(a) (b)

Fig. 10 (a) CM Flash ADC III Transfer Characteristics (b) DNL Vs. Output Code

The CM ADC characteristics are redrawn in Fig. 11(a) with a best fit line plotted alongside actual and ideal characteristics in order to compute Integral Non-Linearity (INL). The dotted line indicates the switching point where code transitions should actually take place. The INL is calculated from Fig. 12 (a) and a maximum INL of -0.25 LSB is obtained, as plotted in Fig. 11 (b).



(a) (b) (c)

Fig. 11 (a)CM Flash ADC III Transfer Characteristic with best fit line (b) INL Vs. Output Code (c) Ideal and actual best fit line

In order to compute the gain and offset error of this ADC, the best fit line for Ideal and Actual ADC transfer characteristics is plotted. The error at the first transition is evaluated to obtain the offset error, which in the current case is -0.1LSB indicating that the first output transition code is obtained earlier than that expected ideally. The gain error is given by the difference in slope of actual best fit line and the ideal best fit line, which is also found to be 0.1LSB for this implementation. Fig. 11 (c) depicts both these errors.

5. Two-Step Flash ADC

Another application of the proposed current comparator, a Two-step Flash ADC is presented herein. Flash ADCs are usually the architectures of choice whenever there is a need for a fast conversion. This is so because the conversion is performed in one step, hence they can achieve very fast conversion rates. However, they suffer from a drawback that the number of comparators to be employed increases exponentially with the increasing number of bits at the output. Since, for N-bit conversion, 2^N-1 comparators are necessary, hence as the value of N increases, so does the number of comparators, thus making Flash ADC a hardware extensive structure. To overcome some of these limitations of Flash architecture and to advantage from its high speed, two-step (semi-flash) architecture is often employed. Although popular in voltage mode, only a few applications of the same have been reported in CM. [22]-[23].

The two-step method employs a coarse quantization in first step and a fine quantization in second step to obtain the desired resolution without extensively increased hardware. However, the speed is compromised as the output appears in two steps instead of parallel.

A 3-bit two-step CM Flash ADC architecture is presented herein that produces the higher order 2 bits through coarse quantization and 1 bit (LSB) through fine quantization. The schema is illustrated in Fig. 12.

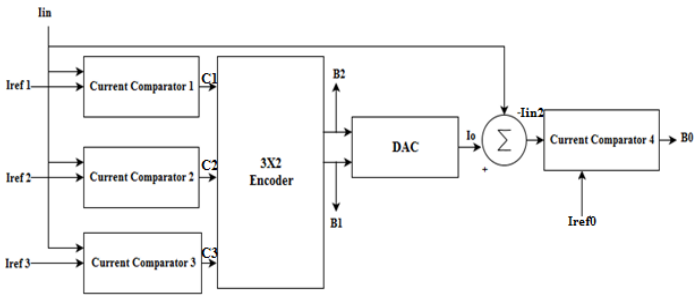


Fig. 12 Two-step 3-bit CM Flash ADC architecture

A two-step 3-bit CM ADC comprises of 4 current comparators, a 3X2 encoder a 2-bit DAC and a current differencing unit. This scheme gives the obvious advantages in terms of the reduced hardware. For a CM Flash ADC, the number of comparators required is 7 which is reduced to 4 in this schema. The encoder size is also down to 3X2 as against 7X3 in the CM Flash architecture. Even though a DAC and a subtractor have been included, yet the overall reduction in the total chip area outweighs the addition of these components.

The conversion takes place in two stages, with most significant bits, B_2 and B_1, being generated in the first stage while the LSB, B_0, is generated in the second stage depending on the on the output values obtained from the first stage.

In first stage, it is required to obtain 2 bits at the output, hence, as in a CM Flash ADC, 3 (2^2-1=3) current comparators are required. These current comparators compare the input current I_{in} to a progressively increasing reference current I_{refi}, where the value of I_{refi} is determined as follows. A step size is calculated as-

$$Step = \frac{I_{inmax} - I_{inmin}}{2^N - 1} \tag{6}$$

Where (I_{inmin}, I_{inmax}) is the input current range.

Based on the value of Step, I_{refi} is calculated as-

$$I_{ref1} = Step\ X\ 2^1 \tag{7}$$

$$I_{ref2} = Step\ X\ 2^2 \tag{8}$$

$$I_{ref3} = Step\ X\ (2^1 + 2^2) \tag{9}$$

The comparison of I_{in} against the respective I_{ref} by the three current comparators results in a 3-bit thermometer code. This code it then converted into corresponding binary code with the help of a 3X2 encoder which finally produces the two higher order bits B2 and B1. The relation between comparator and encoder output is given by:

$$B_1 = \overline{C_2} C_1 + C_3 \tag{10}$$

$$B_2 = C_2 \tag{11}$$

where $\overline{C_2}$ represents the complement of C_2. The CMOS encoder circuit implemented is as shown in Fig. 13.

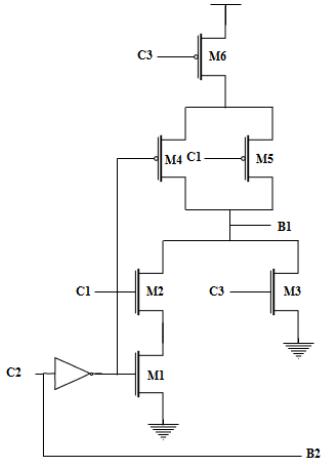


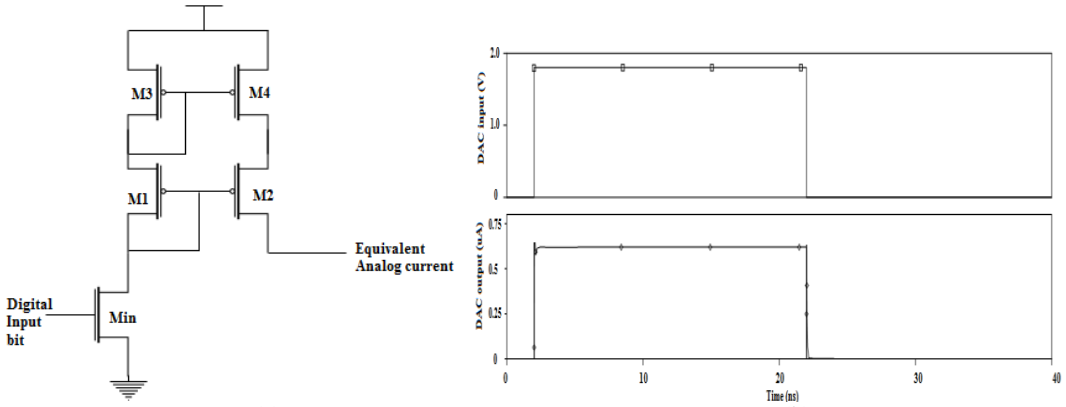
Fig. 13 3X2 CMOS Encoder

In the second stage, the outputs from first stage B_2 and B_1 are converted into an analog signal given by I_o through a DAC. The value of I_o depends upon the combination of B_2B_1 as per the Table I.

Table I DAC Outputs

B_2	B_1	I_o
0	0	0
0	1	$Step\ X\ 2^1$
1	0	$Step\ X\ 2^2$
1	1	$Step\ X\ (2^1 + 2^2)$

A 1-bit DAC as employed for the purpose is shown in Fig. 14(a) and its exemplary output is depicted in Fig. 14 (b). For 2-bits, two such structures are employed.



(a) (b)

Fig. 14(a) 1-bit DAC (b) Output Response

The DAC output I_o is then subtracted from I_{in} through a current differencing circuit identical to that used in the design of the proposed current comparator. The output of this current differencing circuit serves as the input current for the current comparator of second stage or 1-bit

fine Flash ADC. The 1-bit Flash ADC for generating the LSB B_0 is simply a current comparator that compares the value of I_{in2} with I_{ref0} given by-

$$I_{ref0} = Step\ X\ 2^0 \tag{12}$$

The result of this comparison produces the LSB, hence completing the 3-bit conversion process. The second stage does not require an encoder in the present scenario as the output obtained is a single bit i.e. either a '0' or a '1'. Had the number of bits required from the second stage been more, an encoder would also have been required. Hence, the schema gets modified based on the required resolution of the ADC.

5.1 Simulation Results of the CM Flash ADC

The results are verified through simulations using PSPICE. For the purpose of simulations, the input current range has been taken to be 0-3.5μA. Hence, the various values as calculated using the relations described in Eqns. (7)-(9) and (12) are as given in Table II.

Table II Step and I_{refi} Values for I_{in}=2.5μA

Step	I_{ref1}	I_{ref2}	I_{ref3}	I_{ref0}
$\frac{3.5-0}{2^3-1}$	$0.5X\ 2^1$	$0.5\ X\ 2^2$	$0.5\ X\ (2^1+2^2)$	$0.5\ X\ 2^0$
0.5	$1\mu A$	$2\mu A$	$3\mu A$	$0.5\mu A$

The values of I_o as obtained are 1μA, 2μA and 3μA for B_2B_1 '01', '10' and '11' respectively.

A step input current value I_{in} = 2.5μA is applied to these ADCs. For this input, C3C2C1 = '011' and the encoder output B_2B_1 ='10'. Also, as per Table I, the value of I_o is 2 μA. This value of I_o is then subtracted from I_{in} (2.5 μA) to obtain I_{in2} (= 0.5 μA). Finally, I_{in2} is compared to I_{ref0} by 4th current comparator and an output '1' is obtained as B_0 (LSB). Hence for I_{in}=2.5 μA the ADC output obtained is '101'. The circuit response to the input current, I_{in}=2.5μA is recorded in Fig. 15.

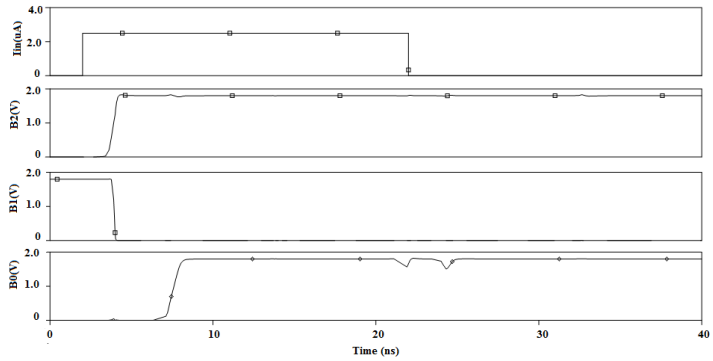
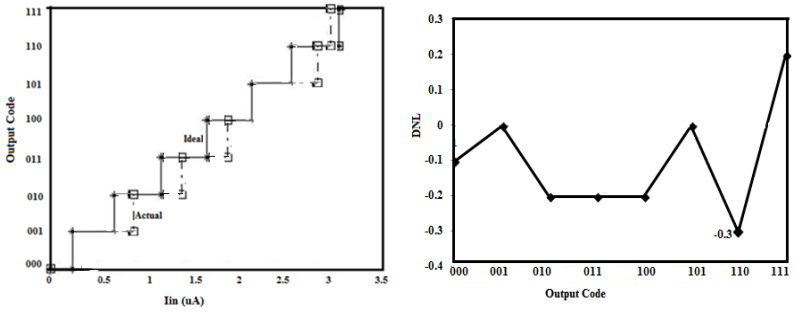


Fig. 15 Output of a Two-step CM Flash ADC based on Proposed Comparator III

The DNL and INL for this implementation of two-step CM Flash ADC is found to be higher than its full Flash counterpart. This is due to the residual inaccuracy that arises when output of one stage is cascaded to the next. The inaccuracy from first stage gets propagated to the next stage, leading to larger inaccuracy, thereby affecting the DNL and INL of the overall architecture [24].

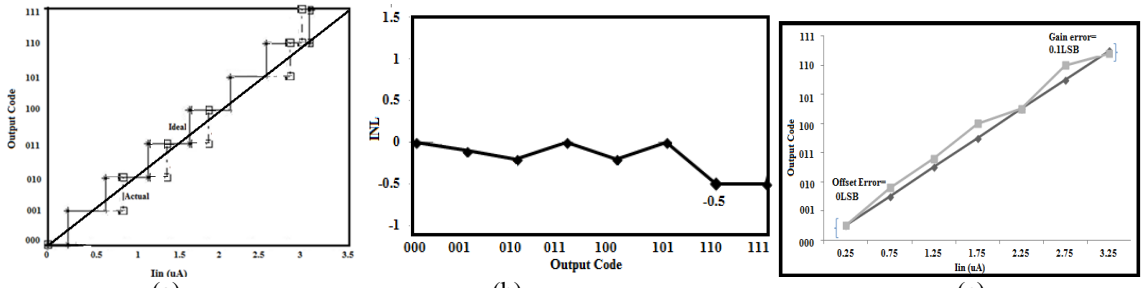
In this case the DNL is found to be -0.3 LSB while INL of -0.5 LSB is obtained. Figures 16(a) and (b) illustrate the transfer characteristics of the two-step CM Flash ADC and DNL vs output code curve of the same respectively.



(a) (b)

Fig. 16 (a) Transfer Characteristics of Two-step Flash ADC using Proposed Comparator IV (b) DNL Vs. Output Code

The INL calculation with respect to the best fit line has been depicted in Fig. 17(a) while Fig. 17(b) shows the variation of INL with respect to the output code.



(a) (b) (c)

Fig. 17 (a) Transfer Characteristics with best fit line for Two-step Flash ADC using Proposed Comparator III (b) INL Vs. Output Code

Figure 17(c) depicts the best fit lines for ideal and actual transfer characteristics of this ADC to evaluate the offset and gain errors. An offset error of 0LSB is observed at the first output code transition indicating that the first code appears at the same instance as ideally expected. The gain error is given by the difference in slope of actual best fit line and the ideal best fit line at the last transition, which is found to be 0.1LSB for this ADC.

Conclusion

A high speed, power efficient modification of Tang's current comparator employing FVF based input stage has been proposed. Performance of the proposed current comparator is compared to that of Tang and the former outperform the later in terms of propagation delay, power dissipation and PDP. The proposed current comparator has been employed to implement a 3-bit CM flash ADC and a two-step 3-bit Flash ADC. The ADC performance parameters for both the implementations have been evaluated and are found to be satisfactory.

REFERENCES

[1] Vlassis, S.; Siskos, S., "High speed and high resolution WTA circuit", in International Symposium on Circuit and Systems, pp 224–227, 1999.

[2] Demosthenous, A.; Taylor, J. , "2.8 V asynchronous high speed current comparator for sequence detection applications", Electronics Letters, Vol. 34, pp. 1714–1715, 1998.

[3] Baru, M.; Oliveira, O.; Silveira, F., "A 2 V rail-to-rail micropower CMOS comparator", Journal of Solid-State Devices Circuits, pp. 9–13, 1997.

[4] Banks, D.I.; Degenaar, P.; Toumazou, C., "A Colour and Intensity Contrast Segmentation Algorithm for Current Mode Pixel Distributed Edge Detection", Eurosensors XIX, 2005.

[5] Banks, D.I., Degenaar, P., Toumazou, C., 2005. Distributed Current Mode Image Processing Filters. Electronics Letters, Volume 41, pp. 1201–1202.

[6] Rius, J.; Figueras, J., "Proportional BIC sensor for current testing", Journal of Electronic Testing, Vol. 3, pp. 387-396, 1992.

[7] Razavi, B., "Analog Integrated Circuit", Tata McGraw Hill Publications, 2000.

[8] Rodríguez-Vázquez, A.; Domínguez-Castro, R.; Medeiro, F.; Delgado-Restituto, M., "High Resolution CMOS Current Comparators: Design and Applications to Current-Mode Function Generation", Analog Integrated Circuits and Signal Processing, Vol. 7, pp. 149-165, 1995.

[9] Traff, H., "Novel approach to high speed CMOS current comparators", Electronics Letters, Vol. 28, pp. 310-312, 1992.

[10] Tang, A.T.K.; Toumazou, C., "High performance CMOS current comparator", Electronics Letters, Vol. 30, pp. 5-6, 1994.

[11] Ravezzi, L.; Stoppa, D.; DallaBetta, G-F., "Simple high-speed CMOS current comparator", Electronics Letters, Vol.33, pp. 1829-1830, 1997.

[12] Min. B.-M.; Kim, S.-W., "High performance CMOS current comparator using resistive feedback network", Electronics Letters, Vol. 34, pp. 2074-2076, 1998.

[13] Chen, L.; Shi, B,; Lu, C., "Circuit Design of a High Speed and Low Power CMOS Continuous-time Current Comparator", Analog Integrated Circuits and Signal Processing, Vol. 28, pp. 293-297, 2001.

[14] Banks, D.; Toumazou, C., “Low-power high-speed current comparator design”, Electronics Letters, Vol. 44, pp.171-172, 2008.

[15] Tang, X.; Pun, K.P., “High-performance CMOS current comparator”, Electronics Letters, Vol. 45, pp.1007-1009, 2009.

[16] Chavoshisan, R.; Hashemipor, O., “A high-speed current conveyor based current comparator”, Microelectronics Journal, vol. 42, pp.28-32, 2011.

[17] Chavoshisan, R.; Hashemipor, O., “Differential current conveyor based current comparator,” International Journal of Electronics and Communications (AEÜ), Vol. 65, pp. 949– 953, 2011.

[18] Iswerya, P.; Gupta, S.; Goel, M,; Bhatia, V.; Pandey, N.; Bhattacharyya, A.,“Delay Area Efficient Low Voltage FVF Based Current Comparator”, IEEE 1st Students Conference on Engineering and Systems (SCES), pp. 1 – 4, 2012.

[19] Ramirez-Angulo, J.; Carvajal., R.G.; Torralba, A.; Galan, J.; Vega-Leal, A.P.; Tombs, J., “The flipped voltage follower: a useful cell for low-voltage low-power circuit design”, IEEE International Symposium on Circuits and Systems, Vol. 3, pp. 615 – 618, 2002.

[20] Ramirez-Angulo, J.; Carvajal, R.G.; Torralba, A.; Galan, J.; Vega-Leal, A. P.; Tombs, J., “Low-Power Low-Voltage Analog Electronic Circuits Using The Flipped Voltage Follower”, in IEEE International Symposium on Industrial Electronics, Vol.4, pp. 1327-1330, 2002.

[21] Flynn, M. P.; Allstot, D. J., “CMOS folding A/D converters with current-mode interpolation”, in IEEE Journal of Solid-State Circuits, Vol. 31, No. 9, pp. 1248-1257, 1996.

[22] Carreira, J. P.; Franca, J. E., “A two-step flash ADC for digital CMOS technology”, in Second International Conference on Advanced A-D and D-A Conversion Techniques and their Applications, pp. 48-51, 1994.

[23] Kim, H.H.; Yoon, K.S., “A 12 bit current-mode folding/interpolation CMOS A/D converter with 2 step architecture,” in The First IEEE Asia Pacific Conference on ASICs, pp. 174-177, 1999.

[24] Song, B.S., “MicroCMOS Design”, CRC Press, September 14, 2011.

HSOA Journal of Cell Biology and Cell Metabolism

Review Article

Molecular Chaperones and Ubiquitin Proteasome System in Tumor Biogenesis: An Overview

Saurabh Kumar Jha[1], Niraj Kumar Jha[1], Pravir Kumar[1] and Rashmi K Ambasta[1,2]*

[1]*Molecular Neuroscience and Functional Genomics Laboratory, Delhi Technological University (Formerly DCE), Delhi, India*

[2]*Department of Biotechnology, Delhi Technological University, Delhi, India*

Abstract

The hallmark feature in cancer is uncontrolled cell-division and altered protein expression. Currently, cancer is one of the most detrimental diseases encountered by a large population across the globe. However, an absolute treatment strategy has still not been achieved by the researchers. Further, molecular mechanism and therapeutic to combat this lethal disease is a baffling issue. Molecular chaperones and ubiquitin proteasome system is mainly responsible for the maintenance of protein homeostasis and thus playing a crucial role in the cancer pathophysiology. Molecular chaperones are a superfamily of proteins which expressions are triggered under physiological, pharmacological and environmental insults and playing a protective role for cell survival. However, beyond a threshold of protection, molecular chaperones are unable to provide proper shape of non functional proteins that accumulate unwanted protein the cellular milieu. In order to get rid off these accumulated proteins ubiquitin proteasome system comes into action where an E3 ligase, specific enzymes of ubiquitination system, play a decisive role in the turnover of many essential regulatory proteins involved in cancer. It also mediates numerous functions, for instance, cell death, cell growth and DNA repair. Since, both molecular chaperones and E3 ligases have been involved in the progression of cancers it is necessary to understand and implement the role of these two molecules to use as diagnostic markers to treat cancer. Herein, we have comprehensively discussed the functional role of molecular chaperones, their differential protein expressions and a possible correction mechanism in cancer. Furthermore, comprehensive information has been documented regarding E3 ligases and their associated role in cancer that may be used as potential diagnostic biomarker for the treatment of various cancers.

***Corresponding author:** Rashmi K Ambasta, Department of Biotechnology, Delhi Technological University, Delhi, India, Tel: +91 9818898638; E-mail: rashmiambasta@gmail.com; rashmiambasta@dce.edu

Citation: Jha SK, Jha NK, Kumar P, Ambasta RK (2016) Molecular Chaperones and Ubiquitin Proteasome System in Tumor Biogenesis: An Overview. J Cell Biol Cell Metab 3: 010.

Received: March 18, 2016; **Accepted:** May 31, 2016; **Published:** June 15, 2016

Keywords: Cancer; E3 ligases; Heat shock proteins; Molecular chaperones; Ubiquitin proteasome pathway

Introduction

The progression of cancer is so silent that it is hard to diagnose at the earlier stages, and it is an equally challenging task for the clinicians to treat this disease at early stage due to many unknown mechanisms with sites and tissues specificity issues. Cancer cells are immensely proliferatives, incursive, and metastatic in nature. The pathological hallmark in cancer is uncontrolled cellular proliferation and altered protein expression where hindrance in chaperoning machinery, and UPS is one of the major reasons. Molecular chaperones and ubiquitin E3 ligases are ubiquitous class of proteins that play an essential role in the conformational quality control of the proteins through interacting with various misfolded proteins, stabilizing and remodeling a wide range of non-native polypeptides [1,2]. Even though constitutively expressed under balanced growth conditions, many chaperones are upregulated upon exposure of heat shock or other insults that constitutively increases cellular protein level and for that reason, it is also known as stress or Heat Shock Proteins (HSPs) [3]. Molecular chaperones act together on unfolded or partially folded protein subunits, for instance, nascent chains emerging from the ribosome and with extended chains being translocated across sub-cellular membranes [4]. In addition, some chaperones are non-specific, and they easily interact with a broad range of protein subunits, while others are restricted to specific targets. They often require ATP binding/hydrolysis for their proper functions [4]. Moreover, they also stabilize the non-native conformation for correct folding of protein subunits [5] and not associate with native proteins nor do they form part of the final folded structures. HSPs were first identified as a group of proteins, which are brought about by heat shock and other kind of sources, including physical and chemical stressors in a broad range of species [6]. The HSPs have been afterwards described as molecular chaperones, which share common property of altering the structures and interactions of other proteins [7].

Importantly, molecular chaperone directs that the HSPs frequently interact in a stoichiometric manner with their substrates and also require high intracellular levels of proteins [6]. This is the reason why HSP28, HSP40, HSP70 and HSP110 genes have developed a highly effective mechanism for their synthesis during stress with transcriptional activation, efficient messenger RNA (mRNA) stabilization and their preferential translation [8] and boosts to become dominantly expressed proteins under such stress scenario [9]. Heat shock factor (hsf) family is the main regulatory machineries for HSP gene transcription, which ensure proper transcriptional activation and equally steep switch-off mechanism after recovery [10]. The hsf gene family comprises heat shock transcription factor 1 (hsf1), acts as central co-ordinator of heat shock stress response. Besides this, heat shock transcription factor 2 (hsf2) and heat shock transcription factor 4 (hsf4) are also involved in stress response but less active with respect to hsf1 [11]. HSP transcription needs activated hsf1, which is itself over-expressed in cancer and play a crucial role in invasion and metastasis [12]. Further, the molecular

mechanisms that connecting increased HSP and hsf1 expression to tumor development are not presently well understood. Since, HSPs are activated only under stress conditions in the normal cells; thus play a decisive role in both cellular homeostasis and the stress response [13]. To maintain the protein homeostasis, cells also encompass a large number of constitutively expressed HSPs which are present in a variety of multiprotein complexes together with many co-factors [8,14]. These HSPs comprise HSP10 and HSP60 multi complexes that direct protein folding; whereas, HSP70 and HSP90 containing complexes are implicated in both generic protein-folding pathways in specific connection with key regulatory proteins within the cell [15]. Most importantly, HSP90 plays a central role in forming complexes with a large number of transcription factors, cellular kinases and other molecules that in turn involved in the cell regulation process. Levels of the HSPs are raised in numerous tumor cells and HSP over-expression marks a poor prognosis in context with cell-survival and response to therapy in specific cancer types [16]. An elevated HSP expression in malignant cells plays a critical role in protection from spontaneous apoptosis associated with malignancy as well as apoptosis caused due to therapy. Further, this mechanism may underlie a highly complex role of HSPs in cancer development and reluctance to treatment [17].

Exposure of cells to stress condition, including oxidative stress, heat shock, heavy metals, inflammation, infection, tissue damage and mutant proteins associated with the genetic disease's result into an inducible expression of HSPs that acts as molecular chaperones [18]. HSPs are commonly found in both prokaryotic and eukaryotic cells and play a pivotal role in the cellular processes [19]. Interestingly, mammalian HSPs are grouped into four major families according to their molecular mass, including HSP90, HSP70, HSP60 and small HSPs [20]. Under physiological stress such as hypoxia, HSPs palying an essential role in the cell protection [21]. Further, HSP27, HSP70 and HSP90 are considered as anti-apoptotic markers, since; they were able to bind to some pro-apoptotic molecules, including cytochrome c and Apaf [22]. In contrast, HSP10 and HSP60 were suggested as pro-apoptotic [23]. It was also revealed that HSP70 increases the tumorigenicity of cancer cells in rodent models and inhibits apoptosis [24] and therefore, increases the survival of cells exposed to a wide range of lethal stimuli. Molecular chaperones have also ubiquitin-dependent proteasome like activity; ensure that damaged and short-lived proteins are degraded efficiently, thereby restoring protein homeostasis and promoting cell-survival [25]. Nevertheless, the altered expression of molecular chaperones and E3 ligases has been noticed in various cancers, including breast, prostate, lungs, and gastric. On contrary, these machineries are also having an opposite effect since, in many instances, it has been involved in inhibiting disease progression. Therefore, this review underlies the potential role of molecular chaperones and well-known E3 ligases in cancer biology. Further, this review will also provide a promising therapeutic strategy for clinicians to design suitable drugs for treating cancers.

An Interlink Between Chaperoning Machinery and Chaperonopathies

The term 'chaperoning system' is postulated in 2008 and notion behind this is consolidated protective machineries that have molecular chaperones, co-chaperones and co-factors of an organism [26]. Chaperonopathies is a pathological condition which comprises chaperones as etiological pathogenic factors while, chaperonotherapy is used as a medical term in which chaperones are used for the treatment of various diseases [27]. This scheme visualizes a physiological system integrated by chaperones, their functionally-related molecules and structures that are present in all tissues, organs and biological fluids. The ultimate fate of this physiological system is pivotal for the control and maintenance of protein homeostasis by correcting and providing functional conformation of proteins in all body fluids and tissues [27]. The chaperoning system also contributes their major input in some other processes, including, receptor assembly, antigen presentation and the formation of complexes with a variety of ligands and several other cellular functions [28]. Further, the term chaperonology, a scientific discipline has been identifiedwhich is dealing with the chaperoning system and includes the study of the genomic sequences of chaperone genes by virtue of applying chaperonomics concept. Chaperones are highly conserved proteins and assist other proteins for proper folding and re-folding [29]. Moreover, when the proteins are irreversibly misfolded, they are destined for degradation [30]. Additionally, these chaperone proteins are involved in regulating immune system, cell differentiation, cell-signaling, gene expression, DNA replication, apoptosis, cellular senescence and oncogenesis [31]. These chaperones are not present only in the tissues but also in fluids such as cell secretion products and have hormone-like activity because they act in locations other than those of their origin. A number of molecular chaperones are HSPs which including HSP110, HSP90, HSP70, HSP60 and so on. These proteins are induced under heat shock insult as well as by other physical and chemical stressors in a broad range of species [32]. Furthermore, these HSPs are encoded in genes that are inducible by stressors, but many others are not HSPs. These HSPs delineate their major input to protein homeostasis and also play other roles more or less unconnected to the maintenance of protein homeostasis. Earlier, HSP genes were categorized according to their molecular mass expressed in kilodalton (kDa) elaborated in table 1. However, recently guidelines for the nomenclature of the human HSP families have been changed. The main motto of this nomenclature system is based on gene symbols, which have been attributed or assigned by the HUGO Gene Nomenclature Committee (HGNC) and are used as the primary identifiers such as entrez gene and ensemble database [45].

A lethal complication of chaperoning machinery is considered to be a morbid condition where molecular chaperone malfunction is an etiopathological issue, and fatal complications (chaperonopathies) may be categorized as familial or acquired. In familial complication, the abnormal function of a chaperone is due to gene mutation [46]. Further, familial complications comprising the diseases of nervous system such as motor neuropathies and ataxias, heart disease includes familial forms of dilated cardiomyopathies and other sporadic forms of congenital diseases. In acquired chaperonopathies mediated complications, the malfunction of a chaperone may be due to morbid post-translational modifications, including oxidation, glycation, phosphorylation and acetylation resulting into loss or gain of function. Among the acquired chaperonopathies mediated complications, diseases are basically related with aging and with dysregulation of the immune system [46]. These fatal conditions may happen in any age. However, genetic chaperonopathies have a fairly early onset, while acquired chaperonopathies become exposed in the elderly, occasionally in association with other diseases. It has also been revealed that few prominent groups of chaperone are represented by the 'chaperonopathies by mistake' in which a molecular chaperone may be normal, although takes part in a cascade which indulges disease progression rather than the disease reversal [47]. In such condition, the pathology can be manifested by two types of pathogenic cascades; first the pathway is usual and comprises the

HSPS	Associated Chaperones	Molecular Weight (kDa)	Functions	References
HSP40	dnaJ, Ydj1, Sis1, Hdj1 and Hdj2	35-54	Associated with protein folding and refolding along with HSP70/ HSC70. It enhances the rate of Adenosine Triphosphatease (ATP) activity and substrate release	[33,34]
HSP60	groEL, HSP60, Cpn60 and HSP60	55-64	Helps in proper folding of proteins and also prevents aggregation of denatured proteins *in vitro*. It may also facilitate protein degradation by the help of proteolytic systems and involves in macrophage activation possibly through Toll-like receptor	[35]
HSP70	DnaK, Kar2, Ssc1, HSC70, HSP70, BIP and Mhsp70	65-80	Assists in proper folding of proteins and also contribute their potential role in protein-trafficking. It has also potential anti-apoptotic like properties. Further, it has been found to be Involved in cell-cycle progression and proliferation	[36,37]
HSP90	HtpG, HSP83, HSP90 and GRP94	81-99	Involves in signal transduction process and also assists proper folding and maintenance of proteins in *in vitro* and crucial for cell-cycle control	[38]
HSP100	ClpA,B,C and HSP104	90	Assists in the resolubilization of heat-inactivated proteins from insoluble aggregates and also plays pivotal role in stress tolerance	[35]
Small HSPs	Ibp A and B, HSP27, A and B crystalline and HSP27	34 or less than 34	Helps in heat inactivation and suppression of proteins in *in vitro*. It has also potential anti-apoptotic like properties	[39,40]
CCT	Hsp70 and TRiC	55-63	Cytosolic molecular chaperone that is involved in Protein folding	[41,42]
HSP10	HSP60	10	Pivotal for protein folding along with HSP60 and modulation of immune system	[43]
HSP 27	HspB1	20-30	Helps in the refolding of denatured proteins and have anti-apoptotic like properties	[44]

Table 1: Heat shock proteins, associated chaperones and their functional significance.

participation of one or more chaperones which develops into part of a morbid process; and second the cascade that includes chaperones is not part of a physiological process within the cell, although comes to be potent and functional in morbid cases. In both situations, the chaperones conduce to disease progression 'by mistake' [46]. In some occasions, autoimmune diseases can also be evoked by molecular chaperone acting as an auto-antigen 'by mistake' or due to molecular mimicry between human and bacterial HSP60 and other human proteins [48,49]. Interestingly, in some cases of neoplasms, chaperones can promote growth and proliferation of tumor cells [46]. Thus, molecular chaperone has both the beneficial and negative impact on the cells, as in normal condition it directs favourable impact on the cell, however, any mutation in its genes leads to morbid ambiance, which is also spelled as chaperonopathies which is a prominent notion as it directs to novel anti-cancer strategies.

Heat Shock Proteins: An Intervenor in Tumor Biogenesis

HSP27

Small HSP, HSP27 acts in an ATP-independent manner and is spotted in the cytosol. It is activated in response to various stresses through transcriptional and post-translational modification, thereby playing numerous roles, including proper folding, maintaining cytoskeleton architecture, cell-differentiation, cell-migration and tumor progression [50-52]. Elevated levels of HSP27 relative to its normal level in non-transformed cells have been detected in numerous cancers, including endometrial, pancreatic, ovarian, breast, lung cancer and leukaemia [53]. However, aberrant expression of HSP27 in cancer is mainly linked with increased resistance to chemotherapy, aggressive tumor behaviour and poor prognosis [5]. HSP27 is activated in various stress conditions by virtue of both transcriptional activation and post-translational modification, especially through phosphorylation. Phosphorylation of HSP27 occurs at mainly three serine residues Ser15, Ser78, Ser82 and its phosphorylation are interceded by the p38 MAPK stress kinase pathway [54]. However, this phosphorylation is a reversible process that regulates the oligomerization of HSP27. Additionally, various phosphorylation frameworks of HSP27 have been found to be linked with the aggressiveness of different cancer types. A recent report has stated that, in HER2 positive breast cancer samples, there are two fold increased in phosphorylation of HSP27 at ser78 but not at ser15 and 82 compared to HER2 negative tumors [55,56]. Therefore, the precise role of HSP27 phosphorylation in the physiology of cancer further needs to be investigated.

HSP27 along with HSP70 also serves as an anti-apoptotic factor by binding and sequestering cytosolic cytochrome c and therefore, creates a blockade for APAF-1 assembly of the apoptosome complex [57-59]. Furthermore, the activation of 'death' receptors such as TNF and TNF receptor superfamily member 6 (FAS, CD95 and APO-1) propels the formation of a death inducing complex for the activation of pro-caspase-8 to activate caspases by inducing the release of cytochrome c [6,60]. The phosphorylation pattern of HSP27 in tumor cells has also appeared distinct and shown different characteristic features as compared to the phosphorylation pattern of HSP27 in untransformed cells. Subsequently, it has been proposed that the diversity of HSP27 phosphorylation isoforms can also signify the useful tumor markers. Moreover, when phosphorylated HSP27 interacts with Daxx protein, it interferes with the interaction between same protein Daxx and Fas thereby blocking the FAS-mediated apoptosis to prevent cell death [61,62].

HSP60

In particular, HSP60 along with its associated chaperonin HSP10 has been identified as an evolutionarily conserved stress response chaperone. It has also been ascertained by few *in vitro* based studies, where HSP60 has found to direct both pro-and anti-apoptotic roles. HSP60 in association with the co-chaperone HSP10 modulates

caspase-3 activation by acting as a chaperone to advance the maintenance of pro-caspase-3, while it forms a stable complex with pro-caspase-3, thereby showing an anti-apoptotic effect [63]. Additionally, it also orchestrates a cytoprotective role through Inhibitors of Apoptosis (IAP) family, as well as inhibition of p53 cascade. Furthermore, elevated expression of both the HSP60 and HSP10 has been observed during prostate, colorectal, breast, leukaemias and exocervical carcinogenesis [64]. Recently, HSP60 has been reported to involve in ovarian cancer where, it has shown different prognosis and treatment response. Further, it is also having a pivotal role in malignant cell-survival [65].

HSP70

Like other HSPs, HSP70 is a molecular chaperone that activates in response to stress. It performs numerous roles under normal condition that include the transport and proper folding of proteins, assembly and dissociation of multi-protein complexes and also involve in degradation of denatured proteins [66]. Further, human cells comprise several HSP70 families based on their particular position in different organelles. This is stress-inducible HSP70 (HSP72 or HSPA1), the constitutively expressed heat shock cognate 70 (HSC70, HSP73 or HSPA8); Glucose regulated protein 78 (Grp78, HSPA5) and HSP70 (Mortalin/HSPA9, Grp75) which is found in nucleus, cytosol, endoplasmic reticulum and mitochondria respectively [67-71]. It has been well documented that HSP70 frequently localizes to the cell membrane in a variety of human tumors but not in the corresponding normal tissues. This activity is crucial for its therapeutic purposes against anti-tumor immunity since, membrane HSPs are the easily accessible targets for specific antibodies [72]. Similarly, HSP 27, HSP70 also performs anti-apoptotic like activity and can act at different key targets to perturb both the intrinsic and extrinsic signaling axis of apoptosis. Furthermore, it was also noticed to involve in caspase independent signaling where, it blocked signaling through inhibition of an Apoptosis-Inducing Factor (AIF) and therefore, mediate chromatin condensation and cathepsins release [73-76].

In cancer tissues, HSP70 is expressed at high levels, and their expression has been routinely linked with poor prognosis of tumors. The precise role of HSP70 in the cancer physiology is remains unsettled. Though, in cancer cells high expression of HSP70 is thought to provide a survival advantage due to its potential to stall apoptosis and senescence [77,78]. HSP70 also acts as the co-chaperone for HSP90 because of its role in the substrate-loading phase of the HSP90, which is important to the stability and function of multiple oncoproteins [79]. Further, elevated expression of HSP70 has also been correlated with therapeutic resistance while, the detailed mechanisms about resistance is still unknown. Moreover, recent evidence suggests that reduced activation of NF-κB, ERK and JNK pathways may be responsible for its therapeutic resistance [80]. Pharmacological inhibition of HSP90 has been found to provoke a compensatory activation of HSP70. This might be since HSP70 is a highly protective protein, which may strongly reduce the cell death effect induced by HSP90 inhibition. Consequently, the potential remedial advantage of regulating HSP70 activity has become striking, particularly dual therapy against both HSP70 and HSP90 [81-84]. It also acts as an inhibitor to progress towards G1 and S phase of the cell-cycle in human tumor cells and can be used as an attractive biomarker for cancers [85].

HSP90

HSP90 is a highly abundant and evolutionarily conserved protein present in the all eukaryotic cells. There are five HSP90 isoforms have been identified so far, which includes the two major cytoplasmic isoforms HPS90α and HPS90β, mitochondrial Tumor necrosis factor Receptor Associated Protein 1 (TRAP1), endoplasmic reticulum localized Grp94 and membrane-associated HSP90N [86]. HSP90 was reported to be expressed in 92.9% of examined tumors; moreover, the invasive samples contain significantly higher levels of HSP90 than the superficial ones. It was also identified that VEGF stimulation caused HSP90 activation, thereby showing anti-apoptotic and survival promoting effects of VEGF [87]. HSP90 often interacts with a huge number of molecules responsible for the development/survival of cancer cells, allowing mutant proteins to gain function while, permitting cancer cells to tolerate the imbalanced signaling. It also plays numerous key roles in angiogenesis, tumor invasion, metastasis, cell regulation, forming complexes with a large number of cellular kinases, transcription factors and other molecules [88].

HSP90 is an imperative molecular-chaperone that modulates the stability and activity of numerous client proteins, for instance, HER2, BCL-ABL, SRC, EGFR, CRAF, AKT, BRAF, MET, VEGFR, FLT3, HIF-1α, androgen and estrogen receptor and telomerase. These proteins directly involve in malignancy and are essential for the transformed phenotype [89]. In fact, elevated expression of HSP90 has been observed in a variety of human malignancies, including lung, breast tumors and leukaemias. In the breast cancer, it was found to associate with various proteins critical in breast cancer progression, such as HER2 and c-SRC [50]. Moreover, it also stabilizes many oncogenic proteins in tumor cells. It can inhibit apoptosis through several interactions. For illustration, it can bind directly with Apaf-1 there by blocking the assembly of apoptosome complex. However, anti-apoptotic action of HSP90 has been revealed by its association with proteins important for generating a survival signal in response to growth factor stimulators. For instance, HSP90 can bind with AKT1, an anti-apoptotic protein to prevent its inactivation and favoring cell-survival. Furthermore, over-expression of HSP90 has been implicated in resistance to senescence due to its pivotal role in telomerase stability [90,91].

HSP110

HSP110 is a component of the quite large multiprotein complex accompanied by the most common heat shock protein HSP70 [92]. HSP90 and HSP70 are particularly prominent regulators of the cellular proliferation, effective anti-apoptotic factors and are concerned in the cancer biology [93]. Molecular fundamental role of HSP110 in cancer cells is not yet fully inferred; nevertheless Hosaka et al., used small interfering RNA (siRNA)-mediated suppression of HSP110 protein expression for *in vitro* apoptosis induction in HCT116 colon cancer cells [94]. This siRNA-induced apoptosis was arbitrated through caspases, but not through the p53 tumor suppressor pathway, even though the HSP110 protein was bound to wild-type p53 protein in HCT116 cells. These results advocate that the constitutive over-expression of HSP110 in cancer cells is concerned in malignant transformation by protecting tumor cells from apoptosis [94]. HSP110 protein is over-expressed in various human tumors, including colon cancer cells, however, not in colorectal adenomas; therefore, proposing that over-expression of HSP110 is a late event in colorectal adenoma-carcinoma sequence [95]. Furthermore, it has been seen that higher levels of HSP110 gene expression were linked with

metastatic disease in comparison to those in tumors of patients with localized disease. Moreover, higher frequency of HSP110 protein positivity in colorectal adenocarcinomas of advanced clinical stages, therefore, this is highlighting consequential upregulation of HSP110 gene expression in tumors compared to paired adjacent non-tumoral tissue and negative trend of HSP110 mRNA levels with overall survival of colorectal cancer patients [95].

HSP110 gene is a favourable molecular forecaster in Colorectal Cancer (CRC). Its association with common clinicopathological information may be the decisive for diagnosis of the lymph node metastatic mediated cancer prognosis, identifying more aggressive tumors and in predicting the clinical outcome thus, might facilitate clinical oncologists in designing more aggressive remedies for subgroups of patients with colorectal cancer [96]. Mutant form of HSP110 in colorectal cancer showing microsatellite instability caused from an aberrantly spliced mRNA and lacking the HSP110 substrate-binding domain. This mutant was expressed at variable levels in almost all microsatellite instability CRC cell lines. Mutated HSP110 weakened both the normal cellular localization of HSP110 and its interaction with other HSPs, thus, opposing the chaperone activity and anti-apoptotic function of HSP110 in a dominant-negative manner. An over-expression of this mutated form of HSP110 resulted in the sensitization of cells to anti-cancer agents such as oxaliplatin and 5-fluorouracil, which are usually medically advised in the adjuvant treatment of people with CRC. HSP110 may thus, establish a crucial determining factor for both prognosis and medication response in CRC [97]. The signaling axis where HSPs mainly trigger their potential role has been elaborating in figure 1. Despite the involvement of molecular chaperones in cancer, the pertinent role of UPS is also needed to be explored to understand its significance in cancer biology.

Figure 1: Pictorial representation of the common mechanism for the role of HSPs in various signaling targets.

Ubiquitin/Proteasome Pathway: A Central Player Of Protein Homeostasis Machineries

The ubiquitin-proteasome pathway is a most important pathway for the targeted degradation of misfolded proteins and triggers an enzymatic cascade which encompasses ubiquitin-activating enzyme E1, ubiquitin-conjugating enzyme, E2 and finally ubiquitin E3 ligase, responsible for a wide range of processes, including cell-cycle progression, control of gene expression, antigen presentation, DNA replication, proliferation and apoptosis. The ubiquitin is, firstly, activated by binding with E1 through a thioester bond formation between a cysteine residue at the active site of E1 and the C-terminus Glycine (G76) of ubiquitin. After activation of ubiquitin in an E1-ubiquitin complex is then transferred to conjugating enzyme E2 and finally ubiquitin is covalently attached to the target protein through a lipopeptide bond between the G76, and process is catalyzed by E3 ubiquitin ligase. Moreover, due to the involvement of multiple steps of reaction, ubiquitin at first covalently attached to substrates to form K48-linked polyubiquitinated conjugates that are rapidly recognized and degraded by the 26S proteasome systems. Several studies have also revealed that proteins can also be monoubiquitinated or polyubiquitinated through K63 linkage, leading to an altered protein profiling and sub-cellular localization, rather than degradation [98,99].

There are several types of malignancies, for example, breast, gastric, colon, renal and cervical cancer has been reported to be associated with altered UPS. Further, there are approximately thousand of E3 ligases in the human genome have been reported so far, that can be differentiated into three major groups based upon their domain structure and substrate recognition. The first group comprises N-end rule ubiquitin ligase that targets protein substrates allowing to destabilize N-terminal residues, including Arg, Lys, His (type, I) and Phe, Trp, Leu, Tyr and Ile (type II). The current example of protein degradation by the Ub-dependent N-end rule cascade is *Drosophila* inhibitor of apoptosis protein. The second type of E3 is HECT known as E6-associated protein, which function is related with oncoprotein E6, responsible for ubiquitin mediated degradation of p53. The third and largest type of E3 ligase is known as the RING family which carries a classic RING finger domain with a linear sequence of Cys-X-Cys-X-Cys-X-His-X-Cys/His-X-Cys-X-Cys-X-Cys, where X can be any amino acid. A RING finger domain attaches to two zinc atoms per molecule, where the first and third pairs of cysteine/histidine form the first binding site, and the second and fourth pairs of cysteine/histidine form the other binding site. Further, E3 ubiquitin ligases exist and proceed as a single peptide (such as Mdm2 and XIAP or as multiple component complexes, for instance, SCF). Through the covalent modification of a massive repertoire of cellular proteins with ubiquitin, E3 ligases control almost all aspects of eukaryotic cellular biological process and function. However, deregulated expression of E3 ligases leads to cancer progression, although over-expression of E3 ligases is associated with reduced pathogenesis of disease. Thus, E3 ligases which find out the specificity of protein substrates and themselves critical enzymes may provide potential cancer targets in addition to cancer biomarkers [100-104]. It also functions in tissue specific and targets specific manner with maximal therapeutic index with minimal toxicity and provides a potential cancer target in addition to cancer biomarkers [105]. This notion, therefore, makes E3 ligase a potential biomarker/forecaster for cancers.

E3 Ligases: A Potential Biomarker for Cancer Diagnosis

CUL4A

Numerous E3 ligases could be oncogenes since frequent deregulation of E3 ligases have been identified in the progression of

various cancers such as breast, prostate, gastric, colorectal cancer and their inhibition direct to growth arrest or trigger apoptosis. CUL4A is a potent E3 ligase having oncogenic properties and involves in a broad range of cellular processes, for instance, chromatin remodeling, cell-cycle progression, hematopoiesis, spermatogenesis, DNA repairs and DNA replication [106]. It is a scaffold protein of the SCF (Skp1/Cullin1/Rbx1/F-box protein) complex, which ubiquitinates a wide range of proteins crucial for signal transduction, cell-cycle progression and transcription [107]. Cullin1 is found to be involved in the prognosis of numerous phenotypes, including adrenocortical carcinoma and squamous-cell carcinoma, childhood medulloblastoma, primary malignant pleural mesotheliomas, hepatocellular carcinomas and human breast, prostate and gastric cancer [108]. Furthermore, their high expression is significantly associated with poorer overall survival and lymph node metastasis. CUL4A is also responsible for neoplastic transformation to the case of breast and ovarian cancers [106]. Moreover, it inhibits the p73 transcriptional activation, which is a structural and functional homologue of p53 and thus highlights its potential in promoting tumorigenesis. On the contrary, it has also been shown to target proto-oncogenic proteins, for instance; N- and C-Myc and c-Jun by employing TRCP4AP/TRUSS and COP1, respectively and lead to stop disease progression [109]. However, Korzeniewski et al., has reported that Cullin1 can also serve as a tumor suppressor by modulating PLK4 protein levels [110].

ARF-BP1

It is a HECT domain E3 ligase that is responsible for degradation of p53 via UPS. Moreover, it also mediates both the p53-dependent and p53-independent tumor suppressive functions of ARF. The ARF-BP1 gene is positioned at Xp11-13 and is found to associate with progression of numerous cancers, including breast and colorectal cancer. In contrast, RING Finger protein 11 (RNF11) is greatly expressed in breast cancer cells; however, their role in disease pathogenesis remains elusive [111]. Further, RNF11 interplays with multiple HECT-domain E3 ligase and Cul1 that provide a bridge to link some substrates to the HECT domain E3 ligase for ubiquitination.

EFP

Another E3 ligase EFP provokes proliferation of breast cancer through facilitating ubiquitin-mediated destruction of a tumor suppressor 14-3-3j in response to IFNs. It is also known as oestrogen-inducible E3 ligase that plays a key role in ubiquitination. Moreover, it is having a potential to modulate a switch from estrogen-dependent to estrogen independent growth of breast cancer. In nude mice, it was noticed that EFP over-expressed MCF-7 (estrogen-dependent breast cancer cells) gained the ability to form tumors [112,113]. Further, it has also been reported that expression of EFP in ER-positive breast cancer cells cause oestrogen mediated degradation of KLF5 (Krüppel-like Factor 5) and ATBF1 protein [112]. These proteins are involved in breast development, differentiation, cell proliferation and carcinogenesis process. Furthermore, using antisense oligonucleotides the EFP expression can be regulated in order to reduce tumor growth. The protein expression of EFP is drastically linked with reduced prognosis of breast cancer and therefore, provides a new potential biomarker and molecular target for various cancers, including, breast, prostate and ovarian cancer [114].

RNF115/BCA2

The BCA2 protein is a RING-type E3 ubiquitin ligase, which gene is located at 1q21.1. BCA2 is found to be upregulated in Estrogen Receptor α (ERα)-positive breast cancer cells. Burger et al., have also reported the upregulated expression of BCA2 in invasive breast cancer along with negative lymph node metastasis, positive estrogen receptor and increased cell survival by using immunohistochemistry and tissue microarray. However, BCA2 functions can be modulated by adopting small interfering RNAs (siRNAs). In response to siRNAs two ERα-positive breast cancer cell lines, MCF-7 and T47D were used that shown reduced cell proliferation and increased protein levels of the cyclin-dependent kinase inhibitor p21Waf/Cip1. This is highlighting that BCA2 is involved in proliferation activity through downregulation of p21 since; protein stability of p21 is negatively regulated by BCA2. Further, BCA2 directly interacts with p21 and provokes them for ubiquitination [115,116].

SKP2

Skp2 E3 ligase plays a decisive role in metabolism, cell-cycle progression, senescence, proliferation and metastasis. Moreover, the over-expression of Skp2 has been reported in numerous phenotypes such as melanoma, lymphomas, nasopharyngeal carcinoma, prostate, pancreatic and breast carcinomas. Skp2 gene is positioned at 5p13, a region found to be associated with amplification of breast cancer cell-lines and act as a potential biomarker for disease prognosis [117]. On the contrary, over-expression of Skp2 has also been associated with a poor prognosis of breast cancer and crucial for proteolytic degradation of p21CIP1, p27KIP1, FoxO1 and p130 by SCF E3 ligase [118]. Moreover, Skp2 inactivation can profoundly control cancer progression by activating a massive apoptosis and cellular senescence.

BTRC1

BTRC1 (h-TrcP1) E3 ligase is involved in progression of numerous tumors such as ovarian, mammary and uterine carcinomas. It has been reported that over-expression of BTRC1 prompts epithelial cell-proliferation and nuclear factor-nB activity and thereby resulting in severe outcomes. It also directs ubiquitin mediated degradation of InB, h-catenin, CDC25A, Emil1 and Smad4 protein. These proteins are involved in various signaling processes and thereby triggering downstream signaling of various transcription factors [119-121].

WWP1

WWP1 is an oncogene, HECT domain containing E3 ligase and located at 8q21. Over-expression of WWP1 is found to be involved in various tumors, including prostate and breast tumor [122]. Moreover, it also provides stability and negatively regulates Large Tumor Suppressor 1 (LATS1: Mst1/2, MOB1, Kibra, etc.) by promoting their degradation through polyubiquitination. Further, degradation of LATS1 is crucial in triggering WWP1-induced increased cell-proliferation in breast cancer cells. The LATS1 is a serine/threonine kinase and having tumor suppressor role which is found to be down-regulated in various human cancers. It has also been reported that WWP1 negatively controls cell migration to CXCL12 by limiting CXCR4 degradation that leads to promote breast cancer bone metastasis. Further, It also regulates the Transforming Growth Factor-h (TGF-h) activity by the ubiquitination of TGF-h receptor 1, Smad2 and Smad4 [123]. Additionally, WWP1 also acts as an E3 ligase for numerous transcription factors, such as KLF2 and KLF5 which are found to be associated with ovarian and breast cancers, respectively [124]. Surprisingly, it also plays a chief role in many other biological processes, for instance, regulation of sodium channels, viral budding and ligand-receptor trafficking [125]. Since these E3 ligases are involved in the disease symptoms of numerous cancers due to their

oncogenic activity, there are many other E3 ligases have been reported, which is having therapeutic potential to target various cancers due to their tumor suppressor activity.

SIAH1

SIAH1 gene is located at 16q12.1 and was first recognized as a tumor suppressor candidate for human hepatocellular carcinomas. It is a RING finger E3 ligase and highly conserved among E3 ubiquitin ligases family, which is involved in tumor suppression and apoptosis [126]. It has been reported that SIAH1 directs the degradation of Kid (KIF22), a chromokinesin like DNA binding protein crucial for normal progression of mitosis and meiosis, transcriptional corepressor CtIP, transcriptional coactivator OBF-1 and cell fate regulator numb by ubiquitination. Additionally, it also induces h-catenin for proteolysis in response to p53 activation and may lead to p53-dependent cell-cycle arrest and apoptosis [127-129]. The ubiquitin ligase complex of SIAH1 gene contains SIAH1 interacting protein, F-box protein Ebi and Skp1 gene. Interestingly, SIAH2, an isoform of SIAH gene plays an important role in diverse signaling pathways and having high sequence similarity with SIAH1 but possess contrary roles in cancer, since SIAH1 more often acting as a tumor suppressor whereas, SIAH2 acts as a proto-oncogene [130].

BRCA1

A widely-known tumor suppressor gene and act as a hub protein for a wide range of cellular processes in order to maintain genomic stability. It contains a RING heterodimer with BARD1 to provide an ubiquitin E3 ligase function that is requisite for its tumor suppressor activity in numerous cancers, including breast and ovarian cancer. However, the function of the BRCA1 gene is often compromised by cancer-associated mutations. In case of breast cancer, BARD1 is mutated at their lower frequency and triggers BRCA1-independent and p53-dependent pro-apoptotic activity. Further, BRCA1 is also involved in homologous recombination and DNA repair in response to DNA damage. Moreover, the activity of these heterodimer can be antagonized by using CDK2 and improved by BRCC36 whose mRNA expression is often elevated in breast cancer. Additionally, this ligase is also responsible for ubiquitination of g-tubulin and RNA polymerase II (Rpb1) which is pivotal for genome stability [131-134].

CHFR and CUL-5

Similarly BRCA1, the CHFR gene also encodes a RING finger domain, possessing E3 ligase activity. It acts as a tumor suppressor gene which was noticed to play an imperative role in mitosis by targeting key mitotic proteins Plk and Aurora A for their ubiquitination. Further, Epigenetic inactivation of CHFR by methylation was found in numerous cancers, including gastric, breast, lung, liver and ovarian cancer [135,136]. In addition to CHFR, CUL-5 also possesses E3 ligase activity and located at 11q22-23. Cul-5 was shown to significantly attenuate cellular proliferation of the T-47D breast cancer cell-line [137]. It also regulates multiple molecular and cellular responses to HSP90 inhibition in human cancer cells.

FBXW7/CDC4

The FBXW7/CDC4 gene is spotted to 4q32 and found to be involved in ubiquitination of several oncoproteins such as cyclin E, c-Myc, c-Jun and Notch that is responsible for its tumor suppressor activity [138]. These oncoproteins are responsible for controlling cell-growth and cell-division. On the contrary, loss of functions of FBXW7/CDC4 due to genomic instability and cell-cycle progression has been reported in various cancers, including gastric and breast cancer [139-141]. Therefore, it can be used as a possible diagnostic biomarker and therapeutic target for various cancers in the future.

Parkin

Parkin is a RING-type E3 ligase, which is responsible for ubiquitination of misfolded proteins. However, mutations in parkin gene are found to be associated with numerous outcomes, such as Parkinson's Disease (PD), mycobacterial infection and cancer. Parkin is also known as RING/HECT hybrid, which is found to be present on chromosome 6q25-q27, the region mainly associated with the prognosis of human breast, ovarian and lung cancer. In breast cell-lines the reduced expression of Parkin gene has been observed [142,143]. It was also noticed that in cell-proliferation parkin was shown to suppress tumourigenicity due to *in vitro* changes. Further, Pael receptor (Pael-R), aSp22 and p38/JTV1 were identified as the parkin substrates in brain cells, although; the targeted substrate in cancer cells remains unsettled [144].

CHIP/STUB1

CHIP/STUB1 is a U-box containing E3 ubiquitin ligase, plays an important role in preventing tumor progression through degradation of numerous oncogenic proteins, including Cyclin D1, Src-3, HIF-1α, NF-κB, c-Myc, MMP-2, VEGF, IL-8, ErbB2 and c-Myc. Its gene is found to be present at 16p13.3, the region associated with papillary carcinomas. Further, Loss of function of CHIP due to methylation has been involved in prognosis of human colorectal cancer. Not only that, in prostate cancer it was also involved in the mitotic process for proliferation. The over-expression of CHIP negatively regulates the sensitivity of TGF-h signaling by targeting Smads for their proteolysis and also promotes the degradative action of Parkin gene [145-147]. Despite these potential E3 ligases, there are numerous other E3 ligases are reported whose activity is needed for maintenance of cancer cells as well as for diagnosis purposes. These E3 ligases and their associated functions in different cancers have been illustrated in table 2.

Conclusion

The main goal of cancer therapies relies on the researcher's endowment to adjust actions to circumstances and has a clear projection pertaining to the aberrant mechanisms that ultimately determine the fate of the pathogenesis and henceforth degeneration through diverse processes. Despite gradual improvement in the field of cancer therapies, still the destined of such therapies hangs on morbid speculation and fragile anticipations. The diverse signaling axis offerings, an interesting opportunity to exploit in the pathology of cancers; furthermore, interrupting critical interactions of the pathways by using potential diagnostic marker such as, E3 ligases and molecular chaperones can solve the "targeted therapy crisis" problem in cancer biology. In doing so, HSPs are concerned with the pathogenesis and development of a range of human cancer types. They primarily participate in crucial mechanisms of tumor cells, including invasiveness, cell proliferation and neoangiogenesis, differentiation, metastasis, and immune system recognition. Since, HSPs are presently considered as biomarkers of carcinogenesis and their expression is correlated with the extent of differentiation and aggressiveness of certain tumors. Therefore, HSPs may also have been potential as forecasters of response to therapy. As well, their use as anti-cancer agents is growing, for instance, as inducers of anti-tumor

S.No.	E3 ligases	Associated functions	Principle phenotypes	References
1	AMFR/RNF45	AMFR plays a critical role in metastasis through ubiquitination of the metastasis suppressor KAI1	Prostate, liver and breast cancer	[148]
2	HACE1	Acts as tumor suppressor. Moreover, abnormal methylation and Rac 1 signaling make it oncogenic	Wilms' tumors, colorectal and breast cancer	[149]
3	PJA1/PRAJA	It plays an important role in downregulation of TGF-β signaling via ubiquitination of the SMAD4 adaptor protein ELF	Gastric cancer	[150]
4	Cbl-b	Cbl-b along with TAM receptors regulate cancer metastasis via natural killer cells	-------	[151]
5	UBE3A/ E6-AP	It interacts with the E6 protein of the human papillomavirus types 16 and 18, and activates p53 for degradation	Breast cancer	[152]
6	HUWE1/MULE	It suppresses RAS-driven skin tumorigenesis in vivo by regulating c-MYC/MIZ1 stability	Skin cancer	[153]
7	RFWD2/COP1	It ubiquitinates several proteins involved in the DNA damage response and apoptosis, including MTA1, p53 and FoxO1. Further, it also inactivates proto-oncogenes (ETV1, ETV4 and ETV5)	Prostate cancer	[154]
8	RNF5	It involves in motility, stress response and regulates cancer progression through cytoskeleton alterations	Breast cancer	[155]
9	RNF13	It contributes to a reduction in the colonization of metastatic tumor cells	Lung and pancreatic cancer	[156]
10	FBXO11	It is associated with HIF-1α for its oncogenic effects. Further, it acts as a tumor suppressor and also to be a potential target for cancer therapy	Gynecological cancer	[157]
11	SPOP	It acts as tumor-suppressor and involved in signal-dependent proteolysis of the oncogenic co-activator SRC-3/AIB1	Liver and breast cancer	[158]
12	SMURF2	It promotes Epithelial-Mesenchymal Transition (EMT) in HPDE6c7 cells and its over-expression inhibits TGF-β-mediated EMT in the cells. Subsequently, it is also found to be involved with metastasis	Pancreatic and breast cancer	[159]
13	RNF31	It stabilizes estrogen receptor α and modulates estrogen-stimulated cell proliferation	Breast cancer	[160]
14	RNF43	RNF43 interacts with NEDL1 and modulates p53-mediated transcription	Colorectal cancer	[161]

Table 2: Potential E3 ligases and their associated functionalities in cancers.

immune responses. Importantly, E3 ligases have also shown the regulatory role in various cancers and lead to protect from a variety of cancers, conversely, it also acts as oncogenes. These E3 ligases have a significant role in motility, cytoskeleton alterations, cell growths, cell-death, DNA repairs and cell-cycle progression. This notion advocates new insights for anticancer therapy. Nevertheless, further research is needed in order to make drugs/compounds in cancer therapeutics a blatant reality.

Acknowledgement

The authors would like to thank SERB/DST for funding the project. The authors would also like to thank the administration of DTU for encouragement and excellent infrastructure provided.

Conflicts of Interest

The authors declare no conflicts of interest.

References

1. Vabulas RM, Raychaudhuri S, Hayer-Hartl M, Hartl FU (2010) Protein folding in the cytoplasm and the heat shock response. Cold Spring Harb Perspect Biol 2: 004390.
2. Chen B, Retzlaff M, Roos T, Frydman J (2011) Cellular strategies of protein quality control. Cold Spring Harb Perspect Biol 3: 004374.
3. Morano KA, Grant CM, Moye-Rowley WS (2012) The response to heat shock and oxidative stress in Saccharomyces cerevisiae. Genetics 190: 1157-1195.
4. Hartl FU, Bracher A, Hayer-Hartl M (2011) Molecular chaperones in protein folding and proteostasis. Nature 475: 324-332.
5. Saibil H (2013) Chaperone machines for protein folding, unfolding and disaggregation. Nat Rev Mol Cell Biol 14: 630-642.
6. Martínez-Paz P, Morales M, Martín R, Martínez-Guitarte JL, Morcillo G (2014) Characterization of the small heat shock protein Hsp27 gene in *Chironomus riparius* (Diptera) and its expression profile in response to temperature changes and xenobiotic exposures. Cell Stress Chaperones 19: 529-540.
7. Requena JM, Montalvo AM, Fraga J (2015) Molecular Chaperones of *Leishmania*: Central Players in Many Stress-Related and -Unrelated Physiological Processes BioMed Research International 2015: 301-326.
8. Tang D, Khaleque MA, Jones EL, Theriault JR, Li C, et al. (2005) Expression of heat shock proteins and heat shock protein messenger ribonucleic acid in human prostate carcinoma *in vitro* and in tumors *in vivo*. Cell Stress Chaperones 10: 46-58.
9. Zhao M, Tang D, Lechpammer S, Hoffman A, Asea A, et al. (2002) Double-stranded RNA-dependent protein kinase (pkr) is essential for thermotolerance, accumulation of HSP70, and stabilization of ARE-containing HSP70 mRNA during stress. J Biol Chem 277: 44539-44547.
10. Calderwood SK, Xie Y, Wang X, Khaleque MA, Chou SD, et al. (2010) Signal Transduction Pathways Leading to Heat Shock Transcription. Sign Transduct Insights 2: 13-24.
11. Akerfelt M, Morimoto RI, Sistonen L (2010) Heat shock factors: integrators of cell stress, development and lifespan. Nat Rev Mol Cell Biol 11: 545-555.
12. Wang MH, Grossmann ME, Young CY (2004) Forced expression of heat-shock protein 70 increases the secretion of Hsp70 and provides protection against tumour growth. Br J Cancer 90: 926-931.
13. Lindquist S, Craig EA (1988) The heat-shock proteins. Annu Rev Genet 22: 631-677.
14. Buchner J (1999) Hsp90 & Co. - a holding for folding. Trends Biochem Sci 24: 136-141.
15. Pratt WB, Toft DO (2003) Regulation of signaling protein function and trafficking by the hsp90/hsp70-based chaperone machinery. Exp Biol Med (Maywood) 228: 111-133.

16. van de Vijver MJ, He YD, van't Veer LJ, Dai H, Hart AA, et al. (2002) A gene-expression signature as a predictor of survival in breast cancer. N Engl J Med 347: 1999-2009.

17. Gyrd-Hansen M, Nylandsted J, Jäättelä M (2004) Heat shock protein 70 promotes cancer cell viability by safeguarding lysosomal integrity. Cell Cycle 3: 1484-1485.

18. Akerfelt M, Morimoto RI, Sistonen L (2010) Heat shock factors: integrators of cell stress, development and lifespan. Nat Rev Mol Cell Biol 11: 545-555.

19. Zügel U, Kaufmann SH (1999) Role of heat shock proteins in protection from and pathogenesis of infectious diseases. Clin Microbiol Rev 12: 19-39.

20. Yang Z, Zhuang L, Szatmary P, Wen L, Sun H, et al. (2015) Upregulation of heat shock proteins (HSPA12A, HSP90B1, HSPA4, HSPA5 and HSPA6) in tumour tissues is associated with poor outcomes from HBV-related early-stage hepatocellular carcinoma. Int J Med Sci 12: 256-263.

21. Fan GC (2012) Role of heat shock proteins in stem cell behavior. Prog Mol Biol Transl Sci 111: 305-322.

22. Purandhar K, Jena PK, Prajapati B, Rajput P, Seshadri S (2014) Understanding the role of heat shock protein isoforms in male fertility, aging and apoptosis. World J Mens Health 32: 123-132.

23. Shan YX, Liu TJ, Su HF, Samsamshariat A, Mestril R, et al. (2003) Hsp10 and Hsp60 modulate Bcl-2 family and mitochondria apoptosis signaling induced by doxorubicin in cardiac muscle cells. J Mol Cell Cardiol 35: 1135-1143.

24. Rérole AL, Jego G, Garrido C (2011) Hsp70: anti-apoptotic and tumorigenic protein. Methods Mol Biol 787: 205-230.

25. Shang F, Taylor A (2012) Roles for the ubiquitin-proteasome pathway in protein quality control and signaling in the retina: implications in the pathogenesis of age-related macular degeneration. Mol Aspects Med 33: 446-466.

26. Tomala K, Korona R (2008) Molecular chaperones and selection against mutations. Biol Direct 3: 5.

27. Cappello F, Marino Gammazza A, Palumbo Piccionello A, Campanella C, Pace A, et al. (2014) Hsp60 chaperonopathies and chaperonotherapy: targets and agents. Expert Opin Ther Targets 18: 185-208.

28. Mayer MP, Bukau B (2005) Hsp70 chaperones: cellular functions and molecular mechanism. Cell Mol Life Sci 62: 670-684.

29. Kampinga HH, Craig EA (2010) The HSP70 chaperone machinery: J proteins as drivers of functional specificity. Nat Rev Mol Cell Biol 11: 579-592.

30. Stolz A, Wolf DH (2010) Endoplasmic reticulum associated protein degradation: a chaperone assisted journey to hell. Biochim Biophys Acta 1803: 694-705.

31. Rappa F, Farina F, Zummo G, David S, Campanella C, et al. (2012) HSP-molecular chaperones in cancer biogenesis and tumor therapy: an overview. Anticancer Res 32: 5139-5150.

32. Mahmood K, Jadoon S, Mahmood Q, Irshad M, Hussain J (2014) Synergistic effects of toxic elements on heat shock proteins. Biomed Res Int 2014: 564136.

33. Qiu XB, Shao YM, Miao S, Wang L (2006) The diversity of the DnaJ/Hsp40 family, the crucial partners for Hsp70 chaperones. Cell Mol Life Sci 63: 2560-2570.

34. Lopez N, Aron R, Craig EA (2003) Specificity of class II Hsp40 Sis1 in maintenance of yeast prion [RNQ+]. Mol Biol Cell 14: 1172-1181.

35. Parsell DA, Taulien J, Lindquist S (1993) The role of heat-shock proteins in thermotolerance. Philos Trans R Soc Lond B Biol Sci 339: 279-285.

36. Mosser DD, Caron AW, Bourget L, Denis-Larose C, Massie B (1997) Role of the human heat shock protein hsp70 in protection against stress-induced apoptosis. Mol Cell Biol 17: 5317-5327.

37. Buzzard KA, Giaccia AJ, Killender M, Anderson RL (1998) Heat shock protein 72 modulates pathways of stress-induced apoptosis. J Biol Chem 273: 17147-17153.

38. Stebbins CE, Russo AA, Schneider C, Rosen N, Hartl FU, et al. (1997) Crystal structure of an Hsp90-geldanamycin complex: targeting of a protein chaperone by an antitumor agent. Cell 89: 239-250.

39. Richards EH, Hickey E, Weber L, Master JR (1996) Effect of overexpression of the small heat shock protein HSP27 on the heat and drug sensitivities of human testis tumor cells. Cancer Res 56: 2446-2451.

40. Trautinger F, Kokesch C, Herbacek I, Knobler RM, Kindås-Mügge I (1997) Overexpression of the small heat shock protein, hsp27, confers resistance to hyperthermia, but not to oxidative stress and UV-induced cell death, in a stably transfected squamous cell carcinoma cell line. J Photochem Photobiol B 39: 90-95.

41. Kubota H (2002) Function and regulation of cytosolic molecular chaperone CCT. Vitam Horm 65: 313-331.

42. Melville MW, McClellan AJ, Meyer AS, Darveau A, Frydman J (2003) The Hsp70 and TRiC/CCT chaperone systems cooperate *in vivo* to assemble the von Hippel-Lindau tumor suppressor complex. Mol Cell Biol 23: 3141-3151.

43. Höhfeld J, Hartl FU (1994) Role of the chaperonin cofactor Hsp10 in protein folding and sorting in yeast mitochondria. J Cell Biol 126: 305-315.

44. Arrigo AP (2007) The cellular "networking" of mammalian Hsp27 and its functions in the control of protein folding, redox state and apoptosis. Adv Exp Med Biol 594: 14-26.

45. Kampinga HH, Hageman J, Vos MJ, Kubota H, Tanguay RM, et al. (2009) Guidelines for the nomenclature of the human heat shock proteins. Cell Stress Chaperones 14: 105-111.

46. Macario AJ, Conway de Macario E (2007) Chaperonopathies and chaperonotherapy. FEBS Lett 581: 3681-3688.

47. Savvateeva-Popova E, Popov A, Grossman A, Nikitina E, Medvedeva A, et al. (2007) Pathogenic chaperone-like RNA induces congophilic aggregates and facilitates neurodegeneration in Drosophila. Cell Stress Chaperones 12: 9-19.

48. Rodolico V, Tomasello G, Zerilli M, Martorana A, Pitruzzella A, et al. (2010) Hsp60 and Hsp10 increase in colon mucosa of Crohn's disease and ulcerative colitis. Cell Stress Chaperones 15: 877-884.

49. Gammazza AM, Bucchieri F, Grimaldi LM, Benigno A, de Macario EC, et al. (2012) The molecular anatomy of human HSP60 and its similarity with that of bacterial orthologs and acetylcholine receptor reveal a potential pathogenetic role of anti-chaperonin immunity in myasthenia gravis. Cell Mol Neurobiol 32: 943-947.

50. Ciocca DR, Oesterreich S, Chamness GC, McGuire WL, Fuqua SA (1993) Biological and clinical implications of heat shock protein 27,000 (Hsp27): a review. J Natl Cancer Inst 85: 1558-1570.

51. Jakob U, Gaestel M, Engel K, Buchner J (1993) Small heat shock proteins are molecular chaperones. J Biol Chem 268: 1517-1520.

52. Garrido C, Brunet M, Didelot C, Zermati Y, Schmitt E, et al. (2006) Heat shock proteins 27 and 70: anti-apoptotic proteins with tumorigenic properties. Cell Cycle 5: 2592-2601.

53. Myung JK, Afjehi-Sadat L, Felizardo-Cabatic M, Slavc I, Lubec G (2004) Expressional patterns of chaperones in ten human tumor cell lines. Proteome Sci 2: 8.

54. Brunet Simioni M, De Thonel A, Hammann A, Joly AL, Bossis G, et al. (2009) Heat shock protein 27 is involved in SUMO-2/3 modification of heat shock factor 1 and thereby modulates the transcription factor activity. Oncogene 28: 3332-3344.

55. Katsogiannou M, Andrieu C, Rocchi P (2014) Heat shock protein 27 phosphorylation state is associated with cancer progression. Front Genet 5: 346.

56. Kim LS, Kim JH (2011) Heat shock protein as molecular targets for breast cancer therapeutics. J Breast Cancer 14: 167-174.

57. Lee SJ, Choi SA, Lee KH, Chung HY, Kim TH, et al. (2001) Role of inducible heat shock protein 70 in radiation-induced cell death. Cell Stress Chaperones 6: 273-281.

58. Zorzi E, Bonvini P (2011) Inducible hsp70 in the regulation of cancer cell survival: analysis of chaperone induction, expression and activity. Cancers (Basel) 3: 3921-3956.

59. Kennedy D, Jäger R, Mosser DD, Samali A (2014) Regulation of apoptosis by heat shock proteins. IUBMB Life 66: 327-338.

60. Elmore S (2007) Apoptosis: a review of programmed cell death. Toxicol Pathol 35: 495-516.

61. Charette SJ, Lavoie JN, Lambert H, Landry J (2000) Inhibition of Daxx-mediated apoptosis by heat shock protein 27. Mol Cell Biol 20: 7602-7612.

62. Ferns G, Shams S, Shafi S (2006) Heat shock protein 27: its potential role in vascular disease. Int J Exp Pathol 87: 253-274.

63. Ghosh JC, Dohi T, Kang BH, Altieri DC (2008) Hsp60 regulation of tumor cell apoptosis. J Biol Chem 283: 5188-5194.

64. Cappello F, David S, Rappa F, Bucchieri F, Marasà L, et al. (2005) The expression of HSP60 and HSP10 in large bowel carcinomas with lymph node metastase. BMC Cancer 5: 139.

65. Ciocca DR, Calderwood SK (2005) Heat shock proteins in cancer: diagnostic, prognostic, predictive, and treatment implications. Cell Stress Chaperones 10: 86-103.

66. Korennykh A, Walter P (2012) Structural basis of the unfolded protein response. Annu Rev Cell Dev Biol 28: 251-277.

67. Wang Q, He Z, Zhang J, Wang Y, Wang T, et al. (2005) Overexpression of endoplasmic reticulum molecular chaperone GRP94 and GRP78 in human lung cancer tissues and its significance. Cancer Detect Prev 29: 544-551.

68. Pratt WB (1998) The hsp90-based chaperone system: involvement in signal transduction from a variety of hormone and growth factor receptors. Proc Soc Exp Biol Med 217: 420-434.

69. Schaffitzel E, Rüdiger S, Bukau B, Deuerling E (2001) Functional dissection of trigger factor and DnaK: interactions with nascent polypeptides and thermally denatured proteins. Biol Chem 382: 1235-1243.

70. Young JC, Barral JM, Ulrich Hartl F (2003) More than folding: localized functions of cytosolic chaperones. Trends Biochem Sci 28: 541-547.

71. Bercovich B, Stancovski I, Mayer A, Blumenfeld N, Laszlo A, et al. (1997) Ubiquitin-dependent degradation of certain protein substrates *in vitro* requires the molecular chaperone Hsc70. J Biol Chem 272: 9002-9010.

72. Murphy ME (2013) The HSP70 family and cancer. Carcinogenesis 34: 1181-1188.

73. Zourlidou A, Payne Smith MD, Latchman DS (2004) HSP27 but not HSP70 has a potent protective effect against alpha-synuclein-induced cell death in mammalian neuronal cells. J Neurochem 88: 1439-1448.

74. Li H, Liu L, Xing D, Chen WR (2010) Inhibition of the JNK/Bim pathway by Hsp70 prevents Bax activation in UV-induced apoptosis. FEBS Lett 584: 4672-4678.

75. Beere HM (2005) Death versus survival: functional interaction between the apoptotic and stress-inducible heat shock protein pathways. J Clin Invest 115: 2633-2639.

76. Juhasz K, Lipp AM, Nimmervoll B, Sonnleitner A, Hesse J, et al. (2013) The complex function of hsp70 in metastatic cancer. Cancers (Basel) 6: 42-66.

77. Powers MV, Jones K, Barillari C, Westwood I, van Montfort RL, et al. (2010) Targeting HSP70: the second potentially druggable heat shock protein and molecular chaperone? Cell Cycle 9: 1542-1550.

78. Gabai VL, Meriin AB, Yaglom JA, Volloch VZ, Sherman MY (1998) Role of Hsp70 in regulation of stress-kinase JNK: implications in apoptosis and aging. FEBS Lett 438: 1-4.

79. Li J, Soroka J, Buchner J (2012) The Hsp90 chaperone machinery: conformational dynamics and regulation by co-chaperones. Biochim Biophys Acta 1823: 624-635.

80. Nahleh Z, Tfayli A, Najm A, El Sayed A, Nahle Z (2012) Heat shock proteins in cancer: targeting the 'chaperones'. Future Med Chem 4: 927-935.

81. Patury S, Miyata Y, Gestwicki JE (2009) Pharmacological targeting of the Hsp70 chaperone. Curr Top Med Chem 9: 1337-1351.

82. Gabai VL, Budagova KR, Sherman MY (2005) Increased expression of the major heat shock protein Hsp72 in human prostate carcinoma cells is dispensable for their viability but confers resistance to a variety of anticancer agents. Oncogene 24: 3328-3338.

83. Bottoni P, Giardina B, Scatena R (2009) Proteomic profiling of heat shock proteins: An emerging molecular approach with direct pathophysiological and clinical implications. Proteomics Clin Appl 3: 636-653.

84. Powers MV, Clarke PA, Workman P (2008) Dual targeting of HSC70 and HSP72 inhibits HSP90 function and induces tumor-specific apoptosis. Cancer Cell 14: 250-262.

85. Neganova I, Lako M (2008) G1 to S phase cell cycle transition in somatic and embryonic stem cells. J Anat 213: 30-44.

86. Sreedhar AS, Kalmár E, Csermely P, Shen YF (2004) Hsp90 isoforms: functions, expression and clinical importance. FEBS Lett 562: 11-15.

87. Dias S, Shmelkov SV, Lam G, Rafii S (2002) VEGF(165) promotes survival of leukemic cells by Hsp90-mediated induction of Bcl-2 expression and apoptosis inhibition. Blood 99: 2532-2540.

88. Whitesell L, Lindquist SL (2005) HSP90 and the chaperoning of cancer. Nat Rev Cancer 5: 761-772.

89. Zhao R, Kakihara Y, Gribun A, Huen J, Yang G, et al. (2008) Molecular chaperone Hsp90 stabilizes Pih1/Nop17 to maintain R2TP complex activity that regulates snoRNA accumulation. J Cell Biol 180: 563-578.

90. Lanneau D, de Thonel A, Maurel S, Didelot C, Garrido C (2007) Apoptosis versus cell differentiation: role of heat shock proteins HSP90, HSP70 and HSP27. Prion 1: 53-60.

91. Ciocca DR, Arrigo AP, Calderwood SK (2013) Heat shock proteins and heat shock factor 1 in carcinogenesis and tumor development: an update. Arch Toxicol 87: 19-48.

92. Easton DP, Kaneko Y, Subjeck JR (2000) The hsp110 and Grp1 70 stress proteins: newly recognized relatives of the Hsp70s. Cell Stress Chaperones 5: 276-290.

93. Romanucci M, Bastow T, Della Salda L (2008) Heat shock proteins in animal neoplasms and human tumours--a comparison. Cell Stress Chaperones 13: 253-262.

94. Hosaka S, Nakatsura T, Tsukamoto H, Hatayama T, Baba H, et al. (2006) Synthetic small interfering RNA targeting heat shock protein 105 induces apoptosis of various cancer cells both *in vitro* and *in vivo*. Cancer Sci 97: 623-632.

95. Slaby O, Sobkova K, Svoboda M, Garajova I, Fabian P, et al. (2009) Significant overexpression of Hsp110 gene during colorectal cancer progression. Oncol Rep 21: 1235-1241.

96. Kim JH, Kang GH (2014) Molecular and prognostic heterogeneity of microsatellite-unstable colorectal cancer. World J Gastroenterol 20: 4230-4243.

97. Dorard C, de Thonel A, Collura A, Marisa L, Svrcek M, et al. (2011) Expression of a mutant HSP110 sensitizes colorectal cancer cells to chemotherapy and improves disease prognosis. Nat Med 17: 1283-1289.

98. Ciechanover A (1998) The ubiquitin-proteasome pathway: on protein death and cell life. EMBO J 17: 7151-7160.

99. Pickart CM (2001) Ubiquitin enters the new millennium. Mol Cell 8: 499-504.

100. Varshavsky A (2003) The N-end rule and regulation of apoptosis. Nat Cell Biol 5: 373-376.

101. Ditzel M, Wilson R, Tenev T, Zachariou A, Paul A, et al. (2003) Degradation of DIAP1 by the N-end rule pathway is essential for regulating apoptosis. Nat Cell Biol 5: 467-473.

102. Scheffner M, Huibregtse JM, Vierstra RD, Howley PM (1993) The HPV-16 E6 and E6-AP complex functions as a ubiquitin-protein ligase in the ubiquitination of p53. Cell 75: 495-505.

103. Freemont PS (2000) RING for destruction? Curr Biol 10: 84-87.

104. Nakayama KI, Nakayama K (2006) Ubiquitin ligases: cell-cycle control and cancer. Nat Rev Cancer 6: 369-381.

105. Sun Y (2006) E3 ubiquitin ligases as cancer targets and biomarkers. Neoplasia 8: 645-654.

106. Sharma P, Nag A (2014) CUL4A ubiquitin ligase: a promising drug target for cancer and other human diseases. Open Biol 4: 130217.

107. Zhao Y, Sun Y (2013) Cullin-RING Ligases as attractive anti-cancer targets. Curr Pharm Des 19: 3215-3225.

108. Hannah J, Zhou PB (2013) The CUL4A ubiquitin ligase is a potential therapeutic target in skin cancer and other malignancies. Chin J Cancer 32: 478-482.

109. Lee J, Zhou P (2012) Pathogenic Role of the CRL4 Ubiquitin Ligase in Human Disease. Front Oncol 2: 21.

110. Korzeniewski N, Zheng L, Cuevas R, Parry J, Chatterjee P, et al. (2009) Cullin 1 functions as a centrosomal suppressor of centriole multiplication by regulating polo-like kinase 4 protein levels. Cancer Res 69: 6668-6675.

111. Chen C, Seth AK, Aplin AE (2006) Genetic and expression aberrations of E3 ubiquitin ligases in human breast cancer. Mol Cancer Res 4: 695-707.

112. Zhao KW, Sikriwal D, Dong X, Guo P, Sun X, et al. (2011) Oestrogen causes degradation of KLF5 by inducing the E3 ubiquitin ligase EFP in ER-positive breast cancer cells. Biochem J 437: 323-333.

113. Urano T, Saito T, Tsukui T, Fujita M, Hosoi T, et al. (2002) Efp targets 14-3-3 sigma for proteolysis and promotes breast tumour growth. Nature 417: 871-875.

114. Horie K, Urano T, Inoue S (2003) Efp as a new molecular target for breast cancer therapy. Anticancer Drugs 14: 1-2.

115. Burger AM, Gao Y, Amemiya Y, Kahn HJ, Kitching R, et al. (2005) A novel RING-type ubiquitin ligase breast cancer-associated gene 2 correlates with outcome in invasive breast cancer. Cancer Res 65: 10401-10412.

116. Wang Z, Nie Z, Chen W, Zhou Z, Kong Q, et al. (2013) RNF115/BCA2 E3 ubiquitin ligase promotes breast cancer cell proliferation through targeting p21Waf1/Cip1 for ubiquitin-mediated degradation. Neoplasia 15: 1028-1035.

117. Hao JJ, Shi ZZ, Zhao ZX, Zhang Y, Gong T, et al. (2012) Characterization of genetic rearrangements in esophageal squamous carcinoma cell lines by a combination of M-FISH and array-CGH: further confirmation of some split genomic regions in primary tumors. BMC Cancer 12: 367.

118. Tedesco D, Lukas J, Reed SI (2002) The pRb-related protein p130 is regulated by phosphorylation-dependent proteolysis via the protein-ubiquitin ligase SCF(Skp2). Genes Dev 16: 2946-2957.

119. Kudo Y, Guardavaccaro D, Santamaria PG, Koyama-Nasu R, Latres E, et al. (2004) Role of F-box protein betaTrcp1 in mammary gland development and tumorigenesis. Mol Cell Biol 24: 8184-8194.

120. Wan M, Huang J, Jhala NC, Tytler EM, Yang L, et al. (2005) SCF(β-TrCP1) controls Smad4 protein stability in pancreatic cancer cells. Am J Pathol 166: 1379-1392.

121. Busino L, Donzelli M, Chiesa M, Guardavaccaro D, Ganoth D, et al. (2003) Degradation of Cdc25A by β-TrCP during S phase and in response to DNA damage. Nature 426: 87-91.

122. Chen C, Zhou Z, Ross JS, Zhou W, Dong JT (2007) The amplified WWP1 gene is a potential molecular target in breast cancer. Int J Cancer 121: 80-87.

123. Yeung B, Ho KC, Yang X (2013) WWP1 E3 ligase targets LATS1 for ubiquitin-mediated degradation in breast cancer cells. PLoS One 8: 61027.

124. Carrano AC, Dillin A2, Hunter T3 (2014) A Krüppel-like factor downstream of the E3 ligase WWP-1 mediates dietary-restriction-induced longevity in Caenorhabditis elegans. Nat Commun 5: 3772.

125. Yang B, Kumar S (2010) Nedd4 and Nedd4-2: closely related ubiquitin-protein ligases with distinct physiological functions. Cell Death Differ 17: 68-77.

126. Cho HS, Kelly JD, Hayami S, Toyokawa G, Takawa M, et al. (2011) Enhanced expression of EHMT2 is involved in the proliferation of cancer cells through negative regulation of SIAH1. Neoplasia 13: 676-684.

127. Bruzzoni-Giovanelli H, Fernandez P, Veiga L, Podgorniak MP, Powell DJ, et al. (2010) Distinct expression patterns of the E3 ligase SIAH-1 and its partner Kid/KIF22 in normal tissues and in the breast tumoral processes. J Exp Clin Cancer Res 29: 10.

128. Susini L, Passer BJ, Amzallag-Elbaz N, Juven-Gershon T, Prieur S, et al. (2001) Siah-1 binds and regulates the function of Numb. Proc Natl Acad Sci USA 98: 15067-15072.

129. Germani A, Prabel A, Mourah S, Podgorniak MP, Di Carlo A, et al. (2003) SIAH-1 interacts with CtIP and promotes its degradation by the proteasome pathway. Oncogene 22: 8845-8851.

130. Knauer SK, Mahendrarajah N2, Roos WP2, Krämer OH3 (2015) The inducible E3 ubiquitin ligases SIAH1 and SIAH2 perform critical roles in breast and prostate cancers. Cytokine Growth Factor Rev 26: 405-413.

131. Silver DP, Livingston DM (2012) Mechanisms of BRCA1 tumor suppression. Cancer Discov 2: 679-684.

132. Starita LM, Machida Y, Sankaran S, Elias JE, Griffin K, et al. (2004) BRCA1-dependent ubiquitination of gamma-tubulin regulates centrosome number. Mol Cell Biol 24: 8457-8466.

133. Dong Y, Hakimi MA, Chen X, Kumaraswamy E, Cooch NS, et al. (2003) Regulation of BRCC, a holoenzyme complex containing BRCA1 and BRCA2, by a signalosome-like subunit and its role in DNA repair. Mol Cell 12: 1087-1099.

134. Clark SL, Rodriguez AM, Snyder RR, Hankins GD, Boehning D (2012) Structure-Function Of The Tumor Suppressor BRCA1. Comput Struct Biotechnol J 1.

135. Hou YC, Deng JY (2015) Role of E3 ubiquitin ligases in gastric cancer. World J Gastroenterol 21: 786-793.

136. Kashima L, Idogawa M, Mita H, Shitashige M, Yamada T, et al. (2012) CHFR protein regulates mitotic checkpoint by targeting PARP-1 protein for ubiquitination and degradation. J Biol Chem 287: 12975-12984.

137. Cheung HW, Ching YP, Nicholls JM, Ling MT, Wong YC, et al. (2005) Epigenetic inactivation of CHFR in nasopharyngeal carcinoma through promoter methylation. Mol Carcinog 43: 237-245.

138. Laszlo GS, Cooper JA (2009) Restriction of Src activity by Cullin-5. Curr Biol 19: 157-162.

139. Wang Z, Inuzuka H, Fukushima H, Wan L, Gao D, et al. (2011) Emerging roles of the FBW7 tumour suppressor in stem cell differentiation. EMBO Rep 13: 36-43.

140. Onoyama I, Tsunematsu R, Matsumoto A, Kimura T, de Alborán IM, et al. (2007) Conditional inactivation of Fbxw7 impairs cell-cycle exit during T cell differentiation and results in lymphomatogenesis. J Exp Med 204: 2875-2888.

141. Wang Z, Liu P, Inuzuka H, Wei W (2014) Roles of F-box proteins in cancer. Nat Rev Cancer 14: 233-247.

142. Cesari R, Martin ES, Calin GA, Pentimalli F, Bichi R, et al. (2003) Parkin, a gene implicated in autosomal recessive juvenile parkinsonism, is a candidate tumor suppressor gene on chromosome 6q25-q27. Proc Natl Acad Sci USA 100: 5956-5961.

143. Tay SP, Yeo CW, Chai C, Chua PJ, Tan HM, et al. (2010) Parkin enhances the expression of cyclin-dependent kinase 6 and negatively regulates the proliferation of breast cancer cells. J Biol Chem 285: 29231-29238.

144. Dawson TM, Dawson VL (2010) The role of parkin in familial and sporadic Parkinson's disease. Mov Disord 25 1: 32-39.

145. Lininger RA, Park WS, Man YG, Pham T, MacGrogan G, et al. (1998) LOH at 16p13 is a novel chromosomal alteration detected in benign and malignant microdissected papillary neoplasms of the breast. Hum Pathol 29: 1113-1118.

146. Inoue Y, Imamura T (2008) Regulation of TGF-beta family signaling by E3 ubiquitin ligases. Cancer Sci 99: 2107-2112.

147. Wang Y, Ren F, Wang Y, Feng Y, Wang D, et al. (2014) CHIP/Stub1 functions as a tumor suppressor and represses NF-κB-mediated signaling in colorectal cancer. Carcinogenesis 35: 983-991.

148. Tsai YC, Mendoza A, Mariano JM, Zhou M, Kostova Z, et al. (2007) The ubiquitin ligase gp78 promotes sarcoma metastasis by targeting KAI1 for degradation. Nat Med 13: 1504-1509.

149. Goka ET, Lippman ME (2015) Loss of the E3 ubiquitin ligase HACE1 results in enhanced Rac1 signaling contributing to breast cancer progression. Oncogene 34: 5395-5405.

150. Yu P, Chen Y, Tagle DA, Cai T (2002) PJA1, encoding a RING-H2 finger ubiquitin ligase, is a novel human X chromosome gene abundantly expressed in brain. Genomics 79: 869-874.

151. Paolino M, Choidas A, Wallner S, Pranjic B, Uribesalgo I, et al. (2014) The E3 ligase Cbl-b and TAM receptors regulate cancer metastasis via natural killer cells. Nature 507: 508-512.

152. Ramamoorthy S, Nawaz Z (2008) E6-associated protein (E6-AP) is a dual function coactivator of steroid hormone receptors. Nucl Recept Signal 6: 006.

153. [No authors listed] (2013) The MULE/HUWE1 E3 ubiquitin ligase is a tumor suppressor. Cancer Discov 3: 32.

154. Lu G, Zhang Q, Huang Y, Song J, Tomaino R, et al. (2014) Phosphorylation of ETS1 by Src family kinases prevents its recognition by the COP1 tumor suppressor. Cancer Cell 26: 222-234.

155. Bromberg KD, Kluger HM, Delaunay A, Abbas S, DiVito KA, et al. (2007) Increased expression of the E3 ubiquitin ligase RNF5 is associated with decreased survival in breast cancer. Cancer Res 67: 8172-8179.

156. Cheng H, Wang A, Meng J, Zhang Y, Zhu D (2015) Enhanced metastasis in RNF13 knockout mice is mediated by a reduction in GM-CSF levels. Protein Cell 6: 746-756.

157. Ju UI, Park JW, Park HS, Kim SJ, Chun YS (2015) FBXO11 represses cellular response to hypoxia by destabilizing hypoxia-inducible factor-1α mRNA. Biochem Biophys Res Commun 464: 1008-1015.

158. Li C, Ao J, Fu J, Lee DF, Xu J, et al. (2011) Tumor-suppressor role for the SPOP ubiquitin ligase in signal-dependent proteolysis of the oncogenic co-activator SRC-3/AIB1. Oncogene 30: 4350-4364.

159. Zhang WL, Zhang JH1, Wu XZ2, Yan T3, Lv W3 (2015) miR-15b promotes epithelial-mesenchymal transition by inhibiting SMURF2 in pancreatic cancer. Int J Oncol 47: 1043-1053.

160. Zhu J, Zhao C, Kharman-Biz A, Zhuang T, Jonsson P, et al. (2014) The atypical ubiquitin ligase RNF31 stabilizes estrogen receptor α and modulates estrogen-stimulated breast cancer cell proliferation. Oncogene 33: 4340-4351.

161. Shinada K, Tsukiyama T, Sho T, Okumura F, Asaka M, et al. (2011) RNF43 interacts with NEDL1 and regulates p53-mediated transcription. Biochem Biophys Res Commun 404: 143-147.

The Author(s) *BMC Bioinformatics* 2016, **17**(Suppl 19):512
DOI 10.1186/s12859-016-1374-1

BMC Bioinformatics

RESEARCH Open Access

Molecular modeling and lead design of substituted zanamivir derivatives as potent anti-influenza drugs

Dhwani Dholakia[1], Sukriti Goyal[2], Salma Jamal[2], Aditi Singh[3], Asmita Das[1] and Abhinav Grover[4*]

From 15th International Conference On Bioinformatics (INCOB 2016)
Queenstown, Singapore. 21-23 September 2016

Abstract

Background: Influenza virus spreads infection by two main surface glycoproteins, namely hemagglutinin (HA) and neuraminidase (NA). NA cleaves the sialic acid receptors eventually releasing newly formed virus particles which then invade new cells. Inhibition of NA could limit the replication of virus to one round which is insufficient to cause the disease.

Results: An experimentally reported series of acylguanidine zanamivir derivatives was used to develop GQSAR model targeting NA in different strains of influenza virus, H1N1 and H3N2. A combinatorial library was developed and their inhibitory activities were predicted using the GQSAR model.

Conclusion: The top leads were analyzed by docking which revealed the binding modes of these inhibitors in the active site of NA (150-loop). The top compound (AMA) was selected for carrying out molecular dynamics simulations for 15 ns which provided insights into the time dependent dynamics of the designed leads. AMA possessed a docking score of −8.26 Kcal/mol with H1N1 strain and −7.00 Kcal/mol with H3N2 strain. Ligand-bound complexes of both H1N1 and H3N2 were observed to be stable for 11 ns and 7 ns respectively. ADME descriptors were also calculated to study the pharmacokinetic properties of AMA which revealed its drug-like properties.

Keywords: Neuraminidase, H1N1, H3N2, NA, Influenza, QSAR

Background

Type A influenza virus, member of orthomyxoviridae family [1] is one of the most lethal and virulent strains of influenza virus which has been responsible for worldwide havoc including seasonal epidemics and major pandemic breakthroughs [2]. Pandemic Influenza could have originated via two major mechanisms, either by direct transmission from birds to humans as in 1918 "Spanish Influenza" virus (H1N1) or via genetic reassortment between avian influenza virus and human influenza virus as happened in the case of 1968 "Hong Kong" influenza virus (H3N2) [3]. It is a highly contagious virus and causes severe respiratory associated problems. Complications include post influenza encephalitis, secondary bacterial pneumonia and change in cardiac electrocardiogram [4, 5].

Subtypes of the type A virus has been classified based on the serological activity of the glycoprotein antigens hemagglutinin (HA) and neuraminidase (NA). Sixteen serotypes of HA have been found to circulate in mammalian and avian hosts. HA is a surface envelop protein of influenza virus and performs crucial viral functions like host recognition and membrane fusion [6]. HA often recognizes sialic acid receptors found in the human upper respiratory tract which act as initial key step of viral infection [7]. The second glycoprotein NA is a sialidase which destroys HA present on the surface of the virus allowing release of the infected viral progeny from infected cell thus preventing their self-aggregation [8]. Thus, inhibiting NA prevents second round of

* Correspondence: abhinavgr@gmail.com; agrover@jnu.ac.in
[4]School of Biotechnology, Jawaharlal Nehru University, New Delhi 110067, India
Full list of author information is available at the end of the article

BioMed Central

© The Author(s). 2016 **Open Access** This article is distributed under the terms of the Creative Commons Attribution 4.0 International License (http://creativecommons.org/licenses/by/4.0/), which permits unrestricted use, distribution, and reproduction in any medium, provided you give appropriate credit to the original author(s) and the source, provide a link to the Creative Commons license, and indicate if changes were made. The Creative Commons Public Domain Dedication waiver (http://creativecommons.org/publicdomain/zero/1.0/) applies to the data made available in this article, unless otherwise stated.

replication of influenza virus therefore culminating further influenza infection. Sequence analysis of nine subtypes of NA separates them into two major phylogenetic groups. Group 1 consists of N1, N4, N5 and N8 while group 2 consists of N2, N3, N6, N7 and N9.

Active site of NA is lined by 150-loop which includes residues from 147 to152 and is present in two forms. First is an open conformation which adopts 150-loop formation and the other is a closed conformation in which active site lacks 150-loop conformation [9]. Analysis of X-ray crystal structure [10] shows an open conformation for NA in group 1 and a closed conformation for those in group 2. However molecular dynamics simulation suggested the presence of 150-loop not only in group 1 but also in group 2 [9]. These findings provide deep insight into the design and synthesis of new NA inhibitors targeting the 150-loop lining cavity. Based on these structures FDA approved drugs [11] like Oseltamivir (Tamiflu), Zanamivir (Relenza) and Peramivir are commercially available to treat infected patients. Oseltamivir, an oral prodrug administered as phosphate, is hydrolysed hepatically to its active form carboxylate while Zanamivir is administered via nasal inhalation because of high polar compounds. To alleviate the potential consequence of suboptimal bioavailability and clumsy inhalational devices, an intravenous peramivir antiviral drug was used. However, this type of treatment has limited control as the developed vaccines frequently become ineffective because of mutation in influenza viral antigen taking place at a rapid rate in forms of antigenic shift or drift resulting in resistance [12]. Thus a search for new influenza drug with broad spectrum activity is the need of hour.

Considerable amount of work has been done to target the 150-loop lining cavity through modification of the existing inhibitors by attaching various additional groups with appropriate size, shape and hydrophobicity [2]. *In silico* methods provide substantial contribution to drug design and development of lead compounds in limited time and resources. Quantitative structure activity relationship (QSAR) is a method of ligand-based drug designing that establishes relationships between structure and inhibitory activity of inhibitors. Group-based QSAR (GQSAR) gives flexibility to traditional QSAR methods by calculating descriptors for the fragment of a molecule rather than calculating descriptors for whole molecule [13–16]. Unlike the traditional QSAR methods, GQSAR can be applied to both congeneric as well as non-congeneric series of compounds.

In this study we developed a novel GQSAR model based on congeneric series of acylguanidine zanamivir derivatives [17–19]. Same set of congeneric series were counter screened against NA of both H1N1 and H3N2. The main purpose of our study was to develop a robust GQSAR model to identify relation between structure and biological activity of the set of zanamivir derivatives as a function of fragments done at substitution site. Developed model predicted the relationship between anti-influenza activity and electro-chemical properties of the derivatives with high efficiency. Various descriptors essential for effective interaction between inhibitors and the active site of target were identified. An attempt has also been made to understand effect of different substituents at the substitution site in the template structure. In addition to building of GQSAR model, a comprehensive computational insights into binding action of lead compound to targets has also been provided.

Methods

Preparation and optimization of data set

Marvin sketch (ChemAxon Ltd., https://www.chemaxon.com/products/marvin/) was used to draw experimentally reported 24 acylguanidine zanamivir derivatives. The compounds were drawn in 2-D format and then converted to 3-D using VlifeEngine module of VLifeMDS [20]. The prepared compounds were minimized using force field batch minimization platform of VlifeEngine ver 4.3 provided by Vlife Sciences, Pune on Intel® Xeon(R).

Calculation of descriptors for GQSAR model development

In this GQSAR study, various descriptors correlating the inhibitory activity of molecules were identified as detailed in our previous publications [13–15]. GQSAR model was built using the GQSAR module of VlifeMDS [15]. The common scaffold, representative of all the structures was used as a template for the GQSAR study. Using Modify module of VLifeMDS, template (Fig. 1) was created by replacing dummy atoms at R1 on the common moiety i.e. template. Optimized set of compounds and template molecule were then imported for template based GQSAR model building. Experimentally reported IC50 values (half maximal inhibitory concentration) were converted to pIC50 scale (–log IC50) to narrow down the range (Additional file 1: Table S1). Thus, a higher value of pIC50 exhibits a more potent compound. These values were then manually incorporated in VLifeMDS. Physicochemical 2-D descriptors were calculated for functional group at substitution site (R1). Total of 101 descriptors out of 343 descriptors were further used for QSAR analysis while rest were removed owing to invariability.

Development of GQSAR model using multiple regression method

For development of a robust and efficient model, the data set of compound was divided into training and test set. The data set was divided into training and test set by random distribution of 70% into training and

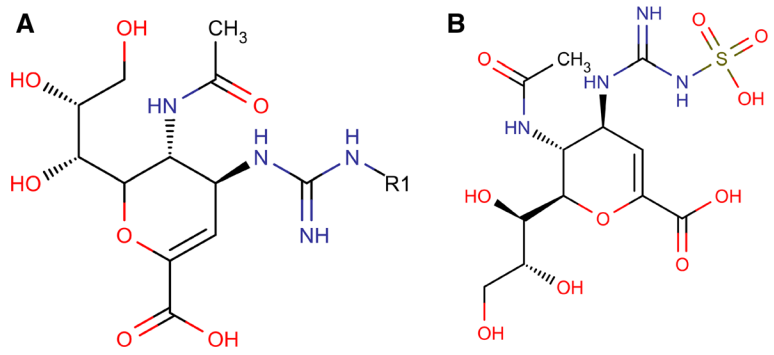


Fig. 1 a Representation of common template for acylguanidine zanamivir derived compounds. **b** Designed novel lead compound AMA

remaining 30% into test set. For GQSAR against NA of H1N1, 16 molecules were grouped into training set while8 molecules namely f, l, n, o, q, t, y and Ae were grouped in test set. For the second NA target of H3N2, 16 molecules were chosen for training set and 8 molecules namely ac, ae, j, m, q, r, w, y were selected for test set. After division of training and test set, the unicolumn statistics for both the training and test sets were calculated which provides validation of the chosen training and test sets. Stepwise-forward method was used as variable selection. The next step involved, building of a GQSAR model using multiple regression analysis which predicts the activity using the selected descriptors. Regression analysis is process which estimates the relationship between a dependent variable and one or more independent variable. For this model Column containing the activity values (pIC50) was selected as dependent variable while rests other were selected as independent variables. In general, multiple regression can be explained in the terms of Eq. 1.

$$Y = \alpha + \beta_0 + \beta_1 X_1 + \beta_2 X_2 + \cdots + \beta_n X_n \qquad (1)$$

Where Y is the independent variable, α is the intercept, β_n is the slope for n^{th} independent variable X.

Validation and evaluation of the developed model

This step was done to test both the stability and predictive ability of the developed GQSAR models. Various statistical parameters [21] like k (number of variables), n (number of compounds), r^2(Squared degree correlation), q^2(cross validated correlation coefficient), Pred_r^2(for external test set), Z score (Randomization test), F-Test, best_ran_q^2 (Highest value of q^2 in randomization test), best_ran_r^2 (highest value of r^2 in randomized test) and standard error were calculated to test goodness of fit of the developed model. For a model to be robust, values should be above threshold i.e. $r^2 > 0.6$, $q^2 > 0.6$, and Pred_$r^2 > 0.5$ [21–23]. Higher values of F-Test and lower values of standard error of Pred_r^2se, r^2_se and q^2_se indicate a statistically reliable model. Internal and external validation of the model was performed as detailed in our earlier publications [13–16].

Development of combinatorial library

Combinatorial library was generated using the Leadgrow module of VLifeMDS by substituting various chemical groups at the substitution site R1 site. The library generated consisted of 189 molecules. Prediction of activity and descriptor for each of the substituted site was calculated using the developed GQSAR model via generic prediction module.

Protein and ligand preparation for docking studies

The protein crystal structure of both H1N1 (PDB ID: 3BEQ) and H3N2 (PDB ID: 4GZ0) were retrieved from protein databank. Since the structures obtained were homomer complex structures, only the monomer chain was selected and rest including water and non-bonded atoms were removed using Accelyrs Viewer lite 5.0 [2, 15, 19]. The combinatorial library compounds with good predicted activity were selected and prepared using Ligprep and protein structure was prepared using Protein Preparation wizard [24–27].

Receptor grid generation

A Glide scoring grid around the receptor was generated using receptor grid generation platform of Schrodinger's Glide modules [28]. This utility of Glide defines receptor structure, determines and mark active site position. All the parameters were kept default and a grid of size 20 × 20 × 20 Å with inner box size of 10 × 10 × 10 Å was generated.

Docking and scoring

The prepared combinatorial library compounds were docked against NA of H1N1 and H3N2 using extra precision GlideXP platform. The selected poses were further minimized on pre-computed OPLS-2005 electrostatic and van der Waals grid for receptor. Ultimately lowest energy poses were subjected to Monte

Carlo minimization and rescored using Glide Score function. The complexes with least XP score (highest magnitude) were selected for molecular dynamics simulations.

ADME prediction

Absorption, distribution, metabolism and elimination (ADME) of the selected compounds were predicted *in silico* using QikProp module of Schrödinger suite [29]. Ligands were initially prepared using LigPrep. It predicts physically significant descriptors and relevant pharmaceutical properties. In addition to the molecular descriptors, QikProp also provides their range values by comparing an individual molecule property with those known 95% drug.

Molecular dynamics simulations

Docked complex of protein and ligand were prepared in protein preparation wizard of maestro. Desmond software was then used to study the molecular dynamics of ligand inside the active site of NA for both H1N1 and H3N2 using the Optimized potentials for liquid simulations 2005 (OLPS) force field [30]. Structures were uploaded in Desmond for further process of molecular dynamics simulations using parameters as mentioned in our earlier publications [16, 31]. The docked complexes were then simulated for 15 ns using above parameters. Frames of trajectory were recorded for each 10 ns time step. The root mean square deviations (RMSD) for the docked complexes were calculated for the entire simulations trajectory with reference to their respective frames. Radius of Gyration and hydrogen bond analysis were carried out for all the frames of 15 ns MD simulation.

Results and discussion

Separation of data into training and test set

A QSAR model was developed for acylguanidine zanamivir derivatives considering the activity and various physiochemical descriptors for both H1N1 and H3N2. Seventy percent of total compounds were selected as training set and the rest as test set. Separation of the dataset into training and test set was validated using unicolumn statistics (Tables 1 and 2) according to which maximum of test should be less than maximum of training set and minimum of test should be greater than minimum of training set [32].

Table 1 Unicolumn statistics for training and test sets for *influenza* H1N1 Neuraminidase inhibitory activity

Data set	Average	Max.	Min.	Std dev	Sum
Training	−2.4963	−1.3032	−4.5955	0.6975	−39.9406
Test	−2.5855	−1.7396	−4.5396	0.8352	−20.6838

Table 2 Unicolumn statistics for training and test sets for *influenza* H3N2 Neuraminidase inhibitory activity

Data set	Average	Max.	Min.	Std dev	Sum
Training	−2.5530	−1.7657	−4.4713	0.6407	−40.8485
Test	−2.5821	−1.4065	−4.5832	0.9057	−20.6564

Analysis of GQSAR models developed against H1N1 and H3N2

A robust GQSAR model was developed which explained correlation between the physiochemical parameters and contribution of each substitution site. Several models were developed and the best model with significant values based on statistical parameters was chosen.

H1N1 model

The chosen model for H1N1 exhibited significant statistical values of r^2 (squared correlation coefficient) = 0.95, q^2 (cross-validated squared correlation coefficient) = 0.90, Pred_r^2 (predicted squared correlation coefficient) = 0.95, F-Test = 92.99 while standard errors were observed to be r^2_se = 0.15, q^2_se = 0.23, Pred_r^2se = 0.18. Low standard error values indicated absolute quality of the model.

Three descriptors namely R1-SdOEindex, R1-6ChainCount and R1-SssSE-index were selected by the model for all the compounds. The model had good internal and external prediction. The model can be given by the Eq. 2.

$$\begin{aligned} plC50 = (23.61 \ * \ R1\text{–}Sd0Eindex) \\ +(47.12 \ * \ R1\text{–}6ChainCount) \\ -(39.90 \ * \ R1\text{–}(SssSEindex) - 5.26. \end{aligned} \quad (2)$$

With n = 16, degree of freedom = 12, ZScore R^2 = 3.35, ZScore Q^2 = 0.69, "n" represents total number of compounds in the training set. The derived QSAR model shows a good correlation between aforementioned descriptors and biological activity as r^2 is 0.95 with minimum standard error of 0.15. The p-value was observed to be < 0.001 for both models. The model incorporates various descriptors as shown in Table 3. R1-SdOEindex which is an electro-*topological* descriptor gives information about the number of –OH groups connected with one double bond. The positive contribution of 58.02% (Fig. 2a) indicates that presence of –OH group increases

Table 3 Physicochemical descriptors with predicted activity values for training and test set for H1N1 model

Column	R1-SdOE-index	R1-6ChainCount	R1-SssSE-index	Prediction
1186	17.51	0	0	−1.1278
1185	17.20	0	0	−1.2019
1189	13.03	2	0	−1.2442

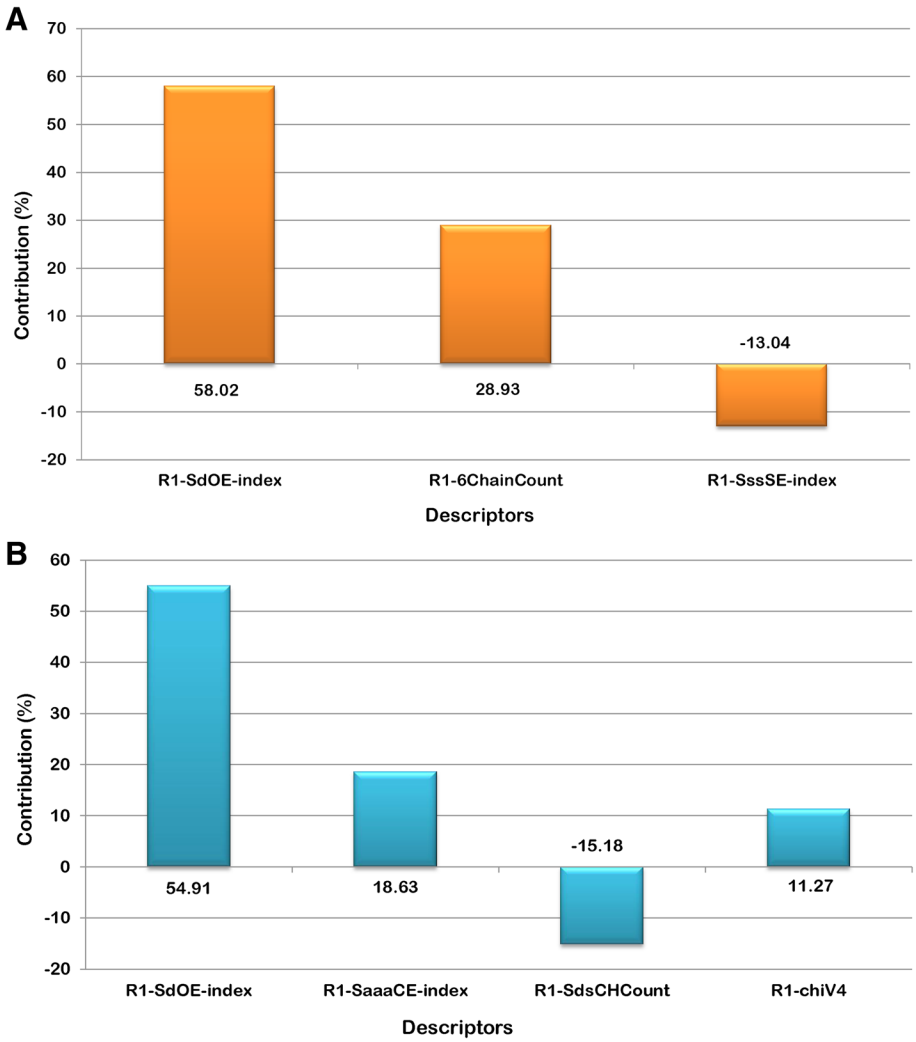


Fig. 2 Contribution plot of GQSAR model developed against (**a**) H1N1 and (**b**) H3N2

the inhibitory activity of the NA inhibitors. The percentage contribution is relative (not absolute) contribution of individual descriptors among the selected descriptors that are important for activity variation. These values are an indication of the relative importance of fragment-specific descriptors towards their contribution in the inhibitory activity of the ligands. Second descriptor, R1-6ChainCount is one of the most influential descriptors which signifies the total number of six-membered rings in a compound. Thus, a positive contribution of 28.93% indicates that the presence of aromatic compounds like phenyl could improve the inhibitory potency of compounds targeting NA. The third descriptor, R1-SssSEindex shows the importance of electronic environment of sulfur atom bonded with two single non-hydrogen atoms in the molecule. A negative contribution value of 13.04% suggests decrease in E-state contribution of either aromatic or free sulfur could improve the inhibitory activity. Thus, it can be deduced that the model is reliable and predictive, which can also be seen in the line graph of observed vs. predicted activity as shown in Fig. 3a and also the radar plots of observed and predicted activity for both training and test set (Fig. 4a and b).

H3N2 model

The model developed against H3N2 also showed satisfactory statistical values with $r^2 = 0.95$, $q^2 = 0.93$, Pred_r^2 = 0.87 and F-test = 61.02 and the standard errors as r^2_se = 0.15, q^2_se = 0.19, Pred_r^2_se = 0.32. A line graph of observed vs. predicted activity is shown in Fig. 3b. Low standard error and high values of internal and external prediction indicate robustness of the model. Thus, it can be inferred that the model is reliable and predictive, which can also be seen in the radar plots of the observed and predicted activity for both training and test set (Fig. 4c and d). Four descriptors were selected for

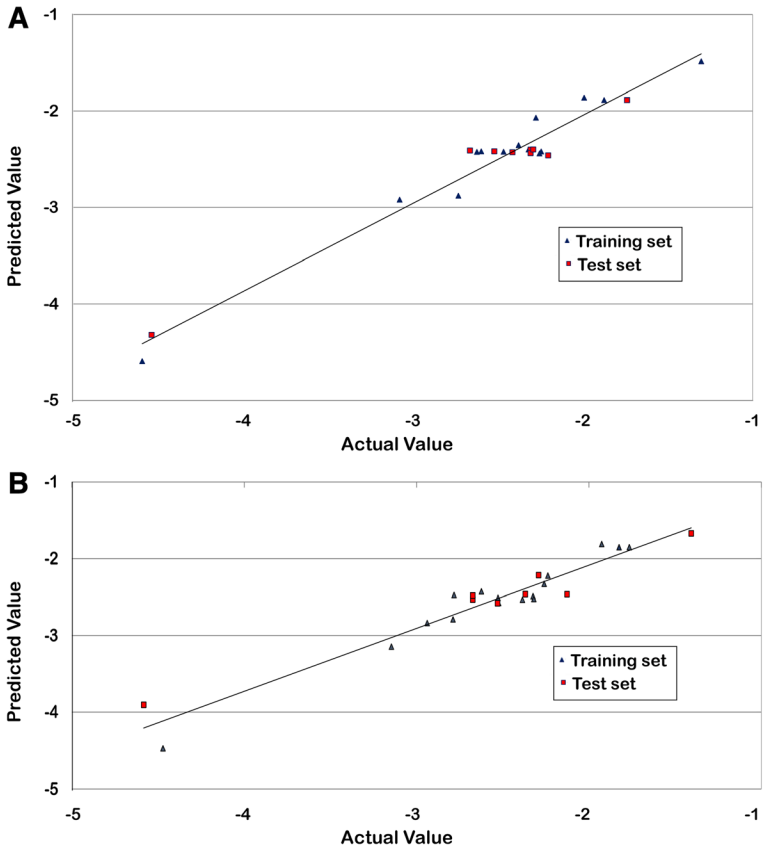


Fig. 3 Graph of observed vs. predicted activity for training and test set of (**a**) H1N1 and (**b**) H3N2

model namely R1-SdOEindex, R1-SaaaCEindex, R1-SdsCHcount, R1-chiV4. The developed model had a good internal as well as external prediction. The model can be explained via Eq. 3.

$$\begin{aligned} plC50 &+ (22.90 * R1{-}Sd0Eindex) \\ &+ (20.31 * R1{-}SaaaCE_index) \\ &- (25.88 * R1{-}SdsCHcount) \\ &+ (26.58 * R1{-}chiV4) - 4.83 \end{aligned} \tag{3}$$

with $n = 16$, degree of freedom = 11, ZScore R^2 = 5.94, ZScore Q^2 = 0.71, "n" represents total number of compounds in the training set.

The equation obtained above contains three physicochemical descriptors as shown in Table 4. Depending on the inhibitory activity of the data set compounds against H1N1 and H3N2, descriptors obtained for both the models were found to be different, indicating that the inhibitory activity of data set compounds is affected by different descriptors (as well as fragments) in the case of H1N1 and H3N2. R1-SdOEindex gives information about number of –OH groups connected with one double bond. The positive contribution of 54.91% (Fig. 2b) indicates that presence of –OH group at R1 position increases the inhibitory activity of the NA inhibitors. The second descriptor, R1-SaaaCEindex is an electro topological descriptor which indicates the number of carbon atoms that are connected with three aromatic bonds. A positive contribution (18.63%) indicates that increase in SaaaCE properties would enhance the inhibitory effect of lead compound. Another descriptor R1-SdsCHcount highlights the number of –CH groups connected with one double and one single bond in a molecule. Negative contribution of 15.18% indicates that increase in length of -CH atoms chain at the substitution site of NA inhibitors could be detrimental to the inhibitory activity. The last descriptor, R1-chiV4 is a steric property descriptor that helps in discriminating molecules according to size, degree of branching, shape and overall flexibility. A positive contribution of 11.27% indicates that increasing the steric properties at R1 will account for increased inhibitory activity.

Combinatorial library analysis and selection of lead compound

Combinatorial library was generated after analyzing the above two models and inhibitory activities of the

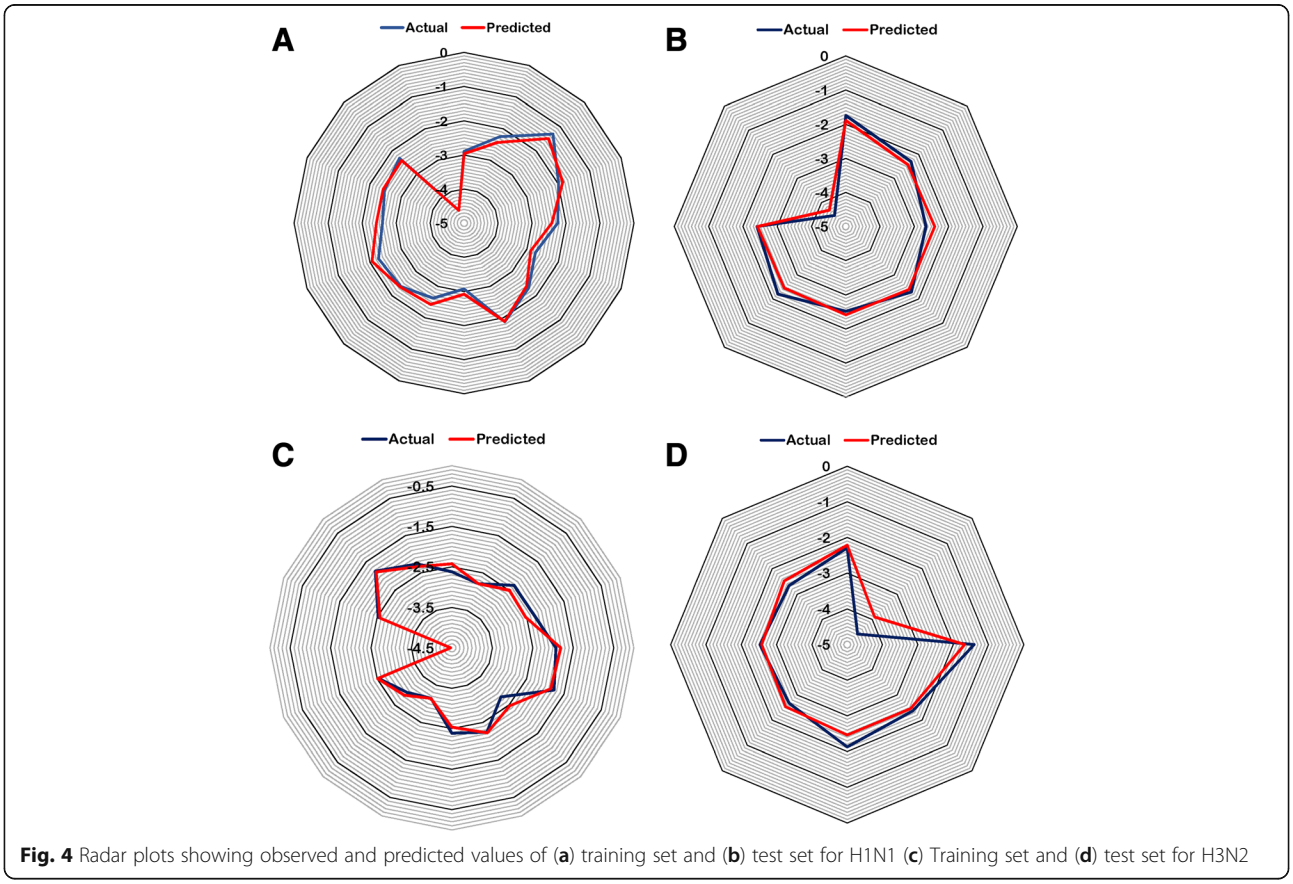


Fig. 4 Radar plots showing observed and predicted values of (**a**) training set and (**b**) test set for H1N1 (**c**) Training set and (**d**) test set for H3N2

developed compounds were predicted. Various substituting groups like alkanes, atoms, aromatic rings, ketone, ester etc. were added. The developed library contained 189 molecules. Molecules having activity values more than that reported in congeneric series were selected and the compound having highest predicted activity was chosen as lead compound [2]. It was seen that lead compound (Fig. 1b) was substituted with sulphite group at R1 position and had good predicted activity value for H1N1 and H3N2. Docking studies were performed on lead compound and further molecular dynamics was also performed to check its stability in aqueous environment.

ADME prediction

ADME properties were predicted using QikProp program (Schrodinger Inc). The IUPAC name of the lead compound docked is *(2R,3R,4S)-3-acetamido-4-{[(sulfoamino)methanimidoyl]amino}f-2-[(1R,2R)-1,2,3-trihydroxypropyl]-3,4-dihydro-2H-pyran-6-carboxylic acid* (AMA), details in the next section. It was found that AMA, highest scoring molecule followed three conditions of Lipinski rule of five. Various descriptors were evaluated for ADMET properties. The range values for each descriptor were given based on the known values of 95% of drugs. Molecular weight of AMA was found to be 412.4 (ideal molecular weight 130–725). Descriptors considered for drug permeability includes molecular volume of solute, hydrogen bond acceptor and liophilicity. Molecular volume of the compound was found to be 1107.4 (range value 500–2000) while hydrogen accepter was found to be 12.8 (range value 2–20). The latter parameter estimates average number of hydrogen bonds that would be accepted by the solute from water molecules in an aqueous solution. Rotatable bond

Table 4 Physicochemical descriptors with predicted activity values for training and test set for H3N2 model

Column	R1-SdOE-index	R1-SaaaCE-index	R1-SdsCHcount	R1-chiV4	Prediction
1186	17.51	0	0	0	−0.823
1185	17.200	0	0	0	−0.894
1184	16.25	0	0	0	−1.112

count is one of the widely used descriptor that inversely correlates with oral bioavailability. Rotatable bonds of this compound had value of 12 (Range 0–15). Various computational parameters were also calculated to analyze the solubility from its 2-D structure. Solvent accessible surface area (SASA) is one influential parameter, which defines the surface area of biomolecule that can be accessed by solvent. It is usually performed using 14 Å radius which generates various components *viz.* total SASA whose value was found to be 618.8 (Range values 300–1000), solute hydrophobic SASA (FOSA) with value 154.1 (Range value 0–750), solute Carbon Pi SASA (PISA) whose value was found to be 25.7 (range value 0–450) and solute weekly polar SASA (WPSA) which includes surface area for all sulphur, halogens and phosphorous atom with a value of 2 (Range value 0–175). Distribution of lead compound in solution is calculated using the ionization potential parameter which affects the availability of the compound for further physical, chemical or biological reactions. The calculated descriptor Solute Ionization Potential (eV) was found to be 9.7 (Range value 7.9–10.5). Various other electrochemical descriptors like Solute Globularity (Sphere = 1) = 0.837 (0.75/0.95) and Solute Electron Affinity (eV) = 1.262 (−0.9/1.7) were also calculated. This lead compound was found to be similar to various compounds like Voglibose 68.40, Valganciclovir 68.04, Aminopterin 65.66, Lisinopril 64.63 and Methotrexate 64.39. All these above parameters suggest that AMA can be a potential drug molecule and a good lead candidate.

Docking and molecular dynamics simulations studies of AMA with H1N1 and H3N2

Docking study of the top scored compound was performed using Glide to study the interaction with crystal structures of H1N1 and H3N2. The lead compound exhibited highest predicted activity in case of both H1N1 and H3N2 models. The activity of this compound was around ten-fold higher than the next candidate as predicted by both the QSAR models. Thus this compound with highest predicted activity was selected for further analysis. The IUPAC name of the lead compound is *(2R,3R,4S)-3-acetamido-4-{[(sulfoamino)methanimidoyl]amino}f-2-[(1R,2R)-1,2,3-trihydroxypropyl]-3,4-dihydro-2H-pyran-6-carboxylic acid* (AMA). Docking of AMA with H1N1 was performed and the binding energy of the compound was found to be −8.26 Kcal/mol. Weak bonding interactions like hydrophobic and hydrogen bonds are vital parameters that stabilize interactions between ligand and protein. AMA formed various hydrogen bonds with protein residues namely Arg152, Arg156, Trp178, Glu277, Asn294, Arg371, Arg292 (Fig. 5a). It also showed hydrophobic interactions with non-polar protein residues *viz.* Glu119, Asp151, Ser 179, Arg224, Glu227 Ser246, Glu276, Asn347 and Tyr406 (Fig. 5b). Post-MD simulations AMA was found to form hydrogen bonds with residues Arg156, Asn294, Glu227, Arg371, Tyr406 (Fig. 5c) and hydrophobic interactions with Glu119, Asp 151, Agr152, Trp178 and Ser179 (Fig. 5d). Two residues of 150-loop (Asp 151 and Arg152) were

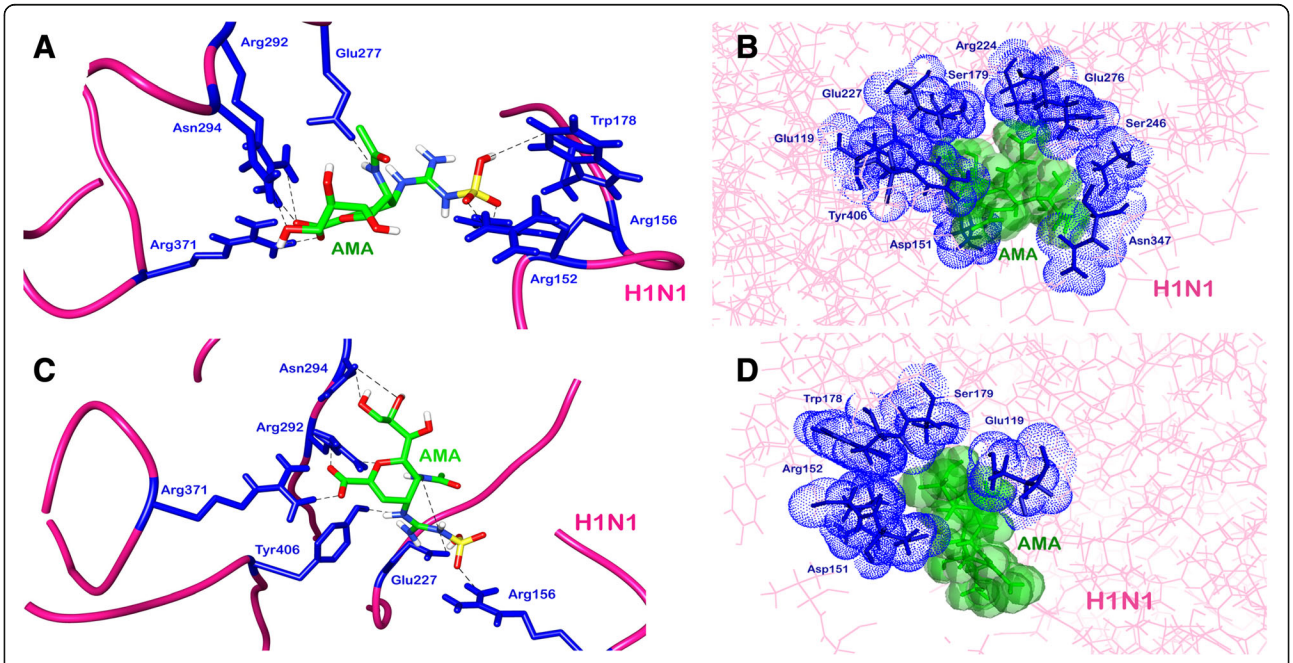


Fig. 5 Molecular interactions of H1N1 Neuraminidase (*pink*) with AMA (*green*) depicting (**a**) hydrogen bond before MD simulations and (**b**) hydrophobic interactions before MD simulations. (**c**) Hydrogen bond after MD simulations and (**d**) hydrophobic interactions after MD simulations

observed to be interacting with AMA. Two hydrogen bonds with Glu 277 and Arg 292 were lost during simulations, however the interaction was stabilised with the ligand forming stronger hydrogen bonds. The number of hydrogen bonds between H1N1 and AMA across simulation can be seen in Additional file 1: Figure S1. The same lead compound, AMA, when docked against H3N2 showed different bonding patterns and binding energy. The compound when docked had a binding energy of −7.00 Kcal/mol. It made hydrogen bonds with Arg118, Glu119, Arg371, Asp151 and Arg292 (Fig. 6a) and hydrophobic interactions via residues Val 149, Tyr 406, Arg430, Lys431 (Fig. 6b). A difference in hydrogen bonding and hydrophobic interactions were observed post-MD simulations. AMA formed hydrogen bonds with protein residues Lys431 and Glu432 (Fig. 6c) while hydrophobic interactions with Val149, Arg292, Arg371, Arg403 and Arg430 (Fig. 6d). In this case, only one residue of 150-loop was observed to be interacting with AMA. Molecular dynamics study was performed on this lead compound and RMSD was recorded for first 15 nanoseconds to study fluctuations and conformational changes in protein which gives a measure of the stability of protein in vivo. The ligand bound protein complex of both H1N1 and H3N2 was found to be stable for a period of 11 ns and 7 ns respectively (Fig. 7). This implied that protein underwent significant structural changes during initial stages and was stable for later stage during simulation.

In order to understand the position of AMA in H1N1 and H3N2 in comparison to zanamivir, the latter inhibitor was docked and superimposed. Additional file 1: Figure S2 shows the relative position of both inhibitors in cavity. Interacting residues can be seen in Additional file 1: Figure S3. AMA in both H1N1 and H3N2 strain was observed to be binding in the cavity in a spreadout fashion by occupying and forming strong interaction with the cavity. Also, the docking score of AMA with H1N1 (−8.26 kcal/mol) and H3N2 (−7.00 kcal/mol) was observed to be better than Zanamivir with H1N1 (−6.66 kcal/mol) and H3N2 (−5.55 kcal/mol), indicating stronger interaction.

Accessible surface area (ASA) analysis of the free and docked complexes was performed by calculating the change in accessible surface area (ASA). In case of H1N1, the change in ASA was around 1411 $Å^2$ while for H3N2, the change was 615 $Å^2$. Though some change was observed in ASA of all residues lining the cavity of H1N1 and H3N2, four residues (Arg118, Glu119, Glu277 and Arg292) of H1N1 exhibited a significant change, indicating their importance in drug binding.

In order to understand the correlation between IC50 values and docking scores of experimentally reported dataset compounds, the two most active compounds and two least active compounds were docked and the values were compared (Additional file 1: Table S2).

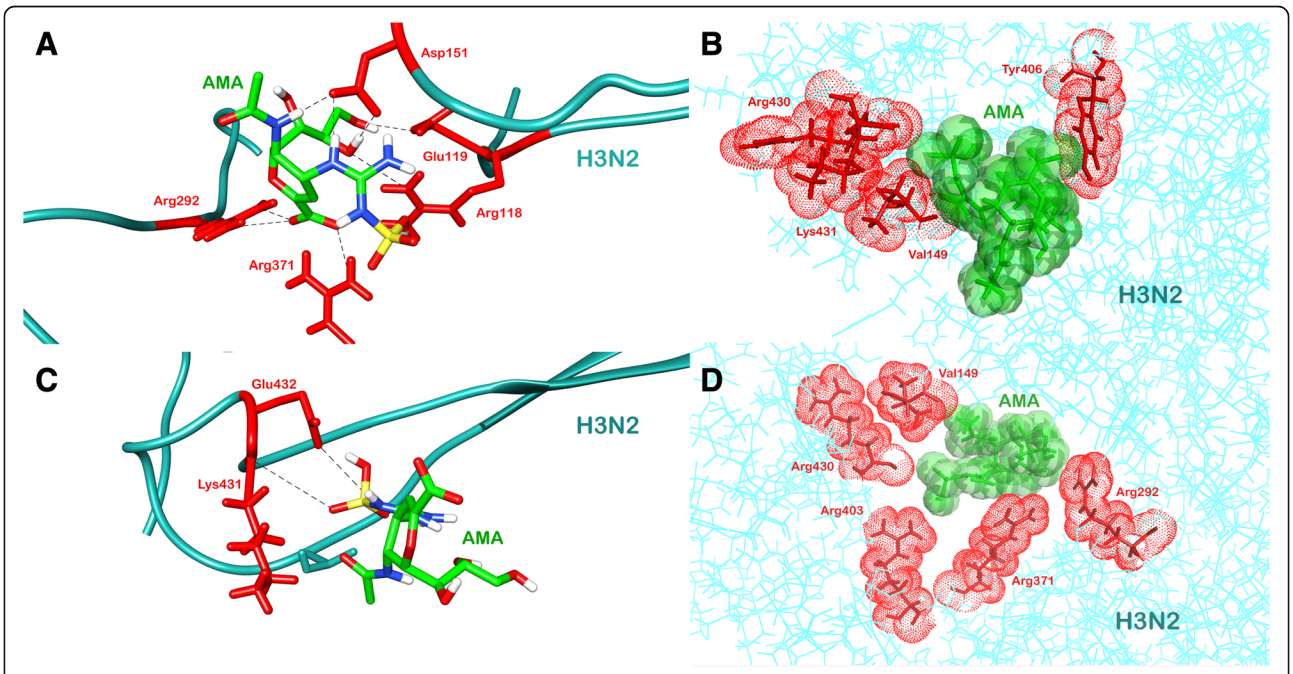


Fig. 6 Molecular interactions of H1N1 Neuraminidase (*pink*) with AMA (*green*) depicting (**a**) hydrogen bond before MD simulations and (**b**) hydrophobic interactions before MD simulations. (**c**) Hydrogen bond after MD simulations and (**d**) hydrophobic interactions after MD simulations

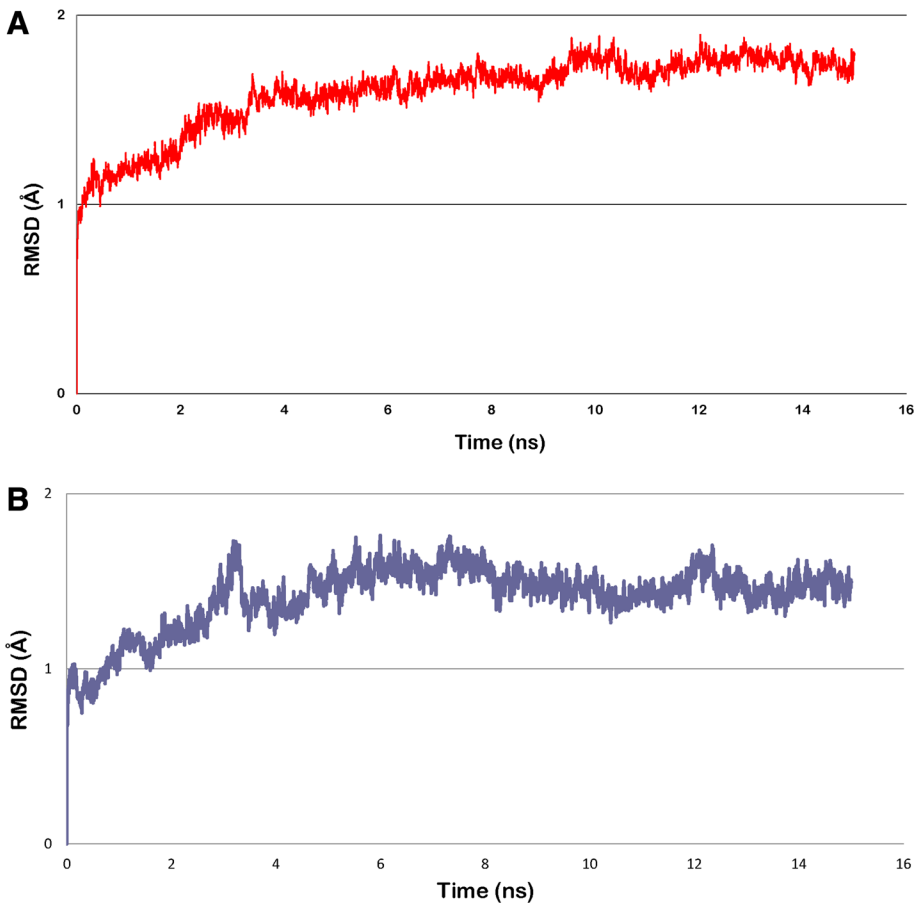


Fig. 7 RMSD plot of molecular dynamics simulations of lead compound against NA of (**a**) H1N1 (**b**) H3N2

Conclusion

The objective of the present work was to gain insight into structural features of zanamivir derivatives for prediction of anti-influenza activity using GQSAR approach. This study demonstrates a correlation between structure and inhibitory activity of these molecules. Two models were generated targeting NA of both H1N1 and H3N2 influenza strains. The developed model generated various descriptors namely R1_SdOE_index, R1_6ChainCount, R1_SssSE-index, R1_SaaaCE_index, R1_SdsCHcount and R1_schiV4 in which two descriptors SssSE-index and SdsCHcount showed negative contribution while rest all showed positive contribution. A positive contribution suggests increase in contribution of that descriptor could be beneficial for inhibitory activity while a negative contribution indicates that those descriptors are detrimental for inhibitory activity. Thus, these contributions provide insights into design of novel molecule with enhanced inhibitory activity. We also developed one novel inhibitor (AMA) using the combinatorial library approach which displayed substantial binding affinity for NA in both H1N1 and H3N2 pandemic influenza strains. AMA was docked against the active site of NA and a satisfactory docking score of −8.26 Kcal/mol and −7.00 Kcal/mol was observed for H1N1and H3N2 respectively. MD simulations of AMA stabilized the ligand bound protein complex which resulted in a steady trajectory for satisfactory time. Complex structure of ligand and protein was found to be energetically stable post MD Simulations. Thus this provides evidence that the novel compound could serve as potent anti-influenza drugs with improved binding properties and low IC50 values than traditional drugs.

Additional file

Additional file 1: Figure S1. Graph depicting number of hydrogen bonds between H1N1 and AMA across simulations. **Figure S2.** Figure comparing the conformation of AMA and Zanamivir in (a) H1N1 and (b) H3N2. **Figure S3.** Interacting residues of (a) H1N1 and (b) H3N2 with Zanamivir. **Table S1:** Structures and anti-influenza activity of acylguanidine zanamivir derivatives. **Table S2.** Table showing correlation between IC50

and docking scores of most and least active dataset compounds. (DOCX 1691 kb)

Acknowledgements
AG would like to thank University Grants Commission, India for the Faculty Recharge position. AG is also thankful to Jawaharlal Nehru University for usage of all computational facilities.

Declarations
This article has been published as part of BMC Bioinformatics Volume 17 Supplement 19, 2016. 15th International Conference On Bioinformatics (INCOB 2016): bioinformatics. The full contents of the supplement are available online https://bmcbioinformatics.biomedcentral.com/articles/supplements/volume-17-supplement-19.

Funding
Publication charges for this article have been funded by Jawaharlal Nehru University.

Availability of data and material
The datasets supporting the conclusions of this article are included within the article and its additional files as Additional file 1.

Authors' contributions
DD, SG, AD and AG designed the methods and experimental setup. DD and SG carried out the implementation of various methods. SJ and AS assisted in the implementation of methods and preparation of manuscript. All the authors wrote and approved the manuscript.

Competing interests
The authors declare that they have no competing interest.

Consent for publication
The authors give their consent for publication of this article.

Ethics approval
Not applicable.

Author details
[1]Department of Biotechnology, Delhi Technological University, New Delhi 110042, India. [2]Department of Bioscience and Biotechnology, Banasthali University, Tonk, Rajasthan 304022, India. [3]Department of Biotechnology, TERI University, New Delhi 110070, India. [4]School of Biotechnology, Jawaharlal Nehru University, New Delhi 110067, India.

Published: 22 December 2016

References

1. Nelson MI, Holmes EC. The evolution of epidemic influenza. Nat Rev Genet. 2007;8:196–205.
2. Neumann G, Noda T, Kawaoka Y. Emergence and pandemic potential of swine-origin H1N1 influenza virus. Nature. 2009;459:931–9.
3. Carrat F, Flahault A. Influenza vaccine: the challenge of antigenic drift. Vaccine. 2007;25:6852–62.
4. Harper SA, Fukuda K, Uyeki TM, Cox NJ, Bridges CB. Prevention and control of influenza, Recommendations of the Advisory Committee on Immunization Practices (ACIP). MMWR Recomm Rep. 2005;54:1–40.
5. Banning M. Influenza: incidence, symptoms and treatment. Br J Nurs. 2005; 14:1192–7.
6. Skehel JJ, Wiley DC. Receptor binding and membrane fusion in virus entry: the influenza hemagglutinin. Annu Rev Biochem. 2000;69:531–69.
7. Wiley DC, Skehel JJ. The structure and function of the hemagglutinin membrane glycoprotein of influenza virus. Annu Rev Biochem. 1987;56:365–94.
8. Gong J, Xu W, Zhang J. Structure and functions of influenza virus neuraminidase. Curr Med Chem. 2007;14:113–22.
9. Amaro RE, Swift RV, Votapka L, Li WW, Walker RC, Bush RM. Mechanism of 150-cavity formation in influenza neuraminidase. Nat Commun. 2011;2:388.
10. Russell RJ, Haire LF, Stevens DJ, Collins PJ, Lin YP, Blackburn GM, Hay AJ, Gamblin SJ, Skehel JJ. The structure of H5N1 avian influenza neuraminidase suggests new opportunities for drug design. Nature. 2006;443:45–9.
11. Gubareva LV, Kaiser L, Hayden FG. Influenza virus neuraminidase inhibitors. Lancet. 2000;355:827–35.
12. Zambon MC. Epidemiology and pathogenesis of influenza. J Antimicrob Chemother. 1999;44(Suppl B):3–9.
13. Goyal S, Dhanjal JK, Tyagi C, Goyal M, Grover A. Novel Fragment-Based QSAR Modeling and Combinatorial Design of Pyrazole-Derived CRK3 Inhibitors as Potent Antileishmanials. Chem Biol Drug Des. 2014;84:54–62.
14. Goyal S, Grover S, Dhanjal JK, Tyagi C, Goyal M, Grover A. Group-based QSAR and molecular dynamics mechanistic analysis revealing the mode of action of novel piperidinone derived protein–protein inhibitors of p 53–MDM2. J Mol Graph Model. 2014;51:64–72.
15. Tyagi C, Gupta A, Goyal S, Dhanjal JK, Grover A. Fragment based group QSAR and molecular dynamics mechanistic studies on arylthioindole derivatives targeting the α-β interfacial site of human tubulin. BMC Genomics. 2014;15:S3.
16. Vats C, Dhanjal JK, Goyal S, Bharadvaja N, Grover A. Computational design of novel flavonoid analogues as potential AChE inhibitors: analysis using group-based QSAR, molecular docking and molecular dynamics simulations. Struct Chem. 2015;26(2):467–76.
17. Lin CH, Chang TC, Das A, Fang MY, Hung HC, Hsu KC, Yang JM, von Itzstein M, Mong KK, Hsu TA, Lin CC. Synthesis of acylguanidine zanamivir derivatives as neuraminidase inhibitors and the evaluation of their bio-activities. Org Biomol Chem. 2013;11:3943–8.
18. Goyal M, Dhanjal JK, Goyal S, Tyagi C, Hamid R, Grover A. Development of dual inhibitors against Alzheimer's disease using fragment-based QSAR and molecular docking. 2014.
19. Goyal S, Jamal S, Shanker A, Grover A. Structural investigations of T854A mutation in EGFR and identification of novel inhibitors using structure activity relationships. BMC Genomics. 2015;16:S8.
20. Singla RK, Bhat GV. QSAR model for predicting the fungicidal action of 1,2,4-triazole derivatives against Candida albicans. J Enzyme Inhib Med Chem. 2010;25:696–701.
21. Golbraikh A, Tropsha A. Predictive QSAR modeling based on diversity sampling of experimental datasets for the training and test set selection. Mol Divers. 2000;5:231–43.
22. Afantitis A, Melagraki G, Sarimveis H, Igglessi-Markopoulou O, Kollias G. A novel QSAR model for predicting the inhibition of CXCR3 receptor by 4-N-aryl-[1,4] diazepane ureas. Eur J Med Chem. 2009;44:877–84.
23. Golbraikh A, Tropsha A. Beware of q2! J Mol Graph Model. 2002;20:269–76.
24. Dhanjal JK, Goyal S, Sharma S, Hamid R, Grover A. Mechanistic insights into mode of action of potent natural antagonists of BACE-1 for checking Alzheimer's plaque pathology. Biochem Biophys Res Commun. 2014;443:1054–9.
25. Dhanjal JK, Grover S, Paruthi P, Sharma S, Grover A. Mechanistic Insights into Mode of Action of a Potent Natural Antagonist of Orexin Receptor-1 by Means of High Throughput Screening and Molecular Dynamics Simulations. Comb Chem High Throughput Screen. 2014;17:124–31.
26. Goyal S, Grover S, Dhanjal JK, Goyal M, Tyagi C, Chacko S, Grover A. Mechanistic insights into mode of actions of novel oligopeptidase B inhibitors for combating leishmaniasis. J Mol Model. 2014;20:1–9.
27. Grover S, Dhanjal JK, Goyal S, Grover A, Sundar D. Computational identification of novel natural inhibitors of glucagon receptor for checking type II diabetes mellitus. BMC Bioinformatics. 2014;15:S13.
28. Halgren TA, Murphy RB, Friesner RA, Beard HS, Frye LL, Pollard WT, Banks JL. Glide: a new approach for rapid, accurate docking and scoring. 2. Enrichment factors in database screening. J Med Chem. 2004;47:1750–9.
29. Jorgensen WL, Duffy EM. Prediction of drug solubility from structure. Adv Drug Deliv Rev. 2002;54:355–66.
30. Jorgensen WL, Tirado-Rives J. Potential energy functions for atomic-level simulations of water and organic and biomolecular systems. Proc Natl Acad Sci U S A. 2005;102:6665–70.
31. Jorgensen WL, Chandrasekhar J, Madura JD, Impey RW, Klein ML. Comparison of simple potential functions for simulating liquid water. J Chem Phys. 1983;79:926–35.
32. Jain SK, Vishwakarma S, Nayak P. 3D QSAR analysis on pyrrolidine derivatives as DPP IV inhibitors. Int J Pharm Biomed Res. 2011;2(3).

International Journal of Research in Engineering and Innovation (IJREI)

Home page http:// www.ijrei.com

Analysis of Calorimetric Measurement Bismuth and Tin System

Kapil [1], C.K Behra[2], Ravinder Kumar[3]

[1]M.Tech Student, Department of Metallurgical Engineering, IIT, BHU Varanasi, India
[2] Department of Metallurgical Engineering, IIT, BHU Varanasi, India
[3]M.Tech Student, Delhi Technological University, New Delhi, India

Keywords

Drop Calorimeter
Calisto Software
Sapphire,
Enthalpy

Abstract

Lead-free soldering alloys with low melting point suitable for use in soldering joints are very essential. Use of lead as a solder is considered dangerous for the environment due to the huge number of printed circuit board and electronic devices, pipe joints etc. needed to be recycled from dumps.

In this work the metallic samples were prepared from Bi in the mass range from 0.75gm. Samples of Sn were dropped into the bath of Bi by using an automatic dropping device System required 40min time interval after every sample of dropped. Calorimetric measurements was done at temperature 830K. The Integral and partial enthalpy of mixing was calculated at this temperatures. The Integral enthalpy of mixing in Bi- Sn system at 830K is endothermic in nature throughout the composition and its maximum value at X_{sn} = 0.6, is 1005.9061 respectively. © 2016, ijrei.com. All rights reserved

1. Introduction

Development of new lead-free solder requires a database. The database will help us to avoid complicated and time consuming experiments. Information on thermodynamic properties such as mixing enthalpies is indispensable for the accurate thermodynamic optimization of phase diagrams, for the development of a lead-free solder database, and for the prediction of physical and chemical properties, such as surface tension and viscosity.

It is not possible so far to substitute lead by any single metal in the conventional lead-tin solder. So the attempt has been made to substitute lead by more than one metal. These systems are called multicomponent metallic solution. Like In- Sn- Bi, In-Sn-Zn, and In-Sn-Bi-Zn

Higher temperatures dramatically reduce the firmness of the solder joint during thermal cycling, due to greater plastic deformation of the solder and recrystallization and grain growth inside the solder. At such high temperatures, the mechanical properties of the conventional alloys Sn62/Pb36/Ag2 (melting point 179°C) and Sn63/Pb37 (melting point 183°C) deteriorate. In the manufacturing environment, the only risk is caused by breathing in floating, dried powder particles, or through the occurrence of gross mistakes in safety measures. A greater danger lies in the contamination of groundwater and soil by electronics scrap (disposal of electronic circuit and solder dross). Several proposals have been made to ban the use of lead in electronics.

2. Experimental Setup & Procedure

- All experimental measurements were performed by using the calorimetric drop method. Calorimetric measurements were carried out by using the MHTC96 high temperature drop calorimeter from Setaram, France.
- It is a calorimeter with a thermopile of 20 thermocouples and a graphite tube resistance furnace operating up to 1723K. Control and data evaluation were performed using the software provided by the manufacture. To prevent oxidation of the samples all measurements were taken in a atmosphere of flowing argon.
- All measurements were carried out in an alumina crucible.

Corresponding author: Kapil
Email address: kapil.tyagipr@gmail.com
Copyright©ijrei.com

- A motorized dropping device is placed on the top of the calorimeter. 23 samples can be installed at a time into it. It also consists of a vacuum pump.
- An alumina tube connects the furnace to the dropping device. Sample is dropped from dropping device to the alumina crucible (placed in the furnace) by this tube.
- Control and data evaluation were performed using the software provided by the manufacturer

The starting materials are the metals reagent grade as powder. In (purity > 99.9%; 1µm<Ø<2µm), Bi (purity > 99.95%; Ø< 25µm) and Sn (purity > 99.9985%, Ø<20µm). The Stoichiometric mixtures, in the appropriate molar ratio were carefully homogenized inside a glove box under purified argon gas in an agate mortar and compacted into 6mm diameter pellets. The pellets were cut into pieces and transferred from the glove box to the calorimeter using a special Ar-tight container in order to prevent any oxidation with air atmosphere. The Ar gas pressure and time in Analysis chamber is 1.5 bar & 15 min. while for furnace it is 1.5 bar & 2 min 30 sec. The starting samples were placed alternatively in the container with reference •-alumina used for calibration. The enthalpy variations of •-alumina between room and experimental temperatures are well established by Sabbah et al. [1]

Figure 1: Drop Calorimeter Device

Governing Equation

Heat capacity

If there is not a transition or reaction occurring within the sample on the temperature range, the following heat relation is obtained

, " , =

It is needed to repeat sample drops at different temperatures in order to determine the variation of heat versus sample temperature. From the derivation of this curve according to temperature the variation of the sample heat capacity is obtained on the measured temperature range.

Determination of enthalpy of transition

For the temperature range under investigation, the sample can undergo a structure change (melting, crystallization, phase transition ,). The measured heat will contain the heat capacity contribution before and after the transformation and the corresponding heat of transition

, " , = "+ + "+ "+ + " + "+

To obtain the heat of transition, the Cp variation has to be calculated before and transition. The difference between the two curves provides the heat value.

Where

- T_D = Dropping (Room) Temperature
- T_{Tr} = Transformation Temperature
- " = Enthalpy change during transformation
- Tm = Melting Point
- $\int H_{Tf}$ = Enthalpy change during melting
- T_C = Temperature of the Calorimeter at which experiment is carried out.

*Transformation phase may or may not be present in the system. C_p was calculated using the following relation taken from the Metallurgical Thermochemistry book [27].

Cp = a+bT

Where a and b are the constants and T is temperature in Kelvin. Values of a and b are taken from the book. All the experiments was carried out at a calorimeter temperature of 830 K and drop temperature was 293K.

, " , = = . D

Alpha alumina (•-Al2O3) was used for the calibration of the calorimeter for each experiment. Alpha alumina does not react with the molten alloy of Bi-Sn due to its high melting point. Molecular weight of the •-Al2O3 = 101.9613. $\int H$ Reaction for •-Al2O3 is zero. The molar enthalpy difference for •-Al2O3 Standard Reference Material 720 was taken from Standard Reference Material 720 Synthetic Sapphire certificate issued by National Bureau of Standards Certificate, Washington.

, " , = D

4.1.3 Enthalpy calculation:

The measured enthalpy (integrated heat flow at constant pressure) is given by

$$" = , " , + "$$

Where the number of moles of the added sample is $H_{sample, Tc}$ enotes molar enthalpies at calorimetric temperature and $H_{sample, TD}$ denotes molar enthalpies at drop (room) temperature. $\Delta H_{reaction}$ is the enthalpy of reaction due to addition of i. number of moles.

Because of the relatively small mass added the Partial enthalpy can be directly calculated as

$$" = \frac{"}{\quad}$$

The integral enthalpy of mixing was calculated by summarizing the respective reaction enthalpies and division by the total molar amount of substance.

$$" = \frac{S"}{(+ S)}$$

Calibration constant (K) calculation:

Calibration constant was calculated using area under the peak of dropped α-Al_2O_3 samples

$$" = , " ,$$

$$= \frac{}{"}$$

Where n_i is the number of moles of dropped α-Al_2O_3 samples. A is area under the peak in micro-volt second (m-s). " is the heat absorbed in joule by n_i number of moles of α-Al_2O_3.

Results & Discussion

Molten Bi Held at temperature 38 K according to pre-set time range in program and Sn dropped in the crucible at a regular interval of 40 mins with the help of motorizing dropping device.

Graph-1: Peak areas with enthalpy values

Table1 Molar mixing Enthalpies with composition

Xsn	ΔH_{MIX} (Joule/mole)
0.1	40.27759
0.2	151.754
0.3	292.1128
0.4	469.3475
0.5	570.039
0.6	605.922
0.7389	569.9107
0.8093	450.1246
0.832	392.1039
0.8498	339.8457
0.8642	286.1929
0.8861	229.9907
0.8946	165.0691
0.9019	85.15358

Calibration constant was calculated using area under the peak of dropped α-Al_2O_3 samples

Table2: Partially Enthalpies with730 Kcomposition[5]

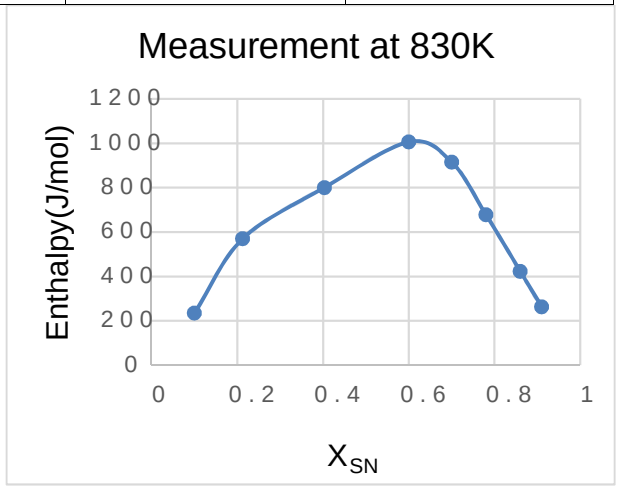
Xsn	Partial Enthalpy (J/mole)
0.1	1352.665878
0.2	606.035198
0.3	515.5397029
0.4	945.0941891
0.5	883.0229295
0.6	667.9512507
0.7389	535.4989169
0.7796	106.1237565
0.832	-3.890277147
0.8642	-30.5927125
0.8946	-104.2914341
0.9019	-370.2476901

Table- 3: Integral Enthalpies of mixing at 830K

X_{sn}	€• MIX (J/mol)
	Experimental valuesat 830K
0.1	234.92128
0.2126	570
0.40295	745
0.6	1005.9061
0.7	915.2765
0.78	678.7265
0.86	423.5942
0.91	263.36614

Comparison of Model values [3] to experimental values

	€• MIX (J/Mole)	
	Experimental values at 730K	Theoretical Values at 608K
0.1	135.2776	20.91
0.2	221.754	62.73
0.3	292.1128	83.64
0.4	469.3475	104.55
0.5	589.039	154.55
0.6	612.922	346.37
0.7	570.678	104.55
0.8	400.126	62.64
0.9	165.1536	2091



Partial Enthalpy values at 830K

X_{sn}	€• partial (J/mol)
	Experimental values at 830K
0.1	2364.1027
0.2126	2058.12752
0.40295	1158.32547
0.6	628.76927
0.7	137.91588
0.78	-89.168
0.86	-122.07893
0.91	-98.79091

Variation of Mixing Enthalpies with X_{sn} [5]

comparison data analysis between Literature data & our experimental data

we find that first the value of Enthalpy is increasing with composition of Sn and at X_{SN} = 0.59, the value of Enthalpy is Maximum for all the temperatures. This is an agreement with the literature. That means at this point reaction is more Endothermic in nature and after this composition Enthalpy goes on decreasing as shown in Fig. R. Hultgrenet[3] have got the maximum value of enthalpy at X_{sn} = 0.6 is „† $_{mix}$ = 146.37 J/mol at 608K1. we have obtained the maximum values of enthalpy at X_{sn} = 0.6 is † $_{mix}$=1005.9061 J/mol at 830K, and is „† $_{mix}$ = 612.33 J/mol at 730 K [5]. It has been observed that enthalpy of mixing in the system Bi- Sn is more endothermic in nature with the temperature.

It is observed that partial enthalpy of mixing decreases temperature. The experimental values show some scatter from the literature [3,4]. The reason for the scatter may be due to different techniques used for the experimental measurement in the Bi-Sn system. The second reason may be the experiments are carried out at different temperatures. For example the Partial enthalpies values obtained from the literature are calculated values from EMF measurement but our values are obtained directly from the enthalpy measurement by calorimeter at 730K and 830 K.

Conclusion

The Enthalpy change of Bi- Sn system is measured at temperature 608K & 830K by Drop calorimetric technique and following conclusions are made. The Integral enthalpy of mixing in Bi- Sn system at 608K and 830K is endothermic in nature throughout the composition and its maximum value at X_{sn} = 0.6, is 346.37 J/mol and 1005.9061 respectively

The partial molar enthalpy of Sn is endothermic in nature and decreases with the composition of tin for most of the composition except Sn rich composition.

The experimental values are compared with the literature and found some scatter due to difference in experimental constraints.

References

[1] R. Sabbah, Xu-Wu An, J.S. Chickos, M.L. Planas Leitão, M.V. Roux, Thermochim.Acta 331 (1999) 93–204.

[2] O.Kubaschewski, E.LL. Evans, C.B. Alcock, "Metallurgical Thermochem" V4 (1967) [28]

[3] R. Hultgren, Raymond L.Orr, Philip D. Anderson. Selected values of Thermodynamic properties of metals and alloys V2(1963), pp 549-554

[4] Hing-feng Yanga, Feng-ling Chena, Wojciech Gierlotkaa Hsiehc, Li-ling Huanga Materials Chemistry and Physics 112 (2008) pp. 94–103.

[5] Kapil, Sunil kumar, Avnish kumar, calorimetric measurement on Bi-Sn system IJRMET VOL5 spl nov2014

Optical logic operation using universal NOR gate

Preeti Rani[1], Yogita Kalra[1] and R. K. Sinha[1,2]

[1]TIFAC-Centre of Relevance and Excellence in Fiber Optics and Optical Communication, Department of Applied Physics, Delhi Technological University (Formerly Delhi College Of Engineering, University of Delhi), Bawana Road, Delhi-110042, India
[2]CSIR-Central Scientific Instruments Organization (CSIO), Sector-30C, Chandigarh-160 030, India

Author e-mail address: dr_rk_sinha@yahoo.com

Abstract: The design of AND optical logic gate using the combination of universal NOR gates has been reported. The proposed AND gate exhibits a contrast ratio of 21.8 dB and a bit rate of 0.416 Tb/s.

OCIS codes: (230.0230) Optical devices; (230.5298) Photonic crystals; (230.3750) Optical logic devices;

1. Introduction

Photonic crystals [1] provide a versatile platform to design various optical devices due to their certain unique properties such as low loss, compact, low power consumption, high speed and better confinement. Recently, with the increase in the speed of the telecommunication over the electronic systems, the optical logic gates have received considerable attention in switching, decision-making, regenerating, and basic or complex computing. Logic gates are the basic designs useful for the designing of complex systems like processors and networks. In recent years, different schemes have been adopted for the designing of all optical logic gates such as Mach-Zehnder interferometer [2], interferometry [3] and photonic crystals [4-10]. In this paper, we have reported a photonic crystal (PhC) based design of AND optical logic gate using the combination of three universal NOR gates as shown in figure 1. The PhC structure is composed of air holes in silicon of refractive index 3.5. The radius of air holes 'r' has been taken as, r = 0.3a, where 'a' is the lattice constant.

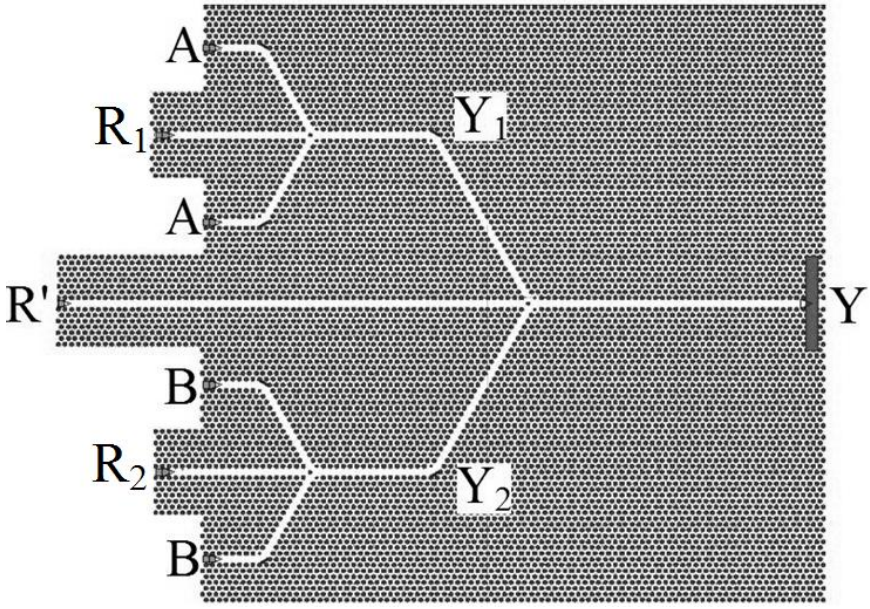


Fig.1. Schematic representation of AND gate using combination of NOR gates

Initially, a single NOR gate has been designed which is operational at a wavelength of 1.55μm, as verified using the plane wave expansion (PWE) method. Further, the three such NOR gates have been arranged in such a way that the combined structure behaves as an AND optical logic gate. The designed structure is operational at a wavelength of 1.55 μm and has been analyzed using the finite difference time domain (FDTD) method. The input to the NOR gate 1 is A and the input to the NOR gate 2 is B as shown in figure 1. The outputs of NOR gate 1 and NOR gate 2 i.e. Y_1 and Y_2 respectively act as inputs for NOR gate 3. The operation of optical AND logic gate is as follows:
(i) when the input A and B are low i.e. A = 0, B = 0.

For the NOR gate1 the reference signal R_1 is launched with light having phase angle $\varphi = 0^\circ$ then logic 1 is obtained at the output Y_1. For the NOR gate2 reference signal R_2 is launched with light having phase angle $\varphi = 0^\circ$ then logic 1 is obtained at the output Y_2. Output Y_1 and Y_2 as the input signals for the NOR gate 3 along with the reference signal R' with the light having the phase angle $\varphi = \pi$ gives logic 0 at the output port Y.

(ii) When A = 0 and B = 1 with light having phase angle $\varphi = 0^\circ$.

For the NOR gate1, A = 0 and the reference signal R_1 is launched with light having phase angle $\varphi = 0^\circ$ then logic 1 is obtained at the output Y_1. For the NOR gate2, B = 1 and reference signal R_2 is launched with light having phase angle $\varphi = \pi$ then logic 0 is obtained at the output Y_2. Output Y_1 and Y_2 as the inputs signals for the NOR gate 3 along with the reference signal R' with the light having the phase angle $\varphi = \pi$ gives logic 0 at the output port Y.

(iii) When A = 1 with light having phase angle $\varphi = 0^\circ$ and B = 0.

For the NOR gate1, A=1 and the reference signal R_1 is launched with light having phase angle $\varphi = \pi$ then logic 0 is obtained at the output Y_1. For the NOR gate2, B=0 and reference signal R_2 is launched with light having phase angle $\varphi = 0^\circ$ then logic 1 is obtained at the output Y_2. Output Y_1 and Y_2 act as the inputs signals for the NOR gate 3 along with the reference signal R' with the light having the phase angle $\varphi = \pi$ gives logic 0 at the output port Y.

(iv) When both the input ports A and B are excited with light signal having phase angle $\varphi = 0^\circ$, along with the reference signals R_1 and R_2 with phase angle $\varphi = \pi$, logic 0 is obtained at the output Y_1 and Y_2 for NOR gate 1 and 2 respectively. Outputs Y_1 and Y_2 as the input signals for the NOR gate 3 along with the reference signal R' with the light having the phase angle $\varphi = 0^\circ$ gives logic 1 at the output port Y.

The results obtained for the proposed AND gate have been summarized in table 1 for all possible combinations which indicate that the truth table for the AND optical logic gate has been successfully realized.

Table 1 Truth table for AND logic gate where output Y is in terms of input power P

Input A ($\varphi = 0^\circ$)	Input ($\varphi = 0^\circ$)	Reference signal (R_1)	Reference signal (R_2)	Reference signal (R')	Logic Output	Output Y
0	0	1($\varphi = 0^\circ$)	1($\varphi = 0^\circ$)	1($\varphi = \pi$)	0	0.0051 P
0	1	1($\varphi = 0^\circ$)	1($\varphi = \pi$)	1($\varphi = \pi$)	0	0.2270 P
1	0	1($\varphi = \pi$)	1($\varphi = 0^\circ$)	1($\varphi = \pi$)	0	0.2318 P
1	1	1($\varphi = \pi$)	1($\varphi = \pi$)	1($\varphi = 0^\circ$)	1	0.7172 P

The contrast ratio for the proposed AND optical logic designed with the universal NOR gates have been obtained to be 21.48dB. Further, other optical logic gates can also be realized using the combination of universal NOR gates. The response time for the proposed design has been determined using time evolving curve of the output power. At steady-state, the time taken to reach output power from 0 to 90% of the average output power (P_{av}) is ct = 200.86μm or t = 2.34 ps. This time consists of two parts one of which is time due to transmission delay i.e. t_1 = 1.74 ps and another is time taken by output power to climb from 0.1% to 90% of P_{av} i.e. t2 = 0.542 ps. It has been expected that the falling time from P_{av} to 10% of P_{av} is approximately equal to t_2. Thus, a narrow pulse width of $2t_2$ = 1.2 ps can be produced and hence the response time of 2.4 ps has been achieved if the ON and OFF time of the signal is same which leads to a bit rate of 0.416 Tbit/s.

2. Conclusion

In this paper, we have proposed the design for AND optical logic gate based on the phenomenon of optical interference effect using the combination of universal NOR logic gates. The performance of the proposed PhC structure has been analyzed by PWE method and simulated using FDTD method. The high value of contrast ratio and realized truth table indicate that the proposed design can be used for the realization of all optical logic circuits.

3. Acknowledgement

Authors gratefully acknowledge (i) the initiatives and support provided by establishment of the TIFAC-Centre of Relevance and Excellence in Fiber Optics and Optical Communication at Delhi College of Engineering, now DTU, Delhi through “Mission REACH” program of Technology Vision-2020, Government of India, (ii) support through DST-RMES (Indo-Russian) joint research project on “All-Dielectric, Plasmonic and Hybrid Photonic Nanostructures".

4. References

[1] John D Joannopoulos, Johnson SG, Winn JN and Meade RD, "Photonic Crystals: Molding the Flow of Light (2nd ed.)", Princeton NJ: Princeton University Press, ISBN 978-0-691-12456-8 (2008).
[2]Y. A. Zaghloul and A. R. M. Zaghloul, Complete all-optical processing polarization-based binary logic gates and optical processors, Optics Express 14, 9879-9895(2006).
[3] P. Sahu, “All-optical switch using optically controlled two mode interference coupler,” Applied Optics 5,1 2601-2605(2012).
[4]C. J. Wu, C. P. Liu and Z. Ouyang, “Compact and low-power optical logic NOT gate based on photonic crystal waveguides without optical amplifiers and nonlinear materials”, Applied Optics 51, 680-685 (2012).
[5] P. Rani, Y. Kalra and R. K. Sinha, Realization of AND gate in Y shaped photonic crystal waveguide, Optics Communications 298, 227-231(2013).
[6]Y. Ishizaka, Y. Kawaguchi, K. Saitoh and M. Koshiba, “Design of ultra compact all-optical XOR and AND logic gates with low power consumption”, Optics Communications 284, 3528-3533 (2011).
[7] T. A. Ibrahim, K. Amarnath, L. C. Kuo, R. Grover, V. Van, and P.-T. Ho, “Photonic logic NOR gate based on two symmetric microring resonators,” Opt. Lett. 29, 2779–2781(2004).
[8] S. K. Tripathy, S. Sahu, C. Mohapatro and S.P. Dash, “Implementation of optical logic gates using closed 2D photonic crystal structure,” Optics Communications, 285 (13-14), 3234–3237 (2012).
[9]Parisa Andalib and Nosrat Granpayeh, “All-optical ultra compact photonic crystal AND gate based on nonlinear ring resonators,” J. Opt. Soc. Am. B 26, 10-16 (2009).
[10] Jibo Bai, Junqin Wang, Junzhen Jiang, Xiyao Chen, Hui Li, Yishen Qiu, and Zexuan Qiang, “Photonic NOT and NOR gates based on a single compact photonic crystal ring resonator,” Applied Optics 48, 6923-6927(2009).

International Journal of Research in Science and Technology http://www.ijrst.com

(IJRST) 2016, Vol. No. 6, Issue No. IV, Oct-Dec **e-ISSN: 2249-0604, p-ISSN: 2454-180X**

POLICY ISSUES ON CLOUD COMPUTING IN INDIA- A COMPARATIVE LANDSCAPE

***Dr. Rajat Agarwal, **Vatsal Chanana, ***Rishabh Chanana**

**Assistant Professor,Department of Management Studies,*
Indian Institute of Technology, Roorkee, India
***Student, Netaji Subhas Institute of Technology, University of Delhi, New Delhi, India*
****Student, Delhi Technological University, New Delhi, India*

ABSTRACT

Cloud computing allows business organizations to focus on their business requirements and align IT strategically through dynamic provisioning of resources and applications. Similarly, in the Government and public sector, cloud computing offers scope for reduction in cost of service delivery. For countries like India, this can be a game changer as it may bring huge savings in cost of e-governance infrastructure, which can permit the alternative usage of funds for core development activities. To ensure the adoption of cloud computing, it is imperative that a policy framework on cloud computing is finalized so that business and government organizations can reap its benefits. This paper highlights some of the key policy issues that require attention, particularly for government and public sector in India. The paper highlights key policy issues related to cloud such as data protection, data sovereignty, cloud standards, security requirements, etc. through a comparative landscape of the policies of the developed world. A strategic policy framework/roadmap for cloud in India has also been suggested

Keywords
Cloud computing; cloud policy; ICT policy; e-governance; Digital India; cloud standards

1. INTRODUCTION

Recent advances such as high computer penetration, high-speed broadband at a lower cost, 3G, 4G technology, high-efficiency servers and amendment in storage technologies, etc., along with the business needs and economic factors together have led to the engenderment of an offering called cloud computing or simply 'Cloud'. The National Telecom Policy 2012 (NTP-2012) of India aims to "take new policy initiatives to ensure rapid expansion of new services and technologies at globally competitive prices by addressing the concerns of cloud users and other stakeholders, including specific steps that need to be taken for lowering the cost of service delivery."[1]

According to National Institute of Standards and Technology (NIST), USA, "Cloud computing is a model for enabling

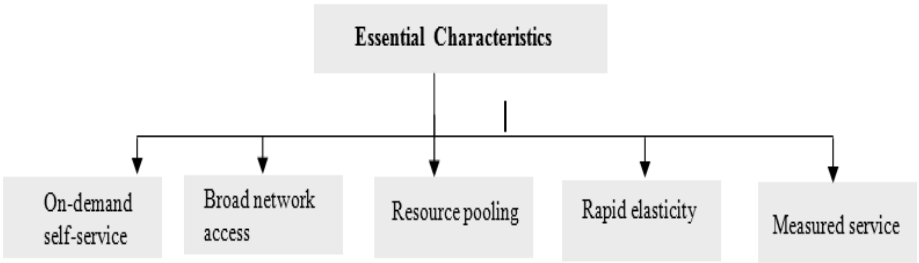
IJRST

ubiquitous, convenient, on-demand network access to a shared pool of configurable computing resources (e.g., networks, servers, storage, applications, and services) that can be rapidly provisioned and released with minimal management effort or service provider interaction."[2]

In other words, cloud refers to the sharing of hardware, development platforms and software resources over the internet on a pay-per-use or subscription basis.By leveraging the cloud a shared pool of configurable computing resources can be accessed on -demand basis. The cloud has led to a transmutation in the way in which the IT services are procured and utilized.

With the increasing competition and change in business environment, the traditional IT models, may not be able to utilize the resources efficiently and will hamper the organization development in gaining a competitive edge while requiring an immense investment. The organizations can transform their business models and acquire a competitive edge by leveraging the benefits from cloud computing adoption.The main proposal of cloud is to revamp the present IT infrastructure model from Capital Expenditure (CAPEX) model into an Operational Expenditure (OPEX) model. Along with the cost benefits, cloud computing allows an organization to focus on their core business activities while parting the task related to run IT services and infrastructure in the hands of cloud service providers(CSPs). The cloud empowers organization to establish virtual and open business processes and permitting its stakeholders (customers, business partners, suppliers, etc.) to connect and do business more efficiently [3]. Utilizing the cloud services, the governments can provide e-services more efficiently to the resident and launch e-Governance initiatives more expeditiously and likewise locally, state government and other public partners can be empowered to adopt e-Governance for providing better services to stakeholders without establishing IT infrastructure.

As per NIST, this cloud model is composed of five essential characteristics, three service models, and four deployment models.



IRST

Cloud Service Models		
Software as a Service (SAAS) The capability provided to the consumer is to use the provider's applications running on a cloud infrastructure.	**Platform as a Service (PaaS)** The capability provided to the consumer is to deploy onto the cloud infrastructure consumer-created or acquired applications created using programming languages, libraries, services and tools supported by the provider.	**Infrastructure as a Service (IaaS)** The capability provided to the consumer is to provision processing, storage, networks, and other fundamental computing resources where the consumer is able to deploy and run arbitrary software, which can include operating systems and applications.

Fig 1: Cloud Essential Characteristics

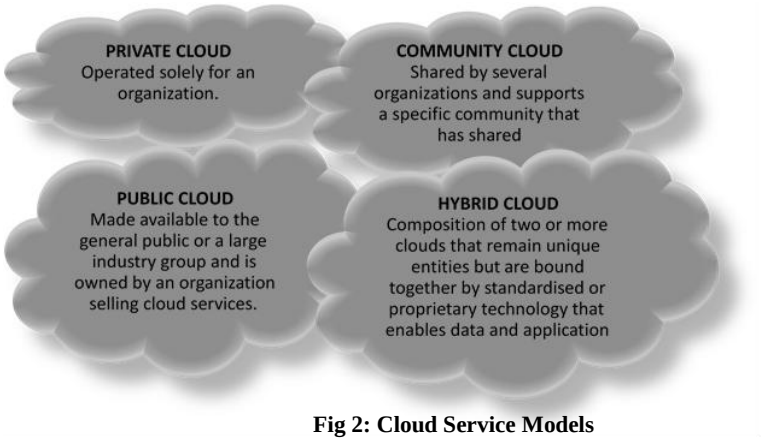


Fig 2: Cloud Service Models

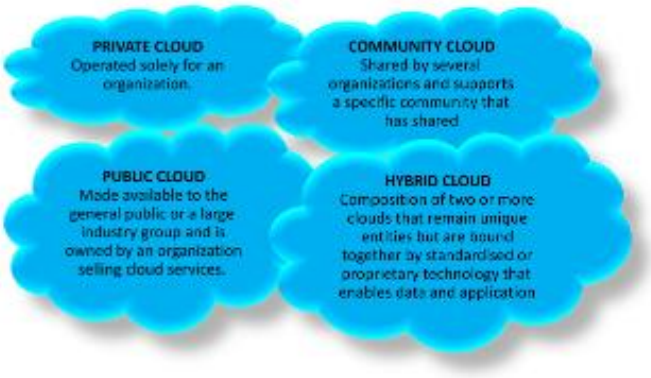


Fig 3: Cloud deployment models

With the above introduction as the base, the remaining sections of this paper are organized as follows: section 1.1 covers the cloud computing scenario in India; section 2 covers a summary of key identified issues related to cloud computing; section 3 presents a comparative summary ofcloud policies in selected other countries of the world; section 4 covers the cloud initiatives in India and finally section 5 presents a strategic roadmap for enabling cloud in India and also highlights the scope for future work.

1.1 The "Cloud' of Computing in India

India with its booming economy is growing at an expeditious pace in domestic IT sector with a USD 60 Billion IT and BPO industry, thereby exhibiting enormous potential to act as a hub for distributing cloud services and also to get the benefitsof cloud computing as a consumer. Cloud computing services have immense opportunity in Indian market as a large number of small and medium enterprises (SMEs) can potentially utilize reliable and scalable applications that facilitate expansion of their business at a lower technological cost.

Other areas where the cloud computing can have a sounding impact in India include sectors like education, automotive, health, Information Technology (IT) & IT enabled services (ITES) and Government. Utilizing the cloud, the government can launch e-Governance initiatives more expeditiously and with lower infrastructure and operating costs.A prevalent cloud platform will allow government bodies and partners at different level to adopt e-Governance without establishing IT infrastructure. Along with the above mentioned advantages, adoption of the cloud will provide Indian Information Technology (IT) & IT enabled services (ITES) sector an opportunity to provide cloud based services globally.

Public cloud services are accepted widely by the Indian companies as compared to the private cloud services. According to Gartner, "the spending on cloud will rise to $ 2 billion by 2018 from $638 million in 2014; there was an increase of almost 34 percent from 2013 to 2014". Many research reports predict enormous growth in cloud computing in India. [4] The National Association for Software and Services Companies (NASSCOM) in association with Deloitte has recently released a study report predicting that the cloud computing market in India is projected to grow by $16 Billion in 2020 with new businesses contributing to sixty percent of this growth. [8]A latestsurvey conducted by Gartner to determine the cloud adoption trends in different sectorsin India reports that public cloud services arebeing preferred by most of the organizations in India.According to the survey 53 percent of the organizations in India are currently using cloud services, while another 43 percent are pointing plans to adopt cloud based services in coming future.

Also the revenues generated from different cloud models by 2018 are forecasted as; $735 million from Software as a Service (SaaS), $121 million from Platform as a Service (PaaS) and Infrastructure as a Service (IaaS) is predicted to grow to $295 million by 2018 in India". [4] According to IDC, "Digital data in India is projected to shoot up to 2.3 million petabytes in 2020. This slowly leads to an information explosion with cloud in the middle, as more and more Indian companies are looking to

leverage the cost advantages of the cloud".[5]

2. KEY ISSUES IN ADOPTION OF CLOUD COMPUTING

A review of technical and management literature suggests that embracing the cloud by organizations to achieve improved financial and operational efficiency is still a risk-based decision rather than technology based decision. This is even more relevant for public sector wherein the assessment of risk of an IT solution is of paramount importance. Some of the key issues related to cloud computing include the following:

- *Data Security:*For the organizations migrating to the cloud unauthorized access to their data and data protection are the two main concerns which also act as a hindrance in cloud adoption**.** This concern primarily stems from the environment wherein their data and software are running on someone else's physical infrastructure.[3][6]
- *Interoperability and Portability:*Every cloud service provider has its own manner of providing cloud services. How cloud customers interact with their cloud vary for different service providers leading to cloud application programming interface (API) propagation. [7] In general, the interfaces and APIs of cloud accommodations are not standardized and different providers use different APIs due to which, it can be arduous to peregrinate from one cloud provider to another.
- *Service Level Agreement (SLA):*Another key aspect to be considered by the organizations before migrating to the cloud is to obtain the required guarantees from the service provider on services that their business needs.Typically, these guarantees are provided through service level agreements (SLAs) negotiated between the providers and consumers. Constrained control of the organizations over the application on the cloud makes SLA a crucial aspect to consider while migrating to cloud. SLA should be simple to verify easily and must cover most of the consumer expectations of addressing concerns on integrity and confidentially of the application[3][6]
- *Reliability and Availability:*Applications migrated to cloud must be subjected to the arrangements for the disaster recovery. As modern enterprises applications are now critical, these must be reliable and available to support the smooth operations. Backup plans must work properly in the event of failure and in case of the disastrous or catastrophic failure, recovery plans must come into force with minimum disruption.[3][6]
- *Service Delivery and Billing:*Migrating to the cloud means paying for the resources used, that is an OPEX model for cost especially for the application with varying needs. Here the planning and evaluation of the expense will be troublesome until the cloud service providers have similar benchmarks to offer. So the organizations need to estimate application usage, OPEX cost and migration cost before settling on the choice to move into the Cloud. [3][6]

IJRST

- *Network and Support:*With the business operations migrating to cloud, network failure is a real risk. Any failure will lead to the hindrance of the operations of the organization.
- *Change in IT Organization:*Acquiring the cloud computing services will affect the IT organization of the businesses, as has been the case with other technology shifts. Migration to cloud requires up-gradation in the skills of the IT team (especially in architecture, implementation and operation) and the migration will lead to the loss of control by IT team due to which the role of IT organization of the business may change**.**
- *Data Subject and Jurisdiction:*Globally, in cloud major source of the continuous tension between the cloud service providers and regulators are data sovereignty and jurisdiction.Generally, the local law of the place is applicable on the data storage. Different governments have different local laws, which are imposed on the cloud users or data providers. Lack of harmonized regulation for cloud computing can lead to a jurisdictional problem. Because of the fragmented data storage and processing, data may spread over multiple locations in different countries, which makes it difficult to trace as well as to determine which regulations will govern that data.[3][6]
- *Data Privacy:*Another big challenge that affects the cloud services is data privacy. To protect and secure the data over the cloud every country government have some data privacy law with which the service providers are expected to comply to. These laws substantially affect the foreign companies to provide the services to the consumer in different countries and hence creating a challenge for cross border cloud service providers**.**[3][6]

3. GLOBAL CLOUD POLICIES AND PRACTICES

One of the fundamental change that cloud computing has brought in is the removal of geographical boundaries in offering services and data transmission. Cloud service providers cater to the needs of cross-border organizations (in addition to home customers) and use service delivery methods which necessitates cross border transmission. Many countries have examined the main policy challenges on the issues highlighted in the preceding section viz., data security, data privacy, data localization, etc. associated with the cross border provision of cloud services and are making attempts to address them through domestic policies and international cooperative agreements. The continuous evolution of cloud technology has necessitated the emergence of policy environments covering the areas like data privacy, security, and cross border flow of data. In addition, many developing countries are examining their domestic infrastructure and regulatory challenges related to cloud computing. Given below are some of the policy initiatives taken by counties in different parts of the world to address the main policy requirements for cloud computing.

3.1 European Union (EU)

The European Union cloud strategy aims to evolve contract terms and conditions that cover areas like data location, data transfer, data ownership, data disclosure, data preservation, liability of cloud

IJRST

providers and subcontracting.

- *Standards and Certification***:** The European Commission is working for the development of EU-wide voluntary cloud certification schemes. This will ensure interoperability between cloud providers. The EU is also aiming to develop a meta framework of cloud security certification schemes which compares schemes with regard to the security requirements of individual organizations.[9]
- *Code of Conduct for Cloud Service Providers:* Cloud customers must be able to trust a cloud service provider before they entrust their data and applications to them. They must ensure that personal data is handled by the cloud service provider in accordancewith the EU data protection directive and its applicable national transpositions. The cloud computing strategy states that the European Commission will aim to develop a code of conduct for CSPs to support the application of data protection rules. [10]
- *Service Level Agreements (SLAs):* The European commission is working to evolve model terms and conditions for cloud computing related service level agreements as part of the contracts between cloud providers and cloud users. In order to implement this, a subgroup on service level agreements within the cloud select industry group has been established. The EU is working on coming out with reference SLAs for cloud service providers. [11]
- *Data Privacy:* The EU favors a "baseline common level of privacy to protect the data privacy rights of Europeans regardless of where data is transferred and processed". The EU data privacy directive states that the transfer of personal data which is being processed from a third country may take place only if the third country ensures an adequate level of protection.
- *Data Localization:*The EU data retention directive requires service providers to retain certain identified data for all communications for 6–24 months. The purpose is that these identified data may be made available to law enforcement agencies. A reformed EU's data protection regime by the European Commission in 2012 named as the General Data Protection Regulation (GDPR) aimed to establish a single Europe wide dataprotection law.

3.2 United States

- The United States follows a self-regulatory approach. The regulations typically cover the use of personal data in some sensitive sectors such as healthcare and financial services etc.
- In the US, there is no single, national law regulating the collection and use of personal data. Instead, a number of federal and state laws, and regulations exist and these appear to overlap.
- In the United States, the Digital Due Process initiative was created in 2010. The initiative is aimed at a clearer standard for U.S. government and law enforcement access to electronic communications and personal data.
- The US government's Cloud strategy focuses on the following:

IJRST

- High federal security requirements
- Adopting new technologies
- Ancillary technologies
- Technical know how
- IT expenditure

3.3 United Kingdom

The UK operates within the framework of the European Union, particularly with respect to the EU wide Data Protection Directive and its strong engagement in the EU Cloud strategy.

- *Data Protection and Privacy*:The UK has implemented the Data Protection Act - updated in 1998 and also a local implementation of the EU Directive 95/46/EC passed in 1995. It is administered by an independent Information Commissioner's Office (ICO) which is able to intervene in both public and private sectors based on public interest priorities. The ICO also adjudicates on freedom of information measures.
- *Data Localization and Data Security:* Although individual projects, especially individual public sector procurements, may have specific localization requirements, at the policy level, there is a clear recognition that some sectors require specific regulators to impose data curation requirements (e.g. Banking).
- *Standardization and Data Portability*:Apart from some security-based information sharing partnerships, the UK Government supports independent standardization. As such , it drives the UK engagement in international formal standardization efforts both via the National Standards body and also through the UK delegations to ISO, IEC and ITU.

4. INDIA'S INITIATIVES TO PROMOTE CLOUD COMPUTING

Digital India, a flagship project of the current Indian Government aims to create the IT and telecom infrastructure, provide electronic delivery of services and also bring in empowerment to citizens through IT. The program aims to transform India into a knowledge economy. Consequently, there is a noteworthy open door for empowering Indian markets for quickened acceptance of Cloud Computing. There is an opportunity for the government and industry to accomplice, to drive selection of cloud in India and fabricate India as a significant center point for conveying cloud solutions. Cloud computing has also been identified as one of the thrust areas in the National IT policy. Some Key Initiatives that embody the fast appropriation and deployment of cloud computing are highlighted below

4.1 Meghraj (Government of India cloud)

For the effective delivery of e-services by leveraging the cloud computing, Department of Electronics and IT (DeitY), Government of India has launched Meghraj (GI Cloud) [12], a national cloud initiative.

services to citizens by the Government is expected to have a very large participation by IT industry and therefore lead to a larger cloud proliferation in the country. The 'empowerment' pillar can bring in the required skill for cloud computing.

- *Cloud Policy Guidelines:* The Government of India and Indian IT industry will need to work collaboratively to bring out India specific guidelines on various issues related to cloud in India. At the minimum, these include the following:
    - Code of conduct for cloud service providers
    - Model contracting guidelines with cloud Service providers including the service level agreements
    - Data privacy and access to data by government agencies
    - Data localization
    - Development of meta security standards framework for Indian conditions
    - Cloud taxation policies
    - Data protection
    - Standardization and data portability

The above two foundational elements of the framework, i.e. digital India program management and cloud guidelines can be supported by the three implementation pillars as given below:

- *Promotion***:** There is a big potential for awareness creation, particularly in the small business on the advantages of cloud. A joint industry-government awareness plan can actually help drive the demand for cloud based services.
- *Capacity Building:* The Indian IT and ITES industry will need a huge skill base to serve the growing demand for the same. Accordingly, a planned capacity building program with cloud as the key component may help achieve the same.
- *Change Management:* A structured change management initiative on migration of existing applications and infrastructure to cloud can help increased proliferations.

5.1 Suggestions for Future Work

Based on the study above, the following can be taken up as future areas for research/study:

- Identification of success parameters for cloud in the larger Digital India programs
- Guidelines on key issues related to cloud in India
- Framework for the promotion and awareness plan on cloud in India
- Structure of the capacity building for cloud in India

IJRST

- Change management framework for migration to cloud for Indian organizations

6. REFERENCES

[1] *National Telecom Policy 2012* , Ministry of Communication & IT, Department of Telecommunication, New Delhi, 2012

[2] Peter, M. and Timothy G., "*The NIST Definition of Cloud Computing"*, U.S. Department of Commerce, 2011

[3] Chandeajit, B., "The Indian Cloud Revolution", Confederation of Indian Industry, 2012

[4] Gartner, http://www.gartner.com/newsroom/id/2869417

[5] N. Venkateswaran, A STUDY ON EXPOSURE TOWARDS CLOUD COMPUTING IN INDIA, *International Journal of Development Research*, Vol. 4, Issue, 6, pp. 1308-1311, June, 2014

[6] Nitin, K., "*The Cloud- Changing the Business Ecosystem*", KPMG,2011

[7] Cloud API Propagation and the Race to Zero (Cloud Interoperability),http://www.elasticvapor.com/2009/01/cloud-APIpropagation-and-race-to-zero.html

[8] *Deconstructing the "Cloud": The New Growth Frontier for Indian IT-BPO Sector*, NASSCOM,http://www.nasscom.in/deconstructing-"cloud"new-growth-frontier-indian-itbpo-sector

[9] European union Agency for Network and Information Security, https://resilience.enisa.europa.eu/cloud-computing-certification

[10] European commission, https://ec.europa.eu/digital-agenda/en/cloud-select-industry-group-code-conduct

[11] European commission,\https://ec.europa.eu/digital-agenda/en/news/cloud-service-level-agreement-standardisation-guidelines

[12] GI Cloud Initiative (Meghraj,)http://deity.gov.in/content/gi-cloud-initiative-meghraj

[13] NIC Cloud, https://cloud.gov.in/

[14] National Knowledge Network, www.nkn.in/

[15] Institute for Development and Research in Banking Technology, www.idrbt.ac.in/ibcc.html

[16] CDAChttp://cdac.in/index.aspx?id=cloud_ci_cloud_computing

IJRST

Neural Comput & Applic
DOI 10.1007/s00521-016-2817-3

ORIGINAL ARTICLE

Recommender system with grey wolf optimizer and FCM

Rahul Katarya[1] · **Om Prakash Verma**[1]

Received: 16 September 2016 / Accepted: 19 December 2016
© The Natural Computing Applications Forum 2016

Abstract Recommender systems are contributing a significant aspect in information filtering and knowledge management systems. They provide explicit and reliable recommendations to the users so that user can get information about all products in e-commerce domain. In the era of big data and large complex information delivery system, it is impossible to get the right information in the online environment. In this research work, we offered a novel movie-based collaborative recommender system which utilizes the bio-inspired gray wolf optimizer algorithm and fuzzy c-mean (FCM) clustering technique and predicts rating of a movie for a particular user based on his historical data and similarity of users. Gray wolf optimizer algorithm was applied on the Movielens dataset to obtain the initial clusters, and also the initial positions of clusters are obtained. FCM is used to classify the users in the dataset by similarity of user ratings. Our proposed collaborative recommender system performed extremely well with respect to accuracy and precision. We analyzed our proposed recommender system over Movielens dataset which is available publically. Various evaluation metrics were utilized such as mean absolute error, standard deviation, precision and recall. We also compared the performance of projected system with already established systems. The experiment results delivered by proposed recommender system demonstrated that efficiency and performance are enhanced and also offered better recommendations when compared with our previous work [1].

✉ Rahul Katarya
rahulkatarya@dtu.ac.in

[1] Department of Computer Science and Engineering, Delhi Technological University, Delhi, India

Keywords Recommender systems · Collaborative filtering · Gray wolf optimizer · Fuzzy c-mean · Movie

1 Introduction

Recommender systems are now mostly used in all e-commerce applications and knowledge management systems. Recommender systems are responsible for delivering accurate and reliable information to the specific users [1–5]. Recommender systems collect the relevant information and preferences for the users or group of users. For example, if a new user is registered on the Amazon Web site, then recommendation engine will first try to investigate the behavior and pattern of that user, and if recommender system is unable to provide sufficient recommendations, then this type of problem is known as cold-start problem [6–8]. In this situation, the system is unaware of the new user's choices and likes, but as soon as the user spends the time on the Web site and browses the web pages of Amazon Web site, then he will get the recommendation of the products which he likes. Various applications and business applications such as tourism, entertainment, web intelligence and online shopping have seen the power of recommender system, and still it is moving toward its mature phase. RSs work on the various filtering procedures such as collaborative filtering (CF), context based, content based (CB), hybrid and social based. CF approach is the most widely used tactic which is adopted by the recommender systems [9–13]. In the CF-based system, the recommendation is suggested on the basis rating provided by the users. For example, if users have given the ratings to an e-commerce Web site of various items such as camera, washing machine and juicer mixer, then recommender system will suggest the products

Published online: 27 December 2016

for delaying the performance of the tag-based recommender system such as ambiguity, sparsity and redundancy. These such issues were taken into consideration and an algorithm was presented which relied on the deep neural networks and formed a system which had an abstract form of a tag-based recommender system [33]. A literature survey based on interactive recommender system was accomplished by researchers in which they focused on serious problems of recommender systems such as collaborative filtering, contextual information, controllability, diversity and cold start [34]. In the recommender systems, sometimes the information of the users is not complete and has some missing and faulty information because these impact recommender systems failed to understand what products should be recommended. Based on these errors and mistakes, some authors termed it as natural noise in the recommender system [35]. This natural noise was reduced and managed by presenting a system which employed the fuzzy-based methods and provided an efficient recommender system. Evolutionary computation is an emerging research area which is applied to the different interdisciplinary areas of computer science, web technologies and electronics. A survey was conducted for the involvement of evolutionary computation in the recommender system and tracked down the areas of information retrieval, knowledge management and web personalization [36]. Authors considered the papers which were based on recent technologies and themes of RS. They furthermore examined the issues of recommender systems such as novelty, diversity and serendipity. Authors categorized and explained the research work done so far, with evolutionary computation, genetic algorithm, evolutionary programming, genetic programming, feature weighting approaches, clustering-based methodologies and latent models. As soon as recommender system influence is increasing on big data, then online social networks are also growing tremendously in which the products reviews and ratings are shared by online users who can be friends or strangers. Various Web sites such as Flickr, Amazon and Flipkart have millions of users, and they exchange their experiences, lifestyle involvements, check-ins or point of interests, product ratings and reviews. In this regard for web social networks, a study was performed which categorized the social information into three major parts such as social web search, social search and social recommender systems [37]. They also sub-divided all these components majorly into the indexing, result ranking, query recommendations, social content search, collaborative search, user recommendation, item recommendation and topics recommendations. Recommender systems apart from the recommendation to online recommendation have a significant impact on other domains also which are essential for activities such as web intelligence and information retrieval from big data. The researchers performed a study related to the application of recommender systems in other substantial domains and categorized them as electronic (government, resource services commerce, shopping, library, business, learning, tourism and group activities) [38]. In the similar type of study, the performance and behavior of recommender system were analyzed in the e-learning environments [39]. They suggested and examined the techniques for recommender systems as association rule mining, content based, matrix factorization, tensor factorization and collaborative filtering. Another literature survey was conducted by the authors in which they deeply studied the recommender systems [40]. They studied the recommender systems on the various important factors such as evaluation procedures, offline and online evaluation with different types of accuracy issues. We analyzed the behavior of users who have rated the movie on the scale 1 to 5 and demonstrated that our proposed system is better than the other existing systems. A collaborative recommender system was presented with the utilization of genetic algorithm in which researchers focused on the various similarity measures [41]. A literature review of the bio-inspired algorithm was conducted, in which author surveyed various important swarm algorithms with their applications [42]. A new meta-heuristic algorithm was named as kidney-inspired and considered four components [43]. Recommender systems for groups are productive and effectual in nature because information can be shared very easily and fastly. A group recommender system was designed to analyze the sentiments of human in online microblogs in which authors focused on the TV and movies applications [44]. A similar work related to the mining of news was presented by the researchers in which they adopted fuzzy systems [45]. A multi-objective system was introduced in which authors proposed a new evolutionary algorithm for long tail recommendations [46]. A tag-based recommender system based on the deep neural network was offered by authors in which they utilized the two Last.Fm and Delicious [47]. An evolutionary algorithm was proposed which was based on the discretization and cut points. This algorithm followed the multivariate tactic and chromosome deduction methodology with the utilization of various benchmark datasets [48].

3 Proposed recommender system

In this segment, we will present the projected RS which is assimilated by the FCM and gray wolf optimizer. The fuzzy c-mean is well-known clustering algorithm which is applied to the Movielens dataset. The gray wolf optimizer was used in our work as it performed efficiently and delivered superior result in the optimization process when compared to other meta-heuristic methodologies [24].

In Fig. 1, we demonstrated the workflow of our anticipated RS in which first the Movielens dataset is

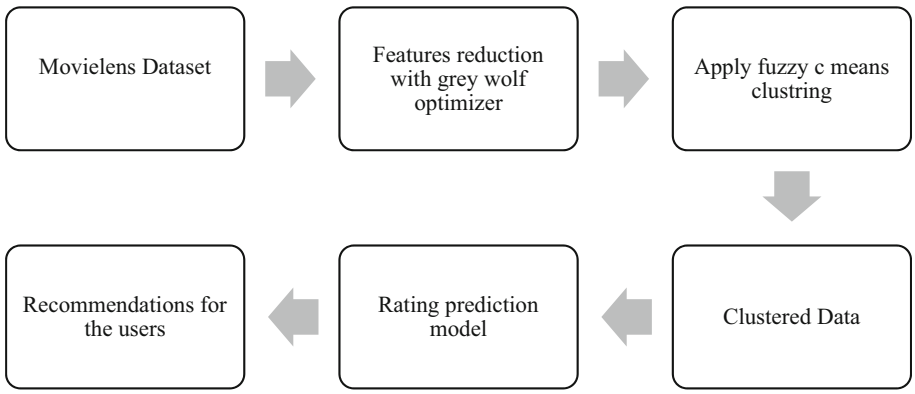


Fig. 1 Workflow of proposed collaborative movie recommender system

engaged and then gray wolf optimizer is applied to find the initial locations of the clusters. When we received the initial positions with the help of gray wolf optimizer, then FCM is used to classify the users in Movielens dataset by applying similarity of the user ratings. The useful recommendations are delivered to the users who received the effects of FCM and gray wolf optimizer.

Fig. 2 Pseudocode of proposed collaborative movie recommender system

1. Load the GWO culture X_i (i = 1, 2, ..., n) // X_i represents random cluster positions in Movielens dataset.
2. Initialize r, R, and Q // r, R and Q are coefficient points.
3. Estimate the appropriateness of each explorer negotiator
4. X_α =finest explorer negotiator
5. X_β =2nd finest explorer negotiator
6. X_δ =3rd finest explorer negotiator
7. While (z < Most number of iterations) // z represents current iteration.
   - 7.1 for respective explorer negotiator
     - 7.1.1 Refresh the spot of the present explorer negotiator.
   - 7.2 end for
   - 7.3 Refresh r, R and Q.
   - 7.4 Determine the appropriateness of entire explorer negotiators.
   - 7.5 Refresh X_α, X_β, & X_δ
   - 7.6 z=z+1
8. end while
9. Return X_α // represents positions of centroids given by the grey wolf optimizer for Movielens data.
10. Randomly select cluster centre // Fuzzy c-means.

F matrix represents an association between clusters for Movielens dataset of users.

11. Load F= [f_{lm}] matrix, F(0)
12. Estimate the f_{lm} using:

$$f_{lm}^{m} = 1 \Big/ \sum_{k=1}^{c} \left[\frac{\|(X_l - c_m)\|}{\|(X_l - c_k)\|}\right]^{\frac{2}{n-1}}$$ // represents association between i^{th} and j^{th} cluster in Movielens.

13. set k=0
14. At k-step: determine the midpoints B(k)=[c_m] with F(k)

$b_m = \frac{\sum_{l=1}^{N} f_{lm}^{n} . x_l}{\sum_{l=1}^{N} f_{lm}^{n}}$ // represents the new position of the jth cluster for Movielens dataset.

15. Refresh F(k), F(k+1)

$$f_{lm}^{m} = 1 \Big/ \sum_{k=1}^{c} \left[\frac{\|(X_l - c_m)\|}{\|(X_l - c_k)\|}\right]^{\frac{2}{n-1}}$$

16. If || F(k+1) - F(k)||< ε, then discontinue; else go back to step 12.
17. Return newly formed clusters and cluster centers for the Movielens users.

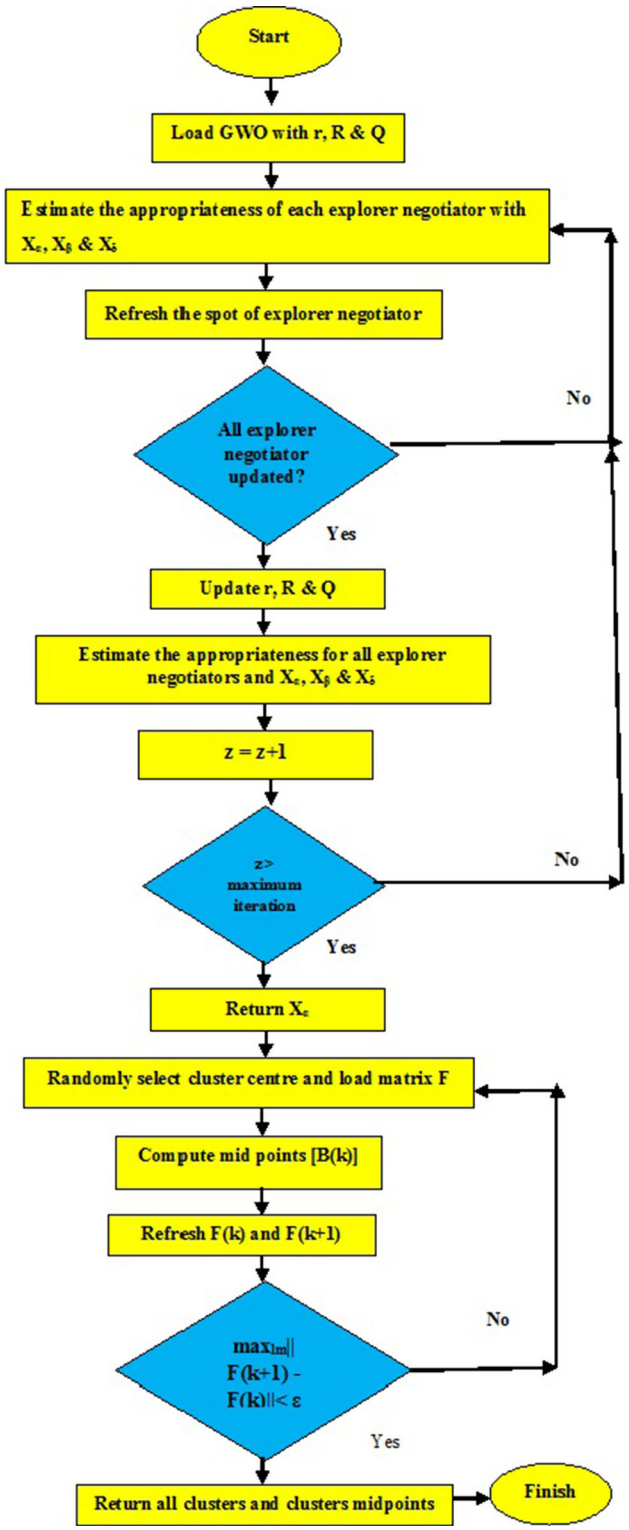


Fig. 3 Detailed flowchart of proposed collaborative movie recommender system

In Fig. 2, we demonstrated the pseudocode of our proposed recommender system, where initial data are loaded in GWO culture with three explorer negotiators and FCM is applied finally. Whereas in Fig. 3, we have demonstrated the detailed working flow process with all three coefficient points such as r, R and Q which are valid for clusters. Figures 2 and 3 demonstrate the proposed recommender system in which first Movielens data are initialized. With the help of gray wolf optimizer, features of movies in which users have rated them are initialized. Then, we estimated the appropriateness of respective explorer negotiator and designated as finest according to their positions. Then, we refreshed the spots of recent explorer negotiator. We will check whether all the explorer negotiators are refreshed or not; if they are not updated, then again we will refresh the spot of existing explorer negotiator. After this process, all the coefficients points r, R and Q are updated, and appropriateness value of all the explorer negotiator is calculated which is present in the form of users, who have rated the movies. After the implementation of gray wolf optimization in Movielens dataset, then users' centers of a particular cluster are selected randomly. The results generated by grey wolf optimization technique were later on adopted by FCM. A membership matrix is initialized, and then, center vectors are calculated. Membership matrices are updated with the help of user rating and movie ratings which are retrieved by the vectors. Finally, all the clusters and clusters centers are returned with effective ratings which are estimated by the help of a mean absolute error, precision and recall.

Table 1 Assessment of state of the art methods with different metrics

Method/system	MAE	SD	Precision	Recall
K-means	0.7	0.62	0.53	0.43
PCA-K-means	0.64	0.73	0.57	0.48
K-means-improved	0.69	0.65	0.52	0.42
SOM-cluster	0.79	0.08	0.31	0.23
FCM	0.77	0.53	0.49	0.38
UPCC	0.83	0.67	0.17	0.28
KM-PSO-FCM	0.74	0.77	0.54	0.41
PCA-SOM	1.96	1.15	0.16	0.15
PCA-GAKM	0.92	0.18	0.49	0.33
GAKM-cluster	0.78	0.13	0.37	0.45
PCA	1.99	1.48	0.19	0.22
Proposed	0.68	0.54	0.55	0.49

4 Experiment outcomes and investigation

In this segment, we will discuss the analysis of experiments of the projected RS which was performed on the Movielens dataset (http://grouplens.org/datasets/movielens/). We performed all these experiments on the system which has a configuration as Intel I3 processor, 8 GB RAM and Python 2.7.10 environment.

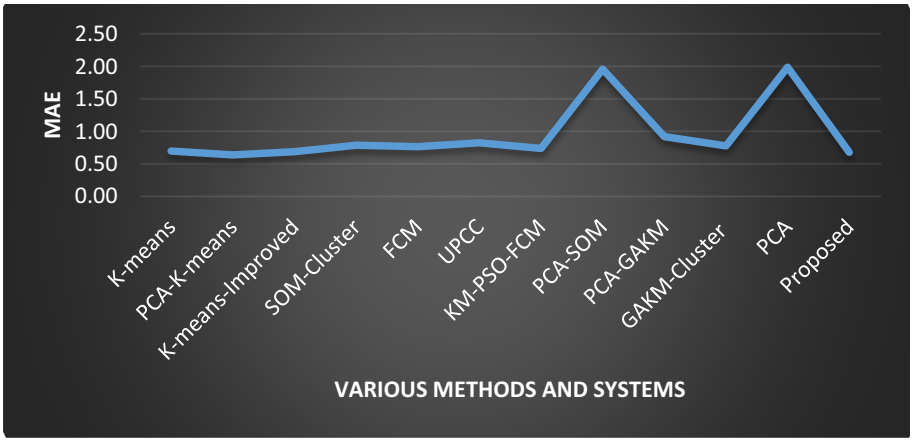


Fig. 4 Comparison of various methods and systems for MAE

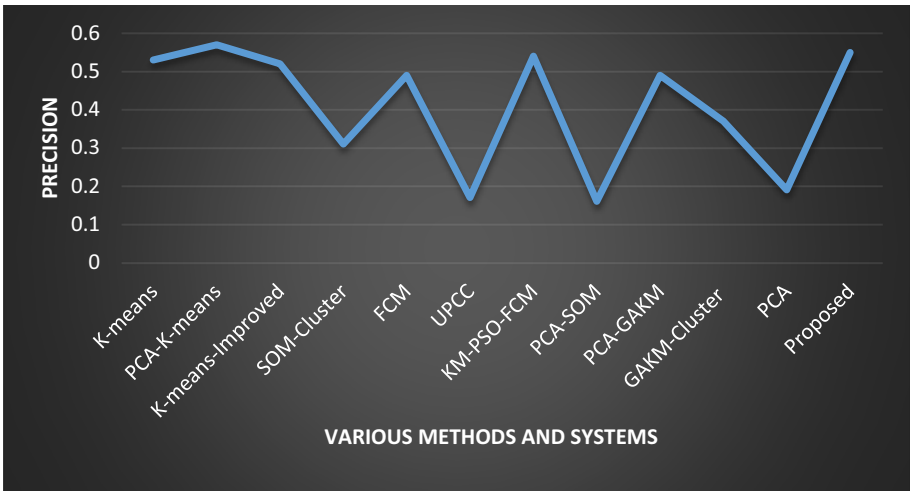


Fig. 5 Comparison of various methods and systems for precision

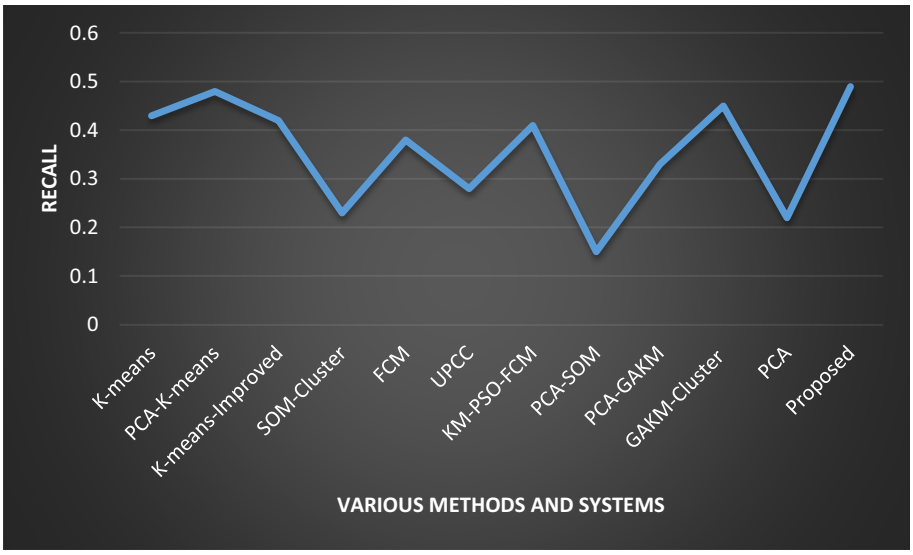


Fig. 6 Comparison of various methods and systems for recall

4.1 Dataset and evaluation procedures

For the evaluation of our proposed recommender system, we considered the Movielens dataset which is available publically. The University of Minnesota collected the dataset for the GroupLens research project. The Movielens dataset contains the 100, 000 ratings (1–5) and 943 users who have rated 1682 movies. Every user from 943 has

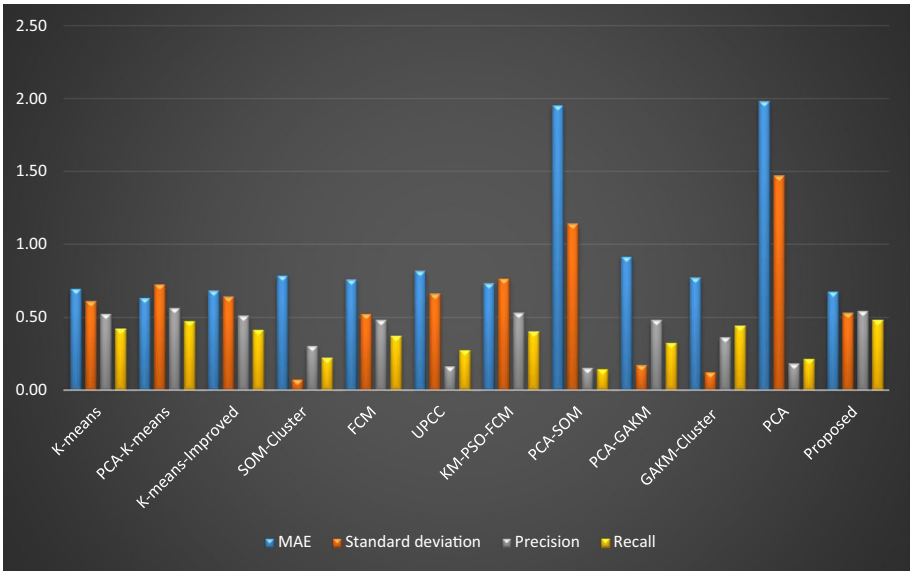


Fig. 7 Comparison of the state of art methods and systems with various metrics

rated at least 20 movies. To understand the behavior of the user's recommendation quality, we adopted some evaluation matrices. We calculated means absolute error (MAE) which is the most popular metric to understand the conduct of a recommender system. We also calculated the precision and recall for the proposed system, so that we can analyze the interest of users in a particular movie or collection of movies.

$$\text{MAE} = \frac{\sum \| o_{gh} - s_{gh} \|}{G} \tag{1}$$

$G =$ entire amount of expected movies, o_{gh} = expected value for user g on item h, $s_{gh} =$ real rating.

$$\text{Precision} = \left| \frac{\text{Interesting} \cap \text{Top}N}{N} \right| \tag{2}$$

$$\text{Recall} = \left| \frac{\text{Interesting} \cap \text{Top}N}{|\text{Interesting}|} \right| \tag{3}$$

If the MAE value is small, then prediction accuracy is superior. And if precision and recall values are high, then recommender system's prediction accuracy is better.

4.2 Results

In this segment, we mentioned the outcomes and comparisons which were performed on various already existing systems by adopting Movielens dataset of 100 K.

In Table 1, we have compared proposed system with other existing systems. The proposed system has a mean absolute error as 0.68, which is much better than PCA and PCA-SOM methods. K-means, PCA-K-means, K-means-improved, SOM-Cluster, FCM, KM-PSO-FCM and GAKM-Cluster have MAE ranges from 0.64 to 0.78. Some of the methods did not respond well, for example, SOM-Cluster, UPCC, PCA-GAKM, PCA-SOM, and PCA has 0.79, 0.83, 0.92, 1.96 and 1.99, respectively. As far as other evaluation metrics is concerned such as standard deviation, precision and recall, our proposed system also delivered enhanced results.

In Figs. 4, 5 and 6, comparisons of different systems are compared by MAE, precision and recall, respectively.

In Fig. 7, all evaluation metrics such as mean absolute error, standard deviation, precision and recall are compared for the different existing systems and the proposed system.

So we concluded from Fig. 7 and Table 2 that our proposed system performed well with valuable recommendations and performance for the Movielens dataset.

Table 2 Comparison of speed of different methods and systems for Movielens dataset

Method	Time (in seconds)
K-means	24.75
PCA-K-means	67.56
K-means-improved	23.48
SOM-cluster	89.11
FCM	42.67
UPCC	181.23
KM-PSO-FCM	140.43
PCA-SOM	152.89
PCA-GAKM	31.25
GAKM-cluster	332.31
PCA	19.65
Proposed	66.45

5 Conclusion and future work

Recommender systems are helpful for the organizations and e-commerce business in such manner that they help the users to choose relevant products from billions of products. Similarly, companies will get to know their customer more in depth such as their behaviors, likes and patterns. We have presented a new and efficient collaborative movie-based recommender system. Our proposed recommender system performed superiorly when compared with already existing systems. As suggested, recommender system delivered the mean absolute error, standard deviation, precision and recall as 0.68, 0.54, 0.55 and 0.49, respectively. The performance of proposed system with respect to time is also superior as compared to existing systems. As far as future work is a concern, we will apply this system by including demographic features, sentiments, machine learning and big data environment. We can also enhance the quality of our proposed recommender system by including some important factors such as privacy, trust within the group, contextual information and application of hybrid systems.

References

1. Katarya R, Verma OP (2016) A collaborative recommender system enhanced with particle swarm optimization technique. Multimed Tools Appl 75:1–15
2. Ortega F, Hernando A, Bobadilla J, Kang JH (2016) Recommending items to group of users using Matrix Factorization based Collaborative Filtering. Inf Sci (Ny) 345:313–324
3. Bobadilla J, Ortega F, Hernando A, Gutiérrez A (2013) Recommender systems survey. Knowl-Based Syst 46:109–132
4. Katarya R, Verma OP (2016) Recent developments in affective recommender systems. Phys A Stat Mech Appl 461:182–190
5. Katarya R, Jain I, Hasija H (2014) An Interactive Interface for Instilling Trust and providing Diverse Recommendations. In: 2014 IEEE international conference on computer and communication technology (ICCCT). pp 17–22
6. Ji K, Shen H (2016) Jointly modeling content, social network and ratings for explainable and cold-start recommendation. Neurocomputing 218. doi:10.1016/j.neucom.2016.03.070
7. Zhao WX, Li S, He Y et al (2016) Connecting social media to e-commerce: cold-start product recommendation using microblogging information. IEEE Trans Knowl Data Eng 28:1147–1159
8. Son LH (2016) Dealing with the new user cold-start problem in recommender systems: a comparative review. Inf Syst 58:87–104
9. Da Silva EQ, Camilo-Junior CG, Pascoal LML, Rosa TC (2016) An evolutionary approach for combining results of recommender systems techniques based on collaborative filtering. Expert Syst Appl 53:204–218
10. Zhou Q (2016) Supervised approach for detecting average over popular items attack in collaborative recommender systems. IET Inf Secur 10:134–141
11. Yang Z, Xu L, Cai Z (2015) Re-scale adaboost for attack detection in collaborative filtering recommender systems. Knowl-Based Syst 100. doi: 10.1016/j.knosys.2016.02.008
12. Liang X, Xia Z, Pang L, et al. (2016) Measure prediction capability of data for collaborative filtering. Knowl Inf Syst 49(3):975–1004. doi:10.1007/s10115-016-0920-5
13. Hernando A, Bobadilla J, Ortega F (2016) A non negative matrix factorization for collaborative filtering recommender systems based on a bayesian probabilistic model. Knowl-Based Syst 97:188–202
14. Xu Y, Yin J (2015) Engineering Applications of artificial intelligence collaborative recommendation with user generated content. Eng Appl Artif Intell 45:281–294
15. Puglisi S, Parra-Arnau J, Forné J, Rebollo-Monedero D (2015) On content-based recommendation and user privacy in social-tagging systems. Comput Stand Interfaces 41:17–27
16. Puglisi S, Parra-Arnau J, Forné J, Rebollo-Monedero D (2015) On content-based recommendation and user privacy in social-tagging systems. Comput Stand Interfaces 41:17–27
17. Zhao WX, Li S, He Y, et al. (2015) Exploring demographic information in social media for product recommendation. Knowl Inf Syst 49(1):61–89. doi: 10.1007/s10115-015-0897-5
18. Katarya R, Verma OP (2015) Restaurant recommender system based on psychographic and demographic factors in mobile environment. In: 2015 IEEE international conference on green computing internet things. pp 907–912
19. Al-Shamri MYH (2016) User profiling approaches for demographic recommender systems. Knowl-Based Syst 100:1–13
20. Moradi P, Gholampour M (2016) A hybrid particle swarm optimization for feature subset selection by integrating a novel local search strategy. Appl Soft Comput 43:1–14
21. Capdevila J, Arias M, Arratia A (2016) GeoSRS: a hybrid social recommender system for geolocated data. Inf Syst 57:111–128
22. Pessemier T De, Dhondt J, Martens L (2016) Hybrid group recommendations for a travel service. Multimed Tools Appl 1–25. doi10.1007/s11042-016-3265-x
23. Mirjalili S, Saremi S, Mirjalili SM, Coelho LDS (2016) Multi-objective grey wolf optimizer: a novel algorithm for multi-criterion optimization. Expert Syst Appl 47:106–119
24. Mirjalili S, Mirjalili SM, Lewis A (2014) Grey wolf optimizer. Adv Eng Softw 69:46–61
25. Emary E, Yamany W, Hassanien AE, Snasel V (2015) Multi-objective gray-wolf optimization for attribute reduction. Procedia Comput Sci 65:623–632
26. Emary E, Zawbaa HM, Hassanien AE (2016) Binary grey wolf optimization approaches for feature selection. Neurocomputing 172:371–381
27. Koohi H, Kiani K (2016) User based collaborative filtering using fuzzy c-means. Measurement 91:134–139
28. Cannon RL, Dave JV, Bezdek JC (1986) Efficient implementation of the fuzzy c-means clustering algorithms. IEEE Trans Pattern Anal Mach Intell 8:248–255
29. Havens TC, Bezdek JC, Leckie C et al (2012) Fuzzy c-means algorithms for very large data. IEEE Trans Fuzzy Syst 20:1130–1146
30. Bezdek JC, Ehrlich R, Full W (1984) FCM: the fuzzy *c*-means clustering algorithm. Comput Geosci 10:191–203
31. Boratto L, Carta S, Fenu G (2016) Investigating the role of the rating prediction task in granularity-based group recommender systems and big data scenarios. Inf Sci (Ny) 378:1–20
32. Wang W, Zhang G, Lu J (2016) Member contribution-based group recommender system. Decis Support Syst 87:80–93
33. Zuo Y, Zeng J, Gong M, Jiao L (2016) Tag-aware recommender systems based on deep neural networks. Neurocomputing 204:1–10
34. He C, Parra D, Verbert K (2016) Interactive recommender systems: a survey of the state of the art and future research challenges and opportunities. Expert Syst Appl 56:9–27

35. Yera R, Castro J, Martínez L (2016) A fuzzy model for managing natural noise in recommender systems. Appl Soft Comput 40:187–198
36. Horváth T, de Carvalho ACPLF (2016) Evolutionary computing in recommender systems: a review of recent research. Nat Comput 1–22. doi:10.1007/s11047-016-9540-y
37. Bouadjenek MR, Hacid H, Bouzeghoub M (2016) Social networks and information retrieval, how are they converging? A survey, a taxonomy and an analysis of social information retrieval approaches and platforms. Inf Syst 56:1–18
38. Lu J, Wu D, Mao M et al (2015) Recommender system application developments: a survey. Decis Support Syst 74:12–32
39. Klašnja-Milićević A, Ivanović M, Nanopoulos A (2015) Recommender systems in e-learning environments: a survey of the state-of-the-art and possible extensions. Artif Intell Rev 44:571–604
40. Beel J, Gipp B, Langer S, Breitinger C (2015) Research-paper recommender systems: a literature survey. Int J Digit Libr 17(4):305–338. doi:10.1007/s00799-015-0156-0
41. Gang L, Chun-ling H, Sheng-bing C (2015) Research on recommender system based on ontology and genetic algorithm. Neurocomputing 187:1–6
42. Kar AK (2016) Bio inspired computing—a review of algorithms and scope of applications. Expert Syst Appl 59:20–32
43. Jaddi NS, Alvankarian J, Abdullah S (2017) Kidney-inspired algorithm for optimization problems. Commun Nonlinear Sci Numer Simul 42:358–369
44. Li H, Cui J, Shen B, Ma J (2016) An intelligent movie recommendation system through group-level sentiment analysis in microblogs. Neurocomputing 210:1–10
45. Iglesias JA, Tiemblo A, Ledezma A, Sanchis A (2016) Web news mining in an evolving framework. Inf Fusion 28:90–98
46. Wang S, Gong M, Li H, Yang J (2016) Multi-objective optimization for long tail recommendation. Knowl-Based Syst 104:145–155
47. Zuo Y, Zeng J, Gong M, Jiao L (2016) Tag-aware recommender systems based on deep neural networks. Neurocomputing 204:1–10
48. Ramírez-Gallego S, García S, Benítez JM, Herrera F (2016) Multivariate Discretization Based on Evolutionary Cut Points Selection for Classification. IEEE Trans Cybern 46:595–608

Optik 132 (2017) 164–170

Contents lists available at ScienceDirect

Optik

journal homepage: www.elsevier.de/ijleo

Original research article

SBS based slow-light generation in rectangular lattice graded-index photonic crystal fiber: Design and analysis

Sandeep Yadav [a], Ajeet Kumar [a,*], Than Singh Saini [b], Ravindra Kumar Sinha [b]

[a] Advanced Photonics Simulation Laboratory, Delhi Technological University, Delhi 110042, India
[b] CSIR-Central Scientific Instruments Organization, Chandigarh 160030, India

ARTICLE INFO

Article history:
Received 2 June 2016
Received in revised form
13 December 2016
Accepted 15 December 2016

Keywords:
Nonlinear optics
Stimulated brillouin scattering
Photonics crystal fiber

ABSTRACT

Theoretical analysis of stimulated Brillouin scattering based slow-light in As_2Se_3 based chalcogenide photonic crystal fiber has been reported. A maximum time-delay of 252.8 ns has been achieved for 1 m long fiber at input pump power of 9.8 mW. A maximum gain of 99 dB/m has been obtained for the same input pump-power. The simulated results indicate that the time-delay can be tuned by varying the input pump-power and the size of the air holes to obtain tunable features. We feel that the comprehensive theoretical investigation carried out in this paper have potential impact in the design and development of slow-light based photonic devices.

© 2016 Published by Elsevier GmbH.

1. Introduction

The Slow-light is a key method for the potential alternates of electronic delay lines in the telecommunications because such tunable delays helps in various digital signals processing functions that are very useful in communication systems. This method is quite helpful in accurate and fine control of an optical delay in high bit-rate systems such as time-division-multiplexers, data equalization using tapped-delay-lines, and optical correlation where the control of light within fraction of time is very tough [1,2]. There are many other applications of slow-light such as optical buffering, microwave photonics, optical memories, optical signal processing and precise interferometric instruments [3–5]. This technique also provides anticipative solution of broadband and tunable time-delay for microwave and milli-meter wave systems [6,7].

Slow-light is ultimately a technique that alters the propagation of pulses through any medium to generate unusual effects including time delay that refers to slow propagation velocities. As we all know that a monochromatic light travels at the phase velocity given by V_P

$$V_p = \frac{\omega}{k} = \frac{c}{n} \tag{1}$$

where, ω is angular frequency, k is the wave number, c is the speed of light in vacuum and n is the refractive index of the medium. From the above Eq. (1), it can be concluded that V_P is dependent on the refractive index of the material. As a pulse of light is generated by the interference of large number of sinusoidal waves and each of them has their own phase velocity. In a dispersive material, n varies with the wavelength and hence each component of wave packet will travel at different

* Corresponding author.
E-mail address: ajeetdph@gmail.com (A. Kumar).

http://dx.doi.org/10.1016/j.ijleo.2016.12.048
0030-4026/© 2016 Published by Elsevier GmbH.

phase velocities. Therefore we need to define another velocity known as group velocity (V_G) to analyse the movement of the wave packets

$$V_G = \frac{d\omega}{dk} = \frac{c}{n_G} \tag{2}$$

and

$$n_G = n(\omega) + \omega \frac{dn(\omega)}{d\omega} \tag{3}$$

Therefore, the relation between the group velocity and the refractive index is give as

$$V_G = \frac{c}{n(\omega) + \omega \frac{dn(\omega)}{d\omega}} \tag{4}$$

Thus by increasing the denominator of Eq. (4), we can reduce the group velocity of the wave packet.

Previously, slow-light has been achieved using various techniques. *Hau* et al. has achieved slow-light using electromagnetically induced transparency (EIT) [8]. *Bigelow* et al. has explained coherent population oscillation (CPO) method to achieve slow-light [9]. Raman-assisted optical parametric amplification has been used by *Shumakher* et al. [10]. Inspite of these method, other methods of slow light are also introduced which include stimulated Raman scattering (SRS), stimulated Brillouin scattering (SBS) and slow-light relaying on dispersive media [11–17]. Among all the methods SBS is preferred because it is simple, flexible and easy to handle in fiber geometry. The optical fiber components based on it can be easily realised. The slow-light resonance is tunable within optical communication wavelength.

Earlier, slow-light has been studied in the fiber of various material having different non-linear refractive indices. Initially silica was used as a material in step index optical fiber by *Schneider* et al. [18] to acquire effective time-delay. But it was observed that the length of the fiber is of kilometre range to achieve effective time-delay. Hence to reduce the length of the fiber, a lot of efforts were made by changing the material with higher non-linear refractive indices like tellurite, As_2S_3 chalcogenide and As_2Se_3 chalcogenide [19–25]. Some researcher have used photonic crystal fibers (PCF) instead of conventional fibers for analysis of slow-light and found better time delay in PCF. *Yang* et al. have designed a short length PCF for SBS based slow-light application [26]. *Woodward* et al. [27] characterized silica based PCF pumped with 532 nm to study SBS of visible light. Another material chosen was tellurite by *Ohishi* et al. [28]. They observed a maximum time delay of 74 ns for a 200 m long PCF pumped with input pump power of 19.7 mW [28]. A maximum time delay of 88 ns has been reported by *Saini* et al. in 1 m long PCF pumped with 140 mW input pump power [29]. For the first time, chalcogenide was used by *Pant* et al. for the study of slow light [30]. They reported a time delay of 23 ns for a 7 cm long chalcogenide rib waveguide [30]. *Song* et al. [31] has reported a time-delay of 37 ns for a 5 m long conventional fiber with As_2Se_3 material pumped with 60 mW power and 60 ns Gaussian pulses. Recently, a single mode PCF structure has been reported in As_2Se_3 based chalcogenide glass for the time-delay of 137 ns in 1 m long PCF pumped with 100 mW [32].

In this paper, we have deliberated a new graded-index PCF structure with rectangular-core for the analysis of SBS based slow-light. The intrinsic material parameters of As_2Se_3 based chalcogenide has been taken from Ref. [23,31]. Other parameters of PCF like effective mode area (A_{eff}), maximum threshold pump power (P_{max}), minimum pump power required for SBS (P_{min}), time-delay and Brillouin gain (G) has been simulated numerically. From the simulated results it is experienced that the time-delay of the PCF depends mainly on A_{eff} which can be tuned either by changing the diameter of the air holes or by changing the pitch of the air holes in the PCF structure.

2. Theory of SBS based slow light

SBS is a non-linear optical phenomenon which can be used for development of new laser sources, slow-light devices and distributed fiber sensors. It is a process of interaction of two counter propagating waves, one is known as strong pump wave and another is termed as weak stokes wave.

$$\nu_{pump} = \nu_{stokes} + \nu_B \tag{5}$$

If Eq. (5) is satisfied by the two waves then an acoustic wave is generated which emits photons from the pump to stokes wave and the interference of these two waves will stimulate the SBS process. Here ν_{pump} and ν_{stokes} are the frequencies of the pump wave and stokes wave respectively and ν_B is the Brillouin frequency [33].

Let I_P and I_S be the intensities of the pump wave and the stokes wave and α_P and α_S be the fiber losses at pump and stokes waves respectively and g_B is the Brillouin gain coefficient, then the coupled nonlinear differential equation for pump and stokes is given by

$$\frac{dI_P}{dz} = -g_B I_P I_S - \alpha_P I_P \tag{6}$$

$$-\frac{dI_s}{dz} = +g_B I_P I_S - \alpha_S I_S \tag{7}$$

Assuming the pump wave is undepleted and ($\alpha_P \approx \alpha_S$) = α, then the solution of above differential Eqs. (6) and (7) is given by relation

$$I_S(0) = I_S(L)\exp\left(\frac{g_B P_0 L_{eff}}{A_{eff}} - \alpha L\right) \tag{8}$$

with

$$L_{eff} = \frac{[1-\exp(-\alpha L)]}{\alpha} \tag{9}$$

where L_{eff} is the effective length of the PCF, L is the real of the PCF and α is the material loss coefficient, P_0 is the input pump power, A_{eff} is the effective mode area of the propagating mode in the PCF.

The Brillouin gain can be expressed as

$$g_B(\Omega) = \left(\frac{g_P(\Gamma_B/2)^2}{(\Omega-\Omega_B)+(\Gamma_B/2)^2}\right) \tag{10}$$

where, Γ_B is the SBS line width, g_P is the peak value of the Brillouin gain at $\Omega = \Omega_B$ and given by relation

$$g_P = g_B(\Omega_B) = \frac{2\pi n^7 {p_{12}}^2}{c{\lambda_P}^2 \nu_A \Delta_{\nu_B}} \tag{11}$$

where, $\Delta_{\nu B}$ is the Brillouin gain bandwidth, ν_A is the acoustic velocity, n is the refractive index of the material of the fiber, p_{12} is the longitudinal elasto-optic coefficient, c is the velocity of the light, λ_P is the wavelength of the pump wave.

Every designed PCF has its own capacity to work below some threshold power above which the output pulse will be distorted. That maximum power is termed as $P_{\max}$ and can be calculated by using Eq. (12) [34]

$$P_{\max} = 21\frac{A_{eff}}{K g_B L_{eff}} \tag{12}$$

In the same way, we can calculate the minimum pump power required to initiate the SBS effect using the relation [34]

$$P_{\min} = \frac{\alpha A_{eff} L}{K g_B L_{eff}} \tag{13}$$

where, K is the polarization factor and depends on the polarization properties of the PCF. We have used $K = 0.667$, which is appropriate for the fiber with low birefringence and very high polarization factor like chalcogenide.

The time delay that is induced due to the SBS per unit length by slow-light fiber devices can be expressed as [35]

$$\frac{\Delta_{t_d}}{L_{eff}} = \frac{P_P g_0 K}{\Gamma_B} \tag{14}$$

where, Δ_{td} is the time-delay achieved, P_P is the input pump-power, g_0 is the inherent material gain coefficient as $g_0 = g_B/A_{eff}$.

Similarly the Brillouin gain (G) has been calculated by using the relation [36]

$$Gain = 10\log\left(\exp\left(g_B K\left(\frac{P_P}{A_{eff}}\right)L_{eff}\right)\right) \tag{15}$$

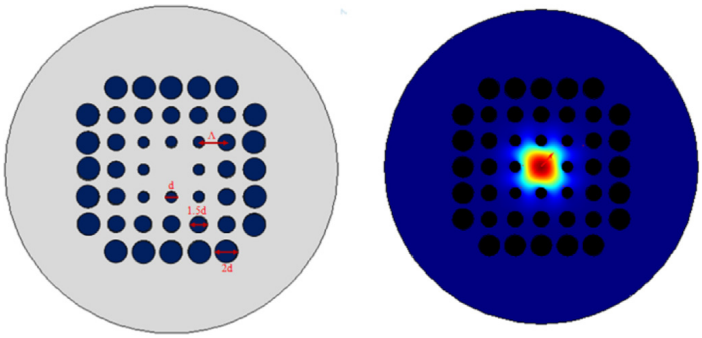
3. Design of the proposed PCF

We have designed a graded-index PCF for the study of SBS based slow-light. The transverse cross-sectional view and the normalized electric field pattern of the fundamental mode of the PCF have been shown in Fig. 1(a) and (b) resepectivly.

We have used As_2Se_3 as the material of the PCF in which air-holes are arranged in rectangular manner. The reason for opting rectangular lattice is to avoid the birefringence effect of the design of the PCF. The diameters of the air-holes in successive rectangular ring is kept increasing to obtain graded-index refractive index profile in the cladding region. In our design, there are 3 layers of the air-holes having the diameters of air holes *d*, *1.5d*, and *2d* for first, second and third layer respectively. The refractive index of the As_2Se_3 material has been calculated by using the Sellemier equation for a wavelength of 1.55 μm [37]. The distance between the centres of two consecutive air holes is known as the pitch (Λ) of the PCF, which is kept constant in our design to 1 μm. The diameters of the air holes have been varied to find the effective mode area (A_{eff}) and the confinement loss.

4. Results and discussion

For The inherent properties of the As_2Se_3 chalcogenide material such as: SBS linewidth (Γ_B = 13.2 MHz), Brillouin gain coefficient (g_B = 6.0 × 10 − 9 m/W) have been taken from the Ref. [23]. The refractive index of the As_2Se_3 chalcogenide has been found by using Sellemier equation form Ref. [37].



(a) (b)

Fig. 1. **(a)** Transverse cross-sectional view of the proposed graded-index photonic crystal fiber; (b) normalized electric field pattern of propagating mode in proposed graded-index photonic crystal fiber with Λ = 1 μm and d = 0.5 μm.

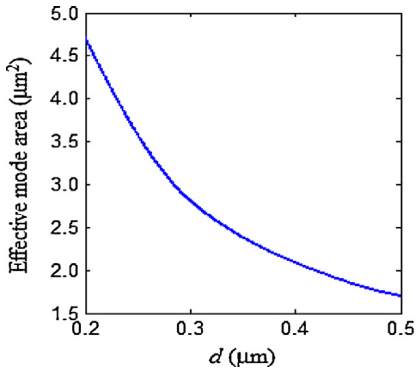


Fig. 2. Variation of A_{eff} with the diameter (d) of the air holes.

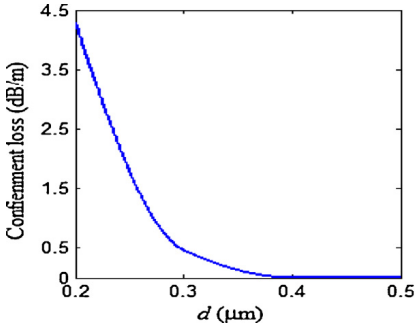


Fig. 3. Variationof confinement loss with diameter (d).

The first parameter calculated in our simulation is effective mode area (A_{eff}) of the designed graded index PCF. For the calculation of A_{eff}, we had varied the diameter (d) of the air holes. A_{eff} plays a very important role in the non-linear effects of the PCF. It depends on the Air filling fraction of the PCF. Air filling fraction of the PCF is defined as the ratio of the diameter of the air-holes (d) and the distance between the centres of the air-hole i.e. pitch (Λ). Since, in our simulation the pitch is kept constant to 1 μm so the air filling fraction (i.e. d/Λ) is mainly dependent on diameter (d) of the air holes. So, as the diameter of the air-holes kept on increasing, the value of A_{eff} will decrease due to core size reduction. The variation of the A_{eff} has been shown in Fig. 2. From our calculations the value of A_{eff} is 1.72 μm^2 for $d = 0.5$ μm.

Another important parameter calculated by us is the confinement loss of the designed graded index PCF. The confinement loss of the PCF basically depends on the confinement of the light in the core region. As the diameter of the air holes increases the difference between the refractive indices of the core and cladding also increases which leads to the higher confinement of light and thus the confinement loss keeps on decreasing with increasing the diameter of the air-holes which is shown in Fig. 3.

P_{max} and P_{min} are two important parameters for the calculation of time delay. Fig. 4 represents how the values of P_{max} and P_{min} vary with the increasing diameter of the air-holes. From which we can see that as the diameter of the air-holes increases, the value of both P_{max} and P_{min} decreases, it is because of the strong confinement of the modal field within the

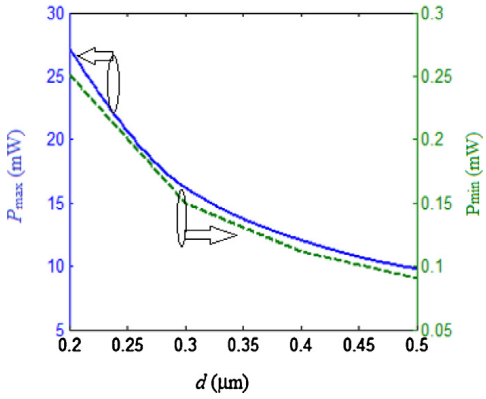


Fig. 4. P_{max} and P_{min} varied with diameter (d).

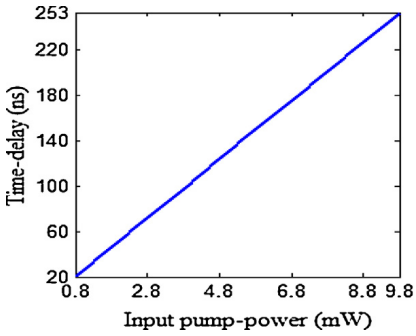


Fig. 5. Variation of the Time-delay with input pump-power.

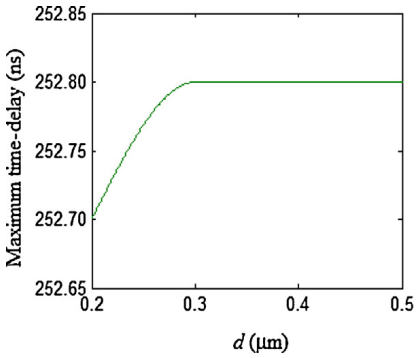


Fig. 6. Maximum time-delay varying with respect to diameter of the air holes.

core on increasing *d*. There is a small kink near $d \sim 0.28$ μm, which can be explain by considering the confinement loss profile of the PCF structure which is shown in Fig. 3. Initially the slop of the loss profile is large on increasing *d*. After $d \sim 0.28$ μm the slop of the loss profile start to decrease. Since the P_{min} is directly proportional to the loss coefficeint, the slop of the P_{min} curve is also start to decrease after $d \sim 0.28$ μm. The value of P_{max} and P_{min} are 9.81 mW and 0.09 mW for $d = 0.5$ μm.

The time-delay in the PCF structure is depend on the input pump-power. The value of P_{max} and P_{min} are 9.81 mW and 0.09 mW for $d = 0.5$ μm. The variation of the time-delay with that of the input pump-power has been shown in Fig. 5 within the variation ranging from 0.8 mW to 9.8 mW. A maximum time-delay of 252.8 ns has been achieved for the maximum input pump-power of 9.8 mW for 1 m long PCF. The time-delay increases with the input pump-power due to stimulated effect, where the optical fields substantially contribute to the phonon population.

Fig. 6 represents the variation of the maximum time-delay for different values of the *d*. From this figure we can easily conclude that the maximum time delay remains the same for all the values of the diameter, but the main advantage of increased diameter is that the input power required for the maximum time-delay has been reduced. As we can see P_{max} for $d = 0.4$ is 12.06 mW whereas the same P_{max} for $d = 0.5$ is 9.81 mW. For both the input pump-powers the maximum time-delay achieved is 252.8 ns. Hence it can be easily concluded that the PCF with more diameter of air holes is superior to the PCF with lesser diameter of air holes. It is because of ethe reduction in the losses as well as effective mode area of the propagating mode on incresing *d*.

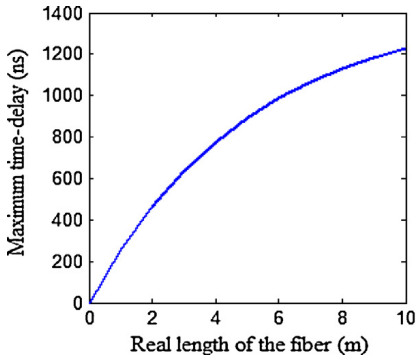


Fig. 7. Maximum time-delay varying with real length of the fiber.

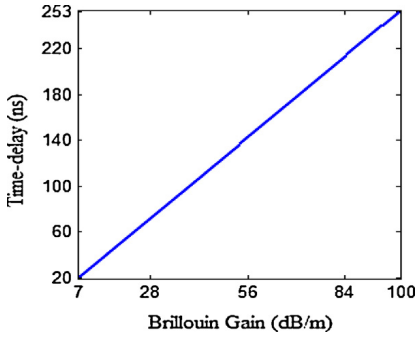


Fig. 8. Time-delay varying with the Gain of the PCF.

The variation of the maximum time delay for $d = 0.5\,\mu m$ has been shown in Fig. 7. From Fig. 7 we can conclude that initially the maximum time-delay keeps on increasing and then gets stable after some length. We have plotted the graph for the length of upto 10 m and a maximum time delay of around 1200 ns has been achieved.

Brillouin gain is also another very important parameter for a PCF structrure. As the diameter of the air-holes increases the light beam is confined within the core and hence there is a great enhancement in the Brillouin scattering which leads to greater Brillouin gain as shown in Fig. 8.

5. Conclusion

A novel highly nonlinear rectangular-core graded-index photonic crystal fiber structure in As_2Se_3 chalcogenide glass has been designed and analysed for slow-light applications based on SBS. A maximum time-delay of 252.8 ns has been achieved for low input power of 9.8 mW. Also a maximum Brillouin gain of 99.78 dB/m has been simulated with such a small power requirements. Our results has been found better than earlier reported works in Refs. [19,20,32]. Using the proposed PCF strrucutre larger time-delay and very high Brillouin gain have been obtained with lower pump-power. The time-delay can be tuned by varying the diameter of the air-holes and the pump power, and hence the tuneable features of the slow-light can be achieved. The designed graded index PCF is expected to have the potential applications in the realization of compact slow-light based photonic devices.

Acknowledgements

The authors gratefully acknowledge the TUN-IND bilateral research project, Department of science and Technology, Govt. of India.

References

[1] D.J. Blumenthal, P.R. Pruncal, J.R. Sauer, Photonic packet switches: architectures and experimental implementations, Proc. IEEE 82 (1994) 1650–1667.
[2] G.M. Gehring, R.W. Boyd, A.L. Gaeta, D.J. Gauthier, A.E. Willner, Fiber-based slow-light technologies, J. Lightwave Technol. 26 (2008) 3752–3762.
[3] J.T. Mok, B.J. Eggleton, Expect more delays, Nature 433 (2005) 811–812.
[4] S. Rawal, R.K. Sinha, R.M. De La Rue, Slowlight miniature devices with ultra-flattened dispersion in silicon-on-insulator photonic crystal, Opt. Exp. 17 (2009) 13315–13325.
[5] S. Rawal, R.K. Sinha, R.M. De La Rue, Silicon-on-insulator photonic crystal miniature devices with slow light enhanced third-order nonlinearities, J. Nanophoton. 6 (2012) 063504.
[6] M. Santagiustina, G. Eisenstien, L. Thevenaz, J. Capmany, J. Mork, J.P. Reithmaier, A. De Rossi, S. Sales, K. Yvind, S. Cambrie, J. Bourderionnet, Slow light devices and their applications to microwaves and photonics, IEEE Photon. Soc. Newslett. 26 (2012) 5–12.

[7] J. Capmany, I. Gasulla, S. Sales, Microwave photonics: harnessing the speed of light, Nat. Photon. 5 (2011) 731–733.
[8] L.V. Hau, S.E. Harris, Z. Dutton, C.H. Behroozi, Light speed reduction to 17 metres per second in an ultracold atomic gas, Nature 397 (1999) 594–598.
[9] M.S. Bigelow, N.N. Lepeshkin, R.W. Boyd, Superluminal and slow-light propagation in a room-temperature solid, Science 301 (2003) 200–202.
[10] E. Shumakher, A. Willinger, R. Blit, D. Dahan, G. Eisenstein, Large tunable delay with low distortion of 10 Gbit/s data in a slow light system based on narrow band fiber parametric amplification, Opt. Exp. 14 (2006) 8540–8545.
[11] J. Sharping, Y. Okawachi, A. Gaeta, Wide bandwidth slowlight using a Raman fiber amplifier, Opt. Exp. 13 (2005) 6092–6098.
[12] S.H. Wang, L.Y. Ren, Y. Liu, Y. Tomita, Zero-broadening SBS slow light propagation in an optical fiber using two broadband pump beams, Opt. Exp. 16 (2008) 8067–8076.
[13] L.Y. Ren, Y. Tomita, Transient and nonlinear analysis of slow-light pulse propagation in an optical fiber via stimulated Brillouin scattering, J. Opt. Soc. Am. B 26 (2009) 1281–1288.
[14] D. Dahan, G. Eisenstien, Tunable all optical delay via slow and fast light propagation in a Raman assisted fiber optical parametric amplifier: a route to all optical buffering, Opt. Exp. 13 (2005) 6234–6248.
[15] A. Kobyakov, M. Sauer, D. Chowdhury, Stimulated Brillouin scattering in optical fibers, Adv. Opt. Photon. 2 (2010) 1–59.
[16] E.P. Ippen, R.H. Stolen, Stimulated Brillouin scattering in optical fibers, Appl. Phys. Lett. 21 (1972) 539–540.
[17] T. Baba, Slow light in photonic crystals, Nat. Photon. 2 (2008) 465–473.
[18] T. Schneider, D. Hannover, M. Junker, Investigation of Brillouin scattering in optical fibers for the generation of millimeter waves, J. Lightwave Technol. 24 (2006) 295–304.
[19] G. Qin, H. Sotobayashi, M. Tsuchiya, A. Mori, T. Suzuki, Y. Ohishi, Stimulated Brillouin scattering in a single mode tellurite fiber for amplification, lasing and slow light generation, J. Lightwave Technol. 26 (2008) 492–498.
[20] T.S. Saini, A. Kumar, R.K. Sinha, Slow light generation in single mode tellurite fibers, J. Modern Opt. 62 (2015) 508–513.
[21] K.S. Abedin, Stimulated Brillouin scattering in single-mode tellurite glass fiber, Opt. Exp. 14 (2006) 11766–11772.
[22] K.S. Abedin, G.W. Lu, T. Miyazaki, Slow light generation in single mode Er-doped tellurite fiber, Electron. Lett. 44 (2008) 16–17.
[23] K.S. Abedin, Observation of strong stimulated Brillouin scattering in single-mode As_2Se_3 chalcogenide fiber, Opt. Exp. 13 (2005) 10266–10271.
[24] C. Florea, M. Bashkanshy, Z. Dutton, J. Sanghera, P. Pureza, I. Aggarwal, Stimulated Brillouin scattering in single-mode As_2S_3 and As_2Se_3 chalcogenide fibers, Opt. Exp. 14 (2006) 12063–12070.
[25] J.H. Lee, T. Tanemura, K. Kikuchi, T. Nagashima, T. Hasegawa, S. Ohara, N. Sugimoto, Experimental comparison of a Kerr nonlinearity figure of merit including the stimulated Brillouin scattering threshold for state-of-art nonlinear optical fibers, Opt. Lett. 30 (2005) 1698–1700.
[26] S. Yang, H. Chen, C. Qiu, M. Chen, M. Chen, S. Xie, J. Li, W. Chen, Slow-light delay enhancement in small core pure silica photonic crystal fiber based on Brillouin scattering, Opt. Lett. 33 (2008) 95–97.
[27] R.I. Woodward, E.J.R. Kelleher, S.V. Popov, J.R. Taylor, Stimulated Brillouin scattering of visible light in small-core photonic crystal fibers, Opt. Lett. 39 (2014) 2330–2333.
[28] Y. Ohishi, G. Qin, M. Liao, C. Chaudhari, T. Suzuki, Opto electronics and communications, Conference, 2009 (OECC 2009)14th, IEEE, paper no. TuD1, 978-1-4244-4103 (2009), http://dx.doi.org/10.1109/OECC.2009.5222772.
[29] T.S. Saini, A. Kumar, R.K. Sinha, Proc. photonics, in: 12th International Conference on Fiber Optics and Photonics @ OSA 2014, IIT Kharagpur, WB, India, Dec 13–16, (2014) T3A.28, 2014.
[30] R. Pant, A. Byrnes, C.G. Poulton, E. Li, D.Y. Choi, S. Madden, B.L. Davies, B.J. Eggleton, Photonic-chip-based tunable slow and fast light via stimulated Brillouin scattering, Opt. Lett. 37 (2012) 969–971.
[31] K.Y. Song, K.S. Abedin, K. Hotate, M.G. Herraez, L. Thevenaz, Highly efficient Brillouin slow and fast light using As2Se3 chalcogenide fiber, Opt. Exp. 14 (2006) 5860–5865.
[32] T.S. Saini, A. Kumar, R.K. Sinha, Analysis and design of single-mode As_2Se_3-chalcogenide photonic crystal fiber for generation of slow light with tunable features, IEEE J. Sel. Top. Quant. Electron. 22 (2016) 4900706.
[33] G.P. Agrawal, Nonlinear Fiber Optics, Academic Press, California, 2002.
[34] R.G. Smith, Optical power handling capacity of low loss optical fibers as determined by stimulated raman and brillouin scattering, Appl. Opt. 11 (1972) 2489–5865.
[35] K.Y. Song, M.G. Herraez, L. Thevenaz, Observation of pulse delaying and advancement in optical fibers using stimulated Brillouin scattering, Opt. Exp. 13 (2005) 82–88.
[36] J.S. Sanghera, C.M. Florea, L.B. Shaw, P. Pureza, V.Q. Nguyen, M. Bashkansky, Z. Dutton, I.D. Aggarwal, Nonlinear properties of chalcogenide glasses and fibers, J. Non-Cryst. Solids 354 (2008) 462–467.
[37] W. Yuan, 2–10 μm mid-infrared super continuum generation in As2Se3 photonics crystal fiber, Laser Phys. Lett. 10 (2013) 095107.

Volume 4, Issue 1 (2016) 361-363 ISSN 2347 - 3258
International Journal of Advance Research and Innovation

Search for Eco-friendly Alternatives Refrigerants in Vapor Compression Refrigeration Systems for Reducing Global Warming and Ozone Depletion

R. S. Mishra
Department of Mechanical Engineering, Delhi Technological University, Delhi, India

Article Info

Article history:
Received 15 January 2016
Received in revised form
10 February 2016
Accepted 28 February 2016
Available online 15 March 2016

Keywords
Sustainable Technologies,
Green Technologies,
Sustainable Development,
Alternative Refrigerants,
Eco Friendly Refrigerants,
Reduction in global warming,
Reduction in ozone depletion

Abstract

In the Make India and Green India Program, the use of eco-friendly refrigerants is well demonstrated due to global warming and ozone depletion.
This paper highlights the use of R-290 refrigerant is the best alternative and second alternative is R600a. and third is R-152a. Due to flammable nature of these eco-friendly refrigerants, these refrigerants can only be used by using safety measures, otherwise R134a and R410a and R404a are easily available in the markets can be used. The performance of R134a gives better than using R410a and R404a, however for larger Industrial applications R 717 and R744 can be used. Even in mixing of nano-particles mixed with R718 in the secondary circuit and R1234yf for low temperature applications gives better first law and second law performance as compared to R134arefrigerant To replace, R134a, R1234yf (of zero ODP and 4 GWP) and R1234ze (GWP=6, and Zero ODP) are recommended, although these refrigerants gives 5 to 10% less performance than using R134a. Although the performance of R134a is better than R134a using nano particles mixing in R718 but R1234ze can replace R134a for higher temperature applications. The best first law and second law performances have been found using copper nano materials mixed with R718 in secondary evaporator circuit as compared to TiO2 nano particles

1. Introduction

Sustainable development is a process in which development can be sustained for generations. It also focuses attention on inter generational fairness in the exploitation of development opportunities while social development is a function of technological advancement, and also the technological advancement, in turn is a function of scientific know how for a streamlined development of the society. Technology is one of the crucial determinants of sustainable development. Technological import through collaborations has been one of the most important sources of technological inputs for Indian conditions. The use of technologies originating in rich countries often ten to create many social, ecological and resource problems in poor countries. The exploitation of the vast natural resources through progressive development of science, engineering and technology that has brought about the vast changes in the civilization and society from the stone age to the present high technology era. In facts, the mad race for industrialization and economic development has resulted in over exploitation of natural resources, leading to a situation where the two worlds of mankind- the biosphere, lithosphere and hydrosphere of his inheritance and the techno sphere of his creation, are out of balance with each other, indeed on a collision path. To facilitate optimal utilization of finite natural resources for ensuring a sustainable benefit steam for better quality of life on the one hand and to simultaneously keep in mind the conservation of natural resources on the other hand, it is essential that the technology conservation process must be made as efficient as possible. Therefore sustainable economic development depends on the careful choice of technologies and judicious management of resources for productive activities to satisfy the changing human needs without degrading the environment or depleting the natural resources base.

Corresponding Author,
E-mail address: professor_rsmishra@yahoo.co.in
All rights reserved: http://www.ijari.org

2. Vapor Compression Refrigeration Systems

Refrigeration is a technology which absorbs heat at low temperature and provides temperature below the surrounding by rejecting heat to the surrounding at higher temperature. Simple vapor compression system which consists of four major components compressor, expansion valve, condenser and evaporator in which total cooling load is carried at one temperature by single evaporator but in many applications like large hotels, food storage and food processing plants, food items are stored in different compartment and at different temperatures. Therefore there is need of multi evaporator vapor compression refrigeration system. The systems under vapor compression technology consume huge amount of electricity, this problem can be solved by improving first law and second law performances of system.

Performance of systems based on vapor compression refrigeration technology can be improved by following:

- The performance of refrigerator is evaluated in term of COP which is the ratio of refrigeration effect to the net work input given to the system. The COP of vapor compression refrigeration system can be improved either by increasing refrigeration effect or by reducing work input given to the system.
- It is well known that throttling process in VCR is an irreversible expansion process. Expansion process is one of the main factors responsible for exergy loss in

cycle performance because of entering the portion of the

- Refrigerant flashing to vapor in evaporator which will not only reduce the cooling capacity but also increase the size of evaporator. This problem can be eliminated by adopting multi-stage expansion with flash chamber where the flash vapors is removed after each stage of expansion as a consequence there will be increase in cooling capacity and reduce the size of the evaporator.
- Work input can also be reduced by replacing multi-stage compression or compound compression with single stage compression.
- Refrigeration effect can also be increased by passing the refrigerant through sub cooler after condenser to evaporator.
- Use of nano particles mixed with R718 in the secondary evaporator circuit
- Use of nano particles directly mixed with eco-friendly
- refrigerants in the primary circuit
- Use of nano particles coating in the VCR condenser tubes.

3. Appropriate Refrigeration Technologies for Sustainable Development

The efforts under the Montreal protocol to protest the Ozone layer, the alternative refrigerants have been proposed as substitutes for ozone depleting substances. HFCs (Hydro-fluoro carbons) PFCs (Perfluro carbons) have zero ODP potential but they are producer of green house gases and are subjected to limitation and reduction commitments under UNFCC (United Nations Framework Convention on Climate change). With the entry into force of Kyoto protocol on 16th February 2005 developed countries have already planning and implementing rational measures intended to contribute towards meeting green house gas reduction targets during the first commitment period of Kyoto protocol (2008-2012). The countries have also started together with developing countries to size up projects that qualify under Kyoto clean development mechanism. In the developing countries the conversion of CFCs to alternate is still a major issue. In this paper the first law and second law analysis of various eco friendly refrigerants have been carried out which will help in deciding about the path to be followed to satisfy Montreal and Kyoto protocol. R-22 is the refrigerant used for window type air conditioning systems long back.

4. Use of Eco-friendly Refrigerants

Due to Montreal protocol and Kyoto protocol and the provision of 1990 clean air act specifying phasing out the use of R-22 by the year 2030 due to ozone depleting potential around 0.055 as compared to the alternate refrigerants which have zero ozone depleting potential (ODP) and zero global warming potential (GWP) and some other alternate refrigerants which have less ODP & GWP. The energy (first law) analysis and second law (exergy) analysis of vapor compression refrigeration systems have been carried out for reducing irreversibility's occurring in the various components in the vapor compression refrigeration systems in terms of performance parameters such as COP, EDR, Exegetic efficiency, percentage of exergy destruction in components (i.e. condenser, compressor, throttle valve and evaporator) to total exergy destruction in the system for air conditioning system of 1.5 ton capacity for seven eco-friendly refrigerants such as (R-134a, R-404a, R-407C, R-502, propane (R-290), isobutene (R-600a), butane (R-600)) . These performance parameters have been evaluated for varying condenser temperatures in the range from 303 K to 333K and evaporator temperatures in the range from 253 to 278K of 1.5 ton capacity of vapor refrigeration systems by using eco friendly refrigerants. It was observed that R-290 (zero ODP & zero GWP) and R-600 (butane of zero ODP and zero GWP) and R-600a (isobutene of zero ODP and zero GWP) are best alternatives if its flammable problem will mitigate and the next option are R-134a (of zero ODP and 1300 GWP), R-407c(of zero ODP and 1530), R-404a (zero ODP and 3260 GWP)and R-410a (of zero ODP & 1730 GWP), R507a, R125, R227ea, and R236ef for replacing R-11, R12, R22 and R502 with minor modification in the existing design of vapor refrigeration systems (i.e. larger size of compressors in case of R-134a , which increases the cost of the vapor compression refrigeration system.

5. Methods for Improving First and Second Law Performance of Vapor Compression Refrigeration Systems Using Eco-friendly Nano Refrigerants

Mishra[1] Simple VCR with liquid vapor heat exchanger , flash intercooler, flash chamber, water intercooler, liquid subcooler and stages in compression(double stage and triple stage) Mishra [2] conducted detailed analysis of vapor compression refrigeration systems using thirteen eco-friendly refrigerants Mishra [3] observed that there is a 12% to 19% improvement in the first law efficiency using nano particles mixed with R718 in the secondary evaporator circuit of VCR and suggested that higher improvement occurs using copper particles mixed with R718 and low improvement occurs using TiO2 in R134a Mishra [2] also observed the improvement in the second law thermal performance of vapor compression refrigeration system by mixing Al2O3 in R718 in secondary evaporator circuit and various eco-friendly refrigerants in the primary evaporator circuit. The lowest performance was observed by using R410a in the primary evaporator circuit Based on the literature it was observed that researchers have gone through detailed first law analysis in terms of coefficient of performance and second law analysis in term of exergetic efficiency of simple vapor compression refrigeration system with single evaporator. Researchers did not go through the nano mixed eco-friendly refrigerant in the secondary evaporator and R1234yf and R1234ze used in the primary circuit of evaporator in terms of improving first and second law efficiency of vapor compression refrigeration systems.

6. Results and Discussions

Table 1 to 3 gives the variation of first law efficiency in terms of coefficient of performance and second law efficiency using R1234ze refrigerant in the primary circuit and R-718 with nano mixed refrigerant in the evaporator circuit. It was observed that performance of R1234yf and R1234ze is acceptable as compared with R1234a. Even then

mixing circuit, the performance of R1234yf gives better performance than R1234ze and R1234a. The worst performance is observed using R410a

Table: 1. Performance evaluation of vapor compression refrigeration system using R1234ze eco-friendly refrigerants in primary circuit and following nano materials mixed with R718 in the secondary circuit

Nano materials	COP	EDR	ETA_II
Copper	5.093	0.5199	0.4801
Al oxide	4.34	0.6239	0.3761
TiO2	3.823	0.644	0.356

Table: 2. Performance evaluation of vapor compression refrigeration system using R1234 yf eco-friendly refrigerants in primary circuit and following nano materials mixed with R718 in the secondary circuit

Nano materials	COP	EDR	ETA_II
Copper	5.293	0.5071	0.4929
Al oxide	4.36	0.5666	0.4334
TiO2	3.832	0.6721	0.3279

Table: 3. Performance evaluation of vapor compression refrigeration system using R134 a eco-friendly refrigerants in primary circuit and following nano materials mixed with R718 in the secondary circuit

Nano materials	COP	EDR	ETA_II
Copper	5.193	0.5194	0.4806
Al oxide	4.35	0.6239	0.3761
TiO2	3.82	0.654	0.346

Similarly the effect of nucleate heat transfer in terms of enhancement factor is showing the percentage improvement in the first law efficiency as shown in Table 4 and 5 respectively**.** The effect of computed nano refrigerant property for enhancement factor and first law efficiency is shown in Table-5. It was observed the best performance is achieved using R1234yf which can replace R134a for low temperature and R1234ze for higher temperature applications

Table: 4. nucleate heat transfer coefficient enhancement factor and First law improvement (COP enhancement) based on nano-particle used in R718 and eco-friendly refrigerants in primary circuit

Refrigerant	Enhancement factor	COP enhancement
R1234yf	3.54	23 %
R1234ze	2.38	18%
R134a	2.3	19%

Table: 5. Effect of Computed nano-refrigerents property in terms of enhancement factor on first law improvement

Refrigerant	Enhancement factor	COP Enhancement
R1234 yf	2.04	23 %
R 1234ze	1.7	19%
R134a	2.24	21

7. Conclusions & Recommendations

On the basis of theoretical computational analysis, and five test rigs developed by author with extensive experimentation have been conducted in the RAC lab of DTU, it was observed that R-290 refrigerant is the best alternative and second alternative is R600a. And third is R-152a. Due to flammable aspect, these refrigerants can only be used by using safety measures, otherwise R134a and R410a are easily available in the markets can be used. The performance of R134a gives better than using R410a however for larger Industrial applications R 717 and R744 can be used. To replace, R134a , R1234yf (of zero ODP and 4 GWP) and R1234ze (GWP=6, and Zero ODP) are recommended, although these refrigerants gives less 10% performance than R134a.The use of nano particles mixed in the eco-friendly refrigerants and then used gives 8% to 35% improvement in the first law efficiency while using nano particles mixed with water in the secondary circuit and eco-friendly refrigerants in the primary circuit gives 7% to 22% improvement and better performance was observed with mixing copper nano particles.

The following recommendations have been made

(i) Even in mixing of nano particles mixed with R718 in the secondary circuit and R1234yf for low temperature applications gives better first law and second law performance as compared to R134arefrigerant

(ii) Although the performance of R134a is better than R134a using nano particles mixing in R718 but R1234ze can replace R134a for higher temperature applications.

(iii) The best first law and second law performances have been found using copper nano materials mixed with R718 in secondary evaporator circuit as compared to TiO2 nano particles

References

[1] R. S. Mishra, Appropriate Refrigeration Technology for sustainable Development, Int. Journal of IJARI, 3(3), 2014, 405-411

[2] R. S. Mishra et.al. Methods for Improving Thermodynamic Performance of Variable Speed Vapor Compression Refrigeration Systems Using Nanorefrigerent in Primary Circuit, Nature & Environment, 20(2), 2015, 26-47

[1] R. S. Mishra et.al, Irreversibility Optimization Using Energy-Exergy Analysis of Three Stage Vapor Compression Refrigeration Systems with Flash-Intercooler Using eco-friendly Refrigerants (R410a, R290, R600, R600a, R1234yf, R125, R717 And R134A) for Reducing Global Warming and Ozone Depletion, Nature & Environment, 20(2), 2015, 73-89.

Fourth International IEEE Workshop on e-Health Pervasive Wireless Applications and Services 2016

Security Framework for Portable NFC Mobile Based Health Record System

Divyashikha Sethia, Daya Gupta
Department of Computer Science and Engineering
Delhi Technological University (DTU)
New Delhi, India
sethiadivya@gmail.com

Huzur Saran
Department of Computer Science and Engineering
Indian Institute of Technology Delhi (IIT-D)
New Delhi, India
saran@cse.iitd.ac.in

***Abstract*—A portable healthcard on the patient mobile device can integrate Patient Health Records (PHRs) dispersed on various Hospital Information Systems (HIS) to provide a highly available medical history for correct diagnosis and treatment.In this paper, we present a broad overview of the design issues for the security framework of a novel NFC and Secure Element-based healthcard on a mobile device known as S-MAPLE (Secure Mobility-Assisted PortabLE) healthcard. We provide detailed design for Role-Based Access Control (RBAC) with selective read and write access. Evaluation results on Android-based devices indicate satisfactory performance results for delays due to security overheads.**

***Keywords*-PHR; NFC; Secure Element; RBAC; Attribute-Based Encryption; HL7**

I. Introduction

Patient Health Record (PHR) should be highly reliable, secure and available 24/7 for providing the complete health history of the patient for correct medical treatment. When PHRs gets dispersed across several Hospital Information Systems (HIS), it becomes challenging to collect records for a complete health history. People visit many hospitals due to mobility across different countries for work or tourism requirements, such as in developed countries across Europe. In developing countries, patients may have to visit physicians in various hospitals due to different specialisations and expertise. However, to get the right medical treatment, patient history must be readily available at the time of need. Due to the dispersal of PHRs, there is a requirement of storing them at a common place such as cloud. However, it has challenges of integration and problem of 24/7 availability in places with poor infrastructure and connectivity. Hence there is a requirement of a portable device that can integrate dispersed PHRs and retain in the form of a healthcard.

In our previous work [1], we have proposed a novel NFC-based mobile healthcard, which can maintain health records on a patient mobile device, to provide reliable and highly available health history. However, it lacks integration of health records in standard formats and provides limited security features with symmetric encryption and authentication. Although the mobile device of the patient can retain all the health information, it is vulnerable to threats. Hence, it is important to maintain privacy and security of the healthcard [2] as also stated in the regulations of Health Insurance Portability and Accountability Act (HIPAA) and the European Data Protection Directive 95/46/EC. It must address issues such as confidentiality, integrity, availability and non-repudiation of health records through techniques of encryption, authentication, selective authorization, digital signatures, scalable key distribution and revocation, the delegation of keys, audit logs and loss of healthcard.

In this paper, we present a broad overview of the design issues for the security framework of an S-MAPLE (Secure Mobility-Assisted PortabLE) healthcard on the patient mobile device. We briefly discuss the proposed solutions for the security requirements. Due to the limitation of space we present detailed design for the Role Based Access Policy (RBAC) with selective read and write access feature.

The S-MAPLE healthcard integrates dispersed PHRs using standard HL7 format. It retains all medical information including prescription, lab test reports, prescribed and current medications from various hospitals. Different authorised medical professionals access it by just tapping healthcard to their mobile device, using low energy wireless communication interfaces such as NFC [3] and Bluetooth. After reviewing the health history, the medical professional updates or writes a new prescription or lab tests through a secure tap. Both S-MAPLE healthcard application and reader application of the mobile devices of patient and medical professional respectively parse the health records and graphically visualise data for viewing and analysing the records.

The S-MAPLE healthcard uses a hardware tamper resistant SE (Secure Element) in the form factor of a microSD card, for storing cryptographic credentials. It organises the information into various sections. Since different stakeholders such as physician, nurse, lab technician and pharmacist must access the sections according to their roles, they must have selective privileges for each section. The S-MAPLE healthcard is supported by a cloud-based Healthsecure service to manage credentials and provide a data sync on a secure digital vault.

The health records are encrypted using Proxy-based Ciphertext Attribute-Based Encryption (CP-ABE) scheme [4] along with AES for encrypting the healthcard for fine-grained control and providing RBAC (Role Based Access Control) with selective read and write access. The Healthsecure Ser-

978-1-5090-0724-0/16/$31.00 ©2016 IEEE

vice can store every access of the healthcard in the audit logs. The stakeholders must renew cryptographic credentials periodically. The Proxy-based CP-ABE scheme supports direct user revocation which does not require re-encryption and re-distribution of cryptographic credentials.

We have developed a prototype of S-MAPLE healthcard and medical professional mobile application on Android devices. Evaluation results indicate that there are acceptable delays of the security policy overheads for a secure healthcard access. The average access time to read ten records is less than ten seconds which involves, mutual authentication, NFC communication for automatic Bluetooth pairing, encrypted transmission over Bluetooth, transferring secure healthcard and proxy-based CP-ABE decryption of records.

The rest of the layout of the paper consists of preliminaries in section II and related Work in section III. Section IV discusses the broad overview of the S-MAPLE healthcard security framework requirements and their solutions followed by details of the design for Selective Role-based Access Control. We mention the implementation and evaluation in section VI, security analysis for selective RBAC in section VII followed by conclusion in section VIII.

II. Preliminaries

In this section, we describe background information for security framework.

A. NFC and security threats

NFC [1] is an upcoming wireless technology which provides simple interfaces for communication between devices as well as access to NFC, RFID and smart card tags [6]. NFC enabled mobile device can operate in various modes as discussed in [1]. For a contactless card, there are two modes. First is hardware card emulation which requires SE and another is Host Card Emulation (HCE) in which mobile device emulates a software based contactless card without the need for the SE. Although NFC ensures that communication between devices happens when they are nearby there are some vulnerabilities [5] such as untrusted communication channel, lack of encryption, eavesdropping, a man in the middle attack and denial of service.

Relay attack is a form of a man in the middle attack, in which attacker masquerades itself as an authorised reader by relaying the information received from the card to an actual reader at a remote location and by relaying back the response. It can be prevented using Distance Bounding Protocols, Location based services and Multi-factor authentication [6].

B. Secure Element

A secure element (SE) is a tamper-resistant region and comprises typically of a one chip secure microcontroller, which is capable of securely hosting applications and their confidential and cryptographic data.There are three different form factors of SE: Universal Integrated Circuit Card (UICC), embedded SE and microSD. Both the UICC and microSD are removable [3]. In the context of smart cards, an application protocol data unit (APDU) is the communication unit for access of a smartcard by a reader. ISO/IEC 7816-4 Organization [7] defines the structure of the APDU commands namely command and response APDUs along with security and commands for interchange. Java Card supports applets to be run securely on smart cards and similar resource constrained devices. The applets can process only incoming command requests and respond by sending data or response status words back to the reader device.

C. Attribute Based Encryption

Data must be encrypted to allow access by only trusted and authorised users. Traditional Public-key encryption technique requires different keys for encryption and decryption but involves complex key management when a group of users share decryption key. Attribute-Based Encryption (ABE) [8] provides fine-grained access control to a group of users that must access a ciphertext. It involves usage of plain text attributes and access policy to define the ciphertext and decryption keys such that each user can have a different decryption key. It has two variations. First is Ciphertext ABE (CP-ABE) which associates ciphertext with an access policy and attributes to the decryption keys. The decryption key decrypts the ciphertext only when its corresponding attributes can satisfy the access policy. The stakeholders can be assigned different combinations of attributes based on their roles. Hence CP-ABE can provide Role-Based Access Control (RBAC). The other policy Key-Policy ABE is the reverse since it associates attributes with the ciphertext and access policies to the decryption keys. ABE is collusion-free since users cannot aggregate their attributes together to decrypt the ciphertext.

Since RBAC is useful for health record access by various stakeholders [2], CP-ABE can be used for encrypting them. It provides public-key functionality. The public key encrypts the health record with an access policy. It associates set of attributes to the private key which can decrypt if it satisfies the access policy. CP-ABE can be formally be defined by four algorithms [8]:

- SETUP: It takes security parameters and generates public key PK and Master Secret Key as MK.
- ENCRYPT(PK, D, P): It takes data D, Public key PK and access policy P to generate ciphertext CT.
- KEYGEN(MK, S): It takes the Master Secret Key MK and set of attributes S to create a Secret attribute key SK.
- DECRYPT(CT, SK): It decrypts the ciphertext CT to plaintext D if the set of attributes S in SK satisfy the policy P that was used to generate ciphertext CT.
- DELEGATE(SK,$\tilde{S}$): It takes as input the secret key SK based on set of attributes S and $\tilde{S} \subseteq$ S. It outputs a delegation key $\tilde{SK}$ for set of attributes $\tilde{S}$.

D. Revocation in ABE

There are several variations of ABE and revocation schemes as discussed in [9]. We require user based direct revocation which does not involve ciphertext re-encryption and key-revocation. PIRATTE (Proxy-based Immediate Revocation of

Attribute-based Encryption) [4] suggests a Proxy-based CP-ABE scheme in which a proxy server assists in partial decryption process and hence can enforce direct selective revocation of a user. It uses broadcast revocation scheme and Shamir's secret sharing [4] that creates shares of a secret which can be reconstructed using t + 1 shares. Each user has a single share of the secret key. For regular operation, it depends on the distributor to broadcast t random shares which can be combined with the user share to reconstruct the secret. The scheme can revoke up to t users by broadcasting their shares instead of random ones and hence revokes each of the users since they cannot combine their share with the t shares received to generate the secret uses this technique through the assistance of a Proxy server which participates in the secret reconstruction in the decryption process. The revocation scheme has two phases:

- INIT: This phase is before SETUP phase for the implementation of Proxy-Based CP-ABE [4] scheme which support revocation. A server managing credentials generate a random polynomial P of degree t. For each user, u it generates random identity I_u and sends a personal key $<I_u>$to the user u.
- REVOKE: It uses a list of random identities of t users who can be revoked I_{u1},..., I_{ut}. It chooses random r and sets new key as $g^{rP(0)}$. It broadcasts the message g^r, $<I_{u1}, g^{rP(I_{u1})}>$,.....,$<I_{ut}, g^{rP(I_{ut})}>$. Each revoked user can compute $g^{rP(I_u)}$ and is unable to combine it with broadcast values using Lagrange's interpolation to obtain $g^{rP(0)}$. In the case of non-revoked user broadcaster would have sent random broadcast values which could be combined with the user share $g^{rP(I_u)}$ to generate $g^{rP(0)}$.

The Proxy-based CP-ABE [4] scheme also supports multi-authority and single authority delegation so that user can delegate the secret key to another user to assist in decryption temporarily and can revoke it later. The limitation of this revocation scheme is that it can revoke only t users.

III. Related Work

A. Portable Health Records on Mobile Devices

Portable health records should be retained on the mobile device of a patient for offline personal access as well as access by authorised stakeholders. We have proposed an NFC-based system for storing health records on the patient mobile device [1]. However, it does not specify how to integrate health records in a standard format and provides limited security features of symmetric encryption and authentication. In this paper, we have proposed S-MAPLE healthcard which can integrate health records on the patient mobile device and also provide a broad overview of the advanced security requirements to ensure security and privacy of health records.

An iPhone application is suggested in [10] to store health records on the mobile device encrypted using CP-ABE. The main health records reside on the cloud. The health records on the mobile device may not be up to date. They are retained only for the offline purpose and not to be shared or updated by the medical professional. We offer a unique record management for a portable healthcard on a patient mobile device which is most recent and provides backup on a secure digital cloud. We have developed a prototype on Android based mobile device with NFC and Bluetooth interfaces for S-MAPLE healthcard. We use SE which is hardware tamper resistant to store credentials on a microSD card. Multiple stakeholders can access it by tapping it on his mobile device. It provides provenance of data when an update is written as well as provides 24/7 availability of health information with the patient. [11] suggests using trusted virtual machine environment for processing of secure health records. [12] suggests usage of a smartcard for a secure prescription to preserve the anonymity of medical professional as well as patient illness. We use smartcard on SE for our healthcard credential management on S-MAPLE healthcard. [13] provides a medical card with extra space and Bluetooth interface for throughput. Our unique work involves maintaining similar large card on the patient mobile device which is secure yet easy to retain and access.

B. ABE and Revocation

There are several revocation schemes related to CP-ABE which involve direct, indirect and hybrid revocation [9]. [14] requires re-encryption of the ciphertext. Since patient device retains encrypted healthcard, it is not feasible to re-encrypt or redistribute keys every time a HealthSecure service revokes a stakeholder. [15] suggests usage of a broadcast variation of ABE for revocation, delegation and uses searchable encryption. In this scheme, the length of ciphertext grows proportionally to the number of revoked users. A scalable EHR scheme is proposed in [16] using Multi-Authority ABE, but it uses revocation technique which requires re-encryption of data.Studies such [17] have used CP-ABE toolkit and cross compiled it on Android device and find satisfactory performance. We have implemented and tested the Proxy-Based CP-ABE [4] toolkit for RBAC with selective read and write access. It supports direct user revocation without re-encrypting the ciphertext and re-distributing the keys to stakeholders. It also supports delegation of credentials.

IV. Broad Overview of the S-MAPLE healthcard Security Framework

In this section, we describe the broad overview of the requirements for the security framework along with suggested solutions for providing privacy and security for S-MAPLE healthcard. Fig. 1 shows the main notations of the paper, The System Architecture of the S-MAPLE healthcard is shown in Fig. 2. The NFC-based health record system in [1] does not integrate health records and has limited security features of symmetric encryption and authentication. We consider a mobile device to retain health records from various hospitals as a list of HL7 records encapsulated in a JSON-based healthcard. The healthcard must be stored in an encrypted format so that only trusted application on a mobile device can access it. It must be available through simple yet secure communication by the mobile device of a stakeholder through low energy

Term	Description
Idp,Idm	Patient and Medical Professional unique identifier
H,H'	Unencrypted,ABE encrypted healthcard
Section i	i={1-5} ith section on the healthcard
KERabe	ABE encryption key for read policy for healthcard
KEWabei	ABE encryption key for write policy for section i
ri	Random number for section i
rei	E(KEWabei,ri) encrypted random number for ith section
CP	**Patient Credentials**
{KPpub,KPpri	Patient Public and Private RSA keys
KDRPabe,KDWPabe	Patient CP-ABE decryption key Read/Write access
RW = {re1..re5}}	List of Write policy ABE encrypted random numbers
CM	**Medical Professional Credentials**
{KMpub, KMpri	Medical professional Public and Private RSA keys
Non emergency:	
KDRMabe	Medical professional CP-ABE Read Access decryption key
KDWMabei}	Medical professional CP-ABE Write Access decryption key for write access for ith section
Ksym	Symmetric session key generated after Mutual Authentication
Sigp,Sigm	Signature from patient/medical professional access
Updatei	Update from medical professional for ith section

Fig. 1. Main notations

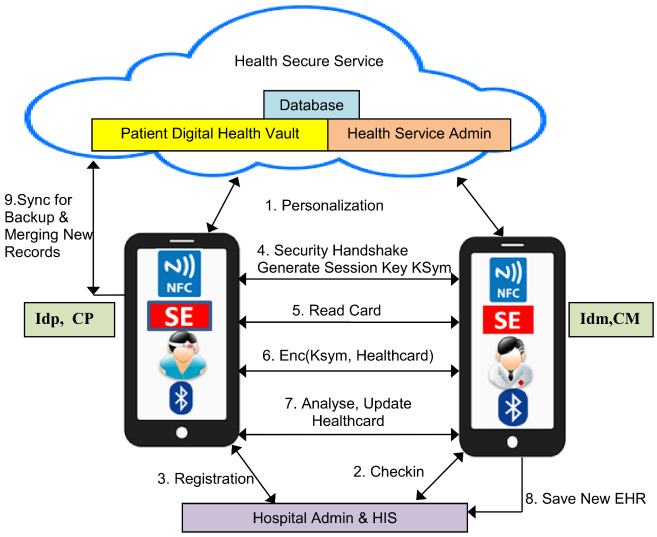


Fig. 2. System Architecture [1]

wireless interfaces such as NFC and Bluetooth. The medical professional must be able to access only authorised sections of the health card with selective read and write access rights.

For example when a patient takes his card to a cardiologist, the physician must be able only to read previous records. Based on the previous health records and current vitals he should be able to update the current vitals, diagnosis, allergies, health status, prescriptions and tests required in the current visit record. The patient could take his healthcard to the pharmacist who would tap to seek medications prescribed and should not be able to see other information related to illness for the privacy of the patient. He should update the information associated with medication prescribed in the visit record. Similarly, the lab technician must have selective access to read and update only the Lab test and immunisation sections. The mobile device on medical professional must not be able to store the records and must have a unique secure session with the patient mobile healthcard. To support secure communication the mobile devices of patient and medical professional could have minimal interaction for cryptographic support through a HealthSecure service on the cloud.

In the case of theft the patient healthcard credentials must be revoked, and there should be a mechanism to refurbish the lost healthcard on patients new mobile device.

A. Healthcard Layout

The S-MAPLE healthcard consists of prescriptions from various hospitals in a standard HL7 format from different department such as cardiology, endocrinology and organises them into different sections as in Figure 3. It is organised into various sections of basic vital signs, Diagnosis for allergies and diseases, advanced vital signs, medication, lab tests and immunisation and observations that must be available in the emergency situation. Various stakeholders can access the card with different read and write permissions, which is defined by the CP-ABE access policy. Each stakeholder gets a decryption key based on attributes that match their roles. They can decrypt a section only if attributes in encryption key can satisfy the access policy of the healthcard. Healthsecure service encrypts each section with using a read access policy and a corresponding random number write access policy as mentioned in the following subsections of the paper.

B. Security Requirements and Solutions

The S-MAPLE healthcard must retain credentials on secure storage and allow authorised stakeholders to access healthcard and perform read/write on specific subsections. It must fulfill the security goals of confidentiality, integrity and availability (CIA). The healthcard contains all visit health records of the patient and must keep them confidential so that there is no unauthorised access. Integrity is important so that the health data which is sensitive for the life of the patient reflects the right medications, diagnosis and health vitals. Availability ensures that the right records of the patient are available at the right time to the right medical professional for timely treatment. It is important to address concerns for security and privacy of health records [18]. The following requirements must be met to fulfill the goals:

- *Credential Storage*. The mobile devices of the patient and medical professional must retain credentials for decrypting the healthcard, storing their unique identity so that there is trust between a valid patient and an authorised medical professional. We use an SE on microSD card of a mobile device stores cryptographic credentials. It is a hardware tamper resistant and works as a smart-card which retains Java Card based applets which are accessible through APDU commands from secure internal applications as well as an external reader through the NFC controller of the mobile device.
- *Key Distribution*. The decryption keys must be scalable based on RBAC policy and must be stored safely to preserve privacy and security of patient.We use Proxy-based CP-ABE scheme for fine-grained access control and ease of key distribution. An access policy comprising

Stakeholder	Basic Vitals	Allergies /Disease	Advan. Vitals	Medic	Lab/ Immun	Emerg / Admin
Doctor	RW	RW	RW	RW	RW	R
Nurse	RW	R	R	R	R	R
Pharmacist	--	--	--	RW	--	R
Lab Tests	--	--	--	--	RW	R
Emergency	RW	RW	RW	RW	RW	RW
Patient	R	R	R	R	R	R
Admin	R	R	R	R	R	RW
Read Policy	ACRB	ACRB	ACRB	ACRM	ACRL	ACRALL
Write Policy	ACWBV	ACWSP	ACWSP	ACWM	ACWL	ACWADM

Fig. 3. HealthCard sections and Stakeholders access rights

a set of attributes encrypts the healthcard. A different set of attributes that can satisfy the access policy can be distributed to the stakeholders based on their roles. Hence each stakeholder can have his decryption key and can access the healthcard with different privileges.

- *Mutual Authentication*. Patient health records and identity are critical for the well-being of the patient. The mutual authentication ensures that a malicious medical professional cannot access the healthcard and provide wrong treatment. Likewise, it also stipulates that a fake patient cannot seek costly medications or treatment that are not covered under the insurance on behalf of a valid patient. It must ensure that a valid patient is seen by an authorised medical professional to prevent any malicious medical frauds such as causing harm to the patient or a fake patient seeking unauthorised expensive medical treatment or medications on behalf of a valid patient.The Healthsecure service provides unique identifiers and certificates for mobile devices of the patient and the medical professional which they store on the SE of the mobile device. For a secure hospital visit, the patient registers in the hospital for an OPD (Out Patient Department) session to seek a medical appointment with the medical professional. After tapping their mobile devices, they mutually authenticate each other to ensure that the right patient is getting proper care from the authorised doctor.
  The mutual authentication values and computations are generated on the SE and communicated over wireless low energy communication interfaces like NFC or Bluetooth. A symmetric one-time use key KSym is created in the process which is used for further encrypting communication between patient and medical professional.
- *Data confidentiality*. It must ensure that the healthcard is accessed securely by approved stakeholders and ensure the privacy of the patient.The healthcard is encrypted using Proxy-based CP-ABE scheme by the trusted cloud-based Healthsecure service and hence can be accessed only by stakeholders that have the authorised decryption key. The hardware tamper resistant SE on the mobile device stores the decryption key which is obtained by the S-MAPLE healthcard and the reader application on the mobile device of medical professional to decrypt and access the healthcard. Hence healthcard information is confidential. We also provide selective access to the sections so that stakeholders can access them based on their roles and help retain the privacy of the patient. For example, a pharmacist must be able to view and update only the section related to medications and should not be able to access the list of ailments and treatments being taken by the patient.
- *Data integrity*. An authorised stakeholders must update the relevant sections on the healthcard correctly so that the data does not get corrupt.The Proxy-based CP-ABE scheme in our framework provides RBAC for selective read and write access for various sections by multiple stakeholders, which ensures that authorised stakeholders are writing the updates on the permitted healthcard sections and also provides provenance of health records.
- *Data availability*. The right data must be available to the stakeholders at the right time to provide timely treatment. The patient mobile device retains the integrated health records on the S-MAPLE healthcard. It is highly available to be accessed directly by a simple tap by authorised stakeholders over low energy interfaces of NFC and Bluetooth. It provides ease of mobility to the patient as well as can provide correct diagnosis and treatment since complete medical history is available to the patient.
- *User revocation*. Any unusual action must lead to revocation of the credentials of the stakeholder so that the healthcard is not accessible with backward and forward secrecy. The CP-ABE decryption key of a stakeholder is associated with time-based attributes. A valid stakeholder renews the credentials periodically otherwise attributes in the decryption key do not satisfy the access policy and decryption fails. However, even when the key is not expired, the server can revoke a stakeholder by maintaining a revocation list. Every time he contacts the proxy server on the Healthsecure service for decryption; it checks if the stakeholder id is in the revocation list and sends a share to the stakeholder which will not allow him to decrypt.
- *User delegation*. The medical profession such as a senior physician should be able to delegate his cryptographic credentials for temporary assistance in work by a junior doctor especially in crowded hospitals or training purposes. The physician can revoke the keys after some duration The patient could also delegate temporary cryptographic credentials and portion of healthcard to family or friends for a drug or report collection on his behalf. The member can take the delegated portion on his card and use temporarily delegated keys to retrieve the card from the lab technician and tap it back on the patient card. Each stakeholder receives a decryption key with a set of attributes that satisfy access policy. With Proxy-based CP-ABE [4] scheme, a stakeholder can delegate some of the attributes of a user in the form of a delegation key which can be used to decrypt temporarily on behalf of the user.
- *Audit logs*. An Audit log must store information for every access of the card, to resolve non-repudiation. The

Name	Description	Policy
ACRALL	Read access by all stakeholders	AND(OR(AND(AND(hosp>=1,hosp<=10), OR(pharmacy, lab, AND(AND(department>=1,department<=10), OR(doctor , nurse)), admin, emergency, AND(id=12,pateint), AND (time>=1,time<=4))

Fig. 4. CP-ABE Read Access Policy ACRALL

Name	Description	Policy
ACWB	Write access to section for basic vitals	AND(wobb,OR(doctor,nurse,emergency))
ACWSP	Write access to sections for allergies, advanced vitals	AND(wobs,OR(AND(doctor,department),emergency))
ACWM	Write access to section for medications	AND(wmed,OR(doctor,pharmacy,emergency))
ACWL	Write access to section for lab tests	AND(wlab,OR(doctor,pharm,emergency))
ACWADM	Write access to section admin data	AND(wadm,OR(admin,patient))

Fig. 5. Write Access Policies

certificates of patient and mobile device sign each update on the healthcard and stores them along with timestamps in the Audit log on the trusted Healthsecure service.

- Theft of device. In the case of theft of device malicious user must not be allowed to access healthcard and should provide recovering healthcard on a new device with new credentials. The patient mobile device syncs all updates for the S-MAPLE healthcard on the HealthSecure server which merges it with the healthcard, re-encrypts the card sends to the patient. It uses a secure kiosk to tap and store a backup on the data sync through HTTPS. We assume the server to be trusted and use it only for storing the backup. On theft of the device, the patient informs HealthSecure Service, which will then revoke old patient credentials so that healthcard is not accessible. It re-encrypts the healthcard and restores on the new patient mobile device with new cryptographic credentials.
- *Emergency* The healthcard must be available with special privileges to emergency personnel access to complete medical history and provide timely diagnosis and treatment.In our security framework, an authorised emergency personnel seeks decryption key from the server for special access after validating Public-key certificate credentials stored in the SE of his mobile device.In the case of emergency, normal access policy is overridden, and the emergency staff accesses the patient's health records. An emergency key issued to the emergency staff, is revoked after some duration.

C. Selective Role-Based Access Control

In this section, we discuss the details for the design of Role-Based Access Control (RBAC) selective access control for a secure access of the S-MAPLE healthcard.

We encrypt the healthcard using Proxy-based CP-ABE [4] scheme, to provide RBAC and ease of decryption key distribution between different stakeholders. Each section on healthcard has selective read and write access policy. A stakeholder has set of attributes on a single decryption key which can satisfy different policies of different encrypted sections. The different sections and their read and access policies are as shown in figure 3. The read access policy ACRALL which allows stakeholders to read all sections is shown in figure 3. It allows read access by a patient with id=12, hospitals with ids in the range of 1-10, and time range in slots 1-4. The slot number could indicate valid time slots for credentials which must renew them periodically. SE retains the decryption key associated with a set of attributes. A stakeholder can access the healthcard after mutual authentication. However, each stakeholder has different write access for various sections. Figure 5 shows the write policies for each section.

To offload computations from a mobile device, we outsource the task of encryption to HealthSecure service which is trusted. It encrypts the sections of the healthcard as well as a set of random numbers for write access policy.

The card applets that manage credentials can be setup during a personalization phase in a secure environment by the HealthSecure service as shown in step 1 of Fig 6. 6.It allocates a unique identifier Id/Im to the patient and medical professional, public-key certificates used in mutual authentication and Proxy-Based CP-ABE decryption key for RBAC with selective read and write access.

A stakeholder taps his mobile device to the S-MAPLE healthcard on the patient mobile device to access the health records. It uses low-energy wireless interfaces of NFC and Bluetooth. However, before accessing it must undergo mutual authentication. It generates a symmetric key KSym for the one-time session between patient and medical professional as shown in step 2.

A stakeholder first reads the healthcard and accesses the concerned sections by decrypting with his share of ABE key. However once read does not indicate that it can be updated.

To achieve write access policy, the S-MAPLE healthcard application has a list of random numbers ri for each section i, encrypted with the write CP-ABE policy of the section as rei. When stakeholder requests to write to a section, patient challenges it with the encrypted rei for the section. If the stakeholder has to write with his mobile device, he must decrypt rei using his share of write CP-ABE key and in response returns ri'=ri+1 to the patient along with the update for the section. If the patient finds received ri' same as ri, then it allows the update to be written to the healthcard else reject it. Steps 3-11 in figure 6 show the read and write steps.

For every read or write access to the healthcard, the proxy server helps in partial decryption and revokes in case the user is in the revocation list. Reader signs the action of access with the private key and sends signed hash of the update in the event of write. Patient doubly signs it with the time stamp and his private key to store in the audit logs. This way both the patient and medical professional interacting in the session have signed and save their actions on the audit logs as shown in steps 9,11 and 12 in figure 6.

When an emergency personnel tries to access the card, he seeks the decryption key from the server for special access after validating Public-key certificate credentials stored in the SE of his mobile device as shown in step 6 in 6. The key is revoked later after a duration as shown in step 12. All updates

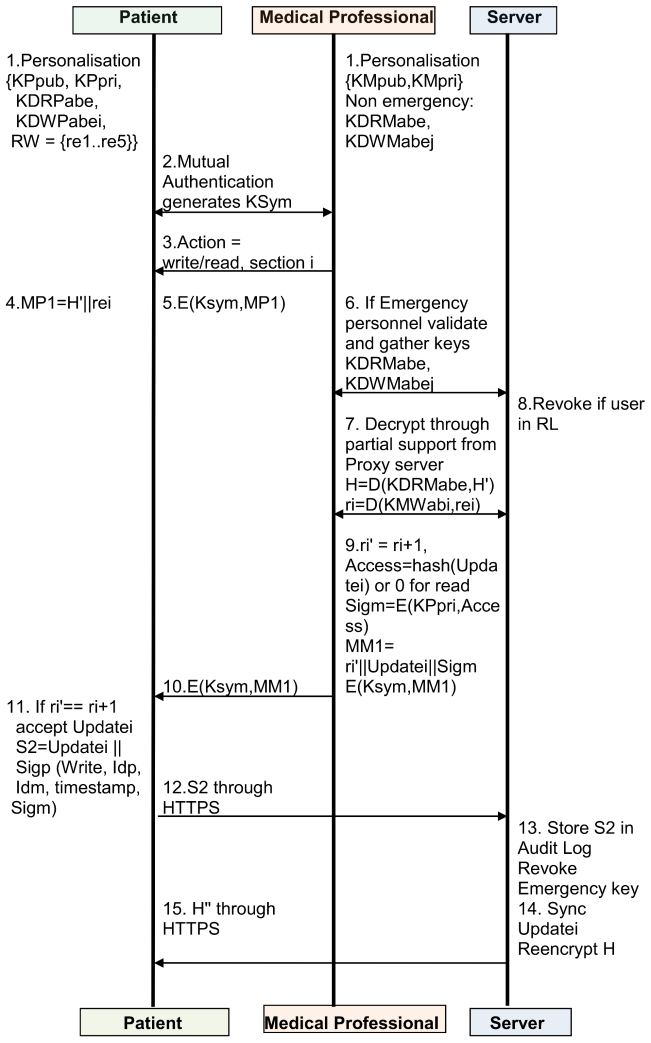


Fig. 6. Sequence Diagram

to the healthcard are stored on a secure digital vault as shown in step 13. The Healthsecure service merges the updates with the old healthcard and restores the re-encrypted healthcard on the patient mobile device as shown in steps 14-15.

V. Implementation and Evaluation

We have developed an S-MAPLE healthcard application and a reader application for mobile devices of patient and medical professional respectively. The reader application accesses the S-MAPLE healthcard using low energy interfaces of NFC and Bluetooth by a simple tap. We use the following for the implementation:

- 2 Sony Xperia M2 devices running Android 5.0.0 (Lollipop) which supports NFC and Bluetooth.
- PIRATTE library [19][20] represents a Proxy-based CP-ABE scheme which encrypts the health records and supports direct revocation and delegation. It has been deployed on Android mobile device using Android Native Development Kit (NDK) tool.
- GO-Trust secure microSD cards [21] provides Java card chip for SE on the microSD cards.
- Android SDK and Android Studio.
- MongoDB and Python interpreter to implement a server for the HealthSecure service and proxy-based decryption support for proxy-based CP-ABE.

The patient application assists parsing of HL7-based records on the S-MAPLE healthcard. The parsed data is used for graphical visualisation of previous vitals signs as well as retrieving past prescriptions, lab tests medications. Similar visualisation is feasible after the reader application retrieves the authorised sections. It can also tap on the S-MAPLE healthcard to write updates back on the healthcard securely.

We have evaluated the prototype for an encrypted healthcard with ten records with a size of 57 KB and a revocation list consisting of ten users on the proxy server. It uses interfaces of NFC and Bluetooth for communication. The following are some of the average timings results after iterative testing:

- Encryption on server: 4197 ms
- NFC transactions: 575 ms
- Transfer over Bluetooth: 5119 ms
- Proxy decryption support: 1864 ms
- Device decryption: 2143 ms
- Net decryption time: 4007 ms
- Net access time: 9701 ms

It outsources encryption to a server. The S-MAPLE healthcard application and the reader application decrypt the encrypted healthcard with the help of a proxy-server. The read time involves time from tap to the visualisation of the health card. It involves time for mutual authentication, NFC transfer of Bluetooth address, Bluetooth automatic pairing, transfer of healthcard, followed by decryption using the server. We find the net time to access ten health records is less than 10 sec which is acceptable for a secure interaction between the S-MAPLE healthcard and the reader application.

Figure 7 shows the testing results for access of S-MAPLE healthcard for encryption, decryption and read access time. We observe the CP-ABE encryption and decryption timings do not get affected by the increase in the number of records. However, the read time increases significantly since it also involves the time for communication which increases with the number of records. We also observe that the decryption and encryption timings are not affected by increasing the number of users in the revocation list on the proxy server.

VI. Security Analysis for RBAC with selective access control

Confidentiality of healthcard is maintained by encrypting it using proxy-based CP-ABE scheme for partial decryption on the server and supporting direct revocation and delegation. HealthSecure service offloads encryption on a trusted server. The cryptographic credentials are stored safely on a hardware tamper resistant SE on the mobile devices. The

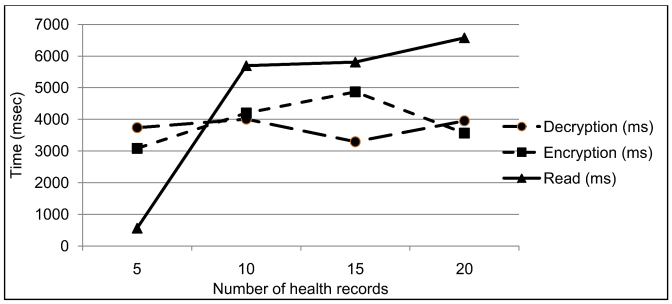


Fig. 7. Testing Results

credentials are setup in a personalisation phase. A secure mutual authentication handshake over NFC tap, along with location sensors provide countermeasures to relay attack to prevent frauds from medical professional or patient as well as phishing attacks. The HealthSecure Service provides minimal communication overheads for decryption.The role based selective access control for read and write access helps maintain all the sections on the healthcard reliably. A stakeholder cannot access restricted sections.It retains the privacy of the patient, along with data confidentiality and integrity of the updates on the healthcard.The Proxy-CP-ABE scheme helps in direct revocation of the user without re-encryption or key distribution. However, it has a limitation of a maximum number of users to be revoked. The healthcard is stored in a secure digital vault on the cloud and is used to revoke old credentials and restore new credentials and copy of the healthcard on a new mobile device.

VII. Conclusion

In this paper, we provide a broad overview of the requirements and possible solutions for the security framework for an S-MAPLE healthcard on the patient mobile device. The proxy-based CP-ABE scheme is used for RBAC with selective read and write access to various sections on the healthcard and provides confidentiality, integrity and privacy of the patient.It can provide highly available and reliable health records for efficient treatment. The testing results indicate that the timings for mutual authentication, communication and decryption are tolerable for a secure interaction between patient and medical professional. If we store credentials on alternates such as TEE Trustzone from ARM processor or High-speed SEs, the access time will be faster and will improve the results. We can also implement improved CP-ABE schemes for scalable revocation of users.

References

[1] D. Sethia, H. S. Daya Gupta, T. Mittal, and U. Arora, "NFC based secure mobile healthcare system," in *Proc. IEEE Communication Systems and Networks(COMSNET'2014)*, Jan. 2014, pp. 749–760.

[2] J. L. Fernndez-Alemn, I. C. Seor, P. ngel Oliver Lozoya, and A. Toval, "Security and privacy in electronic health records: A systematic literature review," *Elseiver Journal of Biomedical Informatics*, vol. 46, p. 541562, 2013.

[3] V. Coskun, B. Ozdenizci, and K. Ok, "A survey on near field communication (nfc) technology," *Springer Wireless Personal Communications*, vol. 71, pp. 2259–2294, 2013.

[4] S. Jahid, P. Mittal, and N. Borisov, ""PIRATTE: Proxy-based immediate revocation of attribute-based encryption"," in *arXiv preprint arXiv*, 2012.

[5] A security analysis of nfc implementation in the mobile proximity payments environment . [Online]. Available: http://www.mobeyforum.org/w/wp-content/uploads/NFCSecurityAnalysis_Part1_FINAL1.pdf

[6] S. Drimer and S. J. Murdoch, "Keep your enemies close: Distance bounding against smartcard relay attacks," *USENIX Security*, vol. 2007, 2007.

[7] Iso 7816 part 4 interindustry commands for interchange apdus. [Online]. Available: http://www.cardwerk.com/smartcards/smartcard-standard/ISO78164.aspx

[8] J. Bethencourt, A. Sahai, and B. Waters, "Ciphertext-policy attribute-based encryption," in *Proc. IEEE Symposium on Security and Privacy(SP'2007)*, 2007, pp. 321–334.

[9] L. Pang, J. Yang, and Z. Jiang, "A survey of research progress and development tendency of attribute-based encryption," *Hindwai The Scientific World Journal*, vol. 2014, 2014.

[10] J. A. Akinyele, M. W. Pagano, and M. D. Green, "Securing electronic medical records using attribute-based encryption on mobile devices," in *Proc.ACM Security and privacy in smartphones and mobile devices*, 2011, pp. 75–86.

[11] A. Dmitrienko, Z. Hadzic, H. Lhr, A.-R. Sadeghi, and M. Winandy, "Securing the access to electronic health records on mobile phones," in *Biomedical Engineering Systems and Technologies*, ser. Communications in Computer and Information Science. New York: Springer-Verlag, 2011.

[12] Y. Yang, X. Han, F. Bao, and R. H. Deng, "A smart-card-enabled privacy preserving e-prescription system," *IEEE Transactions on Information Technology in Biomedicine*, vol. 8, pp. 47 – 58, 2004.

[13] E. S. Hall, D. K. Vawdrey, C. D. Knutson, and J. K. Archibald, "Enabling remote access to personal electronic medical records," *IEEE Engineering in Medicine and Biology Magazine*, vol. 23, pp. 133 – 139, 2003.

[14] S. Y. Worcester, C. Wang, K. Ren, and W. Lou, "Attribute based data sharing with attribute revocation," in *Proc. IEEE 5th ACM Symposium on Information, Computer and Communications Security (ASIACCS)*, 2010, pp. 261–270.

[15] S. Narayan, M. Gagn, and R. Safavi-Naini, "Privacy preserving ehr system using attribute-based infrastructure," in *Proc. ACM Workshop on Cloud computing security workshop*, 2010, pp. 47–52.

[16] M. Li, L. S. Yu, Y. Zheng, K. Ren, and W. Lou, "Scalable and secure sharing of personal health records in cloud computing using attribute-based encryption," *IEEE Transactions on Parallel and Distributed Systems*, vol. 24, pp. 131 – 143, 2012.

[17] M. Ambrosin, M. Cont, and T. Dargahi, "On the feasibility of attribute-based encryption on smartphone devices," in *Proc.ACM IoT challenges in Mobile and Industrial Systems(IoY-Sys)*, 2015, pp. 49–54.

[18] J. L. Fernndez-Alemn, I. C. Seor, P. ngel Oliver Lozoya, and A. Toval, "Security and privacy in electronic health records: A systematic literature review," *Elseiver Journal of Biomedical Informatics*, vol. 46, p. 541562, 2013.

[19] S. Jahid, P. Mittal, and N. Borisov, "Easier: Encryption-based access control in social networks with efficient revocation," in *Proceedings of the 6th ACM Symposium on Information, Computer and Communications Security*, 2011, pp. 411–415.

[20] Implementation of piratte: Proxy-based immediate revocation of attribute-based encryption. [Online]. Available: https://bitbucket.org/hatswitch/piratte

[21] "Go-trust secure microsd java." [Online]. Available: http://www.go-trust.com/products/microsd-java/

Slow-Light Generation Based on Stimulated Brillouin Scattering in Single-Mode Er-Doped Tellurite Photonic Crystal Fibers

Shubham Sharma[1], Varsha Jain[1], Ajeet Kumar[1,*], Than Singh Saini[2]
[1]*Advanced Photonics Simulation Research Laboratory, Department of Applied Physics, Delhi Technological University, Delhi-110 042, INDIA*
[2]*CSIR-Central Scientific Instruments Organization, Chandigarh-160030, INDIA*
[*]*ajeetdph@gmail.com*

Abstract: We report theoretical study of single-mode Er-doped tellurite PCF for generation of slow-light with tunable features based on stimulated Brillouin scattering. We obtained time-delay of 145 ns at pump power of 516mW in 2m Er-doped tellurite PCF.
OCIS codes:(290.5900) Scattering, stimulated Brillouin; (060.5295) Photonic crystal fibers; (190.4370) Nonlinear optics, fibers; (060.2370) Fiber optics sensors.

1. Introduction

"Slow light" can be defined as reducing the group velocity of optical pulse. This can be achieved by interacting the light pulse with the medium in which light is propagating. The interest on the topic of slow light increasing day-by-day because of the many applications such as, data synchronization, optical memories, optical buffering, optical signal processing, microwave photonics. Various phenomena have been proposed to slow down the velocity of light such as Electromagnetically Induced Transparency (EIT) [1], Coherent Population Oscillation (CPO) [2], Stimulated Raman Scattering (SRS) [3], Stimulated Brillouin Scattering (SBS) [4], Soliton Collision [5]. Among all these phenomena, Stimulated Brillouin Scattering, have attracted recent research in generation of slow light in optical fibers, due to because it leads to the application of slow-light in telecommunication systems with moderate pump power and operation at room temperature and tunable wavelength working range [4,6].

Use of engineered structure particularly PCF offers a promising approach to shrink the length of fiber from kilometers [7]to few meters at desired Brillouin gain and time delay. The shape and strength of Brillouin gain depends on overlap between the optical and acoustic modes. Small-core photonic crystal fiber have tighter confinement of both sound and light so as to enhance acousto-optic interaction [8]. Pant et al. reported first time the maximum delay of ~23 ns in 7 cm long chalcogenide rib waveguide [9]. It has been confirmed that tellurite fibers are one of the most promising medium for Brillouin fiber laser, amplifiers and slow-light generation [10]. Therefore, features of tunable slow-light are investigated in high refractive index tellurite photonic crystal. Recent work on tellurite [11] indicate the tunable pump power between 12.3 and 1100 mW for 2 m long Er-doped tellurite fiber.

In this work, we have designed and analyzed Er-doped tellurite photonic crystal fiber. The influences of PCF characteristics such as allowable pump power range for undistorted output pulse and time-delay experienced by the pulse for Er-doped tellurite PCF have been numerically simulated. Simulated results indicate that time-delay experienced by optical pulse can be tuned with pump power and tunable features can be obtained. Pump power can be tuned between 5.8mW to 516 mW for 2 m long Er-doped tellurite PCF.

2. Theory of Stimulated Brillouin Scattering

In the process of SBS a high intensity pump wave interacts nonlinearly with a signal wave with the help of an acoustic wave, all travelling in the longitudinal direction inside the core of the fiber. This creates travelling density variations (i.e. acoustic wave) in the medium. This low frequency acoustic wave travels in one direction in the fiber creating travelling modulations of refractive index in the core. These periodic changes in the refractive index of the fiber essentially create a dynamic Bragg grating along the fiber. This travelling grating (moving with acoustic velocity v_A) is responsible for scattering the high power pump wave into a frequency downshifted wave called Stokes wave. When the counter-propagating continuous signal wave has the same downshift as the stokes wave, the signal wave experiences high gains [12].

3. Design of proposed Photonic Crystal Fiber

To study the generation of SBS based tunable slow-light, we have proposed a single-mode PCF design which consists of array of circular air holes arranged in hexagonal lattice pattern in the cladding region. As shown in Fig. 1, the diameter of the circular air holes is kept identical is represented by "*d*", except the innermost layer of air holes

whose diameter is "*1.5d* " and the pitch (i.e. center to center distance between any two consecutive air holes) is represented by "*Λ*". In our simulation, the pitch (*Λ*) is kept constant at 2 µm and diameter is varied from 0.6 µm to 1.0 µm to change the effective-mode-area of PCF. The refractive index of Er-doped tellurite PCF has been taken

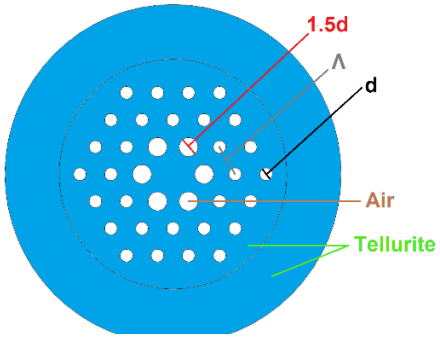


Fig. 1. Transverse cross sectional view of proposed PCF.

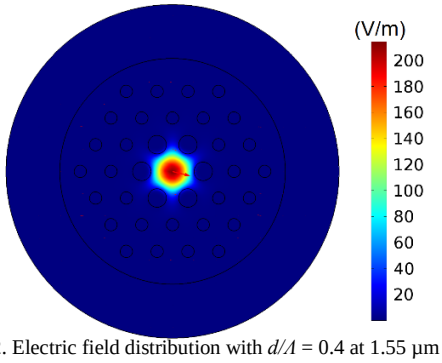


Fig. 2. Electric field distribution with *d/Λ* = 0.4 at 1.55 µm in the proposed Er-doped tellurite PCF

equal to 1.98 at 1.55 µm [13]. In order to ensure single-mode operation in the proposed PCF the value of *d/Λ* must be less than 0.5 [8]. Therefore, we have chosen *d/Λ*equal to 0.4 for ensuring proper single-mode operation.Figure 2illustrates the 2D surface plot of the incident electromagnetic wave in the proposed Er-doped tellurite PCF.

4. Results and Discussion

The simulation of pump and signal wave propagating over a 2-m long Er doped Tellurite PCF is carried out using the following parameters, fiber material loss = 0.51 dB/m (i.e. α = 0.117/m), the polarization factor, K = 0.667, the Brillouin gain coefficient, g_B = 1.47 × 10−10 m/W, Brillouin gain bandwidth, Δv_B = 23 MHz [14], and the length of the PCF = 2 m. Using the above parameters, the influence of *d/Λ* on effective mode area (A_{eff}) of propagating mode in Er-doped tellurite PCF has been illustrated in Fig. 3. Effective mode area of PCF can be controlled by tuning the *d/Λ* and so is nonlinearity.Increasing *d/Λ* effectively increases the nonlinearity of PCF. Simulated results show effective mode area of the fundamental mode is equal to 6.45 µm^2 at *d/Λ* = 0.4 for Er-doped tellurite PCF.

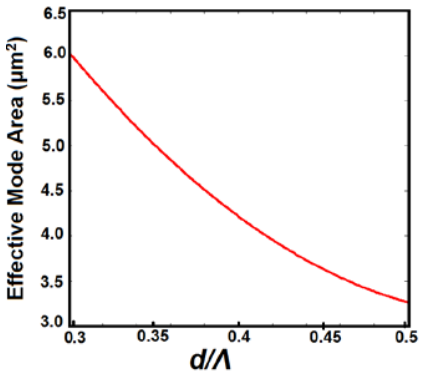


Fig. 3. Effective mode area of propagating mode in Er-dopedtellurite PCF

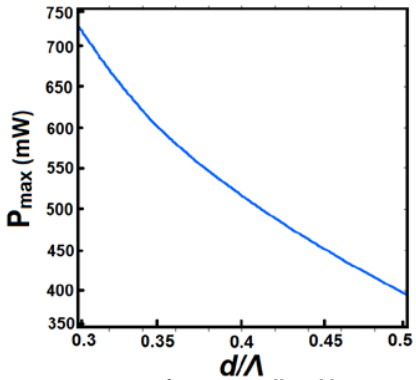


Fig. 4. Variation of *maximum allowable pump power* with *d/Λ*

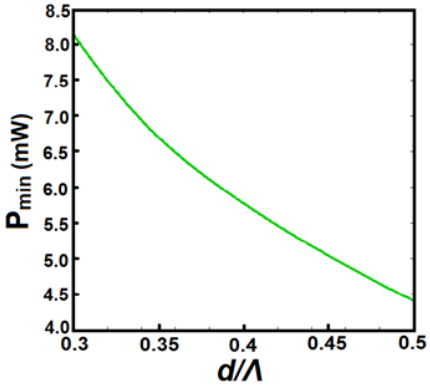


Fig. 5. Threshold pump power for inducing SBS in variation with *d/Λ*

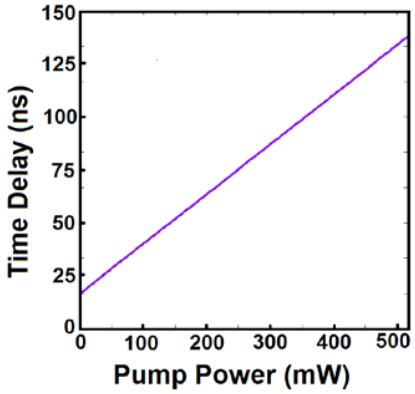


Fig. 6. Dependence of time delay produced on pump power

Fig. 4shows the effect of d/Λ on pump power. When the value of the d/Λ increases, the core area decreases, thus confining the field within a smaller region. This decreases the maximum pump power of PCF. The value of P_{max} is equal to 516.5mW when d/Λ = 0.4 for Er-doped tellurite PCF.The minimum pump power indicates the threshold for inducing stimulated Brillouin scattering in the PCF. Below this power the PCF does not show any nonlinear effects. The value of P_{min} is equal to 5.8mW when d/Λ = 0.4 for Er-doped tellurite PCF as shown in Fig. 5. Fig. 6 illustrates the variation total time-delay with the pump power. The maximum time-delay using 2 m doped tellurite fiber has been obtained up to 145.3 ns at 516 mW of maximum allowable pump power.

5. Conclusion

In conclusion, we have designed and analyzed a highly nonlinear Er doped tellurite photonic crystal fiber structure for tunable slow light generation based on stimulated Brillouin scattering. We have calculated PCF characteristics for slow-light such as maximum allowable pump power and time-delay designed PCF. Our simulation results indicate that maximum time-delay of 145 ns can be achieved using 2 m long Er doped tellurite PCF pumped with 516 mW of pump power. The results of this work are found to be better than earlier reported work in the conventional tellurite PCF [15], as producing time delay of ~145 ns requires less pump powers when the air hole structure is designed as shown. Simulated results indicate that the use of engineered structures like photonic crystal fiber, reduces the length and required pump power for producing comparable delays. Thus, effectively, time delay can be tuned with pump power. The slow light nonlinear enhancement in the designed photonic crystal fibers has the potential to contribute in advancement of the field of integrated nonlinear optics to lower operating powers and ultra-compact devices.

.

6. References

1. J. Zhang, G. Hernandez, and Y. Zhu, "Slow light with cavity electromagnetically induced transparency.," Opt. Lett. **33**, 46–48 (2008).
2. S.-W. Chang, P. Kondratko, H. Su, and S. L. Chuang, "Slow Light Based on Coherent Population Oscillation in Quantum Dots at Room Temperature," Quantum Electron. IEEE J. **43**, 196–205 (2007).
3. J. Sharping, Y. Okawachi, and A. Gaeta, "Wide bandwidth slow light using a Raman fiber amplifier.," Opt. Express **13**, 6092–6098 (2005).
4. Y. Okawachi, M. S. Bigelow, J. E. Sharping, Z. Zhu, A. Schweinsberg, D. J. Gauthier, R. W. Boyd, and A. L. Gaeta, "Tunable all-optical delays via brillouin slow light in an optical fiber," Phys. Rev. Lett. **94**, 1–4 (2005).
5. J. T. Mok, C. M. de Sterke, I. C. M. Littler, and B. J. Eggleton, "Dispersionless slow light using gap solitons," Nat. Phys. **2**, 775–780 (2006).
6. K. Y. Song, M. Herráez, and L. Thévenaz, "Observation of pulse delaying and advancement in optical fibers using stimulated Brillouin scattering.," Opt. Express **13**, 82–88 (2005).
7. T. Schneider, D. Hannover, and M. Junker, "Investigation of Brillouin scattering in optical fibers for the generation of Millimeter waves," J. Light. Technol. **24**, 295–304 (2006).
8. R. K. Sinha, A. Kumar, and T. S. Saini, "Analysis and Design of Single-Mode As2Se3-Chalcogenide Photonic Crystal Fiber for Generation of Slow Light with Tunable Features," IEEE J. Sel. Top. Quantum Electron. **22**, 1–6 (2016).
9. R. Pant, A. Byrnes, C. G. Poulton, E. Li, D.-Y. Choi, S. Madden, B. Luther-Davies, and B. J. Eggleton, "Photonic-chip-based tunable slow and fast light via stimulated Brillouin scattering," Opt. Lett. **37**, 969–971 (2012).
10. T. Fiber and T. . O. Qin, G.; Sotobayashi, H.; Tsuchiya, M.; Mori, A.; Suzuki, "Stimulated Brillouin Scattering in a Single-Mode Slow Light Generation," Lightwave **26**, 492–498 (2008).
11. T. Singh Saini, A. Kumar, and R. Kumar Sinha, "Slow light generation in single-mode tellurite fibers Slow light generation in single-mode tellurite fibers," J. Mod. Opt. **627**, 508–513 (2015).
12. L. Thévenaz, "Slow and fast light in optical fibres," Nat. Photonics **2**, 474–481 (2008).
13. X. Peng, F. Song, S. B. Jiang, N. Peyghambarian, M. Kuwata-Gonokami, and L. Xu, "Fiber-taper-coupled L-band Er3+-doped tellurite glass microsphere laser," Appl. Phys. Lett. **82**, 1497–1499 (2003).
14. K. S. Abedin, G.-W. Lu, and T. Miyazaki, "Slow light generation in singlemode Er-doped tellurite fibre," Electron. Lett. **44**, 16 (2008).
15. V. Jain, S. Sharma, T. S. Saini, A. Kumar, and R. K. Sinha, "Design and analysis of single-mode tellurite photonic crystal fibers for stimulated Brillouin scattering based slow-light generation," Appl. Opt. **55**, 6791–6796 (2016).

14.139.251.187 {ts '2016-12-26 04:26:59'}

Volume 4, Issue 3(2016) 496-497 ISSN 2347 - 3258
International Journal of Advance Research and Innovation

Study of Natural Gas Engine using non-premixed combustion model

Raj Kumar Singh, Aditya Kumar Singh, Aditya Anand
Department of Mechanical Engineering, Delhi Technological University, Delhi, India

Article Info

Article history:
Received 25 January 2016
Received in revised form
20 February 2016
Accepted 28 February 2016
Available online 15 June 2016

Keywords
Combustion model;

Abstract

Direct injection natural gas engines are used in many heavy duty vehicles. Similar to diesel engines, high thermal efficiency and power density is maintained in such direct injection natural gas engines. In such engines, natural gas is injected directly into the combustion chamber. Then the gas mixes with the high pressure air in the combustion chamber and combustion occurs. The main objective is to simulate a cycle, from the end of the compression stroke to 50° after TDC. Simulation would be done keeping methane as fuel. A 30 degree sector of a 4-stroke engine which corresponds to one fuel injector hole is modeled. Since combustion simulation is to be studied, the simulation starts at 20 degree crank angle (CA) before the start of injection (SOI) and ends at 50 degree CA after top dead center (TDC). A simplified model of the engine with no valves is modeled since during the entire combustion process, both the valves remain closed.

1. Geometry and Mesh Generation

Dynamic meshing method is used for meshing the combustion chamber. For efficient meshing the combustion chamber is decomposed in several zones. The principle of decomposition is to divide the complicated combustion chamber into several different zones with either simpler geometry or less mesh movement. That is, in some zones, the geometry is complicated, but the mesh will not move much during the computation process. The mesh in those zones is much easier to handle. Once the mesh is generated with fair quality, the mesh will stay in such way though out the entire computational process. For zones with moving boundaries, the geometry is made to be simple such as between two parallel surfaces. The mesh in those zones is not only easy to generate but also the mesh is easy to manage during the piston and valve moving process. The makes the re-meshing process much more robust, efficient, and reliable. With the division, the complex geometry of the entire chamber is broken down into four much simpler geometry, the ports, the head zone, the cylinder zone, and the bowl-in-piston zone. [1] Because of large movement of piston, must use a kind of mesh that able to be swept when piston moves up and again generate when piston moves down. For this part hexahedral elements are used while for part where valves move tetrahedral elements are used. [2]

There are three methods to update the meshes of a moving boundary:

- Smoothing
- Layering
- Re meshing

In the present work a 30° sector of a combustion chamber having bore of 120mm and stroke of 220mm with one injector is modeled. Since combustion simulation is to be studied, the simulation starts at 20° crank angle before injection and 50° crank angle after top dead centre. A simplified model of combustion chamber with no valves is modeled since during the entire combustion process, both the valves remain closed. This way the geometrical complexity of piston head is simplified and is thus easier to mesh. Four dynamic mesh zones are defined namely

- fluid-outer
- bowl
- bowl:019
- wall top outer

Layering methods is used for dynamic meshing of the moving piston boundary. Height based layering method is used with split factor of 0.4 and collapse factor of 0.1. To define an initial volume and to describe the motion of moving zones In-Cylinder motion is described with table 1 parameters.

Table 1 Input parameters

Parameter	Value
Crank Shaft Speed (rpm)	2000
Starting Crank Angle (deg)	360
Crank Period (deg)	720
Crank Angle Step Size (deg)	0.25
Piston Stroke (mm)	120
Connecting Rod Length (mm)	220
Piston Stroke Cutoff (mm)	0
Minimum Valve Lift (mm)	0

2. Result and Discussion

An IC engine performance was characterized by measuring the profiles of in-cylinder CH_4 mole fraction and temperature variations during engine cycle. During the measurements, significant variations in the selected parameters were observed within the combustion chamber. This comparison provided the baseline information for the selection of an appropriate kinetic model (mechanism) of oxidation of natural gas in IC engine. The mesh generated is

Corresponding Author,
E-mail address: rajkumardce@dce.ac.in
All rights reserved: http://www.ijari.org

as shown in figure 2. The simulation was done with the following fuel charge mixture as described Table 2.

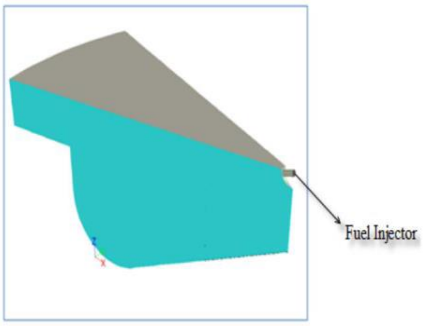


Fig. 1: Sector Geometry of a Direct Injection Natural Gas Engine

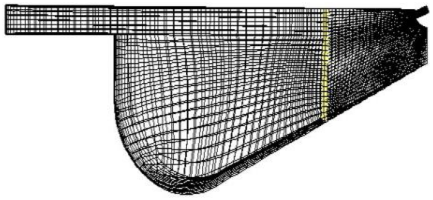


Fig.2 Mesh

Table 2 Fuel composition

Species	Fuel	Oxid
ch4	1	0
n2	0	0.78992
o2	0	0.21008

.

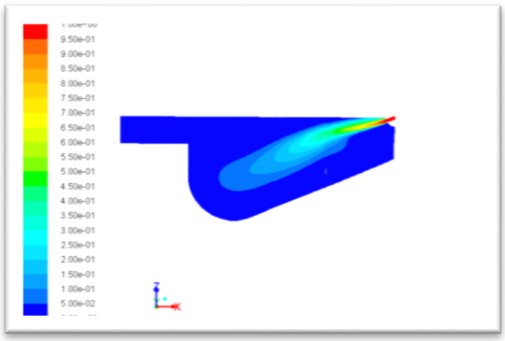


Fig. 3 Contours of CH4 mass fraction (10° after SOI)

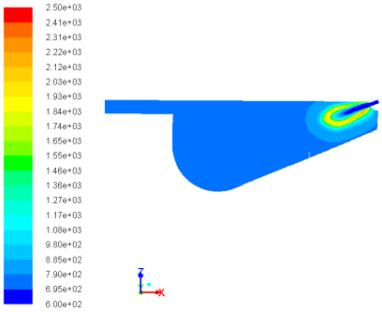


Fig. 4 Static Temperature (1.25° after ignition)

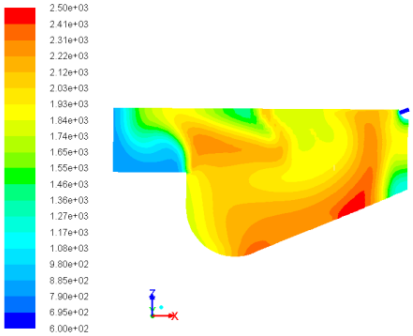


Fig. 5 Static Temperature (30° after ignition)

The simulation is started from 20° before the start of injection and ends at 50° after top dead center. No valves are modeled because the valves are closed between these crank angle periods.

3. Conclusions

The combustion characteristics of a natural gas engine was completed and the presented CFD based computational approaches can strongly contribute to improve the performance, efficiency and emissions of the combustion chambers beside allowing possibilities for investigating the effect of alternative fuels concerning the expected goals and taking care for the requirements and standards.

References

[1]. Rapid Mesh Generation, Dynamic Mesh Management for Kiva-3v Jianwen Yi
[2]. Flow Simulation in Engine Cylinder with Spring Mesh M.H. Shojaeefard and A.R. Noorpoor
Department of Automotive Engineering, Iran University of Science and Technology, Narmak, Tehran, Iran
[3]. Serag-Eldin, M. A., Spalding, D. B., Computations of Three-dimensional Gas Turbine Combustion
Chamber Flows, ASME J. Engineering for Power, Vol. 101, pp. 326-336, 1979.
[4]. Ghenai C., Combustion of Syngas Fuel in Gas Turbine Can Combustor, Advances in Mechanical
Engineering, Volume 2010, Article ID 342357, 2010.
[5]. N. T. Weiland, C. R. Bedick, P. A. Strakey, Stability, Emissions, and Boundary Conditions for a Model Validation Combustor, Spring Technical Meeting of the Central States Section of the Combustion Institute, https://www.combustioninstitute.org/upload_resources/12S-109.pdf, April 22-24, 2012.
[6]. Abraham, J, Bracco, FV. Reitz, RD. Comparisons of Computed and Measured Premixed Charge Engine, Combustion and Flame, 60, 1985, 309-322.
[7]. Peters N. Turbulent Combustion, Cambridge University Press, 2000.
[8]. Bray K. NC. Libby PA. Recent Developments in the BML Model of Premixed Turbulent Combustion, Turbulent Reacting Flow. Academic Press, London, 1994.

Supercontinuum Generation in $Ge_{11.5}As_{24}Se_{64.5}$ based Chalcogenide Few-Mode Fiber

Priti[1], Ajeet Kumar[1]*, Than Singh Saini[2]

[1]*Advanced Photonics Simulation Research Lab., Department of Applied Physics, Delhi Technological University, Delhi-110042, India*
[2]*CSIR-Central Scientific Instruments Organization, Sector-30, Chandigarh-160 030, India*
**ajeetdph@gmail.com*

Abstract: We report the supercontinuum generation spanning 2 µm-13 µm in a few-mode step index fiber of 10mm length pumped with 50 fs laser pulses of 4 kW peak power at 3.1µm pump wavelength.

OCIS codes:(320.6629)Supercontinuum generation; (320.2250)Femtosecond phenomena; (260.2030)Dispersion; (190.4390) Nonlinear optics.

1. Introduction

Supercontinuum generation is the broadening of the spectrum of input pulse due to third order non-linearity of the media when an input pulse of picosecond or femtosecond duration is launched into the fiber. The nonlinear property of the media results in the generation of the new frequencies within the pulse spectrum. The phenomenon of supercontinuum generation was first time observed in gaseous and solid non-linear media in 1970 [1].

Multimode fibers were studied in 1980s for mode coupling and intermodal energy transfer [2]. But they were outdated due to high intermodal dispersion. Again multimode fiber is used for mode division multiplexing by exciting each mode separately to increase the transmission capacity of communication system [3]. Also they are used to enhance the performance of single mode to nonlinear devices that are based on higher order modes [4].

Chalcogenide glasses such as $As_2S_{3,}As_2Se_3$, $Ge_{11.5}As_{24}Se_{64.5}$ and $Ge_{11.5}As_{24}S_{64.5}$ are very suitable for nonlinear applications such as supercontinuum generation and slow-light generation due to their high nonlinearity and wide transparency in mid-infrared region[5-10]. Out of these chalcogenide glasses, $Ge_{11.5}As_{24}Se_{64.5}$ has very high thin film forming ability due to high thermal and optical stability even under intense illumination [11].

In this paper, we studied the effect of variation of the core radius of the step index fiber on the dispersion. The zero dispersion is obtained around 3.4 µm in a 10mm length fiber. The fiber is pumped with a secant pulse of temporal duration (T_{FWHM}) of 50 fs with 4000 W peak power at a wavelength of 3.1 µm which is far below zero dispersion wavelength (ZDW) for generating supercontinuum. The fiber generated the output pulse spectrum in mid-infrared region (MIR) from 2 µm to 13 µm region.

2. Design of the fiber

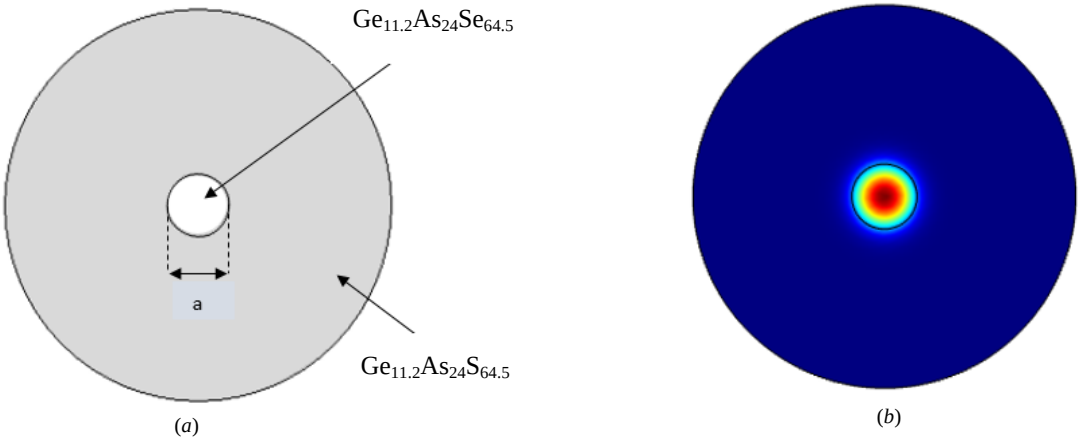


Fig.1(a). Schematic cross-section of step index fiber structure; (b) Electric field distribution of fundamental mode at 3.1 µm

The cross-sectional view of the fiber is shown in the fig.1(a) having a core radius of '*a*' which is fabricated with $Ge_{11.5}As_{24}Se_{64.5}$ chalcogenide glass material having refractive index, n_1=2.614 and cladding is fabricated with$Ge_{11.5}As_{24}S_{64.5}$ chalcogenide glass having a lower refractive index, n_2=2.284. The core material is having a nonlinear refractive index, $N_2=4.8\times10^{-18}$ m^2/W and fiber having the propagation loss of 0.05 dB/mm.

The electric field distribution of the fundamental mode is shown in the Fig.1(b) having the maximum field intensity at the center of core of fiber.

3. Numerical results and discussion

The variation of the dispersion of the material with the varying wavelength is shown in the Fig.2(a). At the pump wavelength 3.1 µm, minimum dispersion is obtained with core radius, a=1.7 µm. With this core radius, the number of modes are increased to 5, so this fiber is known is called few-mode fiber.The effective mode area is 6.09 μm^2 and corresponding non-linear coefficient, γ is 1431 W^{-1} km^{-1} as calculated from Fig.2(b). at pump wavelength 3.1 µm.

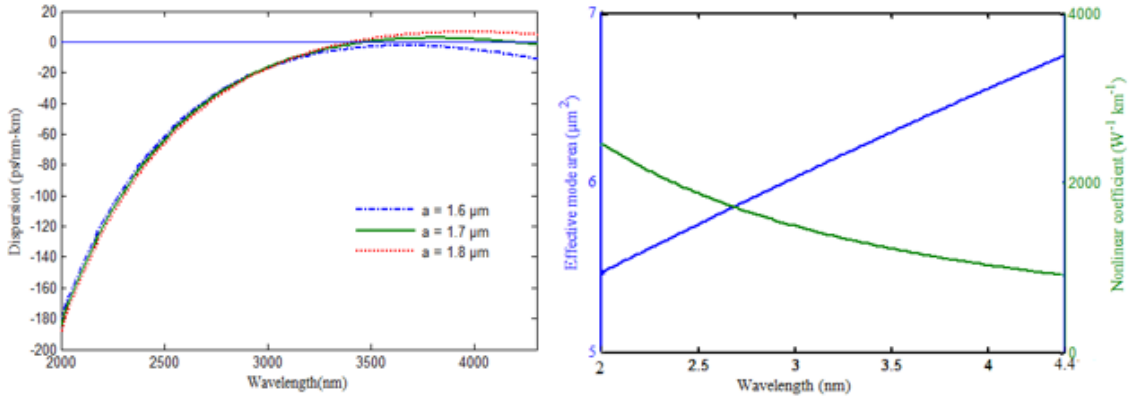


Fig.2. (a) Effect of the variation of the core radius of the fiber on dispersion at pump wavelength 3.1 µm; (b) Variation of the effective mode area of the propagating mode and corresponding nonlinear coefficient of fiber with wavelength variations.

The calculated output spectra of supercontinuum generation areshown in the Fig.4. It is to be noticed that output spectra become constant in the spectral range of 2µm to 13µm at the 10mm length of fiber with peak power 4000 W provided by 50 fs pulse.

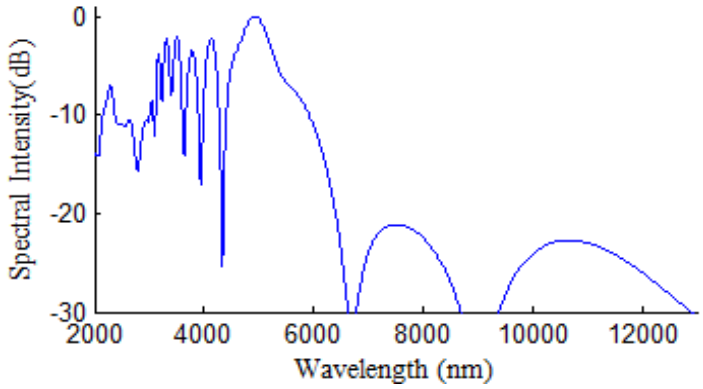


Fig.4. Broadening of output spectra obtained at 10 mm length of fiber using peak power of 4000 W of incident pulse with pulse duration of 50 fs.

For the simulation of SC, the parameters taken for calculation are shown in table-1 where f_R represents the fractional response of delayed Raman response.

Table-1. Parameters used for the generation of supercontinuum(SC)

Parameters	Fiber length	Propagation Loss(α)	f_R[12]	τ_1 [12]	τ_2[12]
Unit	mm	dB/mm	Null	fs	fs
Value	10	0.05	0.031	15.5	230.5

4. Conclusion

A design of the step index fiber generating few modes with $Ge_{11.5}As_{24}Se_{64.5}$ chalcogenide glass has been demonstrated for mid-infrared SCG. A flat-top dispersion curve having dispersion of -11.36 ps/(nm × km) at pump wavelength of 3.1 μm have obtained. Multimode fibres with large effective mode area may lead to generation of supercontinuum with higher energy, so the light sources will be of higher energy and also the transmission capacity of a communication system can be increased with this fibre.

References

[1] R. R. Alfano and S. L. Shapiro, *Phys. Rev. Lett.* **24**, 584 (1970).

[2] S. Berdagué and P. Facq, "Mode division multiplexing in optical fibers," Appl. Opt. 21, 1950–1955 (1982).

[3] D. J. Richardson, J. M. Fini, and L. E. Nelson, "Space-division multiplexing in optical fibres," Nat. Photonics 7, 354–362 (2013).

[4] A. Efimov, A. J. Taylor, F. G. Omenetto, J. C. Knight, W. J. Wadsworth, and P. Russell, "Nonlinear generation of very high-order UV modes in microstructured fibers," Opt. Express 11, 910–918 (2003).

[5] J. L. Adam and X. Zhang, Chalcogenide Glasses: Preparation, Properties and Applications, 1st ed. (Woodhead Publishing, 2013).

[6] T. S. Saini, A. Kumar, R. K. Sinha, "Broadband mid-infrared supercontinuum spectra spanning 2 – 15 μm using As_2Se_3 chalcogenide glass triangular-core graded-index photonic crystal fiber," *IEEE/OSA J. Lightwave Technol.*33(18), (2015) 3914 – 3920.

[7] T. S. Saini, A. Kumar, R. K. Sinha, "Broadband mid-IR supercontinuum generation in As_2Se_3 based chalcogenide photonic crystal fiber: A new design and analysis," *Opt. Commun*. 347, (2015), 13 – 19.

[8] T. S. Saini, A. Kumar, R. K. Sinha, "Stimulated Brillouin scattering based tunable slow light in tellurite photonic crystal fiber," *Proc.* Photonics 2014: 12th International Conference on Fiber Optics and Photonics @ OSA 2014, IIT Kharagpur, WB, India, December 13-16, 2014, T3A.28.

[9] R. K. Sinha, A. Kumar, T. S. Saini, "Analysis and Design of Single-Mode As_2Se_3-Chalcogenide Photonic Crystal Fiber for Generation of Slow Light with Tunable Features," *IEEE J. Sel. Topics Quant. Electron.* 22(2), (2016), 4900706.

[10] T. S. Saini, A. Kumar, R. K. Sinha, "Slow light generation in single-mode tellurite fibers," *J. Modern Optics* 62(7), (2015),508 – 513.

[11] P. Ma, D. Y. Choi, Y. Yu, X. Gai, Z. Yang, S. Debbarma, S. Madden, and B. Luther-Davies, "Low-loss chalcogenide waveguides for chemical sensing in the mid-infrared," Opt. Express **21**(24), 29927–29937 (2013).

[12] M. R. Karim, B. M. A. Rahman, and Govind P. Agrawal, "Mid-infrared supercontinuum generation using dispersion-engineered $Ge_{11.5}As_{24}Se_{64.5}$chalcogenide channel waveguide," Opt. Express 23, 6903-6914 (2015)

14.139.251.107 {ts'2016-12-26 04:27:54'}

International Conference on Communication and Signal Processing, April 6-8, 2016, India

The Smart Number Plate

Vanshaj Sikri

***Abstract*—Although much has been professed about the fruitfulness of smart cars, road crash statics cast a shadow on the veracity of those claims. Gruesome reports on car crashes and related deaths are affirmation to the fact that we are nowhere near to the smart car paradigm. The two most prominent causes for these deaths are over-speeding on the part of driver and a delayed response by emergency service providers in case of a mishap. The given paper proposes a Smart Number Plate as a solution to these problems. The number plate is equipped with an accelerometer that continuously measures the acceleration of the car and if the acceleration is greater than 4g (g=9.8 m/s^2) it alerts the relatives of the driver and the emergency service providers by sending an SMS consisting of location coordinates obtained via GPS module. The number plate is also equipped with GPRS module that sends vehicle's location coordinates and details (number and model) on a server in case vehicle exceeds the speed limit. This data can be accessed by police control room via website and expeditious action can be taken against the defaulters. A website consisting of a Google map to display location coordinates of vehicle is also developed. Additionally, the Smart Number Plate is provided with an ultrasonic proximity sensor to assist vehicle in parking it appropriately. The Smart Number Plate is also tested for its ability to resist false positive detections of accidents under simulated environment. The paper adds an element of smartness in the vehicle's number plate and takes us a step closer to the smart vehicle paradigm.**

***Index Terms*—over speeding alert, parking assist system, smart car, smart number plate, vehicle crash detection.**

I. INTRODUCTION

As per the records of Indian Government, 4, 97, 686 road accidents were reported in the year 2011 [1]. A staggering 1, 42, 485 people were killed in road mishaps [2]. Attributable causes can be many, ranging from over speeding and drunken driving [3] to slow response by emergency service providers (ESPs) [4] and abysmal road infrastructure [3].

Advancements in the field of software development and embedded systems have yielded potent technologies that can partly tame the problem of feeble crash detection and alert dissemination methods. To hasten up the process of crash alert dissemination, researchers have proposed variegated methods based on Vehicular Ad-Hoc Networks (VANETs), GSM transmission, RF transmission, etc. Virtually all methods to detect vehicle crash use accelerometer, Airbag trigger signal from OBD-II (On-Board Diagnostic system) interface, map-matching or an admixture of two or more. Some even provide a GUI for the user to interact with in-vehicle sensors as well as external ones [5, 10, 12].

Hitherto all the efforts ([5], [9]-[11], [12]-[14]) to reduce the number of people killed in car accidents focused mainly on effective communication of accident to ESPs and discounted over speeding as a potential cause; But, according to [6], 37% of accidents were caused due to over speeding. 40% of fatal road accidents in New South Wales are speed related [7]. So, it is impossible to bring down the number of deaths without finding a prudent solution to the problem of over speeding. Also, researchers who have proposed solutions for the problem of over speeding do not include the role of police. In [8], authors have presented an in-vehicle system that records events of traffic violations such as: exceeding speed limit, ignoring stop sign, and disregarding forbidden turning. The system is designed to warn drivers in case they violate traffic rules and issues acoustical message for the same. The system also records parameters like vehicle speed, GPS location, and photographs of the surroundings on a database for offline analysis. Albeit the given system is a great attempt to avoid accidents caused by driver's inattention, but it cannot convey willful violation by the driver to police control room in real time. In [7], authors evaluate a self-contained on-board speed advisory system that alerts drivers when speed limit is exceeded. Again, this system fails to include the role of police.

The given paper offers an ingenious remedy to the problem of over speeding as well as abysmal alert dissemination. A Smart Number Plate has been proposed that alerts police control room in case a vehicle exceeds the predefined speed limit. Also, the Smart Number Plate apprise the ESPs and relatives of the driver in case the vehicle crashes somewhere. Additionally, the Smart Number Plate is equipped with an ultrasonic proximity sensor that aids in parking the vehicle in a limited expanse. Smart Number Plate's ability to localize a vehicle also creates a new set of capabilities for it such as locating stolen vehicles, fleet management and highway congestion control. Moreover, it will also reduce the amount of police force needed to nab the defaulters and manage traffic. The proposed system was also tested for its robustness to avoid detection of false positives for accident alert. Fig. 1 shows the architecture of the proposed system, and Fig. 2 illustrates the working of the proposed system.

V. Sikri is with the Electronics and Communication Engineering Department, Delhi Technological University, Delhi, India (e-mail: vanshajsikri@gmail.com).

978-1-5090-0396-9/16/$31.00 ©2016 IEEE

IEEE Advancing Technology for Humanity

The rest of the paper is organized as follows. The Related Work section II discusses different crash detection and alert systems in detail. System Implementation section III delineates hardware and software of the prototype and details algorithm implemented. Additionally, it shows the website developed and S-O-S message that is sent to the relatives and ESPs. Section IV, Prototype Testing and Discussion, outlines test results of the prototype. Finally, the paper is concluded in Section V.

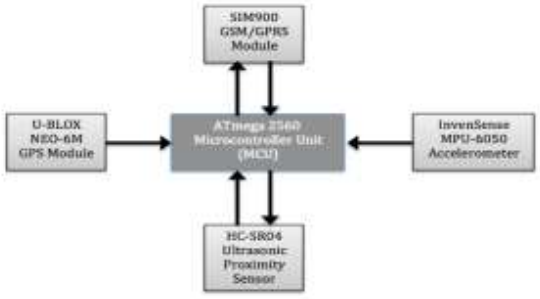


Fig. 1. System Architecture



Fig. 2. System Overview

II. RELATED WORK

There are multitudes of vehicle crash detection techniques currently available. Many researchers have proposed hardware as well as software solution to rein in the problem of inefficient crash detection. Furthermore, many have come up with innovative methods that amalgamate hardware and software approach to yield robust crash detection technique.

In [9], the author exploits the capabilities of Vehicular Ad-hoc Networks (VANETs) to effectively detect car crashes. Additionally the method described in this paper can be used to broadcast a warning message to every car within a fixed range so that drivers of other cars can decide whether they need to change the route or not.

In [10], authors present a canny approach to upgrade the obsolete in-vehicle accident detection systems. They have proposed an application, WreckWatch, which detects accidents based on the inputs from smartphone-based sensors (accelerometer). WreckWatch ignores any acceleration events below 4g (g=9.8 m/s^2). Authors first address issues associated with detecting traffic accidents such as preventing false positives by using mobile context information and monitoring on board sensors to detect large accelerations. Authors also analyzed the ability of their system to resist false positives. Finally, authors discuss how their system can be used to reduce overall traffic congestion and increase preparedness of emergency responders. Reference [5] proposes an android based application. The application constantly monitors the vehicle, via Bluetooth, for airbag trigger signal issued by OBD-II interface. The application simultaneously calculates the acceleration (G-force) experienced by the passengers when there is an accident. The application uses accelerometer readings and airbag trigger signal to determine whether an accident occurred or not. If the accident is detected, the application sends details about the accident through an e-mail or an SMS to pre-defined destinations and calls ESPs. Even though these applications are an innovative approach to tackle the issue, they will probably fail to attract masses because they use a smart phone. It is highly possible that the driver might forget to carry his/her smart phone while travelling. Furthermore, as these applications are always polling sensors, they will drain out the battery faster.

In [11], authors have proposed an intelligent Accident Detection and Reporting System (ADRS) that uses low cost RF modules, a microcontroller, an LCD and an accelerometer to accurately detect an accident and effectively convey the emergency message to ESPs.

In [12], authors have proposed an android application called HDy Copilot that uses vehicle's ODB-II interface and smartphone's sensors to detect accidents. The novelty of the proposed technique is that the application broadcasts accident alerts by three sources. The first is the vehicular network, by transmitting a Decentralized Environmental Notification Message (DENM) message containing a Road Hazard Warning via the IT2S platform. The second is an eCall to the Emergency Medical System (EMS). Third is by sending an SMS, containing the eCall minimum set of data.

In [13], authors have designed an accident detection and alert system for motorcycles. The system examines acceleration via an accelerometer, pressure change on body of vehicle via piezo film sensor and tilt of the vehicle via simple pendulum tilt meter to characterize occurrence of an accident. Alert dissemination is done via SIM300 module. In [14], authors have proposed an innovative method by coalescing Map-Matching technique and location coordinates calculation via GPS to indicate occurrence of an accident. When speed of vehicle falls below the safe threshold speed, the system will signalize occurrence of an accident if the system is found outside the road network. The proposed system assumes that in events of crash, the vehicle will veer away from the road and map-matching module will catch that deviation.The methodology proposed is unique; but if the vehicle does not go off the road network in case of an accident, then the proposed method will have the opposite effect.

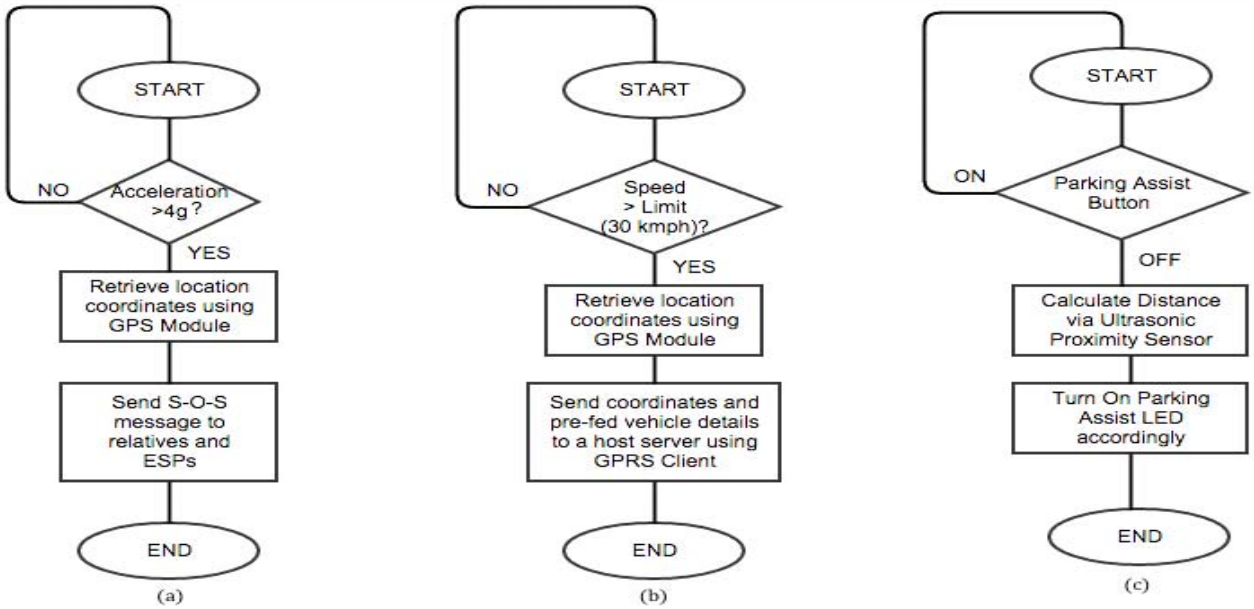


Fig. 3. Algorithm for Accident Alert (a) functionality; Algorithm for issuing Over Speeding Alert (b); Algorithm for Parking Assist (c) functionality.

III. SYSTEM IMPLEMENTATION

The given section discusses the algorithm implemented for the Smart Number Plate in detail. Fig.3 shows the algorithm executed for three functionalities. Hardware and Software details are also elucidated in the given section.

A. Accident Alert

The InvenSense MPU-6050 accelerometer constantly polls the acceleration of the vehicle. If the acceleration exceeds 4g, accident is detected and alert is issued to the relatives of the driver and ESPs. Any acceleration value below 4g is ignored. Table I summarizes the accident's severity and the corresponding acceleration range in g's. Values of Table I were estimated based on full frontal crash test results from 2007 Chevrolet suburban. Thereafter, GPS location coordinates are obtained from the U-BLOX NEO-6M module. The GPS module returns a stream of data in National Marine Electronics Association (NMEA) standard. Fig. 4 shows the stream of data coming from the GPS module. Out of these strings only $GPRMC sentence is useful for the proposed system. The module was so configured that it only returned $GPRMC string. After receiving the string, it is parsed via NMEA message parser to obtain Latitude and Longitude of the vehicle. After extracting the coordinates from the string, SIM900 GSM/GPRS module is used to send an alert message consisting those location coordinates to ESPs and relatives of the driver. Fig. 5 shows the alert message issued when accident is detected.

TABLE I

ACCELEROMETER THRESHOLDS FOR ACCIDENT DETECTION

G Range	Accident Severity
0-4g	No Accident
4-20g	Mild Accident
20-40g	Medium Accident
40+g	Severe Accident



Fig. 4. NMEA sentences received from GPS module.



Fig. 5. Accident Alert message issued to relatives and ESPs.

B. Over Speeding Alert

Out of the scads of benefits NMEA string message provides, one is its capability to convey the speed of vehicle on which the GPS module is attached. The proposed system exploits this ability to detect any vehicle that exceeds the speed limit. The speed limit of a particular road can be obtained via Google Road API [15], but because of questionable accuracy of the method, the given paper used a predefined speed limit of 30 km/h. The $GPRMC string also provides speed over ground in knots (1 knot =1.852 km/h). After converting the speed in km/h, it is compared with predefined speed limit. If the vehicle exceeds the speed limit, microcontroller unit (MCU) commands the SIM900 GPRS module to send the location coordinates of vehicle and vehicle details such as model of the vehicle and vehicle number via standard HTTP POST operations to the host server. As the vehicle information is made available on the server, location coordinates, vehicle number and vehicle model are accessed and displayed on a website consisting of a Google map. This information can be availed by Police Control Room. The system will aid the police to judiciously allocate their limited work force. Also, this system will create a sense of fear in the mind of driver thereby restraining his/her whim to exceed the speed limits. Fig. 6 shows the website that was developed.

The website is based on PHP and MySQL backend. The server is hosted on [16]. The script has a two-way function. If data are HTTP posted to the server, it stores it on the backend database otherwise it renders the last record from the database using Google maps API and HTML. All the previous requests stay in the database for any future reference.

C. Parking Assist

The Smart Number Plate is also equipped with HC – SR04 ultrasonic proximity sensor that can help park a vehicle. It is cheap and provides 2cm – 400cm non-contact measurement function. When the distance to an object is to be calculated, Trig pin is pulled to high level for more than 10us impulse and the module starts ranging. When the ultrasonic wave encounters an object, it is reflected back to the sensor and the sensor pulls the Echo pin at low level when it detects the reflected wave. The Echo pin will be at high level for different durations depending on the distance to object. Distance to an object can be found out using (1).

$$\text{Distance} = (\text{Duration of High Level}) \times 340 \div 2 \quad . \tag{1}$$

Here, Duration of High level of Echo pin is in seconds and speed of ultrasonic wave is taken as 340 m/s.

When the user presses the parking assist button, ultrasonic sensor calculates the distance between the vehicle and nearby object. When the distance is greater than 50 cm, MCU switches on no LED. When the distance is between 25 – 50 cm, MCU switches on the corresponding LED, and when the distance is between 10 - 25 cm, MCU switches on the other LED. Fig. 7 shows the console used for parking assist. This can be placed inside the car.

IV. PROTOTYPE TESTING AND DISCUSSION

Fig. 9 shows the prototype of the proposed Smart Number Plate. In order to evaluate the viability of the prototype, accelerometer measurements were taken during normal car operation. Events such as travelling a straight path, turning and sudden stopping were tested to assay the ability of the system to resist detection of false positives. The accelerometer was so positioned that the x-axis faced forward and any changes in acceleration on this axis formed the basis for accident detection. Thereafter, the accelerometer readings were plotted on a graph as shown in Fig. 8. Here, x-axis represents time and y-axis represents acceleration value in g's. It can be observed that none of the reading on the 3 axes exceeded the 4g threshold.

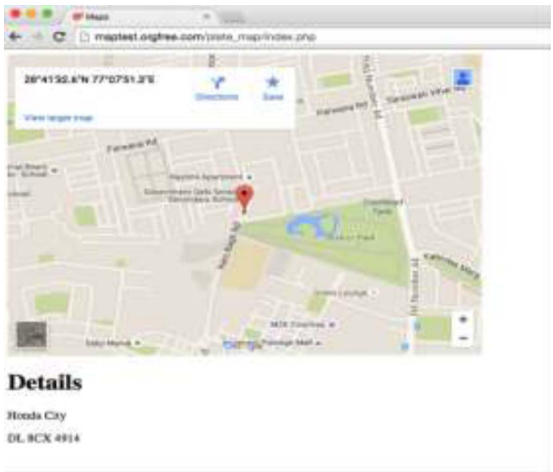


Fig. 6. Website developed to show over speeding vehicle.

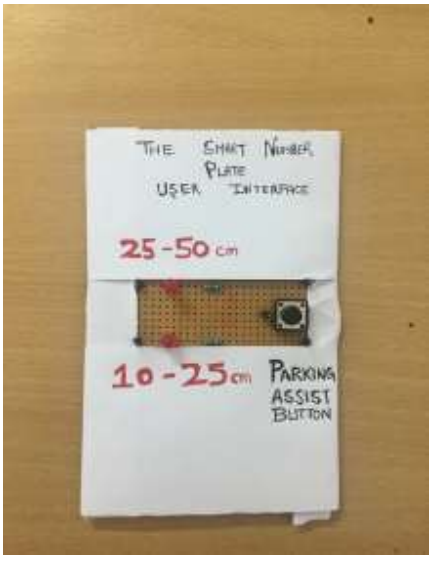


Fig. 7. Parking Assist Interface

V. CONCLUSION AND FUTURE WORK

The given paper proposed a prototype of Smart Number Plate that can rein in the problem of deaths caused by over speeding vehicle and tardy response by ESPs. The prototype is a concerted effort towards realization of a quintessential

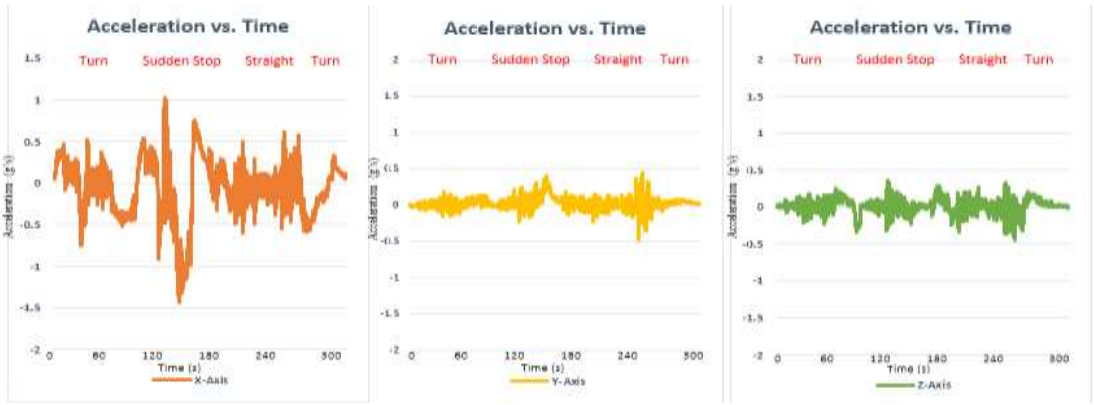


Fig. 8. Accelerometer readings along X, Y, and Z Axis in events of turning, sudden stop, and straight line motion.

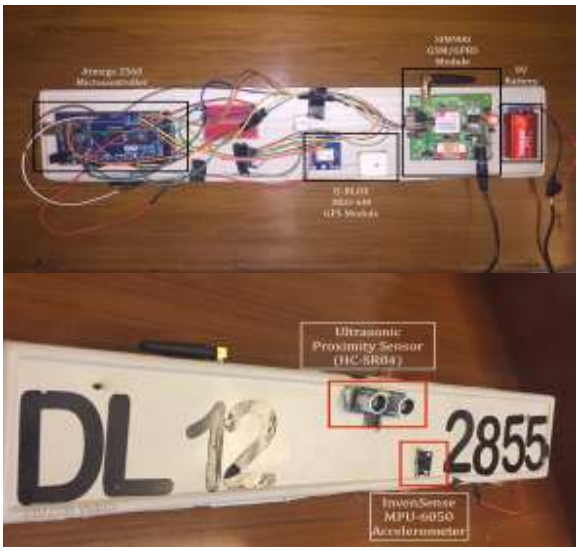


Fig. 9. Backside and Front of the prototype for smart number plate.

smart car that can take swift measures to avoid accidents or in case of accidents. Additionally, an in-built GPS facility of Smart Number Plate opens up a lot of opportunities ranging from judicious deployment of traffic police personnel to limit highway congestion, to expeditious deployment of medical services to needy vehicles on highway. The prototype was also tested for accuracy under controlled environment. The results obtained affirmed the robustness of the prototype in preventing false positives. In future, I would like to validate results in a real crash test.

REFERENCES

[1] Government of India. (2014, April 30). [Online]. Available: https://data.gov.in/catalog/total-number-persons-killed-road-accidents-india

[2] Government of India. (2014, April 30). [Online]. Available: https://data.gov.in/catalog/total-number-road-accidents-india

[3] Law Offices of Michael Pines APC. [Online]. Available: https://seriousaccidents.com/legal-advice/top-causes-of-car-accidents/

[4] P. Kendall. Thousands die from ambulance delays [Online]. Available: http://www.dailymail.co.uk/health/article-55521/Thousands-die-ambulance-delays.html

[5] J. Zaldivar, C.T. Calafate, J.C. Cano, and P. Manzoni, "Providing accident detection in vehicular networks through OBD-II devices and android-based smartphones," in *Proceedings of the 36th IEEE Conference on Local Computer Networks (LCN)*, Bonn. 4-7 October 2011,pp.813-819.

[6] Dipak K Dash. (2015, July 19). 16 deaths every hour [online]. Available: http://timesofindia.indiatimes.com/india/16-deaths-every-hour-Indian-roads-claim-the-maximum-number-of-lives-in-2014/articleshow/48128946.cms

[7] M. Paine, D. Paine, M. Griffiths, and G. Germanos, "In-vehicle intelligent speed advisory systems," in Proceedings of the 20th International Conference on the Enhanced Safety of Vehicles, 2007.

[8] N. Aliane, J. Fernandez, S. Bemposta, and M. Mata, "Traffic violation alert and management," in *Proceedings of the 14th International IEEE Conference on Intelligent Transportation Systems*, Washington, DC, Oct. 2011, pp. 1716–1720.

[9] S.J.Weiner, Feasibility of a 802.11 VANET Based Car Accident Alert System, Northeastern University.

[10] C. Thompson, J. White, B. Dougherty, A. Albright, and D. C. Schmidt, "Using smartphones to detect car accidents and provide situational awareness to emergency responders," in *3rd International Conference MOBILWARE'10*, Chicago, USA, 2010, pp. 29-42.

[11] R.K.Megalingam, R.N.Nair, S.M.Prakhya, " Wireless vehicular Accident Detection and Reporting System", in *2nd International Conference on Mechanical and Electrical Technology (ICMET)*, Singapore, 2010, 636-640.

[12] B.Fernanded, V.Gomes, J.Ferreira, A.Oliveira, " Mobile Application for Automatic Accident Detection and Multimodal Alert", in *IEEE 81st Vehicular Technology Conference (VTC Spring)*, Glasgow, 2015, pp.1-5.

[13] F.B.Basheer *et al.*, "Design of Accident Detection and Alert System for Motor Cycles", in *Global Humanitarian Technology Conference: South Asia Satellite (GHTC-SAS)*, Trivandrum, 2013, pp.85-89.

[14] M.S. Amin, M.A.S. Bhuiyan, M.B.I. Reaz, S.S. Nasir, "GPS and Map matching based vehicle accident detection system", *in IEEE Student Conference on Research and Development (SCOReD)*, Putrajaya, 2013, pp.520-523.

[15] Google. [Online]. Available: https://developers.google.com/maps/documentation/roads/intro

[16] Free Web Hosting Area. [Online]. Available: http://freewebhostingarea.com/

Progress In Electromagnetics Research B, Vol. 71, 167–181, 2016

Theoretical Modelling of Kelvin Helmholtz Instability Driven by an Ion Beam in a Negative Ion Plasma

Kavita Rani[1] and Suresh C. Sharma[2, *]

Abstract—An ion beam propagating through a magnetized plasma having positive ions K^+ (Potassium ions), electrons and negative ions SF_6^- (Sulphur hexafluoride ions) drives Kelvin Helmholtz Instability (KHI) via Cerenkov interaction. For two modes, K^+ and SF_6^-, the frequency and the growth rate of the unstable wave increase with the relative density of negative ions. It is observed that the beam has destabilizing effect on the growth rate of KHI in the presence of negative ions. However, at the large concentration of the negative ions beam stabilizes the growth rate of KHI. An increase in mass of negative ions also stabilizes the growth rate of KHI modes. It is also observed that increase in ion beam velocities and densities play a significant role in changing the growth rate of KHI modes. Moreover, the finite geometry effects tend to modify the dispersion properties and growth of KHI modes.

1. INTRODUCTION

The study of Kelvin Helmholtz instability has received great attention in various geophysical and astrophysical situations such as Earth's polar cusps [1], Earth's Magnetosphere [2–5], Comet tails [6] and Ion Loss on Mars [7] etc..

Kelvin Helmholtz instability (KHI) is low frequency perturbation that may arise due to relative motion between the different layers of a conductive, magnetized and incompressible heterogeneous fluid that feeds on the ambient flow energy. The instability may arise in the plasma streaming parallel to the magnetic field whose velocity varies in the direction perpendicular to the magnetic field [8]. The study of the KHI for magnetized compressible fluids showed that the KHI may occur if the relative speed between two adjacent layers exceeds the root mean square Alfven speed between the layers [9]. The essential features of KHI were later on confirmed by experimental observations of Q-machine [10]. The Landau damping has a stabilizing effect on the Kelvin Helmholtz instability [11].

It was observed that the excitation of KHI in a magnetized plasma having positively charged dust grains is easier than negatively charged dust grains due to reduction in the critical shear with increase in the quantity $Z\varepsilon$ (where Z is the charge state and ε is the ratio between dust density and the ion density) for the positive ions [12]. The presence of negative ions has a destabilizing effect on the KHI in a plasma for ion acoustic and electrostatic ion cyclotron (EIC) waves [13]. An et al. [14] have investigated the unstable nature of KHI in a plasma having negative ions and found that the wave amplitude grows as the concentration of negative ions increases. However, relatively large negative ion concentration has stabilizing effect on the K-H instability.The stabilizing effect of negatively charged dust grains on the K-H instability in a magnetized Cesium plasma have also been studied [15].

Moreover, the study of negative ions in the plasma has found to be a source of motivation due to their potential applications in surface plasma technologies [16] such as ion implantation, chemical

Received 23 September 2016, Accepted 17 November 2016, Scheduled 2 December 2016
* Corresponding author: Suresh C. Sharma (suresh321sharma@gmail.com).
[1] Department of Applied Physics, Bhagwan Parshuram Institute of Technology, Sector-17, Rohini, New Delhi 110 089, India. [2] Department of Applied Physics, Delhi Technological University (DTU), Shahbad Daulatpur, Bawana Road, Delhi 110 042, India.

vapour deposition (CVD), etching in ultra-large scale integration (ULSI) fabrications, macro and Nano particles creations [17, 18].

The destabilizing effect of ion beam has been studied by Sharma and Srivastava [19] on the excitation of ion cyclotron (IC) waves in a plasma cylinder with negative ions. Sharma and Gahlot [20] have studied that an ion beam propagating through the magnetized plasma cylinder with negative ions drives electrostatic ion acoustic waves to instability via Cerenkov interaction. The results of their theory showed the increase in phase velocity and unstable mode frequency with negative ions and are in compliance with the experimental observations of Song et al. [21] The dispersion properties of various ion wave modes are modified in the presence of negative ions [22–24]. Various plasma instabilities have been studied in the plasma having negative ions with and without beam. It has been observed earlier in ion beam plasma systems that the beam plays an important role in growth of instabilities [25, 26].

In this paper, we develop a theoretical model on KHI driven by an ion beam in a negative ion plasma as no work on the effect of ion beam on KHI in a magnetized plasma having negative ions has been reported so far. We also study the effects of finite boundaries on the growth of KHI modes as it is observed that finite geometry effects tend to reduce the growth of waves and instabilities [27]. We choose SF_6^- negative ions as SF_6 has a large electron capture cross section for low-energy electrons in Q-machine plasmas [21]. In Section 2, we carry out the instability analysis for two modes (positive ion K^+ and negative ion SF_6^-). The plasma and beam responses are obtained using fluid theory. We obtain the mode frequencies and the growth rate for both the modes using first order perturbation theory. Results and discussions are given in Section 3. Section 4 concludes the results obtained.

2. INSTABILITY ANALYSIS

Consider a fully ionized multi-component collisionless plasma consisting of electrons, positive ions K^+ (Potassium ions) and negative ions SF_6^- (Sulphur hexafluoride ions) immersed in the magnetic field B_s. The magnetic field is the positive z-direction and equilibrium densities of components $j(= e, +, -)$ vary along negative x-direction as $n_{0j} = \overline{n_{0j}} e^{-\lambda x}$, where for different components, $\overline{n_{0j}}(=$ constant) and λ is the e-folding wave vector of the density gradient [15]. Equilibrium densities of electrons, positive ions and negative ions are represented as $n_{0e}(= (1-\varepsilon)n_p), n_{0+} = n_p$ and $n_{0-} = \varepsilon n_p$, where $\varepsilon(= n_{SF_6^-} \big/ n_{K^+})$ is the relative density of negative ions and n_p is the plasma density. Their charges, masses and temperatures are denoted by $(-e, m_e, T_e), (e, m_+, T_+)$ and $(-e, m_-, T_-)$, respectively. The equilibrium velocity vectors of each components are given by $v_{0j} = (0, v_{0yj}, v_{0zj}(x))$ with $v_{0yj}(=$ constant). An ion beam with velocity $v_{0b} \parallel \hat{z}$, mass m_b, density $n_{0b} \ll n_{0+}$ propagates through plasma along the magnetic field.

Apply quasineutrality on the beam plasma system so that $en_{0e} - en_{0+} - en_{ob} + en_{0-} \approx 0$ as we have taken plasma density $\gg$ beam density.

The motion of all the three plasma species (electrons, positive ions and negative ions) is described by the momentum and continuity equations following the treatment of Sharma & Srivastava [19] (cf. Eqs. (1)–(6)).

Now the equilibrium is perturbed by an electrostatic perturbation to the potential

$$\phi_1 = \phi(r) e^{-i(\omega t - \vec{k}\cdot\vec{r})}. \tag{1}$$

The first order quantities are assumed to vary as $e^{-i(\omega t - k_y y - k_z z)}$. The response of plasma electrons to the perturbation may be derived from the momentum conservation equation, i.e.,

$$m_e \frac{d\vec{v_e}}{dt} = -e\vec{E} - \frac{e}{c}\vec{v_e} \times \vec{B_s} - \frac{\nabla(n_e T_e)}{n_e}. \tag{2}$$

We obtain electron, positive ion and negative ions perturbed density from the mass conservation equation as

$$n_{1e} = n_{0e} \frac{e\phi_1}{T_e}. \tag{3}$$

$$n_{1+} = \frac{n_{0+}e\phi_1}{m_+}\frac{\left(\frac{\nabla_\perp^2}{\left(\omega_{c+}^2-\Omega_+^2\right)}+\frac{k_z^2}{\Omega_+^2}+\frac{\lambda k_y\omega_{c+}}{\Omega_+\left(\omega_{c+}^2-\Omega_+^2\right)}-\frac{k_yk_z\omega_{c+}}{\Omega_+^2\left(\omega_{c+}^2-\Omega_+^2\right)}\frac{\partial v_{0z+}}{\partial x}\right)}{\left(1-\frac{\nabla_\perp^2 v_{t+}^2}{\left(\omega_{c+}^2-\Omega_+^2\right)}-\frac{k_z^2v_{t+}^2}{\Omega_+^2}-\frac{\lambda k_yv_{t+}^2\omega_{c+}}{\Omega_+\left(\omega_{c+}^2-\Omega_+^2\right)}+\frac{k_yk_zv_t{}^{+2}\,\omega_{c+}}{\Omega_+^2\left(\omega_{c+}^2-\Omega_+^2\right)}\frac{\partial v_0z+}{\partial x}\right)}. \quad (4)$$

$$\text{and } n_{1-} = \frac{-n_{0-}e\phi_1}{m_-}\frac{\left(\frac{\nabla_\perp^2}{\left(\omega_{c-}^2-\Omega_-^2\right)}+\frac{k_z^2}{\Omega_-^2}-\frac{\lambda k_y\omega_{c}-}{\Omega_-\left(\omega_{c-}^2-\Omega_-^2\right)}+\frac{k_yk_z\omega_{c}-}{\Omega_-^2\left(\omega_{c-}^2-\Omega_-^2\right)}\frac{\partial v_0z-}{\partial x}\right)}{\left(1-\frac{\nabla_\perp^2\,v_t{}^{-2}}{\left(\omega_{c-}^2-\Omega_-^2\right)}-\frac{k_z^2v_{t-}^2}{\Omega_-^2}+\frac{\lambda k_yv_{t-}^2\omega_{c-}}{\Omega_-\left(\omega_{c-}^2-\Omega_-^2\right)}-\frac{k_yk_zv_{t-}^2\omega_{c}-}{\Omega_-^2\left(\omega_{c-}^2-\Omega_-^2\right)}\frac{\partial v_{0z-}}{\partial x}\right)}, \quad (5)$$

where $v_{t+}[=(\frac{T_+}{m_+})^{1/2}]$ and $v_{t-}[=(\frac{T_-}{m_-})^{1/2}]$ are the thermal velocities of positive and negative ions, $\omega_{c+}(=eB_s/m_+c)$ and $\omega_{c-}(=eB_s/m_-c)$ are the positive and negative ions cyclotron frequencies and $\Omega_+[=\omega-k_yv_{0y+}-k_zv_{0z+}]$ and $\Omega_-[=\omega-k_yv_{0y-}-k_zv_{0z-}]$ are the Doppler shifted wave frequencies for positive and negative ions, respectively.

Following the analysis of Sharma and Srivastava [19], the ion beam density perturbation is given by

$$n_{1b} = \frac{n_{0b}e(k_y^2+k_z^2)\phi_1}{m_b(\omega-k_zv_{0b})^2}, \quad (6)$$

where $k_y=k_\perp$ and $(k_y^2+k_z^2)\approx k^2(=k_\perp^2+k_z^2)$.

2.1. Infinite Boundary Effects

Using Eqs. (3)–(6) in the Poisson equation, $\nabla^2\phi_1=4\pi(n_{1e}e-n_{1+}e-n_{1b}e+n_{1-}e)$, we obtain,

$$1-\frac{\omega_{p+}^2v_{te}^2}{\omega_{pe}^2}\frac{\left(k_z^2-\frac{k_y^2\Omega_+^2}{\left(\omega_{c+}^2-\Omega_+^2\right)}+\frac{\lambda k_y\omega_{c+}\Omega_+}{\left(\omega_{c+}^2-\Omega_+^2\right)}-\frac{k_yk_z\omega_{c+}}{\left(\omega_{c+}^2-\Omega_+^2\right)}\frac{\partial v_{0z+}}{\partial x}\right)}{\left(\Omega_+^2-k_z^2v_{t+}^2+\frac{k_y^2v_{t+}^2\Omega_+^2}{\left(\omega_{c+}^2-\Omega_+^2\right)}-\frac{\lambda k_yv_{t+}^2\omega_{c+}\Omega_+}{\left(\omega_{c+}^2-\Omega_+^2\right)}+\frac{k_yk_zv_{t+}^2\omega_{c+}}{\left(\omega_{c+}^2-\Omega_+^2\right)}\frac{\partial v_{0z+}}{\partial x}\right)}$$
$$-\frac{\omega_{p-}^2v_{te}^2}{\omega_{pe}^2}\frac{\left(k_z^2-\frac{k_y^2\Omega_-^2}{\left(\omega_{c-}^2-\Omega_-^2\right)}-\frac{\lambda k_y\omega_{c-}\Omega_-}{\left(\omega_{c-}^2-\Omega_-^2\right)}+\frac{k_yk_z\omega_{c-}}{\left(\omega_{c-}^2-\Omega_-^2\right)}\frac{\partial v_{0z-}}{\partial x}\right)}{\left(\Omega_-^2-k_z^2v_{t-}^2+\frac{k_y^2v_{t-}^2\Omega_-^2}{\left(\omega_{c-}^2-\Omega_-^2\right)}+\frac{\lambda k_yv_{t-}^2\omega_{c-}\Omega_-}{\left(\omega_{c-}^2-\Omega_-^2\right)}-\frac{k_yk_zv_{t-}^2\omega_{c-}}{\left(\omega_{c-}^2-\Omega_-^2\right)}\frac{\partial v_{0z-}}{\partial x}\right)}=\frac{\omega_{pb}^2(k_y^2+k_z^2)v_{te}^2}{\omega_{pe}^2\left(\omega-k_zv_{0b}\right)^2} \quad (7)$$

where $\omega_{p+}[=(4\pi n_{0+}e^2/m_+)^{1/2}]$, $\omega_{p-}[=(4\pi n_{0+}e^2/m_-)^{1/2}]$, $\omega_{pb}[=(4\pi n_{0b}e^2/m_b)^{1/2}]$, $\omega_{pe}[=(4\pi n_{0e}e^2/m_e)^{1/2}]$ and $v_{te}[=(\frac{T_e}{m_e})^{1/2}]$ are the positive ion plasma frequency, negative ion plasma frequency, beam plasma frequency, electron plasma frequency and electron thermal velocity, respectively.

Equation (7) can be simplified further as

$$1-\frac{c_+^2}{(1-\varepsilon)}\frac{A^2}{\left(\Omega_+^2-v_{t+}^2A^2\right)}-\frac{\varepsilon c_-^2}{(1-\varepsilon)}\frac{B^2}{\left(\Omega_-^2-v_{t-}^2B^2\right)}=\frac{\omega_{pb}^2(k_y^2+k_z^2)v_{te}^2}{\omega_{pe}^2\left(\omega-k_zv_{0b}\right)^2}, \quad (8)$$

where $c_+(=T_e/m_+)^{1/2}$, $c_-(=T_e/m_-)^{1/2}$ are the positive ion and negative ion sound speeds, respectively,

$$A^2 = \left(k_z^2-\frac{k_y^2\Omega_+^2}{\left(\omega_{c+}^2-\Omega_+^2\right)}+\frac{\lambda k_y\omega_{c+}\Omega_+}{\left(\omega_{c+}^2-\Omega_+^2\right)}-\frac{k_yk_z\omega_{c+}}{\left(\omega_{c+}^2-\Omega_+^2\right)}\frac{\partial v_{0z+}}{\partial x}\right). \quad (9)$$

$$\text{and } B^2 = \left(k_z^2-\frac{k_y^2\Omega_-^2}{\left(\omega_{c-}^2-\Omega_-^2\right)}-\frac{\lambda k_y\omega_{c-}\Omega_-}{\left(\omega_{c-}^2-\Omega_-^2\right)}+\frac{k_yk_z\omega_{c-}}{\left(\omega_{c-}^2-\Omega_-^2\right)}\frac{\partial v_{0z-}}{\partial x}\right). \quad (10)$$

Equation (8) can be rewritten as

$$\left(\Omega_+^2 - P_+^2A^2\right)\left(\Omega_-^2 - P_-^2B^2\right) - \alpha A^2B^2 = \frac{\omega_{pb}^2(k_y^2+k_z^2)k^2v_{te}^2}{\omega_{pe}^2\left(\omega - k_zv_{0b}\right)^2}\left(\Omega_+^2 - v_{t+}^2A^2\right)\left(\Omega_-^2 - v_{t-}^2B^2\right), \tag{11}$$

where $P_+^2 = v_{t+}^2 + \frac{c_+^2}{(1-\varepsilon)}$, $P_-^2 = v_{t-}^2 + \frac{\varepsilon c_-^2}{(1-\varepsilon)}$, and $\alpha = \frac{\varepsilon c_+^2 c_-^2}{(1-\varepsilon)^2}$.

Equation (11) is the dispersion relation of an ion beam driven KHI in a plasma having negative ions. In the absence of beam, i.e., $n_{0b} \to 0$ or$\omega_{pb} = 0$, Eq. (11) reduces to

$$\left(\Omega_+^2 - P_+^2A^2\right)\left(\Omega_-^2 - P_-^2B^2\right) - \alpha A^2B^2 = 0. \tag{12}$$

Equation (12) is the dispersion relation of D'Angelo and Song [13] (cf. Eq. (26)). To study the interaction of an ion beam with positive and negative ions, we evaluate Eq. (8) for two different modes (i.e., K^+ and SF_6^- ion modes).

2.1.1. Beam Plasma Interaction with Positive Ions (K^+)

In the limit $\omega \sim \omega_{c+}$ and positive ion Larmor radius is less than the perpendicular wavelength of the positive ion mode, Eq. (8) can be rewritten as

$$1 - \frac{c_+^2}{(1-\varepsilon)}\frac{A^2}{\left(\Omega_+^2 - v_{t+}^2A^2\right)} = \frac{\omega_{pb}^2(k_y^2+k_z^2)v_{te}^2}{\omega_{pe}^2\left(\omega - k_zv_{0b}\right)^2}. \tag{13}$$

Equation (13) can be further rewritten as

$$(\Omega_+^2 - P_+^2A^2) = \frac{\omega_{pb}^2(k_y^2+k_z^2)v_{te}^2}{\omega_{pe}^2(\omega - k_zv_{0b})^2}(\Omega_+^2 - v_{t+}^2A^2). \tag{14}$$

We are looking for solutions when the beam is in Cerenkov resonance with the positive ion KHI mode. In the limit of long perpendicular wavelength, i.e., $k_y^2\Omega_+^2 \ll \omega_{c+}^2$, also, for low frequency approximations, i.e., $\Omega_+^2 \ll \omega_{c+}^2$ and in the absence of beam, i.e., $n_{0b} \to 0$ or $\omega_{pb} = 0$. Hence Eq. (14) gives

$$\left(\Omega_+^2 - \frac{\lambda k_yP_+^2}{\omega_{c+}}\Omega_+ - k_z^2P_+^2 + \frac{k_yk_zP_+^2}{\omega_{c+}}\frac{\partial v_{0z+}}{\partial x}\right) = 0, \tag{15}$$

and $\omega \cong k_zv_{0b}$.

Equation (16) corresponds to the positive ion KHI mode and $\omega \approx k_zv_{0b}$ corresponds to the beam mode. Let us write $\Omega_+ = \Omega_{r+} + i\Omega_{i+}$ and assume that wave is either weakly damped or growing (i.e., $|\Omega_{i+}| \ll \Omega_{r+}$). In the presence of beam, Eq. (15) can be simplified as

$$\zeta_+^2 - \frac{\Lambda_1\beta_1}{r}\zeta_+ - \frac{\gamma_1}{r}(\gamma_1 - \beta_1S_1) = 0, \tag{16}$$

where $\zeta_+ = \frac{\Omega_+}{\omega_{c+}}$ (here, $\zeta_+ = \zeta_{r+} + i\Gamma_+$), $\Lambda_1 = \lambda\rho_1$, $\beta_1 = k_y\rho_1$, $\gamma_1 = k_z\rho_1$, $S_1 = \frac{1}{\omega_{c+}}\frac{\partial v_{0z+}}{\partial x}$, $\rho_1^2 = \frac{\rho_+^2}{\omega_{c+}^2}$ (here, $\rho_+^2 = \mathrm{P}_+^2 - \frac{\omega_{pb}^2(k_y^2+k_z^2)v_{t+}v_{te}}{\omega_{pe}^2(\omega-k_zv_{0b})^2}$) and $r = (1 - \frac{\omega_{pb}^2(k_y^2+k_z^2)v_{te}}{\omega_{pe}^2(\omega-k_zv_{0b})^2})$.

Hence Eq. (16) gives the dispersion relation of Ion beam driven KHI for normalized positive ion mode. In the absence of beam (i.e., $\omega_{pb} \to 0, r = 1$), we can recover the dispersion relation of D'Angelo & Song [12] (cf. Eq. (23)) in the limit $\varepsilon \to Z\varepsilon$. For $T_e \simeq T_i$, we can recover the dispersion relation of D'Angelo [9] (cf. Eq. (15)). From Eq. (16) the maximized normalized growth rate $\Gamma_+(= \Omega_{i+}/\omega_{c+})$ can be found as

$$\Gamma_+ = \left[\frac{1}{4}\beta_1^2\left(\frac{S_1^2}{r} - \frac{\Lambda_1^2}{r^2}\right)\right]^{1/2}. \tag{17}$$

In the absence of beam and for $\varepsilon \to Z\varepsilon$, Eq. (17) is similar to the growth rate of Luo et al. [15] (cf. Eq. (2)).

2.1.2. Beam Plasma Interaction with Negative Ions (SF_6^-)

In the limit $\omega \sim \omega_{c-}$ and negative ion Larmor radius is less than the perpendicular wavelength of negative ion mode, Eq. (8) can be rewritten as

$$1 - \frac{\varepsilon c_-^2}{(1-\varepsilon)} \frac{B^2}{\left(\Omega_-^2 - v_{t-}^2 B^2\right)} = \frac{\omega_{pb}^2 (k_y^2 + k_z^2) v_{te}^2}{\omega_{pe}^2 \left(\omega - k_z v_{0b}\right)^2}. \tag{18}$$

Equation (18) can be further rewritten as

$$\left(\Omega_-^2 - P_-^2 B^2\right) = \frac{\omega_{pb}^2 \left(k_y^2 + k_z^2\right) v_{te}^2}{\omega_{pe}^2 \left(\omega - k_z v_{0b}\right)^2} \left(\Omega_-^2 - v_{t-}^2 B^2\right). \tag{19}$$

Again, we are looking for solutions when the beam is in Cerenkov resonance with the negative ion KHI mode. In the absence of beam, i.e., $\omega_{pb} = 0$ as $n_{0b} \to 0$, following the same procedure as was done earlier for positive ion mode, in the limit of long perpendicular wavelength, i.e., $k_y^2 \Omega_-^2 \ll \omega_{c-}^2$ and for low frequency approximations, i.e., $\Omega_-^2 \ll \omega_{c-}^2$, Eq. (19) gives

$$\left(\Omega_-^2 + \frac{\lambda k_y P_-^2}{\omega_{c-}} \Omega_- - k_z^2 P_-^2 - \frac{k_y k_z P_-^2}{\omega_{c-}} \frac{\partial v_{0z-}}{\partial x}\right) = 0, \tag{20}$$

and $\omega \cong k_z v_{0b}$.

Equation (20) corresponds to the negative ion KHI mode and $\omega \approx k_z v_{0b}$ corresponds to the beam mode. Let $\Omega_- = \Omega_{r-} + i\Omega_{i-}$. Assuming that the wave is either weakly damped or growing (i.e., $|\Omega_{i-}| \ll \Omega_{r-}$). Then in the presence of beam, Eq. (20) can be simplified in the same manner as was done for positive ion KHI mode as

$$\zeta_-^2 + \frac{\Lambda_2 \beta_2}{r} \zeta_- - \frac{\gamma_2}{r} (\gamma_2 + \beta_2 S_2) = 0, \tag{21}$$

where $\zeta_- = \frac{\Omega_-}{\omega_{c-}}$(here, $\zeta_- = \zeta_{r-} + i\Gamma_-$), $\Lambda_2 = \lambda\rho_2$, $\beta_2 = k_y\rho_2$, $\gamma_2 = k_z\rho_2$, $S_2 = \frac{1}{\omega_{c-}} \frac{\partial v_{0z-}}{\partial x}$, $\rho_2^2 = \frac{\rho_-^2}{\omega_{c-}^2}$ (here, $\rho_-^2 = \mathrm{P}_-^2 + \frac{\omega_{pb}^2 k^2 v_{t-}^2 v_{te}^2}{\omega_{pe}^2 (\omega - k_z v_{0b})^2}$), and $r = (1 - \frac{\omega_{pb}^2 k^2 v_{te}^2}{\omega_{pe}^2 (\omega - k_z v_{0b})^2})$.

Equation (21) gives the dispersion relation of ion beam driven KHI for normalized negative ion mode. From Eq. (21), the maximized normalized growth rate $\Gamma_-(= \Omega_{i-}/\omega_{c-})$ can be found as

$$\Gamma_- = \left[\frac{1}{4}\beta_2^2 \left(\frac{S_2^2}{r} - \frac{\Lambda_2^2}{r^2}\right)\right]^{1/2}. \tag{22}$$

In the absence of beam and for $\varepsilon \to Z\varepsilon$, Eq. (22) reduces to the growth rate expression of Luo et al. [15] (cf. Eq. (2)).

2.2. Finite Boundary Effects

Consider a plasma cylinder of radius a_1 consisting of electrons, positive ions K^+ (Potassium ions) and negative ions SF_6^- (Sulphur hexafluoride ions) immersed in the magnetic field B_s acting along positive z-direction and equilibrium densities of components $j(= e, +, -)$ vary along negative x-direction as $n_{0j} = \overline{n_{0j}} e^{-\lambda x}$ as for infinite boundaries. An ion beam with velocity $v_{0b} \parallel \hat{z}$, mass m_b, density $n_{0b} \ll n_{0+}$, and radius r_b propagates through plasma cylinder along the magnetic field. The other parameters are same as infinite geometry of plasma waveguide. Poisson equation can be simplified as a second order differential equation in ϕ_1, which can be rewritten for axially symmetric case as

$$\frac{\partial^2 \phi_1}{\partial r^2} + \frac{1}{r} \frac{\partial \phi_1}{\partial r} + p^2 \phi_1 = -\frac{\omega_{pb}^2 k^2 \phi_1}{(\omega - k_z v_{b0})^2}, \tag{23}$$

$$\text{where } p^2 = -k_z^2 - \frac{\omega_{pe}^2}{v_{te}^2} \left[1 - \frac{c_+^2}{(1-\varepsilon)} \frac{A_1^2}{\left(\Omega_+^2 - v_{t+}^2 A_1^2\right)} - \frac{\varepsilon c_-^2}{(1-\varepsilon)} \frac{B_1^2}{\left(\Omega_-^2 - v_{t-}^2 B_1^2\right)}\right] \tag{24}$$

$$\text{Also, } A_1^2 = \left(k_z^2 - \frac{k_\perp^2\Omega_+^2}{\left(\omega_{c+}^2 - \Omega_+^2\right)} + \frac{\lambda k_\perp \omega_{c+}\Omega_+}{\left(\omega_{c+}^2 - \Omega_+^2\right)} - \frac{k_\perp k_z \omega_{c+}}{\omega_{c+}^2 - \Omega_+^2}\frac{\partial v_{oz+}}{\partial x}\right) \tag{25}$$

$$\text{and } B_1^2 = \left(k_z^2 - \frac{k_\perp^2\Omega_-^2}{\left(\omega_{c-}^2 - \Omega_-^2\right)} - \frac{\lambda k_\perp \omega_{c-}\Omega_-}{\left(\omega_{c-}^2 - \Omega_-^2\right)} + \frac{k_\perp k_z \omega_{c-}}{\omega_{c-}^2 - \Omega_-^2}\frac{\partial v_{oz-}}{\partial x}\right). \tag{26}$$

In the absence of beam, i.e., $\omega_{pb} = 0$ as $n_{0b} \to 0$, the solution of Bessel equation Eq. (23) is given by

$$\phi_1 = AJ_0(p_m r), \tag{27}$$

where A is a constant, and the functions $J_o(p_m r)$ is called the zeroth-order Bessel functions of the first kind. At $r = a_1$, ϕ_1 must vanish, hence, $J_o(p_m a_1) = 0$, i.e., $p_m = \frac{x_n}{a_1}\,(n = 1, 2, \ldots), x_n$, are the zeros of the Bessel function $J_o(x)$.

If $J_o(x) = 0$ then $x = 2.404$ hence, $p_m = \frac{2.404}{a_1}$.

In the presence of the beam, the solution wave function ϕ_1 can be expressed in a series of orthogonal sets of wave functions:

$$\phi_1 = \sum\nolimits_m A_m J_o(p_n r). \tag{28}$$

Now substituting the value of Eq. (28) in Eq. (23), multiplying both sides of Eq. (23) by $rJ_o(p_n r)$ and integrating over r from 0 to a_1 (where a_1 is the plasma radius), retaining the dominant mode ($m = n$) only, we get

$$p^2 - p_m^2 = -\frac{\omega_{pb}^2 k^2 I}{(\omega - k_z\, v_{bo})^2}, \tag{29}$$

where $I = \frac{\int_0^{r_b} rJ_o(p_m r)J_o(p_n r)dr}{\int_0^{a_1} rJ_o(p_m r)J_o(p_n r)dr}$ and $k^2 = p_m^2 + k_z^2$.

Using the value of p^2 in Eq. (29) and simplifying, we obtain

$$1 - \frac{c_+^2}{(1-\varepsilon)}\frac{A_1^2}{\left(\Omega_+^2 - v_{t+}^2 A_1^2\right)} - \frac{\varepsilon c_-^2}{(1-\varepsilon)}\frac{B_1^2}{\left(\Omega_-^2 - v_{t-}^2 B_1^2\right)} = \frac{\omega_{pb}^2\left(p_m^2 + k_z^2\right)v_{te}^2 I}{\omega_{pe}^2\left(\omega - k_z v_{0b}\right)^2}. \tag{30}$$

Equation (30) is same as Eq. (8) of Infinite boundary analysis. On further simplifying Eq. (30), we get the similar dispersion relation as Eq. (11)

$$\left(\Omega_+^2 - P_+^2 A_1^2\right)\left(\Omega_-^2 - P_-^2 B_1^2\right) - \alpha A_1^2 B_1^2 = \frac{\omega_{pb}^2\left(p_m^2 + k_z^2\right)v_{te}^2 I}{\omega_{pe}^2\left(\omega - k_z v_{0b}\right)^2}\left(\Omega_+^2 - v_{t+}^2 A_1^2\right)\left(\Omega_-^2 - v_{t-}^2 B_1^2\right), \tag{31}$$

where $P_+^2 = v_{t+}^2 + \frac{c_+^2}{(1-\varepsilon)}$, and $P_-^2 = v_{t-}^2 + \frac{\varepsilon c_-^2}{(1-\varepsilon)}$, now we study the two modes of KHI for finite boundary effects in the same way as was done for infinite geometry effects.

2.2.1. Beam Plasma Interaction with Positive Ions (K^+)

In the limit $\omega \sim \omega_{c+}$ and positive ion Larmor radius is less than the perpendicular wavelength of the positive ion mode, Eq. (30) can be rewritten as

$$1 - \frac{c_+^2}{(1-\varepsilon)}\frac{A_1^2}{\left(\Omega_+^2 - v_{t+}^2 A_1^2\right)} = \frac{\omega_{pb}^2\left(p_m^2 + k_z^2\right)v_{te}^2 I}{\omega_{pe}^2\left(\omega - k_z v_{0b}\right)^2}. \tag{32}$$

Equation (32) can be further simplified in the absence of beam, i.e., $n_{0b} \to 0$ or $\omega_{pb} = 0$, in the limit of long perpendicular wavelength, i.e., $k_y^2\Omega_+^2 \ll \omega_{c+}^2$ and also, for low frequency approximations, i.e.,$\Omega_+^2 \ll \omega_{c+}^2$, to obtain the solutions when the beam is in Cerenkov resonance with the positive ion KHI mode. Hence Eq. (32) gives

$$\left(\Omega_+^2 - \frac{\lambda p_m P_+^2}{\omega_{c+}}\Omega_+ - k_z^2 P_+^2 + \frac{p_m k_z P_+^2}{\omega_{c+}}\frac{\partial v_{0z+}}{\partial x}\right) = 0, \tag{33}$$

and $\omega \cong k_z v_{0b}$.

Equation (33) corresponds to the positive ion KHI mode and $\omega \approx k_z v_{0b}$ corresponds to the beam mode. Following the same procedure as for infinite boundary, in the presence of beam, Eq. (32) can be further simplified as

$$\zeta_+^2 - \frac{\Lambda_1'\beta_1'}{r_1}\zeta_+ - \frac{\gamma_1'}{r_1}\left(\gamma_1' - \beta_1' S_1\right) = 0, \tag{34}$$

where $\zeta_+ = \frac{\Omega_+}{\omega_{c+}}(\zeta_+ = \zeta_{r+} + i\Gamma_+)$, $\Lambda_1' = \lambda\rho_1'$, $\beta_1' = p_m\rho_1'$, $\gamma_1' = k_z\rho_1'$, $S_1 = \frac{1}{\omega_{c+}}\frac{\partial v_{0z+}}{\partial x}$, $\rho_1'^2 = \frac{\rho_+'^2}{\omega_{c+}^2}$ (here, $\rho_+'^2 = P_+^2 - \frac{\omega_{pb}^2(p_m^2+k_z^2)v_{t+}^2 v_{te}^2 I}{\omega_{pe}^2(\omega-k_z v_{0b})^2}$) and $r_1 = (1 - \frac{\omega_{pb}^2(p_m^2+k_z^2)v_{te}^2 I}{\omega_{pe}^2(\omega-k_z v_{0b})^2})$.

Hence Eq. (34) gives the dispersion relation of ion beam driven KHI for normalized positive ion mode. From Eq. (34) the maximized normalized growth rate $\Gamma_+(= \Omega_{i+}/\omega_{c+})$ can be found as

$$\Gamma_+ = \left[\frac{1}{4}\beta_1'^2\left(\frac{S_1^2}{r_1} - \frac{\Lambda_1'^2}{r_1^2}\right)\right]^{1/2}. \tag{35}$$

2.2.2. Beam Plasma Interaction with Negative Ions (SF_6^-)

In the limit $\omega \sim \omega_{c-}$ and negative ion Larmor radius is less than the perpendicular wavelength of negative ion mode, Eq. (30) can be rewritten as

$$1 - \frac{\varepsilon c_-^2}{(1-\varepsilon)}\frac{B_1^2}{\left(\Omega_-^2 - v_{t-}^2 B_1^2\right)} = \frac{\omega_{pb}^2\left(p_m^2 + k_z^2\right)v_{te}^2 I}{\omega_{pe}^2\left(\omega - k_z v_{0b}\right)^2}. \tag{36}$$

Equation (36) can be further simplified to obtain solutions when the beam is in Cerenkov resonance with the negative ion KHI mode. In the limit of long perpendicular wavelength, i.e., $k_y^2\Omega_-^2 \ll \omega_{c-}^2$ and for low frequency approximations, i.e., $\Omega_-^2 \ll \omega_{c-}^2$, and in the absence of beam, i.e., $\omega_{pb} = 0$ as $n_{0b} \to 0$, Eq. (36) gives

$$\left(\Omega_-^2 + \frac{\lambda p_m P_-^2}{\omega_{c-}}\Omega_- - k_z^2 P_-^2 - \frac{p_m k_z P_-^2}{\omega_{c-}}\frac{\partial v_{0z-}}{\partial x}\right) = 0, \tag{37}$$

and $\omega \cong k_z v_{0b}$.

Equation (37) corresponds to the negative ion KHI mode and $\omega \approx k_z v_{0b}$ corresponds to the beam mode. Again following the same procedure as for infinite geometry, in the presence of beam, Eq. (37) can be simplified as

$$\zeta_-^2 + \frac{\Lambda_2'\beta_2'}{r_1}\zeta_- - \frac{\gamma_2'}{r_1}\left(\gamma_2' + \beta_2' S_2\right) = 0, \tag{38}$$

where $\zeta_- = \frac{\Omega_-}{\omega_{c-}}(\zeta_- = \zeta_{r-} + i\Gamma_-)$, $\Lambda_2' = \lambda\rho_2'$, $\beta_2' = p_m\rho_2'$, $\gamma_2' = k_z\rho_2'$, $\frac{1}{\omega_{c-}}\frac{\partial v_{0z-}}{\partial x} = S_2$, $r_1 = (1 - \frac{\omega_{pb}^2(p_m^2+k_z^2)v_{te}^2 I}{\omega_{pe}^2(\omega-k_z v_{0b})^2})$ and $\rho_2'^2 = \frac{\rho_-'^2}{\omega_{c-}^2}$, (here, $\rho_-'^2 = P_-^2 + \frac{\omega_{pb}^2(p_m^2+k_z^2)v_{t-}^2 v_{te}^2 I}{\omega_{pe}^2(\omega-k_z v_{0b})^2}$). Hence Eq. (38) gives the dispersion relation of an ion beam driven KHI for normalized negative ion mode. From Eq. (38), the maximized normalized growth rate $\Gamma_-(= \Omega_{i-}/\omega_{c-})$ can be found as

$$\Gamma_- = \left[\frac{1}{4}\beta_2'^2\left(\frac{S_2^2}{r_1} - \frac{\Lambda_2'^2}{r_1^2}\right)\right]^{1/2}. \tag{39}$$

The dispersion relations and the growth rate expressions obtained for finite boundaries of plasma waveguide are same as for infinite boundaries under certain limit.

3. RESULTS AND DISCUSSION

In the calculations, we have used plasma parameters for the experiments of An et al. [14] with some modification for infinite and finite boundary analysis of KHI modes. Using Eqs. (15) & (33) for the positive ions (K^+), we plot in Figs. 1(a) & 1(b) the dispersion curves of KHI with positive ion plasma for infinite and finite boundaries of plasma waveguide, respectively and using Eqs. (20) & (37) for negative ions (SF_6^-), the dispersion curves of KHI with negative ion plasma are plotted in Figs. 2(a) & 2(b), for infinite and finite boundaries of plasma waveguide, respectively, for the following parameters: plasma density $n_p = 1.0 \times 10^{11}\,\mathrm{cm}^{-3}$, positive ion density $n_{0+} = n_p$, relative

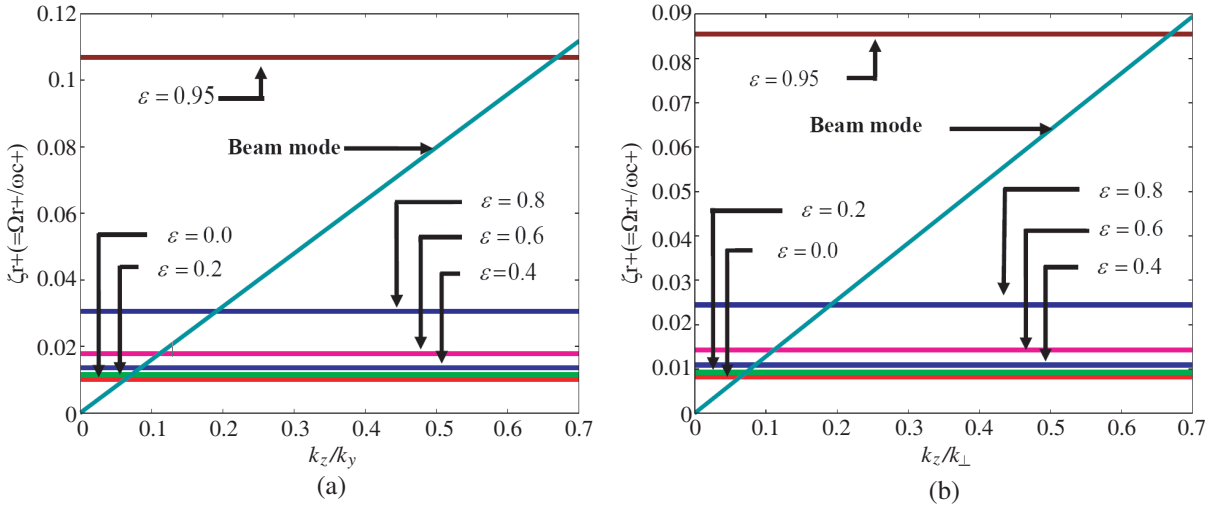


Figure 1. Dispersion curve between normalized real frequency of positive ion $\zeta_{r+}(= \Omega_{r+}/\omega_{c+})$ of the KHI for different values of the relative density of negative ions ε as a function of normalized wave vector k_z/k_y for (a) infinite and $k_z/k_\perp$, for (b) finite plasma boundary. The parameters are given in the text.

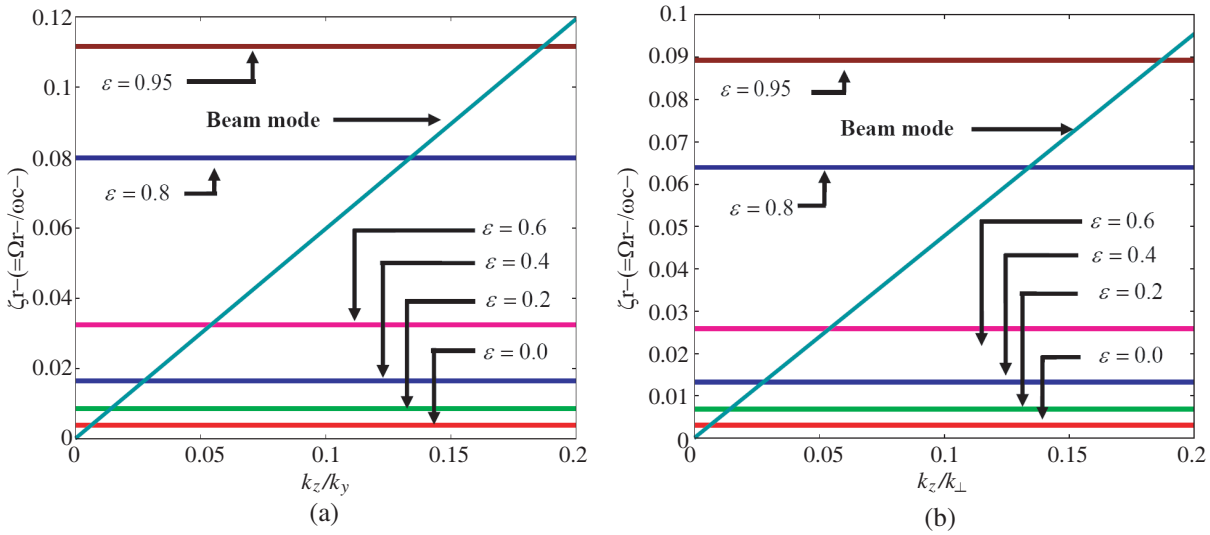


Figure 2. Dispersion curve between normalized real frequency of negative ion $\zeta_{r-}(= \Omega_{r-}/\omega_{c-})$ of the KHI for different values of relative density of negative ions ε as a function of normalized wave vector k_z/k_y for (a) infinite and $k_z/k_\perp$, for (b) finite plasma boundary. The parameters are same as Fig. 1.

Table 1. From Fig. 1 (ion beam + plasma with positive ions) we obtain the unstable wave frequencies Ω_{r+} (rad/sec) from normalized wave frequencies $\zeta_{r+}(=\Omega_{r+}/\omega_{c+})$, normalized wave vector k_z/k_y, axial wave vectors $k_z\,(\mathrm{cm}^{-1})$ and wavelength $\lambda_z\,(\mathrm{cm})$ for different values of ε & for infinite geometry case $k_y = 1.0\,\mathrm{cm}^{-1}$.

ε	k_z/k_y	$k_z\,(\mathrm{cm}^{-1})$	$\lambda_z\,(\mathrm{cm})$	Ω_{r+}/ω_{c+}	$\Omega_{r+}\,(\mathrm{rad/sec})$
0.0	0.063378	0.063378	99.09	0.010078	9.897×10^3
0.2	0.071544	0.071544	87.86	0.010357	10.171×10^3
0.4	0.084618	0.084618	74.22	0.013432	13.190×10^3
0.6	0.111554	0.111554	56.30	0.017895	17.572×10^3
0.8	0.190716	0.190716	32.93	0.030739	30.186×10^3
0.95	0.667368	0.667368	9.41	0.106673	104.753×10^3

Table 2. From Fig. 2 (ion beam + plasma with positive ions) we obtain the unstable wave frequencies Ω_{r+} (rad/sec) from normalized wave frequencies $\zeta_{r+}(=\Omega_{r+}/\omega_{c+})$, normalized wave vector $k_z/k_\perp$, axial wave vectors $k_z\,(\mathrm{cm}^{-1})$ and wavelength $\lambda_z\,(\mathrm{cm})$ for different values of ε for finite geometry case, where $k_\perp = p_m = 2.404/a_1 = 0.8\,\mathrm{cm}^{-1}$.

ε	$k_z/k_\perp$	$k_z\,(\mathrm{cm}^{-1})$	$\lambda_z\,(\mathrm{cm})$	Ω_{r+}/ω_{c+}	$\Omega_{r+}\,(\mathrm{rad/sec})$
0.0	0.064201	0.051361	122.38	0.008395	8.244×10^3
0.2	0.070755	0.056604	110.95	0.009237	9.071×10^3
0.4	0.083794	0.067035	93.77	0.010911	10.715×10^3
0.6	0.112377	0.089902	69.92	0.014472	14.212×10^3
0.8	0.190716	0.152573	41.16	0.024518	24.077×10^3
0.95	0.669015	0.535212	11.74	0.085240	83.706×10^3

density of negative ions $\varepsilon(=n_{SF_6^-}/n_{K^+}) = 0.0, 0.2, 0.4, 0.6, 0.8, 0.95$, electron temperature $T_e \simeq \mathrm{K}^+$ ion temperature $T_+ = 0.2\,\mathrm{eV}$, SF_6^- ion temperature $T_- = 0.2T_e$, plasma radius $a_1 = 3\,\mathrm{cm}$, beam radius $r_b = 2.5\,\mathrm{cm}$, guide magnetic field $B_s \simeq 4 \times 10^3\,\mathrm{Gauss}$ and $k_y \approx 1.0\,\mathrm{cm}^{-1}$, $k_z \approx 0 - 0.7\,\mathrm{cm}^{-1}$ and $\lambda \approx 2\,\mathrm{cm}^{-1}$. For finite geometry of plasma waveguide, k_y is given by the solution of Bessel function as $k_\perp = p_m = \frac{2.404}{a_1} = 0.84\,\mathrm{cm}^{-1}$, where a_1 = radius of cylindrical plasma waveguide. Real part of wave frequencies for positive and negative ion modes $\zeta_{r+}(=\Omega_{r+}/\omega_{c+})$ and $\zeta_{r-}(=\Omega_{r-}/\omega_{c-})$ have been plotted as a function of normalized wave vector k_z/k_y (for infinite geometry) & $k_z/k_\perp$ (for finite geometry) for different values of relative density of negative ions (cf. Figs. 1(a), 1(b), 2(a) & 2(b)) for both the positive and negative ion modes, respectively for infinite and finite geometry of waveguide. We have also plotted the beam mode for potassium ion beam energy $E_b = 0.5\,\mathrm{eV}$ or $v_{0b}[=(\frac{2E_b}{m_b})^{1/2}] = 1.567 \times 10^5\,\mathrm{cm/s}$. The frequencies and the corresponding wave numbers of the unstable waves are obtained by the point of intersections between the beam mode and positive ion KHI mode, for infinite and finite geometry of plasma waveguide and are given in Tables 1 & 2 and that for negative ion plasma KHI mode for infinite and finite geometry of plasma waveguide are given in Tables 3 & 4.

From Tables 1–4, we can say that the unstable wave frequencies of the KHI for positive as well as negative ion mode increase with the relative density of negative ions in the presence of beam. The frequency of positive ions increases by a factor ~ 0.33 when ε changes from 0.0 to 0.4 and increases by a factor ~ 1.28 when ε varies from 0.4 to 0.8 and by a factor ~ 2.47 with increase of ε from 0.8 to 0.95 for infinite geometry of plasma while for finite geometry of waveguide the frequency of positive ions increases by a factor ~ 0.30 when ε changes from 0.0 to 0.4 and increases by a factor ~ 1.25 when ε varies from 0.4 to 0.8 and by a factor ~ 2.47 with increase of ε from 0.8 to 0.95. The frequency of negative ions is found to increase by a factor ~ 3.26 when ε changes from 0.0 to 0.4 and increases by a factor ~ 3.76 when ε varies from 0.4 to 0.8 and by a factor ~ 0.39 with increase of ε from 0.8 to 0.95 for infinite boundaries and for finite boundaries the frequency of negative ions is found to increase by a

Table 3. From Fig. 3 (ion beam + plasma with negative ions) we obtain the unstable wave frequencies Ω_{r-} (rad/sec) from normalized wave frequencies $\zeta_{r-}(=\Omega_{r-}/\omega_{c-})$, normalized wave vector k_z/k_y, axial wave vectors $k_z\,(\mathrm{cm}^{-1})$ and wavelength $\lambda_z\,(\mathrm{cm})$ for different values of ε for infinite geometry case $k_y = 1.0\,\mathrm{cm}^{-1}$.

ε	k_z/k_y	$k_z\,(\mathrm{cm}^{-1})$	$\lambda_z\,(\mathrm{cm})$	Ω_{r-}/ω_{c-}	Ω_{r-} (rad/sec)
0.0	0.006216	0.006216	1011.23	0.003935	1.039×10^3
0.2	0.014382	0.014382	437.04	0.008683	2.292×10^3
0.4	0.027902	0.027902	225.07	0.016779	4.430×10^3
0.6	0.054029	0.054029	116.34	0.032412	8.557×10^3
0.8	0.133775	0.133775	46.94	0.079877	21.088×10^3
0.95	0.187176	0.187176	33.55	0.111142	29.342×10^3

Table 4. From Fig. 4 (ion beam + plasma with negative ions) we obtain the unstable wave frequencies Ω_{r-} (rad/sec) from normalized wave frequencies $\zeta_{r-}(=\Omega_{r-}/\omega_{c-})$, normalized wave vector $k_z/k_\perp$, axial wave vectors $k_z\,(\mathrm{cm}^{-1})$ and wavelength $\lambda_z\,(\mathrm{cm})$ for different values of ε for finite geometry case, $k_\perp = p_m = 0.8\,\mathrm{cm}^{-1}$.

ε	$k_z/k_\perp$	$k_z\,(\mathrm{cm}^{-1})$	$\lambda_z\,(\mathrm{cm})$	Ω_{r-}/ω_{c-}	Ω_{r-} (rad/sec)
0.0	0.006451	0.005161	1216.82	0.003279	0.866×10^3
0.2	0.014618	0.011694	537.03	0.007004	1.849×10^3
0.4	0.027441	0.021953	286.33	0.013285	3.507×10^3
0.6	0.054255	0.043404	144.82	0.026080	6.885×10^3
0.8	0.133775	0.107020	58.68	0.064001	16.896×10^3
0.95	0.187176	0.149741	41.94	0.089359	23.591×10^3

factor ~ 3.05 when ε changes from 0.0 to 0.4 and increases by a factor ~ 3.82 when ε varies from 0.4 to 0.8 and by a factor ~ 0.40 with increase of ε from 0.8 to 0.95. It can also be seen from the Tables 1–4 that the axial wave vector k_z increases with increasing ε. This result is similar to the analytical result of Chow and Rosenberg [28], where the wave is unstable because k_z increases with the relative density of negatively charged dust grains $\delta(=\frac{1}{1-Z\varepsilon})$.

We plot Fig. 3(a) using Eqs. (16) & (34), for normalized real frequency of KHI for positive ions and Fig. 3(b) using Eqs. (21) & (38), for normalized real frequency of KHI for negative ions as a function of relative density of negative ions ε in the absence and presence of beam for the same parameters as used for plotting Fig. 1 and Fig. 2, respectively, for infinite and finite geometry of plasma waveguide. It is observed that the unstable modes frequencies increase with the relative density of negative ions for both positive ion and negative ion modes under both infinite and finite boundaries of plasma waveguide. It is also observed that the KHI unstable modes frequencies slightly increase in the presence of beam at high concentration of negative ions. This result is in line with the experimental results obtained for electrostatic Ion Cyclotron waves (EICW) [29] (cf. Fig. 3, page No. 1555) and Ion Acoustic waves (IAW) [21] (cf. Fig. 1, page No. 285) in plasma with negative ions where the frequency of EICW and phase velocity of IAW increases with relative concentration of negative ions. For finite boundaries of plasma waveguide, the frequencies of KHI modes are lesser than for infinite boundary effects. These results are in line with the results for finite geometry effects obtained by Prakash et al. [27].

Using Eqs. (17) & (35), we plot Fig. 4(a), the normalized growth rate $\Gamma_+(=\Omega_{i+}/\omega_{c+})$ for positive ion mode of KHI, and using Eqs. (22) & (39), we plot Fig. 4(b), the normalized growth rate $\Gamma_-(=\Omega_{i-}/\omega_{c-})$ for negative ion KHI mode showing infinite and finite boundary effects, as a function of relative density of negative ions $\varepsilon(=0.0-1.0)$, respectively in the absence as well as in the presence of beam for the same parameters used for plotting Fig. 3 and for beam density $n_{b0} = 2.5 \times 10^8\,\mathrm{cm}^{-3}$ and the shear parameters $S_1 \simeq S_2(=0.7)$. It is observed that at a constant $\varepsilon = 0.7$ the growth rate of KHI for positive

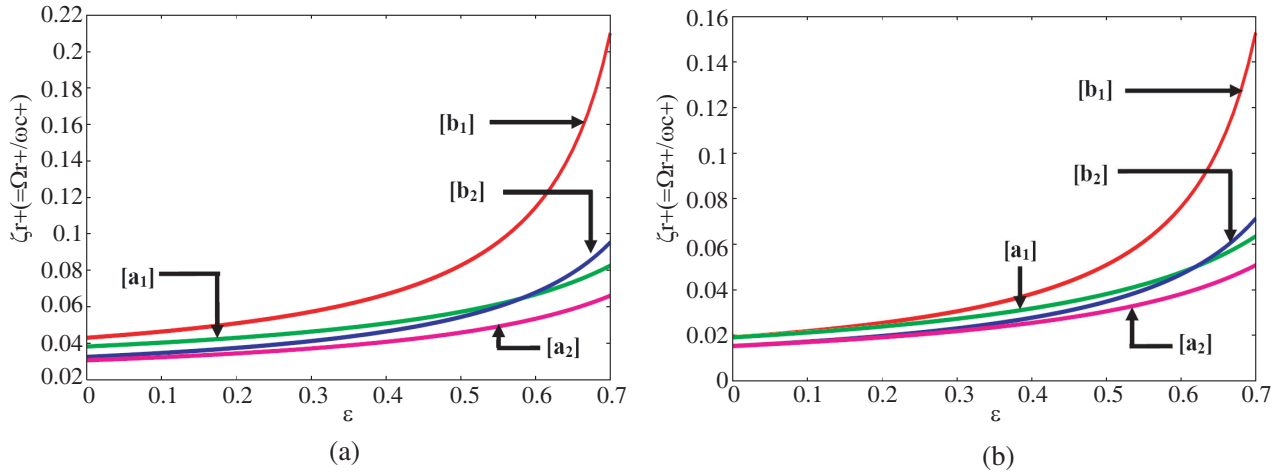


Figure 3. Normalized real frequency $\zeta_{rj}(=\Omega_{rj}/\omega_{cj})$ of the KHI (where $j(=+$ or $-)$, for positive ion and negative ion, respectively) for negative ions as a function of relative density of negative ions ε for infinite plasma boundary [a1] — in the absence of beam [b1] — in the presence of beam, and for finite plasma boundary, [a2] — in the absence of beam and [b2] — in the presence of beam for the parameters same as Fig. 2. (a) For Positive ion, (b) for Negative ion.

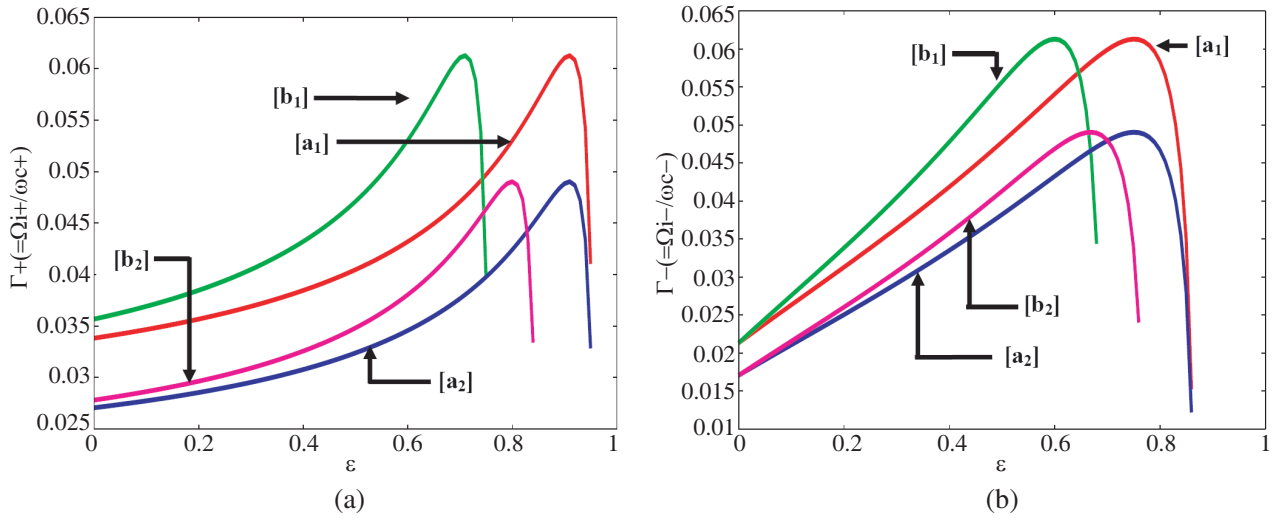


Figure 4. Normalized growth rate $\Gamma_j(=\Omega_{ij}/\omega_{cj})$ of the KHI (where $j(=+$ or $-)$, for positive and negative ions, respectively) as a function of the relative density of negative ions ε for infinite plasma boundary [a1] — in the absence of beam, [b1] — in the presence of beam, and for finite plasma boundary [a2] — in the absence of beam and [b2] — in the presence of beam for the same parameters as Fig. 3 and for beam density $n_{b0} = 2.5 \times 10^8\,\mathrm{cm}^{-3}$. (a) For Positive ions, (b) for Negative ions.

ions shoots up to 30% when the ion beam is switched on for infinite geometry of plasma waveguide. On the other hand for cylindrical waveguide, the growth rate of KHI positive ion mode increases only up to 14% in the presence of beam. For negative ions, at $\varepsilon = 0.6$ the growth rate of KHI increases up to 13% for infinite geometry in presence of beam while for finite geometry case increases only up to 8% in the presence of beam. From Figs. 4 (a) & (b), we can say that the growth rate of the KHI for both positive and negative ion modes increases with relative concentration of negative ions in the presence of beam for infinite as well as for finite geometry. Moreover, our results show the stabilizing effect of KHI for large concentration of negative ions. The results are in line with the experimental observations

of An et al. [14] (cf. Figs. 4 & 5 on page No. 50). It is also observed that the effect of beam on the destabilization of the KHI is prominent at large shear parameter and for large value of ε. This result is in line with the theoretical predictions of D'Angelo and Song [13] (cf. Figs. 1–5 on page No. 44–45), i.e., the growth rate of KHI is larger for large concentration of negative ions and for large shear parameters.

We also plot in Figs. 5 & 6 the normalized growth rate of KHI for the positive and negative ions, respectively, in presence of beam as a function of relative density of negative ions ε for different relative masses of negative ions (m_-/m_+) using the same parameters as that used for plotting Fig. 4, for infinite and finite geometries. From Figs. 5 & 6, it is observed that the KHI mode is stabilized for both the ion modes with increasing the relative mass of negative ions for infinite geometry of waveguide. These results are similar to the theoretical results of D'Angelo and Song [13] (cf. Fig. 6 on page No. 45). It is observed that the finite geometry effects further lowers the growth rate of positive ion while for negative ion growth rate of KHI shows an increase with relative mass of negative ions up to small values of ε and then decreases for large values of ε.

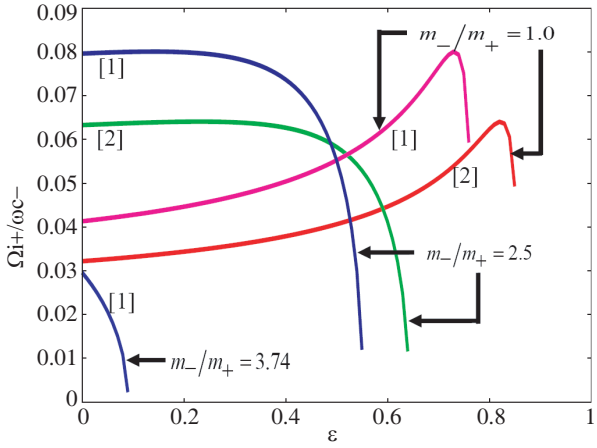


Figure 5. Normalized growth rate Ω_{i+}/ω_{c-} of the ion beam driven KHI for positive ions as a function of the relative density of negative ions ε for different relative masses of negative ions $m_-/m_+(= 1.0, 2.5, 3.74)$, [1] — for infinite boundary and [2] — for finite boundary of plasma waveguide. The parameters are same as Fig. 4.

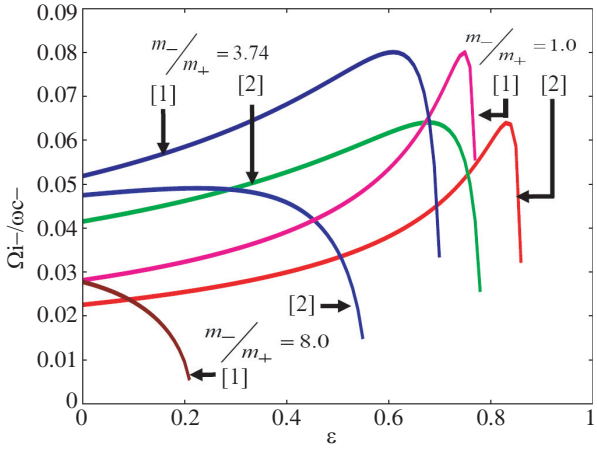


Figure 6. Normalized growth rate Ω_{i-}/ω_{c-} of the ion beam driven KHI for negative ions as a function of the relative density of negative ions ε for different relative masses of negative ions $m_-/m_+(= 1.0, 3.74, 8.0)$, [1] — for infinite boundary and [2] — for finite boundary of plasma waveguide for the same parameters as Fig. 4.

To investigate the effect of ion beam energies and densities on the growth rate of KHI in the presence of negative ions in the plasma, we plot the growth rate of KHI for both positive and negative ion modes as a function of relative density of negative ions in Figs. 7(a) & (b), respectively, for different values of beam velocities $v_{0b}[= (2E_b/m_b)^{1/2}] = 1.57 \times 10^5$, 3.57×10^5 and 7.0×10^5 cm/s, and Figs. 8(a) & (b), respectively, for different values of beam densities $n_{0b}(= 2.5 \times 10^7,\ 2.5 \times 10^8,\ 7.5 \times 10^8)\,\mathrm{cm}^{-3}$. Other parameters are the same as Fig. 4. It is found that the growth rate of KHI decreases at high beam energies or velocities while an increase of ion beam density boosts the growth rate of KHI modes.

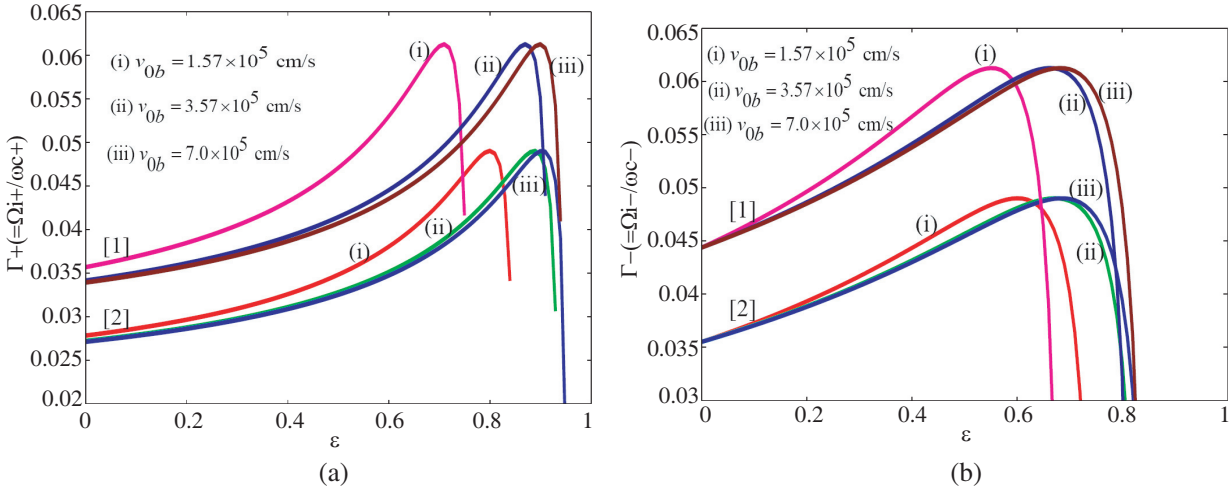


Figure 7. Normalized growth rate $\Gamma_j(= \Omega_{ij}/\omega_{cj})$ of the ion beam driven KHI (where $j(= +$ or $-)$, for positive and negative ions, respectively) as a function of the relative density of negative ions ε for different ion beam velocities $v_{0b}(= 1.57 \times 10^5, 3.57 \times 10^5, 7.0 \times 10^5)$ cm/s, [1] — for infinite boundary and [2] — for finite boundary of plasma waveguide, for the same parameters as Fig. 4, for (a) Positive ions, (b) Negative ions.

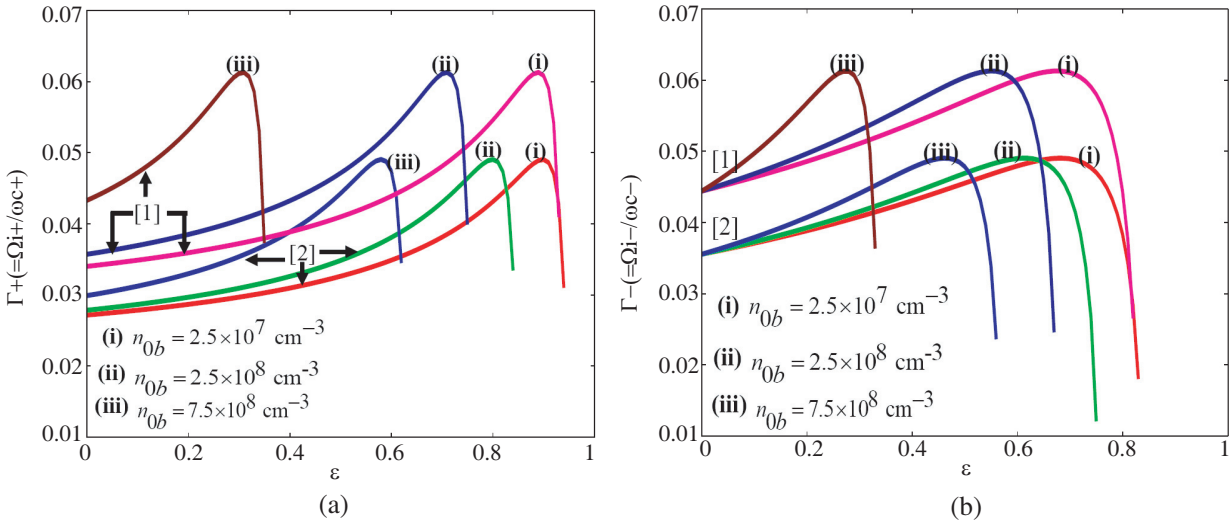


Figure 8. Normalized growth rate $\Gamma_j(= \Omega_{ij}/\omega_{cj})$ of the ion beam driven KHI (where $j(= +$ or $-)$, for positive and negative ions, respectively) as a function of the relative density of negative ions ε for different ion beam densities, $n_{0b}(= 2.5 \times 10^7, 2.5 \times 10^8, 7.5 \times 10^8)\,\mathrm{cm}^{-3}$, [1] — for infinite boundary and [2] — for finite boundary of plasma waveguide, for the same parameters as Fig. 7, for (a) Positive ions, (b) Negative ions.

4. CONCLUSIONS

The Kelvin Helmholtz instability (KHI) in a magnetized plasma having positive and negative ions is driven by an ion beam via a Cerenkov interaction.

The effect of beam on the growth of KHI is more prominently seen at high concentration of ε Our results are in line with the theoretical predictions of D'Angelo and Song [13] (cf. Figs. 1–5). It is also observed that KHI mode in presence of negative ions is destabilized up to $\varepsilon \leq 0.7$ and beyond this limit it is stabilized. This result is in line with the experimental observations of An et al. [14] (cf. Figs. 4 & 5 on page No. 50). Our results show stabilization of KHI mode up to $\varepsilon \leq 0.6$ in the presence of negative ions and the ion beam. The results also show that the KHI mode is stabilized in presence of heavier negative ions in the potassium plasma which is similar to the result obtained by D'Angelo and Song [13] (cf. Fig. 6 on page No. 45). A comparison of finite and infinite geometry effects describe that the frequency and growth rate of KHI is reduced for cylindrical plasma waveguide, it may be due to reduction in beam plasma interaction region [27]. The results showing increase in frequency and growth rate of Low frequency KHI modes are in line with the experimental observations of electrostatic ion Cyclotron waves [29] and Ion Acoustic waves [21] in negative ion plasma. An increase in beam energy reduces the growth rate of KHI while increase of beam density enhances the growth rate of the KHI modes. Our theoretical model of KHI driven by an ion beam in negative ion plasma may be validated via laboratory and space plasma experiments in near future.

In addition, our results of KHI, in general, may be useful for understanding the instabilities in the negative ion plasma in the material processing [30–32] (as the velocity shear instability and negative ions in plasma plays an important role in surface technologies) beam plasma system [33] (as ion beam tends to excite the instabilities in plasma) various fluids phenomena [34] such as Magneto hydrodynamic flows and the properties of Earth's ionosphere [2–7, 35] such as solar wind, ion loss on Mars and energy transport in space etc. However, the results need to be verified for above applications via experiments/simulations for definite evidences as we have basically emphasized on the laboratory plasma.

REFERENCES

1. D'Angelo, N., "Ultralow frequency fluctuations at the polar cusp boundaries," *J. Geophys. Res.*, Vol. 78, No. 7, 1206–1209, 1973.
2. Pu, Z. Y. and M. G. Kivelson, "Kelvin Helmholtz instability at magnetopause: Energy flux into magnetosphere," *J. Geophys. Res.*, Vol. 88, No. A2, 853–861, 1983.
3. Miura, A., "Kelvin Helmholtz instability for supersonic shear flow at the magnetospheric boundary," *Geophys. Res. Lett.*, Vol. 17, No. 6, 749–752, 1990.
4. Hasegawa, H., M. Fujimoto, T. D. Phan, H. Réme, A. Balogh, M. W. Dunlop, C. Hashimoto, and R. T. Dokoro, "Transport of solar wind into Earth's magnetosphere through rolled-up Kelvin-Helmholtz vortices," *Nature*, Vol. 430, No. 7001, 755–758, 2004.
5. Migliuolo, S., "Velocity shear instabilities in the anisotropic solar wind and the heating of ions perpendicular to the magnetic field," *J. Geophys. Res.*, Vol. 89, No. A1, 27–36, 1984.
6. Ershkovich, A. I., "Kelvin-Helmholtz instability in type-1 comet tails and associated phenomena," *Space Sci. Rev.*, Vol. 25, No. 1, 3–34, 1980.
7. Penz, T., N. V. Erakaev, H. K. Biernet, H. Lammer, U. V. Amerstorfer, H. Gunell, E. Kallio, S. Barabash, S. Orsini, A. Milillo, and W. Baumjohann, "Ion loss Mars caused by Kelvin-Helmholtz instability," *Planet. Space Sci.*, Vol. 52, No. 13, 1157–1167, 2004.
8. Chandrasekhar, S., *Hydrodynamic and Hydromagnetic Stability*, Chap. XI, 481, Clarendon Press, Oxford, 1961.
9. D'Angelo, N., "Kelvin-Helmholtz instability in a fully ionized plasma in a magnetic field," *Phys. Fluids*, Vol. 8, No. 9, 1748–1750, 1965.
10. D'Angelo, N. and S. V. Goeler, "Investigation of Kelvin Helmholtz instability in a cesium plasma," *Phys. Fluids*, Vol. 9, No. 2, 309–313, 1966.
11. Smith, C. G. and S. V. Goeler, "The Kelvin-Helmholtz instability in a collisionless plasma model," *Phys. Fluids*, Vol. 11, No. 12, 2665–2668, 1968.

12. D'Angelo, N. and B. Song, "The Kelvin-Helmholtz instability in dusty plasmas," *Planet. Space Sci.*, Vol. 38, No. 12, 1577–1579, 1990.
13. D'Angelo, N. and B. Song, "Kelvin-Helmholtz instability in a plasma with negative ions," *IEEE Trans. Plasma Sci.*, Vol. 19, No. 1, 42–46, 1991.
14. An, T., R. L. Merlino, and N. D'Angelo, "The effect of negative ions on the Kelvin-Helmholtz instability in a magnetized potassium plasma," *Phys. Lett. A*, Vol. 14, No. 1–2, 47–52, 1996.
15. Luo, Q. Z., N. D'Angelo, and R. L. Merlino, "The Kelvin-Helmholtz instability in a plasma with negatively charged dust," *Phys. Plasmas*, Vol. 8, No. 1, 31–35, 2001.
16. Ostrikov, K., "Surface science of plasma exposed surfaces — A challenge for applied plasma science," *Vacuum*, Vol. 83, No. 1, 4–10, 2008.
17. Ostrikov, K., S. Kumar, and H. Sugai, "Charging and trapping of macroparticles in near-electrode regions of fluorocarbon plasmas with negative ions," *Phys. Plasmas*, Vol. 8, No. 7, 3490–3497, 2001.
18. Ostrikov, K., "Colloquium: Reactive plasmas as a versatile nano fabrication tool," *Rev. Mod. Phys.*, Vol. 77, No. 2, 489–511, 2005.
19. Sharma, S. C. and M. P. Srivastava, "Ion beam driven ion cyclotron waves in a plasma cylinder with negative ions," *Phys. Plasmas*, Vol. 8, No. 3, 679–686, 2001.
20. Sharma, S. C. and A. Gahlot, "Ion beam driven ion-acoustic waves in a plasma cylinder with negative ions," *Phys. Plasmas*, Vol. 15, No. 7, 0737051–0737056, 2008.
21. Song, B., N. D'Angelo, and R. L. Merlino, "Ion-acoustic waves in a plasma with negative ions," *Phys. Fluids B*, Vol. 3, No. 2, 284–287, 1991.
22. An, T., R. L. Merlino, and N. D' Angelo, "Lower hybrid waves in a plasma with negative ions," *Phys. Fluids B*, Vol. 5, No. 6, 1917–1918, 1993.
23. D'Angelo, N. and R. L. Merlino, "Electrostatic ion-cyclotron waves in a plasma with negative ions," *IEEE Trans. Plasma Sci.*, Vol. 14, No. 3, 285–286, 1986.
24. Rosenberg, M. and R. L. Merlino, "Ion-acoustic instability in a dusty negative ion plasma," *Planet. Space Sci.*, Vol. 55, No. 10, 1464–1469, 2007.
25. Yatsui, K. and Y. Yamamoto, "Heating of plasma ions by a modulated beam," *Phys. Letters*, Vol. 30A, No. 2, 135–136, 1969.
26. Chang, R. P., "Lower hybrid beam-plasma instability," *Phys. Rev. Lett.*, Vol. 35, No. 5, 285–288, 1975.
27. Prakash, V., S. C. Sharma, Vijayshri, and R. Gupta, "Ion beam driven resonant ion-cyclotron instability in a magnetized dusty plasma," *Phys. Plasmas*, Vol. 21, No. 3, 0337011–0337016, 2014.
28. Chow, V. W. and M. Rosenberg, "Electrostatic ion cyclotron instabilities in negative ion plasmas," *Plasma Phys.*, Vol. 3, No. 4, 1202–1211, 1996.
29. Kim, S. H., J. R. Heinrich, and R. L. Merlino, "Electrostatic ion-cyclotron waves in a plasma with heavy negative ions," *Planet. Space Sci.*, Vol. 56, No. 11, 1552–1559, 2008.
30. Tyagi, R. K., R. S. Pandey, and A. Kumar, "Surface coating by velocity shear instability in plasma," *Theoretical Foundations of Chem. Engg.*, Vol. 46, No. 5, 508–514, 2012.
31. Stoffels, E., W. W. Stoffels, and G. M. W. Kroesen, "Plasma chemistry and surface processes of negative ions," *Plasma Sources Sci. Technol.*, Vol. 10, No. 1, 311–317, 2001.
32. Kuznetsova, V. P., S. Yu. Tarasov, and A. I. Dmitriev, "Nanostructuring burnishing and subsurface shear instability," *Journ. of Mat. Processing Tech.*, Vol. 217, No. 1, 327–335, 2015.
33. Rosenberg, M. and P. K. Shukla, "Instability of ion flows in bounded dusty plasma systems," *Phys. Plasmas*, Vol. 5, No. 10, 3786, 1998.
34. Matsuoka, C., "Kelvin-Helmholtz instability and roll-up," *Scholarpedia*, Vol. 9, No. 3, 11821, 2014.
35. Moore, T. W., K. Nykyri, and A. P. Dimmock, "Cross-scale energy transport in space plasmas," *Nature Physics*, 2016, doi:10.1038/nphys3869.

2nd International Conference on Recent Innovations in Science, Technology, Management and Environment
Indian Federation of United Nations Associations, Qutab Institutional Area, New Delhi (India) (ICRISTME-16)
20 November 2016, www.conferenceworld.in ISBN: 978-93-86171-11-5

TOPIC: A STUDY OF SENSE OF WELL-BEING AND PERCEIVED QUALITY OF LIFE OF PEOPLE IN CENTRAL GUJARAT.

Rajesh Handa[1], Dr. G.C.Maheshwari[2]

[1]*Rajesh Handa, Management, Manish Institute of Management, Gujarat, (India)*
[2]*Dr. G.C.Maheshwari, Management, Delhi Technological University, Delhi (India)*

ABSTRACT

The paper examined the perceived quality of life in Central Gujarat of Gujarat state, with a 400 adult sample. It investigated first the relation between demographic characteristics and perceived quality of life and then the relation between Life domain satisfaction and perceived quality of life. Employing descriptive approaches through a modi fied questionnaire. The survey instrument measures the residents' life satisfaction in many Life domains: satisfaction with government, Infrastructure, Work-life, Material possession, Relationships, Self-development, Physical health, Environmental quality, Children's education, Recreation activity & Spirituality. EFA, Multiple Regression analysis, PLS-SEM and CB-SEM techniques used to predict perceived life-satisfaction.

Keywords: Well-being, Perceived Quality of Life, Life-Satisfaction

I. INTRODUCTION

Quality of life and its assessment is a challengeable task; still to improve it is a primary goal of any government & Individuals too. By many years we are measuring quality of life in terms of HDI (Human development Index) and accordingly ranking of the nations takes place which shows their well-being and quality of life in the country. HDI is an objective approach to access quality of life. But the second approach to measure Quality of life is subjective approach which we called perceived quality of life or happiness. Many researches has contributed their work in measuring PQOL or happiness of the nations and now a days World happiness Index is one of popular approach to measure the quality of life. As we noticed countries like Bhutan had focused on GNP (Gross national happiness) instead of GDP. This study is also an approach towards measuring PQOL of Individuals in Central Gujarat of Gujarat state.

II. OBJECTIVES

1. To access global life satisfation of the inhabitants of Central-Gujarat.
2. To examine whether quality of life varies with sex, age, marital status, education status and income level or not.

3. To assess different domains this affects the quality of life like satisfaction with government, Infrastructure, Work-life, Material possession, Relationships, Self-development, Physical health, Environmental quality, Children's education and Recreation activity.

III. RESEARCH METHODOLOGY

- Research type: Quantitative Research.
- Descriptive Research.
- Universe: Central-Gujarat.
- Data used: Primary.
- Data Collection Tool: Structured Questionnaire
- Data Collection method: Survey (personal interaction).
- Survey method: Convenience Sampling (Non-Probability).
- Sample unit: People (ordinary resident).
- Sample Size: 400.
- Software used: Microsoft-Excel 2010, SPSS version 21, AMOS 21 & SMART PLS.

IV. LIMITATIONS OF THE STUDY

1. Under certain time limit 422 samples has collected, out of which 400 samples became part of this study.
2. Sampling frame was not present. Non-random, Convenience sampling method has used.
3. Respondent has limited to working class people with certain age, education and income limitation.

V. RESEARCH TOOLS USED

1. Global life satisfaction scale.
2. Life domain satisfaction scale

VI. RELIABILITY CHECK

Life domain satisfaction scale

Case Processing Summary

		N	%
Cases	Valid	400	100.0
	Excluded	0	.0
	Total	400	100.0

a. List wise deletion based on all variables in the procedure.Table:1

Reliability Statistics

Cronbach's Alpha	N of Items
.941	53

Table: 2

***Interpretation*:** Cronbachs Alpha value **0.941 > 0.7**. This is a good sign of reliability.

VII. RESEARCH HYPOTHESIS

Hypothesis 1: Males and females vary significantly in their perceived QOL.

Hypothesis 2: Individuals belonging to different age groups vary significantly in their perceived QOL.

Hypothesis 3: Individuals belonging to different education status vary significantly in their perceived QOL.

Hypothesis 4: Individuals belonging to different marital status vary significantly in their perceived QOL.

Hypothesis 5: Individuals belonging to different income groups vary significantly in their perceived QOL.

Hypothesis 6: Sense of well-being is influenced by different domains of life. To determine which of these domains of life such as satisfaction with government, Infrastructure, Work-life, Material possession, Relationships, Self-development, Physical health, Environmental quality, Children's education and Recreation activity are related to global satisfaction or PQOL.

VIII. HYPOTHESIS TESTING

1. HO: There is no significant difference between Males and females in their PQOL.

   H1: There is significant difference between Males and females in their PQOL.

Independent Samples Test

		Levene's Test for Equality of Variances		t-test for Equality of Means						
		F	Sig.	t	df	Sig. (2-tailed)	Mean Difference	Std. Error Difference	95% Confidence Interval of the Difference	
									Lower	Upper
Life Satisfaction	Equal variances assumed	9.771	.002	-.043	398	.966	-.003	.061	-.122	.116
	Equal variances not assumed			-.040	214.891	.968	-.003	.065	-.131	.126

Table: 3

Interpretation: Here, p-value **0.002 < 0.05**, so we reject our null hypothesis. Alternate hypothesis is accepted. There is significant difference between Males and females in their perceived QOL.

2. H0: There is no significant difference Individuals belonging to different age groups vary significantly in their perceived QOL.

H1: There is significant difference between individuals belonging to different age groups vary significantly in their perceived QOL.

ANOVA

Life Satisfation

	Sum of Squares	df	Mean Square	F	Sig.
Between Groups	.476	2	.238	.738	.479
Within Groups	127.964	397	.322		
Total	128.440	399			

Table: 4

Interpretation: Here, p-value **0.479 > 0.05**, so we accept our null hypothesis.There is no significant difference between individuals belonging to different age groups varies significantly in their perceived QOL**.**

3. H0: There is no significant difference between Individuals belonging to different education status in their perceived QOL.

H1: There is significant difference between Individuals belonging to different education status vary significantly in their perceived QOL.

ANOVA

Life Satisfation

	Sum of Squares	df	Mean Square	F	Sig.
Between Groups	5.114	3	1.705	5.473	.001
Within Groups	123.326	396	.311		
Total	128.440	399			

Table: 5

Interpretation: Here, p-value **0.001 < 0.05**, so we reject our null hypothesis. Alternate hypothesis accepted.There is significant difference between Individuals belonging to different education status in their perceived QOL.

4. H0: There is no significant difference between Individuals belonging to different marital status in their perceived QOL.

H1: There is significant difference between Individuals belonging to different marital status vary significantly in their perceived QOL.

ANOVA

Life Satisfation

	Sum of Squares	df	Mean Square	F	Sig.
Between Groups	1.866	1	1.866	5.868	.016
Within Groups	126.574	398	.318		
Total	128.440	399			

Table: 6

Interpretation: Here, p-value **0.016 < 0.05**. So we reject our null hypothesis. Alternate hypothesis accepted There is significant difference between Individuals belonging to different marital status in their perceived QOL.

5. H0: There is no significant difference between Individuals belonging to different income groups in their perceived QOL.

H1: There is significant difference between Individuals belonging to different income groups vary significantly in their perceived QOL.

ANOVA

Life Satisfation

	Sum of Squares	df	Mean Square	F	Sig.
Between Groups	5.355	2	2.677	8.636	.000
Within Groups	123.085	397	.310		
Total	128.440	399			

Table: 7

Interpretation: Here, p-value **0.000 < 0.05.** So we reject our null hypothesis. Alternate hypothesis accepted. There is significant difference between Individuals belonging to different income groups vary significantly in their perceived QOL.

6. Ho: There is no significant relationship between Sense of well-being and different domains of life.

H1: There is significant relationship between Sense of well-being and different domains of life.

IX. REGRESSION ANALYSIS

Variables Entered/Removed

Model	Variables Entered	Variables Removed	Method
1	Recreation Activity, Children's Education, Environmental Quality, Physical Health, Self-development, Relationships, Material Possess, Worklife, Infrastructure, Government.	.	Enter

a. Dependent Variable: Life Satisfaction b. All requested variables entered.

Table:8

Model Summary	R	R Square	Adjusted R Square	Std. Error of the Estimate	Durbin-Watson
Model	.823[a]	.677	**.669**	.326	1.637

Table: 9

a. Predictors: (Constant), Recreation Activity, Children's education, Environmental Quality, Physical Health, Self-development, Relationships, Material Possess, Work life, Infrastructure, Government

Interpretation: *The Adjusted R square value tells us that our model accounts for 66.9% of variance which indicate it is a good model*

ANOVA[a]

Model		Sum of Squares	df	Mean Square	F	Sig.
1	Regression	86.977	10	8.698	81.601	.000[b]
	Residual	41.463	389	.107		
	Total	128.440	399			

a. Dependent Variable: Life Satisfaction

a. Predictors: (Constant), Recreation Activity, Children's education, Environmental Quality, Physical Health, Self-development, Relationships, Material Possess, Worklife, Infrastructure, Government

Table:10

Interpretation: p<.05 the model is significant.

Coefficients

Model		Unstandardized Coefficients		Standardized Coefficients	t	Sig.	Collinearity Statistics	
		B	Std. Error	Beta			Tolerance	VIF
1	(Constant)	3.670	.016		224.824	.000		
	Government	.182	.016	.321	11.139	.000	1.000	1.000
	Infrastructure	.221	.016	.390	13.525	.000	1.000	1.000
	Worklife	.226	.016	.399	13.840	.000	1.000	1.000
	Material Possess	.176	.016	.311	10.787	.000	1.000	1.000
	Relationships	.020	.016	.035	1.200	.231	1.000	1.000
	Self-development	.063	.016	.111	3.842	.000	1.000	1.000
	Physical Health	.127	.016	.223	7.754	.000	1.000	1.000
	Environmental Quality	.053	.016	.094	3.266	.001	1.000	1.000
	Children's education	.119	.016	.209	7.256	.000	1.000	1.000
	Recreation Activity	.128	.016	.226	7.839	.000	1.000	1.000

a. Dependent Variable: Life Satisfation

Table:11

Interpretation: All predictors variable's p <.05 except Relationship satisfation. T values of all predictor variables are high except Relationship satisfation. So, all predictors variable are significant except Relationship satisfaction.

Multicollinearity check: No tolerance value less than 0.2 and no VIF value greater than 5 found.

X. VALIDITY CHECK: *Partial Least Square Structural Equation Modelling (PLS-SEM)*

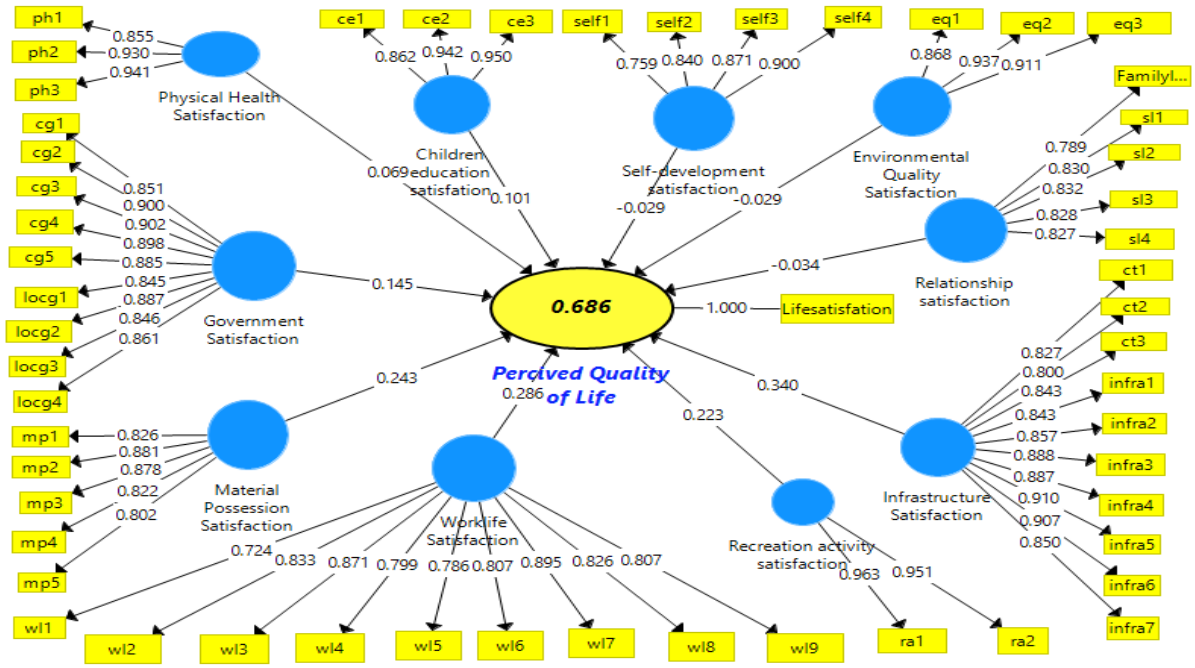


Fig 1

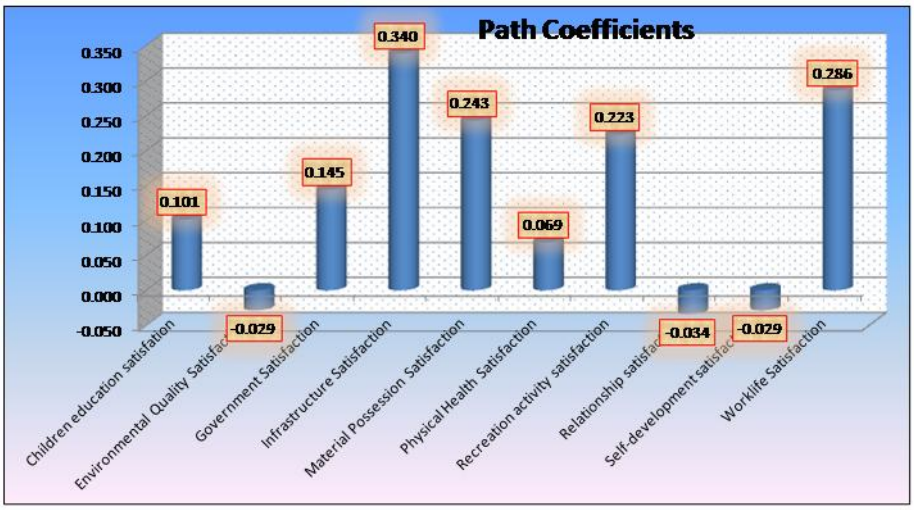


Fig 2

Outcomes

Variables	AVE	Composite Reliability	Cronbachs Alpha	Path Coefficients
Children education satisfation	0.844	0.942	0.906	0.101
Environmental Quality Satisfaction	0.820	0.932	0.890	-0.029
Government Satisfaction	0.766	0.967	0.962	0.145
Infrastructure Satisfaction	0.743	0.966	0.961	0.340
Material Possession Satisfaction	0.709	0.924	0.897	0.243
Physical Health Satisfaction	0.827	0.935	0.895	0.069
Recreation activity satisfaction	0.916	0.956	0.909	0.223
Relationship satisfaction	0.675	0.912	0.881	-0.034
Self-development satisfaction	0.712	0.908	0.864	-0.029
Worklife Satisfaction	0.669	0.948	0.938	0.286

Table: 12

Convergent Validity and Construct validity check

AVE values all variables are >0.50 (Accepted)

Composite Reliability values of all variables are > 0.70 (Accepted)

Cronbachs alpha values of all variables are >0.70 (Accepted)

Discrininant Validity										
Fornell-Lacker Criterion										
	Children education satisfation	Environmental Quality Satisfaction	Government Satisfaction	Infrastructure Satisfaction	Material Possession Satisfaction	Physical Health Satisfaction	Recreation activity satisfaction	Relationship satisfaction	Self-development satisfaction	Worklife Satisfaction
Children education satisfation	0.918									
Environmental Quality Satisfaction	0.202	0.906								
Government Satisfaction	0.290	0.468	0.875							
Infrastructure Satisfaction	0.327	0.533	0.759	0.862						
Material Possession Satisfaction	0.273	-0.144	-0.092	-0.113	0.842					
Physical Health Satisfaction	0.231	0.216	0.253	0.283	0.274	0.909				
Recreation activity satisfaction	0.208	0.213	0.306	0.296	0.332	0.523	0.957			
Relationship satisfaction	0.163	-0.049	-0.074	-0.047	0.316	0.071	0.058	0.821		
Self-development satisfaction	0.252	0.106	0.123	0.091	0.478	0.238	0.326	0.090	0.844	
Worklife Satisfaction	0.295	0.095	0.111	0.107	0.334	0.265	0.341	0.445	0.301	0.818

Table: 13

Discriminant validity check: The diagonal values (in bold) are the square root of AVE while other values are the correlation between the respective constructs. Here, discriminant validity is achieved when a diagonal value bold is higher than the value in its column.

XI. CONCLUSION

[1] In Central-Gujarat people are generally satisfied as per global life satisfation or perceived QOL.

[2] In Central-Gujarat, perceived QOL is varying with sex. Females are comparative more satisfied than man.

[3] In Central-Gujarat, perceived QOL is does not vary with age.

[4] In Central-Gujarat, perceived QOL varies significantly with education status. Graduate & above and professional degree holder groups are equally more satisfied than education group of below matric and matric & above.

[5] In Central-Gujarat, perceived QOL vary significantly with marital status of Individuals.

[6] Bachelors are more satisfied than marrieds.

[7] In Central-Gujarat, perceived QOL significantly varies income level. Higher income group found more satisfied followed by middle income group. Lower income group are less satisfied.

[8] In Central-Gujarat, perceived QOL is significantly affected by chosen domains of life. Worklife satisfaction, Infrastructure satisfaction, Government satisfaction, Material possession satisfaction, Recreation activity, Physical health and children education were more significant in one's global satisfation in life. Self-development and Environmental Quality are less significant. Relationship satisfaction is insignificant.

REFERENCES

[1] W. Asyraf, & B. Afthanorhan (2013), A comparison of partial least square structural equation modeling (PLS-SEM) and covariance based structural equation modeling (CB-SEM) for confirmatory factor analysis, International journal of engineering science and innovative technology (IJESIT), Vol.2, Issue 5, pp 198-205.

[2] P. Conceicao & R. Bandura (2008), Measuring Subjective Well-being: A Summary Review of the Literature United Nations Development Programme, USA.

[3] S. Dasgupta & S. Majumdar (2000), Sense of well-being and perceived quality of life in Culcutta, In Advance in quality of life theory and research, Kluwer Academic publishers, Netherlands, Pp 65-79.

[4] E. Diener, R. Emmons, R, Larsen & S. Griffen (1985), The Satisfaction with Life. Scale, Journal of Personality Assessment, 49, 1.

[5] N. Gjoksi (2010), National approaches to measure wealth and well-being in the context of sustainable development. ESDN Case Study No.4.

[6] I. Gough (2003), Human Well-being: Bridging Objective and Subjective Approaches. ESPANET Conference, 13-15 November, 2003, Copenhagen.

[7] R, Haq (2009). Measuring Human Wellbeing in Pakistan: Objective versus Subjective Indicators, European Journal of Social Science, Volume 9, 3.

[8] S, Hicks, J, Newton, J, Haynes & J. Evans (2011), Measuring Children's and Young People's Well-being, Office for National Statistic and BRASS, Cardiff University.

[9] D. Kahneman (2006), Developments in the Measurement of Subjective Wellbeing, Journal of Economic Perspective, Volume 20, Number 1, Pages 3-24.

[10] D. Kahneman, E. Diener & N. Schwarz (1999). Well-being: The Foundations of Hedonic Psychology, Russell SAGE Foundation, New York.

[11] T. Kashdan (2002), The Assessment of Subjective Wellbeing (Issues Raised By the Oxford Happiness Questionnaire). Personality and Individual Difference, 36, 1225-1232.

[12] M. Rapley (2003), Quality of Life Research, SAGE Publications, New Delhi.

[13] C. Smith, & P. M. Clay (2010), Measuring Subjective and Objective Well-being: Analysis from Five Marine Commercial Fisheries. Human Organization, Volume 69, No.2.

2nd International Conference on Recent Innovations in Science, Technology, Management and Environment
Indian Federation of United Nations Associations, Qutab Institutional Area, New Delhi (India) (ICRISTME-16)
20 November 2016, www.conferenceworld.in ISBN: 978-93-86171-11-5

TOPIC: A STUDY OF SENSE OF WELL-BEING AND PERCEIVED QUALITY OF LIFE OF PEOPLE IN NORTH GUJARAT & CENTRAL GUJARAT

Rajesh Handa[1], Dr. G.C.Maheshwari[2]

[1]*Rajesh Handa, Management, Manish Institute of Management, Gujarat, (India)*

[2]*Dr. G.C. Maheshwari, Management, Delhi Technological University, Delhi, (India)*

ABSTRACT

The paper examined the perceived quality of life in Central and North-Gujarat of Gujarat state, with a 267 adult sample. It investigated first the relation between demographic characteristics and perceived quality of life and then the relation between Life domain satisfaction and perceived quality of life. Employing descriptive approaches through a modified questionnaire. The survey instrument measures the residents' life satisfaction in many Life domains: Government satisfaction, Material possession satisfaction, Spirituality satisfaction, Recreation activity satisfaction, Physical health satisfaction, Environmental quality satisfaction and career satisfaction. EFA, Multiple Regression analysis, CB-SEM techniques used to predict perceived life-satisfaction and validate the model of Perceived Quality of Life.

Keywords: Well-Being, Perceived Quality of Life, Life-Satisfaction, Government Satisfaction, Spirituality.

I. INTRODUCTION

Quality of life and its assessment is a challengeable task; still to improve it is a primary goal of any government & Individuals too. By many years we are measuring quality of life in terms of HDI (Human development Index) and accordingly ranking of the nations takes place which shows their well-being and quality of life in the country. HDI is an objective approach to access quality of life. But the second approach to measure Quality of life is subjective approach which we called perceived quality of life or happiness. Many researches has contributed their work in measuring PQOL or happiness of the nations and now a days World happiness Index is one of popular approach to measure the quality of life. As we noticed countries like Bhutan had focused on GNP (Gross national happiness) instead of GDP. This study is also an approach towards measuring PQOL of Individuals in North & Central Gujarat.

II. OBJECTIVES

1. To access global life satisfation of the inhabitants of North Gujarat and Central Gujarat.
2. To examine whether perceived quality of life varies with sex, age, marital status, education status and income level or not.
3. To assess different domains of life satisfaction thus affects the overall life satisfaction of Individuals.

III. RESEARCH METHODOLOGY

- Research type: Quantitative Research.
- Descriptive Research.
- Population: North Gujarat and Central Gujarat.
- Data used: Primary.
- Data Collection Tool: Structured Questionnaire
- Data Collection method: Survey (personal interaction).
- Survey method: Convenience Sampling (Non-Probability).
- Sample unit: People (ordinary resident).
- Sample Size: 267 respondents.

IV. LIMITATIONS OF THE STUDY

1. Under certain time limit 300 samples has collected, out of which 267 sample became part of this study.
2. Sampling frame was not present. Non-random, Convenience sampling method has used.
3. Respondent has limited to working class people with certain age, education and income limitation.

V. RESEARCH TOOLS USED

1. Global life satisfaction scale.
2. Life domain satisfaction scale.

VI. RELIABILITY CHECK

1. Global life satisfaction scale.

Reliability Statistics

Cronbach's Alpha	N of Items
.710	5

Table: 1

***Interpretation*:** Cronbachs Alpha value **0.710 > 0.7**. This is a good sign of reliability.

2. Life domain satisfaction scale.

Reliability Statistics

Cronbach's Alpha	N of Items
.927	38

Table: 2

***Interpretation*:** Cronbachs Alpha value **0.927 > 0.7**. This is a good sign of reliability.

VII. RESEARCH HYPOTHESIS

Hypothesis 1: People are not neutral towards their perceived QOL.

Hypothesis 2: Males and females vary significantly in their perceived QOL.

Hypothesis 3: Individuals belonging to different age groups vary significantly in their perceived QOL.

Hypothesis 4: Individuals belonging to different education status vary significantly in their perceived QOL.

Hypothesis 5: Individuals belonging to different marital status vary significantly in their perceived QOL.

Hypothesis 6: Individuals belonging to different income groups vary significantly in their perceived QOL.

Hypothesis 7: Individuals belonging to Central Gujarat and North-Gujarat vary significantly in their perceived QOL.

Hypothesis 8: Individuals belonging to rural and urban vary significantly in their perceived QOL.

Hypothesis 9: Sense of well-being is influenced by different domains of life. To determine which of these domains of life are related to global satisfaction or PQOL?

VIII. HYPOTHESIS TESTING

1. HO: Peoples are neutral about their perceived quality of life.

   H1: People are not neutral about their perceived quality of life

One-Sample Test

	Test Value = 4					
	t	df	Sig. (2-tailed)	Mean Difference	95% Confidence Interval of the Difference	
					Lower	Upper
sw	20.643	266	**.000**	1.07566	.9731	1.1782

Table: 3

Interpretation: Here, p-value **0.000 < 0.05**, so we reject null hypothesis. Alternate hypothesis is accepted. People are not neutral about their perceived quality of life. Peoples are somewhat satisfied toward their perceived quality of life.

2. HO: There is no significant difference between Males and females in their PQOL.

   H1: There is significant difference between Males and females in their PQOL.

Independent Samples Test

	Levene's Test for Equality of Variances		t-test for Equality of Means						
	F	Sig.	t	df	Sig. (2-tailed)	Mean Difference	Std. Error Difference	95% Confidence Interval of the Difference	
								Lower	Upper

sw	Equal variances assumed	5.676	**.018**	.033	262	.974	.00367	.11103	-.21496	.22231
	Equal variances not assumed			.031	153.395	**.975**	.00367	.11724	-.22794	.23528

Table: 4

Interpretation: Here, p-value **0.975 > 0.05**, so we fail to reject null hypothesis. Null hypothesis is accepted. There is no significant difference between males and females in their perceived QOL.

3. H0: There is no significant difference Individuals belonging to different age groups in their perceived QOL.

H1: There is significant difference between individuals belonging to different age groups in their perceived QOL.

ANOVA

sw

	Sum of Squares	df	Mean Square	F	Sig.
Between Groups	8.152	2	4.076	5.832	.003
Within Groups	182.415	261	.699		
Total	190.567	263			

Table: 5

sw

Tukey HSD[a,b]

Age	N	Subset for alpha = 0.05	
		1	2
36-45	50	5.0040	
26-35	204	5.0441	
46-55	13		5.8462
Sig.		.981	1.000

Table: 6

Means for groups in homogeneous subsets are displayed.

a. Uses Harmonic Mean Sample Size = 29.462.

b. The group sizes are unequal. The harmonic mean of the group sizes is used. Type I error levels are not guaranteed.

Interpretation: Here, p-value **0.003 < 0.05**, so we reject null hypothesis. Alternate hypothesis accepted.There is significant difference between individuals belonging to different age groups varies significantly in their perceived QOL**.**

Individual of age group of 46-55 years are comparative more satisfied than rest of two.

4. H0: There is no significant difference between Individuals belonging to different education status in their perceived QOL.

H1: There is significant difference between Individuals belonging to different education status vary significantly in their perceived QOL.

ANOVA

sw

	Sum of Squares	df	Mean Square	F	Sig.
Between Groups	1.634	2	.817	1.129	.325
Within Groups	188.933	261	.724		
Total	190.567	263			

Table: 7

sw

Tukey HSD[a,b]

Education	N	Subset for alpha = 0.05
		1
Graduate	53	4.9509
Post graduate or above.	203	5.0926
Below graduate	11	5.3636
Sig.		.187

Table: 8

Means for groups in homogeneous subsets are displayed.

a. Uses Harmonic Mean Sample Size = 26.154.

b. The group sizes are unequal. The harmonic mean of the group sizes is used. Type I error levels are not guaranteed.

Interpretation: Here, p-value **0.325 > 0.05**, so we fail to reject null hypothesis. Null hypothesis accepted.There is no significant difference between Individuals belonging to different education status in their perceived QOL.

5. H0: There is no significant difference between Individuals belonging to different marital status in their perceived QOL.

H1: There is significant difference between Individuals belonging to different marital status vary significantly in their perceived QOL.

Group Statistics

	Marital status	N	Mean	Std. Deviation	Std. Error Mean
sw	Unmarried	61	4.8328	.86347	.11056
	Married	206	5.1476	.83647	.05828

Table: 9

ANOVA

sw

	Sum of Squares	df	Mean Square	F	Sig.
Between Groups	4.107	1	4.107	5.770	.017
Within Groups	186.460	262	.712		
Total	190.567	263			

Table: 10

Interpretation: Here, p-value **0.017 < 0.05**. So we reject our null hypothesis. Alternate hypothesis accepted .There is significant difference between Individuals belonging to different marital status in their perceived QOL. Married individuals are significantly more satisfied in their PQOL than unmarried.

6. H0: There is no significant difference between Individuals belonging to different income groups in their perceived QOL.

H1: There is significant difference between Individuals belonging to different income groups vary significantly in their perceived QOL.

ANOVA

sw

	Sum of Squares	df	Mean Square	F	Sig.
Between Groups	4.823	2	2.411	3.388	.035
Within Groups	185.744	261	.712		
Total	190.567	263			

Table: 11

sw

Tukey HSD[a,b]

Income	N	Subset for alpha = 0.05	
		1	2
Lower income group	95	4.9011	
Middle income group	140	5.1429	5.1429
Higher income group	32		5.3000
Sig.		.253	.557

Table: 12

Means for groups in homogeneous subsets are displayed.

a. Uses Harmonic Mean Sample Size = 61.326.

b. The group sizes are unequal. The harmonic mean of the group sizes is used. Type I error levels are not guaranteed.

Interpretation: Here, p-value **0.000 < 0.05.** So we reject our null hypothesis. Alternate hypothesis accepted. There is significant difference between Individuals belonging to different income groups vary significantly in their perceived QOL.

PQOL of higher income group is significantly higher than lower income group.

7. H0: There is no significant difference between Individuals belonging to Central Gujarat and North-Gujarat in their perceived QOL.

H1: There is significant difference between Individuals belonging to Central Gujarat and North-Gujarat vary significantly in their perceived QOL

Group Statistics

	Residence3	N	Mean	Std. Deviation	Std. Error Mean
sw	North-Gujarat	125	5.1376	.81018	.07247
	Central-Gujarat	142	5.0211	.88541	.07430

Table: 13

Independent Samples Test

		Levene's Test for Equality of Variances		t-test for Equality of Means						
		F	Sig.	t	df	Sig. (2-tailed)	Mean Difference	Std. Error Difference	95% Confidence Interval of the Difference	
									Lower	Upper
sw	Equal variances assumed	.414	**.520**	1.116	265	**.265**	.11647	.10438	-.08904	.32199
	Equal variances not assumed			1.122	264.593	.263	.11647	.10379	-.08788	.32083

Table: 14

Interpretation: Here, p-value **0.265 > 0.05.** So we accept our null hypothesis. There no significant difference between in PQOL of Individuals belonging to Central Gujarat and North-Gujarat.

8. H0: There is no significant difference between Individuals belonging to Rural Gujarat and Urban Gujarat in their perceived QOL.

H1: There is no significant difference between Individuals belonging to Rural Gujarat and urban Gujarat in their perceived QOL.

Group Statistics

	Residence2	N	Mean	Std. Deviation	Std. Error Mean
sw	Rural	46	5.1609	.84708	.12490
	Urban	221	5.0579	.85317	.05739

Table: 15

Independent Samples Test

		Levene's Test for Equality of Variances		t-test for Equality of Means						
		F	Sig.	t	df	Sig. (2-tailed)	Mean Difference	Std. Error Difference	95% Confidence Interval of the Difference	
									Lower	Upper
sw	Equal variances assumed	.019	**.889**	.745	265	**.457**	.10295	.13810	-.16896	.37486
	Equal variances not assumed			.749	65.413	.457	.10295	.13745	-.17152	.37742

Table: 16

Interpretation: Here, p-value **0.457 > 0.05.** So we accept our null hypothesis. There no significant difference between in PQOL of Individuals belonging to Rural Gujarat and Urban Gujarat.

9. Ho: There is no significant relationship between overall life satisfaction and different domains of life.
H1: There is significant relationship between overall life satisfaction and different domains of life.

IX. REGRESSION ANALYSIS

Model Summary[b]

Model	R	R Square	Adjusted R Square	Std. Error of the Estimate	Durbin-Watson
1	.638[a]	.407	**.391**	.66467	**1.951**

Table: 17

a. Predictors: (Constant), Career satisfaction, Physical_health_satisfaction, Spirituality satisfaction, Recreation_activity_satisfaction, Government satisfaction , Material_possession_satisfaction, Environmental_quality_satisfaction

b. Dependent Variable: sw

Interpretation: *The Adjusted R square value tells us that our model accounts for 39% of variance which indicate it is a respective model as per social science research.*

ANOVA[a]

Model		Sum of Squares	df	Mean Square	F	Sig.
1	Regression	78.408	7	11.201	25.354	**.000[b]**
	Residual	114.423	259	.442		
	Total	192.832	266			

Table: 18

a. Dependent Variable: sw

b. Predictors: (Constant), Career satisfaction, Physical health satisfaction, Spirituality satisfaction, Recreation activity satisfaction, Government satisfaction , Material possession satisfaction, Environmental_quality_satisfaction

Interpretation: p<.05 the model is significant. Null hypothesis rejected, alternate hypothesis accepted. There is significant relationship between overall life satisfaction and different domains of life.

Coefficients

Model		Unstandardized Coefficients		Standardized Coefficients	t	Sig.	Collinearity Statistics	
		B	Std. Error	Beta			Tolerance	VIF
1	(Constant)	5.079	.041		124.555	.000		
	Government satisfaction	**.353**	.042	.402	8.383	.000	.998	1.002
	Material possession satisfaction	.092	.042	.107	2.225	.027	.994	1.006
	Spirituality satisfaction	**.171**	.041	.200	4.186	.000	.999	1.001
	Recreation activity satisfaction	**.211**	.041	.246	5.143	.000	.998	1.002
	Physical health satisfaction	.094	.042	.109	2.258	.025	.992	1.008
	Environmental quality satisfaction	**.252**	.042	.290	6.037	.000	.992	1.008
	Career satisfaction	.140	.041	.164	3.427	.001	.998	1.002

Table: 19

Interpretation: All predictors variable's p <.05 except Relationship satisfaction. T values of all predictor variables are high except Relationship satisfation. So, all predictors variable are significant except Relationship satisfaction.

Multicollinearity check: No tolerance value less than 0.2 and no VIF value greater than 5 found. There is no sign of presence of multicollinearity.

Assumptions Check:

1. Mean of residuals is zero: satisfied.

2. Residuals are normally distributed: satisfied.
3. Error (Residual) variances are constant (Homoscedascity): satisfied.
4. There is no Multicollinearity: satisfied.
5. There is no auto co-relation ($\therefore$ Durbin Watson value 1.951 $\cong$ 2.00 and this is cross-sectional data): satisfied.

X. VALIDITY ANALYSIS: PATH DIAGRAM

Covariance Based Structural Equation Modeling (CB-SEM).

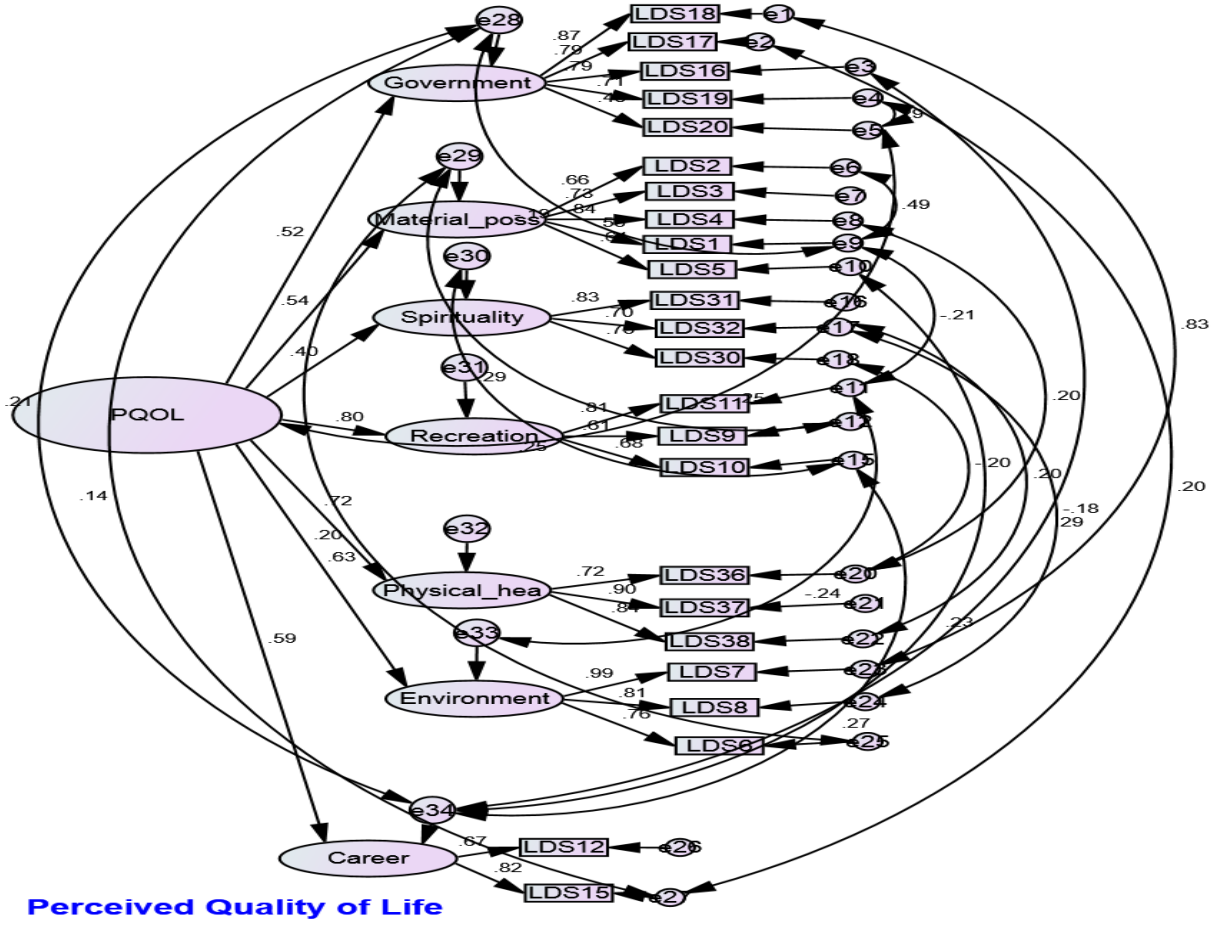


Fig: 1

XI. MODEL FIT SUMMARY

	Index	Level of acceptance	Observed value	Literature	Comments
Absolute fit	Chi-square	P > 0.05	0.051	Wheaton et. Al. (1997)	**Accepted**
	RMSEA	RMSEA < 0.08	0.024	Browne and Cudeck (1993)	**Accepted**
	GFI	GFI > 0.90	0.928	Joreskog and Sorbom (1984)	**Accepted**
Incremental fit	AGFI	AGFI > 0.90	0.904	Tanaka and Huba (1985)	**Accepted**
	CFI	CFI > 0.90	0.988	Bentler (1990)	**Accepted**

	TLI	TLI > 0.90	0.986	Bentler and Bonett (1980)	**Accepted**
	NFI	NFI > 0.90	0.922	Bollen (1989)	**Accepted**
Parsimonious fit	Chisq/df	Chisq/df < 5.0	1.159	Marsh and Hocevar (1985)	**Accepted**

Table: 20

XII. CONCLUSION

1. People of North Gujarat and Central Gujarat are somewhat satisfied towards overall life satisfaction.
2. Perceived Quality of life does not associated with gender difference.
3. Perceived Quality of life is associated with different age groups. People of age group 46-55 years are more satisfied compare to age group 26-35.
4. Perceived Quality of life does not associated with education status of individuals.
5. Perceived Quality of life is associated with marital status. Married are comparative more satisfied than unmarried in their PQOL.
6. Perceived Quality of life is associated with income level of individuals. Higher income group found more satisfied followed by middle income group than Lower income group in PQOL.
7. Perceived Quality of life does not associated with different geographical areas of Gujarat like here North-Gujarat & South Gujarat.
8. Perceived Quality of life does not associate with different areas of Gujarat based on urban and rural.
9. Perceived quality of life is associated with different domains of life.The study found that all seven domains of life: Government satisfaction, Material possession satisfaction, Spirituality satisfaction, Recreation activity satisfaction, Physical health satisfaction, Environmental quality satisfaction and career satisfaction are significant in model. Domains like Government satisfaction, Recreation activity satisfaction and Environmental quality satisfaction show high significance in the PQOL model.

REFERENCES

[1] W. Asyraf, & B. Afthanorhan (2013), A comparison of partial least square structural equation modeling (PLS-SEM) and covariance based structural equation modeling (CB-SEM) for confirmatory factor analysis, International journal of engineering science and innovative technology (IJESIT), Vol.2, Issue 5, pp 198-205.

[2] P. Conceicao & R. Bandura (2008), Measuring Subjective Well-being: A Summary Review of the Literature United Nations Development Programme, USA.

[3] S. Dasgupta & S. Majumdar (2000), Sense of well-being and perceived quality of life in Culcutta, In Advance in quality of life theory and research, Kluwer Academic publishers, Netherlands, Pp 65-79.

[4] E. Diener, R. Emmons, R, Larsen & S. Griffen (1985), The Satisfaction with Life. Scale, Journal of Personality Assessment, 49, 1.

[5] N. Gjoksi (2010), National approaches to measure wealth and well-being in the context of sustainable development. ESDN Case Study No.4.

[6] I. Gough (2003), Human Well-being: Bridging Objective and Subjective Approaches. ESPANET Conference, 13-15 November, 2003, Copenhagen.

[7] R, Haq (2009). Measuring Human Wellbeing in Pakistan: Objective versus Subjective Indicators, European Journal of Social Science, Volume 9, 3.

[8] S, Hicks, J, Newton, J, Haynes & J. Evans (2011), Measuring Children's and Young People's Well-being, Office for National Statistic and BRASS, Cardiff University.

[9] D. Kahneman (2006), Developments in the Measurement of Subjective Wellbeing, Journal of Economic Perspective, Volume 20, Number 1, Pages 3-24.

[10] D. Kahneman, E. Diener & N. Schwarz (1999). Well-being: The Foundations of Hedonic Psychology, Russell SAGE Foundation, New York.

[11] T. Kashdan (2002), The Assessment of Subjective Wellbeing (Issues Raised By the Oxford Happiness Questionnaire). Personality and Individual Difference, 36, 1225-1232.

[12] M. Rapley (2003), Quality of Life Research, SAGE Publications, New Delhi.

[13] C. Smith, & P. M. Clay (2010), Measuring Subjective and Objective Well-being: Analysis from Five Marine Commercial Fisheries. Human Organization, Volume 69, No.2.

applied optics

Ultra broadband mid-IR supercontinuum generation in $Ge_{11.5}As_{24}Se_{64.5}$ based chalcogenide graded-index photonic crystal fiber: design and analysis

A. G. N. Chaitanya,[1] Than Singh Saini,[1] Ajeet Kumar,[1,*] and Ravindra Kumar Sinha[2]

[1]Advanced Photonics Simulation Research Laboratory, Department of Applied Physics, Delhi Technological University, Delhi–110042, India
[2]Central Scientific Instruments Organization (CSIR), Chandigarh–160030, India
*Corresponding author: ajeetdph@gmail.com

Received 26 July 2016; revised 4 November 2016; accepted 12 November 2016; posted 14 November 2016 (Doc. ID 272426); published 13 December 2016

In this paper, we report design and numerical analysis of a $Ge_{11.5}As_{24}Se_{64.5}$ based chalcogenide glass graded-index photonic crystal fiber structure for mid-IR ultra broadband supercontinuum generation. The proposed dispersion engineered photonic crystal fiber offers a zero dispersion wavelength at a pump wavelength of 2.8 μm. To simulate the supercontinuum generation spectrum, the orders of dispersion coefficient up to the ninth order are considered. Simulated results indicate that an ultra broadband supercontinuum spectrum spanning 1–16 μm has been achieved using a 10 mm long photonic crystal fiber structure pumped with 50 fs secant hyperbolic pulses of 3 kW at a −30 dB spectral intensity level. To the best of our knowledge, this is the first time such broad supercontinuum spectrum has been reported. This ultra broadband mid-IR supercontinuum spectrum is applicable in many diverse fields, including medical, defense, metrology, and spectroscopy. © 2016 Optical Society of America

OCIS codes: (190.0190) Nonlinear optics; (190.4370) Nonlinear optics, fibers; (320.6629) Supercontinuum generation.

https://doi.org/10.1364/AO.55.010138

1. INTRODUCTION

Supercontinuum generation (SCG) is a process that broadens a high-intensity ultrashort pulse when it is propagated through a nonlinear optically transparent medium. This phenomenon was first discovered by Alfano and Shapiro [1,2]. The broadening of the spectra is mainly due to the interplay of linear effects such as dispersion and nonlinear effects such as self-phase modulation (SPM), cross-phase modulation (CPM), four-wave mixing (FWM), stimulated Raman scattering (SRS), and solitons dynamics at pump wavelength [3,4]. The study of SCG has gained importance since the spectrum generated due to this process has high spatial coherence and has been found useful in many applications in the fields of frequency metrology, optical coherence tomography, molecular spectroscopy, biomedical imaging, gas sensing, food quality control, and early cancer detection [5–12].

The mid-IR region is important because the fundamental molecular vibration absorption bands are stronger compared to the overtones and combination absorption bands are situated in the near-IR region. The composition of the molecular structure of the substance can be thoroughly understood with the help of mid-IR spectroscopy and non-intrusive diagnostics [13].

SCG has been used on various optically transparent materials including silica. The primary requirement of SCG is that the material must have a high nonlinear coefficient and be optically transparent in the region of continuum generation, viz., near-IR and mid-IR region. A number of experimental, analytical, and numerical investigation have been carried out on silica, ZBLAN [14–16], tellurite [17–19], and bismuth [20–25] fibers. The nonlinear refractive index of ZBLAN is 2×10^{-20} $m^2\,W^{-1}$ and is almost the same as that of silica [26]. Therefore, long fibers with high pulse energy are required for SCG [27]. Spectrum spanning from ultraviolet to IR can be generated using ZBLAN. The nonlinear refractive index of tellurite is 4×10^{-19} $m^2\,W^{-1}$ and of bismuth lies between 30×10^{-20} and 1.1×10^{-18} $m^2\,W^{-1}$ [28,29]. Both these materials have a higher nonlinear refractive index compared to silica and have high transparency in the mid-IR region.

Chalcogenide glasses contain one or more elements from group 16 of the periodic table (S, Se, and Te, but excluding O) covalently bonded to network formers such as As, Sb, Ge, and Si, etc. [30]. These glasses have a nonlinear refractive index at least two orders higher than that of the silica glasses and an excellent IR and mid-IR transmission window up to

20 μm [31]. These two factors have made chalcogenide an excellent choice for fabricating mid-IR nonlinear photonic devices. The SCG in this region also covers most of the molecular fingerprint spectral region and is a natural choice for IR and mid-IR SCG [32]. Recently, a number of experimental and numerical investigations have been carried out in chalcogenide waveguides [27,33–35] and fibers [36–41]. Yu *et al.* have experimentally demonstrated supercontinuum (SC) spectrum spanning from 2.9 to 4.2 μm using a 6.6 cm As_2S_3 rib waveguide at a pump wavelength of 3.26 μm having a pulse width of 7.5 ps and peak power of 2 kW [33]. Yu *et al.* numerically demonstrated SC spectrum spanning beyond 10 μm using a dispersion engineered $Ge_{11.5}As_{24}Se_{64.5}$ rib waveguide at a pump wavelength of 4 μm having a pulse width of 250 fs [34]. Yu *et al.* experimentally demonstrated a broadband SC spanning from 1.8 to 7.5 μm using a 1 cm rib waveguide at a pump wavelength of 4 μm using a 320 fs pulse [34]. Salem *et al.* numerically demonstrated SC spanning from 3.14 to 6.33 μm using a tapered As_2S_3 PCF at a pump wavelength of 4.7 μm and a pulse energy of 100 pJ [36]. Petersen *et al.* experimentally demonstrated SC spanning from 1.4 to 13.3 μm using concatenated fibers (a 10 m long fluoride fiber and 10 cm long chalcogenide fibers were concatenated) at pump wavelength of 6.3 μm having a pulse width of 100 fs and peak power of 520 kW [39]. Yu *et al.* experimentally demonstrated SC spanning from 1.8 to 10 μm using a step index chalcogenide fiber at a pump wavelength of 4 μm having a pulse width of 330 fs and peak power of 3 kW [41]. Hudson *et al.* experimentally demonstrated SC spanning from 1.6 to 5.9 μm using a step index fiber at a pump wavelength of 3.1 μm having a pulse width of 67 fs and pulse energy of 18 μJ [38]. Karim *et al.* numerically demonstrated SC spanning from 3 to 11 μm and beyond using a dispersion engineered $Ge_{11.5}As_{24}Se_{64.5}$ PCF at a pump wavelength of 3.1 μm having peak power of 3 kW [42]. Saini *et al.* numerically demonstrated SC spanning from 2 to 15 μm using a triangular core graded index PCF at pump wavelength of 4.1 μm having a pulse width of 50 fs and peak power of 3 kW [13]. The best results achieved in the earlier reported investigations are SC spanning from 1.4 to 13.3 μm [39] at a peak power of 520 kW and 2–15 μm [13].

In this paper, we have reported what we believe is a novel graded-index photonic crystal fiber (GI PCF) structure that offers an ultra-broadband supercontinuum spectrum using relatively low peak power. The structure offers excellent control over dispersion characteristics. The proposed GI PCF structure is able to generate ultra broadband SC spectrum spanning 1–16 μm in only a 10 mm length when it is pumped with femtosecond laser pulses with low peak power of 3 kW at 2.8 μm.

The paper has been organized into six sections. The first section provides a brief introduction explaining previous investigations and the reason to choose chalcogenide glass as a material. The second section is dedicated to linear and nonlinear analysis of the material since both are required to solve the nonlinear Schrodinger wave equation. In the third section, we discuss the effect of the design principle of the proposed GI PCF. In the fourth section, we discuss the effect of various parameters on dispersion and also the variation of effective mode area and nonlinear coefficient (γ) with respect to wavelength. In the fifth section, we discuss the supercontinuum generation, and variation of spectrum against various parameters. In the sixth section, we draw our conclusions.

2. METHOD OF ANALYSIS

The SCG is governed by the following nonlinear Schrodinger equation (NLSE) [4]

$$\frac{\partial A}{\partial z}+\frac{\alpha}{2}A-\left(\sum_{n\geq 2}\beta_n\frac{i^{n+1}}{n!}\frac{\partial^n A}{\partial t^n}\right)=i\gamma\left(1+\frac{i}{\omega_0}\frac{\partial}{\partial t}\right)\left[A(z,t)\int_{-\infty}^{\infty}R(t')|A(z,t-t')|^2\mathrm{d}t'\right]. \quad (1)$$

In Eq. (1), the terms on LHS signify the linear effect. The terms on RHS indicate the nonlinear effects. The term β_n is called the dispersion parameter of nth order and term γ is called the nonlinear coefficient. Both these terms can be optimized by proper design. Dispersion is optimum, if the dispersion curve lies in normal region and has a zero-dispersion wavelength (ZDWL). The nonlinear coefficient will have optimum value, if the effective mode area of the fundamental mode is minimal. The aim of the design is to satisfy the above two conditions to achieve a broader and a flat continuum.

A. Linear Characteristics

Dispersion engineering in a PCF involves achieving ZDWL with a flat dispersion curve. The wavelength dependent refractive index is calculated using Sellmeier's equation [3]

$$n(\lambda)=\sqrt{1+\frac{A_1\lambda^2}{\lambda^2-B_1^2}+\frac{A_2\lambda^2}{\lambda^2-B_2^2}}, \quad (2)$$

where $A_1=5.78525$, $A_2=0.39705$, $B_1=0.28795$, $B_2=30.39338$, and λ is the pump wavelength in micrometers.

This equation is incorporated to calculate effective mode index of fundamental mode using COMSOL Multiphysics, a full vectorial finite element (FEM) based software. The dispersion D is calculated using the relation [43]

$$D(\lambda)=-\frac{\lambda}{c}\frac{d^2n_{\mathrm{eff}}}{d\lambda^2}. \quad (3)$$

The dispersion obtained using Eq. (3) is comprised of both material and waveguide dispersion since Sellmeier's equation is considered while calculating n_{eff} of the propagating mode.

Using the value obtained in Eq. (3), dispersion parameters are calculated by expanding $\beta(\omega)$ by the Taylor series as [4]

$$\beta(\omega)=\beta(\omega_0)+\beta_1(\omega_0)(\omega-\omega_0)+\frac{1}{2!}\beta_2(\omega_0)(\omega-\omega_0)^2+\ldots, \quad (4)$$

where, $\beta_n=d^n\beta/d\omega^n$. The first term on the RHS of Eq. (4) is the effective refractive index of the propagating mode, the second term is the group velocity, and the third term denotes the group velocity dispersion (GVD) of the pulse. We have

considered the value of dispersion coefficient up to the 9th order.

B. Nonlinear Characteristics

The RHS of Eq. (1) comprises of nonlinear terms and nonlinear effects like nonlinear coefficient γ, SPM, CPM, FWM, and SRS. The nonlinear coefficient γ is given by [4]

$$\gamma = \frac{2\pi n_2}{\lambda A_{\text{eff}}(\lambda)} \ \text{m}^{-1}\,\text{W}^{-1}, \tag{5}$$

where n_2 is the nonlinear refractive index of the material. The n_2 for $Ge_{11.5}As_{24}Se_{64.5}$ chalcogenide glass material is 4.3×10^{-18} m^2/W at 3.1 μm and $\alpha = 0.6$ dB/cm [44]. A_{eff}, called the effective mode area, is a function of the wavelength and is given by [4]

$$A_{\text{eff}}(\lambda) = \frac{\left(\int\int_{-\infty}^{\infty}|E|^2 \text{d}x\text{d}y\right)^2}{\left(\int\int_{-\infty}^{\infty}|E|^4 \text{d}x\text{d}y\right)}. \tag{6}$$

The effective mode area is design dependent and can be minimized by design. The effective mode area has an influence on dispersion, hence an optimized value should be chosen such that both the dispersion and effective mode area at pump wavelength are minimum.

The nonlinear response $R(t')$ takes into account the electronic and nuclear contribution. It is expressed as [4]

$$R(t') = (1 - f_R)\delta(t' - t_e) + f_R h_R(t'), \tag{7}$$

where f_R is the fractional contribution of Raman response of total linear response.

For $Ge_{11.5}As_{24}Se_{64.5}$ chalcogenide glass, f_R is 0.031 [44]. The $h_R(t')$ is the Raman response function and contains information on the vibration of the molecules of the matter as light passes through it. It is given by [4]

$$h_R(t') = \frac{\tau_1^2 + \tau_2^2}{\tau_1 \tau_2^2} \exp\left[-\frac{t'}{\tau_2}\right] \sin\left(\frac{t'}{\tau_1}\right), \tag{8}$$

where $\tau_1 = 1/\Omega_R$ in femtoseconds, called Raman period, Ω_R is the vibration frequency of molecule, and τ_2 is damping time of vibrations in femtoseconds.

For $Ge_{11.5}As_{24}Se_{64.5}$ chalcogenide glass, $\tau_1 = 15.5$ fs and has a life time $\tau_2 = 230.5$ fs [41].

The shape of the input pulse is a hyperbolic secant pulse and is represented by the following relation [4]

$$A(z = 0, t) = \sqrt{P_0}\,\text{sec}\,h\left(\frac{t}{t_0}\right), \tag{9}$$

where $t_0 = T_{\text{FWHM}}/1.7627$ and P_0 is the peak power of the applied input pulse.

3. DESIGN PRINCIPLE OF GI PCF

The transverse cross-sectional view of the designed PCF structure has been established in Fig. 1. As illustrated in Fig. 1, we have proposed what we believe is a novel design with three layers of the air holes arranged in a hexagonal lattice pattern in $Ge_{11.5}As_{24}Se_{64.5}$ chalcogenide glass. The x and y-coordinates of the center of the air holes are represented by $x = \Lambda n\ \cos(\theta)$ and $y = \Lambda n\ \sin(\theta)$, respectively, with $n = 1, 2, 3$, and Λn is the distance between the centers of the air holes in nth ring of

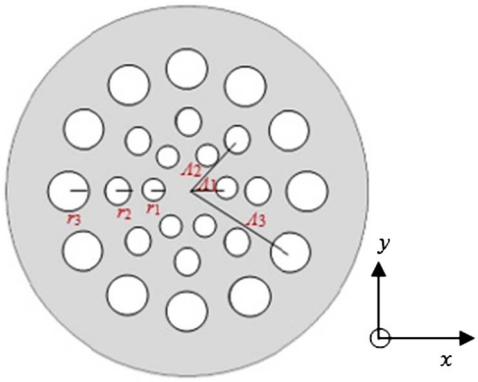


Fig. 1. Transverse cross-section of the proposed GI PCF.

air holes from the center of the PCF structure. Θ represents the angle subtended between x-axis and the line joining the center of the PCF to the center of air holes. More specifically, the inner ring of air holes consists of the six air holes at $\theta = 0°$, 60°, 120°, 180°, 240°, and 300°. The middle ring of air holes consists of eight air holes at $\theta = 0°$, 45°, 90°, 135°,180°, 225°, 270°, and 315°. Similarly, the outer ring (i.e., third ring) of air holes consists of twelve air holes at $\theta = 0°$, 30°, 60°, 90°, 120°, 150°, 180°, 210°, 240°, 270°, 300°, and 330°.

The radii of the air holes in the inner, middle, and outer ring are represented by r_1, r_2, and r_3, respectively, with $r_1 < r_2 < r_3$. The air filling fraction (r_n/Λ_n) increases gradually when increasing the order of the rings of the air holes. In other words, the effective refractive index of the cladding monotonically decreases as we move outward from the center of the core of the PCF. Hence, the structure is named as "graded-index." The hexagonal-shaped core and graded-index profile increases the confinement of the electric field and also results in a monotonically decreasing refractive index profile. The proposed design has a strong control over the dispersion profile and ZDWL. From the fabrication point of view, the reported PCF structure can be fabricated using the well-known "stack-and-draw" technique. Figure 2 shows the simulated electric field of the fundamental mode propagating a 2.8 μm wavelength.

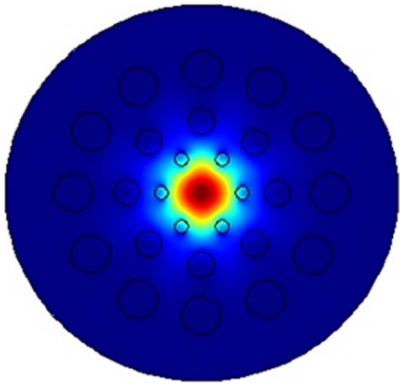


Fig. 2. Electric field distribution of fundamental mode propagating in PCF at a 2.8 μm wavelength.

4. DISPERSION CHARACTERISTICS

The six geometrical parameters (i.e., Λ_1, Λ_2, Λ_3, r_1, r_2, and r_3) have a diverse influence on the dispersion characteristics of the proposed design. A thorough analysis by varying all six parameters has been carried out and the design has been optimized to obtain minimum dispersion at a pump wavelength of 2.8 μm with a minimum effective mode area. The variation in dispersion characteristics due to variation in Λ_1 has been displayed in Fig. 3. If Λ_1 is increased, the effective mode area increases and ZDWL shifts toward a shorter wavelength. The dispersion at 2.8 μm wavelength varied from −2.62 ps/nm km at $\Lambda_1 = 1.68$ μm to −0.69 ps/nm km at $\Lambda_1 = 1.75$ μm. The effective mode area varied from 5.66 μm^2 to 5.30 μm^2 as Λ_1 was varied from 1.75 to 1.70 μm.

The variation in the dispersion characteristic due to a variation in the radius of the air hole of the inner ring has been illustrated in Fig. 4. The variation in the radius has a significant influence on the dispersion characteristics. As the radius of the air hole is increased, the ZDWL shifts toward a shorter wavelength. The effective mode area also decreases with an increase in the radius of the air hole. The increase in the radius of the air hole increases the area of the air holes, thus decreasing the overall effective index of the design.

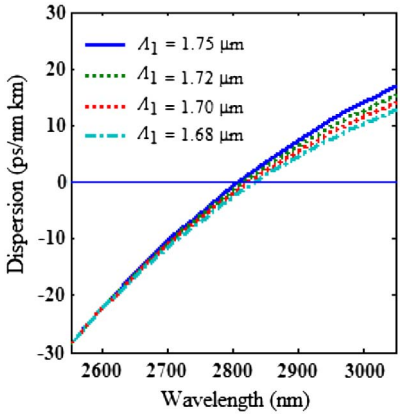


Fig. 3. Dispersion characteristics due to a change in the pitch of the inner ring.

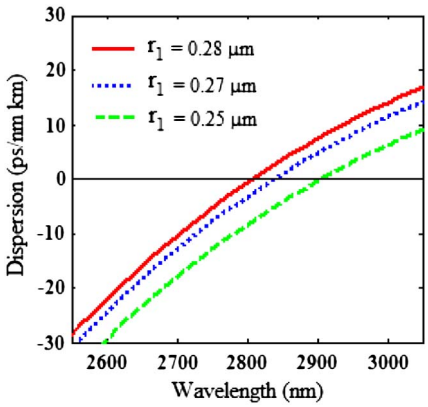


Fig. 4. Dispersion characteristics due to a change in the radius of the air hole of the inner ring.

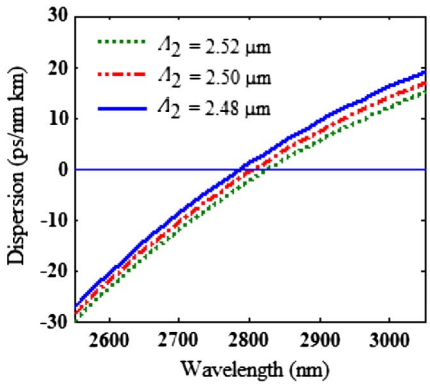


Fig. 5. Dispersion characteristics due to a change in the position of the air hole of the second ring.

The dispersion varies from −8.37 to −0.69 ps/nm km as r_1 is increased from 0.25 to 0.28 μm at pump wavelength. The effective mode area changes from 5.88 μm^2 to 5.56 μm^2 for the above change in r_1.

Figure 5 illustrates the variation in the dispersion characteristics with respect to a variation in Λ_2. ZDWL shifts toward a longer wavelength with an increase in Λ_2. The dispersion varies from 1.09 to −2.42 ps/nm km as Λ_2 is increased from 2.48 to 2.52 μm. The effective mode area changes from 5.52 to 5.59 μm^2 for the above variation.

The variation of the dispersion characteristics due to a variation in air hole radius r_2 is shown in Fig. 6. As r_2 increases, the ZSWL shifts toward a shorter wavelength. The dispersion at 2.8 μm wavelength varied from −3.629 to 2.262 ps/nm km as r_2 is increased from 0.38 μm to 0.42 μm. The effective mode area decreased from 5.61 μm^2 to 5.51μm^2 for the above said variation in r_2.

The variation in the dispersion characteristics due to a variation in Λ_3 has been shown in Fig. 7. As Λ_3 increases ZDWL shifts toward the longer wavelength by a very small value. The dispersion value varied from −0.60 ps/nm km to −0.72 ps/nm km as Λ_3 is varied from 3.88 μm to 3.92 μm. There is no significant change in the effective mode area. Since this variation is small, the dispersion curve for the different value tends to overlap as the size of the graph is reduced.

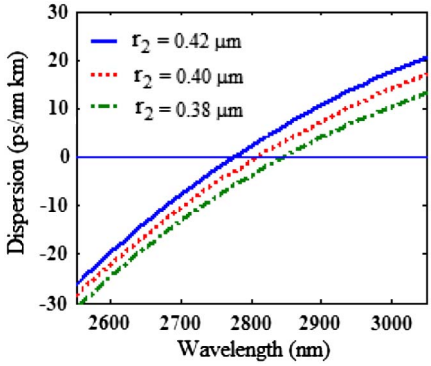


Fig. 6. Dispersion characteristics due to a variation in the radius of the air hole of the second ring.

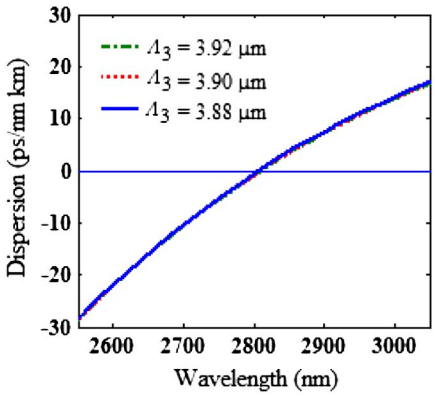


Fig. 7. Dispersion characteristics due to a variation in the position of the air hole of the third ring.

Figure 8 shows the variation in the dispersion characteristics due to a variation in radius r_3. As r_3 increases, ZDWL shifts toward a shorter wavelength. The dispersion varies from −0.6 ps/nm km to −0.34 ps/nm km as r_3 is increased from 0.58 μm to 0.64 μm. There is no significant change in the effective mode area for the above said variation in the r_3. From the above discussion, it can be noted that an increase in the radius r_n ($n = 1, 2, 3$) shifts the ZDWL toward a shorter wavelength and an increase in Λ_n ($n = 1, 2, 3$) shifts ZDWL toward a longer wavelength.

At $\Lambda_1 = 1.75$ μm, $\Lambda_2 = 2.50$ μm, $\Lambda_3 = 3.80$ μm, $r_1 = 0.28$ μm, $r_2 = 0.40$ μm, and $r_3 = 0.60$ μm, a dispersion of −0.6 ps/nm km has been obtained with an effective mode area 5.55 μm^2, at a pump wavelength of 2.8 μm.

The dispersion characteristics between 1–12 μm wavelength have been shown in Fig. 9. The structure has high dispersion until 2 μm in a normal dispersion region. It has minimum dispersion at pump wavelength, anomalous dispersion between 3–5 μm, and normal disperion between 5 and 12 μm. From the dispersion characteristics, it is evident that the structure has a flat dispersion over a wide range. This helps for an efficient continuum generation.

Figure 10 illustrates a variation of the effective mode area and nonlinear coefficient γ with respect to wavelength. The effective mode area (blue solid line) increases with an increase

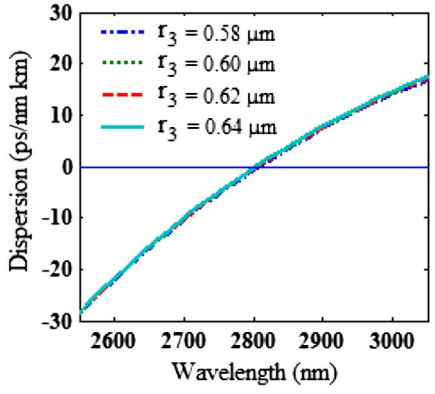


Fig. 8. Dispersion characteristics due to a variation in the radius of the air hole of the third ring.

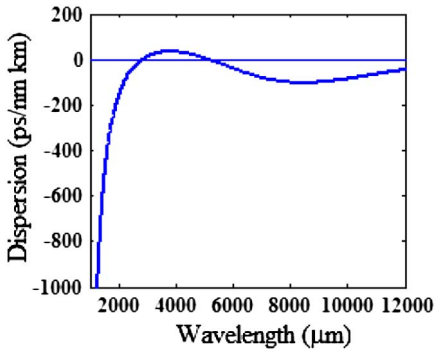


Fig. 9. Dispersion characteristics of the proposed design.

in wavelength. On the other hand, the nonlinear coefficient (green dotted line) decreases with an increase in wavelength. At a pump wavelength of 2.8 μm, the structure has an effective mode area of 5.55 μm^2, a confinment loss of 0.16 dB/mm, and a nonlinear coefficient γ of 1722 W^{-1} km^{-1}.

5. SUPERCONTINUUM GENERATION

The SCG has been generated by solving Eq. (1) using MATLAB. The LHS of Eq. (1) has a dispersion parameter βn, where n is the order of dispersion. Up to the 9th order of dispersion has been considered for this simulation. During the course of the simulation, it was observed that increasing the dispersion until the 9th order had a significant bearing on the output spectrum. An increase beyond the 9th order of dispersion had no impact on the output continuum. Hence, the 9th order of dispersion was chosen. The influence of various parameters like pulse power, pulse width, and fiber length (l) has been analyzed and shown in Figs. 11–13.

When there is a short high intensity pulse incident on a nonlinear fiber, in a very small effective mode area, the intensity dependence of the refractive index leads to SPM. Since the dispersion is minimal around the pump wavelength, spectral

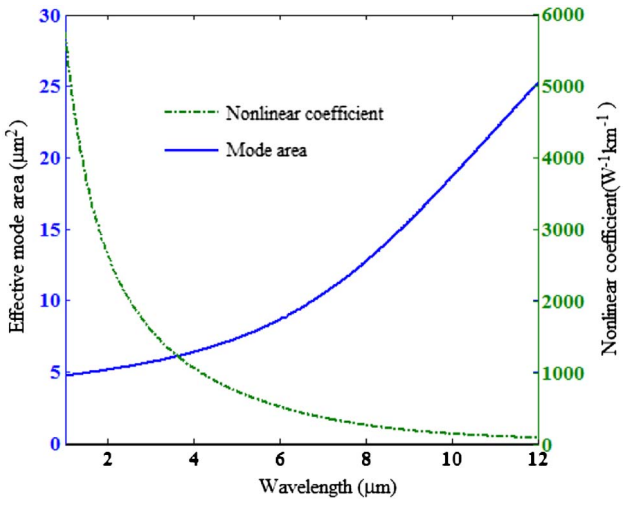


Fig. 10. Variation of the nonlinear coefficient and the effective mode area against the wavelength.

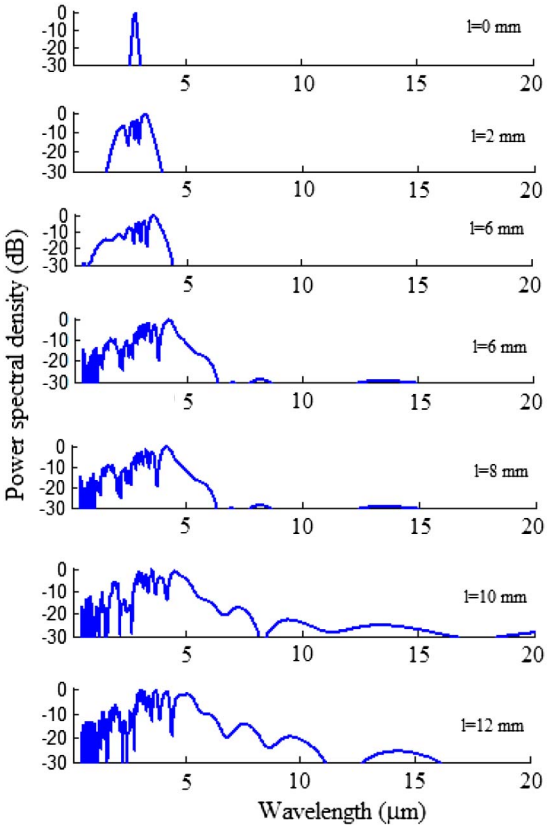


Fig. 11. Effect of the fiber length on SCG.

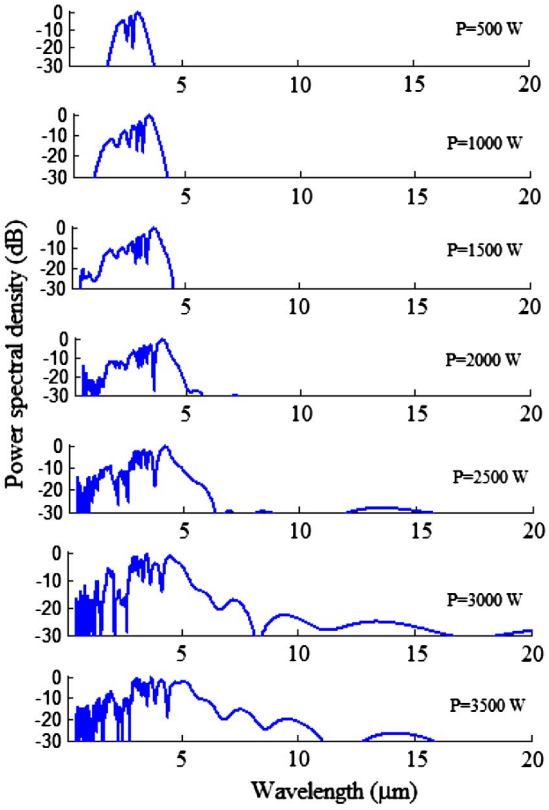


Fig. 13. Effect of the peak power on SCG.

broadening without a change in pulse shape occurs, leading to a symmetrical broadening of the pulse. Since more than one optical field is co-propagating in a very small effective area, CPM occurs, leading to further broadening of the pulse. These two nonlinear phenomenon are responsible for an initial broadening of the spectrum. FWM occurs when photons from one or more waves are annihilated and new photons are created at different frequencies such that net energy and momentum are conserved during the interaction. For this interaction, the phase-matching condition should be satisfied. Dispersion engineering plays an important role in determining the efficiency of FWM. Dispersion flattening along the length of the fiber is also important for a wider spectrum. Since the fiber dimensions along the length don't vary, dispersion flattening is achieved along the length of the fiber.

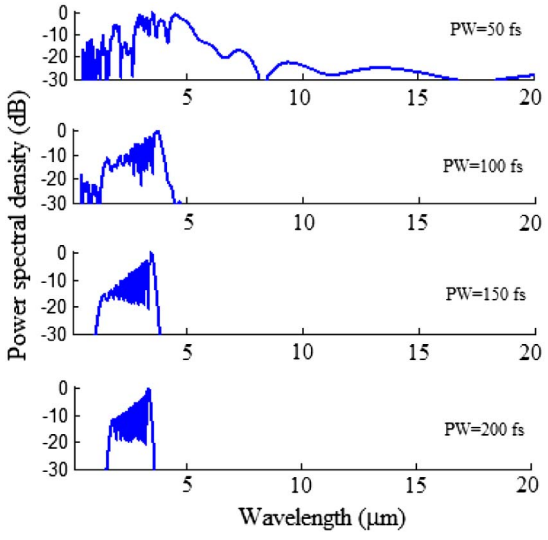


Fig. 12. Effect of the pulse width on SCG.

To study the effect of fiber length on SCG, a secant hyperbolic pulse with a pulse width of 50 fs and peak power of 3000 W has been used for simulation and analysis. Spectrum has been obtained for various lengths of fiber from 0 mm to 12 mm in steps of 2 mm. As the pulse propagates inside the fiber, initially SPM occurs followed by CPM, FWM, and SRS [4]. As the pulse propagates along the fiber, the high intensity electric fields interact with each other and with dielectric media, which results in spectral broadening. At $l = 10$ maximum broadening occurs, indicating that the entire nonlinear process is complete. During further propagation along the fiber, there is no spectral broadening; instead the pulse experiences attenuation losses especially at the extreme longer and shorter wavelength region.

The effect of a variation in pulse width on SCG has been studied by varying a secant hyperbolic shape pulse from 50 fs to 200 fs in steps of 50 fs. The length of the PCF is 10 mm and the peak power is 3000 W. Spectrum for the above-mentioned pulse width are illustrated in Fig. 11. At a shorter pulse width, the rate of change of intensity is high and will result in an effective SPM. This will be followed by other nonlinear

phenomenon like CPM, FWM, and SRS. This results in a broader continuum. As the pulse width is increased, the rate of change of intensity reduces the SPM. Thus, the overall continuum broadening reduces. The spectral broadening decreases as the pulse width increases from 50 fs to 100 fs.

If a broader spectrum must be obtained at larger pulse width, then the pulse should have a higher peak power. The additional power will compensate for the decrease in the rate of change of intensity.

The effect of a variation in the peak power of the pulse on SCG has been studied using a 10 mm chalcogenide glass fiber with a secant shape pulse of pulse width 50 fs. SRS is responsible for continuum broadening on a longer wavelength region (Stokes wave) and is intensity dependent. At low power, the intensity is low and hence the generation of a Stokes wave is limited. As the pulse power is increased the intensity also increases, increasing the generation of a Stokes wave. This leads to a broadening of the spectrum mainly in the longer wavelength region. The spectrum broadening occurs until a certain peak power and a further increase has no effect on the spectrum broadening since the Stokes wave generated will be limited to a certain wavelength. This additional increase in power negates the losses experienced by the spectrum in the extremely short and long wavelength regions; i.e., the Stokes and anti-Stokes waves generated will have an increased intensity. At a higher power, the new waves generated due to FWM will have a higher intensity since the energy in this process is conserved [4].

6. CONCLUSION

We have reported what we believe is a novel $Ge_{11.5}As_{24}Se_{64.5}$ based chalcogenide glass graded-index photonic crystal fiber structure for ultra broadband mid-infrared SCG. The proposed structure possesses a very high nonlinearity ($\gamma = 1722\ W^{-1}\,Km^{-1}$) and very low and flat dispersion of -0.60 ps/nm km at a pump wavelength of 2.8 μm. An ultra broadband supercontinuum spectrum spanning 1–16 μm has been obtained using 10 mm long GI PCF pumped with femtosecond laser pulses with a peak power of 3 kW. Such an ultra-broadband supercontinuum spectrum is expected to have profound applications in various fields and specific applications of mid-IR supercontinuum generation include spectroscopy, optical coherence tomography, frequency comb generation, early cancer detection, food quality control, security, and sensing.

Acknowledgment. The authors gratefully acknowledge the initiative and support toward the establishment of the TIFAC-Center of Relevance and Excellence in Fiber Optics and Optical Communication at Delhi Technological University (formerly Delhi College of Engineering) Delhi, through the Mission REACH program of Technology Vision 2020 of the Government of India.

REFERENCES

1. R. R. Alfano and S. L. Shapiro, "Emission in the region of 4000 to 7000Å via four-photon coupling in glass," Phys. Rev. Lett. **24**, 584–587 (1970).
2. R. R. Alfano and S. L. Shapiro, "Observation of self-phase modulation and small scale filaments in crystals and glasses," Phys. Rev. Lett. **24**, 592–594 (1970).
3. M. R. Karim, B. M. A. Rahman, and G. P. Agrawal, "Dispersion Engineered $Ge_{11.5}As_{24}Se_{64.5}$ nanowire for super continuum generation: a parametric study," Opt. Express **22**, 31029–31040 (2014).
4. G. P. Agrawal, *Non-Linear Fiber Optics*, 5th ed. (Academic, 2013).
5. J. M. Dudley and J. R. Taylor, "Ten years of nonlinear optics in photonic crystal fiber," Nat. Photonics **3**, 85–90 (2009).
6. K. M. Hilligsøe, T. V. Andersen, H. N. Paulsen, C. K. Nielsen, K. Mølmer, S. Keiding, R. Kristiansen, K. P. Hansen, and J. J. Larsen, "Supercontinuum generation in photonic crystal fiber with two zero dispersion wavelength," Opt. Express **12**, 1045–1054 (2004).
7. J. Hu, C. R. Menyuk, L. B. Shaw, J. S. Sanghera, and I. D. Aggarwal, "Maximizing bandwidth of supercontinuum generation in As_2Se_3 chalcogenide fibers," Opt. Express **18**, 6722–6739 (2010).
8. I. D. Aggarwal and J. S. Sanghera, "Development and application of chalcogenide glass optic fiber at NRL," J. Optoelectron. Adv. Mater. **4**, 665–678 (2002).
9. B. Dabas and R. K. Sinha, "Design of highly birefringent chalcogenide glass PCF: a simplest design," Opt. Commun. **284**, 1186–1191 (2011).
10. J. M. Dudley, G. Genty, and S. Coen, "Supercontinuum generation in photonic crystal fiber," Rev. Mod. Phys. **78**, 1135–1184 (2006).
11. H. Ademgil and S. Haxha, "Highly nonlinear birefringent photonic crystal fiber," Opt. Commun. **282**, 2831–2835 (2009).
12. S. Haxha and H. Ademgil, "Novel design of photonic crystal fibers with low confinement losses, nearly zero ultra flattened chromatic dispersion, negative chromatic dispersion and improved effective mode area," Opt. Commun. **281**, 278–286 (2008).
13. T. S. Saini, A. Kumar, and R. K. Sinha, "Broadband mid-infrared supercontinuum spectra spanning 2–15 μm using As_2Se_3 chalcogenide glass triangular-core graded-index photonic crystal fiber," J. Lightwave Technol. **33**, 3914–3920 (2015).
14. X. Zhu and N. Peyghambarian, "High power ZBLAN glass fibers: review and prospect," Adv. OptoElectron. **2010**, 1–23 (2010).
15. C. Xia, Z. Xu, M. N. Islam, and F. L. Terry, Jr., M. J. Freeman, A. Zakel, and J. Mauricio, "10.5 W time-averaged power mid-IR supercontinuum generation extending beyond 4 μm with direct pulse pattern modulation," IEEE J. Sel. Top. Quantum Electron. **15**, 422–434 (2009).
16. G. Qin, X. Yan, C. Kito, M. Liao, C. Chaudhari, T. Suzuki, and Y. Ohishi, "Ultrabroadband supercontinuum generation from ultraviolet to 6.28 μm in a fluoride fiber," Appl. Phys. Lett. **95**, 161103 (2009).
17. S. Wang, E. M. Vogel, and E. Snitzer, "Tellurite glass: new candidate for fiber devices," Opt. Mater. **3**, 187–203 (1994).
18. G. Ghosh, "Sellmeier coefficients and chromatic dispersion for some tellurite glasses," J. Am. Ceram. Soc. **78**, 2828–2830 (1995).
19. P. Domachuk, N. A. Wolchover, M. Cronin-Golomb, A. Wang, A. K. George, C. M. B. Cordeiro, J. C. Knight, and F. G. Omenetto, "Over 4000 nm bandwidth of mid-IR supercontinuum generation in sub-centimeter segments of highly nonlinear tellurite PCFs," Opt. Express **16**, 7161–7168 (2008).
20. R. Buczynski, H. T. Bookey, M. Klimczak, D. Pysz, R. Stepien, T. Martynkien, J. E. McCarthy, A. J. Waddie, A. K. Kar, and M. R. Taghizadeh, "Two octaves supercontinuum generation in lead-bismuth glass based photonic crystal fiber," Materials **7**, 4658–4668 (2014).
21. J. Gopinath, H. Shen, H. Sotbayashi, E. Ippen, T. Hasegawa, T. Nagshima, and N. Sugimoto, "Highly nonlinear Bismuth-oxide fiber for smooth supercontinuum generation at 1.5 μm," Opt. Express **12**, 5697–5702 (2004).
22. G. Bramibilla, F. Koizumi, V. Finazzi, and D. J. Richardson, "Supercontinuum generation in tapered bismuth silicate fibres," Electron. Lett. **41**, 795–797 (2005).
23. J. T. Gopinath, H. M. Shen, H. Sotobayashi, E. P. Ippen, T. Hasegawa, T. Naashima, and N. Sugimoto, "Highly nonlinear bismuth-oxide fiber for supercontinuum generation and femtosecond pulse compression," J. Lightwave Technol. **23**, 3591–3596 (2005).
24. J. H. V. Price, T. M. Monro, H. Ebendorff-Heidepriem, F. Poletti, P. Horak, V. Finazzi, J. Y. Y. Leong, P. Petropoulos, J. C. Glanagan,

G. Brambilla, X. Feng, and D. J. Richardson, "Mid-IR supercontinuum generation from nonsilica microstructured optical fibers," IEEE J. Sel. Top. Quantum Electron. **13**, 738–749 (2007).
25. R. Buczynski, H. T. Bookey, D. Pysz, R. Stepien, I. Kujawa, J. E. McCarthy, A. J. Waddie, A. K. Kar, and M. R. Taghizadeh, "Supercontinuum generation up to 2.5 μm in photonic crystal fiber made of lead-bismuth-galate glass," Laser Phys. Lett. **7**, 666–672 (2010).
26. C. Agger, C. Peterson, S. Dupont, H. Steffensen, J. K. Lyngsø, A. L. Thomsen, J. Thogersen, S. R. Keiding, and O. Bang, "Supercontinuum generation in ZBLAN fibers—detailed comparison between measurement and simulation," J. Opt. Soc. Am. B **29**, 635–645 (2012).
27. C. Wei, X. Zhu, R. A. Norwood, F. Song, and N. Peyghambarian, "Numerical investigation on high power mid-infrared supercontinuum fiber lasers pumped at 3 μm," Opt. Express **21**, 29488–29504 (2013).
28. X. Feng, J. Shi, M. Segura, N. M. White, P. Kannan, X. Zhang, and W. H. Loh, "Towards water-free tellurite glass fiber for 2–5 μm non-linear applications," Fibers **1**, 70–81 (2013).
29. M. F. S. Ferreira, *Nonlinear Effects in Optical Fibers* (Wiley, 2011).
30. X. Gai, T. H. A. Prasad, S. Madden, D.-Y. Choi, R. Wang, D. Bullas, and B. L. Davies, "Progress in optical waveguides fabricated from chalcogenide glasses," Opt. Express **18**, 26635–26646 (2010).
31. N. Granzow, S. P. Stark, M. A. Schmidt, A. S. Tverjanovich, L. Wondraczek, and P. St. J. Russell, "Supercontinuum generation in chalcogenide silica step-index fibers," Opt. Express **19**, 21003–21010 (2011).
32. X. Gai, D. Choi, S. Madden, Z. Yang, R. Wang, and B. Luther-Davies, "Supercontinuum generation in the mid-infrared from a dispersion engineered As_2S_3 glass rib waveguide," Opt. Lett. **37**, 3870–3872 (2012).
33. Y. Yu, X. Gai, T. Wang, P. Ma, R. Wang, Z. Yang, D. Choi, S. Madden, and B. Luther-Davies, "Mid-infrared supercontinuum generation in chalcogenides," Opt. Mater. Express **3**, 1075–1086 (2013).
34. Y. Yu, B. Zhang, X. Gai, P. Ma, D. Choi, Z. Yang, R. Wang, S. Debbarma, S. J. Madden, and B. Luther-Davies, "A broadband, quasi-continuous, mid-infrared supercontinuum generated in a chalcogenide glass waveguide," Laser Photon. Rev. **8**, 792–798 (2014).
35. H. Liang, P. Krogen, R. Grynko, O. Novak, C. L. Chang, G. J. Stein, D. Weerawarne, B. Shim, F. X. Kärtner, and K. H. Hong, "Three-octave-spanning supercontinuum generation and sub-two-cycle self-compression of mid-infrared filaments in dielectrics," Opt. Lett. **40**, 1069–1072 (2015).
36. A. B. Salem, R. Cherif, and M. Zghal, "Tapered As_2S_3 chalcogenide photonic crystal fiber for broadband mid-infrared supercontinuum generation," in *Frontiers in Optics 2011/Laser Science XXVII*, OSA Technical Digest (Optical Society of America, 2011), paper FMG6.
37. I. Kubat, C. R. Petersen, U. V. Moller, A. Seddon, T. Benson, L. Brilland, D. Mechin, P. M. Moselund, and O. Bang, "Thulium pumped mid-infrared 0.9–9 μm supercontinuum generation in concatenated fluoride and chalcogenide glass fibers," Opt. Express **22**, 3959–3967 (2014).
38. D. D. Hudson, M. Baudisch, D. Werdehausen, B. J. Eggleton, and J. Biegert, "1.9 octave supercontinuum generation in a As_2S_3 step-index fiber driven by mid-IR OPCPA," Opt. Lett. **39**, 5752–5755 (2014).
39. C. R. Petersen, U. Moller, I. Kubat, B. Zhou, S. Dupont, J. Ramsay, T. Benson, S. Sujecki, M. Abdel-Moneim, Z. Tang, D. Furniss, A. Seddon, and O. Bang, "Mid-infrared supercontinuum covering the 1.4–13.3 μm molecular fingerprint region using ultra-high NA chalcogenide step-index fiber," Nat. Photonics **8**, 830–834 (2014).
40. U. Moller, Y. Yu, I. Kubat, C. R. Petersen, X. Gai, L. Brilland, D. Mechin, C. Caillaud, J. Troles, B. Luther-Davies, and O. Bang, "Multi-milliwatt mid-infrared supercontinuum generation in a suspended core chalcogenide fiber," Opt. Express **23**, 3282–3291 (2015).
41. Y. Yu, X. Gai, C. Zhai, S. Qi, W. Guo, Z. Yang, R. Wang, D. Choi, S. Madden, and B. Luther-Davies, "1.8–10 μm mid-infrared supercontinuum generation in a step-index chalcogenide fiber using low peak pump power," Opt. Lett. **40**, 1081–1084 (2015).
42. M. R. Karim, B. M. Rahman, Y. O. Azabi, A. Agrawal, and G. P. Agrawal, "Ultrabroadband mid-infrared supercontinuum generation through dispersion engineered chalcogenide microstructured fibers," J. Opt. Soc. Am. B **32**, 2343–2351 (2015).
43. J. M. Senior, *Optical Fiber Communication, Principles and Practice*, 3rd ed. (Pearson Education, 2010).
44. M. R. Karim, B. M. A. Rahaman, and G. P. Agrawal, "Mid-infrared supercontinuum generation using dispersion engineered $Ge_{11.5}As_{24}Se_{64.5}$ chalcogenide channel waveguide," Opt. Express **23**, 6903–6914 (2015).

14.139.251.107 {ts '2016-12-13 23:38:57'}

Journal of Fundamentals of Renewable Energy and Applications

Singh et al., J Fundam Renewable Energy Appl 2016, 6:6
DOI: 10.4172/2090-4541.1000218

Research Article Open Access

Understanding Various Technologies with Perspective of Energy and Environmental Audit: Review

Harwinder Singh[1], Aftab Anjum[2*], Mohit Gupta[3], Aadish Jain[4] and Amrik Singh[5]

Department of Mechanical Engineering, Delhi Technological University, India

Abstract

The present paper is based on understanding the energy audit in a holistic approach. India is a great developing country, economy and energy plays a vital role as fuel for development. As the demand is increasing rapidly, production of energy on the same slope is somewhat difficult. With exponential rise in demands, energy deficit is also rising with each passing day. Hence, judicial use of energy and energy audit becomes an important. The energy audit helps in improving the overall efficiency of the system thereby lowering down energy consumption and the costs in terms of economics. It also helps us determining the energy inflows, outflows and inefficient components. The work has been emphasized on environmental audit along with its importance on protecting the environment. This paper explains various technological aspects, needs and positives related to energy and environmental audit thereby giving an overview of it.

Keywords: Energy audit; Environmental audit; Water conservation; Electrical devices; Mechanical equipment

Introduction

The cost of the energy is going up with the depletion in the current energy resources. The industrial sector is a major contributor towards this trend. So, an overall need arises to reduce down the energy costs which can be considerably achieved by enhancing the working efficiency of the various processes, equipment and operations involved in the industry. The energy efficiency can be further improved by switching over to the renewable sources of energy, creating awareness and a dedicated monitoring of the systems. The Government of India has passed various legislations and amendments to shift the focus towards energy efficiency. Bureau of Energy Efficiency (BEE) was made for defining certain energy standards, providing guidelines, accrediting various organizations for energy audits, carrying out the projects related to energy efficiency and carrying out the research activities related to the energy efficiency equipment [1].

Energy and Environmental Audit

Energy audit

Energy audit enables us to work upon the various inefficiencies in the existing system and analyzing the components thereby ensuring the energy conservation. It tells about the utilization of energy in a given system.

Environmental audit

Environmental audit surge in pollution levels in our country India has ensued in higher environmental risks. Hence the need for sustainable development is emphasized in every quarter be it policy formations, project clearances, future planning or management of already existing infrastructure and industry. While energy audit of a setups concentrates mainly on the energy efficiency of the system. Environmental audit will take care of preserving environment, natural resources such as water, air, land etc. Environmental audit cater to the issues such as Material balance, non-hazardous waste generation and disposal, hazardous waste generation and disposal, characteristics of waste for recycle or reuse along with short term and long term impact on local environmental conditions including air and water quality [1].

Main aim

Main aim of energy and environmental audit is to minimize the energy requirement and waste production with least environmental effect and without affecting the output during any process like residential, industrial, governmental and commercial or any other process.

Positives and need for energy and environmental audit are:

- Energy cost reduction
- Preventive maintenance and
- Quality control programs
- Waste prevention and reduction
- Compliance with regulatory requirements
- Option for adoption energy conservation technologies
- Profit maximization
- Optimization of available resources

Energy and environmental audit can be classified into the following two types

- Preliminary audit
- Detailed audit

Preliminary audit: Preliminary audit is a relatively simple exercise:

- Make energy consumption chart for every process in the organization
- Identify the scope for improvement in effectiveness (and the easiest areas for attention)

***Corresponding author:** Aftab Anjum, Department of Mechanical Engineering, Delhi Technological University, Bawana Road, Delhi-110042, India, Tel: 91-9971193915; E-mail: aftabanjum915@gmail.com

Received August 26, 2016; **Accepted** October 18, 2016; **Published** October 20, 2016

Citation: Singh H, Anjum A, Gupta M, Jain A, Singh A (2016) Understanding Various Technologies with Perspective of Energy and Environmental Audit: Review. J Fundam Renewable Energy Appl 6: 218. doi:10.4172/20904541.1000218

Copyright: © 2016 Singh H, et al. This is an open-access article distributed under the terms of the Creative Commons Attribution License, which permits unrestricted use, distribution, and reproduction in any medium, provided the original author and source are credited.

- Look out for immediate (low cost) improvements
- Spot areas for more detailed and process specific study

Detailed audit: Detailed energy auditing is carried out in three phases: Phase I, II and III.

- **Phase I - pre audit phase:** Establishment is identified for audit. Basic information is collected regarding location, surrounding, climatic conditions, inputs of establishment in form of energy and raw materials, outputs, waste generation, management and disposal.
- **Phase II - audit phase:** Identification type of energy consumed in various departments include major processes, preparation of material balance sheets (includes raw materials, products, by products etc.), data regarding energy cost and tariff and latest regional energy policy. Process and material flow charts include sources of energy supply (e.g. electricity from the grid or self-generation). Potential for alternative energy sources such as solar energy, geothermal etc., process improvements and modifications and the induction of co-generation systems (combined heat and power generation).
- **Phase III - post audit phase:** After conducting audit energy manager/energy auditor should report and file observations to the top management about findings and possible recommendations if any, for effective communication and implementation.

The methods like present value criterion, average rate of return criterion and payback period criterion etc. are used for the economic analysis of the investments.

Electrical Energy Devices

Electrical energy devices collectively consume large amount of electrical power and also incurring large amount of distributed losses. In the current scenario when the energy deficit is large energy efficiency and audit are the need of the hour to plug these distributed losses one by one. Energy audit of these systems becomes essential so as to identify the inefficiencies in the system and can help in reducing this energy deficit.

Motors

An electric motor converts electrical energy into mechanical energy. They are classified as DC (Direct Current) motors and AC (Alternating Current) motors. Further AC motors are classified as AC induction and AC synchronous motors. They are mainly used to provide power to the various equipment. While selecting an electric motor for a process, aspects like reliability, inventory, availability, breakdown torque and operating conditions should be considered.

The efficiency of an electric motor can be written mathematically as:

$$Efficiency(\%) = \frac{Watts(input) - Watts(output)}{Watts(input)}$$

Losses: Losses can be described as the energy fees charged by the motor in order to convert electrical energy into the mechanical energy. They can be further classified into four categories

- Power Losses includes stator and rotor losses which can account for even more than half of the total losses occurring in the motor.
- Friction losses
- Magnetic core losses
- Stray load losses

Conductivity of the material, operating conditions, overall weight of the machine and lubrication are the major factors influencing the efficiency of motors. By giving considerable attention to above losses can be minimized.

Conservation of energy: The amount of energy consumed can be saved by operational improvements which include - balanced supply, improved controls, maintenance and retrofit improvements which look for the replacement of old, oversized and inefficient motors with the new and efficient ones.

Induction motors operate at lagging power factor because of the magnetizing current that is drawn by the motor, the incorporation of capacitors helps in enhancing the power factor thereby reducing energy charges, kVA demand and voltage drop and increased overall efficiency. Use of flat belt drives, variable speed drives and energy-saving controllers also contributes towards the saving of energy.

Illumination

A lumen can be defined as a measurement of light output from a tube or a bulb whereas illumination is the distribution of light on a horizontal surface which is measured in lux or foot-candles. Efficacy can be defined as the ratio of the light output to the electric power the lamp consumes. Efficacy is measured in Lumens per watt (LPW). It should be noted that efficacy should not be confused with the term efficiency which is unit-less quantity.

Quality of illumination: Quality is basically the visibility factor during work conditions and denotes how much people feel visually comfortable. Glare, which is the extra brightness from a direct light source, should be removed for having good quality lighting. The ability of the light source to render the same colors as sunlight does is termed as CRI (Color rendering index).

Types of illumination source: The four basic types of lighting lamps are as follows

- **Incandescent:** Most common types of incandescent lights are tungsten halogen, reflector lamps and standard incandescent.
- Fluorescent
- Compact Fluorescent
- **High intensity discharge:** Common types are mercury vapour, high pressure sodium and metal halide.

Increasing efficiency: Energy efficiency can be improved by replacing the lamps or entire fixtures thereby lowering the wattage, using day lighting, improving light controls, preserving illumination and ensuring simple maintenance. The devices used for regulating the lights are called lighting control like snap switches, timers, photocells, occupancy sensors and dimmers etc.

Transformer

Transformers are used to step up or step down the AC (Alternating Current) voltage. Transformers operate on the Faraday's law of induction. Operating losses in the transformers are namely no-load loss and load loss. No-load losses can be further categorized as eddy current losses, hysteresis losses, I^2R losses and di-electric losses whereas load losses are basically the coil losses.

The net losses for a transformer can be described mathematically as:

$L_p = L_N + (P/P_R)^2 \times L$

Where,

$L_{p=}$ Total power loss in kW

L_N = No-load loss in kW

L = Load loss in kW

P = Actual load on transformer in kVA

P_R = Rated power of transformer in kVA

Identifying the load is an important factor in determining system load curve which will also provide us with the information of peak loads and base load periods. Proper monitoring of the load curves can help to manage the peak loads.

The demands can be controlled in a centralized manner, in a timed bound manner and can also be controlled manually. The prime objective of the transformer audit is to ensure that quality of power to different load centers is high and overall efficiency is better.

Power quality

Power quality is the severity of variations in the power supplied to the customers and deviations from the standard frequency of 50 Hz. If the power received has a pure sinusoidal waveform, it is considered as the clean power. Nowadays a term 'dirty power' is used to describe the contaminations in the clean power.

A harmonic is basically a part of the waveform having a frequency which is an integral multiple of fundamental power line frequency. Harmonic problems should be corrected or prevented from an industrial facility.

Harmonics can be reduced by the following methods:

- Power system design
- Isolation transformer
- Line reactors
- Harmonic trap filters
- K-factor transformers
- Applying tuned filters

Energy Management

Energy Management is the program aimed at reducing the organization's electricity bills and negative environmental impacts. The important hardware components of any energy management information system are:

- Field Transducers
- Power monitor modules
- Programmable logic controllers
- Communications network
- Centralized personal computer

Mechanical Energy Devices

Boilers

Boilers are employed in the industries to act as a heat source for various process applications. Boilers are basically classified as fire tube and water-tube boilers.

Evaluation of boiler efficiency: Efficiency of the boilers can be evaluated by either the direct methods or the indirect methods.

The formula used for the direct method is

Boiler Efficiency = (Heat output/ Heat input) × 100 = (Steam flow rate × (Steam enthalpy- feed water enthalpy) × 100)/ (Fuel firing rate × Gross calorific value).

Indirect methods aims at calculating the various heat losses, namely dry flue gas loss (L_{fg}), heat loss due to the moisture in the fuel (L_{mf}), heat loss due to moisture from burning hydrogen in the fuel (L_{hf}), heat loss due to the moisture in air (L_{ma}), heat loss due to Carbon monoxide (CO) in flue gas (L_{co}), heat loss due to un-burnt carbon in bottom ash (L_{ubb}), heat loss due to un-burnt carbon in fly ash (L_{ubf}), heat loss due to sensible heat in fly ash (L_{sf}) and loss due to surface radiation and convection (L_{rc}). All these losses are calculated in terms of percentage, added and then subtracted from 100 to obtain the thermal efficiency of the boiler.

Thermal efficiency of boiler (%) = 100-(Total losses in %)

Energy conservation measures for a boiler:

- **Excess air flow rate:** Stoichiometric flow rates are possible only for theory calculations and certain amount of excess air flow rates are required for the complete combustion of fuel. This additional amount of air is known as excess air flow which is also to be controlled as large amount of excess air can negatively impact the working of boiler by reducing the average temperature of the fire ball, reduces radiative heat transfer, increased stack losses by reducing the flue gas temperature and increase in the flue gas flow rate will also contribute to losses.
- **Burner and nozzle size:** The size of burner and nozzle must be adequately designed for optimal performance and cost effective maintenance. We should replace the nozzles with the better designed advanced burners where ever possible for advantage.
- **Control of temperatures of working fluid as well mass flow rate of heat carrier:** There are circumstances when a single source of heat is used for different process and there temperature may be different. Hence its adequate design may maximize efficiency of the system.
- **Proper insulation:** This is the first and easiest way to minimize losses. Where ever required proper insulation must be given to minimize heat loss to the environment as heat losses mainly occur at higher temperatures and this result in direct loss in availability of the system.

Waste heat recovery: Waste heat recovery from the flue gases can be done by:

- **Feed water preheating using economizer**: The water entering the boiler is pre-heated using the thermal energy of the flue gases in the equipment known as economizer before the flue gases are exhausted.
- **Combustion air-preheat:** The combustion chamber is provided with the air which is pre-heated in the air preheater utilizing the waste heat from the flue gases.

- **Improvement of condensate recovery:** Feeding the boiler with the steam condensate will also reduce the load of sensible heating for boiler.
- **Optimization of blow-down:** Though blow- down is necessary for the efficient working of boiler but frequency of blow-down is also an important factor.

Compressed air network

Compressed air is used in almost all types of industrial applications and accounts for a major share of electricity used in some of plants. Compressors are mainly classified into dynamic or centrifugal compressors and positive displacement types which are further divided into categories on the basis of principle of functioning. The distribution of compressed air is equally important as its generation. Normally the compressors are located at a central place in the plant and the compressed air travels a long distance through pipes to the point of usage. This results in large pressure drops due to long pipe lines and large number of pipe fittings. An efficient compressed air distribution system must include the proper pipe sizing, surface finish of the duct, minimum number of sudden bends and fittings for minimum pressure drops and leakages [2].

Compressor selection: Selection of compressor must be done considering the main factors [1] such as number of units required, cost of operation, installation cost and quality of air to be delivered by the compressor.

Monitoring performance and testing: Monitoring performance and testing of the working of compressor must be done on the factors stated [1]:

- Pump-up or capacity test
- Specific power consumption
- Compressor efficiency or isentropic efficiency
- Quality of air intake
- Compressor cooling
- Compressor operating pressure
- Capacity control and power consumption

Steam distribution systems

Steam has always been the most preferred working fluid for numerous plants for heating and drives, but the ever rising cost of fossil based fuels has made it necessary to adopt measures to reduce energy losses in steam distribution network. Some of the major considerations for designing a steam distribution network are named below [3,4]:

- **Pipe layout in plant:** Layout network must be so designed to minimize the steam travel from point of steam generation to utilization. Generally underground piping is not preferred.
- Pipe sizing
- Steam quality
- Moisture separation
- Insulation

All sections of hot pipes, valve bodies, unions, flanges and mechanical traps, such as floats, buckets and bodies of disc traps should be insulated.

Refrigeration and air-conditioning

The process of taking heat from a source of lower temperature and delivering it at a relatively high temperature level with the help of an external agent is known as Air conditioning and same concept can be used to either keep the desired space at a temperature lower or higher than surroundings depending on the requirement.

Main mechanisms: Mainly two mechanisms namely vapour compression system and vapour absorption system are employed for the job.

Vapour compression system: The heat absorbed by the evaporation of a liquid refrigerant in the evaporator at a controlled lower pressure after that increase the pressure of low-pressure vapour coming from the evaporator, with the use of compressor, heat removed from the high-pressure vapour in the condenser so that vapour can liquefy or condenses after this reduces the pressure of the high-pressure liquid to a level needed in the evaporator by using the throttling device [5].

Vapour absorption system: This refrigeration system is a heat-operated system. In this system two pressure levels like evaporating and condensing pressure levels are to be created. Compressor in this system is replaced by absorber and generator. A solution is known as absorbent is circulated between the absorber and generator with the help of a solution pump. The absorbent in the absorber draws the refrigerant vapour formed in the evaporator, thus maintaining a low pressure in the evaporator. In generator, the absorbent is heated, therefore releasing the refrigerant vapour at a high pressure and to be condensed in condenser. Thus the suction function of the compressor is performed by the absorbent in the absorber and the generator performs the function of compression and discharge [6].

An air-conditioning and refrigeration plant is efficient when all the system components like compressor and the condenser, the evaporator and the condenser cooling are working in matched conditions. This means that under peak operating conditions they must perform to their optimum output.

Energy conservation opportunities [1]:

Changes on system operating parameters:

- Increasing the chilled water temperature set point
- Installation of variable speed drives
- At air-handling units in fan motors
- At cooling tower fan motors

Changes on system operation:

- Enthalpy control/dry bulb economizer
- Dry bulb economizer
- Enthalpy control
- Reduced minimum outdoor air
- Exhaust air control

Changes on system design:

- Retrofit of central fans for variable air volume usage
- Forward-curved fan systems

- Fans with vortex vanes
- Conversion of dual-duct constant volume to variable air volume
- Heat recovery system
- Use evaporative cooling for comfort cooling in dry areas

Fans and blowers

Fans and blowers are widely used in industrial and commercial applications for ventilation and industrial process requirements. These are categorized into two different types based on the path of the airflow (centrifugal and axial) and blade shape (centrifugal and axial fan). Blowers are also classified into centrifugal and positive displacement type.

Performance: Performance is typically defined by plot of developed pressure and power required over a range of fan generated airflow. Performance of fan is also strictly depends upon the fan enclosure and duct design

Fan efficiency: Fan efficiency is the ratio of power imparted to the air streams to the power delivered by the motor.

In any fan system, the resistance to airflow (pressure) increases when the flow of air is increased. Bends and elbows in the inlet or outlet ducting can change the velocity of air, thereby changing the fan characteristics. Fans often serve a wide range of operating conditions. To accommodate demand changes, flow is controlled by four principle methods: vanes, pitch, outlet dampers and fan speed control [1].

Cooling tower

Cooling tower is a waste heat rejection device which is employed to reject the heat into the atmosphere. It basically removes the heat with the help of cooling water. Hence the performance of the tower is directly related to the temperature of the cooling water.

Categories: Cooling towers can be further categorized according to the way in which air is fed to the tower as 'natural draft' and 'mechanical draft'.

Mechanical draft:

- **Forced draft:** In this type of tower the fan is placed at the bottom from which air is forced into the tower. It is well suited for indoor applications.
- **Induced draft:** The movement of air in this arrangement is either counter flow or crossed flow.
- **Wet dry tower:** It employs an air-cooled heat exchanger, suited for high temperature applications.

Natural draft:

- **Atmospheric tower:** The movement of air in this type of tower is in horizontal fashion.
- **Spray pond:** Two arrangements with fan which involves spraying of the warm water for evaporation and without fan which works on the ejector principle.

Range, approach, cooling tower effectiveness and Performance of the cooling tower: Range of a cooling tower can be mathematically expressed as,

Range (°C) = Temperature of the water out from the cooling tower - Temperature of the inlet water

Whereas approach is,

Approach (°C) = Temperature of the water out from the cooling tower- Design wet bulb temperature

Cooling tower effectiveness (%) = Range/ (Range + Approach)

Performance of the cooling tower depends upon the heat dissipation(Kcal/h), heat load, approach, wet bulb temperature, size of the tower and fill media (film fill, low-clog film fill and splash fill).

There are various instruments which are used during the energy audit of cooling towers.

- **Anemometer:** Used to measure the flow rate of air.
- **Power analyser:** It analyses the electrical parameters of the pump and fan.
- **Sling hygrometer:** Measures dry bulb and wet bulb temperatures of air.
- **Flow meter:** Measures water flow-rate.
- **Temperature indicator:** It uses a thermocouple and measures the water temperature.

Alternate working fluids

Water and steam are the most common heat carriers. However there are problems such as high operating pressures along with leakage losses etc. associated with such systems.

Alternative fluids such as mineral oil, synthetic oil and various other nanofluids are also being used and systems are proved to be much more efficient in its functioning. Some of the advantages of such a system are:

- High operating Temperatures such as 300°C at atmospheric pressure
- Wide range of temperature for stable working
- No need for feed water treatment
- No heat loss related to condensation or Flash steam
- No risk of corrosion
- No need for anti-freeze agents
- Lower maintenance cost
- Quite in operations
- Easy to operate
- Uniform pressures for complete cycle

Internal combustion engines

These engines although deliver High quality of power, but are relatively less efficient. Studies have shown that out of total energy supplied to the engine only 26-28% is available. Nearly 34% of energy is lost to exhaust, 30% in engine cooling and around 10% is dissipated to overcome frictional losses. There are several ways suggested to improve its efficiency by Fuel conservation by operating on design points, proper engine loading, proper lubrication which could reduce frictional losses. Waste heat recovery mechanisms such as turbo charger, hot water generation, vapour absorption refrigeration system are also advised for specific systems to maximize the efficiency of engine where ever possible. Further I.C. engines require regular servicing and timely renewal of lubricants and oil well for proper functioning.

Water Audit and Conservation

Water audit and conservation with the exponential urban and

industrial development along with population, the available quantity of water and its quality has reduced drastically as compared to past decades. In a report by IWRS 2004 it was reported that there was demand of 22 bcm (billion cubic meters) of water in 1995-97 and according to National commission the estimated demand of water stand at 70 bcm by 2025 and 103 bcm by 2050. This data shows the urgency with which the issue of water conservation has to be dealt with:

Classification

The water conservation measures can be broadly classified into technological advancements and habitual practices. The former is used in industrial and commercial users where new installations in water management can significantly affect the setup profitability in future.

Technological advancements: Technological advancements majorly include water recirculation, reuse and recycle. There are few applications such as low flow fixtures, water less urinals, planned landscape irrigation, etc. are used in many commercial projects.

Habitual practices: Changes in behavior of individuals and society as a whole can contribute to great amount of water conservation.

The measures for water conservation may also depend upon the factor of usage of the conservation system by social or industrial/commercial establishment. As a social establishment may use this as a policy towards environment and responsibility towards nature and future generations but industrial establishments may also have ulterior motives of profit maximization of reduction in input cost etc. [7,8].

Conservation

There are several ways suggested for water conservations:

- Rain water harvesting
- Recycle, recirculate, reuse
- Low flow fixtures
- Planned landscape irrigation
- Alternative technologies

Solar Energy

Many reviews have been conducted by engineers and researchers are very important and informative to understand solar technologies [9]. As India is energy deficient country and the demand of energy is enormous and the deficit is also very large. This energy deficit can't be fulfilled by any single energy source but to a great extent can be controlled with the help of solar energy technologies applied to various uses such as power generation [10] or energy source for various industrial applications. There is huge potential for solar thermal and solar photovoltaic (PV) technologies to be applied in the industries which can reduce the demand of energy on the grid.

Some solar thermal technologies are:

- Flat plate collector
- Evacuated tube collector
- Parabolic trough concentrator
- Parabolic dish concentrator
- Compound parabolic concentrator

Solar thermal and PV technologies can be used for power generation, air-conditioning, water heating or process heating, waste heat recovery and many other methods [11] as discussed by S. Mekhilef and R. Saidur, which directly or indirectly utilize solar heat as energy source and reduce the energy budget for the setup.

Conclusion

Energy generation is a complicated issue than its expenditure and therefore it becomes very important to follow the judicious use of the available energy. Energy and environment conservation is not the responsibility of a single person or a group of persons. The society as a whole has to become aware and act aptly for sustainable development. Many government agencies are also working to spread awareness by means of advertisement campaigns such as Petroleum Conservation Research Association (PCRA), BEE and Green Energy Rating Agencies such as GRIHA etc. It has also been observed that with minor changes in Habitual practices by society major amount of energy waste can be plugged, this will also result in lower Energy bills for households as well as commercial establishments. Many electrical devices such as Motor, Transformer, illumination devices along with power quality issues have also been discussed.

References

1. Abbi YP, Jain S (2006) Hand Book on Energy Audit and Environment Management. The Energy and Resources Institute (TERI) pp: 1-302.
2. Efficient Utilization of Steam - Energy Efficiency Office, U.K.
3. Bureau of Energy Efficiency.
4. Prakash A (2013) Improving the Performance of Vapour Compression Refrigeration System by using Sub- Cooling and Diffuser. IJEBEA 1: 88-90.
5. Kaushik S, Singh S (2014) Thermodynamic Analysis of Vapor Absorption Refrigeration System and Calculation of COP. IJRASET 2: 73-80.
6. Abbi YP, Jain S (2006) Hand Book on Energy Audit and Environment Management. The Energy and Resources Institute (TERI) pp: 1-302.
7. Feldbeuer SL (2005) Furnace Optimization; Meeting the Need to Reducing Cost. Abbott Furnace.
8. Indian Water Resources Society (2004) Efficiency of water resources.
9. Kesari JP, Gupta M, Jain A, Ojha AK (2015) Review of the Concentrated Solar Thermal Technologies: Challenges and Opportunities in India. IJRSI 2: 105-111.
10. Singh H, Singh P (2014) A Review About Solar Thermal Power Technology And Its Use In India.
11. Mekhilef S, Saidur R, Safari A (2011) A Review On Solar Energy Use In Industries. Renewable and Sustainable Energy Reviews.

Citation: Abdallah SB, Frikha N, Gabsi S (2016) Numerical Investigations of Coupling a Vacuum Membrane Desalination System with a Salt Gradient Solar Pond. J Fundam Renewable Energy Appl 6: 218. doi:10.4172/20904541.1000218